Occurrence of Parasitic and Bacterial Pathogen in Ornamental and Wild Populations of Siamese Fighting Fish (*Betta splendens*) in a Region of Thailand
Piyapan Manklinniam et.al.

Siamese fighting fish

(*Betta splendens*)
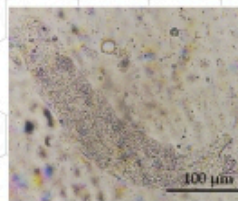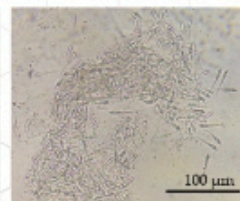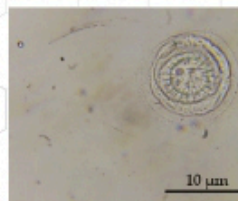
Wild Siamese fighting fish

Granulomas infection in ornamental Siamese fighting fish

Dark brown capsules observed in tissue samples infected with Mycobacterium

LC853090.1 *Aeromonas veronii* WWKMITL-02 - This study
KF661548.1 *Aeromonas veronii* B7
HM358836.1 *Aeromonas sobria* NQ090701
MN894075.1 *Aeromonas hydrophila* RTFL 243
X74674.1 *Aeromonas caviae* ATCC 15468T
MH619508.1 *Escherichia coli* IADCAMB11
KT982478.1 *Vibrio vulnificus* MCCB 371
MG438529.1 *Mycobacteroides chelonae* BN 1983
AB291543.1 *Mycobacterium marinum* NJB0419
LC853089.1 *Mycobacterium marinum* WWKMITL-03 - This study
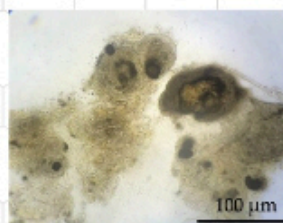NR113366.1 *Mycobacterium marinum* ATCC 927
LC556329.1 *Halobacterium salinarum* NBRC 14715

ASEAN Journal of Scientific and Technological Reports (AJSTR)

List of Contents

List of Contents

Utilisation of Reclaimed Asphalt Pavement for Improving Substandard Subbase

Trongrit Lickachai[1], and Panu Promputthangkoon[2*]

[1] Pangnga Rural Road Office, Department of Rural Roads, Thailand

[2] Faculty of Engineering, Rajamangala University of Technology Srivijaya, 90000, Thailand

[*] Correspondence: panupptk@gmail.com

Abstract: This research attempted to improve substandard subbase by mixing it with reclaimed asphalt pavement. Three substandard soils, namely Soils A, B, C, and RAP, were collected from Phangnga, Southern Thailand. Each soil was mixed with the RAP having the soil to RAP by-weight ratios of 100:0, 90:10, 80:20, 70:30, 60:40, and 50:50. A whole RAP, namely sample D, was also studied, resulting in a total of 19 soil-RAP mixtures. Several testing techniques were carried out to obtain the best mixture for being employed as a subbase. Besides basic properties, the compaction test was conducted to obtain optimum water content. Consequently, such water was employed to prepare samples for the CBR test. Considering overall compaction behaviour, it was found that the maximum dry density gradually increases with the increase of RAP content from 0% up to 30%. After that, it decreased steadily with further increases in RAP from 40% to 50%. Strikingly, all soils had the maximum dry densities when mixed with 30% RAP. As such, the CBR results unsurprisingly showed the same trend, i.e., the maximum values occurred when the mixtures contained 30% RAP. The CBR values for the samples A70R30, B70R30, and C70R30 were 11.0%, 15.9%, and 25.1%, respectively. This indicates that only soil C mixed with 30% RAP qualifies for subbase. These results suggest that 30% of RAP is the most appropriate portion to be mixed with substandard subbase soil to achieve a qualified subbase.

Keywords: Reclaimed asphalt pavement; Substandard subbase; Road construction

1. Introduction

According to the Department of Highways, Thailand, a total of 80,694.355km of roads, including 6,279.653km of concrete pavement, 74,375.009km of asphaltic concrete pavement, and 39.693km of compacted soil pavement, were supervised by the Department of Highways [1]. Additionally, 49,653.785km of minor roads were administered by the Department of Rural Roads, Thailand, the majority of which–46,236.177km–are asphaltic concrete pavement [2]. Considering these numbers, it is evident that most road networks in Thailand are asphaltic concrete pavement. Note that the fact also applies to other countries. Because Thailand is located in a tropical climate, asphaltic pavement is more prone to deterioration than other countries located in mild climate areas. Furthermore, overloaded trucks are normal in the country, exponentially increasing the degree of road damage. As a result, the asphaltic concrete pavement in Thailand requires either repair or even replacement more often than it should be. Consequently, when peeled, an enormous quantity of such deteriorated pavement needs to be

managed somewhat. From this information, there is no doubt that the same problem of managing waste worldwide is vital. Nowadays, the term RAP has been used for either reclaimed asphalt pavement or recycled asphalt pavement material. The RAP, as shown in Fig. 1, is asphaltic concrete retrieved from deteriorated pavement utilising ripping, cold milling, or hot milling, depending on the availability of machines. Then, it is crushed to be smaller in order to obtain the required sizes concerning intended usage.

Authorities, organizations, and research institutes have long been inspecting a solution for using RAP; otherwise, a huge area is essential for storing this waste. Considering its composition, recycling it back as asphaltic pavement seems quite sensible. It should be noted that the RAP may be employed in the forms of hot recycled asphalt (HRA) or cold recycled asphalt (CRA). Advantages and disadvantages for both HRA and CRA can be found in Saeed et al. [4]; Wang et al. [5]; Arámbula-Mercado et al. [6]; Mollenhauer et al. [7]; Taherkhani et al. [8]; Chegenizadeh et al. [9]; DOH [10].

Figure 1. Example of reclaimed asphalt pavement [3]

Table 1. Typical properties of RAP [11]

No.	Parameter	Value	Unit
1	Density	1900 - 2250	kg/m³
2	Moisture content	Max. 3 - 5	%
3	Asphalt content	5-6	%
4	Asphalt penetration at 25 degrees Celsius	10 – 80	Penetration unit
5	Compacted density	1500 - 1980	kg/m³

Generally, asphaltic concrete is constructed by binding mineral aggregates together using bitumen. Note that the bitumen is interchangeably called asphalt. When the RAP is employed, the compositions include bitumen, coarse aggregate, and RAP. In other words, some aggregate is reduced to some degree by introducing the RAP, resulting in lower construction costs. Bearing in mind that typical properties of RAP slightly vary due to the origin of its compositions. However, one can find the typical properties of RAP reported by Kumar et al. [11], as shown in Table 1.

The HRA has been the most popular for pavement recycling, especially when mixing the RAP with conventional asphalt. For such cases, the RAP acts as a conventional aggregate but has properties quite different from those of common aggregates; the bitumen acts as a binder. It is no surprise if one would think that, in terms of load-bearing capacity, the conventional asphaltic concrete pavement is better than that of pavements built by employing the RAP. However, Mittal et al. [12] showed that adding RAP improves the performance of bituminous mixes. Furthermore, based on laboratory tests by Mittal et al. [12], employing 20% of RAP improved the properties. It should be noted that their findings were based on laboratory work, one must consider actual field conditions as well as machine and construction techniques to be utilised. In addition, Saberi and Mohamed [13] showed that soil mixed with 20% RAP could be employed as road shoulder material. Hasan et al. [14] also found that RAP-soils mixtures have a better resilient modulus of subgrade, thereby increasing the resistance to applied confining pressure. To stabilise a soil that has some plasticity,

ASEAN J. Sci. Tech. Report. **2025**, *28*(3), e257089.

3 of 11

adding a small amount of cement when mixed with RAP was recommended by Edeh et al. [15]. They showed that adding some cement could also reduce the RAP portion in a mixture to obtain the best results.

Khosla et al. [16], investigated the optimum asphalt binder contents (OAC) to be mixed with RAP. According to their study, the RAP was first blended with virgin aggregates to have desired gradations, and the RAP varied between 8% and 45%. It was found that the optimum asphalt content ranged from 5.4% to 6.0%. These findings suggested that the first step in employing RAP as the asphaltic pavement is to obtain an appropriate mixture between the RAP and virgin aggregate. Then, the OAC is obtained by varying its contents to achieve an optimum mix.

Ariffin [3] stated that roadways' performance when employing RAP degrades with time because the pavement is constructed from recycled, hardened asphalt pavement. Therefore, ongoing research is considering using bio-based rejuvenators because they have tiny molecules that can fill the void. As such, the overall performance is improved somewhat. Ariffin investigated the addition of rubber seed oil (RSO) as a rejuvenator for RAP. The RAP had an asphalt content of 4.04%. The sample was prepared in the Marshall compactor mould of 100mm diameter. It had an RAP of 1000g, and the RSO and water content were 3.25% and 3-5%, respectively. The bitumen required for laboratory tests, including bulk unit weight, air voids, Marshall stability, and Marshall flow, was 40.4g, corresponding to 4.04%. The mix design employed the two temperature levels of 0°C and 45°C; the results are shown in Table 2.

Table 2. Result for Mashall mix design for 0°C and 45°C [3]

Water content (%)	Avg. SG bulk		Avg. air voids (%)		Avg. stability (kN)		Avg. flow (mm)	
	0°C	45°C	0°C	45°C	0°C	45°C	0°C	45°C
3	2.12	2.09	16.92	18.00	12.80	12.67	3.05	3.01
4	2.14	2.14	16.01	15.89	13.02	12.93	2.91	2.97
5	2.13	2.14	16.24	16.05	12.71	12.58	3.52	4.05

Plati et al. [17] studied the possibility of employing RAP as unbound pavement layers. Please note that most RAP research has emphasised on recycling as asphaltic concrete pavement; thus, information concerning the unbound pavement is scarce. By making use of the RAP, it would benefit the environment in terms of waste management. The RAP used in their study was from a milling process of rehabilitating a pavement section. Then, the RAP was mixed with virgin aggregate (VA), which had varied proportions. Five blends were studied: A, B, C, D, and E. The percentage ratios between RAP and VA for the respective five blends were 0:100, 10:90, 20:80, 30:70, and 40:60. Next, several laboratory tests, both basic and engineering properties, were carried out to obtain suitable results. For the modified Proctor test, Plati et al. reported that the optimum moisture contents for the blends narrowly vary from 5.9% to 6.9%. As the proportion of RAP gradually increased, it was found that the maximum dry density was progressively decreased; the maximum density of 2,196 kg/m^3 was found for blend A, and the minimum density of 2041 kg/m^3 was found for blend D, showing only slight difference. For the CBR test, the results revealed that the higher the RAP portions, the lower the CBR values. Nonetheless, the minimum CBR obtained from blend E (40% RAP and 60% VA) was still just over 50%, but indicating enough strength. Plati et al. also conducted the triaxial test to obtain other strength parameters for more complex problems.

It has been shown that most studies concerning RAP emphasise on mixing it with bitumen to recycle it back as asphaltic pavement. However, considering its shape, size, and properties, the RAP has a high potential to be employed as a subbase. In addition, if properly mixed with other granular materials, the mixture may also be directly employed to construct a Macadam Road. Nonetheless, for both cases, several tests must first be carried out in order to obtain appropriate proportions.

This research attempted to improve substandard subbase soil by mixing it with RAP. Three substandard subbase soils obtained from Phangnga, located in Southern Thailand, were mixed with the RAP obtained from the same region to achieve the objectives. Each soil-RAP mixture had varied mixing ratios. Then, basic and engineering properties were determined using the testing standards provided by the Department of Rural Roads, Thailand.

2. Materials and Methods

According to the standards provided by DRR [18], subbase materials must have a CBR of 25% or higher. When tested using the modified Proctor method at 95% of maximum dry density, the CBR value is one of the most important parameters. Other properties of a suitable soil include less than or equal to 35% of the liquid limit and a plasticity index of not more than 11%. Table 3 displays the gradations of materials suitable for being employed as a subbase for road construction. It should be noted herein that having natural soil with such required properties is almost impossible. Therefore, mixing two or more soils in order to obtain a targeted property is not unusual.

Table 3. Gradation of material suitable for subbase [18]

Sieve size	Percentage passing of material				
	Type A	Type B	Type C	Type D	Type E
2''	100	100	-	-	-
1''	-	-	100	100	100
3/8''	30 – 65	40 – 75	50 – 85	60 – 100	-
# 10	15 – 40	20 – 45	25 – 50	40 – 70	40 – 100
# 40	8 – 20	15 – 30	15 – 30	25 – 45	20 – 50
# 200	2 – 8	5 – 20	5 – 15	5 – 20	6 - 20

Table 4. Soil to RAP ratios by weight

Sample number				Soil to RAP ratio (by weight)	Note
Soil A	Soil B	Soil C	D (Milling)		
A100R0	B100R0	C100R0	-	100:0	
A90R10	B90R10	C90R10	-	90:10	
A80R20	B80R20	C80R20	-	80:20	
A70R30	B70R30	C70R30	-	70:30	
A60R40	B60R40	C60R40	-	60:40	
A50R50	B50R50	C50R50	-	50:50	
-	-	-	R100	0:100	100% of RAP

In this study, a total of three soils from Phangnga Province were chosen, but from different areas, as a base material to be mixed with RAP, namely Soil A, Soil B, and Soil C, as shown in Fig. 2. In addition, the RAP was also collected from the same province. Fig. 3 illustrates the equipment and processes for milling the RAP. Previous studies [19-23] show that even though RAPs were collected from different places, their properties are quite similar. This may be because the constituents of asphaltic concrete, no matter where it is constructed, are very much the same. Nonetheless, for the consistency of test results, only one source of RAP was chosen; it was also from the same province of Phangnga. To obtain the optimum proportion in terms of the highest CBR, each soil was mixed with the RAP having the soil to RAP by-weight ratios of 100:0, 90:10, 80:20, 70:30, 60:40, and 50:50. In addition, 100% of RAP, namely sample D, was also included for the laboratory work so that they could be compared for further analysis. This resulted in 19 samples for laboratory tests, as shown in Table 4.

Besides basic properties such as soil classification and Atterberg limits, the following tests were carried out to achieve this study's objectives: modified compaction test and California Bearing Ratio test. The compaction test during operation is shown in Fig. 4, while Fig. 5 displays the procedures for the CBR test. Although all laboratory tests were conducted according to the standards set by the Bureau of Testing Research and Development, the Department of Rural Roads, Thailand, the methods are indeed based on the international standard, namely ASTM.

ASEAN J. Sci. Tech. Report. **2025**, *28*(3), e257089.

5 of 11

Figure 2. Soil sampling (a) soil A (b) soil B (c) soil C

Figure 3. Collecting the RAP (a) milling machine (b) milling machine in operation (c) pavement after RAP peeled (d) depth of peeled surface (e) pile of milled RAP (f) collecting RAP

Figure 4. Compaction test (a) preparation of soil and RAP (b) soil compaction test in operation (c) taking measurements for density calculation

Figure 5. California Bearing Ratio test (a) sample preparation (b) sample being compressed (c) soaked samples for swelling determination

ASEAN J. Sci. Tech. Report. **2025**, 28(3), e257089.

6 of 11

3. Results and Discussion

The main objective of this study was to improve a soil that is not good enough as a subbase by mixing it with RAP. Commonly, a soil that could be employed as a subbase should have a CBR of 25% or higher. Several factors affect the compaction and CBR behaviours, but one of the most important factors is size distribution characteristics. Fig.6 displays the size distribution curves for Soils A, B, and C as well as the RAP employed in this study. Soil A was classified as clay with low plasticity according to the Unified Soil Classification System, CL. In contrast, soils B and C were classified as SM, mostly sand-sized material with some silt and clay. It can be seen that only Soil C has a size distribution similar to that of the RAP. In addition, soil A has the smallest range of soil particles. These characteristics would provide insight into what will happen when conducting the compaction and CBR tests.

Table 5 summarises the laboratory work carried out by this study, including sample number, maximum dry density, 95% of maximum dry density, optimum water content, soaked CBR, and swelling of soaked samples. For all soils A, B, and C, when considering overall compaction behaviour, it was found that the maximum dry density gradually increases with increasing RAP from 0% to 30%. Subsequently, when the RAP was increased to 40% and then 50%, the maximum dry density decreased with the increase of RAP. Strikingly, the maximum densities for all soils were met at the same mixture with the RAP of 30%. Hence, it was interesting to look at this result by plotting their corresponding compaction curves obtained from the compaction test, as shown in Fig. 7 (a), (b), and (c) concerning the sample numbers A70R30, B70R30, and C70R30. From the figure, the maximum dry densities for the sample numbers A70R30, B70R30, and C70R30 are 1.521, 1.616, and 1.719 g/cm³. When considering their size distribution characteristics, as shown in Fig. 6, it suggests that the greater the range of soil particles–soil mass has a wide range of particle sizes–the higher the maximum dry density. This is because soil with a broader particle size range would be highly compactable, resulting in higher density. Results similar to these findings are also found from Alhaji and Alhassan [24]; they concluded that the maximum dry density of black cotton soil mixed with RAP was achieved when the RAP content was about 30%. Nonetheless, Suebsuk et al. [25] reported that the maximum dry density of lateritic soil mixed with RAP was obtained when the RAP content was 50%. It should be noted that, however, their soil contained a higher amount of fine.

Fig. 8 (a) shows the relationship between maximum dry density versus the increase of percentage RAP, while Fig.8 (b) displays the corresponding optimum water content versus the percentage RAP. It revealed that the maximum density occurs at the same amount of RAP of 30%, as already discussed. Nonetheless, when considering the optimum water content, it showed that the higher the percentage of RAP, the greater the OWC. This may be because as the RAP portion is gradually higher, more water is required for the compaction test.
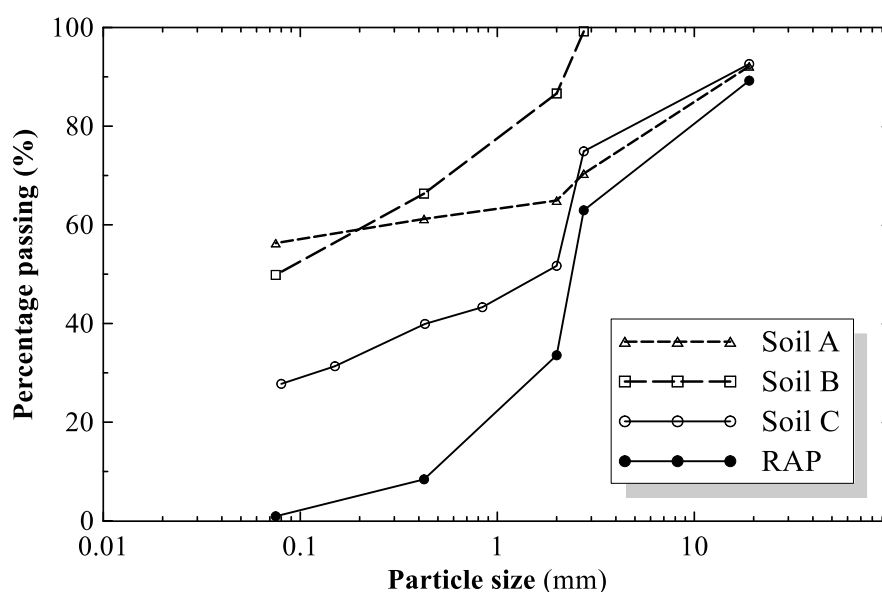
Figure 6. Size distribution curves for all three soils and the RAP

ASEAN J. Sci. Tech. Report. **2025**, *28*(3), e257089.

7 of 11

Table 5. Summary of laboratory work results

Soil	Sample no.	Max. dry density (g/cm³)	95% of Max. dry density (g/cm³)	Optimum moisture content (%)	Soaked CBR (%)	Swelling (%)
A	A100R0	1.455	1.382	14.7	7.9	8.4
	A90R10	1.487	1.412	15.0	8.8	6.8
	A80R20	1.510	1.435	15.7	9.6	5.8
	A70R30	1.521	1.445	16.1	11.0	3.5
	A60R40	1.505	1.429	17.0	9.1	2.9
	A50R50	1.485	1.411	17.6	8.3	2.8
B	B100R0	1.567	1.429	10.9	13.2	4.4
	B90R10	1.585	1.506	11.5	13.4	3.9
	B80R20	1.595	1.516	12.8	14.6	3.5
	B70R30	1.616	1.535	13.2	15.9	3.0
	B60R40	1.588	1.508	14.0	14.2	2.8
	B50R50	1.577	1.429	14.2	13.8	2.2
C	C100R0	1.601	1.521	12.8	16.5	4.9
	C90R10	1.665	1.582	13.5	17.3	4.3
	C80R20	1.698	1.631	15.0	21.5	3.4
	C70R30	1.719	1.633	16.1	25.1	2.9
	C60R40	1.657	1.574	17.6	22.3	2.3
	C50R50	1.641	1.559	19.7	17.6	1.8
D	R100	1.921	1.825	10.9	20.9	0.3

The CBR values for all soils A, B, and C having zero RAP were 7.9, 13.2, and 16.5%, respectively, corresponding to the sample numbers A100R0, B100R0, and C100R0, of which are lower than the standard CBR value of 25% for being employed as subbase. In addition, for the whole milled RAP sample (sample number R100), the CBR was just 20.9%; it is quite high compared to all soils, but it is still not good enough.

The changes in CBR values versus the increase in percentage RAP are shown in Fig. 9 (a), while Fig. 9 (b) displays their corresponding swelling values versus the percentage RAP. The CBR behaviour showed the same trend as found in the compaction test: the CBR gradually increased with the increase of the RAP portion from 0% up to 30%, then gradually decreased till the maximum RAP portion of 50%. The most interesting point, however, is the swelling results. It was found that they steadily and gradually decreased with the increase in the percentage of RAP. As mentioned before, the maximum dry density and CBR for all soils A, B, and C were maximum when the percentage of RAPs was 30%. Consequently, the percentage swelling values for soils A, B, and C are the lowest when the mixtures contain 30% RAP. This means that when 30% RAP was added, even when fully soaked, the void ratios were also the lowest. Hence, the finding strongly confirms that the 30% RAP is the optimum value for mixing with the tested soils to obtain the best parameters for being subgrade material. Nonetheless, for all of the samples studied, only the sample number C70R30 is qualified as a subbase material. As such, the findings imply that even though to be mixed with RAP, soil must be carefully chosen to obtain the required results: soil should have a wide range of particle sizes with a small amount of clay. This is because higher clay content in soil may cause a swelling value to increase substantially, thereby posing the instability of a road. It should be noted herein that these results, particularly of the sample C70R30, show a promising sign because other studies tend to add some substance, such as cement, to achieve a similar CBR. Still, no other materials are required for this study. Thus, it helps in terms of both cost and environment. This is because employing cement, for example, could generate a more significant carbon footprint, thereby worsening pollution.

ASEAN J. Sci. Tech. Report. **2025**, *28*(3), e257089.

8 of 11
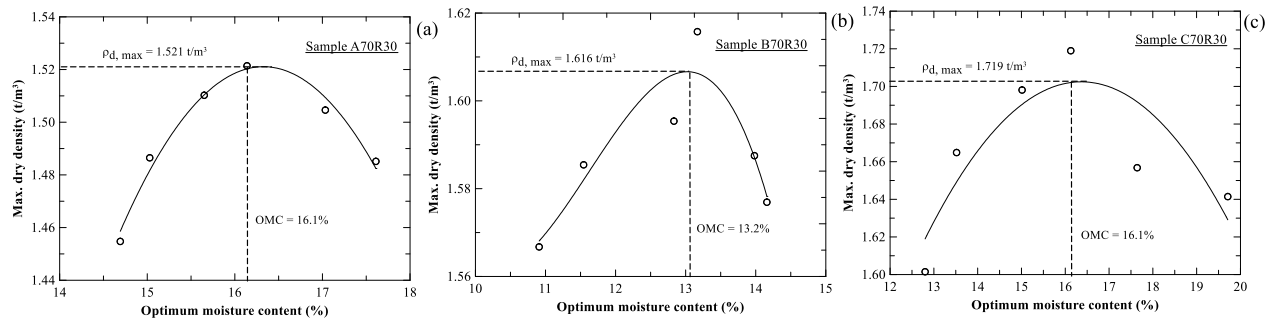
Figure 7. Maximum dry densities for (a) sample A70R30 (b) sample B70R30 (c) sample C70R30
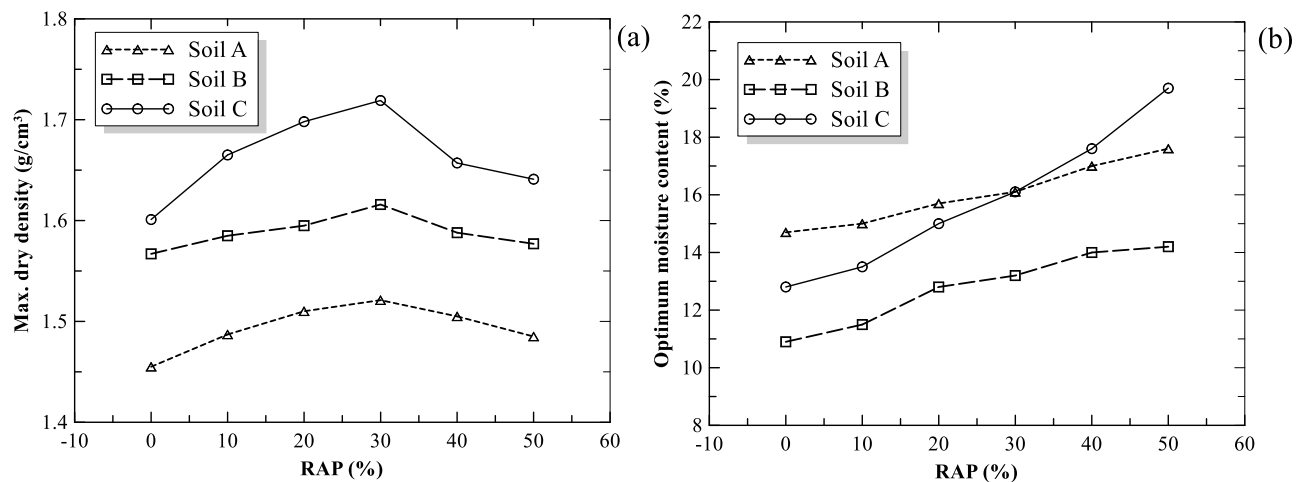
Figure 8. (a) Maximum dry density versus percentage RAP (b) Optimum water content versus percentage RAP
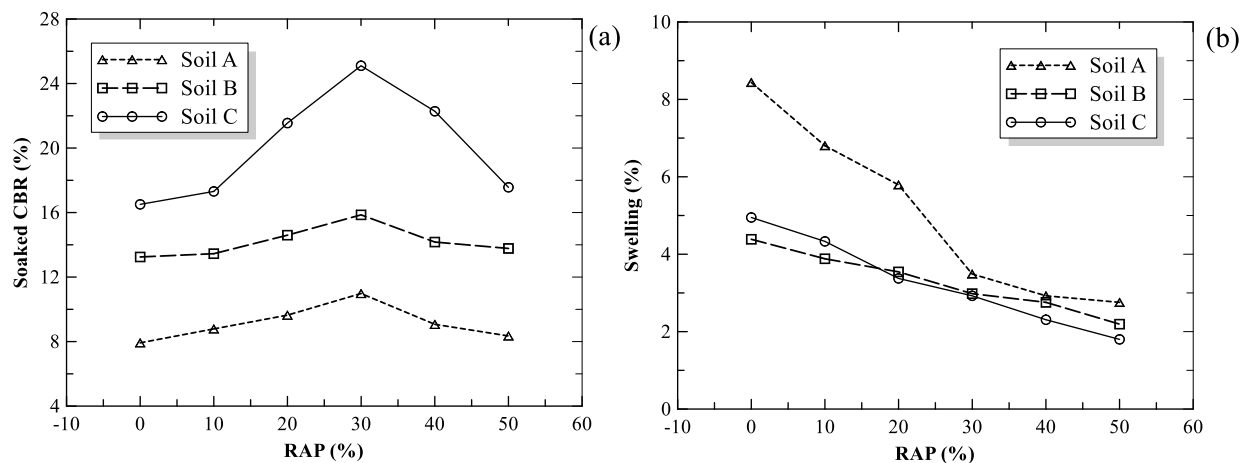
Figure 9. (a) Soaked CBR versus percentage RAP (b) Swelling versus percentage RAP

4. Conclusions

Road networks are vital for economic growth. The construction, however, requires a great deal of natural material, especially soil and rock. Even though both materials are abundant, not all encountered soil and rock are appropriate for road construction: they must possess specific characteristics that can keep up with traffic loads and ambient weather. When a road project has been committed, one of the most priority tasks is to source materials as close to the site as possible. This is because if the main materials are quite far from the project, transportation costs would be so high that it is not viable. As such, soil close to the project but with substandard quality could be employed with some modifications.

ASEAN J. Sci. Tech. Report. **2025**, *28*(3), e257089.

9 of 11

This research attempted to improve soil that is unsuitable for being employed as a subbase by mixing it with RAP. Three substandard subbase soils, namely Soils A, B, and C, were collected from different areas in Phangnga province, Southern Thailand. In addition, the RAP was also milled in the same province. Both basic properties and engineering properties for the soil-RAP mixtures were determined in laboratory using the standards set by the Department of Rural Roads, Thailand. Note that even though the testing standards were domestic, they are equivalent to the international standards set by, for example, ASTM. The soil-to-RAP ratios by weight of each soil type for the laboratory work were 100:0, 90:10, 80:20, 70:30, 60:40, and 50:50. In addition, testing a whole RAP was also carried out so that all results would be compared and contrasted. This resulted in a total of 19 mixtures that were tested and examined. From the laboratory tests and analyzed data, the following points have been drawn:

(1) The classification results show that soil A is classified as CL, while soils B and C are classified as SM.

(2) The CBRs for the sample numbers A100R0, B100R0, and C100R0 were 7.9%, 13.2%, and 16.5%, respectively. They were lower than the standard value of 25% for being employed as a subbase. Even though the whole RAP (sample number R100) had a CBR of 20.9%, which is quite greater than that of all soils, it was still not good enough. Hence, all sampled soils met the requirement for this study: they must have a CBR lower than 25%.

(3) For all soils, the maximum dry density gradually increases with the increase of the RAP portion from 0% to 30%. Then, they steadily decrease with the further increase of the RAP portion from 40% to 50%. The maximum values for soils A, B, and C are 1.521, 1.616, and 1.719 g/cm^3, respectively; they occur when the samples contain an RAP of 30%. This means soil C has the highest capability for being compacted.

(4) The CBR behaviors were similar to those of the compaction test results. The maximum CBR values for all soil occur when the samples also contain an RAP of 30%. The maximum CBR for soils A, B, and C are 11.0, 15.9, and 25.1%, respectively. These results indicate that only soil C mixed with 30% of RAP could be used as a road construction subbase material.

(5) When considering the CBR results, one should also examine their corresponding swelling potential. In this study, it is striking that all samples with 30% RAP also have the lowest swelling. This means that the results obtained from this study firmly validate that when the soils were mixed with 30% of RAP, they were most effective regarding compaction ability and puncture resistance.

Even though the results from this study confirm the possibility of mixing substandard subbase soil with RAP to be employed as a subbase in road construction, we should carry out more studies. This is because only three soil types were tested; if more soil types are to be studied, their results would be beneficial for further comparison to confirm the feasibility of this kind of modification. Furthermore, other substances, such as cement and lime, may be included in mixtures to assess their effects. If only a small percentage of cement and lime are required for a soil-RAP mixture to have enough CBR, a wider range of soil types may then be applied by this modification technique. Therefore, one would not worry when a road construction project is close to substandard soil. Please note that this study did not concern the permeability behaviour; if interested, however, one can find the behaviour from Akinwumi [26], Gowda et al. [27], and Russo et al. [21]. Additionally, if the unconfined compression is concerned, one should investigate the study conducted by Lima et al. [28]. They mixed RAP with pure soil using a percentage of RAP ranging from 0% to 80%, with and without the addition of cement. Other similar studies can also be found in [29-31].

5. Acknowledgements

References

[1] DOH. Statistical summary of transportation engineering for executive, Department of Highways, Thailand. **2022.**

[2] DRR. Road networks. Department of Rural Roads, Thailand. **2024**.

[3] Ariffin, N. Investigating mechanical properties of reclaimed asphalt pavement rejuvenated with rubber seed oil. Bsc Dissertation. Universiti Teknologi Petronas. **2022**.

[4] Saeed, S. M.; Sutanto, M. H.; Napiah, M.; Usman, A.; Batari, A.; Aman, M. Y.; Aliyu Yaro, N. S. Optimization of rubber seed oil content as bio-oil rejuvenator and total water content for cold recycled asphalt mixtures using response surface methodology. *Case Studies in Construction Materials*. **2021**, *15.* https://doi.org/10.1016/j.cscm.2021.e00561.

[5] Wang, Y.; Leng, Z.; Li, X.; Hu, C. Cold recycling of reclaimed asphalt pavement towards improved engineering performance. *Journal of Cleaner Production*. **2018,** *171*, 1031-1038. https://doi.org/10.1016/j.jclepro.2017.10.132

[6] Arámbula-Mercado, E.; Chavarro-Muñoz, S.J.; Moseley, H. Performance of Hot and Cold Recycled Mixtures with High Reclaimed Asphalt Pavement Content. *Journal of the Transportation Research Board*. **2020**, *2674(9)*, https://doi.org/10.1177/0361198120931510

[7] Mollenhauer, K.; Graziani, A.; Gaudefroy, V.; Presti, D.L.; Bjurström, H.; Winter, M.; Mignini, C.; Giancontieri, G. Cold recycled asphalt for pavements with optimized resource and energy efficiency: proposal for harmonized mix and pavement design. *Transport Research Arena (TRA) Conference*. **2023**, *72*, 3031-3038. https://doi.org/10.1016/j.trpro.2023.11.851

[8] Taherkhani, H.; Firoozei, F.; Bazaz, J.B. Evaluation of the mechanical properties of the cement treated cold-in-place recycled asphalt mixtures. *International Journal of Transportation Engineering*. **2016,** *3(4)*, 301-312.

[9] Chegenizadeh, A.; Tufilli, A.; Arumdani, I.S.; Budihardjo, M.A.; Dadras, E.; Nikraz, H. Mechanical properties of cold mix asphalt (CMA) mixed with recycled asphalt pavement. *Infrastructures*. **2022**, *7(45)*, 1-14. https://doi.org/10.3390/infrastructures7040045

[10] DOH. Asphalt hot-Mix recycling, Standard no. DH-S 410/2542, Department of Highways, Thailand. **1999**.

[11] Kumar, P.; Kumar, R.; Aslam, M. Design of Bituminous Mix using Reclaimed Asphalt Pavement (RAP), *International Research Journal of Engineering and Technology (IRJET)*. **2019**, *6(11)*, 3614-3618.

[12] Mittal, A.; Bose, S.; Nagabhushaha, M. N. Recycling of Pavements an Approach Suitable for Sustainable Development (in Hindi). Nirman Surbhi, Rashtriya Sangoshti. Nirman Samagriya Vision 2030. Central Road Research Institute, New Delhi. **2010**.

[13] Saberi, S.S.; Mohamed, A. Characterization of soil for road shoulders mixed with reclaimed asphalt pavement waste. *Bilge International Journal of Science and Technology Research*. **2023**, *7(1)*. 22-32. https://doi.org/10.30516/bilgesci.1218789

[14] Hasan, M.M.; Islam, M.R.; Tarefder, R.A. Characterization of subgrade soil mixed with recycled asphalt pavement. *Journal of Traffic and Transportation Engineering (English Edition)*. **2018**, *5(3)*, 207-214. https://doi.org/10.1016/j.jtte.2017.03.007

[15] Edeh, J.E.; Eberemu, A.O.;Agnes, O. Lateritic soil stabilization of reclaimed asphalt pavement as flexible highway pavement materials. *Advanced Materials Research*. **2012**, *367*, 3-11. https://doi.org/10.4028/www.scientific.net/AMR.367.3

ASEAN J. Sci. Tech. Report. **2025**, *28*(3), e257089.

11 of 11

[16] Khosla, N.P.; Ramoju, S.S.; Prabu, N. Determining Recycled Asphalt Binder Limits Contributed by Waste Materials. North Carolina State University in Cooperation with North Carolina Department of Transportation. **2015**.

[17] Plati, C.; Tsakoumaki, M.; Gkyrtis, K. Physical and mechanical properties of reclaimed asphalt pavement (RAP) incorporated into unbound pavement layers. *Applied Science*. **2023**, *13(1)*, 1-16. https://doi.org/10.3390/app13010362

[18] DRR. Standard for subbase material, DRR Standard 202-2557. Department of Rural Roads, Thailand. **2014.**

[19] Widayanti, A.; Soemitro, A.A.; Ekaputri, J.J.; Suprayitno, H. Physical and mechanical properties of asphalt concrete contain reclaimed asphalt pavement from national road in East Java Province Indonesia. *Advances in Engineering Research*. **2019**, *186*, 9-15. https://doi.org/10.2991/apte-18.2019.3

[20] Montañez, J.; Caro, S.; Carrizosa, D.; Calvo, A.; Sánchez, X. Variability of the mechanical properties of Reclaimed Asphalt Pavement (RAP) obtained from different sources. *Construction and Building Materials*. **2020**, *230*, 116968, ISSN 0950-0618, https://doi.org/10.1016/j.conbuildmat.2019.116968

[21] Russo, N.; Filippi, A.; Carsana, M.; Carsana, M.; Lollini, F.; Redaelli, E. Recycling of RAP (Reclaimed Asphalt Pavement) as aggregate for structural concrete: experimental study on physical and mechanical properties. *Discover Civil Engineering*. **2024**. *1:99*, https://doi.org/10.1007/s44290-024-00101-y

[22] Rinkal, D.; Zala, L.B.; Amin, A.A. Reclaimed asphalt pavement (RAP) – A review. International Research *Journal of Modernization in Engineering Technology and Science*. **2021**, *03(05)*, 3076-3084.

[23] Widayanti, A; Soemitro, R.A.A.; Ekaputri, J.J.; Suprayitno, H. Characterization of reclaimed asphalt pavement (RAP) as a road pavement material (National Road Waru, Sidoarjo). *MATEC Web of Conferences*. **2018**, *181*. https://doi.org/10.1051/matecconf/201818105001

[24] Alhaji, M.M.; Alhassan, M. Effect of reclaimed asphalt pavement stabilization on the microstructure and strength of black cotton soil. *International Journal of Technology*. **2018**, *4*, 727-736. https://doi.org /10.14716/ijtech.v9i4.435

[25] Suebsuk, J.; Suksan, A.; Horpibulsuk, S. Strength assessment of cement treated soil-reclaimed asphalt pavement (RAP) mixture. *Goetech., Const. Mat. & Env*. **2014**, *6(2)*, 878-884. https://doi.org/10.21660/2014.12.3262

[26] Akinwumi, I.I. Plasticity, strength, and permeability of reclaimed asphalt pavement and lateritic soil blends. *International Journal of Scientific & Engineering Research*. **2014**, *5(6)*, 631-636.

[27] Gowda, S.; Kavana, N.; Nithesh, B.N.; Rachana, M.; Gowda, S.P. Study on effect of reclaimed asphalt pavement on permeability of subgrade. *Journal of Emerging Technologies and Innovative Research*, **2019**, *6(5)*, 319-323.

[28] Lima, D.; Arrieta-Baldovino, J.; Izzo, R.L.S. Sustainable use of recycled asphalt pavement in soil stabilization. *Civil Engineering Journal*. **2023**, *9(09)*, 2315-2329. https://doi.org/10.28991/CEJ-2023-09-09-016

[29] Almeida, G.; Sales, L.C.; Cavalcante, E. Geotechnical properties analysis of soil, reclaimed asphalt pavement (RAP) and Portland cement mixtures for use as pavement layers. *Geociências*. **2024**, *43(2)*, 223-235.

[30] Ghanizadeh, A. R.; Rahrovan, M.; Bafghi, K.B. The effect of cement and reclaimed asphalt pavement on the mechanical properties of stabilized base via full-depth reclamation. Construction and Building Materials. **2018**, *161*, 165-174. https://doi.org/10.1016/j.conbuildmat.2017.11.124

[31] Al-Fatlawy, R.A.; Ali, T.S.; Fakhraldin, M.K.; Hussain, N.A.; Abd, I.Y. Improvement in the California bearing ratio of subbase soil by recycled asphalt pavement and cement. *Open Engineering*. **2023**, *13*(1), 1-7. https://doi.org/10.1515/eng-2022-0449

Development of Cement-Based Composites Using Screw Pine Leaf Waste for Sustainable Community Products

Rarin Khuawaraphan[1], Supranee Wunsri[2], Palachai Khaonuan[3], Kosin Teeparuksapun[4], and Noppadon Podkumnerd[5]*

[1] College of Hospitality and Tourism, Rajamangala University of Technology Srivijaya Trang Campus, Trang, 92150, Thailand

[2] Faculty of Liberal Arts, Rajamangala University of Technology Srivijaya, Songkhla, 90000, Thailand

[3] Faculty of Liberal Arts, Rajamangala University of Technology Srivijaya, Songkhla, 90000, Thailand

[4] Faculty of Liberal Arts, Rajamangala University of Technology Srivijaya, Songkhla, 90000, Thailand

[5] Faculty of Liberal Arts, Rajamangala University of Technology Srivijaya, Songkhla, 90000, Thailand

* Correspondence:Noppadon.p@rmutsv.ac.th

Abstract: This study demonstrates an innovative approach to waste material valorization through the development of reinforced fiber cement using screw pine (*Pandanus tectorius* Blume) leaf waste (SLW). First, the researchers study fiber cement composites with SLW, cement, and water in different ratios. The results showed that the 1:30:30 (w/w) ratio gave the highest compressive strength of 15.35 kg/cm²; the density was 1,100±0.08 kg/m³, and water absorption was 38.38 ± 1.61%. Then, the researchers studied the water absorption reduction of this fiber cement by coating it with a water-repellent for 15 minutes. The results indicated that the water absorption value was reduced to 33.78 ± 1.31%. Next, the researchers applied this fiber cement production method to produce cement pots, which were found to be well-formed and, when tested for compressive strength, had a value of 11.09 ± 0.23 kg/cm² and a water absorption value of 34.95 ± 2.23%. Later, the researchers conducted a study on customer satisfaction and cost-benefit analysis from the production of fiber cement pots; the result showed that the customer had an average satisfaction of 4.402 ± 0.101, which was very satisfactory. The production capacity is 1,000 pots, costing 12,600 baht, and the average cost per pot is 12.60 baht. If sold at 35 baht per pot, there will be a gross profit margin of 64.00%. Finally, this technology was transferred to the Khlong U-Tapao Watershed Community's weaving industry in Songkhla, Thailand, creating a sustainable revenue stream while supporting community-based tourism (CBT) initiatives.

Keywords: Cement pots; Screw pine leaf waste (SLW); Khlong U-Tapao Watershed Community

1. Introduction

The growing interest in turning agricultural waste into value-added products results from the emphasis on sustainable development and the circular economy. Plant-based lignocellulose fibers (LFs), which contain different amounts of cellulose, hemicellulose, and lignin, have shown great promise as composite reinforcement materials, especially for building applications. Due to their appealing qualities—such as increased durability, higher compressive strength, flexibility, lightweight, cost-effectiveness, and environmental sustainability—the incorporation of these natural fibers into cement-based composites has accelerated significantly since the 1990s [1-4]. Numerous

ASEAN J. Sci. Tech. Report. **2025**, *28*(3), e256615.

2 of 12

agricultural waste streams have been the subject of in-depth research on using natural fiber reinforcement in concrete and cement-based products. The effective use of date palm fibers for reinforcing concrete [5], palm fibers in concrete bricks [6], and palm oil fibers in cement fiber board manufacturing [7] are noteworthy examples. These applications demonstrate the versatility and effectiveness of natural fibers in enhancing both the mechanical and physical properties of cement-based materials while providing environmental benefits through waste reduction. Screw pine (*Pandanus tectorius* Blume) (Figure 1), locally known as "Ka-Ra-Ket" in Thailand, "Mengkuang" in Malaysia, and "Woromo" in Indonesia, is a prevalent plant species in Southeast Asia [4,8,9]. This plant, characterized by its distinctive screw pine leaves, is particularly abundant in Thailand's Khlong U-Tapao Watershed Community, which serves as a primary material for traditional weaving. The community produces various items through local wisdom practices, including mats, storage containers, and bags. However, this production will generate a large amount of SLW, primarily from leaf preparation and cutting processes, creating a potential environmental burden if left unmanaged.

Figure 1. Screw pine (*Pandanus tectorius* Blume) (Photo by the author)

Khlong U-Tapao Watershed Community uses local wisdom to produce weaving products for daily use from screw pine leaves such as mats, storage containers, and bags (Figure 2A-C). However, in the production of screw pine leaf weaving products, it creates waste materials, as shown in Figure 3. These waste materials are generated during various production steps, including the process of preparing screw pine leaves and the cutting process. SLW is generated each year, and if there is no effective management, it will become the community's waste in the future.

Figure 2. Screw pine leaf basketry products, A) mat, B) handbag, and C) storage container (Photo by the author)

ASEAN J. Sci. Tech. Report. **2025**, *28*(3), e256615.

3 of 12

Figure 3. Screw pine leaf production: A) preparation of screw pine leaf, B) production of basketry product, and C) SLW (Photo by the author)

In the context of Thailand's commitment to the Bio-Circular-Green (BCG) economic model and sustainable development goals, finding innovative ways to utilize such agricultural waste is crucial. The Khlong U-Tapao Watershed Community's screw pine weaving industry presents an opportunity to demonstrate how traditional craft waste can be transformed into valuable products while addressing environmental concerns and supporting community development. This research aims to develop and optimize a method for producing cement pots reinforced with SLW, creating a practical solution for waste utilization while generating additional income opportunities for the community. The specific objectives include determining the optimal mixture ratios of SLW, cement, and water for pot production, evaluating the physical and mechanical properties of the reinforced cement composites, developing a water-resistant treatment process to enhance product durability, analyzing the economic viability of production and facilitating technology transfer to the community. The significance of this research extends beyond waste management, as it presents a model for integrating traditional craft waste into modern, sustainable products while supporting CBT initiatives. This approach aligns with Thailand's BCG economic model, promoting sustainable development that balances social, economic, and environmental considerations. Through this research, we demonstrate how local agricultural waste can be transformed into valuable products, creating a circular economy model that benefits both the environment and the community. The findings contribute to the growing knowledge of natural fiber reinforcement in cement-based materials while providing a practical framework for community-level implementation of sustainable waste management solutions.

2. Materials and Methods

2.1 Preparation of SLW

SLW was obtained from the screw pine weaving group, Mae Thom Sub-district, Bang Klam District, Songkhla Province. It was cut into small pieces with a size of 1 inch long. The SLW was dried using sunlight. After that, the SLW was blended using a high-speed blender (Otto BE-127A; Thailand) at 6,000 rpm for 30 seconds to separate fibers from the leaves. The SLW was stored in a plastic bag to protect them from moisture at room temperature.

2.2 Optimization of mixtures ratio of fiber cement composites

In general, the production of fiber cement composites uses three types of raw materials: cement, water, and lignocellulosic fiber [3]. Therefore, this experiment investigated 4 mixture ratios of cement, water, and SLW, as shown in Table 1. A control experiment was performed where SLW was not. After that, pour the mixture into a 20L plastic container and mix it well using a mud mixer (Stanley-SDR1400; China) at 480 rpm for 5 minutes. The studied mixture was investigated by forming the sample into a square shape with a dimension of 50 x 50 x 20 mm (width x length x thickness). It was then dried at 100-110°C using a hot air oven (Binder ED260; Germany) and allowed to cool before being tested for density and water absorption tests according to the ASTM C 642-21 method [10]. The specimens were baked at 100-110°C in a hot air oven for 24 hours and cooled. They were weighed using an electric balance (Sartorius Quintix3102-1S; Germany) and immersed in water for 24 hours. The specimens were then weighed again. After completing the above process, the sample's percentage of water absorption was analyzed The compressive strength test according to the

ASEAN J. Sci. Tech. Report. **2025**, 28(3), e256615.

4 of 12

ASTM C39/C39M-21 method [11], was investigated using a compression testing machine (Marshall testing machine S215PA171; Italy. The date wer anzlyed for variance using one-way ANOVA, and differences between group means were compared using Duncan's Multiple Range Test (DMRT), at a significance level of 0.05. The strongest and weakest samples were used to study the structure using a Trinocular Fluorescence Stereo Microscope (TFSM) (Leica M205FCA, Germany).

Table 1. Optimization of raw materials ratios

Specimen	SLW (g)	Cement (g)	Water (g)
S1	1.0	10.0	10.0
S2	1.0	20.0	20.0
S3	1.0	30.0	30.0
S4	1.0	40.0	40.0
Control	-	10.0	10.0

2.3 The water-repellent coating of fiber cement composites reinforced with SLW

The water-repellent coating of the cement composites reinforced with SLW was investigated using the optimized mixture ratio of fiber cement composites from the previous experiment. In this experiment, the NK GUARD S-80 (NICCA Chemical) was used to increase the water-repellent properties of the fiber cement composites reinforced with SLW. The water-repellent coating method was modified from Podkumnerd *et al*. [12], Briefly, the NK GUARD S-80 was mixed with water at a ratio of 2:8 (w/w) in a 250 mL beaker. After that, the specimens were soaked in the mixture three different times (5, 15, and 30 minutes) and further studied for water resistance, the water absorption test according to the ASTM C 642-21 method [10].

2.4 Production of cement pots reinforced with SLW

Cement pots reinforced with SLW were produced using the best-performing ingredients from experiment 2.2 and poured into plastic molds, covered with a hemp sack to prevent water evaporation, and left for 24 hours. After that, it was removed from the mold and left to dry for 7 days. They were then dried in a hot oven at 100-110°C for 24 hours and left to cool. The waterproof coating was performed by immersing the pots in a 10L container filled with water-repellent for the appropriate time from Experiment 2.3 and then baking at 100-110°C for 24 hours. The fabricated pots were tested for water absorption according to the ASTM C 642-21 method [10] and for compressive strength according to the ASTM C39/C39M-21 method [11].

2.5 Customer Satisfaction Analysis

After transferring technology for producing cement pots reinforced with SLW to the community, the researchers study customer satisfaction, according to Kotler and Keller [13]. Customer satisfaction analysis emphasizes the Expectation-Disconfirmation Model and various methods businesses use to measure and manage customer perceptions. One of the most commonly used satisfaction measurement scales consists of five levels: 5= Very Satisfied, 4= Satisfied, 3= Neutral, 2= Dissatisfied, and 1= Very Dissatisfied. The questionnaire data on the satisfaction of the sample group was collected between May - June 2023 using a sample group of people living in Bang Klam District, Songkhla Province, selected using Yamane's formula [14]. After that, the data were analyzed for the mean and standard deviation. The evaluation criteria were a rating scale according to Likert [15], which has 5 levels: 4.51-5.00 most satisfied, 3.51-4.50 very satisfied, 2.51-3.50 moderately satisfied, 1.51-2.50 slightly satisfied, and 1.00-1.50 least satisfied.

2.6 Cost-benefit analysis

The researchers analyzed the cost and return on the product to enable the community to effectively sell the produced products and generate additional income for the community.

Total costs analysis according to Horngren *et al*. [16].

Total Cost	=	Direct Material + Direct Labor + Manufacturing overhead
		Break-even point, according to Garrison *et al*. [17].
Break-event point	=	Fixed cost / Contribution margin ratio
		According to Cooper and Kaplan [18], the gross profit margin ratio.
Gross Profit margin ratio	=	(Gross profit x 100) / Sale revenue

2.7 Technology transfer to the community

The technology for producing cement pots reinforced with SLW was transferred to the Screw Pine Leaf Basketry Products Group in the Khlong U-Tapao Watershed Community, located in Mae Thom Sub-district, Bang Klam District, Songkhla Province. This initiative aims to enhance the value of waste materials and support CBT activities within the community.

3. Results and Discussion

3.1 Characteristics of SLW

The transformation of SLW through processing revealed distinct physical changes. The initial waste material, characterized by its fibrous nature, underwent significant modification through the blending process. This processing step was crucial in achieving optimal fiber separation, directly impacting the material's bondability with cement. The processed fibers demonstrated improved potential for cement matrix adhesion, a critical factor for the composite's structural integrity. Figure 4A shows the SLW. After blending, SLWs were obtained, as shown in Figure 4B. These SLWs will further improve the adhesion to the cement.
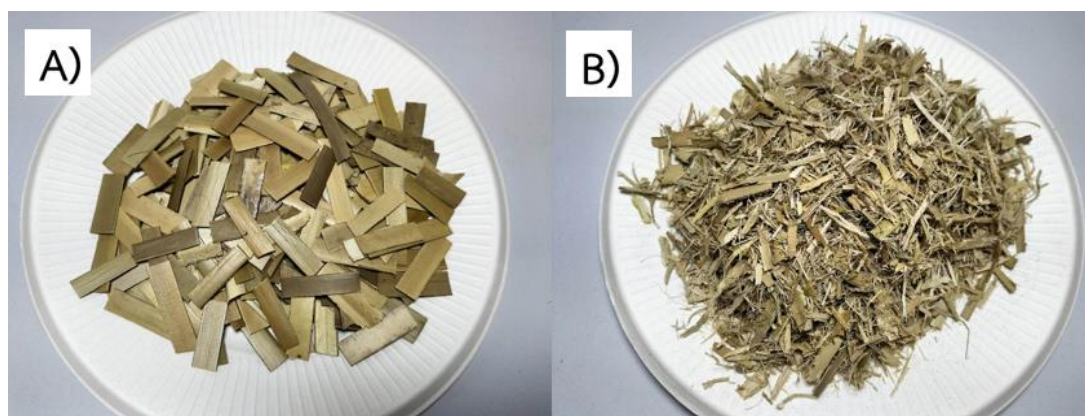
Figure 4. A) SLW and B) SLWs after the blending step

3.2 Mixtures ratios for fiber cement composites

From the forming of fiber cement composites with SLW using 4 different specimens, it was found that it could be formed (shown in Figure 5). When considering the characteristics of the formed samples, it was found that S1 gave a lot of SLW, but they were not very tightly bonded together. However, when the amount of cement was used, namely S2, S3, and S4, it was found that the fibers bonded together more tightly. This result is consistent with the report of Faridul Hasan *et al.* [1]. Mixing lignocellulose, cement, and water was an efficient, cheap, and easy way to fabricate the pots. However, the proportion of lignocellulose needs to be optimized.

ASEAN J. Sci. Tech. Report. **2025**, *28*(3), e256615.

6 of 12
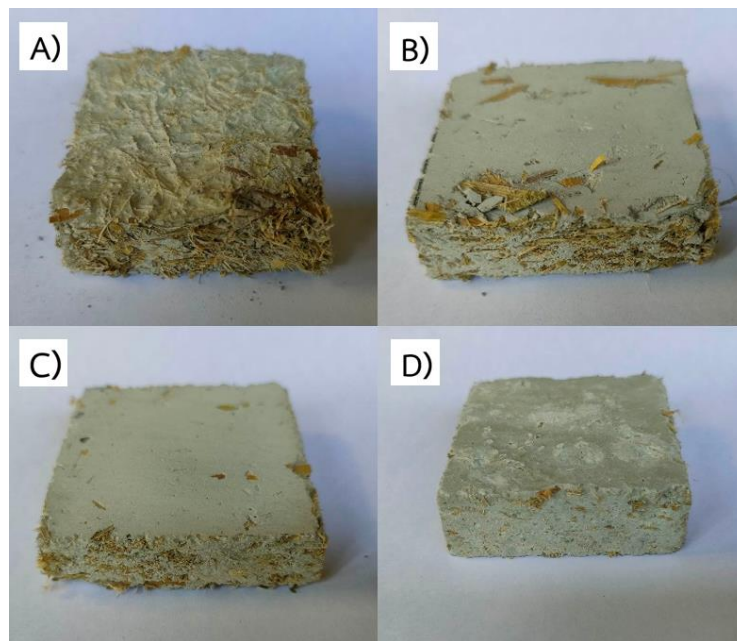
Figure 5. Characteristics of specimens of cement reinforced with SLW at different mixture ratios of SLW: A) S1, B) S2, C) S3, and D) S4

The results of the density test of the specimens are shown in Table 2. It showed that when the amount of cement was increased, it resulted in a higher sample density. In specimen 1, the density was 860 ± 0.09 kg/m³, and this was different at a significance level of 0.05 from S2, S3, and S4 with densities of 1,040 ± 0.09, 1,100 ± 0.08, and 1,180 ± 0.08 kg/m³, respectively. The density of the sample obtained from S2-S4 meets the Thai Industrial Standard, TIS standards. 878-2537 defines industrial product standards (cement-bonded particleboards: high density) that must have an average density in the range of 1,100–1,300 kg/m³ [19].

The specimen's properties for water penetration were tested; the result is shown in Table 2. It was found that increasing the amount of cement in the mixture decreased water absorption. The water absorption in S1 was 53.19 ± 3.09%, which was different from S2, S3, and S4 (40.36 ± 2.21, 38.38±1.61%, and 36.35 ± 1.97%, respectively) at a significance level of 0.05. It can be seen that using a larger amount of SLW has a great effect on water adsorption because it creates more cavities in the sample, resulting in better water retention and water-holding capacity. This is consistent with another report that increased the ratio of sawdust from *Anogeissus leiocarpus* in cement, which increased water absorption and swelling of concrete by 135.76% and 16.67%, respectively [20].

Table 2. Density and water absorption test results

Specimen	Density* (kg/m³)	Water absorption* (%)
S1	860 ± 0.09[a]	53.19 ± 3.09[c]
S2	1,040 ± 0.09[b]	40.36 ± 2.21[b]
S3	1,100 ± 0.08[bc]	38.38 ± 1.61[ab]
S4	1,180 ± 0.08[bc]	36.35 ± 1.97[a]
Control	1,210 ± 0.08[c]	35.11 ± 0.63[a]

* Different characters in each column illustrated the average comparison by DMRT at a significantly different level of 0.05.

From the compressive strength test with a compression testing machine, it was found that using an optimum amount of SLW had a significant effect on the strength of the sample. The use of SLW with cement in S3 gave the highest compressive strength of 15.35 kg/cm², which was different from the other specimen at a significance level of 0.05, followed by S2 with a compressive strength of 14.02 ± 0.48 kg/cm², and followed by S4

ASEAN J. Sci. Tech. Report. **2025**, 28(3), e256615.

7 of 12

(10.24 ± 0.66 kg /cm^2). S1 gave a compressive strength of only 3.37 ± 0.76 kg/cm^2 (Table 3). However, excessive use of SLW decreases mechanical strength due to a decrease in cementitious cohesion. This is consistent with the research of Usman *et al.* [21], who reported that the compressive strength of samples with sawdust (SD) decreased with increasing percentage of SD. The decreased compressive strength may be due to the larger SD particles, which increased the air content in the samples, resulting in increased overall porosity and weaker internal structure. This result is consistent with the images recorded with TFSM at 15X and 50X magnification, as shown in Figure 6 and Figure 7. Excess SLW can cause weakly bound (Figure 6A and Figure 7A), resulting in many cavities and thus less compressive strength.

Table 3. Compression resistance tested by compression testing machine

Specimen	Compressive strength* (Kg/cm^2)
S1	3.37 ± 0.76[b]
S2	14.02 ± 0.48[d]
S3	15.35 ± 0.63[e]
S4	10.24 ± 0.66[c]
Control	1.62 ± 0.24[a]

*Different characters in each column illustrated average comparison by DMRT at significantly different at the 0.05 level
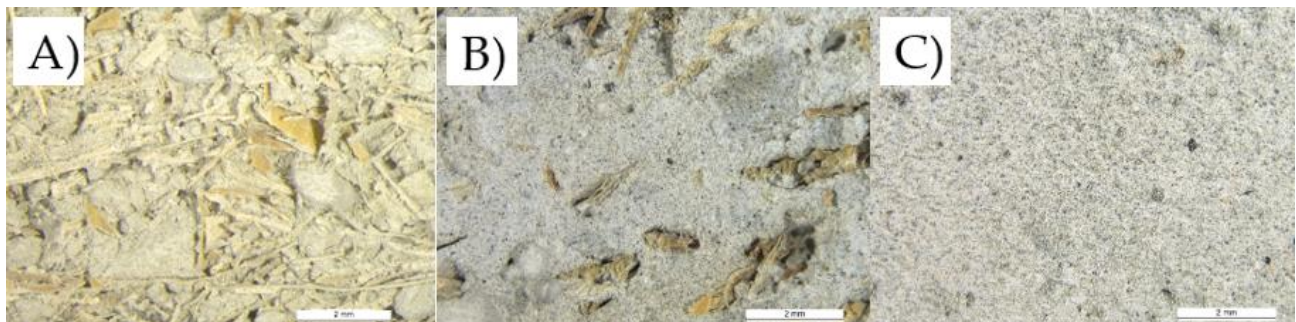
Figure 6. Photos recorded with TFSM of cement reinforced with SLW at 15X magnification A) S1 (1:10:10), B) S2 (1:30:30), and C) control
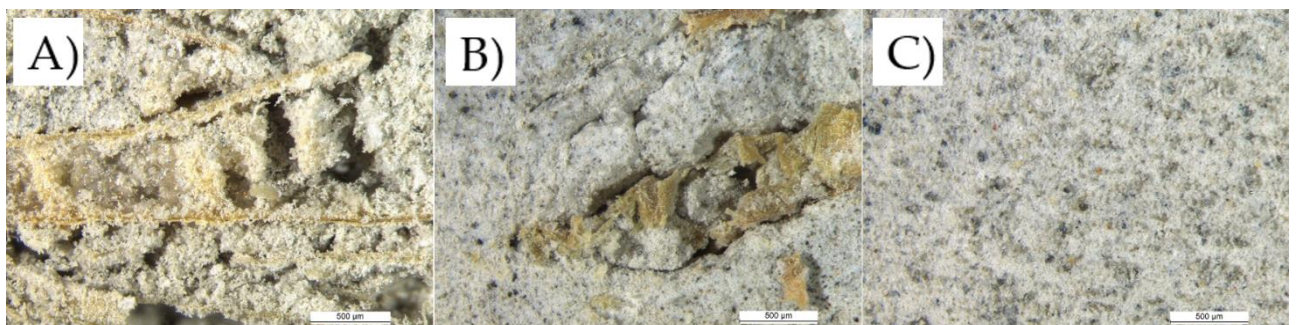
Figure 7. Photos recorded with TFSM of cement reinforced with SLW at 50X magnification A) S1 (1:10:10), B) S2 (1:30:30), and C) control

3.3 The water-repellent coating of fiber cement composites reinforced with SLW

The study results of using fiber cement composites reinforced with SLW showed good water absorption (Table 2). Therefore, the researchers studied the method of reducing water absorption by applying the water-repellent coating to coat the samples with the best compressive strength, S2 and S3 (Table 4). It was found that soaking the samples in a water-repellent coating resulted in a more significant reduction in water absorption. S2, soaked in the water-repellent coating for 0, 5, 15, and 30 minutes, gave the percentage of water absorption of 45.17 ± 0.98%, 39.27 ± 0.69%, 34.18 ± 0.5%, and 32.52 ± 1.45%, respectively. It was found that soaking

the samples for 15 and 30 minutes gave water absorption values that were not significantly different at the confidence level of 0.05. S3 gave the percentage of water absorption values of 44.01 ± 0.79%, 37.54 ± 1.48%, 33.78 ± 1.31%, and 31.81 ± 1.12%, respectively. It was also found that soaking the samples for 15 and 30 minutes gave water absorption values that were not significantly different at the confidence level 0.05.

Table 4. Water absorption of fiber cement composites reinforced with SLW after coating by using the water-repellent coating at different durations

Time (Minute)	Water absorption (%)	
	S2	S3
0	45.17 ± 0.98[c]	44.01 ± 0.79[c]
5	39.27 ± 0.69[b]	37.54 ± 1.48[b]
15	34.18 ± 0.57[a]	33.78 ± 1.31[a]
30	32.52 ± 1.45[a]	31.81 ± 1.12[a]

*Different characters in each column illustrated the average comparison by DMRT at a significantly different level of 0.05.

3.4 Production of cement pots reinforced with SLW

The results of the previous experiments showed that the production of fiber cement composites reinforced with SLW using S3, which uses SLW together with cement in a ratio of 1:30, gives the highest compressive strength, highest density, and lowest water absorption rate. Coating fiber cement composites reinforced with SLW in the water-repellent coating (NK GUARD S-80) for 15 minutes can reduce water absorption. Therefore, researchers have applied this method to produce cement pots reinforced with SLW. The method started by mixing raw material and pouring it into a mold modified from plastic pots (Figures 8A and 8B). This fabrication method was easy, cheap, and suitable for the community. After the mixture had solidified well, the pot was removed from the mold, polished with sandpaper, and dried with sunlight. The weight of the resulting pot was approximately 600 g with a capacity of 360 mL (Figure 8A). The compressive strength of the pot was 11.09 ± 0.23 kg/cm². After coating with water-repellent and testing by soaking the pot in water-repellent coating for 15 minutes, an average water absorption of only 34.95 ± 2.27% was obtained.
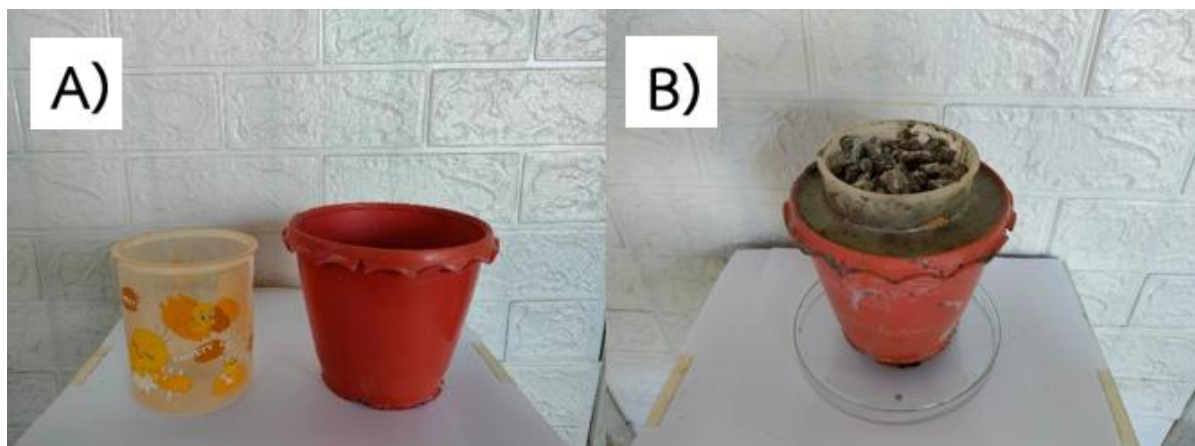
Figure 8. Fabrication of cement pot reinforced with SLW A) An experiment was set up with pot molds. B) Pot forming

The fabrication of cement pots reinforced with SLW can be an alternative way to manage waste in the community. This is consistent with Lertwattanaruk, P., and Suntijitto [22], who investigated the use of coconut coir and oil palm fibers, waste materials from the agricultural industry, to produce roof sheet and siding materials. It was found that both types of natural fibers, at a ratio of 5% by weight of cement in the mixed proportion, resulted in products with physical and mechanical properties according to the specified standards. A set of cement pots reinforced with SLW was fabricated with a pot and a pot pad (Figure 9A) and used for growing small plants such as cacti and Glochidion (Figure 9B) so that the community can use it as a community product.

ASEAN J. Sci. Tech. Report. **2025**, *28*(3), e256615.

9 of 12
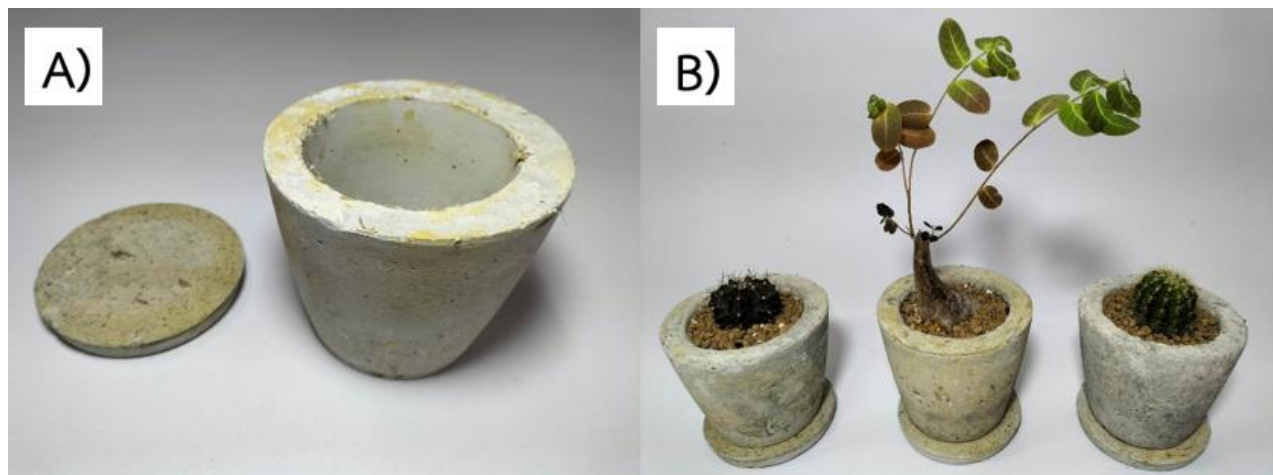
Figure 9. A) The cement pot reinforced with SLW B) planting of small plants in the pots

3.5 Customer satisfaction analysis

The product satisfaction analysis of the sample group, shown in Table 5, found that the average satisfaction in all aspects was 4.402 ± 0.101, which was at a high level. The aspect of usability had the highest average of 4.669±0.088, followed by the aspect of product quality, with an average of 4.463 ± 0.097; the aspect of design and beauty, with an average of 4.377 ± 0.092; and the aspect of value for money, with an average of 4.101 ± 0.117.

Table 5. Product satisfaction evaluation

Evaluation criteria	Satisfaction level ($\bar{x}$±S.D.)	Evaluation results
Product Quality	4.463 ± 0.097	very satisfied
Design and beauty	4.377 ± 0.092	very satisfied
Value for money	4.101 ± 0.117	very satisfied
Usability	4.669 ± 0.088	most satisfied
The average satisfaction	**4.402 ± 0.101**	**very satisfied**

3.6 Cost-benefit analysis

Total cost analysis (Table 6) shows that the production of 50 pots per production cycle costs 1,580 baht, and the average total cost per pot is 31.60 baht. The production of 500 pots per production cycle costs 6,800 baht, and the average total cost per pot is 13.60 baht. If producing up to 1,000 pots per production cycle, it costs 12,600 baht, and the average total cost per pot is only 12.60 baht. From the data, it can be seen that production costs will be significantly reduced when there is continuous production in large quantities.

Table 6. Total cost analysis

Specification	50 pots	500 pots	1,000 pots
Direct materials (DM)	125	1,250	2,500
Direct labor (DL)	250	2,500	5,000
Manufacturing overhead-variable cost (OHVC)	205	2,050	4,100
Manufacturing overhead-fixed cost (OHFC)	1,000	1,000	1,000
Total cost (baht)	**1,580**	**6,800**	**12,600**
Averrage cost/pice (baht)	**31.60**	**13.60**	**12.60**

Break-even analysis (Table 7) found that if the selling price of a pot is set at 35 baht per pot, at least 43 pots must be produced per cycle to reach the break-even point. However, when the pots are sold together with the plants for 100 baht per set, the break-even point is 15 sets per production cycle. Therefore, selling the pots with the plants is an interesting way to achieve a better break-even point.

ASEAN J. Sci. Tech. Report. **2025**, *28*(3), e256615.

10 of 12

Table 7. Break-even point analysis

Specification	Pot	Pot+Plant
Selling Price (Baht)	35	100
Direct Materials (DM)	2.5	2.5
Direct Labor (DL)	5	5
Manufacturing Overhead-Variable cost (OHVC)	4.1	24.1
Manufacturing Overhead-Fixed cost (OHFC)	1,000	1,000
Break-even point	42.74	14.61

Gross profit margin analysis (Table 8) shows that the production of 500 pots will have a gross profit margin of 61.14%, and the production of 1,000 pots will have a similar gross profit margin of 64%. The gross profit margin from producing 1,000 pots was found to be 66.40%, and when producing pots with plants, the gross profit margin was found to be 61.40%. The data shows that higher volume production will result in higher gross profit margins, resulting in lower total production costs.

Table 8. Gross Profit Margin analysis

Specification	500 Pots	1,000 Pots	500 (Pots+Plants)	1,000 (Pots+Plants)
Selling Price (Baht)	17,500	35,000	50,000	100,000
Cost of Sales (Baht)	6,800	12,600	16,800	32,600
Gross Profit Margin (%)	**61.14%**	**64.00%**	**66.40%**	**61.40%**

3.7 Technology transfer to the community

To generate an income from waste materials and to create a learning site for tourism in the screw pine weaving community, Khlong U-Tapao Watershed, Songkhla Province, the fabrication technology of cement pots reinforced with SLW was transferred to the screw pine leaf basketry products group, Mae Tom Sub-district, Bang Klam District, Songkhla Province (Figure 9). The community has applied the production process of cement pots reinforced with SLW as a part of CBT activity, which has received good interest from tourists.

Figure 9. A) technology transfer to the community, B) production of pots to promote CBT

4. Conclusions

The work presented the strategy for product development of cement-based composites using SLW from weaving production in Khlong U-Tapao Watershed Community, Mae Thom Sub-district, Bang Klam District, Songkhla Province. SLW from the community's basketry production process could be used as reinforced material for cement pots. The ratios of raw materials, including SLW, cement, and water, play a key role in compressive strength. The optimum ratio of the material was 1:30:30 (w/w), and the highest compressive strength was 15.35±0.63 kg/cm^2. The density was 1,100±0.08 kg/m^3, meeting the Thai Industrial standard, TIS 878-2537 requirement. The water absorption property of the pot can be controlled by using a

ASEAN J. Sci. Tech. Report. **2025**, *28*(3), e256615.

11 of 12

water-repellent substance, which could reduce water adsorption from 38.38 to 33.78%. When this process was used to produce cement pots mixed with fiber, it was found that the cement pots refocused with SLW produced had the same properties as fiber cement composite with SLW. From the study of customer satisfaction, it was found that customers were delighted. The production capacity is 1,000 pots, costing 12,600 baht, and the average cost per pot is 12.60 baht. If sold at 35 baht per pot, there will be a gross profit margin of 64.00%. Therefore, cement pots reinforced with waste material, such as SLW, can be an alternative way to manage waste. The prototype pots from this research use 20 grams of fiber per pot, and larger amounts of SLW can be used when producing larger pots. When the technology is transferred to the community, it can generate income directly by selling pot and indirectly as it can be part of the activity in CBT.

5. Acknowledgements

References

[1]   Faridul Hasan; K.M.; Horváth, P. G.; Alpár, T. Lignocellulosic Fiber Cement Compatibility: A State of the Art Review. *Journal of Natural Fibers*, **2021.** https://doi.org/10.1080/15440478.2021.1875380.

[2]   Karade, S.R. Cement-bonded composites from lignocellulosic wastes. *Construction and Building Materials*, **2010**, *24*, 1323-1330. https://doi.org/10.1016/j.conbuildmat.2010.02.003.

[3]   Olaoye, R.A.; Oluremi, J. R.; Ajamu, S.O. The use of fibre waste as complement in concrete for a sustainable environment. *Innovative Systems Design and Engineering*, **2012**, *4*(9), Special Issue. 91-98.

[4]   Sheltami, R.M.; Abdullah, I.; Ahmad, I.; Dufresne, A.; Kargarzadeh, H. Extraction of cellulose nanocrystals from mengkuang leaves (Pandanus tectorius). *Carbohydrate Polymers*, **2012**, *88*, 772-779. https://doi.org/10.1016/j.carbpol.2012.01.062.

[5]   Kriker, A.; Debicki, G.; Bali, A.; Khenfer, M.M.; Chabannet, M. Mechanical properties of date palm fibres and concrete reinforced with date palm fibres in hot-dry climate. *Cement & Concrete Composites*, **2005**, *27*, 554-564. https://doi.org/10.1016/j.cemconcomp.2004.09.015.

[6]   Asrial; Antariksa; Leksono, A.S.; Indriyani, S. Palmyra Fiber as Additional Materials on Solid Concrete Brick of Aggregate. *Mediterranean Journal of Social Sciences*, **2017**, *8*(1), 410-418. https://doi.org/10.5901/mjss.2017.v8n1p410.

[7]   Momoh, E.O.; Osofero, A.I. Recent developments in the application of oil palm fibers in cement composites. *The Frontiers of Structural and Civil Engineering*, **2020**, *14*(1), 94-108. https://doi.org/10.1007/s11709-019-0576-9.

[8]   Abduh, M.Y.; Manurung, R.; Faustina, A.; Affanda, E.; Siregar, I.R.H. Bioconversion of Pandanus tectorius using black soldier fly larvae for the production of edible oil and protein-rich biomass. *Journal of Entomology and Zoology Studies*, **2017**, *5*(1), 803-809.

[9] Sahakitpichan, P.; Chimnoi, N.; Thamniyoma, W.; Ruchirawat, S.; Kanchanapoom, T. Aromatic rutinosides from the aerial roots of *Pandanus tectorius*. *Phytochemistry Letters*, **2020**, *37*, 47–50. https://doi.org/ 10.1016/j.phytol.2020.04.008.

[10] ASTM C642-21. Standard Test Method for Density, Absorption, and Voids in Hardened Concrete; American Society for Testing and Materials: West Conshohocken, PA, USA, **2022**. ttps://doi.org10.1520/C0642-13.10.

[11] ASTM C39/C39M-21. Standard Test Method for Compressive Strength of Cylindrical Concrete Specimens. ASTM International, West Conshohocken, PA, USA, **2023.** ttps://doi.org10.1520/C0039_C0039M-21.

[12] Podkumnerd, N.; Wunsri, S.; Rattanankit, T. Product development process of nipa paper from nipa palm (*Nypa fruticans* Wrumb.) waste materials for sustainability of Palian Rever basin community. *Journal of Community Development and life Quality*, **2019**, *7*(3), 271-282. (In Thai)

[13] Kotler, P. and Keller, K. L. *Marketing management* (15th ed.). Pearson, 2016.

[14] Yamane, T. *Statistic:An introductory statistics* (2nd ed.). Harper & Row, 1973.

[15] Likert, R. A technique for the measurement of attitudes. *Archives of Psychology*, **1932**, *22*(140), 1-55.

[16] Horngren, C. T.; Datar, S. M.; Rajan, M. V. *Cost accounting: A managerial emphasis* (14th ed.). Prentice Hall, **2012**.

[17] Garrison, R. H.; Noreen, E. W.; Brewer, P. C. *Managerial accounting* (17th ed.). McGraw-Hill Education, **2021**.

[18] Cooper, R.; Kaplan, R. S. Measure costs right: Make the right decisions. *Harvard Business Review*, **1988**, *66*(5), 96-103.

[19] Ministry of Industry. Thai Industrial standard, TIS. 878-2537, Cement bonded particle boards: High density. Thailand Industrial Standards Institute, Bangkok. **1994**.

[20] Ogunjobi, K.M.; Ajibade, M.A.; Gakenou, O. F.; Gbande, S. Physical and mechanical properties of cement-bonded particle board produced from *Anogeissus leiocarpus* (DC.) Guill and Perr wood species. *African Journal of Agriculture Technology and African Journal of Agriculture Technology and Environment*, **2019**, *8*(1), 192-199.

[21] Usman, M.; Khan, A.Y.; Farooq, S.H.; Hanif, A.; Tang, S.; Khushnood, R.A.; Rizwan, S.A. Eco-friendly self-compacting cement pastes incorporating wood waste as cement replacement: A feasibility study. *Journal of Cleaner Production*, **2018**, *190*, 679-688. https://doi.org/10.1016/j.jclepro.2018.04.186.

[22] Lertwattanaruk, P.; Suntijitto, A. Properties of Natural fiber cement materials containg coconut coir and oil palm fibers for manufacture of buliding material. *Journal of Architectural/Planning Research and Studies*, **2012**, *9*(1), 113-124. (In Thai) https://doi.org/10.56261/jars.v9i1.168602

Prevalence, Antimicrobial Resistance, and Genetic Relationship of Methicillin-Resistant *Staphylococcus aureus* from Meats, Hat-Yai, Thailand

Pharanai Sukhumungoon[1*], Lalita Nuwilai[2], Marisa Boontaworn[3], and Pattamarat Rattanachuay[4]

[1] Faculty of Science, Prince of Songkla University, Songkhla, 90110, Thailand

[2] Faculty of Science, Prince of Songkla University, Songkhla, 90110, Thailand

[3] Faculty of Science, Prince of Songkla University, Songkhla, 90110, Thailand

[4] Faculty of Science and Technology, Prince of Songkla University, Pattani campus, Pattani, 94000, Thailand

* Correspondence: pharanai82@gmail.com

Abstract: Methicillin-resistant *Staphylococcus aureus* (MRSA) is a dangerous pathogen that can cause serious illnesses, leading to morbidity and mortality worldwide. Food items, especially meats, can contaminate it. In this study, a total of 100 meat samples were investigated for MRSA. The results demonstrated the MRSA prevalence in meats as 2.84% (4/141 isolates). Three MRSA strains were obtained from pork, while 1 from beef (p-value < 0.05). It was discovered that all 4 MRSA showed the same virulence gene profiles. The α-hemolysis and catalase production were positive for all 4 MRSA strains. Antimicrobial susceptibility assay showed that all but one MRSA strains were resistant to streptomycin, chloramphenicol, and tetracycline. MRSA strain LN-4 from beef was resistant to an extra antimicrobial agent, clindamycin. MRSA typing using BOX-PCR discovered that 3 MRSA strains (LN-1 to LN-3) from pork and 1 (LN-4) from beef were identical in DNA fingerprint, suggesting the close genetic relationship among strains from 2 different meat samples. This study demonstrates the presence of MRSA from meats in the south of Thailand. Even though they exist in low amounts, their virulence traits are thought to be harmful and cause diseases. Thus, MRSA contamination in meats should be immediately paid attention to for public health.

Keywords: *Staphylococcus aureus*; *mecA*; MRSA; meat

1. Introduction

Nosocomial infections caused by methicillin-resistant *Staphylococcus aureus* (MRSA) have emerged as important problems worldwide [1-3]. Methicillin resistance is mediated through the *mec* operon, a part of the Staphylococcal cassette chromosome *mec* (*SCCmec*) [4]. MRSA carries *mecA* encoding penicillin-binding protein 2a (PBP2a), responsible for low binding affinity to β-lactam antibiotics [5]. This β-lactam antibiotic-resistant capability reinforces *S. aureus* to be more virulent, thereby exacerbating the severity of the disease and prolonging the therapeutic period [6]. The severity of the disease could be worsened in elderly and immunocompromised patients [7]. In addition to its role in nosocomial infection, MRSA is also associated with intestinal tract infections by producing staphylococcal enterotoxins (SEs) and toxic shock syndrome toxin (TSST) [7]. There was a report of an acute community-acquired

gastroenteritis outbreak involving infection of staphylococcal enterotoxin C-producing MRSA and the consumption of coleslaw from a delicatessen [8]. Thus, foods are thought to be the important vehicle of MRSA. Meat is one of the important vehicles transporting several ferocious bacteria, including MRSA [9-11], and those MRSA strains carry numerous virulence genes and are resistant to antimicrobial agents. Therefore, surveillance of MRSA in food sources, especially meats, remains indispensable to prevent large morbidities and mortalities.

Thus, this study aims to report the prevalence, virulence profiles, antimicrobial susceptibility profiles, and genetic relationship of MRSA from meats marketed in southern Thailand. This information should be of importance to the public health of Thailand.

2. Materials and Methods

2.1 Sample collection

100 meat samples (40 beef, 30 pork, and 30 chicken) were collected from open markets throughout Hat-Yai City, Songkhla province, southern Thailand, from November 2022 to January 2023. Samples were processed within 2 hours, as previously described by Bunnoeng et al. [10]. In short, a 10 g of meat was mixed using a CIR-400 stomacher (Seward, West Sussex, UK) with 90 ml of tryptic soy broth (TSB) (Becton Dickinson, Sparks, MD, USA) for 1 minute. The liquid portion was separated and incubated at 37°C for 6 hours. One hundred µl aliquot of 10^{-3} dilution of the culture broth was spread on Mannitol Salt agar (MSA) (Becton Dickinson) and incubated at 37°C for 18 hours. Five to 10 typical colonies per sample were randomly selected for further molecular analyses.

2.2 MRSA identification by detecting *mecA* and *nuc*

Genomic DNA (gDNA) of the bacterial isolates was prepared as described by Pannuch et al. [12]. In brief, a single colony was cultured in 3 ml of TSB for 3 hours at 37°C with 150 rpm agitation. One ml aliquot of culture solution was boiled for 10 minutes, then placed on ice for 5 minutes, centrifuged at 11,000 *g* for 10 minutes, and the supernatant was diluted 10 folds with sterile deionized water. Amplification of *mecA* and *nuc* was performed as described by Bunnueang et al. [7] using specific primer pairs (Table 1). PCR was performed in a 25-µl reaction mixture comprising 3.0 mM $MgCl_2$, 0.1 mM dNTPs, 0.4 µM each primer pair, 0.5 U Go*Taq* DNA polymerase (Promega, Madison, WI, USA), 1X Go*Taq* Flexi green buffer, and 2 µl of bacterial gDNA. Thermocycling was conducted in a T100TM Thermal Cycler (Bio-Rad, Hercules, CA, USA). The PCR conditions were as follows: 95°C for 3 minutes, followed by 35 cycles of 94°C for 1 minute, 50°C for 1 minute (for both *mecA* and *nuc*), and 72°C for 1 minute, with a final step at 72°C for 5 minutes. Amplified products were analyzed using 1.0 % agarose gel electrophoresis, stained with ethidium bromide, and imaged using WSE-5200 Printpraph 2M gel imaging system (ATTO Corp., Tokyo, Japan). *S. aureus*, which carries both *mecA* and *S. aureus*-specific *nuc* genes, was classified as MRSA.

2.3 Virulence gene assay

Five virulence genes other than *mecA* (*coa*, *luk-PV*, *vWbp*, *spa*, and *sea*) were examined using uni-plex PCR as previously described [13]. The 25-µl reaction consisted of 3.0 mM $MgCl_2$, 0.1 mM dNTPs, 0.4 µM each primer pair (listed in Table 1), 0.5 U Go*Taq* DNA polymerase (Promega), 1X Go*Taq* Flexi buffer, and 2 µl of gDNA solution. Thermocycling conditions were as follows: 95°C for 3 minutes, followed by 35 cycles of 94°C for 1 minute, 50 °C for 1 minute (*coa*, *vWbp*, *sea*) or 55°C for 1 minute (*spa*), or 57°C for 1 minute (*luk-PV*), and 72°C for 1 minute (1.5 minutes for *spa*). The reaction was finalized at 72°C for 5 minutes. Amplicons were analyzed as described above.

2.4 Hemolysis and other virulent characteristics of MRSA

Hemolysis on blood agar and catalase production were also examined to seek their additional virulent characteristics. An overnight bacterial colony was spotted on blood agar for hemolysis assay and incubated at 37°C for 18 hours. Alpha (α), beta (β), or gamma (γ) hemolysis was observed macroscopically. Catalase production assay was examined using a 3% H_2O_2 solution. Additionally, a coagulase tube and slide test using rabbit serum were also employed to observe the coagulation by MRSA.

Table 1. Oligonucleotide primers used in the study

Target gene	Name	Sequence (5′ to 3′)	Amplicon size (bp)	Reference
mecA	mecA1	GTAGAAATGACTGAACGTCCGATAA	310	[28]
	mecA2	CCAATTCCACATTGTTTCGGTCTAA		
luk-PV	luk-PV1	ATCATTAGGTAAAATGTCTGGACATGATCCA	433	[29]
	luk-PV2	GCATCAASTGTATTGGATAGCAAAAGC		
coa	COA1	CGAGACCAAGATTCAACAAG	730	[30]
	COA2	AAAGAAAACCACTCACATCAGT		
vWbp	vWbp-F	GCTGGATTAAATGGTGAAAGTCATG	320	[10]
	vWbp-R	GTTTATTAAAACGTTTTTGATGACC		
spa	SPA1	ATCTGGTGGCGTAACACCTG	1,500	[30]
	SPA2	CGCTGCACCTAACGCTAATG		
sea	SEA-F	GCAGGGAACAGCTTTAGGC	520	[31]
	SEA-R	GTTCTGTAGAAGTATGAAACACG		
nuc	nuc1	GTAGGTGGCAAGCGTTATCC	279	[32]
	nuc2	CGCACATCAGCGTCAG		
boxA	BOXA1R	CTACGGCAAGGCGACGCTGACG	Variable	[15]

2.5 Antimicrobial susceptibility assay

All MRSA strains were examined for their antimicrobial susceptibility using the disk diffusion method [14]. Ten common antimicrobial agents used in this assay were as follows: amikacin (30 μg), ampicillin (10 μg), cephalothin (30 μg), chloramphenicol (30 μg), clindamycin (2 μg), erythromycin (30 μg), gentamicin (10 μg), kanamycin (30 μg), tetracycline (30 μg), and streptomycin (10 μg) (Oxoid Hampshire, UK). Vernier caliper measured the clear zone.

2.6 MRSA typing by BOX-PCR

BOX-PCR of MRSA strains was carried out as previously described by Versalovic et al. [15]. Shortly, a 25-μl reaction mixture comprising 0.2 μM BOXA1R primer (Table 1), 0.2 mM dNTPs, 1X Go*Taq* DNA polymerase buffer (Promega), 3.0 mM MgCl 2, 1.25 U Go*Taq* DNA polymerase (Promega) and 50 ng of DNA [prepared by a glass fiber matrix spin column method (Geneaid, Taipei, Taiwan)] was subjected to thermocycling as described above. Thermocycling condition was as follows: 95°C for 3 minutes; then 30 cycles of 94°C for 3 seconds, 92°C for 30 seconds, 50°C for 60 seconds, and 65°C for 8 minutes. Amplified products were separated using 1.5% agarose gel-electrophoresis at 100V for 1 hour and imaged as described above.

2.7 Statistical analysis

One-way ANOVA was employed to compare the prevalence of MRSA among meat types. Significance was set at p-value < 0.05.

3. Results and Discussion

3.1 Prevalence of MRSA from meats

In this study, we tried to isolate *S. aureus* as much as possible. A total of 141 typical colonies on MSA from 100 meat samples could be obtained. Among them, 4/141 isolates (2.84%) from 2 meat samples (prevalence of 2%) were identified as MRSA (Table 2). Three MRSA were obtained from pork while 1 from beef (p-value < 0.05). The absence of MRSA from chicken in this study was thought that bacterial contamination on meat did not reach the detectable limit. The quantity of bacterial contamination on meat samples varied from study to study. One investigation conducted in the same geographical area in 2013 revealed a high level of MRSA contamination in chicken at 57.14% with 40 MRSA strains isolated [10]. In addition, 37.1% of MRSA prevalence was found in frozen chicken meat in Bangladesh. On top of that, they all were multi-drug resistant strains [16].

The contamination of MRSA (strains LN-1 to LN-4) on meats in this study was found to be from the same open market. *S. aureus* contamination in raw meat and meat products is presumably the result of poor food hygienic handling or contamination directly from the animals themselves [17]. During slaughtering

ASEAN J. Sci. Tech. Report. **2025**, *28*(3), e256114.

4 of 7

processes, MRSA can pollute carcasses, leading to high contamination rates of MRSA on meats at the retail level [18]. Various rates of MRSA contamination in meats have been reported from numerous areas of the world. Many kinds of retail meat were investigated in the Netherlands [19]. They were found to carry MRSA as 10.6%, 10.7%, and 16% in beef, pork, and chicken, respectively [19]. In an additional report from Canada, Weese et al. [20] investigated MRSA in four provinces and found MRSA as 9.6%, 5.6%, and 1.2% in pork, beef, and chicken, respectively. In Thailand, it was thought that the prevalence of MRSA in meats depends, in part, on the time point of sampling and geographical location. This study revealed MRSA isolation rates in pork as 9.38% (3/32 samples), while the study in the same geographical area from Bunnoeng et al. [10] revealed 50% (8/16 samples). This suggests that there can be different MRSA contamination rates in different time intervals. Likewise, Tanomsridachchai et al. [21] investigated MRSA in pork samples in the central part of Thailand and found MRSA at a high level of 44.8% (52/116).

Table 2. Prevalence of methicillin-resistant *Staphylococcus aureus* from meats

Meat type	No. of positive sample / No. of sample (%)	No. of MRSA-positive isolates / Total isolates (%)
Chicken	0/30[C] (0)	0/80 (0)
Pork	1/30[B] (3.33)	3/32 (9.38)
Beef	1/40[A] (2.5)	1/30 (3.33)
Total	2/100 (2)	4/141 (2.84)

Uppercase letters indicate significant differences among meat types (*p*-value < 0.05).

3.2 Virulence gene and other virulent traits

Virulence genes frequently found in *S. aureus* were also investigated in 4 MRSA strains (LN-1 to LN-4) in this study. It was discovered that all 4 MRSA showed the same virulence gene profiles (Table 3) and exhibited catalase production and α-hemolysis on blood agar. Both coagulase tube and slide tests were negative, corresponding to the lack of *coa* and vWbp genes. The absence of important virulence genes in MRSA in this study is unsurprising since a similar phenomenon can be found in our previous work in 2016 [10]. Of 185 MRSA isolates from meats, none exhibited the presence of *coa* (coding for coagulase responsible for plasma clotting), *luk-PV* (coding for Panton-valentine leukocidin, a pore-forming toxin responsible for necrotizing disease), and *sea* (coding for staphylococcal enterotoxin A responsible for food poisoning). However, a few strains revealed the presence of *vWbp* (coding for von Willebrand factor binding protein) and *spa* (coding for Staphylococcal protein A) [10]. It is inconclusively shown that MRSA strains LN-1 to LN-5 are naive since they may be equipped with many virulence factors to combat host defense systems. Catalase production in these MRSA is one of their virulence traits that should not be overlooked since it can protect them from H_2O_2-mediated leukocytic bactericidal mechanism, resulting in bacterial survival [22].

Table 3. Virulence characteristics of 4 MRSA strains isolated from meats

Sample number (meat type)	Strain designation	Virulence gene						Hemolysis	Catalase	Drug resistance
		mecA	*coa*	*luk-PV*	*spa*	*vWbp*	*sea*			
No. 40 (pork)	LN-1	+	-	-	-	-	-	α	+	C, S, TE
	LN-2	+	-	-	-	-	-	α	+	C, S, TE
	LN-3	+	-	-	-	-	-	α	+	C, S, TE
No. 93 (beef)	LN-4	+	-	-	-	-	-	α	+	C, S, TE, DA

*C, chloramphenical; DA, clindamycin; S, streptomycin; TE, tetracycline.

3.3 Antimicrobial susceptibility assay

Antimicrobial susceptibility assay revealed that all but one MRSA strains were resistant to streptomycin, chloramphenicol, and tetracycline. MRSA strain LN-4 from beef also showed extra resistance to clindamycin (Table 3). Various MRSA strains from clinical and raw meat samples around the world are documented to be resistant to many antimicrobial agents [23,18]. In the Western hemisphere, O'Brien et al.

ASEAN J. Sci. Technol. Report. **2025**, *28*(3), e256114.

5 of 7

[23] investigated MRSA from pork products at the retail level in Iowa, Minnesota, and New Jersey, USA. They discovered that MRSA isolates were resistant to clindamycin, erythromycin, and tetracycline at 34.6%, 38.5%, and 65.4%, respectively. Also, Jackson et al. [24] collected retail pork and beef products (100 each) from 14 retail food stores in Athens, Georgia, USA, in 2009 to search for MRSA. Twenty-five percent (1/4 strains) of MRSA from beef samples was shown to resist clindamycin and tetracycline, while 33.3% (1/3 strains) of MRSA from pork was resistant to clindamycin. In the Eastern hemisphere, the antimicrobial resistance rate was much higher. A nationwide investigation of MRSA from numerous retail food items was performed in China between 2011 and 2016 [25]. Among 108 MRSA strains obtained, 41/108 (38%), 86/108 (79.6%), and 71/108 (65.7%) MRSA strains were resistant to chloramphenicol, clindamycin, and tetracycline, respectively. Focusing on tetracycline, the study from China and our present study concord with the work from Pakistan that demonstrated 100% resistance [26]. High bacterial resistance to tetracycline is not surprising since this antimicrobial agent is inexpensive. Thus, it has been extensively used for prophylaxis and therapy of humans and animals. Moreover, it is used at sub-therapeutic levels as an animal growth promoter [27]. More importantly, tetracycline-resistant genes are effectively transferred among bacterial species. Therefore, the effectiveness of this antimicrobial agent in treating MRSA infections should be noted.

3.4 BOX-PCR profiling of MRSA

According to MRSA's genotype and phenotype similarities in this current study, DNA typing using BOX-PCR was performed to seek their genetic relationship. It was revealed that 3 MRSA strains (LN1 to LN-3) from pork and 1 (LN-4) from beef showed identical DNA fingerprints by BOX-PCR (Figure 1) even though MRSA strain LN-4 demonstrated an extra clindamycin resistance compared to the other three. This is probably explained by the dissociation between *boxA* and the clindamycin-resistant gene, resulting in the undisturbed DNA fingerprint. Interspersed repetitive-element PCR (rep-PCR) is broadly employed for bacterial typing since the repetitive elements dispersed throughout the bacterial genome are greatly conserved. BOX elements demonstrate a striking ability for DNA fingerprinting generation among repetitive elements. Among 3 BOX subunits, *boxA* (57 bp), *boxB* (43 bp), and *boxC* (50 bp), only *boxA* is highly conserved [15]. Therefore, *boxA* is used to generate reliable and reproducible DNA fingerprints. BOX-PCR is mainly inexpensive and easy to perform. It is thus an excellent approach for investigating bacterial genetic relationships.
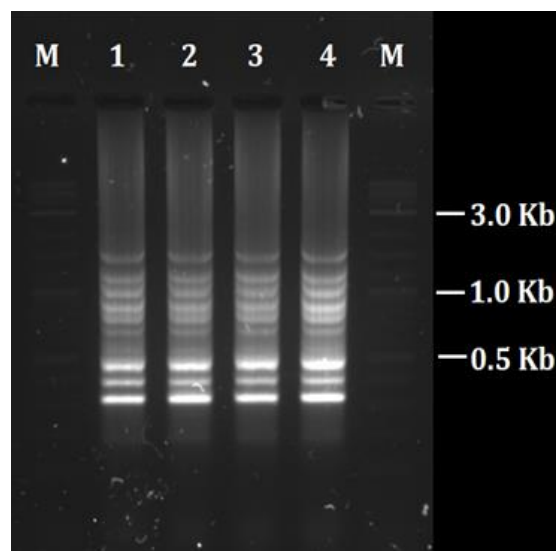
Figure 1. BOX-PCR of MRSA from meats. Lanes 1-4 are MRSA strain LN-1 to LN-4, respectively. Lane M is 2 2-log DNA ladder (New England Biolabs, USA).

4. Conclusions

Pathogenesis by *S. aureus* is a multifactorial process dependent on the presence and expression of several virulence factors. Moreover, some *S. aureus* strains show resistance to various antimicrobial agents. Thus, the contamination of MRSA in meats should be paid immediate attention. Surveillance of MRSA in

meats should be performed to gain data on prevalence and virulence, including the antimicrobial-resistant pattern, for the benefit of the population in Thailand.

5. Acknowledgements

Conflicts of Interest: The authors declare no conflict of interest.

References

[1]　de Sousa, M.A.; Bartzavali, C.; Spiliopoulou, I.; Sanches, S.; Crisóstomo, M.I.; de Lencastre, H. Two international methicillin-resistant Staphylococcus aureus clones endemic in a University hospital in Patras, Greece. *Journal of Clinical Microbiology*. **2003**, *41*, 2027-2032.

[2]　Johnson, A.P.; Pearson, A.; Duckworth, G. Surveillance and epidemiology of MRSA bacteraemia in the UK. *Journal of Antimicrobial Chemotherapy*. **2005**, *56*, 455-462.

[3]　 Witte, W.; Strommenger, B.; Cuny, C.; Heuck, D.; Nuebel, U. Methicillin-resistant Staphylococcus aureus containing the Panton-Valentine leucocidin gene in Germany in 2005 and 2006. *Journal of Antimicrobial Chemotherapy*. 2007, *60*, 1258-1263.

[4]　El Karamany, I.M.; Ibrahim, Y.M.; Abouwarda, A.M.; Essam, T.M.; Amin, M.A. Detection of high levels of methicillin and multidrug resistance among clinical isolates of Staphylococcus aureus. *African Journal of Microbiology Research*. **2013**, *7*, 1598-1604.

[5]　Mostafa, S.I. Molecular typing of methicillin resistant Staphylococcus aureus by spa gene polymorphism. *African Journal of Microbiology Research*. **2013**, *7*, 755-759.

[6]　Carbon, C. Costs of treating infections caused by methicillin-resistant Staphylococci and vancomycin-resistant enterococci. *Journal of Antimicrobial Chemotherapy*. **1999**, *44*, 31-36.

[7]　Bunnueang, N.; Kongpheng, S.; Yadrak, P.; Rattanachuay, P.; Khianngam, S.; Sukhumungoon, P. Methicillin-resistant Staphylococcus aureus: 1-year collection and characterization from patients in two tertiary hospitals, southern Thailand. *Southeast Asian Journal of Tropical Medicine and Public Health*. **2016**, *47*, 234-244.

[8]　Jones, T.F.; Kellum, M.E.; Porter, S.S.; Bell, M.; Schaffner, W. An outbreak of community-acquired foodborne illness caused by methicillin-resistant Staphylococcus aureus. *Emerging Infectious Diseases*. **2002**, *8*, 82-84.

[9]　Sukhumungoon, P.; Nakaguchi, Y.; Ingviya, N.; Pradutkanchana, J.; Iwade, Y.;Seto, K.; Son, R.; Nishibuchi, M.; Vuddhakul, V. Investigation of stx2+ eae+ Escherichia coli O157: H7 in beef imported from Malaysia to Thailand. *International Food Research Journal*. **2011**, *18(1)*, 381-386.

[10]　Bunnoeng, N.; Themphachana, M.; Pewleang, T.; Kongpheng, S.; Singkhamanan, K.; Saengsuwan, P.; Sukhumungoon, P. High prevalence and molecular characterization of methicillin-resistant Staphylococcus aureus isolated from retailed meats, south Thailand. *International Food Research Journal*. 2014, *21*, 569-576.

[11]　Seeyankem, B.; Sae-lim, A.; Puangsiri, W.; Rattanachuay, P.; Sukhumungoon, P. Prevalence, virulence, antibiogram profiles, and genetic relationship of Staphylococcus epidermidis from meat in southern Thailand. *Southeast Asian Journal of Tropical Medicine and Public Health*. **2019**, *50(6)*, 1108-1117.

[12]　Pannuch, M.; Sirikaew, S.; Nakaguchi, Y.; Nishibuchi, M.; Sukhumungoon, P. Quantification of enteropathogenic *Escherichia coli* from retailed meats. *International Food Research Journal*. **2014**, *21*, 547-551.

[13]　Sukhumungoon, P.; Hayeebilan, F.; Yadrak, P.; Kanobthammakul, S.; Nakaguchi, Y.; Saengsuwan, P.; Singkhamanan, K. Molecular characterization and relationship of methicillin-resistant Staphylococcus aureus among strains from healthy carriers and university hospital patients, southern Thailand. *Southeast Asian Journal of Tropical Medicine and Public Health*. **2014**, *45*, 402-412.

[14] Clinical and Laboratory Standards Institute (CLSI). Performance standards for antimicrobial susceptibility testing. *Clinical and Laboratory Standards Institute*, 27th edition, Wayne, USA. **2017**.

[15] Versalovic, J.; Schneider, M.; De Bruijn, F.; Lupski, J.R. Genomic fingerprinting of bacteria using repetitive sequence-based polymerase chain reaction. *Methods in Molecular and Cellular Biology*. **1994**, *5(1)*, 25-40.

[16] Parvin, M.S.; Ali, M.Y.; Talukder, S.; Nahar, A.; Chowdhury, E.H.; Rahman, M.T.; Islam, M.T. Prevalence and multidrug resistance pattern of methicillin resistant S. aureus isolated from frozen chicken meat in Bangladesh. *Microorganisms*. **2021**, *9*, 636. https://doi.org/10.3390/microorganisms9030636.

[17] Normanno, G.; Firinu, A.; Virgilio S, Mula, G.; Dambrosio, A.; Poggiu, A.; Decastelli, L.; Mioni, R.; Scuota, S.; Bolzoni, G.; Di Giannatale, E.; Salinetti, A.P.; La Salandra, G.; Bartoli, M.; Zuccon, F.; Pirino, T.; Sias, S.; Parisi, A.; Quaglia, N.C.; Celano, G.V. Coagulase positive Staphylococci and Staphylococcus aureus in food products marketed in Italy. *International Journal of Food Microbiology*. **2005**, *98*, 73-79.

[18] Boost, M.V.; Wong, A.; Ho, J.; O'Donoghue, M. Isolation of methicillin-resistant Staphylococcus aureus (MRSA) from retail meats in Hong Kong. *Foodborne Pathogens and Disease*. **2013**, *10*, 1-6.

[19] de Boer, E.; Zwartkruis-Nahuis, J.T.M.; Wit, B.; Huijsdens, X.W.; de Neeling, A.J.; Bosch, T.; van Oosterom, R.A.A.; Vila, A.; Heuvelink, A.E. Prevalence of methicillin-resistant Staphylococcus aureus in meat. *International Journal of Food Microbiology*. **2009**, *134*, 52-56.

[20] Weese, J.S.; Avery, B.P.; Reid-Smith, R.J. Detection and quantification of methicillin-resistant Staphylococcus aureus (MRSA) clones in retail meat. *Letters in Applied Microbiology*. **2010**, *51*, 338-342.

[21] Tanomsridachchai, W.; Changkaew, K.; Changkwanyeun, R.; Prapasawat, W.; Intarapuk, A.; Fukushima, Y.; Yamasamit, N.; Kapalamula, T.F.; Nakajima, C.; Suthienkul, O.; Suzuki, Y. Antimicrobial resistance and molecular characterization of methicillin-resistant Staphylococcus aureus isolated from slaughtered pigs and pork in the central region of Thailand. *Antibiotics*. **2021**, *10*, 206.

[22] Das, D.; Bishayi, B. Staphylococcal catalase protects intracellularly survived bacteria by destroying H_2O_2 produced by the murine peritoneal macrophages. *Microbial Pathogenesis*. **2009**, *47*, 57-67.

[23] O'Brien, A.M.; Hanson, B.M.; Farina, S.A.; Wu, J.Y.; Simmering, J.E.; Wardyn, S.E.; Forshey, B.M.; Kulick, M.E.; Wallinga, D.B.; Smith, T.C. MRSA in conventional and alternative retail pork products. *PloS One*. **2012**, *7*, 1-6.

[24] Jackson, C.R.; Davis, J.A.; Barrett, J.B. Prevalence and characterization of methicillin-resistant Staphylococcus aureus isolates from retail meat and humans in Georgia. *Journal of Clinical Microbiology*. **2013**, *51(4)*, 1199–1207.

[25] Wu, S.; Huang, J.; Zhang, F.; Wu, Q.; Zhang, J.; Pang, R.; Zeng, H.; Yang, X.; Chen, M.; Wang, J.; Dai, J.; Xue, L.; Lei, T.; Wei, X. Prevalence and characterization of food-related methicillin-resistant Staphylococcus aureus (MRSA) in China. *Frontiers in Microbiology*. **2019**, *10*, 304.

[26] Sadiq, A.; Samad, M.; Saddam; Basharat, N.; Ali, S.; Roohulla; Saad, Z.; Khan, A.N.; Ahmad, Y.; Khan, A.; Khan, J. Methicillin-Resistant Staphylococcus aureus (MRSA) in slaughter houses and meat shops in capital territory of Pakistan during 2018–2019. *Frontiers in Microbiology*. **2020**, *11*, 577707.

[27] Chopra, I.; Roberts, M. Tetracycline antibiotics: Mode of action, applications, molecular biology, and epidemiology of bacterial resistance. *Microbiology and Molecular Biology Reviews*. **2001**, *65*, 232-260.

[28] Geha, D.J.; Uhl, J.R.; Gustaferro, C.A.; Persing, D.H. Multiplex PCR for identification of methicillin-resistant staphylococci in the clinical laboratory. *Journal of Clinical Microbiology*. **1994**, *32*, 1768-1772.

[29] Lina, G.; Piémont, Y.; Godail-Gamot, F.; Bes M.; Peter, M.O.; Gauduchon, V.; Vandenesch, F.; Etienne, J. Involvement of Panton-Valentine Leuko¬cidin-producing Staphylococcus aureus in primary skin infections and pneumonia. *Clinical Infectious Diseases*. **1999**, *29*, 1128-1132.

[30] Wichelhaus, T.A.; Hunfeld, K.P.; Böddinghaus, B.; Kraiczy, P.; Schäfer, V.; Brade, V. Rapid molecular typing of methicillin-resistant Staphylococcus aureus by PCR-RFLP. *Infection Control & Hospital Epidemiology*. **2001**, *22*, 294-298.

[31] Monday, S.R.; Bohach, G.A. Use of multiplex PCR to detect classical and newly described pyrogenic toxin genes in Staphylococcal isolates. *Journal of Clinical Microbiology*. **1999**, *37*, 3411-3414.

[32] Zhang, K.; Sparling, J.; Chow, B.L.; Elsayed, S.; Hussain, Z.; Church, D.L.; Gregson, D.B.; Louie, T.; Conly, J.M. New quadriplex PCR assay for detection of methicillin and mupirocin resistance and simultaneous discrimination of Staphylococcus aureus from coagulase-negative staphylococci. *Journal of Clinical Microbiology*. **2004**, *42*, 4947-4955.

Konjac Biodegradable Film for Packing Thai Caramel

Anodar Ratchawet[1*], Anan Kanja[2], and Atinut Joradol[3]

[1] Chemistry Department, Faculty of Science and Technology, Chiangmai Rajabhat University, Chiangmai, 50300, Thailand
[2] Chemistry Department, Faculty of Science and Technology, Chiangmai Rajabhat University, Chiangmai, 50300, Thailand
[3] Biology Department, Faculty of Science and Technology, Chiangmai Rajabhat University, Chiangmai, 50300, Thailand
[*] Correspondence: anodar_rat@g.cmru.ac.th

Abstract: This study explores the development of natural, edible packaging materials derived from fresh konjac corms (*Amorphophallus muelleri* Blume.) for producing konjac powder and biodegradable films under controlled casting conditions. The films were formulated using a 1% konjac solution, with glycerol added at varying concentrations (0%, 0.1%, and 0.2% v/v). Among the tested formulations, the film without glycerol demonstrated the best performance. Physical characterization showed an average film weight of 0.4436 ± 0.0071 g (total solution weight: 40.0053 ± 0.0056 g), a thickness of 0.048 ± 0.002 mm, and a tensile strength of 2.497 ± 0.044 N/cm². Water solubility tests revealed that the glycerol-free film dissolved quickly, with an average water permeability time of 1.17 ± 0.03 minutes. When applied as a wrapping material for Thai caramel, the glycerol-free film maintained its structural integrity for over 30 days. It preserved the product's quality for up to three months without mold growth. These findings highlight the potential of konjac-based films as a sustainable, biodegradable alternative to conventional synthetic packaging, particularly for food products like Thai caramel.

Keywords: Thai caramel; Konjac; Biodegradable film; Food wrapping

1. Introduction

The excessive use of plastic packaging has become a significant concern for consumers and the environment. Plastic packaging may contain substances linked to cancer in the lungs, liver, lymph nodes, and skin. Furthermore, the persistent increase in plastic use poses challenges for waste management due to its prolonged decomposition time [1]. To address these issues, natural and biodegradable materials have garnered increasing attention as alternatives to plastic. Konjac, an agricultural cash crop widely cultivated in Thailand, offers promising potential in this context. This biennial plant thrives nationwide and is often found along forest edges or cultivated areas. Renowned for its culinary and medicinal uses, konjac has been a staple in Japanese and Chinese diets for centuries as a healthful food. In Thailand, it is traditionally consumed in rural areas, where it has been used to prepare various dishes and desserts. It is sold in local markets across provinces like Prachin Buri, Phitsanulok, Nan, and Chiang Mai. Every part of the plant—including its tuber, stem, stalk, and young flowers—is utilized in traditional cooking, with the tuber requiring processing to remove potential irritants through methods such as boiling, grilling, or steaming. These components are commonly included in sour soup or red curry, while the flowers are often eaten with chili.[2]

Konjac contains glucomannan, a natural, high-molecular-weight fiber composed of glucose and mannose in a 2:3 ratio. Extracted from the tuber

ASEAN J. Sci. Tech. Report. **2025**, 28(3), e255974.

2 of 14

through a process that removes toxins, glucomannan forms a viscous solution when dissolved in water. Upon drying, this solution transforms into a sticky, rigid film, as shown in Figure 1. Edible films made from konjac glucomannan can extend food shelf life by preventing gas and moisture penetration. These films represent a safer, more degradable alternative to plastic films. Numerous studies have explored konjac-based films' properties and applications. For instance, Piyanus Noiduang et al. [3] investigated starch film production using Chinese water chestnut, revealing that film properties such as thickness, elongation, and water vapor permeability varied with starch and glycerol concentrations. Similarly, konjac films demonstrate remarkable stability in various conditions, including exposure to heat, cold, acidity, and alkalinity. The films are soft, durable, and can be produced in transparent, semi-transparent, and opaque forms. Studies also highlight how blending konjac glucomannan with gelatin and starch can enhance the film's mechanical properties, flexibility, and potential applications in food packaging, including wrapping fruits [4-8].

Additionally, konjac powder exhibits a gel-forming property when mixed with water. This gel promotes satiety, reduces food intake, and absorbs excess fats, cholesterol, and sugars, facilitating their removal. Research by Lamul Wiset et al. [9] further emphasizes the influence of drying temperature and glycerol concentration on konjac film properties, demonstrating improvements in tensile strength, elongation, and water vapor permeability with the addition of glycerol. Such advancements position konjac-based films as a sustainable and functional alternative to conventional plastic packaging. In addition to their environmental benefits, konjac-based films offer significant health advantages, primarily due to their glucomannan content. This natural dietary fiber promotes satiety, aids in reducing cholesterol and sugar absorption, and supports digestive health by enhancing waste elimination. These properties have been associated with preventing colon cancer and managing conditions such as obesity and diabetes [10]. Building on these benefits, the present study seeks to develop edible konjac powder films tailored for wrapping Thai caramel. This innovation addresses environmental waste concerns and adds value to Thailand's abundant konjac resources, showcasing the potential for creating sustainable, functional, and biodegradable packaging solutions.
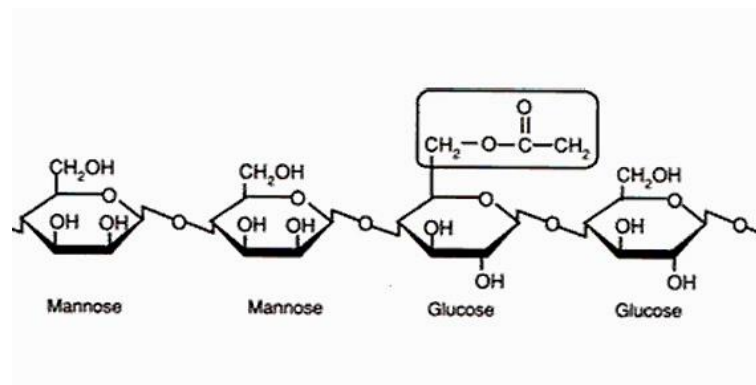
Figure 1. The structure of glucomannan. [10].

Source: http://www.foodnetworksolution.com/

Objective

1. Study methods and suitable conditions for extracting edible konjac powder from fresh konjac tube
2. Investigate the formation of wrapping Thai caramel film from edible konjac powder.
3. To evaluate the impact of edible packaging using films made from konjac powder

2. Materials and Methods

Sample Konjac powder is used in film form. It is a konjac powder extracted from the edible gazelle konjac variety (such as *A. muelleri* Blume found in Mae Wang District, Chiang Mai Province. **Instrument** 1) Analytical balance, AG 245, METTLER TOLEDO, Switzerland. 2) Hot air oven, DLE 500, MERMERT, Germany.

3) High-speed centrifuge, UNIVERSAL 32, Heffich, Germany. 4) Hotplate, stirrer, 1203, JENWAY, the U.S.A. 5) Rotary stirrer (Multifunction Stirrer), Eurostar, IKA, U.S.A. 6) Simple mechanical Tensile Testing Apparatus. 7) Micrometer, Mitutoyo, 103-129 Range 0-25 mm/ 0.001 mm, Japan. 8) Fruit Blender, Y46, Moulinex, France. 9) Simple distillation apparatus. **Chemicals** 1) Sodium Metabisulfite; $Na_2S_2O_5$, Food grade, % Assay = 98.0, MW 190.10, Thailand. 2) Ethyl alcohol; CH_3CH_2OH, Food grade, % Assay = 95.0, Density 0.789 g/mL, MW 46.07, Thailand. 3) Glycerol; $C_3H_5(OH)_3$, Food grade, % Assay = 99.5, Density 1.2570 g/mL, MW 92.09, Thailand. **The experimental method** involves **the extraction of konjac powder**. 1) Rinse the konjac tube with clean water, peel it, and cut it into thin slices. Weigh about 500 grams, add 200 milligrams per liter of sodium metabisulfite ($Na_2S_2O_5$) to about 750 milliliters of 60% ethanol, then mix with a blender until wholly filtered through a thin white cloth. (Wash 3 times with water) and dried at 65°C for 12 hours. 2) Take the konjac powder obtained in step 1, wash it with sodium metabisulfite ($Na_2S_2O_5$) 200 mg/L in 1500 ml 95% ethanol, and then centrifuge carefully. It was filtered through a thin white cloth (washed with water 3 times) and dried at 65 °C for 12 hours. 3) Sieve through a 60-mesh sieve in different sizes. The chemical composition of the extracted konjac powder was analyzed to determine its primary constituents. The analysis included moisture, ash, crude protein, fat, fiber, and carbohydrate content. The procedures were conducted using standard methods to ensure accuracy and reproducibility. **Film formation** 1) Weigh the powder into 10.00 g of konjac and add 1000 ml of water. Then, take the konjac solution to re-separate the sediment by centrifugation at 5000 rpm for 10 minutes. The solution is divided into two parts: the supernatant and the sediment. 3) Remove the clear part and mix with a magnetic stirrer at 1400 rpm for 3 hours. 4) Pour the solution to a known exact weight, about 90 mL, onto a ceramic plate and then dry in a hot air oven at 60 °C for 24 hours. Allow to cool in a desiccator containing silica gel after the specified time. Repeat steps 1) to 4) adding in step 3) 0.1% and 0.2% (v/v) glycerin solutions in 1.00- and 2.00-ml volumes, respectively, and check all film properties such as film appearance, color (by the Lab color system, which also known as the CIELAB system, is widely used in scientific research to measure and describe color), water permeability, etc. **Thai caramel wrapping test** 1) Take a suitable film from the test to wrap the Thai caramel. 2) Observe after 1, 3, 7, 9, 15, 20, 25, 30, and 90 days of packing Thai caramel with and without desiccant and record the results.

3. Results and Discussions

According to the research, it was found that the konjac variety (*A. muelleri* Blume.) from Mae Wang, Chiang Mai, was peeled, cut into small pieces, mixed well with a mixer, and then extracted with an ethanol solution. It was then dried at 65 ° C. After the dried konjac powder was obtained, it was sieved through a 60-mesh sieve. Resulting in smaller particle sizes of less than 150 micrometres; as shown in Figure 2, the yield percentage was 34.92 (0.16). The extraction and drying methods used can influence the particle size of konjac powder. The average percentage composition of konjac powder extracted with 95% ethanol, calculated on a dry weight basis, is presented in Table 1. When observing the film-forming process, the color of the konjac powder was white and yellow. After investigating the functional groups from Konjac films with the FTIR technique, the sample Konjac powder and standard glucomannan powder are compared, as shown in Figures 3A and 3B, respectively. From 3B, the wavenumber range of glucomannan is observed between 4000 and 400 cm^{-1}. The mannose in glucomannan absorbs at 807 and 892 cm^{-1}, stretching methyl groups at 2898 and 2925 cm^{-1}, and a carbonyl group absorption at 1727 cm^{-1}. From Figure 3A, the wavenumber range of glucomannan also spans from 4000 to 400 cm^{-1}. Mannose in glucomannan absorbs at 809 and 879 cm^{-1}, stretching methyl groups at 2885 and 2925 cm^{-1}, and the carbonyl group absorption at 1725 cm^{-1} [11]. In conclusion, the extracted konjac powder contains glucomannan as a significant component. Konjac glucomannan, the primary component of konjac powder, has a high molecular weight, typically ranging from 200,000 to 2,000,000 Daltons. The exact molecular weight can vary depending on the source and processing methods. High molecular weight contributes to its viscosity and film-forming capabilities. [15].

ASEAN J. Sci. Tech. Report. **2025**, *28*(3), e255974.

4 of 14

Figure 2. Extracted konjac powder

Table 1. The average percentage composition of konjac powder

Sample	Moisture	Percentage (Dry Weight)				
		Fat	Protein	Fiber	Ash	Carbohydrate
konjac powder extracted with 95% ethanol	9.14	0.06	3.11	0.79	1.00	95.04
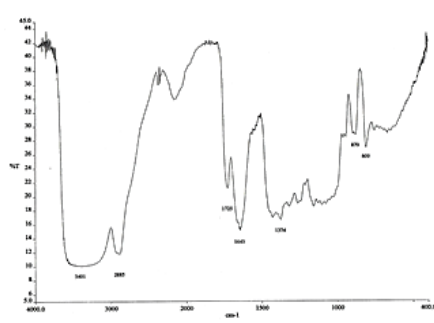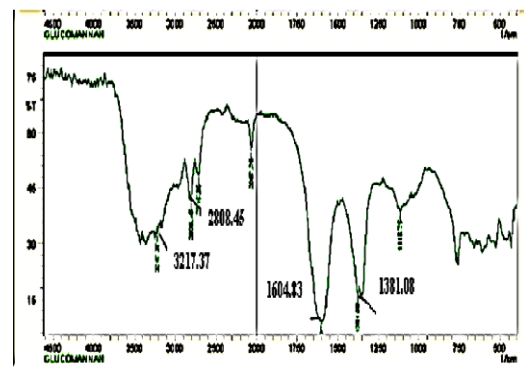
(A)   (B)

Figure 3. (A) Extracted Konjac powder IR spectrum (B) Standard Glucomannan IR spectrum [11].

After the konjac powder was dissolved in water, 0.1 and 0.2% v/v of different glycerol concentrations were added, and no glycerol was added. The powder was then dried at 60 ° C for 24 hours. Film properties are shown in Table 2. The research findings were that the appearance of the films and the weight of the films were similar (the weights are approximately 1.0090 ± 0.0035 g.), the average thickness is approximately 0.050 ± 0.002 mm., and the flexibility of the films depended on the amount of glycerol. High glycerol makes it very flexible. Since glycerol is a plasticizer for polymers, it intercalates between polymer chains and forms hydrogen bonds. This causes a partial loss of symmetry in the glucomannan structure. Films with varying glycerol concentrations were prepared and cut into dimensions of 1 centimeter in width and 3 centimeters in length. Each film was tested for tensile strength using a sandbag tearing method, where the amount of sand required to tear the film was weighed and recorded. The experiment was repeated three times for accuracy. The results indicated that the film without glycerol addition exhibited the lowest tensile strength, while the film with a glycerol concentration of 0.2% (v/v) demonstrated the highest tensile strength [12]. To evaluate water solubility, glycerol films with dimensions of 2 cm × 2 cm were immersed in water under varying conditions. The changes

in the film's structure were monitored at 1-minute intervals for 4 minutes. All films demonstrated solubility in water under the tested conditions. However, glycerol films dissolved more slowly, with the dissolution time increasing proportionally to the glycerol concentration. The color of konjac-based films mixed with glycerol is influenced by Glycerol concentration (affecting transparency and brightness). Konjac powder purity (affecting the base color of the film), Processing conditions (e.g., drying temperature, film thickness). Expected Lab Ranges for Konjac Films: L* (Lightness): Konjac films mixed with glycerol are typically translucent to semi-transparent with L* values in the range of 75-90. A higher glycerol concentration increases transparency, leading to higher L* values (closer to white). a* (Red-Green Axis): Konjac films are generally neutral to slightly yellowish, with a* values ranging from -1.0 to +1.5, indicating minimal redness or greenness. b* (Yellow-Blue Axis): Films tend to have a slight yellow tint due to the natural color of konjac powder and the addition of glycerol. The b* value typically ranges from +5.0 to +15.0. The water permeability study of cutting a membrane of each glycerol concentration differs. The size is 5 cm. width and 5 cm. long and then extended over the mouth of the beaker. Then, 10 drops of distilled water were added to the film. Record the time when the first drop of water penetrates the membrane. Three replicates were made according to Table 3.

Table 2. Film appearances with different concentrations of glycerol

Glycerol Concentration	Film Appearances
No glycerol added	
0.1 % v/v	
0.2 % v/v	

Table 3. The table shows the time that the water had penetrated.

Glycerol Concentration	Water penetration time (min)
No glycerol added	1.17 ± 0.06
0.1 % v/v	10.22 ± 0.81
0.2 % v/v	15.00 ± 0.33

ASEAN J. Sci. Tech. Report. **2025**, *28*(3), e255974.

6 of 14

Table 3 shows the test results. A glycerol concentration of 0.2% (v/v) was found to have the highest water penetration resistance. The choice of packaging characteristics is to take film of different concentrations and cut it to 9 cm. Width and 9 cm. long, then wrapped in Thai caramel. Physical results were recorded according to Table 4. The film without adding glycerol was found to be the most similar to the plastic film (normally, PP was used). So, could you take it to the next test? A study on film was conducted by selecting finished films from a designated environment and using them to package triangular pyramid-shaped candies. Afterwards, the Thai caramel wrapped in konjac film is placed in 2 bags: bag 1 contains a desiccant bag, and bag 2 does not contain a moisture-absorbing bag (desiccant bag). After that, the change characteristics were observed on days 1, 3, 7, 9, 15, 20, 25, 30 and 90 as shown in Tables 5 and 6.

Table 4. Physical characteristics of the film for wrapping the Thai caramel.

Glycerol Concentration	Physical appearance	The appearance of the packaging
No glycerol added	The film is soft and smooth.	
0.1% v/v	The film is slightly flexible.	
0.2% v/v	The film is very flexible.	

Table 5. Table shows the changes in packaging and caramel without desiccant bags.

Packaging Observation Date Of Thai Caramel Wrapping	Physical Appearance	Picture Showing Physical Appearance
Day 1	The film was brown, and the Thai caramel was black and soft	

Table 5. Table shows the changes in packaging and caramel without desiccant bags. (Continued)

Packaging Observation Date Of Thai Caramel Wrapping	Physical Appearance	Picture Showing Physical Appearance
Day 1	The film was brown, and the Thai caramel was black and soft	
Day 3	The brown color of the film remained unchanged, and the Thai caramel did not change.	
Day 7	The brown color of the film remained unchanged, and the Thai caramel did not change.	
Day 9	The brown color of the film was unchanged, and the Thai caramel was black; its softness had not changed.	
Day 15	The brown color of the film was unchanged and the Thai caramel was black, less softness	
Day 20	The brown color of the film was unchanged and the Thai caramel was black and starting to harden a little.	

Table 5. Table shows the changes in packaging and caramel without desiccant bags. (Continued)

Packaging Observation Date Of Thai Caramel Wrapping	Physical Appearance	Picture Showing Physical Appearance
Day 25	The brown color of the film was unchanged and the Thai caramel was black and had to be hardened.	
Day 30	The brown color of the film was unchanged and the Thai caramel was black and rigid.	
Day 90	The film turned yellow from mold, and Thai caramel became black and hard caramel.	

Table 5 revealed that the film had no physical changes within 30 days, but the Thai caramel changed within 1 month because the shelf life of Thai caramel was about 30 days. The film was edited. The mold was about 90 days. Table 6 revealed that the physical properties of the film did not change for 90 days. That's why a film can take more than 90 days.

Table 6. Shows the changes in packaging and caramel with desiccant bags.

Packaging Observation Date Of Caramel Wrapping	Physical Appearance	Picture Showing Physical Appearance
Day 1	The brown color of the film was unchanged, and the Thai caramel had black and Softness	

ASEAN J. Sci. Tech. Report. **2025**, *28*(3), e255974.

9 of 14

Table 6. Shows the changes in packaging and caramel with desiccant bags.

Packaging Observation Date Of Caramel Wrapping	Physical Appearance	Picture Showing Physical Appearance
Day 1	The brown color of the film was unchanged, and the Thai caramel had black and softness	
Day 3	The brown color of the film was unchanged, and the Thai caramel had black and softness	
Day 7	The brown color of the film was unchanged, and the Thai caramel had black and softness	
Day 9	The brown color of the film was unchanged, and the Thai caramel had black and softness	
Day 15	The brown color of the film was unchanged, and the Thai caramel had black and Less softness	
Day 20	The brown color of the film was unchanged, and the Thai caramel had black and slightly hardened.	

ASEAN J. Sci. Tech. Report. **2025**, *28*(3), e255974.

10 of 14

Table 6. Shows the changes in packaging and caramel with desiccant bags.

Packaging Observation Date Of Caramel Wrapping	Physical Appearance	Picture Showing Physical Appearance
Day 20	The brown color of the film was unchanged, and the Thai caramel had black and slightly hardened.	
Day 25	The brown color of the film was unchanged, and the Thai caramel was black and becoming more rigid.	
Day 30	The brown color of the film was unchanged, and the Thai caramel had black and rigid	
Day 90	The brown color of the film was unchanged, and the Thai caramel had black and rigid	

4. Discussions

Based on the experiment, konjac-type gazelle (*A. muelleri* Blume.) from Mae Wang District, Chiang Mai province, was extracted with ethanol and dried at 65 °C. After the dried konjac powder was obtained, it was sieved through a 60-mesh sieve. The experimental results showed that Konjac powder, which has a white-yellow appearance, was used in the study to investigate film formation with different glycerol concentrations. The study examined film formation without glycerol and with 0.1 and 0.2% glycerol (v/v) after film formation with different glycerol concentrations. It was observed that the appearance and weight of the film were similar. In the next step, which included testing the properties of the film from the thickness study, stress study, water solubility study, and film water permeability study, it was found that the glycerol-filled film has the most

ASEAN J. Sci. Tech. Report. **2025**, 28(3), e255974.

11 of 14

suitable properties to develop into an environmental usage. The package thickness was 0.048 ± 0.002 mm, the average tensile strength was 2.497 ± 0.044 N/cm², and the water solubility, all film-forming conditions can dissolve in water, with an average water permeability of 1.17 ± 0.03 minutes. Therefore, as the glycerol content increases, the result is an increase in tensile strength. This suggests that glycerol integrates into the polymer structure of glucomannan by forming bonds with the polymer chains, primarily through hydrogen bonding. These hydrogen bonds draw the molecules closer together, promoting crystallization and enhancing the material's overall strength. Consequently, as the glycerol content increases, the tensile strength of the polymer improves [13]. This is consistent with a study by Danijeal Z. Suput et al. [14], who found that adding glycerol to a konjac solution increased tensile strength. This may be due to the addition of molecular crystals. As a result, it has a higher tensile strength. Another factor influencing the lab values of konjac films with glycerol was that higher Glycerol concentrations increase transparency, leading to higher L∗ values (lighter appearance) while potentially reducing yellow tones (b∗ values). And the film thickness: Thicker films may appear less transparent, reducing L∗ values and increasing b∗ (yellowish tones). As the processing temperature increases, higher temperatures can cause slight browning or degradation of the film, increasing a∗ (redness) and b∗ (yellowness) [15-17] from trying to bring the best quality film instead of plastic to packaging Thai caramel that can be bought as a takeaway and researching the age of Thai caramel from konjac powder after film formation to packaging within 30 days. It has been observed that for 30 days, the Thai caramel appears increasingly stiff. However, the physical properties of the Konjac film did not change. It was concluded that edible konjac film was probably used as a substitute for plastic film to wrap Thai candies. This is consistent with Chupapan Rattananil's study[18] that using konjac film in the packaging of Nam Dok Mai mango varieties can increase the shelf life of mangoes. In addition, Hansa Jakraphan et al. [19] conducted a comprehensive study to develop and enhance the functional properties of carrot-based edible films. The experiment was divided into two main objectives: improving the tensile strength of the films and optimizing their elongation properties. To achieve these goals, pectin and alginate were tested for their ability to enhance film strength, while xylitol was added as a plasticizer to improve elongation. The results indicated that the optimal film properties were obtained by incorporating 3% alginate and 3.75% xylitol, calculated based on the weight of carrot flesh. Alginate significantly increased the film's tensile strength, providing greater rigidity and resistance to tearing, while xylitol, as a sugar substitute, enhanced film elasticity. The carrot-based films demonstrated excellent oxygen transfer resistance, making them suitable for use in packaging products such as candies and fruit preserves, where they effectively prevented quality degradation caused by oxidative reactions. Furthermore, these films contained up to 3465 micrograms of beta-carotene, contributing to their nutritional value. The films retained their functional integrity for up to two months, exhibiting similar mechanical properties to konjac glucomannan-based films. In addition, other biodegradable films, such as those made from chitin and chitosan (1.5%), have been explored for their improved water vapor permeability. Combined with gelatin (2%), these films successfully preserved moisture in Khao Nam Phueng pomelo fruits, extending their shelf life to over 21 days [20-22]. These findings highlight the potential of carrot-based films and other biodegradable materials for food preservation and sustainable packaging applications, aligning with the broader goals of reducing environmental impact. This study successfully developed biodegradable and edible films from konjac powder under controlled conditions. The key findings are: Glycerol acts as an effective plasticizer, enhancing tensile strength and water resistance in konjac films. Films without glycerol exhibited the lowest tensile strength but were most similar to conventional plastic films in appearance. Konjac-based films can effectively serve as sustainable packaging for Thai caramel, with desiccant bags further improving product shelf life. The developed Konjac film offers a promising biodegradable alternative to synthetic packaging, addressing environmental concerns and food preservation requirements.

When comparing conventional polymer films for Thai Caramel packaging and the advantages of Konjac-based films. Currently, polypropylene (PP) films are widely used for packaging Thai caramel due to their low cost, mechanical strength, and moisture barrier properties, effectively preserving the product's quality and texture [23]. Polypropylene, being a synthetic polymer, is non-biodegradable and contributes significantly to environmental pollution through plastic waste accumulation [5]. In contrast, konjac-based films,

ASEAN J. Sci. Tech. Report. **2025**, *28*(3), e255974.

12 of 14

derived from *A. muelleri* Blume, offer numerous advantages over conventional polypropylene films, such as biodegradability and environmental Impact: Konjac-based films are natural, biodegradable materials that decompose under environmental conditions, reducing plastic waste and promoting sustainability [14]. This makes Konjac films particularly relevant in addressing global plastic pollution and environmental degradation concerns. Regarding mechanical properties, these studies have shown that konjac-based films, when plasticized with glycerol, exhibit excellent tensile strength and flexibility [15]. These properties allow konjac films to function effectively as packaging materials for food products like Thai caramel, maintaining their structural integrity during handling and storage. Moreover, moisture and oxygen barrier: konjac-based films provide sufficient moisture and gas permeability resistance, extending the shelf life of food products by preventing oxidative deterioration [6]. This property is essential for products like Thai caramel, which are susceptible to changes in texture and quality due to moisture absorption. As a natural material for consumer safety, konjac films are free from harmful chemical additives, making them safer for consumers and reducing health risks associated with synthetic polymers [24]. Regarding cost comparison, while polypropylene films remain economically advantageous due to their low production cost and mature manufacturing technology, konjac-based films currently incur higher production costs. The cost is primarily attributed to the raw material extraction process and the need for specialized production methods [8]. However, with advancements in production efficiency and increasing consumer demand for eco-friendly products, the cost gap is expected to narrow, making Konjac films a viable alternative in the long term.

Konjac-based films provide a sustainable and functional alternative to synthetic polypropylene films for packaging Thai caramel. Their biodegradability, mechanical strength, and moisture barrier properties align with global efforts to reduce plastic waste and promote environmentally friendly solutions. Further research into cost-effective production methods will enhance their competitiveness and commercial viability in food packaging industries.

It is important to note that this study did not assess the potential for fungal growth on konjac-based films. These films are derived from organic materials and lack preservatives, so they may be prone to fungal contamination if stored unused for extended periods. This limitation was not addressed as the study primarily focused on evaluating the physical and functional properties of the films for packaging applications. Future research should explore strategies to enhance the antifungal properties of konjac-based films. For example, incorporating natural antifungal agents such as chitosan, a biopolymer with well-documented antimicrobial and antifungal properties, could significantly improve their resistance to fungal growth. Chitosan's ability to inhibit a wide range of fungi, including *Aspergillus niger* and *Penicillium* spp., makes it a promising additive for this purpose [25]. Furthermore, integrating plant-derived antimicrobial extracts, such as saffron petal or dragon fruit peel extracts, could complement the antifungal efficacy of the films while maintaining their biodegradability and food safety. [26-27]. By addressing this limitation, konjac-based films could offer enhanced functionality, making them more suitable as sustainable packaging materials for confectionery products like Thai caramel (kalamare), where the prevention of mold growth is crucial for preserving product quality and safety.

4. Conclusions

This study successfully developed edible, biodegradable films derived from Amorphophallus muelleri Blume corms through controlled extraction and film casting. The films, formulated with varying glycerol concentrations, demonstrated distinct physical properties. Glycerol acted as a plasticizer, enhancing tensile strength and water barrier capacity, while the glycerol-free film retained greater similarity to conventional plastic films in texture and transparency. Among the tested formulations, the glycerol-free film exhibited the most favorable characteristics for food wrapping: high water solubility, sufficient tensile strength, and structural integrity maintained for over 30 days. Furthermore, the inclusion of desiccant bags prolonged product shelf life up to 90 days without mold growth, supporting the film's functional viability in food packaging applications. Konjac-based films offer significant advantages over petroleum-based polymers, notably biodegradability, consumer safety, and environmental friendliness. However, their susceptibility to microbial growth under storage remains a concern. Future research should explore strategies to enhance antifungal resistance by incorporating natural agents such as chitosan or plant-based extracts, thereby

ASEAN J. Sci. Tech. Report. **2025**, *28*(3), e255974.

13 of 14

extending storage potential without compromising biodegradability. In conclusion, konjac-derived films represent a promising eco-friendly alternative for food packaging, particularly for confections like Thai caramel. With further development in formulation and production scalability, these materials have the potential to bridge sustainability and commercial application in the packaging industry.

5. Acknowledgement

Author Contributions: "Conceptualization, Ratchawet,A. and Joradol, A..; methodology, Ratchawet,A. and Kanja, A..; software, Joradol, A. and Kanja, A..; validation, Ratchawet,A., Joradol, A. and Kanja, A..; formal analysis, Kanja, A. ; investigation, Ratchawet,A.; resources, Ratchawet,A.; data curation, Ratchawet,A.; writing—original draft preparation, Ratchawet,A.; writing—review and editing, Ratchawet, A. and Joradol, A..; visualization, Ratchawet, A. and Joradol, A..; supervision, Ratchawet, A. and Joradol, A..; project administration, Ratchawet, A.. All authors have read and agreed to the published version of the manuscript." Please turn to the CRediT taxonomy for the term explanation. Authorship must be limited to those who have contributed substantially to the work reported.

Conflicts of Interest: "The authors declare no conflict of interest. The funders had no role in the design of the study; in the collection, analyses, or interpretation of data; in the writing of the manuscript, or in the decision to publish the results".

References

[1]   Pollution Control Department. Plastic and foam to reduce environmental problems. Ministry of Natural Resources and Environment. 2017. Retrieved from http://www.pcd.go.th/public/publications/ (accessed 2022-08-18).

[2]   Villagers in Satun eagerly harvest wild konjac for gourmet dishes. (2021, August 25). The Thaiger. Retrieved December 6, 2024, from https://thethaiger.com/news/national/villagers-in-satun-eagerly-harvest-wild-konjac-for-gourmet-dishes.

[3]   Ekthamsut, K. Effect of scene hydrolyzate on physical properties of edible film from Konjac flour. *Acad. J. Univ. Thai Chamber Commer*. **2010**, *30*(1), 81-89.

[4]   Noiduang, P.; Thaola, L.; Paai, O. Study on the production of the edible film from Water chestnut starch. *J. Agric. Sci.* **2015**, *46*(3) (Special), 665-668.

[5]   Xu, W.; Jia, Y.; Wei, J.; Ning, Y.; Sun, H.; Jiang, L.; Chai, L.; Luo, D.; Cao, S.; Shah, B. R. Characterization and Antibacterial Behavior of an Edible Konjac Glucomannan/Soluble Black Tea Powder Hybrid Film with Ultraviolet Absorption. *RSC Adv.* **2022**, *12*, 32061-32069. https://doi.org/10.1039/D2RA05030G

[6]   Wang, L.; Lin, L.; Guo, Y.; Long, J.; Mu, R.-J.; Pang, J. Enhanced Functional Properties of Nanocomposite Film Incorporated with EGCG-Loaded Dialdehyde Glucomannan/Gelatin Matrix for Food Packaging. *Food Hydrocoll*. **2020**, *108*, 105863. https://doi.org/10.1016/j.foodhyd.2020.105863

[7]   Zhang, L.; Zeng, L.; Wang, X.; Liu, Z. The Influence of Konjac Glucomannan on the Functional and Structural Properties of Wheat Starch. *Food Sci. Nutr.* **2020**, *8*, 2959-2967. https://doi.org/10.1002/fsn3.1607

[8]   Ratchawet, A.; Joradol, A. Preservation of tomato fruit from edible konjac coating. *Naresuan Univ. J. Sci. Technol.* **2017**, *25*(1), 75-91.

[9]   Wiset, L.; Poomsa-ad, N.; Jomlapeertikul, P. Effects of Drying Temperature's and Glycerol Concentrations on Properties of Edible Film from Konjac Flour. Faculty of Engineering, Mahasarakham University, Mahasarakham, Thailand, **2013**. https://doi.org/10.12720/jomb.3.3.171-174

[10]   Tester, R. F.; Al-Ghazzewi, F. H. Beneficial health characteristics of native and hydrolysed konjac (Amorphophallus konjac) glucomannan: Health characteristics of native and hydrolysed konjac glucomannan. *J. Sci. Food Agric.* **2016**, *96*, 3283-3291. https://doi.org/10.1002/jsfa.7571

[11]   Hardikar. S.; Bhosale, A.; Vanave, S.; Kanathe, B. Preparation and Evaluation of Co-Crystals of Carbamazepine with Glucomannan. *Int J Pharm Pharm Sci*, **2017**, *9*(10), 318-320. https://doi.org/10.22159/ijpps.2017v9i10.20656

[12]   Li, B.; Xie, B. Synthesis and Characterization of Konjac Glucomannan/Poly (vinyl alcohol) Interpenetrating Polymer Networks. *J. Appl. Polym. Sci.* **2004**, *93*(6), 2775-2780. https://doi.org/10.1002/app.20769

[13]   Zhang, Y.; Liu, C.; Wang, Q. The development and application of konjac glucomannan-based materials: A review. *International Journal of Biological Macromolecules*, **2019**, *135*, 242-249. https://doi.org/10.1016/j.ijbiomac.2019.05.205

[14]   Suput, D. Z.; Lazic, V. L.; Popovic, S. Z.; Hromis, N. M. Edible films and coatings-sources, properties, and application. University of Novi Sad, Faculty of Technology, 21000 Novi Sad, Bulevar cara Fazara, Serbia, **2015**.

[15]   Fang, Y.; Wu, P. Properties of konjac glucomannan-based films. *Journal of Food Engineering,* **2004**, *63*(1), 67-72. https://doi.org/10.1016/j.jfoodeng.2003.07.004

[16]   Rhim, J. W.; Ng, P. K. W. Natural biopolymer-based films and coatings for food packaging applications. *Critical Reviews in Food Science and Nutrition*, **2007**, *47*(4), 411-433. https://doi.org/10.1080/10408390600846366

[17]   Zhang, Y.; Liu, C.; Wang, Q. The development and application of konjac glucomannan-based materials: A review. *International Journal of Biological Macromolecules*, **2019**, *135*, 242-249. https://doi.org/10.1016/j.ijbiomac.2019.05.205

[18]   Rattananil, C. Production of edible film from konjac powder mixed with Thai herbal extracts to extend the shelf life of mango cv. Nam Dok Mai No. 4. Master's Thesis, Faculty of Science, Chulalongkorn University, **2011**.

[19]   Jakraphan Na Ayudhya, H.; Ketprasert, O. Medicinal plants; Botany and Weed Division, Department of Academic Affairs, Bangkok, 1989.

[20]   Hansa Jakraphan, K.; Sooksai, W. Effect of pectin and alginate on the mechanical properties of carrot-based films. *Journal of Biopolymer Science*, **2018**, *12*(3), 123-130. https://doi.org/10.1021/jbs.2018.01234

[21]   Liu, C., & Wang, Q. Influence of xylitol and other plasticizers on the mechanical properties of edible films. *Polymers,* **2019**, *11*(12), 1952. https://doi.org/10.3390/polym11121952

[22]   Zhang, Y.; Liu, H.; Chen, X. Mechanical properties and elongation at break of composite films from natural biopolymers. *Materials Science and Engineering*, **2020**, *108*(2), 43-50. https://doi.org/10.1016/j.mse.2020.05.012

[23]   Luo, H.; Xie, J.; Wang, J. Recent advances in food packaging materials: Challenges and opportunities. *Food Packaging and Shelf Life*, **2023**, *35*, 101049. https://doi.org/10.1016/j.fpsl.2022.101049.

[24]   Tester, R. F.; Al-Ghazzewi, F. H. Beneficial health characteristics of native and hydrolysed konjac glucomannan. *Journal of the Science of Food and Agriculture*, **2016**, *96*(10), 3283-3291. https://doi.org/10.1002/jsfa.7603

[25]   Nair, S. B.; Alummoottil, N. J.; Moothandasserry, S. S. Chitosan-konjac glucomannan cassava starch-nanosilver composite films with moisture resistant and antimicrobial properties for food packaging applications. *Starch/Stärke*, **2017**, *69*(1-2), 1600210. https://doi.org/10.1002/star.201600210

[26]   Homthawornchoo, W.; Hakimi, N. F. S. M.; Romruen, O.; Rawdkuen, S. Dragon fruit peel extract enriched-biocomposite wrapping film: Characterization and application on coconut milk candy. *Polymers*, **2023**, *15*(3), 720. https://doi.org/10.3390/polym15030720

[27]   Hashemi, S. M. B.; Jafarpour, D. The efficacy of edible film from konjac glucomannan and saffron petal extract to improve shelf life of fresh-cut cucumber. *Food Science & Nutrition*, **2020**, *8*(7), 3128-3137. https://doi.org/10.1002/fsn3.1544

X-ray Shielding Properties of Natural Rubber/BaSO₄ Foam Composites

Narit Klompong[1], Arnon Srisook[2], Pornpana Buaphet[3], Suwit Phethuayluk[4], and Sutthisa Konruang[5*]

[1] Faculty of Science and Fisheries Technology, Rajamangala University of Technology Srivijaya, Trang, 92150, Thailand
[2] Regional Medical Sciences Center 11 Suratthani, 84100, Thailand
[3] Faculty of Science and Digital Innovation0, Thaksin University, Phatthalung, 93210, Thailand
[4] Faculty of Science and Digital Innovation0, Thaksin University, Phatthalung, 93210, Thailand
[5] Faculty of Science and Digital Innovation0, Thaksin University, Phatthalung, 93210, Thailand
* Correspondence: e-mail@e-mail.com; sutthisa@tsu.ac.th

Abstract: In this study, lead-free X-ray shielding materials were fabricated using natural rubber (NR) and barium sulfate (BaSO₄) with various BaSO₄ filler loadings of 0, 50, 75, and 100 phr. The X-ray shielding properties of NR/BaSO₄ foam composites were investigated at X-ray tube voltages of 60, 70, 80, and 90 kVp. The results showed that the X-ray attenuation efficiency increased with higher BaSO₄ filler content and material thickness but slightly decreased with increasing voltages. The X-ray radiation attenuation properties were analyzed using the linear attenuation coefficient (μ_l) and the mass attenuation coefficient (μ_m). The results indicated that both coefficients increased with higher BaSO₄ filler content but decreased as the voltage increased. In contrast, the half-value layer (HVL) decreased with increasing BaSO₄ filler content but increased with higher voltages. In conclusion, NR/BaSO₄ foam composites have great potential for developing flexible and environmentally friendly X-ray shielding materials.

Keywords: Natural rubber foam; Barium sulfate; X-ray shielding

1. Introduction

X-rays are widely used in various industries, including nuclear reactors, airports, agriculture, and medical fields [1-2]. However, overexposure to X-ray radiation can negatively affect users, causing symptoms such as nausea, vomiting, fatigue, diarrhea, headaches, skin burns, and, in severe cases, death [3]. Therefore, it is necessary to develop radiation shielding materials to attenuate and prevent harmful X-ray exposure. Lead (Pb) is the most commonly used material for radiation shielding due to its high atomic number (82), which enables it to absorb radiation efficiently [1]. However, lead is a toxic material that poses significant health and environmental hazards [2]. Additionally, lead is heavy and non-flexible, making it inconvenient for users [4]. As a result, researchers have been exploring alternative materials for X-ray shielding, such as iron oxide (Fe₂O₃) [5], tungsten oxide (WO₃) [6], bismuth oxide (Bi₂O₃) [7], and barium sulfate (BaSO₄) [5]. BaSO₄ is a naturally occurring, non-toxic, and cost-effective material conventionally used in clinical applications [4]. Due to its safety and affordability, BaSO₄ is a promising alternative material for X-ray shielding [2]. Additionally, BaSO₄ has been incorporated into various composite materials, such as natural rubber [1-2, 4, 8], polydimethylsiloxane rubber [5],

ASEAN J. Sci. Tech. Report. **2025**, *28*(3), e256422.

2 of 9

EPDM rubber [3,9], and concrete [10]. Natural rubber (NR) foam composites offer several advantages, including high elasticity, elongation at break, tensile strength, and tear resistance. Therefore, NR/BaSO$_4$ foam composites provide flexibility, lightweight properties, fracture resistance, and high efficiency in radiation shielding [1].

In this study, lead-free X-ray shielding materials were prepared using NR/BaSO$_4$ foam composites with BaSO$_4$ filler loadings of 0-100 phr via the Dunlop method. This method is convenient, reliable, cost-effective, and energy-efficient. The study aimed to evaluate the effects of X-ray tube voltage (60-90 kVp) and material thickness on the X-ray shielding properties of the NR/BaSO$_4$ foam composites.

2. Materials and Methods

2.1 Materials

High-ammonia natural rubber (NR) latex with a 60% dry rubber content was obtained from the Center of Rubber Technology for Community, Faculty of Engineering, Thaksin University, Phatthalung, Thailand. Barium sulfate (BaSO$_4$) particles (0.3 μm) were purchased from Scitrader Co., Ltd., Thailand. The following chemicals were used as additives: sulfur (S), zinc diethyldithiocarbamate (ZDEC), zinc 2-mercaptobenzothiazole (ZMBT), Wingstay®-L, zinc oxide (ZnO), diphenyl guanidine (DPG), and sodium silicofluoride (SSF). These chemicals were acquired from VPK Supply Co., Ltd., Thailand, and were used in an aqueous dispersion form prepared in the laboratory.

2.2 Preparation of NR/BaSO$_4$ foam composites

All ingredients were compounded according to the formulation shown in Table 1 [11]. The NR latex and BaSO$_4$ powders were blended with the other ingredients using mechanical stirring. The resulting foam mixture was poured into a mold (25 × 25 × 0.5 cm³). The NR/BaSO$_4$ foam was vulcanized at 100°C for 1 hour in an oven, following a fabrication process previously described [11].

Table 1. Material formulations for NR/BaSO$_4$ foam composites preparation [11].

Ingredients	Total solid content (%)	Dry weight (phr*)
HA latex	60	100
S	50	2
ZDEC	50	2.5
ZMBT	50	2
Wingstay® L	50	1
ZnO	50	5
DPG	40	2
SSF	20	0.5
BaSO$_4$ (phr)	0, 50,75, 100	

* phr is the ratio unit of weight part of chemicals to 100 wt parts of rubber

2.3 Characterizations

2.3.1 Morphological properties

The NR/BaSO$_4$ foam composite surface morphology was analyzed using a Scanning Electron Microscope (SEM: FEI, Quanta 450 FEG). SEM observations were conducted at a voltage of 5 kV. Before SEM examination, the dried foam samples were vacuum-coated with gold and palladium to enhance conductivity. For morphological analysis, images were captured from three different areas of each NR/BaSO$_4$ sample; however, only a representative image is presented.

2.3.2 Physical properties

The foaming characteristics of NR/BaSO$_4$ foam composites were analyzed based on expansion ratio (ER) and foam porosity (V_f). The expansion ratio reflects the capacity of cellular materials to expand in volume

ASEAN J. Sci. Tech. Report. **2025**, *28*(3), e256422.

3 of 9

during the foaming process. This parameter was determined by calculating the ratio between the density of solid NR (ρ_r = 0.93 g/cm³) and that of NR/BaSO$_4$ foam composites (ρ_f), as described in equation (1) [12].

$$ER = \frac{\rho_r}{\rho_f} \tag{1}$$

Foam porosity, representing the proportion of void spaces within the foam structure, was evaluated using equation (2) [12].

$$V_f = \left(1 - \frac{\rho_f}{\rho_r}\right) \times 100 \tag{2}$$

2.3.3 X-Ray shielding properties

NR/BaSO$_4$ foam composite samples, measuring 3.5 cm × 3.5 cm, were positioned between an X-ray generator (MRAD-A32S, CANON) and an X-ray measuring instrument (X2, RAYSAFE). The samples, with thicknesses ranging from 0.5 cm to 2.5 cm, were exposed to a narrow X-ray beam at tube voltages of 60, 70, 80, and 90 kVp with a current of 200 mA. The exposure time was set to 0.05 seconds. The X-ray tube was placed at a fixed distance of 1 meter from the NR/BaSO$_4$ foam composites, as illustrated in Figure 1. The incident X-ray intensity (I_0) and the transmitted X-ray intensity (I) were recorded.
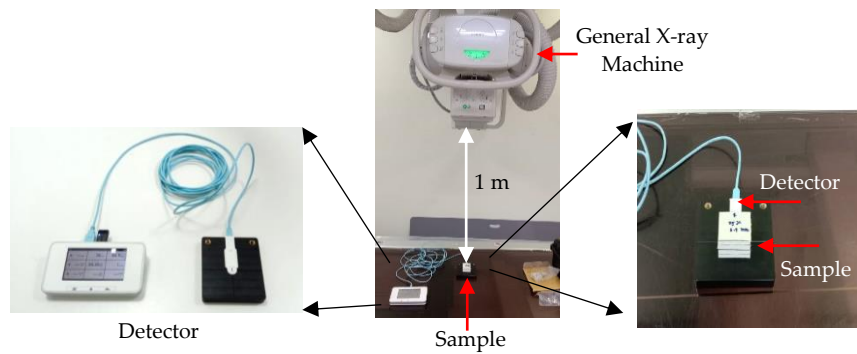
Figure 1. X-ray shielding property experiment setup.

The shielding properties of the NR/BaSO$_4$ foam composites were evaluated based on X-ray attenuation, linear attenuation coefficient (μ_l), mass attenuation coefficient (μ_m), and half-value layer (HVL). The X-ray attenuation efficiency was determined using the following equation (3) [12]:

$$X - ray\ attenuation = \frac{I_0 - I}{I_0} \times 100 \tag{3}$$

Where I and I_0 were the intensity of the transmitted X-ray and the intensity of the incident X-ray, respectively. The linear attenuation coefficients (μ_l) were calculated using the following equation (4) [12]:

$$I = I_0 e^{-\mu_l x} \tag{4}$$

$$ln\left(\frac{I_0}{I}\right) = \mu_l x \tag{5}$$

ASEAN J. Sci. Tech. Report. **2025**, *28*(3), e256422.

4 of 9

A plot of ln(I_0/I) versus thickness (x) was used to determine μ_l the slope of the trendline [8]. The mass attenuation coefficient (μ_m) was obtained using equation (6) :

$$\mu_m = \frac{\mu_l}{\rho} \tag{6}$$

Where ρ represents the density of the NR/BaSO$_4$ foam composites. The density values from a previous study [11] were used for these calculations.

The half-value layer (HVL), which refers to the thickness required to reduce the X-ray intensity by 50%, was determined using equation (7) [13,14] :

$$HVL = \frac{ln\,2}{\mu_l} \tag{7}$$

Table 2. The densities of NR/BaSO$_4$ foam composites with varying contents of BaSO$_4$ [11].

BaSO$_4$ content (phr)	0	50	75	100
Density (g/cm³)	0.59 ± 0.02	0.61 ± 0.02	0.64 ± 0.01	0.70 ± 0.01

3. Results and Discussion

3.1 Morphological properties

Figure 2 presents SEM micrographs that reveal that increasing BaSO$_4$ content (0-100 phr) significantly alters the foam structure. At 0 phr, the foam exhibits a highly porous, uniform structure. At 50 phr, BaSO$_4$ particles are well dispersed, maintaining porosity with thicker cell walls. At 75 phr, pore size decreases, and slight agglomeration appears, affecting homogeneity. At 100 phr, severe particle agglomeration is observed, leading to a denser, less porous structure. While higher BaSO$_4$ loading improves X-ray shielding efficiency, excessive amounts lead to particle agglomeration, reduced foam expansion, and compromised mechanical properties.

(a)

(b)

(c)

(d)
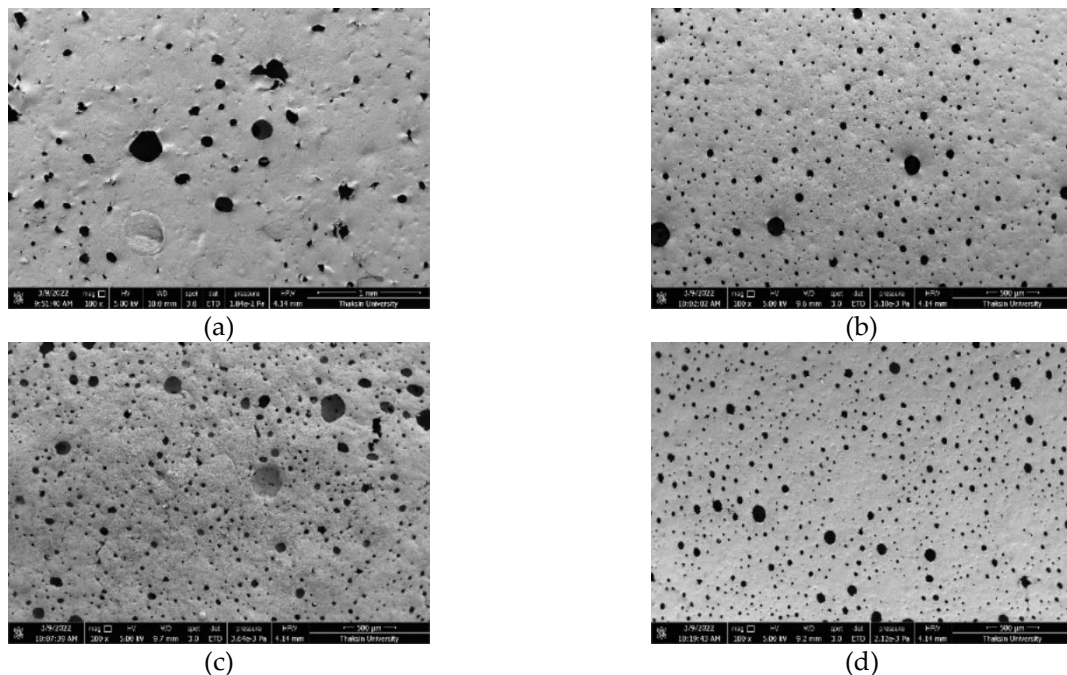
Figure 2. SEM micrographs of NR/BaSO$_4$ foam composites at various BaSO$_4$ filler loadings : (a) 0 phr, (b) 50 phr, (c) 75 phr, and (d) 100 phr.

3.2 Physical properties

Figure 3 illustrates the expansion ratio (ER) and porosity (Vf) of NR/ BaSO$_4$ foam composites with increasing BaSO$_4$ content (0-100 phr). At 0 phr, the foam exhibits the highest ER and porosity, indicating a well-expanded structure. At 50 phr, ER and porosity slightly decrease but remain sufficient for maintaining flexibility. At 75 phr, both properties decline significantly, suggesting restricted foam expansion due to BaSO$_4$ particle interference. At 100 phr, severe reduction in ER and porosity is observed, leading to a denser, less porous structure. Excessive BaSO$_4$ hinders foam formation, reducing void spaces and increasing density.
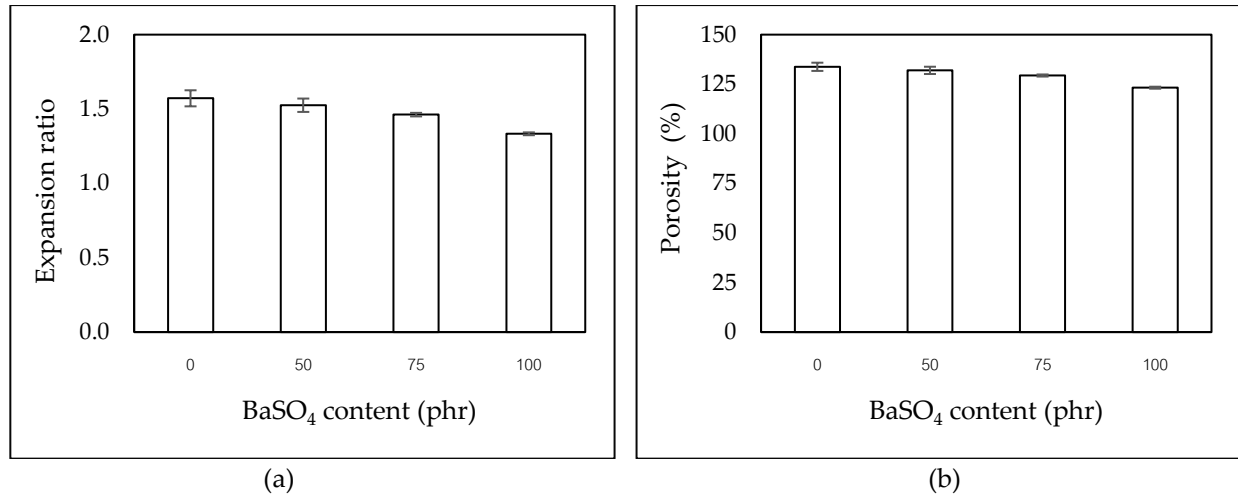
Figure 3. Physical properties of NR/BaSO$_4$ foam composites at various BaSO$_4$ filler loadings : (a) Expansion ratio and (b) porosity

3.3 X-Ray shielding properties

Figure 4 illustrates the X-ray attenuation efficiency of NR/BaSO$_4$ foam composites as a function of BaSO$_4$ content and thickness at different X-ray tube voltages (60-90 kVp). The results show that X-ray attenuation increases with higher BaSO$_4$ content and greater material thickness. At 0 phr, attenuation is lowest, while at 100 phr, it is significantly improved due to the higher density of BaSO4. Increasing the voltage reduces attenuation efficiency since higher-energy X-rays penetrate more easily. Therefore, higher BaSO$_4$ loading enhances shielding effectiveness.
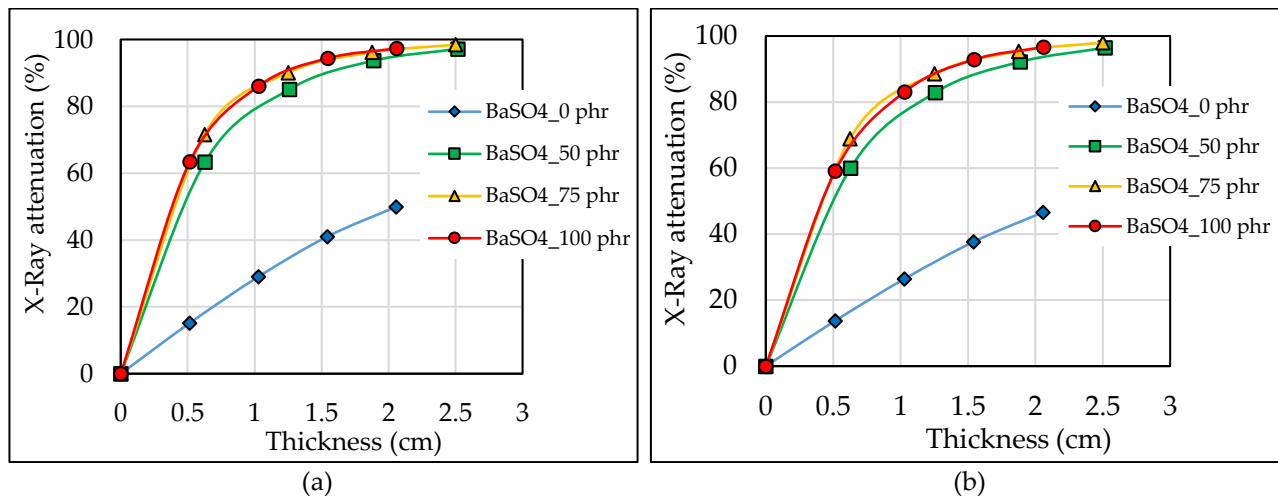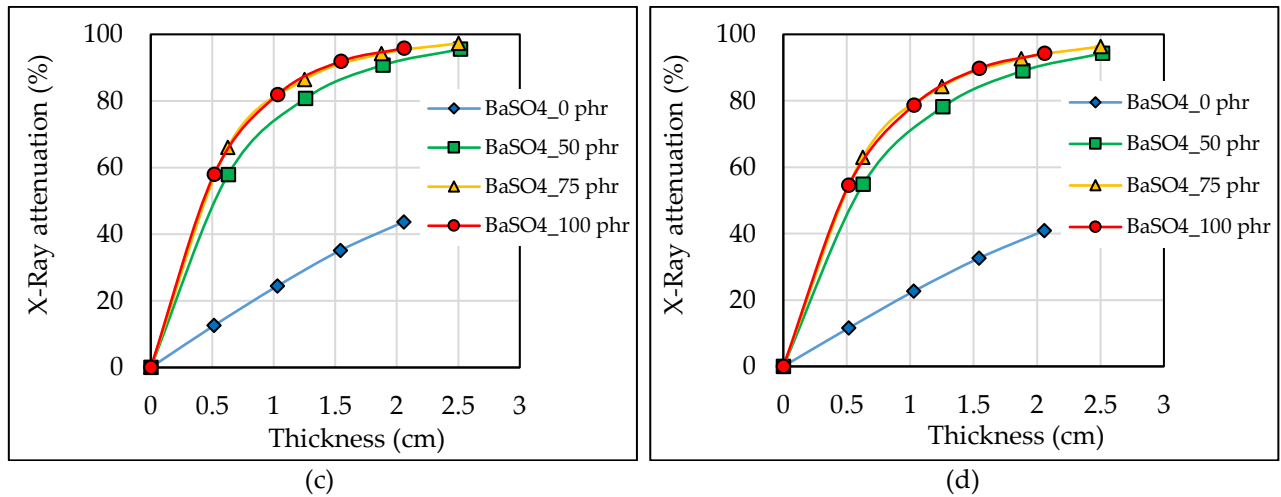
Figure 4. X-ray attenuation of NR/BaSO₄ foam composites as a function of thickness and BaSO₄ contents at different X-ray tube voltages. (a) 60 kV$_P$, (b) 70 kV$_P$, (c) 80 kV$_P$, and (d) 90 kV$_P$.
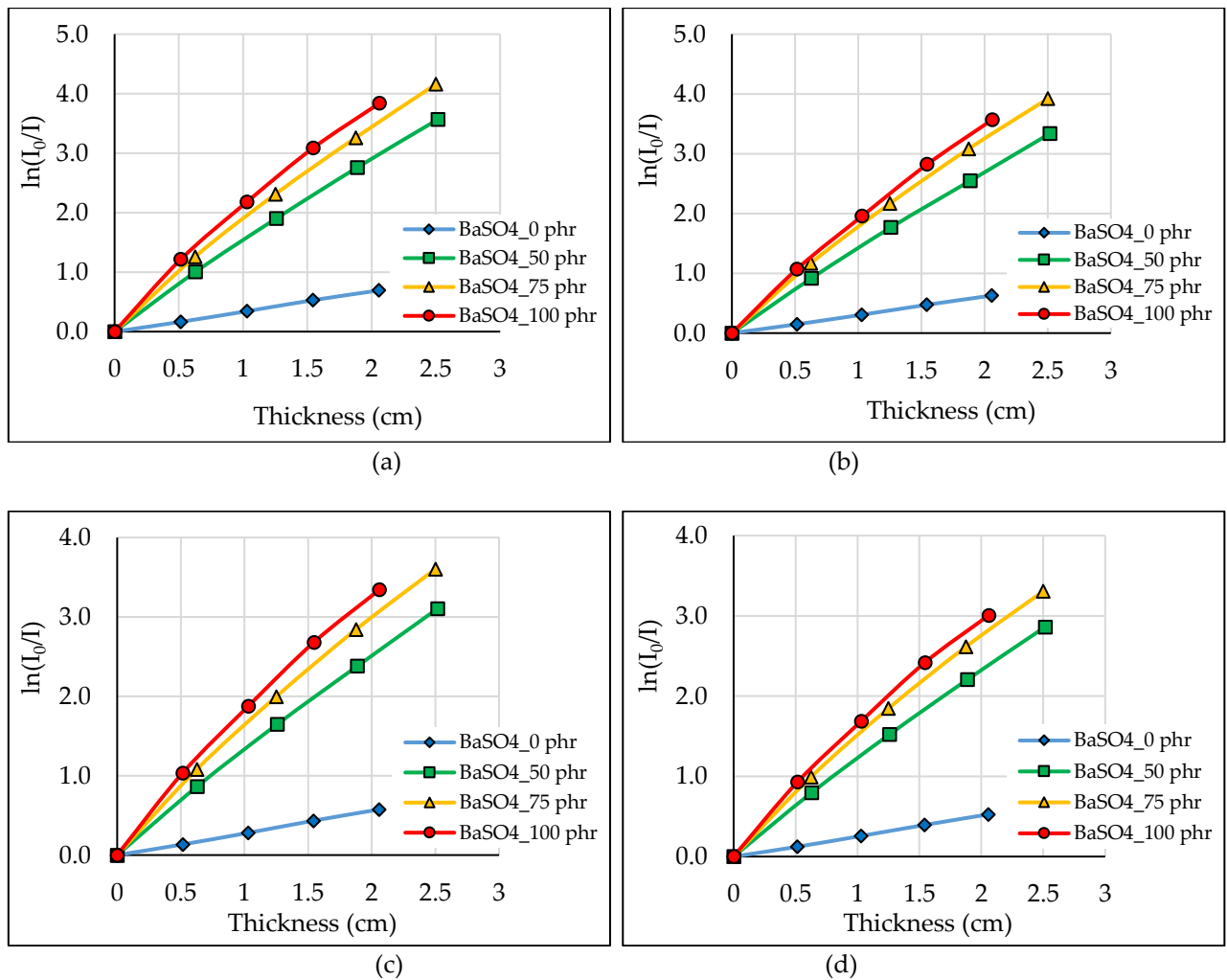
Figure 5. Graph of $ln\left(I_0 / I\right)$ as a function of thickness and BaSO₄ contents at different X-ray tube voltages. (a) 60 kV$_P$, (b) 70 kV$_P$, (c) 80 kV$_P$, and (d) 90 kV$_P$.

ASEAN J. Sci. Tech. Report. **2025**, *28*(3), e256422.

7 of 9
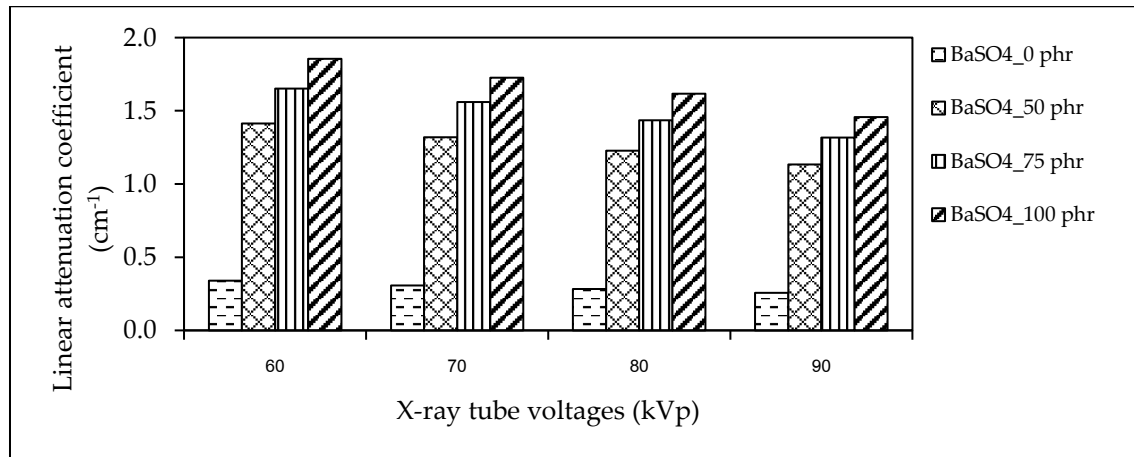
Figure 6. The linear attenuation coefficient of NR/BaSO₄ foam composites with different X-ray tube voltages.

Figure 7 illustrates the mass attenuation coefficient (μ_m) of NR/BaSO$_4$ foam composites at different X-ray tube voltages (60–90 kVp). The results show that μ_m it increases with higher BaSO$_4$ content, confirming that barium sulfate enhances X-ray absorption efficiency due to its high atomic number. However, μ_m it decreases as X-ray voltage increases, indicating that higher-energy X-rays penetrate the material more effectively, reducing attenuation. The trend aligns with expectations, showing that BaSO$_4$-enhanced composites are more effective at lower X-ray voltages, making them suitable for radiation shielding applications.

Figure 8 presents the half-value layer (HVL) of NR/BaSO$_4$ foam composites at different X-ray tube voltages. HVL represents the thickness required to reduce X-ray intensity by 50%, indicating the material's shielding efficiency. The results show that HVL decreases as BaSO$_4$ content increases, confirming that higher BaSO$_4$ loading enhances X-ray absorption, requiring less material thickness for effective attenuation. However, HVL increases with X-ray voltage, indicating that higher-energy X-rays penetrate more easily, reducing shielding efficiency.
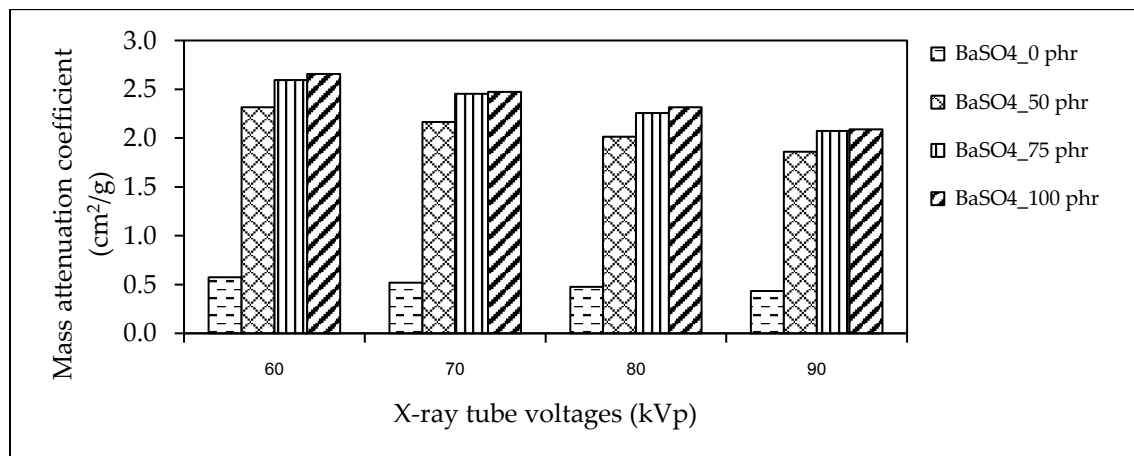
Figure 7. The mass attenuation coefficient of NR/BaSO₄ foam composites with different X-ray tube voltages.

ASEAN J. Sci. Tech. Report. **2025**, *28*(3), e256422.

8 of 9
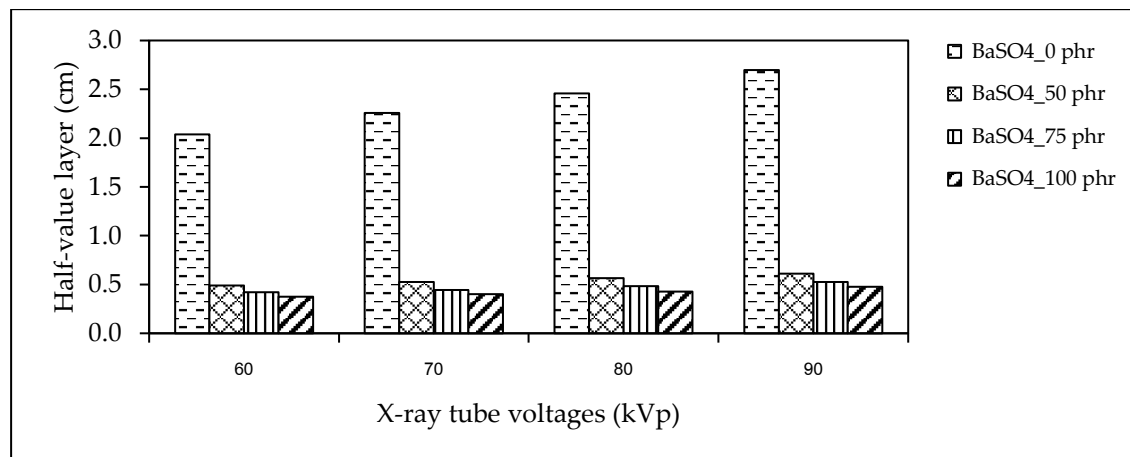
Figure 8. The half-value layer of NR/BaSO₄ foam composites with different X-ray tube voltages.

4. Conclusions

This study confirms that NR/BaSO₄ foam composites exhibit enhanced X-ray shielding efficiency with increasing BaSO₄ content. Higher BaSO₄ loading leads to reduced pore size and increased material density, affecting foam expansion and porosity. The addition of BaSO₄ significantly improves X-ray attenuation, with more excellent absorption observed at lower X-ray voltages. The linear and mass attenuation coefficients increase with BaSO₄ content, confirming enhanced radiation shielding capability. Conversely, the half-value layer decreases as BaSO₄ content rises, indicating better-shielding performance. However, at higher X-ray voltages, attenuation efficiency is reduced due to greater penetration. The results suggest that NR/BaSO₄ foam composites with 75–100 phr BaSO₄ provide an optimal balance between effective X-ray shielding and structural integrity, making them suitable for flexible, lead-free radiation protection materials.

5. Acknowledgements

Conflicts of Interest: The authors declare no conflict of interest.

References

[1] Kalkornsurapranee, E.; Kothan, S.; Intom, S.; Johns, J.; Kaewjaeng, S.; Kedkaew, C.; Chaiphaksa, W.; Sareein, T.; Kaewkhao, J. Wearable and flexible radiation shielding natural rubber composites: Effect of different radiation shielding fillers. Radiat. *Phys. Chem*. **2021**, *179*, 1-8. https://doi.org/10.1016/j.radphyschem.2020.109261.

[2] Mungpayaban, H.; Rindhatayathon, P.; Ninlaphruk, S.; Rueanngoen, A.; Ekgasit, S.; Pengprecha, S. X-ray protective materials from barium sulfate/amorphous cellulose/natural rubber composites. *Radiat. Phys. Chem*. **2022**, *194*, 1-10. https://doi.org/10.1016/j.radphyschem.2022.110011.

[3] Poltabtim, W.; Wimolmala, E.; Saenboonruang, K. Properties of lead-free gamma-ray shielding materials from metal oxide/EPDM rubber composites. *Radiat. Phys. Chem*. **2018**, *153*, 1–9. https://doi.org/10.1016/j.radphyschem.2018.08.036

ASEAN J. Sci. Tech. Report. **2025**, *28*(3), e256422.

9 of 9

[4]   Plangpleng, N.; Charoenphun, P.; Polpanich, D.; Sakulkaew, K.; Buasuwan, N.; Onjun, O.; Chuamsaamarkkee, K. Flexible gamma ray shielding based on natural Rubber/BaSO$_4$ nanocomposites. *Radiat. Phys. Chem*. **2022**, *199*, 1-8. https://doi.org/10.1016/j.radphyschem.2022.110311.

[5]   Kumar, P.; Niranjana, P.T.; Jineesh, A.G. BaSO$_4$ and Fe$_2$O$_3$ Filled polydimethylsiloxane elastomer nanocomposite as x-ray radiation resistant material. *RUAS-SASTech J*. **2018**, *17(1)*, 1-4.

[6]   Onjun, O.; Buasuwan, N.; Rungseesumran, T.; Kamwang, N.; Channuie, J. Natural rubber block as gamma radiation shielding for medical applications. *J. Phys. Conf. Ser 1285.* **2019**, 1-8. https://doi:10.1088/1742-6596/1285/1/012048.

[7]   Poltabtim, W.; Wimolmala, E.; Markpin, T.; Sombatsompop, N.; Rosarpitak, V.; Saenboonruang, K. X-ray shielding, mechanical, physical, and water absorption properties of wood/PVC composites containing bismuth oxide. *Polymers*. **2021**, *13*, 1-16. https://doi.org/10.3390/polym13132212.

[8]   Jaiyen, S.; Phumsuwan, A.; Thongpool, V.; Phunpueok, A. Determination of radiation attenuation coefficients of rubber containing barite. *Appl. Mech. Mater.* **2017**, *866,* 204-207. https://doi.org/10.4028/www.scientific.net/AMM.866.204.

[9]   Cherkasov, V.; Yurkin, Y.; Avdinin, V.; Suntsov, D. Self-adhesion x-ray shielding composite material of EPDM rubber with barite: Mechanical Properties. *Mater. Plast.* **2020**, *57*, 28-36. https://doi.org/10.37358/MP.20.1.5309.

[10]   Akkurt, I.; Akyıldırım, H.; Mavi, B.; Kilincarslan, S.; Basyigit, C. Photon attenuation coefficients of concrete includes barite in different rate. *Ann. Nucl. Energy*. **2010**, *37*, 910–914. https://doi.org/10.1016/j.anucene.2010.04.001.

[11]   Konruang, S.; Srisook, A.; Buaphet, P.; Tayeh, F.; Naebpetch, W. Preparation of Lead-Free X-Ray Shielding materials based on Natural Rubber/Barium Sulfate composites. *ASEAN J. Sci. Technol. Rep.* **2022**, *25,* 59-66. https://doi.org/10.55164/ajstr.v25i2.246574

[12]   Sukkaneewat, B.; Utara, S. Ultrasonic-assisted Dunlop method for natural rubber latex foam production: Effects of irradiation time on morphology and physico-mechanical properties of the foam. *Ultrason. Sonochem.* **2022**, *82*, https://doi.org/10.1016/j.ultsonch.2021.105873.

Leakage Current Modeling for Grounding in Single-Track Electric Mass Transit Systems

Tawat Chuchit[1], Supachai Kaewpoung[2], Wiwat Su-hren[3], Arnon Isaramongkolrak[4], and Tanawat Srirugsa[5*]

[1] Faculty of Engineering, Thaksin University, Phatthalung, 93210, Thailand
[2] Faculty of Engineering, Thaksin University, Phatthalung, 93210, Thailand
[3] Faculty of Engineering, Thaksin University, Phatthalung, 93210, Thailand
[4] Science and Technology, Nakhon Pathom Rajabhat University, Nakhon Pathom, 73000, Thailand
[5] Faculty of Engineering, Thaksin University, Phatthalung, 93210, Thailand
* Correspondence: tanawat.s@tsu.ac.th

Abstract: This study utilizes MATLAB/Simulink to analyze leakage current in the DC electric train power supply system. The objective is to develop simulation models using MATLAB/Simulink to evaluate and compare the simulation results with mathematical and discrete models. The study focuses on three simulation models with a drainage diode: FNRCS, SCCNS, and SCCNS. It examines leakage current behavior and assesses rail voltage characteristics over a distance of 0 to 5.00 km. The simulation results for the FNRCS model indicated a voltage drop from 169.90 V at the initial point to -297.38 V at 5.00 km, along with an increase in leakage current to 14.82 A. These findings align with both the discrete and mathematical models. Compared to the mathematical model, the average increase in leakage current was 40.07%. The simulation results for the SCCNS exhibited behavior similar to that of the FNRCS in terms of both rail voltage and leakage current. The average rail voltage of the SCCNS with a drainage diode was 284.62 V, demonstrating a steady decline. However, the leakage current increased significantly with distance. Compared to the SCCNS, SCCNS with a drainage diode exhibited higher rail voltage in the 0-3.00 km range and lower rail voltage in the 3.00-5.00 km range. The development of MATLAB/Simulink models for the railway power supply system has proven to be a practical approach for analyzing rail voltage and leakage current, offering valuable insights compared to discrete and mathematical models.

Keywords: Leakage current; Rail voltage; MATLAB/Simulink; DC electric rail transit systems

1. Introduction

Power supply systems for electric railroads are now being developed further to improve system efficiency. Consequently, more and more specialist researchers are adopting computer simulation tools to create models. This strategy is becoming more popular because it is difficult to test or alter systems because of the high cost and lengthy installation time, particularly when making changes to the system. For long-term implementation, however, research on minimizing electrical leakage in railway systems has emerged as a crucial component of system analysis [1]. Various study approaches and methodologies are used to understand the effects of electrical leakage and suggest ways to reduce the dangers involved. To evaluate the behavior of electrical leakage in various systems, such as predicting the impacts of soil resistance through simulations, these studies frequently employ numerical approaches and mathematical models [2-3]. Furthermore, designs aimed at lowering the hazards

ASEAN J. Sci. Tech. Report. **2025**, 28(3), e257546

2 of 24

of leaking to the structural integrity of the rails are being developed as part of recommendations for managing electrical leakage in both above-ground and underground railway systems [4-5].

However, Studies of these systems also emphasize how crucial it is to use the right materials and technologies to lower energy loss and improve rail transport systems' safety [6-7]. Furthermore, enhancing railway power supply systems requires assessing the use of materials to reduce electrical leakage [8] and creating methods for identifying electrical leakage in railway transport systems [9]. These efforts aid in developing detection systems and maintenance procedures to monitor electrical leakage precisely [10]. Additionally, electrical leakage analysis in railway power supply systems is essential for advancing and enhancing railway transport systems, especially regarding safety and reducing energy losses in the electrical network [11-12]. The behavior of electrical leakage in three different simulated scenarios has been studied and compared using MATLAB/Simulink simulation tools. A comparison between mathematical and commercially available simulation models has also been conducted [13]. The conductivity between the soil and rails is a crucial factor in determining the features of the leakage current and rail voltage, as evidenced by the findings of earlier research that showed notable variations in the incidence of electrical leakage in each situation [14-15].

Understanding how different environmental conditions, such as humidity, temperature, and rail design, affect electrical leakage requires parameter modeling techniques [16-17]. This emphasizes the necessity of creating new models to help with more accurate calculations and electrical leak detection. Furthermore, studies have concentrated on reducing electrical leakage using novel materials and technologies, which may enhance intercity railway power systems [18-19]. Another important area of study is the effect of electrical leaks on rail structures and how to identify leaks caused by poor design [20-21]. These studies offer strategies for creating maintenance and detection systems that lower the hazards of electrical leaks [22]. These studies, which use engineering analysis and simulation methodologies, are crucial for planning and creating future electrical systems that are safer, more efficient, and more effective, in addition to helping to understand how electrical leakage behaves in electric rail systems. Research in this area is crucial to further the development of high-performance electric rail systems. It focuses on energy-efficient electrical system design, electrical leakage behavior simulation, and guaranteeing safety in future railway transport systems [23-34].

The Direct Current (DC) Railway System is still widely used in many cities worldwide. It was created to ease traffic congestion and promote public transit. The third rail in this system provides power to the trains, while the running rail acts as the driving current's return conductor. Some electrical current leaks or stray currents return to the power station through the ground due to insufficient insulation between the running rail and the ground [25]. Since it is usually challenging to monitor stray currents directly, voltage variations between the ground and the running rail are usually measured instead. The rail potential is the name given to this voltage differential. Furthermore, stray currents are dangerous since, according to the EN-50122-1 standard for DC railway systems, the voltage that can be touched should not be higher than 120 V for longer than 300 seconds. Following EN-50122-2, the rail's voltage shall not surpass 5 V in a 24-hour period [26-28]. Evaluating and regulating the rail voltage is crucial to avoid or lessen such harm. As a result, it is essential to build models for assessing rail voltage and carry out basic research for these evaluations [29-32].

This study aims to create a MATLAB/Simulink model of the electric railway track power supply system to examine leakage current and rail potential voltage. (Figure 1), depicts a DC traction system, which serves as the model's starting point. The EN-50122-2 standard is followed in the design of the railway system's bonding and earthing. Furthermore, the model is constructed following the guidelines for electric train power supply systems, integrating the models of the FNRCS, the SCCNS, and the SCCNS with a drainage diode. The variations in leakage current and rail potential voltage within the system under study are compared using these models.

ASEAN J. Sci. Tech. Report. **2025**, *28*(3), e257546.

3 of 24
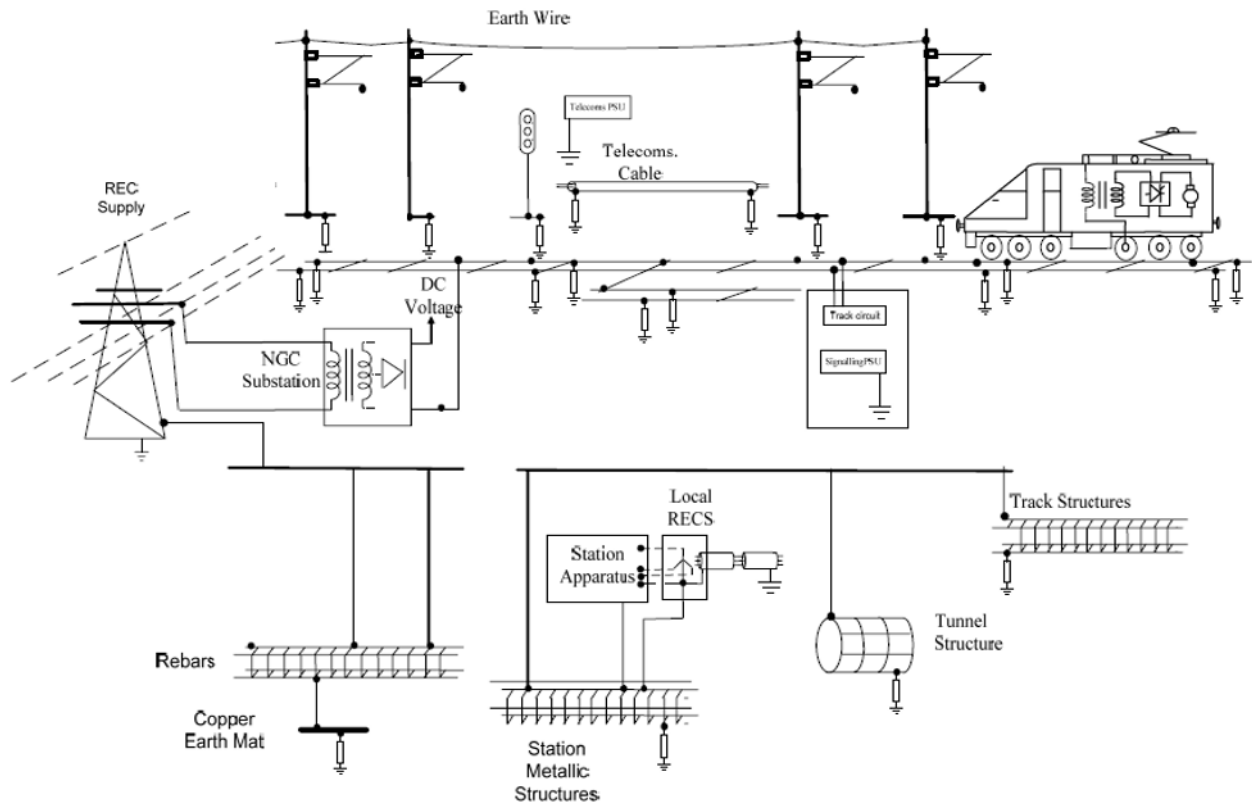
Figure 1. Structural earthing and bonding in the railway system with EN-50122-2 [33].

This grounding setup for DC electric train power supply systems is called the Rail Insulation System (RIS) and its construction (Figure 1). Electric current returns to the power substation via the train wheels and running rails in this arrangement. Due to the absence of electrical insulation between the running rails and the sleepers or other supporting structures, stray currents could seep into different areas of the infrastructure in traditional railway systems. As a result, there were intricate and challenging alternative return routes. To mitigate this problem, contemporary railway systems have integrated electrical insulation between the running rails and supporting elements. This has been shown to minimize corrosion of metallic structures and effectively reduce stray current leakage. The conductance per unit length between the ground and the running rails (track-to-earth) should not be greater than 500 mS/km for open formation systems and 2500 mS/km for closed formation systems, according to the EN-50122-2 standard. To ensure that every component is correctly grounded following EN-50122-2, the system also calls for improved earthing and bonding of metallic structures and reinforced concrete components. Installing low-resistance rail joint bonds across the rail network is necessary to reduce voltage drops along the rails further. The total rail resistance cannot rise by more than 5% due to the extra resistance these bonds add. Both running rails in double-track railway systems need to be connected to ensure efficient current return pathways. Improved safety and operational efficiency are guaranteed by the widespread adoption of this system configuration on Network Rail's DC railway networks in the UK (United Kingdom).

2. Theories and Mathematical models

A thorough grasp of basic ideas and concepts is necessary to create a model for evaluating different electrical parameters in the electric train power supply system. These are necessary for simplifying the process and computing the parameters using simple equations from the system's single-line diagram model. Computer programming tools are used to produce precise calculations while reducing computation complexity and time. The two primary sections of this section address the pertinent theories and mathematical models of the electric train power supply system. According to the established standards, the first section discusses the DC electric traction system's structure and methods for determining leakage current and voltage.

ASEAN J. Sci. Tech. Report. **2025**, 28(3), e257546

4 of 24

The main topics of the second section are the tractive force of the train and the properties of the electrical power needed for train motion. Both sections are essential for creating a model with MATLAB/Simulink, a computer program that effectively computes the necessary values.

2.1 DC Traction Earthing System

The DC Traction Earthing System, a grounding system structure of the DC traction system, is essential for controlling and managing the return current that flows from the traction motors back to the power source. This is crucial for improving railway operations' efficiency and guaranteeing operational safety. The three main types of systems are the floating negative return current system (FNRCS), the sty current collecting net system (SCCNS), and the SCCNS with a drainage diode. Each system functions according to certain principles to safely control return currents and preserve DC railway systems' functionality.

2.1.1. FNRCS

The negative busbar is not grounded from the rectifier substation's output in the FNRCS design. Because the substation isn't directly connected to the ground, the voltage at the negative busbar floats and doesn't always stay at zero. High touch voltage is more likely in this setup, which could endanger operational staff or living things who might unintentionally come into contact with the system. Additional rail potential control devices must be installed to manage the rail voltage and reduce this risk. This configuration of the system (Figure 2). Hong Kong's LRT and Singapore's MRT are two notable train systems that use this basic technique. This article simulates the FNRCS system using a remote ground for grounding, which has an approximate value of zero ohms, as per the RIS.
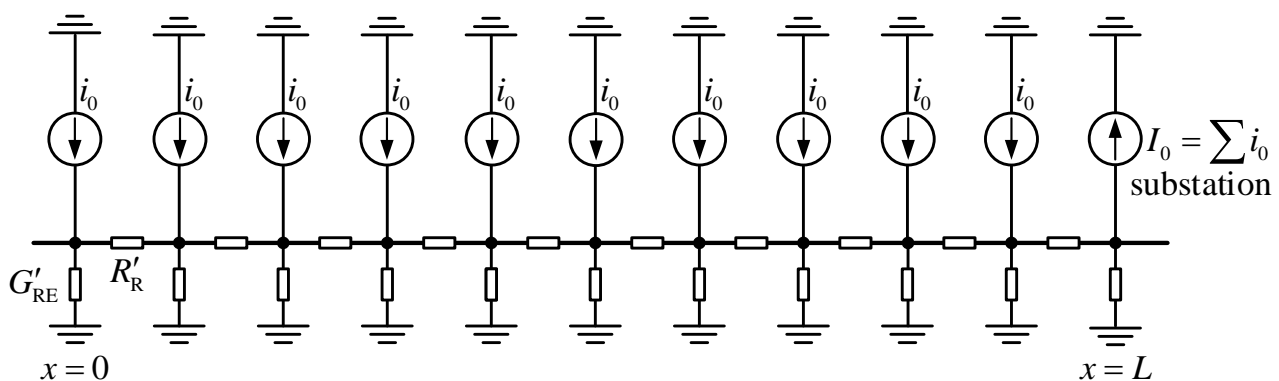
Figure 2. Circuit diagram for FNRCS.

Concerning the non-continuous (discrete) distribution of current sources in the FNRCS, (Figure 2) depicts the structure of discretely distributed current sources. The purpose of this setup is to effectively regulate and control the flow of return current in a DC traction system. Reducing stray current leakage into the ground and preventing corrosion of metallic infrastructure elements, like underground pipelines and railroad tracks, are the goals of the discrete distribution of current sources. The system structure has been converted into a mathematical analysis scheme to efficiently examine and compute the electrical behavior within the FNRCS (Figure 3). This transformation makes it easier to depict how the system operates mathematically by representing the discrete current sources as mathematical current sources. This method makes analyzing the distribution of voltage and current throughout the system easier and more systematic. Additionally (Figure 4), the FNRCS structure's mathematical modeling makes it possible to create an equivalent circuit for assessing the possible drop along a section of railroad track. This analogous circuit faithfully simulates the behavior of electrical currents and voltages across different system components. It usually consists of current sources that replicate return currents and possible stray currents, as well as resistors that represent the resistance of the rails and wires.
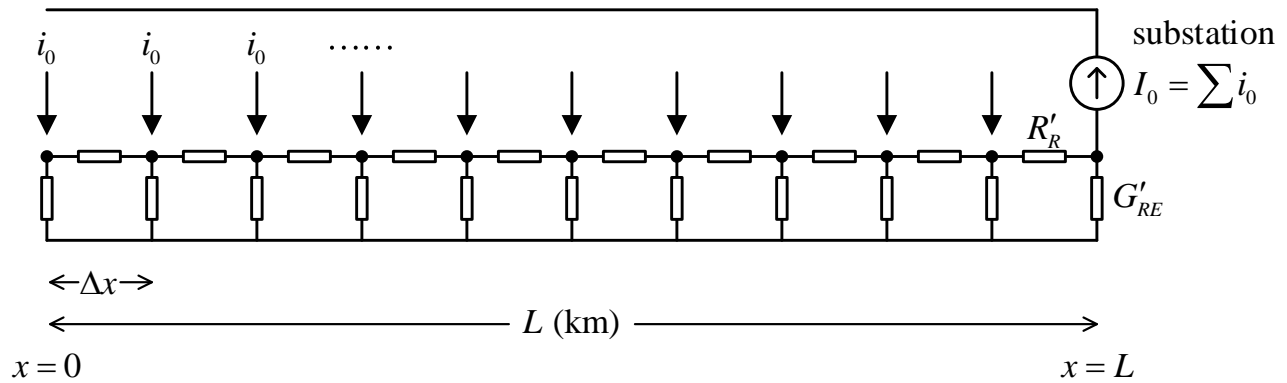
Figure 3. Circuit diagram scheme for the mathematical model.
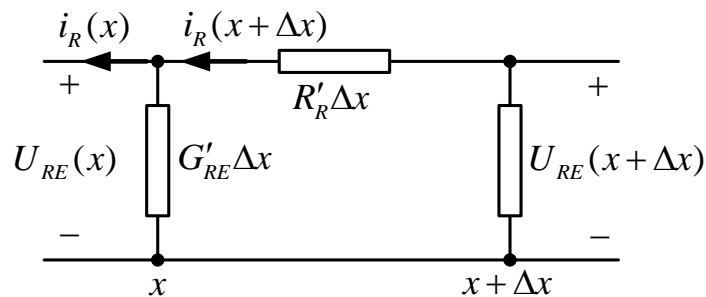
Figure 4. Potential drop along a track element

Using Kirchhoff's voltage law, which is represented in equation (1), the analysis may be completed from (Figure 4). Equation (2) illustrates how to rewrite the problem by setting (), and equation (3) is also obtained by applying Kirchhoff's current law at node (x). Equation (4) can be obtained by further simplifying the equation when ($\Delta x \rightarrow 0$), equation (5) is the final result of taking the derivative of equation (4) concerning (x).

$$-U_{RE}(x+\Delta x)+i_R(x+\Delta x)R_R'\Delta x+U_{RE}(x)=0 \tag{1}$$

$$\frac{dU_{RE}(x)}{dx}=i_R(x)R_R' \tag{2}$$

$$i_R(x+\Delta x)=U_{RE}(x)G_{RE}'\Delta x+i_R(x) \tag{3}$$

$$\frac{di_R(x)}{dx}=U_{RE}(x)G_{RE}' \tag{4}$$

$$\frac{d^2i_R(x)}{dx^2}=\frac{dU_{RE}(x)}{dx}G_{RE}' \tag{5}$$

The result of reformatting equation (5) after substituting equation (2) is equation (6). Equation (7), which is obtained by further rearranging the equation with ($\alpha=\sqrt{R_R'G_{RE}'}$), is obtained. As a result, the form given in equation (8) is used to get the answer for the second-order derivative. If (L) is the length of the distance interval under discussion, and (x) is the beginning point at the power supply station (Figure 3), then (A) and (B) may be

ASEAN J. Sci. Tech. Report. **2025**, 28(3), e257546

6 of 24

found using the conditions at (x = 0) and (x = L), which are (At x = 0: $i_R(0) = 0$) and (At x = L: $i_R(L) = I_0 = i_0 L$). Subsequently, the equations are rewritten as (9) and (10).

$$\frac{d^2 i_R(x)}{dx^2} = i_R(x) R'_R G'_{RE}$$
$$= \alpha^2 i_R(x) \tag{6}$$

$$\frac{d^2 I_R(x)}{dx^2} - \alpha^2 I_R(x) = 0 \tag{7}$$

$$i_R(x) = Ae^{\alpha x} + Be^{-\alpha x} \tag{8}$$

$$0 = A + B \rightarrow A = -B \tag{9}$$

$$i_0 L = Ae^{\alpha L} + Be^{-\alpha L} \tag{10}$$

The equations in (4) and (5) are changed to solve for (A) and (B). Equations (12) and (13) are obtained by reformatting equation (11) and substituting it into equation (8). Following that, the leakage current at position (x) that flows from the rail through the soil at a distance (x) is represented by the current ($i_l(x)$), which is then computed. Equation (14) is the new formulation of the equation.

$$A = \frac{i_0 L}{e^{\alpha L} - e^{-\alpha L}} \text{ and } B = -\frac{i_0 L}{e^{\alpha L} - e^{-\alpha L}} \tag{11}$$

$$i_R(x) = \frac{i_0 L}{e^{\alpha L} - e^{-\alpha L}} e^{\alpha x} - \frac{i_0 L}{e^{\alpha L} - e^{-\alpha L}} e^{-\alpha x}$$
$$= \frac{i_0 L}{e^{\alpha L} - e^{-\alpha L}} \left(e^{\alpha x} - e^{-\alpha x} \right) \tag{12}$$

$$i_R(x) = \frac{i_0 L}{\sinh(\alpha L)} \sinh(\alpha x) \tag{13}$$

$$i_l = i_0 x - i_x = i_0 x - \frac{i_0 L \sinh \alpha x}{\sinh \alpha L} \tag{14}$$

The leakage current ($i_{l\max}$) is then computed by setting the voltage at point (N) to zero, as stated in equation (15). Equation (16) illustrates the reformed equation. Furthermore, equation (17) provides the rail's voltage ($U_{RE}(x)$) at a distance (x) from the power supply station.

$$N = \frac{1}{\alpha} \cosh^{-1} \frac{\sinh \alpha L}{\alpha L} \tag{15}$$

$$i_{l\max} = i_0 \frac{1}{\alpha} \cosh^{-1} \frac{\sinh \alpha L}{\alpha L} - \frac{i_0 L}{\sinh \alpha L} \sqrt{\frac{\sinh^2 \alpha L}{\alpha^2 L^2} - 1} \tag{16}$$

ASEAN J. Sci. Tech. Report. **2025**, *28*(3), e257546.

7 of 24

$$U_{RE}(x) = \frac{1}{G'_{RE}} \frac{di_l}{dx}$$
$$= \frac{i_0}{G'_{RE}} \left(1 - \frac{\alpha L}{\sinh \alpha L} \cosh \alpha x \right)$$

(17)

Moreover, the computational process is made simpler by using mathematical model analysis. Equation (17) can be used to compute the voltage mathematically, and equation (18) can be used to define the node analysis approach, which determines the current at any position (x).

$$i_R(k+1) = \frac{U_{RE}(k+1) - U_{RE}(k-1)}{R'_R \Delta x}$$

(18)

2.1.2. SCCNS

For electric train systems that run on elevated structures or in tunnels, the SCCNS was created especially. This technique installs an SCCNS inside the tunnel or raised structure to stop metallic components from corroding. Furthermore, the net is positioned between the structure and the running rails, and it has incorporated diodes to help return stray currents to the power substation. According to additional research on this system, touch voltage can be increased about two times when an SCCNS is used, as opposed to when the net is not used. The Bangkok Transit System (BTS), created and built by SIEMENS, is a noteworthy case study. By contrasting two configurations, one with metallic bonding in the reinforced concrete structure and another with installing the SCCNS with a drainage diode, SIEMENS assessed the possible effects of stray currents in the elevated structure during the design phase (Figure 5). Stray current levels increased by up to ten times after the SCCNS was implemented, according to the results. Therefore, instead of using drainage diodes or an SCCNS, the BTS constructor chose to ground the metallic elements of the reinforced concrete structure. Based on these results, SIEMENS also advised against using drainage diodes to mitigate stray currents because of their inefficiency in lessening their effects [34].
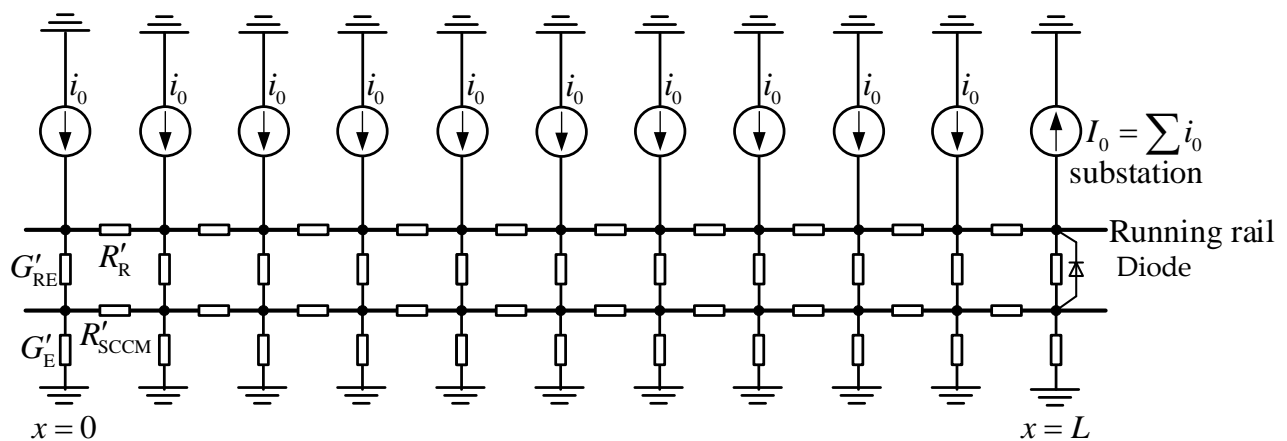
Figure 5. Circuit diagram for SCCNS with a drainage diode.

Installed the SCCNS system in diode-connected and non-diode-connected variants (Figure 5). Equation (19) illustrates how this arrangement uses node analysis to determine the link between (I) and (V). Based on standard standards, this method can be used for basic comparison analysis. (Figure 6), the complex and intricate equations are solved using the matrix form (G). Furthermore, the matrix formulations for the diode-connected and non-diode-connected scenarios are given by equations (20) and (21), respectively, when $I_n^{(R)}$, $I_{n+1}^{(s)}$ is the current entering and exiting node n via the running rail and ground structure, $G_{n,n}$ is represents

ASEAN J. Sci. Tech. Report. **2025**, 28(3), e257546

8 of 24

conductance at position $n \times n$, $V_n^{(R)}$, $V_{n+1}^{(S)}$ is the voltage at node n via the running rail and ground structure and V_d is the voltage across the diode.
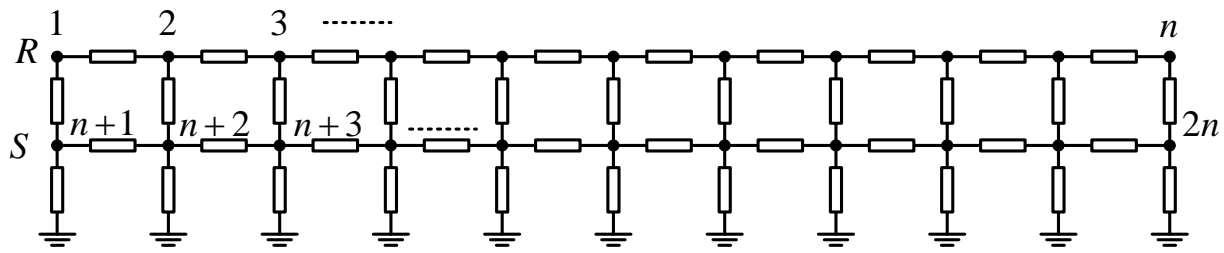
Figure 6. Circuit diagram scheme for mathematical SCCNS model.

$$[I] = [G][V] \tag{19}$$

$$
\begin{bmatrix}
I_1^{(R)} \\
I_2^{(R)} \\
\vdots \\
I_N^{(R)} \\
I_{n+1}^{(S)} \\
I_{n+2}^{(S)} \\
\vdots \\
I_{2n}^{(S)}
\end{bmatrix}
=
\begin{bmatrix}
G_{1,1} & G_{1,2} & \cdots & G_{1,n} & G_{1,n+1} & G_{1,n+2} & \cdots & G_{1,2n} \\
G_{2,1} & G_{2,2} & \cdots & G_{2,n} & G_{2,n+1} & G_{2,n+2} & \cdots & G_{2,2n} \\
\vdots & \vdots & \ddots & \vdots & \vdots & \vdots & \ddots & \vdots \\
G_{n,1} & G_{n,2} & \cdots & G_{n,n} & G_{n,n+1} & G_{n,n+2} & \cdots & G_{n,2n} \\
G_{n+1,1} & G_{n+1,2} & \cdots & G_{n+1,n} & G_{n+1,n+1} & G_{n+1,n+2} & \cdots & G_{n+1,2n} \\
G_{n+2,1} & G_{n+2,2} & \cdots & G_{N+2,n} & G_{n+2,n+1} & G_{n+2,n+2} & \cdots & G_{n+2,2n} \\
\vdots & \vdots & \ddots & \vdots & \vdots & \vdots & \ddots & \vdots \\
G_{2n,1} & G_{2n,2} & \cdots & G_{2n,n} & G_{2n,n+1} & G_{2n,n+2} & \cdots & G_{2n,2n}
\end{bmatrix}
\begin{bmatrix}
V_1^{(R)} \\
V_2^{(R)} \\
\vdots \\
V_n^{(R)} \\
V_{n+1}^{(S)} \\
V_{n+2}^{(S)} \\
\vdots \\
V_{2n}^{(S)}
\end{bmatrix} \tag{20}
$$

$$
\begin{bmatrix}
I_1^{(R)} \\
I_2^{(R)} \\
\vdots \\
I_n^{(R)} \\
I_{n+1}^{(S)} \\
I_{n+2}^{(S)} \\
\vdots \\
I_{2n}^{(S)} \\
V_d
\end{bmatrix}
=
\begin{bmatrix}
G_{1,1} & G_{1,2} & \cdots & G_{1,n} & G_{1,n+1} & G_{1,n+2} & \cdots & G_{1,2n} & 0 \\
G_{2,1} & G_{2,2} & \cdots & G_{2,n} & G_{2,n+1} & G_{2,n+2} & \cdots & G_{2,2n} & 0 \\
\vdots & \vdots & \ddots & \vdots & \vdots & \vdots & \ddots & \vdots & \vdots \\
G_{n,1} & G_{n,2} & \cdots & G_{n,n} & G_{n,n+1} & G_{n,n+2} & \cdots & G_{n,2n} & 1 \\
G_{n+1,1} & G_{n+1,2} & \cdots & G_{n+1,n} & G_{n+1,n+1} & G_{n+1,n+2} & \cdots & G_{n+1,2n} & 0 \\
G_{n+2,1} & G_{n+2,2} & \cdots & G_{n+2,n} & G_{n+2,n+1} & G_{n+2,n+2} & \cdots & G_{n+2,2n} & 0 \\
\vdots & \vdots & \ddots & \vdots & \vdots & \vdots & \ddots & \vdots & \vdots \\
G_{2n,1} & G_{2n,2} & \cdots & G_{2n,n} & G_{2n,n+1} & G_{2n,n+2} & \cdots & G_{2n,2n} & -1 \\
0 & 0 & \cdots & 1 & 0 & 0 & \cdots & -1 & 0
\end{bmatrix}
\begin{bmatrix}
V_1^{(R)} \\
V_2^{(R)} \\
\vdots \\
V_n^{(R)} \\
V_{n+1}^{(S)} \\
V_{n+2}^{(S)} \\
\vdots \\
V_{2n}^{(S)} \\
IV_d
\end{bmatrix} \tag{21}
$$

2.2 Driving of trains in railway systems.

Electric train motion is taken into account by the drive system. Depending on the manufacturer's technology, the electric train's driving motor could be an induction, synchronous, or DC motor. The general motion of the electric train set is the main emphasis of the modeling used to drive it. The traction force, the gradient force, and the electric train's resistance are the main forces driving the motion. (Figure 7) shows how the motion of the electric train was calculated and the forces at play. Equation (22) illustrates Newton's second rule of motion, which serves as the foundation for the fundamental equation used to examine the velocity of the electric train.

ASEAN J. Sci. Tech. Report. **2025**, *28*(3), e257546.

9 of 24

The following definitions of the various parameters are derived (Figure 7) and equation (22). (M_{eff}) represents the effective vehicle mass (kg), (TE) represents the tractive effort (N),(T_R) represents the train resistance (N),(F_{grad}) represents the gradient force (N), and (α) represents the train acceleration (m/s²), where an is positive for uphill motion and negative for downhill motion [35-36].
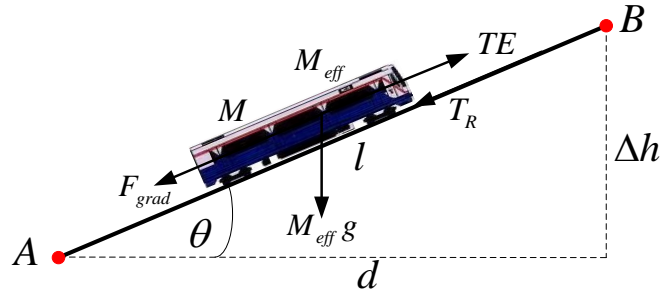
Figure 7. Computerized model for assessing train traction force [35-36].

$$F = TE - F_{grad} - T_R = M_{eff}\alpha \tag{22}$$

2.2.1. *Tractive effort*

The electric locomotive has traction motors to move the train. As a result, the electric locomotive's tractive force must be described for the simulation. This entails using the motor's torque-speed curve directly, where the torque from the motor is converted into tractive force and sent to the wheels via a gear reduction mechanism. The motion of the electric train can be calculated using the resulting tractive force, which the gear ratio has modified. Depending on the train's linear velocity in meters per second (m/s) or kilometers per hour (km/h), the electric train's tractive force graph, which is measured (N), changes. The figure shows the graph as dashed lines at various motor speeds. Plotting of the resulting tractive force with the horizontal axis converted to linear speed occurs after the gear ratio has been modified to account for the wheel radius and gear transmission efficiency. This results in the electric train's tractive force curve (Figure 8).
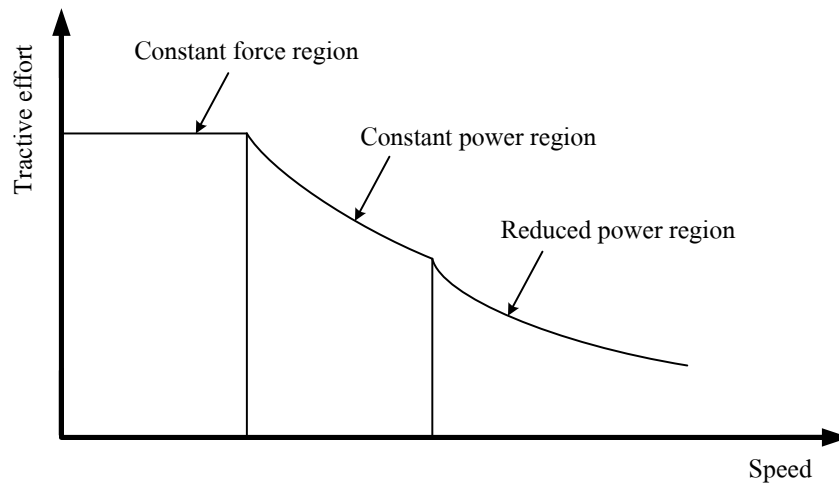
Figure 8. The tractive force of train propulsion and rotational speed of the traction motor.

2.2.2. *Gradient force*

Separate consideration is also given to the gravitational force acting at an inclined angle to the ground. A portion of the train's weight acts on the electric train due to its mass as it moves on a track angled on the ground. According to equation (23), this force can either support or oppose the train's motion. Additionally,

ASEAN *J. Sci. Tech. Report.* **2025**, *28*(3), e257546

10 of 24

the effective weight of the electric train can be computed using equation (24), in which the passenger mass factor is indicated by (λ_w) and the tare weight is represented by (M_t).

$$F_{grad} = \pm M_{eff} \, g \sin \theta \tag{23}$$

$$M_{eff} = M_t (1 + \lambda_w) \tag{24}$$

2.2.3. Train resistance

Generally speaking, the motion of a train encounters resistive forces from air resistance and wheel-rail friction, which are combined to form the resistive force. Equation (25) can be used to determine the train's total resistance. The train's speed (km/h) is represented by (v), and the constant Davis coefficients are (A: kN), (B: kN·h/km), and (C: kN·h²/km²).

$$T_R = A + Bv + Cv^2 \tag{25}$$

2.2.4. Operating Modes of Electric Trains

The operation uses the train's speed-time curve's properties to manage the movement of a train to carry people between two stations. (Figure 9), the train can be operated in four fundamental modes: coasting, braking, cruising or constant-speed, and accelerating. The train's operation may alternate between various modes depending on the intended goals. For example, the train may switch between coasting and accelerating modes to maximize energy efficiency and reduce energy consumption.
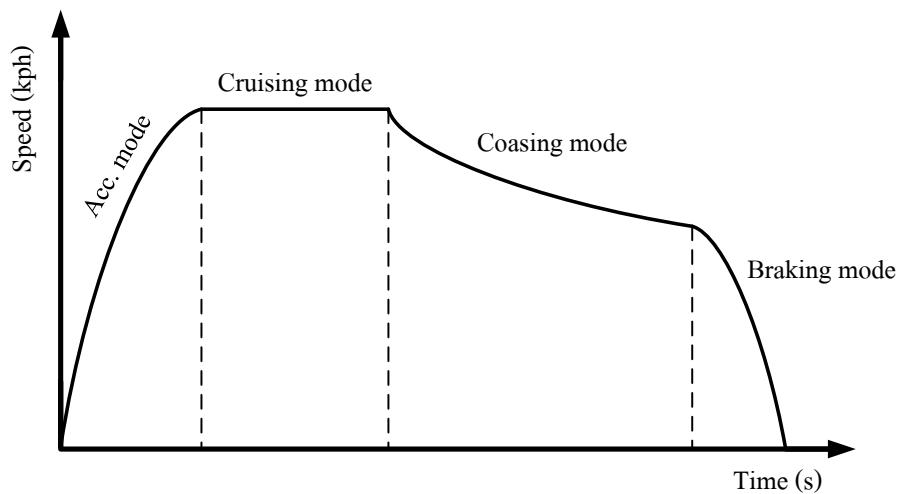
Figure 9. Characteristics of operating modes of electric trains.

According to (Figure 9), the train's operational modes determine the tractive force in each mode, which is determined by the control method. While in the accelerating mode, the train starts to accelerate from the station at a predetermined rate until it achieves the service speed. The train's acceleration is positive during this period ($\alpha_{acc} > 0$), and equation (22) can be used to determine the tractive force. After the train achieves the service speed, it enters the constant-speed mode, which keeps the speed constant until it reaches the coasting mode starting point (L_{coast}), where ($\alpha_{acc} = 0$). In the coasting mode, acceleration becomes negative, and the tractive effort drops to zero ($TE = 0$). On the other hand, when descending a steep hill, the acceleration may be positive. When the train reaches the specified braking distance or the necessary speed, it applies a negative acceleration ($\alpha_{dec} < 0$) and enters the braking mode. The tractive force, train velocity, and the effectiveness of converting mechanical energy to electrical energy (η) affect how much electric power (P : kW)

ASEAN J. Sci. Tech. Report. **2025**, *28*(3), e257546.

11 of 24

is needed to move the train. This can be calculated using equation (26). Additionally, equation (27) illustrates how the relationship can be written in terms of the substation current (I_0: A) and voltage (V_0 : V).

$$P = \frac{TE \times v}{\eta} \tag{26}$$

$$I_0 = \frac{P}{V_0} \tag{27}$$

3. Methodology and Simulation results

This study analyzes leakage current in the electric rail supply system using simulation techniques with MATLAB/Simulink. The intricacy and large-scale factors required to describe the electric rail supply system led to the selection of MATLAB/Simulink. The FNRCS, the SCCNS, and the SCCNS with a drainage diode are the three scenarios that make up the simulation. Using the single-line diagram format, the modeling procedure in all three cases closely adheres to the design and installation guidelines specified in EN-50122-2. These models are then created in MATLAB/Simulink to examine the simulation outcomes. Nevertheless, the three models, FNRCS, SCCNS, and SCCNS with a drainage diode, are commonly employed in current applications. Every model possesses distinct features that render it appropriate for different case studies. These models were chosen as the primary case studies for this research due to their effectiveness in analyzing real-world systems. This holds especially when the models are applied to analyze system behavior in actual environmental contexts. By choosing these models, one can gain a clearer insight into how the system functions and provide analysis results that are precise and applicable to actual circumstances. The following sections provide a methodical presentation of the specific simulation steps.

3.1 Simulation FNRCS model

The simulation settings are listed in the appendix (Table 8) for the FNRCS model (Figure 3), which analyzes the electric rail supply system's leakage current and voltage characteristics. The appendix (Table 7) lists the MATLAB/Simulink tools used to design and simulate these parameters. The FNRCS model was created for MATLAB/Simulink analysis, as shown in the appendix (Figure 19). To compare the outcomes of the discrete and mathematical models, this system was simulated using MATLAB/Simulink. The simulation results for voltage characteristics from the discrete model, mathematical model, and MATLAB/Simulink are presented in (Table 1) and (Table 2), respectively, when the conductance between the rail and earth was set to 0.01 S/km (for good insulation conditions) and 0.10 S/km (for insulation degradation or rainy conditions). Furthermore, (Table 3) and (Table 4), respectively, exhibit the simulation findings for leakage current.

Table 1. The rail voltage results are 0.01 S/km based on the conductance to earth FNRCS model.

No.	Distance (km)	Rail voltage (V)		
		Mathematical model	Discrete model	MATLAB/Simulink
1	0	141.5965	169.8978	169.8978
2	0.50	137.3494	161.4050	161.4050
3	1.00	124.6083	144.4191	144.4191
4	1.50	103.3723	118.9393	118.9393
5	2.00	73.6407	84.9646	84.9646
6	2.50	35.4123	42.4935	42.4935
7	3.00	-11.3147	-8.4758	-8.4758
8	3.50	-66.5422	-67.9455	-67.9455
9	4.00	-130.2726	-135.9180	-135.9180
10	4.50	-202.5085	-212.3964	-212.3964
11	5.00	-283.2531	-297.3837	-297.3837

Table 2. The rail voltage results are 0.10 S/km based on the conductance-to-earth FNRCS model.

No.	Distance (km)	Rail voltage (V)		
		Mathematical model	Discrete model	MATLAB/Simulink
1	0	140.9674	168.9832	168.9832
2	0.50	136.7472	160.5550	160.5550
3	1.00	124.0848	143.6951	143.6951
4	1.50	102.9749	118.3962	118.3962
5	2.00	73.4084	84.6476	84.6476
6	2.50	35.3728	42.4351	42.4351
7	3.00	-11.1480	-8.2595	-8.2595
8	3.50	-66.1739	-67.4575	-67.4575
9	4.00	-129.7282	-135.1843	-135.1843
10	4.50	-201.8380	-211.4684	-211.4684
11	5.00	-282.5338	-296.3425	-296.3425

Table 3. The leakage current results are 0.01 S/km based on the conductance to earth FNRCS model.

No.	Distance (km)	Leakage current (A)		
		Mathematical model	Discrete model	MATLAB/Simulink
1	0	0.0000	0.0000	0.0000
2	0.50	0.7009	0.8495	0.8495
3	1.00	1.3593	1.6565	1.6565
4	1.50	1.9328	2.3786	2.3786
5	2.00	2.3789	2.9733	2.9733
6	2.50	2.6551	3.3981	3.3981
7	3.00	2.7189	3.6106	3.6106
8	3.50	2.5278	3.5682	3.5682
9	4.00	2.0393	3.2285	3.2285
10	4.50	1.2109	2.5489	2.5489
11	5.00	0.0000	1.4869	1.4869

Table 4. The leakage current results are 0.10 S/km based on the conductance to earth FNRCS model.

No.	Distance (km)	Leakage current (A)		
		Mathematical model	Discrete model	MATLAB/Simulink
1	0	0.0000	0.0000	0.0000
2	0.50	6.9780	8.4492	8.4492
3	1.00	13.5340	16.4769	16.4769
4	1.50	19.2457	23.6617	23.6617
5	2.00	23.6906	29.5815	29.5815
6	2.50	26.4454	33.8139	33.8139
7	3.00	27.0864	35.9356	35.9356
8	3.50	25.1889	35.5226	35.5226
9	4.00	20.3269	32.1498	32.1498
10	4.50	12.0734	25.3905	25.3905
11	5.00	0.0000	14.8171	14.8171
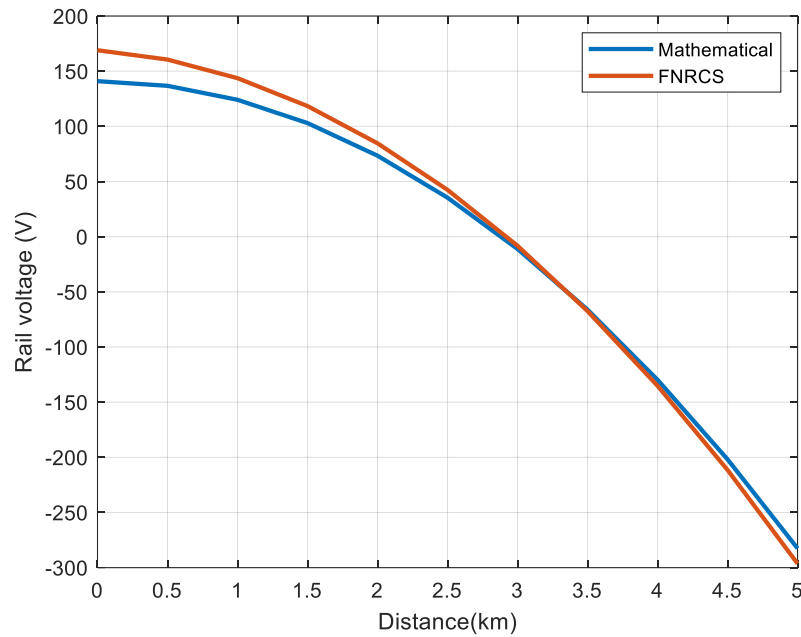
Figure 10. Results in conductance between the rail and earth by varying the rail voltage for the FNRCS model.

Voltage characteristics of the rail were evaluated and compared from (Table 1), which shows the simulation results with the conductance between the rail and earth set at 0.01 S/km for the FNRCS model, and (Table 2), where the conductance is set at 0.10 S/km. The discrete model and the simulation results from MATLAB/Simulink agreed. Consequently, the results of the discrete model were compared to those of the mathematical model. (Figure 10) shows the characteristics of rail voltage. The findings of the comparative simulation indicated an average percentage difference of 8.64% for 0.01 S/km and 8.47% for 0.10 S/km.

Furthermore, by contrasting the discrete and mathematical models, the simulation results for leakage current were examined, as indicated in (Table 3), with the conductance between the rail and earth fixed at 0.01 S/km. The discrete model's results and MATLAB Simulink's simulation results agreed. As seen in (Figure 11), this comparison showed that the leakage current rose by an average of 40.07%.
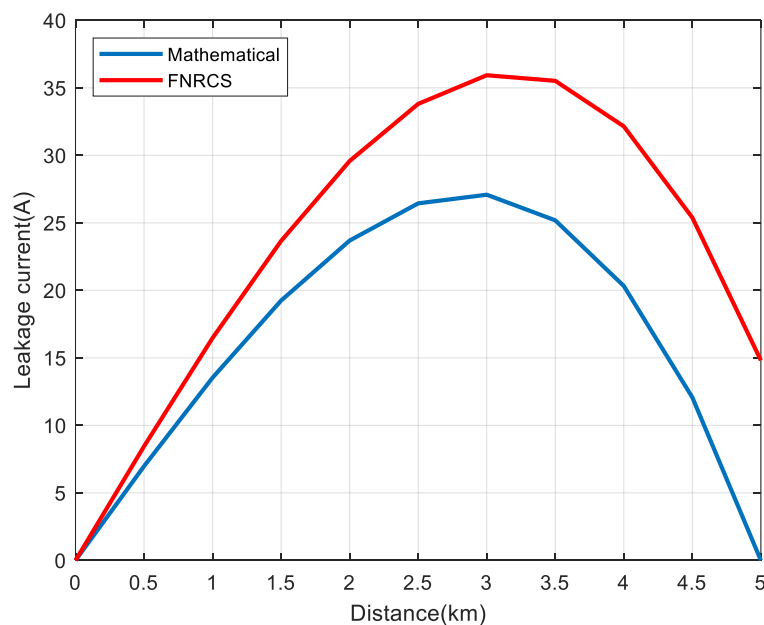
Figure 11. Results leakage current between discrete and mathematical models for the FNRCS model.

ASEAN J. Sci. Tech. Report. **2025**, *28*(3), e257546

14 of 24
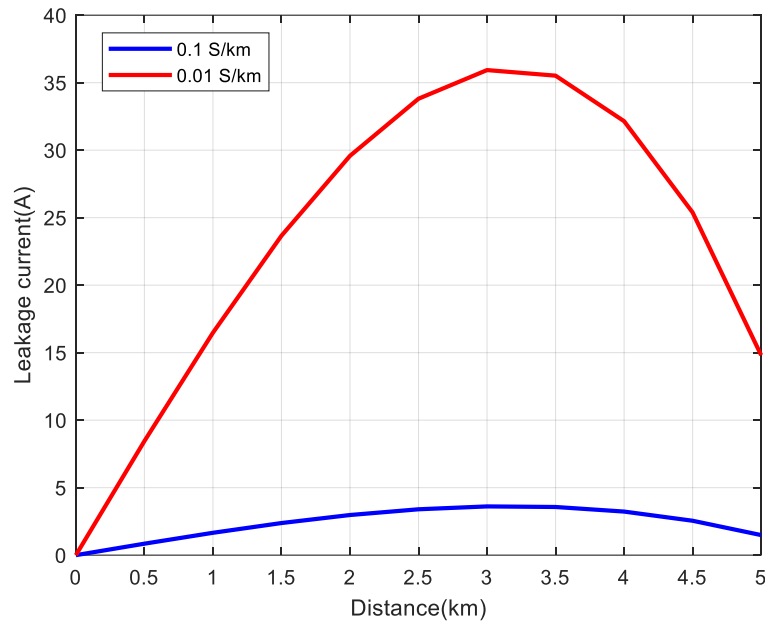
Figure 12. Results leakage current discrete model conductance between rail and earth 0.1 S/km and 0.01 S/km.

With the conductance between the rail and earth set at 0.01 S/km and 0.10 S/km using only the discrete model, the results of the analysis and comparison of leakage current simulations in (Table 3) and (Table 4) indicated that the leakage current dropped by an average of 89.96% and 89.95%, respectively. (Figure 12) shows the results of these findings.

3.2 Simulation SCCNS model

To simulate the SCCNS model, as shown in (Figure 5) and (Figure 6), matrix-based equations in equation (20) were used to examine the electric rail supply system's voltage and leakage current characteristics. The MATLAB/Simulink model creation tools are described in the appendix (Table 7), and the simulation parameters are listed in the appendix (Table 9). The appendix (Figure 20) illustrates how the SCCNS model was subsequently created for MATLAB/Simulink voltage and leakage current analysis. As shown in (Table 5), this system was simulated using MATLAB/Simulink to compare the outcomes with the discrete model. Furthermore, a comparison was made between the FNRCS model (cited in Topic 3.1) and the SCCNS model's simulation findings for rail voltage and leakage current. (Figure 13) shows the results of the simulation for rail voltage, and (Figure 14) shows the results for leakage current. As a result, comparing the simulations of the two models showed that the outcomes nearly matched and followed the same pattern.

Table 5. Results of the simulation for rail voltage and leakage current SCCNS model.

No.	Distance (km)	Rail voltage (V)		Leakage current (A) of Discrete model
		Discrete model	MATLAB/Simulink	
1	0	168.9875	168.9875	0.0000
2	0.50	160.5590	160.5590	8.4102
3	1.00	143.6984	143.6984	16.4016
4	1.50	118.3986	118.3986	23.5552
5	2.00	84.6490	84.6490	29.4512
6	2.50	42.4352	42.4352	33.6693
7	3.00	-8.2606	-8.2606	35.7877
8	3.50	-67.4599	-67.4599	35.3832
9	4.00	-135.1876	-135.1876	32.0309
10	4.50	-211.4725	-211.4725	25.3034
11	5.00	-296.3470	-296.3470	14.7708
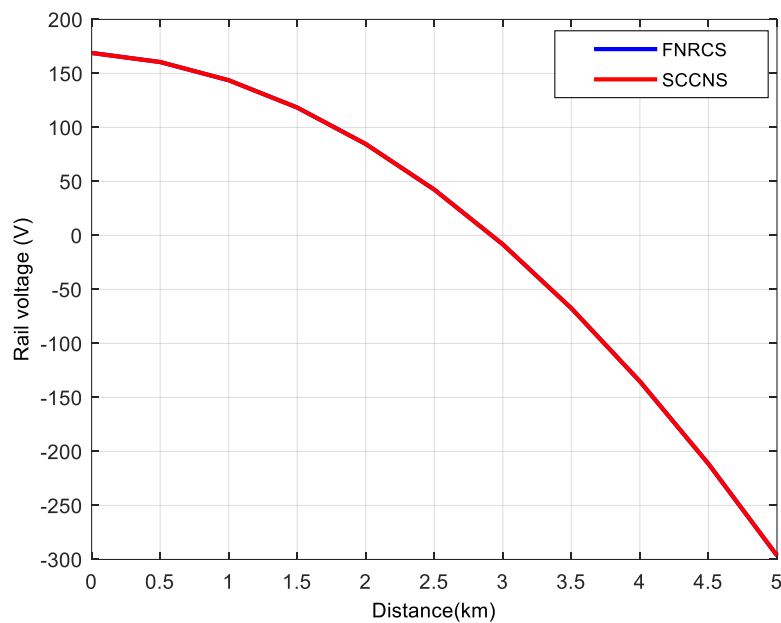
Figure 13. Results rail voltage between FNRCS and SCCNS model.
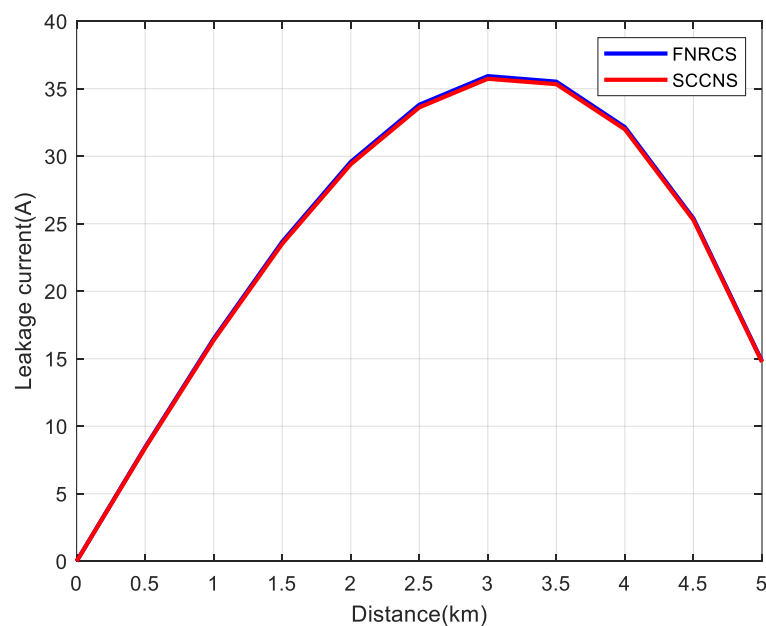
Figure 14. Results show the current leakage between the FNRCS and SCCNS models.

3.3 Simulation SCCNS with a drainage diode model

The voltage and leakage current characteristics in the electric rail supply system were analyzed using matrix-based calculations following equation (21) for the simulation of the SCCNS model with a drainage diode, as shown in (Figure 5) and (Figure 6). The appendix (Table 7) lists the MATLAB/Simulink tools used for model development, and the appendix (Table 10) provides specifics on the system parameters used for the simulation. As seen in the appendix (Figure 21), the SCCNS with a drainage diode model was then created to use MATLAB/Simulink to analyze rail voltage characteristics and leakage current characteristics. To compare the simulation results with the discrete model shown in (Table 6), this system was simulated using MATLAB/Simulink. Furthermore, the rail voltage and leakage current simulation results were compared

ASEAN J. Sci. Tech. Report. **2025**, *28*(3), e257546

16 of 24

between the SCCNS with a drainage diode model and the FNRCS model, which was cited in (Topic 3.1). (Figure 15) and (Figure 16) show the results of the simulations for rail voltage and leakage current, respectively.

Table 6. Simulation results for rail voltage and leakage current SCCNS with a drainage diode model.

No.	Distance (km)	Rail voltage (V)		Leakage current (A) of Discrete model
		Discrete model	MATLAB/Simulink	
1	0	465.4235	465.3942	0.0000
2	0.50	456.9432	456.9140	2.3258
3	1.00	439.9824	439.9532	4.6093
4	1.50	414.5403	414.5110	6.8080
5	2.00	380.6157	380.5865	8.8798
6	2.50	338.2074	338.1782	10.7822
7	3.00	287.3134	287.2842	12.4729
8	3.50	227.9316	227.9024	13.9095
9	4.00	160.0596	160.0303	15.0496
10	4.50	83.6943	83.6650	15.8510
11	5.00	-1.1674	-1.1967	16.2712

A comparison between the FNRCS model and the SCCNS model with a drainage diode (Figure 15) revealed an average difference in the simulated rail voltage of 284.62 V. The voltage profile shows parallel lines with a downward slope. The FNRCS model exhibits a bell-shaped curve (Figure 16), showing the leakage current simulation results. On the other hand, the drainage diode model of the SCCNS shows a constant tendency to rise as the simulated distance grows. This shows an upward-sloping pattern in the leakage current in the SCCNS with a drainage diode model, increasing with the distance of the simulation from the substation starting point.
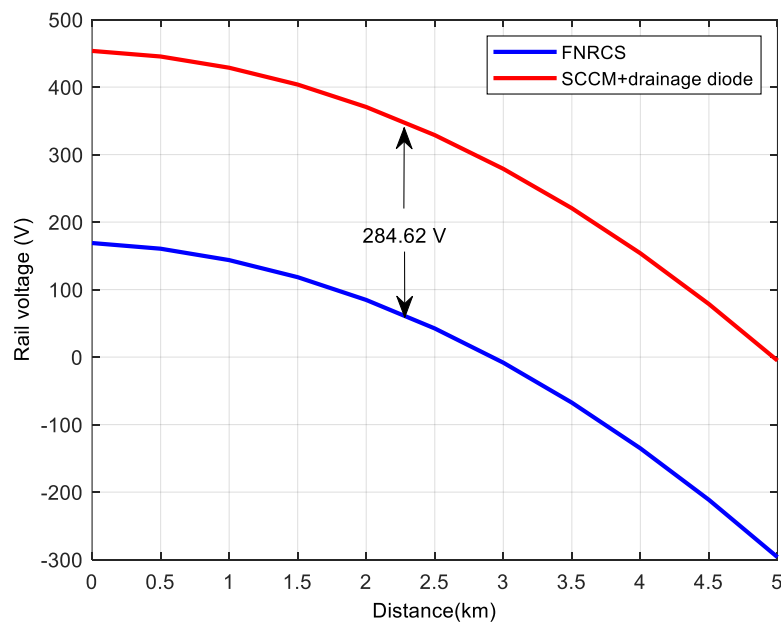
Figure 15. Results rail voltage between FNRCS and SCCNS with a drainage diode model.
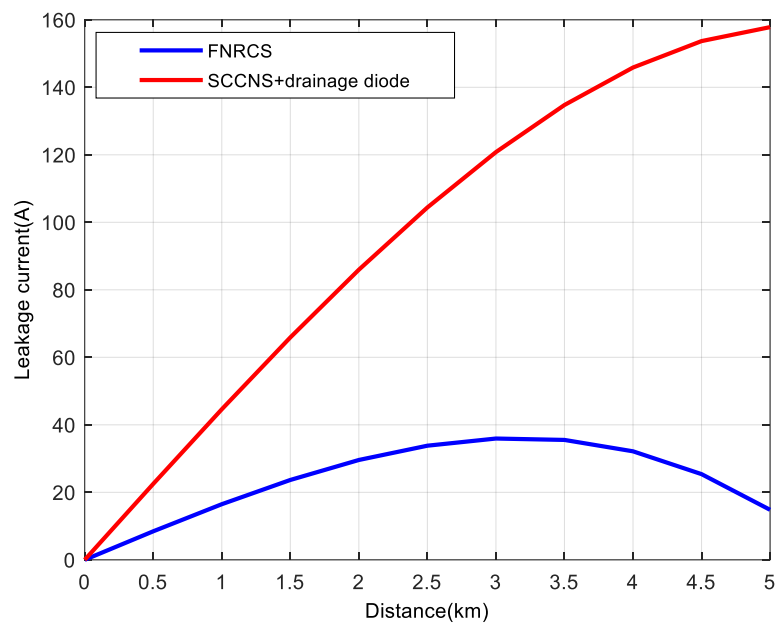
Figure 16. Results leakage current between FNRCS and SCCNS with a drainage diode model.

A comparison between the normal SCCNS model and the SCCNS with a drainage diode model was carried out to illustrate the variations in their simulation outcomes further. At a distance of 3.00 km, where the rail voltage is -0.25 V, it was discovered that the rail voltage profiles intersect. The rail voltage of the SCCNS with a drainage diode model is higher than that of the SCCNS model in the 0-3.00 km range. In contrast, (Figure 17) shows that the rail voltage of the SCCNS with a drainage diode model is lower than that of the SCCNS model in the 3.00–5.00 km range. The SCCNS model shows a bell-shaped curve for the leakage current simulation results (Figure 18). In contrast, the SCCNS with a drainage diode model shows a trend of continuous increase, which is comparable to the pattern seen in (Figure 16).
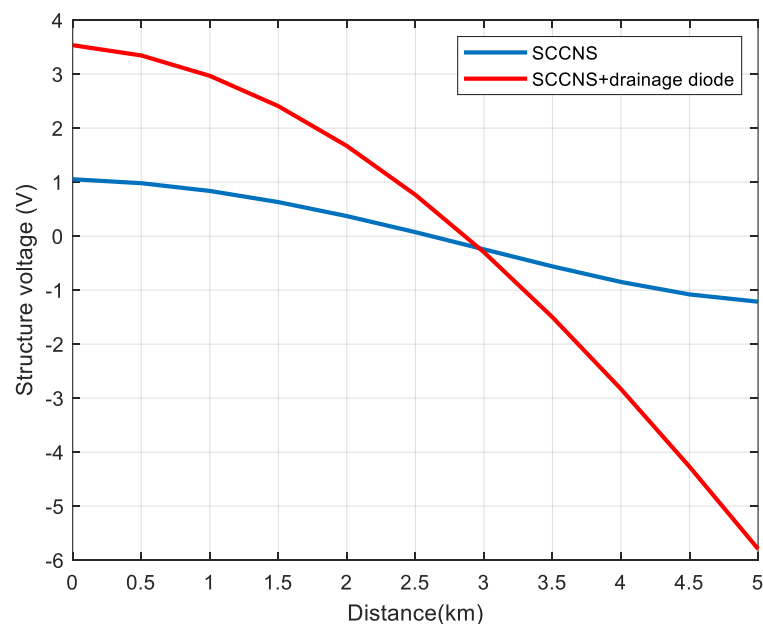
Figure 17. Results of the structure voltage between SCCNS and SCCNS with a drainage diode model.

ASEAN J. Sci. Tech. Report. **2025**, *28*(3), e257546

18 of 24
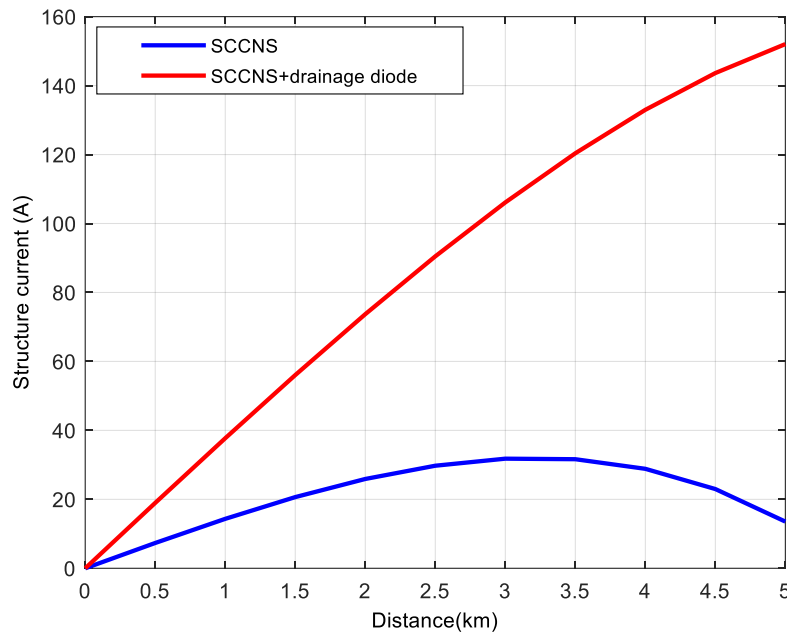
Figure 18. Results structure current between SCCNS and SCCNS with a drainage diode model.

3.4 Summary of simulation results

In this work, the railway power supply system's leakage current was analyzed utilizing simulations that handled huge and complicated parameters using MATLAB/Simulink. The simulation used three scenarios: the FNRCS model, the SCCNS model, and the SCCNS with a drainage diode model. The modeling, which took the shape of a single-line diagram and was created in MATLAB/Simulink for comprehensive simulation result analysis and verification, was based on the EN-50122-2 standard. Between the rail and the earth, conductance values of 0.01 S/km and 0.10 S/km were used to study the voltage and leakage current characteristics for the FNRCS model. The discrete model agreed with the MATLAB/Simulink simulation results. The average voltage deviation relative to the mathematical model was 8.47% for 0.10 S/km and 8.64% for 0.01 S/km. The simulation also revealed an average 40.07% increase in leakage current. Furthermore, an average of 89.96% and 89.95% were found in the leakage current when the conductance values of 0.01 S/km and 0.10 S/km were compared.

The voltage and leakage current characteristics of the SCCNS model were examined using matrix-based models. Regarding both voltage and leakage current behavior, the simulation results in MATLAB/Simulink closely matched the FNRCS model and agreed with the discrete model. The rail voltage for the SCCNS with a drainage diode model was 284.62 V on average, and the graph sloped downward like parallel lines. Three kilometers separated the voltage curves as compared to the SCCNS model. Compared to the SCCNS model, the rail voltage of the SCCNS with a drainage diode model was lower in the 3.00-5.00 km range and higher in the 0-3.00 km range. Furthermore, the bell-shaped curve seen in the SCCNS model contrasted the continuously growing trend of the leakage current in the SCCNS with a drainage diode model. It is clear from the simulation outcomes of the three scenarios that MATLAB/Simulink is a valuable tool for examining railway power supply systems. It offers precise simulation results and makes performance comparisons between various system models easy. The FNRCS, SCCNS, and SCCNS+Diode models are based on different simulation techniques that depend on their operational characteristics. FNRCS is ideal for mathematical modeling because of its continuous behavior. At the same time, SCCNS and SCCNS+Diode, which include switching elements and diodes, necessitate discrete modeling or the use of MATLAB/Simulink to represent their time-dependent behavior accurately. The highest flexibility is offered by MATLAB/Simulink, which supports both continuous and discrete systems, making it applicable to all types of networks with the correct simulation settings. The appendix (Table 11) presents the connection between each model and the simulation technique that corresponds to it.

ASEAN J. Sci. Tech. Report. **2025**, *28*(3), e257546.

19 of 24

4. Conclusions

The FNRCS model, the SCCNS model, and the SCCNS with a drainage diode model are the three models simulated in this work to analyze leakage current in the electric railway power supply system using MATLAB/Simulink. The models were created using the EN-50122-2 standard as a guide. According to the FNRCS model simulation results, the leakage current rose to 14.82 A while the rail voltage dropped from 169.90 V at the beginning to -297.38 V after 5 km. These findings, which had average variances of 8.47% for a conductance value of 0.10 S/km and 8.64% for 0.01 S/km, agreed with both the discrete and mathematical models. The average increase in leakage current over the mathematical model was 40.07%. The simulation results for leakage current and rail voltage for the SCCNS model closely matched those for the FNRCS model. The average rail voltage in the SCCNS with a drainage diode model was 284.62 V, indicating a steady declining trend; however, the leakage current dramatically increased with distance. The SCCNS with a drainage diode showed lower rail voltage in the 3.00-5.00 km range but greater rail voltage in the 0-3.00 km range than the SCCNS model. Overall, the simulation findings show that MATLAB/Simulink is a valuable tool for precisely evaluating and contrasting the performance of power supply systems for electric railways.

5. Acknowledgements

Author Contributions: The simulation strategy and techniques were conceptualized and designed by T.C., S.K., and T.S. It was T.C. and S.K. who implemented the simulation, collected the data, analyzed the results, and came to a conclusion. The authors T.C., S.K., W.S., A.I., and T.S. contributed to the writing and the general content modification.

Conflicts of Interest: The authors of this study hereby state that they have no conflicts of interest.

References

[1]   Bahra, K.S.; Catlow, R.B. Control of stray currents for DC traction systems. In International Conference on Electric Railways in a United Europe, Amsterdam, Netherlands, **1995**, pp. 136-142, https://doi.org/10.1049/cp:19950194.

[2]   Siranec, M.; Regula, M.; Otcenasova, A.; Altus, J. Measurement and Analysis of Stray Currents. *In 20th International Scientific Conference on Electric Power Engineering (EPE), Kouty nad Desnou, Czech Republic*, **2019**, pp. 1-6, https://doi.org/10.1109/EPE.2019.8778072.

[3]   Ogunsola, A.; Sandrolini, L.; Mariscotti, A. Evaluation of Stray Current From a DC-Electrified Railway With Integrated Electric–Electromechanical Modeling and Traffic Simulation. *IEEE Trans. Ind. Appl*. **2015**, 51, 5431-5441, https://doi.org/10.1109/TIA.2015.2429642.

[4]   Niasati, M.; Gholami, A. Overview of stray current control in DC railway systems. In International Conference on Railway Engineering - Challenges for Railway Transportation in Information Age, Hong Kong, **2008**, pp. 1-6, https://doi.org/10.1049/ic:20080043.

[5]   Petkova, P. Stray current control in DC railway systems. In 13th Electrical Engineering Faculty Conference (BulEF), Varna, Bulgaria, **2021**, pp. 1-3, https://doi.org/10.1109/BulEF53491.2021.9690814.

[6]   Sutherland, P.E. Stray current analysis. *In IEEE IAS Electrical Safety Workshop, Toronto, ON, Canada*, **2011**, pp. 1-2, https://doi.org/10.1109/ESW.2011.6164732.

[7]   Pham, K.D.; Thomas, R.S.; Stinger, W.E. Operational and safety considerations in designing a light rail DC traction electrification system. *In IEEE/ASME Joint Railroad Conference, Chicago, IL, USA*, **2003**, pp. 171-189, https://doi.org/10.1109/RRCON.2003.1204663.

ASEAN J. Sci. Tech. Report. **2025**, *28*(3), e257546

20 of 24

[8]   Petkova, P.; Boychev, B. Active stray current protection systems in DC railways. *In 13th Electrical Engineering Faculty Conference (BulEF), Varna, Bulgaria,* **2021**, pp. 1-3, https://doi.org/10.1109/BulEF53491.2021.9690843.

[9]   Fotouhi, R.; Farshad, S. A new novel power electronic circuit to reduce stray current and rail potential in DC railway. *In 13th International Power Electronics and Motion Control Conference, Poznan, Poland*, **2008**, pp. 1575-1580, https://doi.org/10.1109/EPEPEMC.2008.4635491.

[10] Paul, D. DC Stray Current in Rail Transit Systems and Cathodic Protection [History]. *IEEE Ind. Appl. Mag*. **2016**, 22, 8-13, https://doi.org/10.1109/MIAS.2015.2481754.

[11] Tzeng, Y.-S.; Lee, C.-H. Analysis of Rail Potential and Stray Currents in a Direct-Current Transit System. *IEEE Trans. Power Deliv*. **2010**, 25, 1516-1525, https://doi.org/10.1109/TPWRD.2010.2040631.

[12] Hanrob, P.; Kulworawanichpong, T.; Ratniyomchai, T. Reducing Rail Potential and Stray Current with NEG-TPS in DC Electrified Railways. *In International Conference on Power, Energy and Innovations (ICPEI), Nakhon Ratchasima, Thailand*, **2021**, pp. 81-84, https://doi.org/10.1109/ICPEI52436.2021.9690665.

[13] Zaboli, A.; Vahidi, B. Stray Current and Rail Potential Control Strategies in Electric Railway Systems. In Transportation Electrification: Breakthroughs in Electrified Vehicles, Aircraft, Rolling Stock, and Watercraft, *IEEE*, **2023**, pp. 299-323, https://doi.org/10.1002/9781119812357.ch13.

[14] Hoger, M.; Regula, M.; Bracinik, P.; Otcenasova, A. Influence of high voltage power lines on the propagation of stray currents from DC traction. *In ELEKTRO, Krakow, Poland*, **2022**, pp. 1-5, https://doi.org/10.1109/ELEKTRO53996.2022.9803410.

[15] Liu, W.; Li, T.; Zheng, J.; Pan, W.; Yin, Y. Evaluation of the Effect of Stray Current Collection System in DC-Electrified Railway System. *IEEE Trans. Veh. Technol*. **2021**, *70*, 6542-6553, https://doi.org/10.1109/TVT.2021.3084340.

[16] Mariscotti, A. Stray Current Protection and Monitoring Systems: Characteristic Quantities, Assessment of Performance and Verification. *Sensors* **2020**, *20*, 6610. https://doi.org/10.3390/s20226610.

[17] Liang, H.; Wu, Y.; Han, B.; Lin, N.; Wang, J.; Zhang, Z.; Guo, Y. Corrosion of Buried Pipelines by Stray Current in Electrified Railways: Mechanism, Influencing Factors, and Protection. *Appl. Sci*. **2025**, *15*, 264. https://doi.org/10.3390/app15010264.

[18] Georgiev, V.; Petkova, P. Modeling of the influence of different parameters of the power supply system on the magnitude of the stray currents in DC electrified transport. *In 13th Electrical Engineering Faculty Conference (BulEF), Varna, Bulgaria*, **2021**, pp. 1-6, https://doi.org/10.1109/BulEF53491.2021.9690818.

[19] Yu, J.G.; Goodman, C.J. Modelling of rail potential rise and leakage current in DC rail transit systems. *In IEE Colloquium on Stray Current Effects of DC Railways and Tramways, London, UK*, **1990**, pp. 2/2/1-2/2/6.

[20] Lin, S.; Tang, Z.; Chen, X.; Liu, X.; Liu, Y. Analysis of Stray Current Leakage in Subway Traction Power Supply System Based on Field-Circuit Coupling. *Energies* **2024**, *17*, 3121. https://doi.org/10.3390/en17133121.

[21] Lee, C.-H.; Lu, C.-J. Assessment of grounding schemes on rail potential and stray currents in a DC transit system. *IEEE Trans. Power Deliv*. **2006**, 21, 1941-1947, https://doi.org/10.1109/TPWRD.2006.874561.

[22] Tang, Z.; et al. The Influence of Urban Rail Transit's Stray Current on Power Grid and Its Synchronous Monitoring. *In IEEE 4th Conference on Energy Internet and Energy System Integration (EI2), Wuhan, China*, **2020**, pp. 308-312, https://doi.org/10.1109/EI250167.2020.9346946.

[23] Sopharak, A.; Ratniyomchai, T.; Kulworawanichpong, T. Energy Saving Study of Mass Rapid Transit by Optimal Train Coasting Operation. *In International Conference on Power, Energy and Innovations (ICPEI), Chiangmai, Thailand*, **2020**, pp. 25-28, https://doi.org/10.1109/ICPEI49860.2020.9431507.

[24] Ratniyomchai, T.; Hillmansen, S.; Tricoli, P. Optimal capacity and positioning of stationary supercapacitors for light rail vehicle systems. *In International Symposium on Power Electronics, Electrical Drives, Automation and Motion, Ischia, Italy*, **2014**, pp. 807-812, https://doi.org/10.1109/SPEEDAM.2014.6872019.

[25] Zhao, Y.; Xu, J.; Yin, J. Urban rail transit line and station planning optimization based on GIS: Take Haikou city as an example. *In International Conference on Information Control, Electrical Engineering and Rail Transit (ICEERT), Lanzhou, China*, **2021**, pp. 240-247, https://doi.org/10.1109/ICEERT53919.2021.00053.

[26] Radu, P.V.; Lewandowski, M.; Szelag, A.; Steczek, M. Short-Circuit Fault Current Modeling of a DC Light Rail System with a Wayside Energy Storage Device. *Energies* **2022**, 15, 3527. https://doi.org/10.3390/en15103527.

[27] Colella, P.; Pons, E.; Tortora, A. Rail Potential Calculation: Impact of the Chosen Model on the Safety Analysis. *In AEIT International Annual Conference, Bari, Italy*, **2018**, pp. 1-6, https://doi.org/10.23919/AEIT.2018.8577295.

ASEAN J. Sci. Tech. Report. **2025**, *28*(3), e257546.

21 of 24

[28] Kirawanich, P.; Dey, P.; Sumpavakup, C. System-Level Magnetic Interference Modeling in Electrified Monorail System for Track-Side Safety Design. *IEEE Trans. Transp. Electrif.* **2024**, *10*, 4571-4582, https://doi.org/10.1109/TTE.2023.3306999.

[29] Yuan, P.; Mao, W.; Ye, H.; Liu, Y. Model Construction and Analysis of Transformer DC Magnetic Bias Induced by Rail Transit Stray Current. *In IEEE 3rd Conference on Energy Internet and Energy System Integration (EI2), Changsha, China*, **2019**, pp. 1710-1713, https://doi.org/10.1109/EI247390.2019.9061729.

[30] Shao, H.; Yang, X.; He, Y.; Zheng, T.Q. Stray Current and Rail Potential Dynamic Emulator for Urban Rail Transit System. *In IEEE Transportation Electrification Conference & Expo (ITEC), Detroit, MI, USA*, **2023**, pp. 1-6, https://doi.org/10.1109/ITEC55900.2023.10186932.

[31] Kangguan, K.; Hong, S.; Xinde, Z.; Xing, W.; Fan, Z.; Zhuohong, P. Development of a Stray Current Testing Device Based on Harmonic Current Source Technology. *In IEEE International Conference on High Voltage Engineering and Applications (ICHVE), Chongqing, China*, **2022**, pp. 1-4, https://doi.org/10.1109/ICHVE53725.2022.9961760.

[32] Gu, J.; Yang, X.; Zheng, T.Q.; Xia, X.; Zhao, Z.; Chen, M. Rail Potential and Stray Current Mitigation for Urban Rail Transit With Multiple Trains Under Multiple Conditions. *IEEE Trans. Transp. Electrif.* **2022**, *8*, 1684-1694, https://doi.org/10.1109/TTE.2021.3114412.

[33] White, R.D. AC/DC railway electrification and protection. *In IEE ETS Supply AC & DC* 2006, pp. 281-322, https://doi.org/10.1109/ICHVE53725.2022.9961760.

[34] Kiessling, F.; Puschman, R.; Schmieder, A.; Schneider, E. Contact lines for electric railways, SEIMENS, Publicis Publishing, 2nd edition, **2009**.

[35] Lu, S. Optimising power management strategies for railway traction. PhD Thesis, University of Birmingham, **2011**.

[36] Kaewpoung, S.; Sumpavakup, C.; Kulworawanichpong, T. Autotransformer-fed railway power supply model using. *In Advances in Future Manufacturing Engineering: Proceedings of the 2014 International Conference on Future Manufacturing Engineering (ICFME 2014), Hong Kong, December 10-11*, **2014**, *2*, https://doi.org/10.1201/b18474-4.

ASEAN J. Sci. Tech. Report. **2025**, *28*(3), e257546

22 of 24

Supplement Materials

Detailed information regarding the several toolboxes utilized for MATLAB/Simulink model development may be found in the research's supplemental appendix. The parameter settings utilized to simulate the analysis results of the FNRCS, SCCNS, and SCCNS with drainage diode models are also included; these are shown in the following tables and figures.

Table 7. Components of a simulation in the MATLAB/Simulink program.
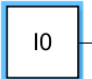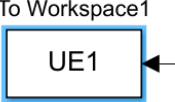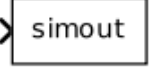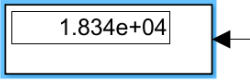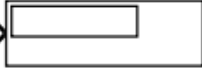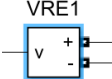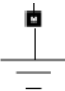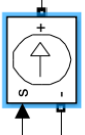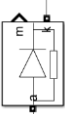
Toolbox	Details	Simulink Library Browser
	powergui	Simscape->Power Systems->Spacialized Technology ->Fundametal Blocks
		Simulink->Sources
		Simulink->Sinks
		Simulink->Sinks
		Simscape->Power Systems->Spacialized Technology -> Fundametal Blocks->Measurements
	Ground	Simscape->Power Systems->Spacialized Technology-> Fundametal Blocks->Elements
	Controlled Current Source	Simscape->Power Systems->Spacialized Technology->Fundametal Blocks->Electrical Sources
	Series RLC Load	Simscape->Power Systems->Spacialized Technology->Fundametal Blocks->Power Electronics
	Didoe	Simscape->Power System->Spacialized Technology->Fundametal Blocks->Element

ASEAN J. Sci. Tech. Report. **2025**, *28*(3), e257546.

23 of 24

Table 8. Parameter for simulation of FNRCS model.

Parameter	Value
Current at Substation (I_0)	10.00 kA
Distance (L)	5.00 km
Sampling (dx)	0.50 km
Rail resistance (R'_R)	0.017 Ω/km
Conductance between rail and earth (G'_{RE})	0.10 S/km, 0.01 S/km

Table 9. Parameter for simulation of SCCNS model.

Parameter	Value
Current at Substation (I_0)	10.00 kA
Distance (L)	5.00 km
Sampling (dx)	0.50 km
Rail resistance (R'_R)	0.017 Ω/km
Conductance between rail and earth (G'_{RE})	0.10 S/km, 0.01 S/km
R'_{SCCNS}	0.02 Ω/km
R_E or G'_E	0.50 Ω/km or 2.00 S/km

Table 10. Parameter for simulation of SCCNS with drainage diode model.

Parameter	Value
Current at Substation (I_0)	10.00 kA
Distance (L)	5.00 km
Sampling (dx)	0.50 km
Rail resistance (R'_R)	0.017 Ω/km
Conductance between rail and earth (G'_{RE})	0.10 S/km, 0.01 S/km
R'_{SCCNS}	0.02 Ω/km
R_E or G'_E	0.50 Ω/km or 2.00 S/km
V_{diode}	0.70 V

ASEAN J. Sci. Tech. Report. **2025**, *28*(3), e257546

24 of 24

Table 11. Model usage for FNRCS/SCCNS/SCCNS+diode systems.

Model	FNRCS	SCCNS	SCCNS+diode
Mathematical	Yes	No	No
Discrete models	Yes	Yes	Yes
MATLAB/Simulink	Yes	Yes	Yes
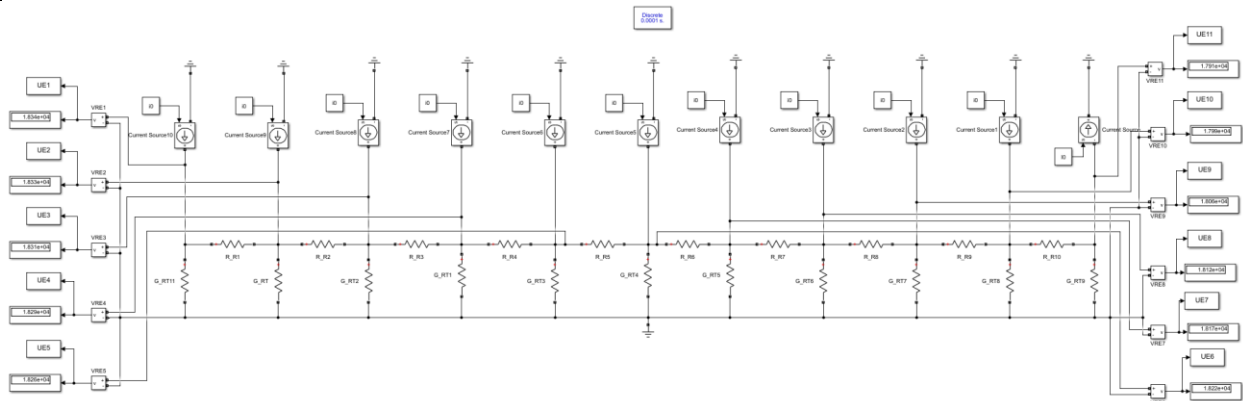
Figure 19. Development FNRCS model in the MATLAB/Simulink program.
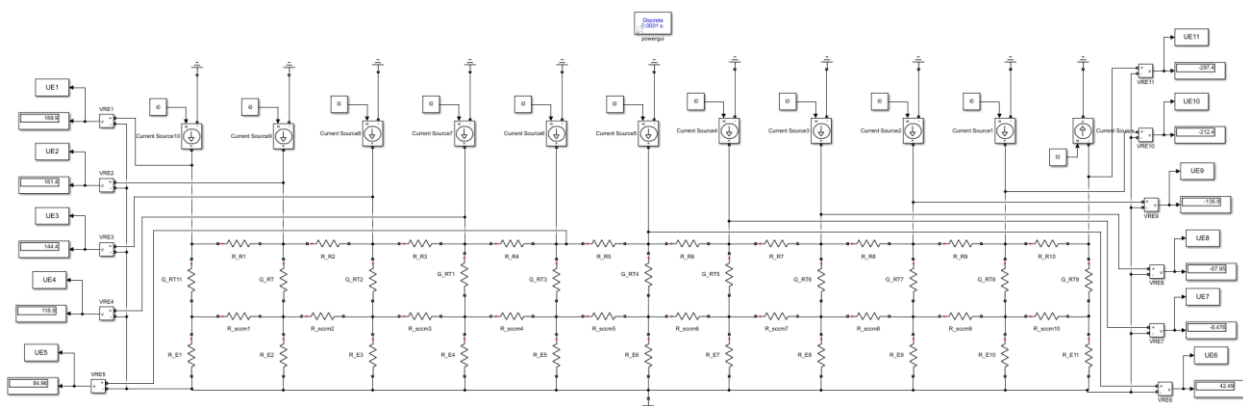
Figure 20. Development SCCNS model in the MATLAB/Simulink program.
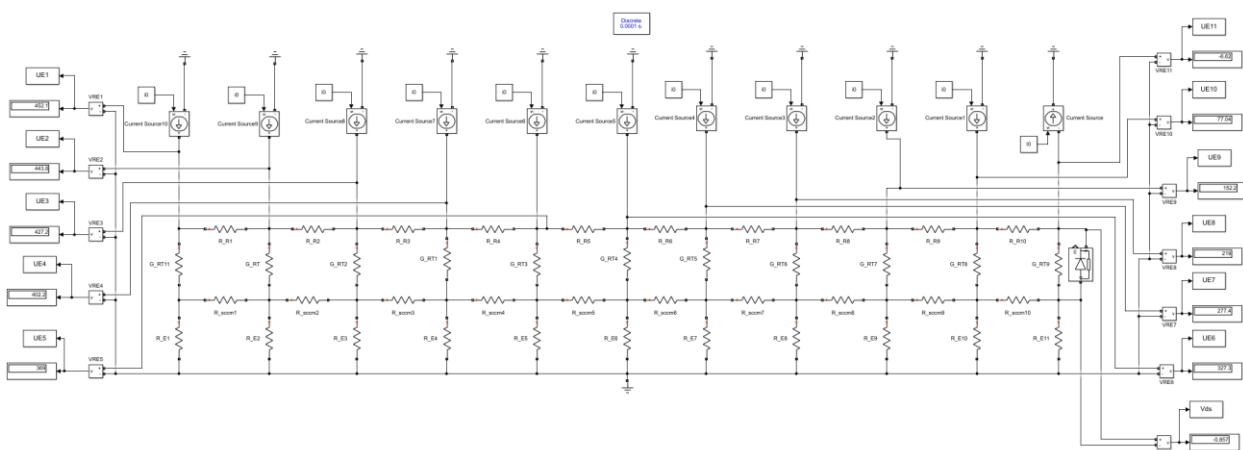
Figure 21. Development of SCCNS with drainage diode model in the MATLAB/Simulink program.

Computational Analysis of Dimples Surface Tube on Heat Transfer Forced Convection Using Turbulence Model of Low Reynolds Number with Different Cases

Sarmad A. Ali¹*, Nour Jamil Alrikaby², and Hanan K. Kadhim³

1. College of Engineering-Al Musayab, University of Babylon, Province of Babylon, 51001, Iraq

2. College of Engineering, University of Thi-Qar, Thi-Qar 64001, Iraq

3. College of Engineering-Al Musayab, University of Babylon, Province of Babylon, 51001, Iraq

* Correspondence: sarmad.ahmed96@uobabylon.edu.iq

Abstract: The researchers aimed to improve the heat transfer process using various industrial engineering techniques to highlight the importance of maximum heat transfer and improvement. In the current numerical study, the Ansys Fluent R23 program was used to enhance the heat transfer rate with a laminar flow in the Reynolds number range of (500-1500) steady state single-phase inside a dimpled tube with three different states heated with a uniform constant heat flux (8000 W/m²) along the flow axis. The effect of the dimples' arrangement on the tube's surface was studied to compare the thermal performance against the empty tube. Comparing the three cases (1, 2, and 3) to the standard tube without a dimple, the heat transfer rates increased by (86.99, 87.22, and 87.47%), respectively. Compared to tubes with two or three dimples, the heat exchanger tube with four dimples on its cross section and linearly towards the flow axis performs much better in terms of thermal-hydraulic performance.

Keywords: Laminar flow; Horizontal tube; Thermal performance factor; Dimples; Friction factor

1. Introduction

Around the world, heat exchangers are widely used in the most important engineering industrial applications. The most appropriate option is necessary to make these devices more convenient than others, reduce their size and cost, and improve their hydrothermal performance and efficiency. The methods of enhancing the heat transfer rate are generally divided into two main parts: the passive and active methods. The current numerical study is focused on using the first method, which has a low cost because it does not require external devices compared to the second method [1]. To achieve the best enhancement of heat transfer by the passive method and using different configurations of the tube surface, such as ribs, dimples, and corrugations, increasing the surface roughness is one of those methods. All the mentioned configurations cause an increase in turbulence, mixing of the flow, and development of the boundary layer. Therefore, the heat transfer rate improves significantly [2, 3]. The pressure loss and heat transfer rate of tubes with a rough surface is significantly increased compared to smooth ones [4-7]. For example, many researchers in their experimental and numerical studies in the recent past

ASEAN J. Sci. Tech. Report. **2025**, *28*(3), e256103.

https://doi.org/10.55164/ajstr.v28i3.256103

ASEAN J. Sci. Tech. Report. **2025**, *28*(3), e256103.

2 of 11

have managed to move away from increasing the surface area of heat transfer and have turned to using dimples on the surface of tubes, causing mixing and disturbance of the boundary layer, thereby improving the thermal efficiency of the heat exchanger Juin Chen et al. and Yu Wang et al. [8 and 9] presented a study of the effect of inserting dimple protrusions to the tube surface to improve thermal performance, the effects of different ribs have been studied by Dennis Leroy Gee and R. L. Webb, J. C. Han and J. S Park [10 and 11] while A. García et al. [12 and 13] presented the realization of the effect of using spiral wires and dimples with axial corrugations to enhance heat transfer and the development of the thermal-hydraulic performance of tubes using CFD in numerical simulation and experimental approach. Ming Li et al. [14] performed numerical simulation using the computational fluid dynamics method to improve the thermal-hydraulic performance of a three-dimensional tube with stable single-phase turbulent flow incompressible. The technique known as the Semi-Implicit Method for Pressure Equations Consistent (SIMPLEC) solves the pressure-velocity coupling. The numerical results showed that the dimpled tube surface in linear order gave a thermal performance and improved high heat transfer compared to the graded configuration. Various geometry parameters such as dimple shape, depth, pitch, and diameter have been shown to affect enhancing heat transfer. M. Z. U. Khan et al. [15] presented a numerical investigation to solve the problem of enhancing heat transfer by the effect of a dimple protrusion in a microchannel of rectangular cross-section using water as the working fluid with a constant heat flux shed on the channel wall as a boundary condition. The coefficient of thermal performance is investigated by calculating the number of Nusselt and the friction factor at a laminar flow range (100-900) of the working fluid inside the channel. Ganesh V. Wafelkar and L. V. Kamble [16] presented an experimental study to overcome the length of the double tube by designing a triple tube for a heat exchanger because it provides a larger transfer heat area than the double tube. The purpose of the study is to evaluate the performance of triple-tube heat exchangers using dimple tubing. Different flow rates of hot and cold fluid are investigated experimentally. The relationship between several performance metrics, including heat exchanger efficacy, friction factor, Nusselt number, and Prandtl number, is also discussed. Farah Nazifa Nourin and Ryoichi S. Amano [17] conducted an experimental and numerical study using six different states of dimples based on the underlying smooth surface to investigate the characteristics of the heat transfer rate of a gas turbine blade inserted with a channel along the turbulent flow axis in the Reynolds number range (6000-50000). The results of the maximum Reynolds number's heat transfer enhancement and friction factor indicated that the leaf-dimpled surface is the optimal cooling channel. On the other hand, half-spherical dimes with a depth-to-diameter ratio of 0.25 had the best thermal performance at the lowest Reynolds number. Kanit Aroonrat and Somchai Wongwises [18 and 19] experimentally studied the condensation process of a two-phase tube flow with a dimpled surface for the development of Thermo-hydraulic performance. The results indicated the heat transfer rate represented by the number of Nusselt improved by (84%) compared to the empty tube. Sarmad A. Ali et al. [20] studied numerically using the finite-volume method of the program (Ansys Fluent) to improve the properties of the working fluid and the forced convective heat transfer of a turbulent flow at Reynolds ranges (3500-7000) single-phase stable three-dimensional. The improvement process involved using three different roller configurations (circular, square, and triangle) with equal hydraulic diameter to achieve the effect on the heat transfer rate represented by the number of Nusselt and the friction factor. The results indicated dimples enhance heat transfer by a ratio of (13, 18, and 21 %) to (square, circular, and triangle) respectively. Sarmad A. Ali [21] presented a numerical study of the optimization of heat transfer by forced convection of fluid flow within a two-dimensional horizontal channel using three different configurations of ribs (quarter circle, square, and triangle) to enhance heat transfer. Several parameters have been studied numerically, including Reynolds numbers, friction factor, pressure drop, and the Nusselt number. The results showed heat transfer improved by (72, 70, and 68%) for configurations (quarter-Circle, Square, and Triangle), respectively. Moreover, as the Reynolds number increases, the number of Nusselt gradually increases, and the friction factor decreases.

The current numerical analysis focuses on increasing the heat transfer rate by forced convection and improving the flow properties of a horizontal circular tube with a dimpled surface in three different cases compared to a smooth tube. A constant heat flux (8000 W/m^2) subjected on the outer wall of the tube along the flow axis in the Reynolds number range (500-1500) is a steady state incompressible single-phase flow. The effect of the change in the number of dimples on the number of Nusselt, the friction factor, the velocity distribution, temperature, and pressure of the fluid was studied numerically. Many previous studies have

dealt with improving heat transfer by turbulent flow, so the current study is concerned with laminar flow because of its importance as a type of fluid flow in various pipes and heat exchangers.

2. Physical Numerical Model

Figure (1) shows the computational domain of a three-dimensional horizontal tube with a length and outer diameter (160 and 30 mm), respectively. Dimples with a diameter of (4 mm) are inserted in three different cases: the first, second, and third cross-section of the tube contains dimples number (2,3, and 4) respectively, as shown in Figure (2). The dimples were linearly distributed over the surface of the tube with an equal spacing (10 mm). In addition, the outer wall is also provided with a uniform constant heat flux of (8000 W.m-2) along the fluid flow axis.
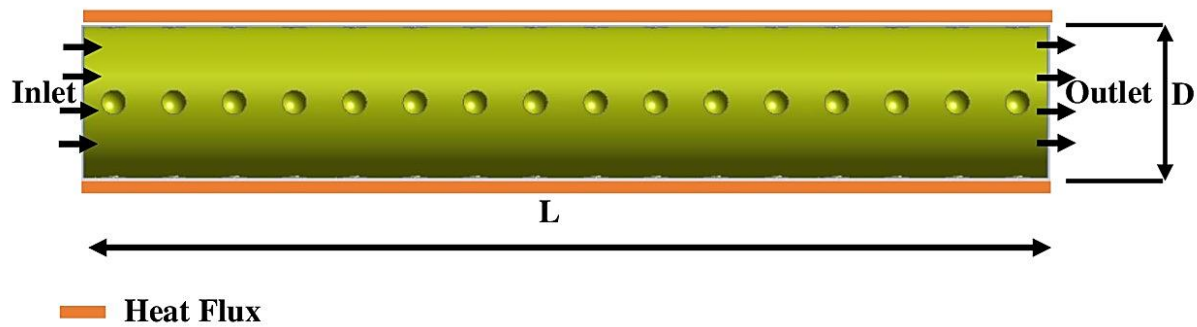
Figure 1. Schematic diagram with dimensions of dimple tube
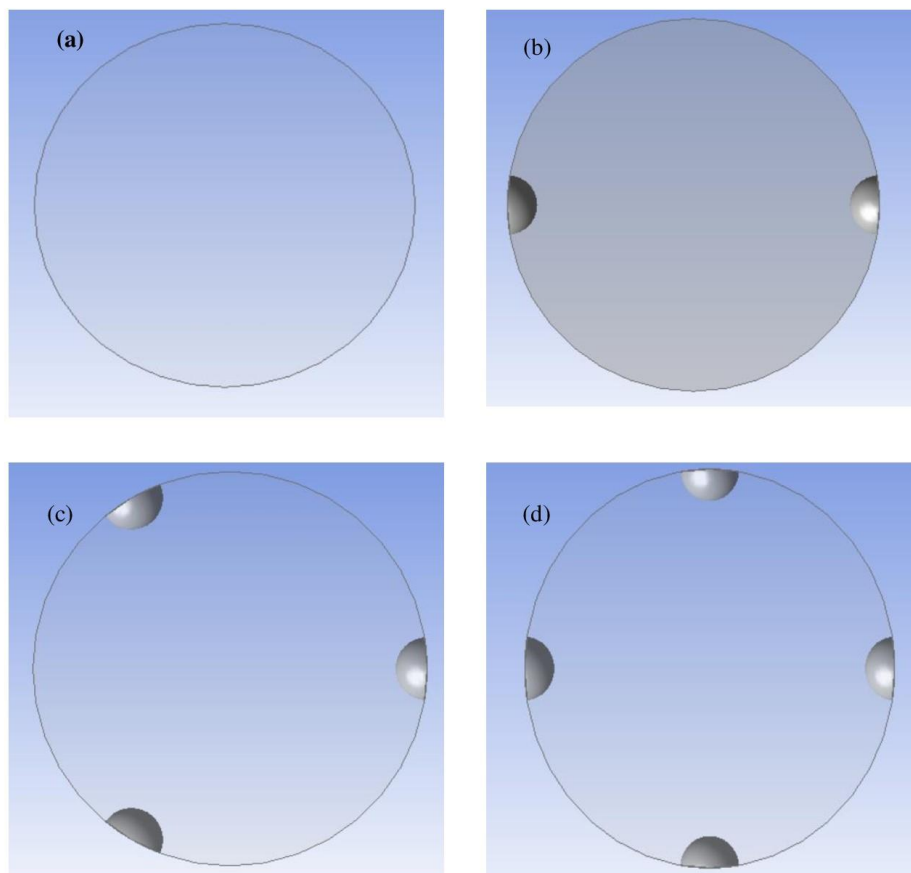
Figure 2. Three different cases of dimples included around the circumference of the tube cross-section: (a) plain, (b) two dimples, (c) three dimples, and (d) four dimples

2.1 Equations of Governing Fluid

The effects of heat transfer by radiation, natural convection, and viscous dissipation these factors are eliminated. The fluid flow in the present study is subject to the steady state with an incompressible three-dimensional laminar flow for all governing equations, including continuity, momentum, and energy. According to the Cartesian system, the governing equations can be written as follows [22]:

$$\frac{\partial u_j}{\partial x_j} = 0 \tag{1}$$

$$\frac{\partial}{\partial x_j}(\rho u_i u_j) = -\frac{\partial p}{\partial x_i} + \frac{\partial}{\partial x_j}[(\mu + \mu_t)(\frac{\partial u_i}{\partial x_i} + \frac{\partial u_j}{\partial x_i})] \tag{2}$$

$$\frac{\partial u_i T}{\partial x_i} = \frac{\partial}{\partial x_j}((\frac{\mu}{\mathrm{Pr}} + \frac{\mu_t}{\mathrm{P_t r}})\frac{\partial T}{\partial j})) \tag{3}$$

Using two transport equations, this two-equation model broadly explains turbulence. Equations for the turbulent kinetic energy dissipated (ε) and turbulent kinetic energy (κ) in turbulence are provided as [23]

$$\frac{\partial}{\partial x_j}(\rho k u_j) = \frac{\partial}{\partial x_j}[(\mu + \frac{\mu_t}{\sigma_k})\frac{\partial k}{\partial x_j}] + \Gamma - \rho\varepsilon \tag{4}$$

$$\frac{\partial}{\partial x_j}(\rho\varepsilon u_j) = \frac{\partial}{\partial x_j}[(\mu + \frac{\mu_t}{\sigma_\varepsilon})\frac{\partial\varepsilon}{\partial x_j}] + C_{1\varepsilon}\Gamma\varepsilon - C_{2\varepsilon}\frac{\varepsilon^2}{k + \sqrt{v\varepsilon}} \tag{5}$$

$$\Gamma = -\overline{uu}\frac{\partial u_i}{\partial x_j} = \frac{\mu_t}{\rho}(\frac{\partial u_i}{\partial x_j} + \frac{\partial u_j}{\partial x_i})\frac{\partial u_i}{\partial x_j} \tag{6}$$

$$\mu_t = \rho C_\mu \frac{k^2}{\varepsilon} \tag{7}$$

The empirical constants in the equations of the turbulent model are:

$$C_\mu = 0.09; C_{1\varepsilon} = 1.47; C_{1\varepsilon} = 1.92; \sigma_k = 1.0; \sigma_\varepsilon = 1.3 \, and \, \mathrm{Pr}_t = 0.85 \tag{8}$$

2.2 Boundary Conditions of Computational Model

For all boundaries of the computational domain, boundary conditions are provided because the governing equations of the flux are located in spatial coordinates. Various boundary conditions can be described as follows:

- Characteristics of the fluid flow at the tube's inlet at a temperature of (300K) and the axial uniform fluid velocity with laminar flow at the Reynolds number range (500-1500). Based on that, turbulent dissipation (ε) and turbulent kinetic energy (k) are calculated.
- The outer wall of the tube is considered to be in a non-slip state, and it is exposed to a constant uniform heat flux.
- Constant temperature conditions are assumed at the extended areas and the tube inlet.
- As a result of the prevailing pressure in the fluid exit area, the pressure outlet boundary condition is applied. Also, all variables in terms of flow have minimal assumed gradients.

2.3 Definition of Parameter

All parameters used for numerical verification of the current study are described for analysis and presentation of results. Based on the laminar flow to analyze the characteristics of the fluid flow and the pressure drop in the tube as follows, the Reynolds number equation and the friction factor can be expressed respectively [24]:

$$\mathrm{Re} = \frac{\rho u_{in} D_h}{\mu} \tag{9}$$

$$f = \frac{2\Delta p D_h}{L\rho u_{in}^2} \tag{10}$$

ASEAN J. Sci. Tech. Report. **2025**, 28(3), e256103.

5 of 11

The coefficient of heat transfer by forced convection and the average Nusselt number by the following equations are calculated [25 and 26]:

$$h_x = \frac{q''}{(T_w - T_f)} \tag{11}$$

$$Nu_m = \frac{D_h}{\lambda} \int_0^L h_x dx \tag{12}$$

3. Solution of Numerical Model

The governing equations with boundary conditions were solved using a commercial program (Ansys Fluent R23) using the finite volume method to solve laminar flow and heat transfer. The pressure-based model was combined with the simple algorithm for the pressure velocity fields. A second-order downwind scheme was used for the equations of momentum, turbulent kinetic energy, and the rate of turbulence dissipation. An achievable (k-ε) model was adopted with improved wall treatment to provide improved predictions of flows close to the wall. The numerical residuals were reduced to (10^{-6}), and the estimated algebraic finite volume equations were repeatedly solved, as shown in Figure (3). After setting the iteration value to 100, the computations begin. Iterations keep on until convergence is achieved. Figure (4) highlights the unstructured hybrid grid of the three-dimensional tube using the tetrahedrons method.
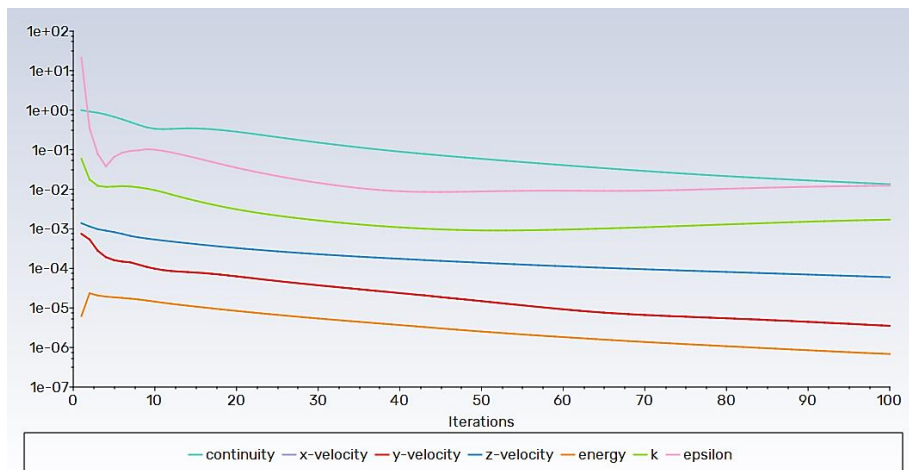
Figure 3. Scaled residuals of the computational model
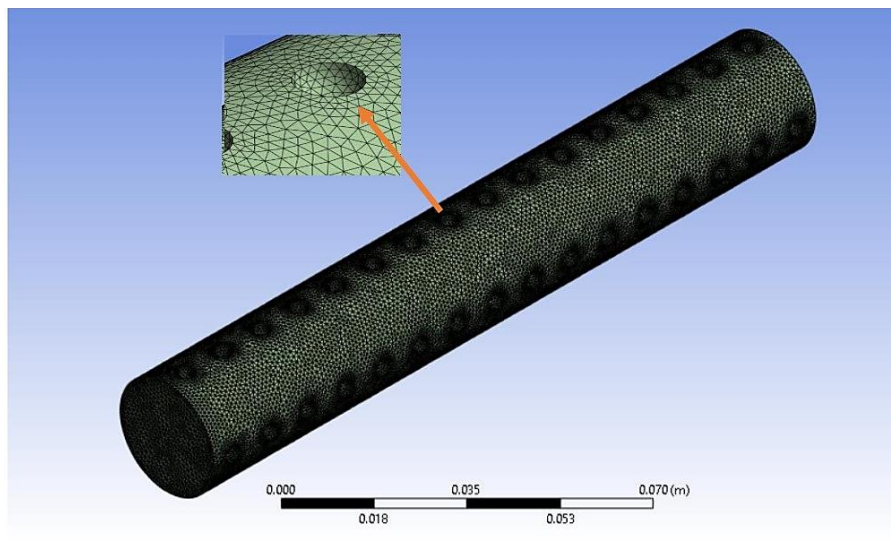
Figure 4. Grid mesh of horizontal 3D tube with a surface dimple

ASEAN J. Sci. Tech. Report. **2025**, *28*(3), e256103.

6 of 11

4. Analysis of Grid Independence

Controlling the size and number of elements and cells in numerical calculations is essential to improve numerical results. This use is called grid independence, so the grid is divided into small parts to achieve accuracy in the mathematical solution. The main principle of the ordinary CFD technique is that at the beginning of the solution, a rough grid is formed, gradually improving so that the detection of changes in values becomes small from the previously specified error. This is problematic in two ways. First, there might be issues when using other CFD software to get a single coarse mesh. Second, refining a mesh by a factor of two or more may require extra time. This is inappropriate behavior for software meant to be an engineering tool with limited production capabilities. Furthermore, the other problems have contributed significantly to the idea that CFD is an incredibly challenging, expensive, and time-consuming approach. The Nusselt number was finally recorded and sorted in each case to establish grid independence ,as shown in Figure (5).
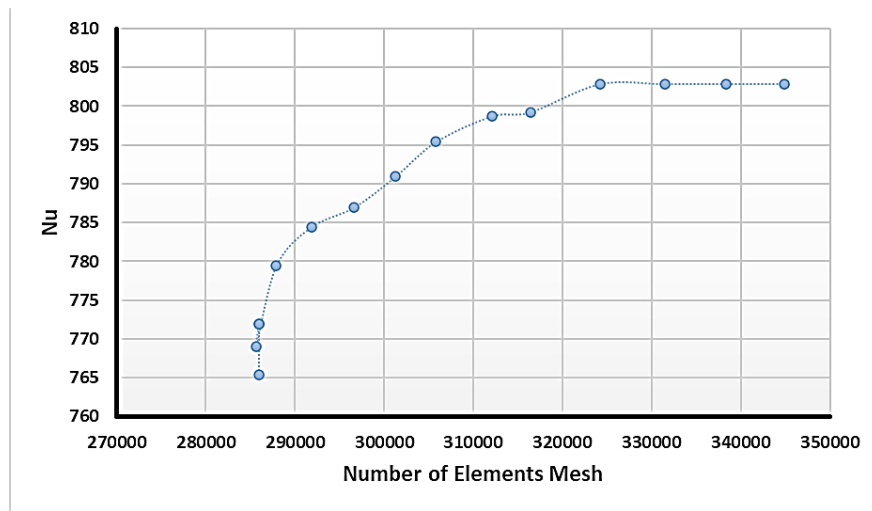
Figure 5. Analysis of grid independence of the computational model

5. Results and Discussions

For variable cases of the surface of a rough, dimpled tube, the change of the Nusselt number against the Reynolds number is shown in Figure (6). As the fluid velocity increases, the Nusselt number gradually increases. Also, by including the dimple on the surface, the Nusselt number increases compared to a tube with a smooth surface. The heat transfer rate of the three cases (1, 2, 3) improved by (86.99, 87.22, and 87.47 %) compared to the ordinary tube without the dimple. The thermal-hydraulic performance of the heat exchanger tube is greatly improved by including four dimples on the tube's cross-section and linearly towards the flow axis compared to the tube with two and three dimples.
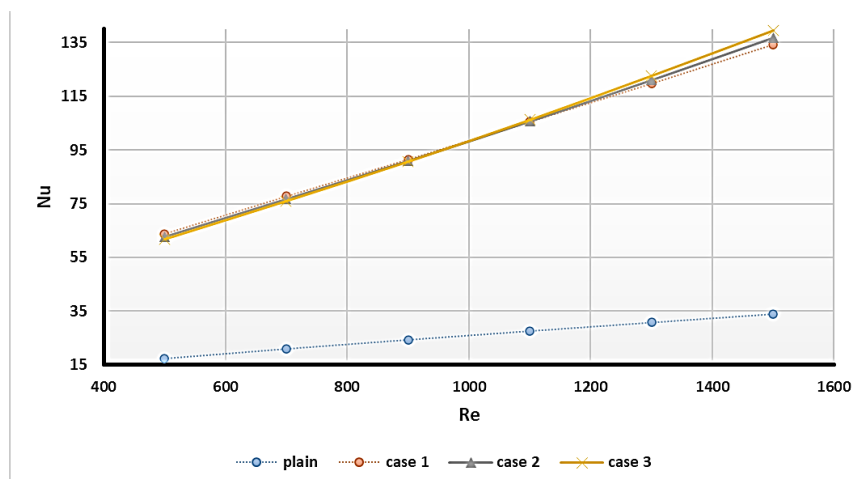
Figure 6. Influence of changing dimples numbering on Nusselt number with Reynolds number

Figure (7) shows the change of the friction factor with the ranges of the Reynolds number. The friction factor can be observed to decrease sharply at first, gradually decreasing by increasing the number of Reynolds using the dimples. The increase in the number of dimples caused an increase in the friction factor, where the third case, including four dimples, gave the highest value of the friction factor compared to the standard tube and the other number of simple cases.
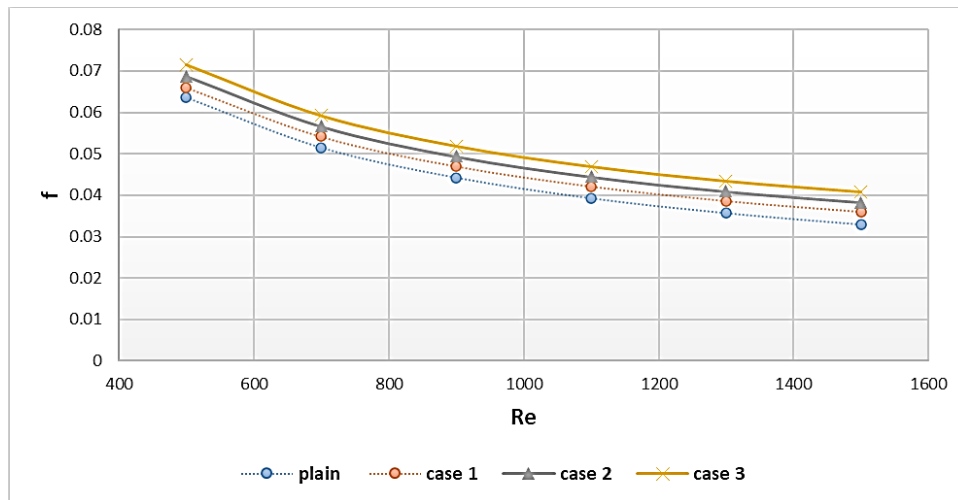
Figure 7. Influence of changing dimples numbering on Nusselt number with Reynolds number

Figure (8) shows the temperature distribution of the water flow with a three-state dimpled tube with an empty smooth tube at a Reynolds number range (1500) and a uniform constant heat flow (8000 W/m²). It can be observed that the average temperature of the fluid gradually increases towards the axis of the fluid flow inside the horizontal tube. Also, the dimples cause a change and deformation of the temperature distribution field. The average temperature is greater in the dimpled tube with the more significant number. It is also evident that the temperature within the tube rises in direct proportion to the number of dimples at the tube wall.
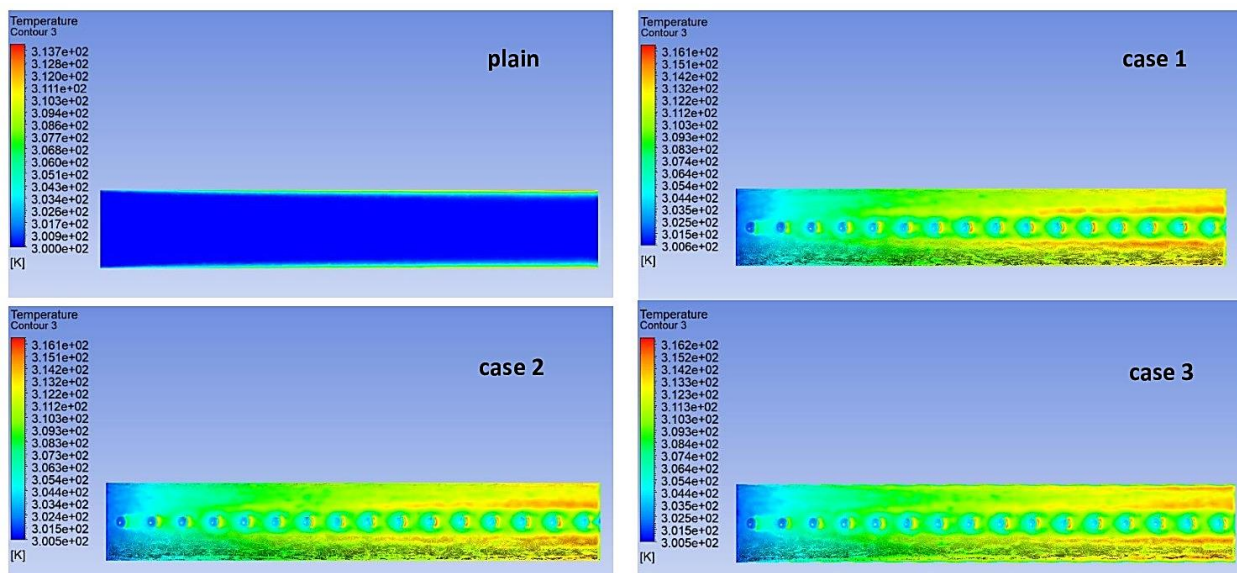
Figure 8. Compassion of Temperature distribution between plain tubes with different case dimples

Figure (9) shows the fluctuations of the fluid velocity distribution with and without dimples on the horizontal tube surface at Reynolds number (1500) and a uniform heat flow along the tube wall. The average

velocity of the fluid can be observed to increase using the three states of the number of dimples. The average velocity of water increases by (5.373, 7, and 4.35) for cases (1,2, and 3) respectively.
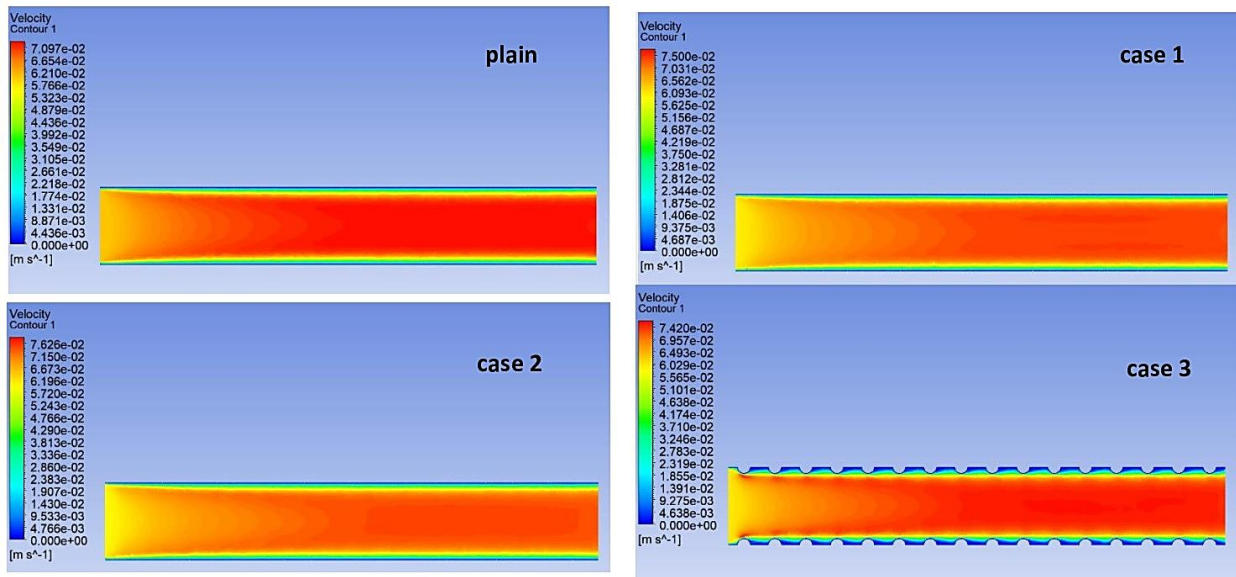
Figure 9. Compassion of velocity distribution between plain tubes with different case dimples

The axial and radial pressure distributions for various numbers of dimpled tubes with a Reynolds number of (1500) and a heat flux of (8000 W/m²) are shown in Figure (10). The pressure variations were less apparent as the tube length increased. The pressure value is more significant in the input tube zone and lower in the output tube region. This figure allows for the observation of several things. The distance between the near-wall tube and the center is where the more excellent pressure value is found. Furthermore, the pressure is reduced in the direction of the tube wall due to this low-velocity value. It should also be mentioned that the pressure within the tube increases with the number of dimples at the tube wall. The tube's higher resistance is what caused this to happen.
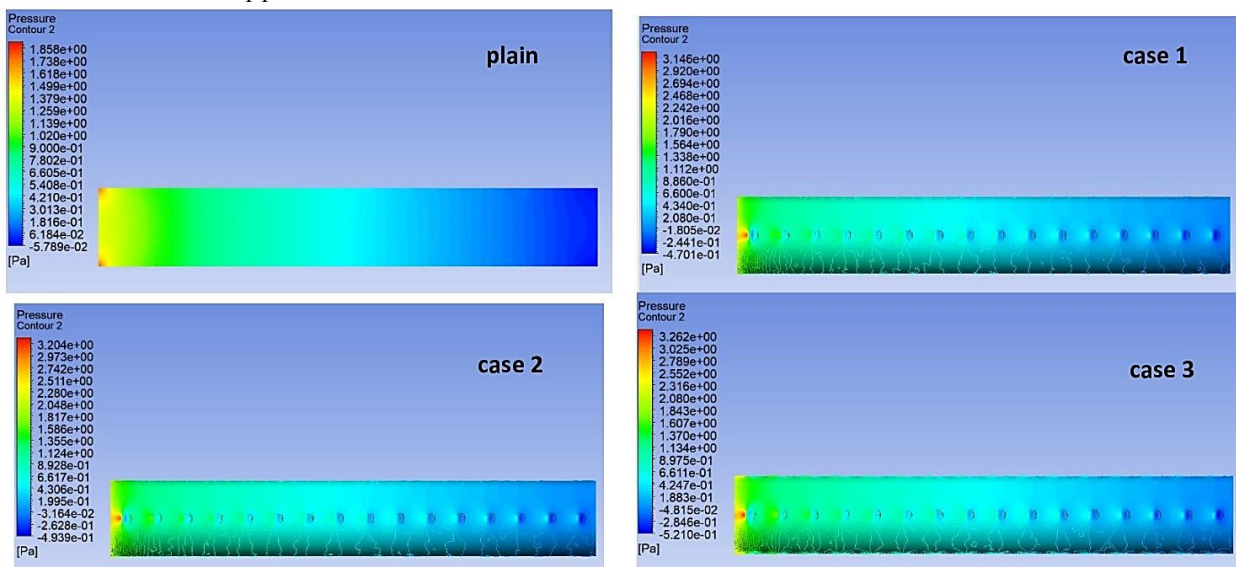
Figure 10. Compassion of pressure distribution between plain tubes with different case dimples

5. Conclusions

In the present study, the effect of increasing the number of dimples on the process of improving the rate of heat transfer by forced convection of laminar flow of water in the Reynolds number range (500-1500) inside a three-dimensional horizontal tube under a constant heat flux along the wall was investigated numerically. In the numerical results, it was mainly concluded that tubes with a dimpled surface are

ASEAN J. Sci. Tech. Report. **2025**, *28*(3), e256103.

9 of 11

considered an appropriate method to enhance heat transfer, thereby increasing the efficiency and thermal performance of the heat exchanger, making it more compact. Compared to the tube without a dimple, the number of Nusselt increased gradually with the dimple and increasing Reynolds number ranges. At the same time, the friction factor decreased with the increase in the Reynolds number and increased with the inclusion of dimples on the surface of the tube. Compared to a normal tube without a dimple, the heat transfer rates of instances 1, 2, and 3 improved by 86.99, 87.22, and 87.47 percent, respectively. Four dimples on the cross-section of the tube and linearly towards the flow axis provide a significant improvement in the heat exchanger tube thermal-hydraulic performance when compared to tubes with two or three dimples.

Nomenclature

D	Tube diameter (m)
f	Dimensionless friction factor
k	Turbulence kinetic energy (m^2/s^2)
L	Tube length (m)
Nu	Dimensionless Nusselt number
p	The pressure of water (Pa)
Pr	Dimensionless Prandtl number
q	Uniform heat flux ($W.m^{-2}$)
Re	Dimensionless Reynolds number
T	Temperature of water (K)
u	Water velocity ($m.s^{-2}$)
μ	Water dynamics viscosity ($N.s.m^{-2}$)
μ_t	Turbulence of water dynamics viscosity ($N.s.m^{-2}$)
ε	Dissipation of heat energy (m^2/s^3)
λ	Water thermal conductivity ($W.m^{-1}. K^{-1}$)
ϱ	Water density ($kg.m^{-3}$)

Subscript

f	fluid
h	Hydraulic
in	Inlet
o	Outlet
t	Turbulence
w	wall

Abbreviations

PEC	Performance Evaluation Criterion
CFD	Computational Fluid Dynamics

6. Acknowledgements

Conflicts of Interest: No conflicts of interest are disclosed by the authors.

References

[1]   Morini, GL. Single-phase convective heat transfer in microchannels: a review of experimental results. *International journal of thermal sciences*. **2004**, *43*(7), 631-651. https://doi.org/10.1016/j.ijthermalsci.2004.01.003

[2] Mangrulkar, CK.; Dhoble, AS.; Chamoli, S.; Gupta, A.; Gawande, VB. Recent advancement in heat transfer and fluid flow characteristics in cross flow heat exchangers. *Renewable and Sustainable Energy Reviews*. **2019**, *113*, 109220. https://doi.org/10.1016/j.rser.2019.06.027

[3] Mohammadi, S.; Mousavi, Ajarostaghi, SS.; Pourfallah, M. The latent heat recovery from boiler exhaust flue gas using shell and corrugated tube heat exchanger: A numerical study. *Heat Transfer*. **2020**, *49*(6), 3797-815. https://doi.org/10.1002/htj.21809

[4] Mangrulkar, CK.; Dhoble, AS.; Abraham, JD.; Chamoli, S. Experimental and numerical investigations for effect of longitudinal splitter plate configuration for thermal-hydraulic performance of staggered tube bank. *International Journal of Heat and Mass Transfer*. **2020**, *161*, 120280. https://doi.org/10.1016/j.ijheatmasstransfer.2020.120280

[5] Abraham, JD.; Dhoble, AS.; Mangrulkar, CK. Numerical analysis for thermo-hydraulic performance of staggered cross flow tube bank with longitudinal tapered fins. *International Communications in Heat and Mass Transfer*. **2020**, *118*, 104905. https://doi.org/10.1016/j.icheatmasstransfer.2020.104905

[6] Mohammed, A.; Al-Gburi, H.; Al-Abbas, A. Experimental study of the thermal performance of corrugated helically coiled tube-in-tube heat exchanger. *Frontiers in Heat and Mass Transfer (FHMT)*. **2023**, *20*. 1-7. https://doi.org/10.5098/hmt.20.17

[7] Zhang, K.; Li, Z.; Yao, J. Numerical study on heat transfer characteristics of corrugated tube phase change thermal energy storage unit. *Frontiers in Heat and Mass Transfer (FHMT)*. **2022**, *19*. https://doi.org/10.5098/hmt.19.5

[8] Chen, J.; Müller-Steinhagen, H.; Duffy, GG. Heat transfer enhancement in dimpled tubes. Applied thermal engineering. **2001**, *21*(5), 535-47. https://doi.org/10.1016/S1359-4311(00)00067-3

[9] Wang, Y.; He, YL.; Lei, YG.; Zhang, J. Heat transfer and hydrodynamics analysis of a novel dimpled tube. *Experimental thermal and fluid science*. **2010**, *34*(8), 1273-81. https://doi.org/10.1016/j.expthermflusci.2010.05.008

[10] Gee, DL.; Webb, RL.; Forced convection heat transfer in helically rib-roughened tubes. *International Journal of Heat and Mass Transfer*. **1980**, *23*(8), 1127-36. https://doi.org/10.1016/0017-9310(80)90177-5

[11] Han, JC.; Park, JS. Developing heat transfer in rectangular channels with rib turbulators. *International journal of heat and mass transfer*. **1988**, *31*(1), 183-95. https://doi.org/10.1016/0017-9310(88)90235-9

[12] García, A.; Solano, JP.; Vicente, PG.; Viedma, A. The influence of artificial roughness shape on heat transfer enhancement: Corrugated tubes, dimpled tubes and wire coils. *Applied Thermal Engineering*. **2012**, *35*, 196-201. https://doi.org/10.1016/j.applthermaleng.2011.10.030

[13] Garcia A, Vicente PG, Viedma A. Experimental study of heat transfer enhancement with wire coil inserts in laminar-transition-turbulent regimes at different Prandtl numbers. *International journal of heat and mass transfer*. **2005**, *48*(21-22), 4640-51. https://doi.org/10.1016/j.ijheatmasstransfer.2005.04.024

[14] Li, M.; Khan, TS.; Al Hajri, E.; Ayub, ZH. Geometric optimization for thermal–hydraulic performance of dimpled enhanced tubes for single phase flow. *Applied thermal engineering*. **2016**, *103*, 639-50. https://doi.org/10.1016/j.applthermaleng.2016.04.141

[15] Khan, MZ.; Akbar, B.; Sajjad, R.; Rajput, UA.; Mastoi, S.; Uddin, E.; Hussain, A.; Younis, MY.; Márquez, FP.; Akram, N. Investigation of heat transfer in dimple-protrusion micro-channel heat sinks using copper oxide nano-additives. *Case Studies in Thermal Engineering*. **2021**, *28*, 101374. https://doi.org/10.1016/j.csite.2021.101374

[16] Wafelkar, GV.; Kamble, LV. Experimental performance analysis of triple tube heat exchanger with dimple tubing. *Int J Adv Sci Res*. **2017**, *6*(4), 810-6.

[17] Nourin, FN.; Amano, RS. Experimental study on flow behavior and heat transfer enhancement with distinct dimpled gas turbine blade internal cooling channel. *Journal of Energy Resources Technology*. **2022**, *144*(7), 072101. https://doi.org/10.1115/1.4052035

[18] Aroonrat, K.; Wongwises, S. Condensation heat transfer and pressure drop characteristics of R-134a flowing through dimpled tubes with different helical and dimpled pitches. *International Journal of Heat and Mass Transfer*. **2018**, *121*, 620-631. https://doi.org/10.1016/j.ijheatmasstransfer.2018.01.001

[19] Aroonrat, K.; Wongwises, S. Experimental investigation of condensation heat transfer and pressure drop of R-134a flowing inside dimpled tubes with different dimpled depths. *International Journal of Heat and Mass Transfer*. **2019**, *128*, 783-793. https://doi.org/10.1016/j.ijheatmasstransfer.2018.09.039

[20] Ali, SA.; Barrak, ES.; Alrikaby, NJ.; Hameed, MR. Numerical Study of Thermal-Hydraulic Performance of Forced Convection Heat Transfer in Dimple Surface Pipe with Different Shapes using Commercial CFD Code. *heat transfer*. **2025**, *125*(2),1-5. https://doi.org/10.37934/arfmts.125.2.115

[21] Ali, SA. Influence of Inserted Different Ribs Configuration in 2D Horizontal Channel on Characteristics Turbulent Fluid Flow and Forced Heat Transfer: A Numerical Investigation. *Journal of Research and Applications in Mechanical Engineering*. **2025**, *13*(1). http://dx.doi.org/10.14456/jrame.2025.15

[22] Ali, SA.; Rasheed, SA. Effect of partially filled porous media on laminar flow and heat transfer via forced convection of fluid flow within a channel at different angles: A numerical study. *InAIP Conference Proceedings*. **2025,** *3169*(1). AIP Publishing. https://doi.org/10.1063/5.0254279

[23] Ali, SA.; Hameed, MR.; Kadhim, HK. Effect of Al2O3/H2O Nanofluid on the Flow and Forced Convection Heat Transfer Enhancement in a Pipe Using Commercial CFD Code. *Iraqi Journal of Industrial Research.* **2024**, *11*(3), 11-24. https://doi.org/10.53523/ijoirVol11I3ID474

[24] Sun, H.; Fu, H.; Yan, L.; Ma, H.; Luan, Y.; Magagnato F. Numerical Investigation of Flow and Heat Transfer in Rectangular Microchannels with and without Semi-Elliptical Protrusions. *Energies*. **2022**, *15*(13), 4927. https://doi.org/10.3390/en15134927

[25] Huang, Z.; Yu, GÁ.; Li, ZY.; Tao, WQ. Numerical study on heat transfer enhancement in a receiver tube of parabolic trough solar collector with dimples, protrusions and helical fins. *Energy Procedia*. **2015**, *69*, 1306-1316. https://doi.org/10.1016/j.egypro.2015.03.149

[26] Ajeel, RK.; Salim, WI.; Hasnan, K. Thermal and hydraulic characteristics of turbulent nanofluids flow in trapezoidal-corrugated channel: Symmetry and zigzag shaped. *Case studies in thermal engineering*. **2018**, *12*, 620-635. https://doi.org/10.1016/j.csite.2018.08.002

Occurrence of Parasitic and Bacterial Pathogen in Ornamental and Wild Populations of Siamese Fighting Fish (*Betta splendens*) in a Region of Thailand

Piyapan Manklinniam[1], Saranya Phunpruch[2, 4], and Worakrit Worananthakij[3, 4*]

[1] School of Science, King Mongkut's Institute of Technology Ladkrabang, Bangkok, 10520, Thailand

[2] School of Science, King Mongkut's Institute of Technology Ladkrabang, Bangkok, 10520, Thailand

[3] School of Science, King Mongkut's Institute of Technology Ladkrabang, Bangkok, 10520, Thailand

[4] Bioenergy Research Unit, School of Science, King Mongkut's Institute of Technology Ladkrabang, Bangkok 10520, Thailand

[*] Correspondence: worakrit.wo@kmitl.ac.th

Abstract: The diversity of fish parasites reflects the diversity of parasites in the water source, providing insights into the effects of pathogens and essential information about parasite-host relationships. Parasitic infections are valuable indicators of the aquatic ecosystem, influenced by various factors. This study aimed to investigate the prevalence and seasonality of parasite species and pathogenic bacteria in Siamese fighting fish (*Betta splendens*) over 12 months, involving sixty ornamental Siamese fighting fish collected from commercial sources and 81 wild Siamese fighting fish from different natural habitats. Parasite prevalence in ornamental Siamese fighting fish (25.00%) was lower than in the wild (34.57%). The protozoa parasite Trichodina was found in both Siamese fighting fish, with the highest prevalence recorded for *Trichodina* sp. in wild Siamese fighting fish. The winter season exhibited the highest parasitic prevalence, with a tremendous diversity of parasites found at each location, followed by the rainy and summer seasons. This study also reported the first finding of *Henneguya* sp. infection in Siamese fighting fish and on the body surface. The prevalence and seasonality of parasite genera were significant in the wild compared to ornamental Siamese fighting fish. Bacterial isolation was performed on internal organs, and isolates were identified using PCR techniques. *Aeromonas veronii* and *Mycobacterium marinum* were detected in ornamental Siamese fighting fish, while *A. veronii* was found in wild Siamese fighting fish. These findings indicate that infections in Siamese fighting fish display seasonal variation and are impacted by their ecology. This information is fundamental for managing the biodiversity of parasites in fish and preventing parasite infections in aquaculture.

Keywords: Fish parasites; Henneguya; Mycobacteriosis; Seasonality of parasites; Wild Siamese fighting fish

1. Introduction

Siamese fighting fish, known as *Betta splendens* (Regan, 1910), belong to the freshwater fish family Osphronemide, Genus Betta, and are of the reproduction bubble nest type. *B. splendens* is the origin of the Siamese fighting fish, which has been utilized in breeding programs alongside ornamental betta fish to develop diverse species, color variations, shapes, and characteristics. This

ASEAN J. Sci. Tech. Report. **2025**, 28(3), e257870.

2 of 13

species is native to Southeast Asia, with several wild types of Siamese fighting fish documented [1]. Siamese fighting fish are popular as ornamental fish due to their vibrant colors and adaptability to small containers with poor-quality water [2]. However, the wild population of Siamese fighting fish is declining due to overexploitation, habitat disruption, and water pollution. Although Siamese fighting fish typically resist diseases, parasites, and bacteria, they can still be susceptible to various infections and diseases in natural habitats and aquaculture systems. [3-6]. Fish diseases caused by various pathogens, including parasites, bacteria, fungi, and viruses, pose a significant challenge in commercial fish farming [7]. The host-parasite relationship is influenced by environmental factors such as season, habitat, and fish behavior [7], and water quality parameters such as pH, temperature, salinity, and dissolved oxygen are affected by anthropogenic activities, further impacting fish health. The prevalence of parasites is strongly influenced by seasonal variations, and bacterial fish diseases also show seasonal patterns [8]. Parasites and bacteria are common culprits leading to illness, mortality, and reduced fish growth [7]. Parasitic infections affect fish in both wild and aquaculture environments across many world regions. Also, bacteria can be found in Siamese fighting fish and cause significant economic damage. The bacterial strains that are commonly encountered and cause harm include *Aeromonas hydrophila*, *A. caviae*, *Pseudomonas alcaligenes*, *Plesiomonas shigelloides*, *Vibrio fluvialis*, *V. cholera*, *Mycobacterium chelonae*, *M. cosmeticum*, *M. mucogenicum*, and *M. senegalense*. [5]. *Mycobacterium* spp. are among the most common bacterial pathogens. Mycobacterium infections, or Mycobacteriosis, are widespread and affect various internal organs, leading to decreased fish production and salability of ornamental fish. The infection can be passed on to the next generation and may even be zoonotic. Despite reported parasite, bacterial, and mycobacterial infections in Siamese fighting fish, no studies have compared wild and ornamental populations [9]. Understanding the diversity of parasites and bacteria is crucial for assessing the impact and causes of diseases, promoting responsible stewardship, and gaining insights into specific host infections. Moreover, this biological diversity data serves as a valuable biological index, reflecting changes in the physical ecosystem, including temperature, pH, salinity, dissolved oxygen, and water pollution, which fluctuate with the seasons. The diversity of parasites in fish accurately mirrors the diversity within the water source, providing valuable information about the effects and damages caused by pathogens and shedding light on the relationships between parasites and their hosts. Various parasitic infections are crucial biological indicators of environmental changes, offering insights into ecosystem health and water quality.

This study's objectives were to monitor the prevalence of parasites, observe their seasonal variation, assess bacterial infections in wild and ornamental Siamese fighting fish, and identify the risks of the disease and contamination to fish farming sites to serve as a guideline for finding treatment in the future. Awareness of native species conservation can influence the prosperity of society and pathogen infection factors. These findings were compared with wild populations collected from various stations. Increased awareness of native species conservation can positively impact social well-being and address pathogen infection factors.

2. Materials and Methods

2.1 Study area and collection of specimens

This study is directed towards examining the prevalence of diverse parasites and bacteria in *Betta splendens*, specifically ornamental Siamese fighting fish, obtained from commercial sources and natural freshwater environments in the central region of Thailand. The Research Ethics Committee and the Animal Care and Use Committee at King Mongkut's Institute of Technology Ladkrabang, Bangkok, Thailand, approved this study on the bacterial isolation method from Siamese fighting fish (Certificate of Approval No. ACUC-KMITL-RES/2020/008). The sampling regime spanned twelve months, commencing in August 2020 and concluding in July 2021, encompassing the rainy, winter, and summer seasons. A total of 60 ornamental Siamese fighting fish, systematically selected at a rate of five specimens per month, were procured from the Chatuchak ornamental fish market in Bangkok throughout the study period. In the case of wild Siamese fighting fish, the specimens were acquired from three distinct sampling stations: station 1 (St01), situated in proximity to residential areas and canals (13°51′00.6″ N 100°28′05.4″ E); station 2 (St02), located near a community wastewater source (13°51′02.3″ N 100°28′05.4″ E); and station 3 (St03), positioned in a local orchard (13°51′05.7″ N 100°28′03.8″ E) (Figure 1). At each station, a maximum of five wild Siamese fighting fish samples were collected, albeit instances of acquiring fewer than five samples arose due to variable factors. pH and temperature data were recorded using a digital pH meter (AZ Instrumen, 8685) to assess the water quality at

ASEAN J. Sci. Tech. Report. **2025**, *28*(3), e257870.

3 of 13

the sampling sites. Salinity levels were measured using a dedicated salinometer (ATC Refractometer Hydrometer), and dissolved oxygen content was determined using a dissolved oxygen test kit (v-color 9780, V-unique, U.S.A.). Subsequently, the collected Siamese fighting fish and water samples were meticulously transported in plastic box aquaria to maintain the vitality of the live specimens. Upon arrival, they were housed in a laboratory fish tank to facilitate subsequent examinations.

2.2 Identification of parasites

Measuring Siamese fighting fish involved recording their length (cm) and weight (g). Subsequently, pathological examinations were conducted to analyze the body surface mucus on all fins and the operculum. Thorough examinations were conducted on the gills, intestines, and internal organs to identify external parasites and endoparasite infestations originating from muscle tissues. A wet mount preparation technique was employed to observe parasites from the sampled Siamese fighting fish, and these parasites were then preserved in 70% alcohol. The examination and identification of parasites utilized a light microscope, with identification based on distinctive morphological features, as outlined in a comprehensive essential guide. The taxonomic classification was confined to genus series within trematode, nematode, acanthocephalan, protozoa, and monogeneans groups. Identification primarily relied on morphological characteristics of fresh specimens, as referenced in standard manuals and scientific papers. Notable sources included Buchmann and Bresciani [10] for protozoa and monogeneans, Bhattacharya [11] for acanthocephalan, Wagner [12] for Myxozoa, Khalil *et al.* [13] for cestode, Gibson *et al.* [14] for trematode, and Anderson *et al.* [15] for the nematode.

Figure 1. Sampling locations in central Thailand: St01 = Station 01, St02 = Station 02, St03 = Station 03.

2.3 Bacterial characterization

The Siamese fighting fish's kidneys, liver, and spleen were enriched in Trypticase soy broth (TSB) and incubated at 30 °C for 24 hours. Following incubation, a loopful was streaked on TSA plates and incubated at 30 °C for 24 hours. After incubation, a single colony representing various morphological types on each plate was selected and re-streaked onto a new TSA plate until a pure culture was obtained. Subsequently, morphological, physiological, and biochemical tests (including the API 20E system) were applied to characterize the isolated bacteria. To isolate *Mycobacterium* spp., the samples were enriched and incubated at 30 °C for 1-4 weeks. The enriched samples were then streaked onto Ogawa medium and incubated at 30 °C for 1-4 weeks. Acid-fast staining (Ziehl-Neelsen) was employed for characterization, and identification was achieved through biochemical tests using the API ZYM system.

Bacterial DNA was extracted for 16s rRNA gene sequencing. The 16s rRNA gene was amplified, and the PCR product was purified. Subsequently, DNA sequencing was performed using the standard Sanger method (U2Bio, Thailand). After obtaining the sequences, the forward and reverse reads were assembled using BioEdit version 7.2.5 software [16]. Species identification was conducted through Nucleotide BLAST (https://blast.ncbi.nlm.nih.gov/Blast.cgi), and the sequences were subsequently submitted to DDBJ (https://www.ddbj.nig.ac.jp/submission-e.html) under accession number LC853089.1 for *Aeromonas veronii* and LC853090.1 for *Mycobacterium marinum*. As both Gram-negative (*A. veronii*) and Gram-positive (*M. marinum*) bacteria were isolated, a phylogenetic tree was constructed using the Neighbor-Joining method [17] based on 16s rRNA gene sequences in MEGA12 software [18]. *Halobacterium salinarum* NBRC14715 (LC556329.1) was selected as the out-group for rooting the tree due to its distant phylogenetic relationship with both study organisms.

2.4 Data analysis

Descriptive analysis was employed to analyze parasites, their habitats, and their prevalence. The prevalence was determined by dividing the number of animals hosting a specific parasite by the total number of animals examined for a given parameter. The percentage (%) was also calculated to measure prevalence. Additionally, bacterial prevalence (%) was calculated by dividing the number of infected animals by the total number examined.

3. Results and Discussion

3.1 Siamese fighting fish measurement

During the period from August 2020 to July 2021, a total of 141 Siamese fighting fish were examined. This comprised 60 ornamental Siamese fighting fish obtained from the market and 81 wild Siamese fighting fish collected from three natural resource sites. The ornamental Siamese fighting fish exhibited an average body length of 5.40±0.86 cm and weights ranging from 0.96±0.42 g. In comparison, the wild Siamese fighting fish had an average body length of 3.74±0.43 cm and weights ranging from 0.64±0.23 g. The wild Siamese fighting fish were collected from three distinct stations. In St01, twenty fish samples were obtained, showcasing advantageous body lengths of 3.68±0.48 cm and weights ranging from 0.62±0.25 g. St02 comprised seventeen fish samples with body lengths averaging 3.53±0.39 cm and weights of 0.52±0.19 g. St03 included forty-four fish samples with body lengths of 4.02±0.42 cm and weights ranging from 0.79±0.25 g.

3.2 Parasite infection and water quality

Parasitological examination revealed that 15 out of 60 ornamental Siamese fighting fish were infected with parasites. The most prevalent was the monogenean *Dactylogyrus* sp. (25.00%), followed by the protozoan *Trichodina* sp. (1.67%). For the wild Siamese fighting fish, 28 out of 81 were parasitized (34.57%), presenting infection with six groups and seven genera of external and internal parasites. There were six groups and seven genera of the fauna of both external and internal parasites, including one genus of monogene (*Gyrodactylus* sp.), two genera of protozoa (*Trichodina* sp. and *Zoothamnium* sp.), one genus of Myxozoa (*Henneguya* sp. present plasmodium in gills and spores found on the body surface and specifically on the lesions present on the fish fins), one genus of nematode (*Proleptus* sp. present adult and cysts), one genus of trematode (*Posthodiplostomum* sp. present adult in muscle and metacercaria in the abdominal cavity), and a genus Pallisentis or spiny headed worm (*Pallisentis nagpyrensis* present cysts) were observed, as shown in Figure 2.

ASEAN J. Sci. Tech. Report. **2025**, *28*(3), e257870.

5 of 13
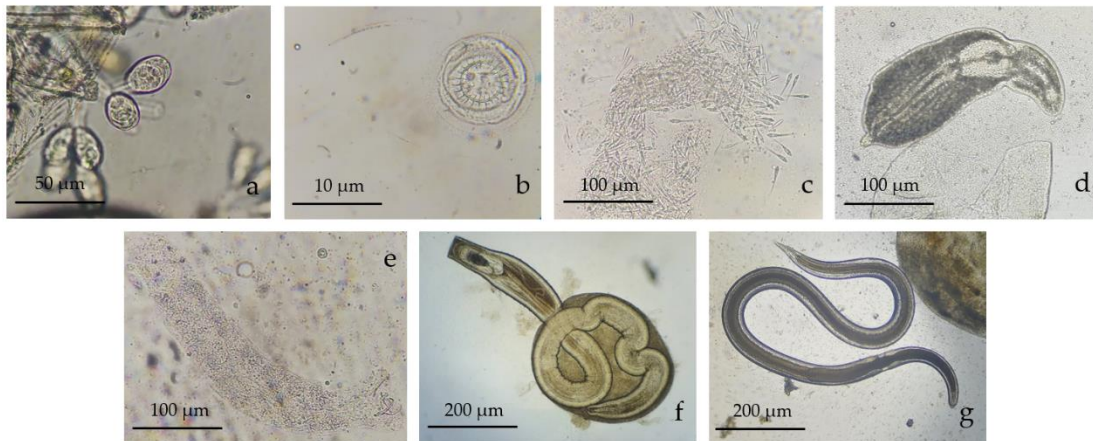
Figure 2. Parasite identification in wild *Betta splendens,* revealing the presence of *Zoothamnium* sp. (a), *Trichodina* sp. (b), *Henneguya* sp. (c), *Posthodiplostomum* sp. hatching from cyst (d), *Gyrodactylus* sp. (e), *Pallisentis* hatching from cyst (f), and *Contracaecum* sp. hatching from cyst (g).

In wild Siamese fighting fish, the highest prevalence (14.81%) was observed for *Trichodina* sp., followed by *Posthodiplostomum* sp. (11.11%), *Proleptus* sp. (9.88%), *Henneguya* sp. (8.64%), *Gyrodactylus* sp. (7.41%), *P. nagpyrensis* (1.23%), and *Zoothamnium* sp. (1.23%) (Table 1). The prevalence of parasites varied for each type among the 141 fish examined. Seasonal variations were noted, with both ornamental and wild Siamese fighting fish primarily infected with external parasites and higher prevalence occurring in the winter season. Ornamental fish showed similar parasite prevalence in summer (53.33%) and the lowest in the rainy season (6.67%). Wild fish exhibited a prevalence of 29.17% in the rainy season, followed by 52.94% in the winter season. *Trichodina* sp. had the highest prevalence in winter (29.41%), followed by the rainy (14.58%) season, and was absent in summer. *Henneguya* sp. (Figure 3.) infections were the second most common among external parasites and varied with the season. Among internal parasites, *Proleptus* sp. exhibited prevalence throughout the year, peaking in winter. *Posthodiplostomum* sp. appeared as both external and internal parasites throughout the year, with the highest cases in summer. Seasonal variations in infection for each parasite are detailed in Table 2. The examination of 81 wild Siamese fighting fish from three stations revealed 28 infected fish. The prevalence of infection varied among the stations, with St01 at 30.00% (6/20), St02 at 17.65% (3/17), and St03 at 43.18% (19/44). Seasonal prevalence of various parasites in wild Siamese fighting fish across different stations is provided in Table 3.

This research examines seasonal variations and environmental disparities in parasite infections among wild Siamese fighting fish. Clinical signs were identified by examining external, internal, and tissue abnormalities in wild Siamese fighting fish, comparing them to ornamental Siamese fighting fish. The study revealed a higher diversity and percentage prevalence of 34.57% in Siamese fighting fish in their natural habitat, in contrast to the low prevalence of 25.00% observed in ornamental Siamese fighting fish. Protozoa (*Trichodina*) and monogenean were the most common parasite genera recovered from ornamental and wild Siamese fighting fish, predominantly during winter. The results indicated seven genera of parasites, with *Trichodina* being the most prevalent, followed by *Posthodiplostomum*, *Proleptus*, *Henneguya*, *Gyrodactylus*, *Pallisentis*, and *Zoothamnium*, respectively. Research studies have consistently reported greater diversity and percentage prevalence of parasite infections that vary according to the season and location. *Trichodina* was predominantly found in winter but was absent in the summer season. Previous studies on parasites in ornamental *B. splendens*, such as Thilakaratne *et al.* [19], reported five species of parasites, including *Dactylogyrus* spp., *Gyrodactylus* spp., *Trichodina* spp., *I. multifiliis*, and *Piscionoodinium* spp. This report marks the first publication of the discovery of *Henneguya* infection occurring on the body surface (pelvic fin) and gills of wild Siamese fighting fish. In the case of infection from *P. nagpyrensis*, an internal parasite was found, and this occurrence was previously unreported. *Henneguya,* a common Myxospore, is highly host-specific, commonly infecting various organs or tissues [20]. Numerous infections have been documented on gill filaments, liver, kidney, spleen, heart, and muscle [21]. In the present study, *Henneguya* infection manifested as illness in specific wild Siamese fighting fish collected from St01 during the rainy season. While *Henneguya* was observed in all seasons at St03, its absence in St02 raises the possibility that water quality or pollution in this location might not

ASEAN J. Sci. Tech. Report. **2025**, *28*(3), e257870.

6 of 13

support the viability of *Henneguya*. The prevalence of *Henneguya* infections was highest in winter (November to January), followed by the rainy season (May to October) and summer (February to April), respectively.

Several infections caused by Myxozoa have posed significant challenges in ornamental fish reared at breeding farms [22]. This parasitic infection may contribute to declining fish reproduction among wild Siamese fighting fish. In line with this report, a noticeable decrease in fish samples was observed at St01, which sometimes could not be collected during the last month of sampling. It can be inferred that the fish population is lower during the winter, summer, and early rainy seasons. Previous studies have provided limited insights into parasites infecting Siamese fighting fish. This study pioneers exploring parasite infections in wild Siamese fighting fish captured in natural freshwater, offering a detailed analysis of the relationship with seasonal variations. Comparative analysis of parasitic infection in wild Siamese fighting fish during seasonal changes revealed peak infections during transitions, such as the shift from winter to summer, the conclusion of winter in March, and the transition from the rainy season to winter in November. This highlights the significant influence of seasons on the parasite population.

Table 1. The overall prevalence of parasite infections in wild Siamese fighting fish and ornamental Siamese fighting fish

Fish examined	Parasites	No. of fish examined	No. of fish Infected	Prevalence (%)	Site of infection
Wild Siamese fighting fish	*Trichodina*	81	12	14.81	Body surface and gills
	Zoothamnium	81	1	1.23	Body surface
	Gyrodactylus	81	6	7.41	Gills
	Henneguya	81	7	8.64	Body surface and gills
	Posthodiplostomum	81	9	11.11	Gills, muscles, and Abdominal
	Pallisentis	81	1	1.23	Abdominal
	Proleptus	81	8	9.88	Abdominal
	Total	81	28	34.57	
Ornamental Siamese fighting fish	*Trichodina*	60	1	1.67	Gills
	Dactylogyrus sp.	60	15	25.00	Gills
	Total	60	15	25.00	

Winter exhibited the highest seasonal prevalence of investigated parasites, followed by the rainy and summer seasons. Each station's seasonal prevalence varied, with the highest parasite prevalence in winter (60.00%) observed in St03. In St01, the highest prevalence (36.84%) occurred only in the rainy season, while St02 recorded the highest prevalence (summer). Parasite prevalence varied according to seasons and stations, as shown in Table 4, indicating the influence of changing environmental parameters on the prevalence of different parasites in different seasons and stations. Examining water quality in March and November revealed parameter alterations, specifically salinity and dissolved oxygen (DO). Interestingly, this finding contrasts with Poulin's [2] observations, suggesting that certain parasites or hosts exhibit distinct infection peaks in the summer while others display no seasonal variations. The prevalence of parasitic infections may, in part, be attributed to the life cycle of each parasite, as indicated by previous reports. Neves *et al.* [23] investigated seasonal variation, noting that host attributes shape the parasite community structure of wild Oscar fish in the Brazilian Amazon. In Thailand, limited reports have associated parasite prevalence with seasonal variations in ornamental fish in natural water.

This research showcases samples of ornamental Siamese fighting fish exhibiting high parasite prevalence in February, April, and March, coinciding with dry weather conditions. The richness of parasite species could be attributed to environmental variability and differences along a latitudinal plot [24]. According to Adugna [25] research, a wide variety of parasites were identified, with the highest prevalence observed in

lakes, surpassing that in farms and ponds. *Trichodina* spp. was detected predominantly in Nile tilapia (*Oreochromis niloticus*)**.** In the case reported by Öztürk and Özer [26], *Aphanius danfordii*, the host of *Gyrodactylus* sp., showed higher prevalence in the spring season, followed by autumn, summer, and winter, respectively.

Seasonal environments affect water parameters, including pH, temperature, and conductivity, influencing parasitic infections in hosts. Temperature and low rainfall are imperative for parasite development [27]. The interaction and relationship between wild Siamese fighting fish size in each location and the prevalence percentages remain unclear. Notably, wild fish exhibited the largest average size in St03, followed by St01 and St02, but the percentages of prevalence and species diversity for parasites were highest in St03, followed by St02 and St01.

Table 2. The prevalence of infection of parasites in examined fish in different seasons

Season	Fish examined	No. of fish examined	Parasite	No. of fish Infected	Prevalence (%)
Rainy	Wild Siamese fighting fish	48	*Trichodina*	7	14.58
			Zoothamnium	1	2.08
			Gyrodactylus	4	8.33
			Henneguya	3	6.25
			Posthodiplostomum	4	8.33
			Proleptus	4	28.57
	Ornamental Siamese fighting fish	30	*Dactylogyrus*	2	6.67
Winter	Wild Siamese fighting fish	17	*Trichodina*	5	29.41
			Gyrodactylus	2	11.76
			Henneguya	3	17.65
			Posthodiplostomum	1	5.88
			Pallisentis	1	5.88
			Proleptus	2	11.76
	Ornamental Siamese fighting fish	15	*Dactylogyrus*	8	53.33
			Trichodina	1	6.67
Summer	Wild Siamese fighting fish	16	*Henneguya*	1	6.25
			Posthodiplostomum	2	12.50
			Proleptus	2	12.50
	Ornamental Siamese fighting fish	15	*Dactylogyrus*	8	53.33

Table 3. The percentage of parasite prevalence in wild Siamese fighting fish examined across different seasons and stations

Parasites	Rainy			Winter			Summer		
	St01 N=19	St02 N=5	St03 N=24	St01 N=1	St02 N=1	St03 N=15	St01 N=0	St02 N=11	St03 N=5
Trichodina	10.53	0	20.83	0	0	33.33	0	0	0
Zoothamnium	5.26	0	0	0	0	0	0	0	0
Gyrodactylus	5.26	0	15.79	0	0	13.33	0	0	0
Henneguya	5.26	0	8.33	0	0	20.00	0	0	20.00
Posthodiplostomum	15.79	0	4.17	0	0	6.67	0	9.09	40.00
Pallisentis	0	0	0	0	0	6.67	0	0	0
Proleptus	0	0	16.67	0	0	13.33	0	6.09	20.00
Total	36.84	0	33.33	0	0	60.00	0	27.27	40.00

ASEAN J. Sci. Tech. Report. **2025**, *28*(3), e257870.

8 of 13

Table 4. Parameters of water quality at each station

Season	Station	Temperature (°C)	Salinity (ppt)	pH	DO (mg/L)
Rainy	01	28.5	0.05	6.55	2.20
	02	27.6	0.06	6.62	1.70
	03	27.4	0.12	6.28	1.20
Winter	01	25.9	0.04	7.43	1.83
	02	25.9	0.07	7.59	1.33
	03	24.5	0.05	7.53	1.67
Summer	01	26.8	0.02	7.19	3.25
	02	26.5	0.04	7.58	1.75
	03	26.4	0.06	7.42	3.00

Figure 3. Normal wild *Betta splendens* (a). Wound in pelvic fin and pectoral fin of wild *B. splendens* (b). *Henneguya* sp. from fins of wild *B. splendens* (c).

3.3 Bacterial infection

The biochemical test, API 20E, and PCR detection resulted in pathogen identification isolated from ornamental Siamese fighting fish from the market. They revealed Gram-negative bacteria, *Aeromonas veronii*, Gram-positive bacteria, and the non-tuberculosis *Mycobacterium marinum*. Mycobacteriosis was investigated in the internal organs of ornamental Siamese fighting fish from markets, liver, spleen, and kidneys. At the same time, no infections were detected in the internal organs of wild Siamese fighting fish. The absence of *Mycobacterium* was confirmed by Ziehl-Neelsen acid-fast testing. This study encompassed both healthy and unhealthy ornamental Siamese fighting fish. Anomalous fish from the local farm exhibited clinical signs such as abdominal distention, big belly or dropsy (Figure 4a), and skin nodules (Figure 4b). Upon investigation of internal organ tissue, dark brown granulomas were identified in the ornamental Siamese fighting fish within a lighter capsule, observed through a wet mount biopsy (Figure 4c). One strain of Gram-negative bacteria (*A. veronii*) was identified in the case of wild Siamese fighting fish. Bacterial isolation targeted Siamese fighting fish's liver, spleen, and kidney. In wild Siamese fighting fish, *A. veronii* infections were detected fewer than in ornamental Siamese fighting fish. The identified bacteria included *A. veronii* and non-tuberculosis *M. marinum*. *M. marinum*, causing granulomatous disease or fish Mycobacteriosis, is known to occur in fish tanks and the culture of live feed for fish [28].

The findings and prevalence of bacterial infections in betta fish of this study revealed the presence of both *A. veronii* and *M. marinum* in ornamental Siamese fighting fish obtained from markets. In contrast, wild Siamese fighting fish showed only a limited presence of *A. veronii* (Table 5). This suggests higher bacterial diversity and infection prevalence in captive fish. Similar findings have been reported in cultured Striped knifejaw fish, where aquacultured populations showed greater gut bacterial diversity than wild fish, possibly due to environmental exposure and aquaculture practices [29]. Conversely, a study on common carp showed lower bacterial diversity in farmed fish than in wild ones [30]. These variations may reflect species differences and farming conditions. Our findings highlight the need for comprehensive comparative studies on microbial communities in cultured versus wild Siamese fighting fish populations to understand better the ecological and health implications of different rearing environments.

Table 5. Prevalence of bacterial infections in wild Siamese fighting fish and ornamental Siamese fighting fish

Bacteria	Prevalence (%)			
	wild Siamese fighting fish			ornamental Siamese fighting fish
	St01	St02	St03	
Aeromonas veronii	15	35.29	15.91	26.67
Mycobacterium marinum	0	0	0	10
Total	15	35.29	15.91	36.67

Dong *et al.* [5] researched the bacterial strains isolated from the skin nodule syndrome of ornamental Siamese fighting fish, identifying 23 different species. Four *Mycobacterium* strains were putatively identified as *M. chelonae*, *M. cosmeticum*, *M. mucogenicum* from the liver, and *M. senegalense* from the nodules. Mandrioli *et al.* [31] presented findings of granulomas in the spleen and other visceral organs of Cichlid fish infected by *M. chelonae* and *M. parascrofulaceum*. This study's results regarding *Mycobacterium* align with previous research, confirming the presence of *M. marinum* in the Siamese fighting fish, consistent with other reports identifying the most common *Mycobacterium* strains in betta fish as *M. marinum* and *M. fortuitum* [3, 32].

In the broader context of bacterial infections in ornamental Siamese fighting fish, studies have identified additional bacteria, including *A. hydrophila* [30], *Pseudomonas* spp., *Edwardsiella tarda*, and *Streptococcus* spp. [9] Walczak *et al.* [31] research, encompassing more than 182 bacterial isolates from ornamental fish, highlighted the prevalence of *A. veronii*, followed by *A. hydrophila*, *Shewanella putrefaciens*, and *Pseudomonas* spp., respectively. While this study reflects a diversity of bacteria similar to previous reports, it is noteworthy that the number of bacteria identified is relatively lower than reported in earlier studies. Previous findings have highlighted variations in bacterial strains contingent on fish species, habitat, and water quality. Specifically, investigations into aquaculture fish have underscored the impact of diverse culture methods on the array of bacterial strains present. Among these strains, *Mycobacterium*, a bacterial species with the potential for transmission through water sources and genetics, stands out. Peeler and Murry [35] detailed that pathogens and diseases originating in the aquaculture of farmed fish are often traced back to wild fish, creating a cycle where these issues can transmit from aquaculture fish to their wild counterparts and then circulate back into the aquaculture system.

In the context of the study area, it was discerned that the surrounding environment, characterized by sewage, pollution, and flooding, played a pivotal role in influencing the release of fish into natural water post-cultivation, thereby impacting the local economy. This environmental influence may contribute to the outcomes observed in the present study, where the prevalence and diversity of parasites and bacteria are shown to hinge on water source conditions and seasonal variations. The sampling protocols of the research, unavoidably influenced by factors like reproductive seasons, summer droughts, and rainy season floods, underscore the complexity of obtaining random fish samples. These uncontrollable elements further accentuate the intricate relationship between environmental dynamics and the study's observed prevalence and diversity of parasites and bacteria.

Figure 4. The clinical signs of ornamental Siamese fighting fish from the market include dropsy symptoms (a) and skin nodule symptoms (b). Additionally, granulomas found on internal organs due to infection in ornamental Siamese fighting fish can be seen in (c) as dark brown inside a lighter capsule visible on a wet mount biopsy.

ASEAN *J. Sci. Tech. Report.* **2025**, *28*(3), e257870.

10 of 13

Phylogenetic analysis revealed two major lineages. The first clade was divided into two subclades, supported by a strong bootstrap value of 97%. The first subclade included *A. veronii* WWKMITL-02 (LC853090.1) isolates separated into a distinct *A. veronii* strain subclade with a bootstrap value of 99%. The current *A. veronii* isolate was clustered among other *Aeromonas* spp. Isolates and distinctly separated from *Vibrio vulnificus*. The second clade included *M. marinum* WWKMITL-03 (LC853089.1) isolates grouped with *M. chelonae*, forming a strongly supported monophyletic group (99% bootstrap support). The phylogenetic relationships, based on 16s rRNA gene sequences of the bacterial isolates, which were submitted to DDBJ, are shown in Figure 5. Although Mycobacterium strains have been isolated from ornamental Siamese fighting fish in farms and markets [9], data regarding their occurrence in wild populations remains limited. Given their ability to persist in aquatic environments and transmit across generations, these infections may pose long-term ecological and economic risks, particularly to the ornamental fish trade. Proactive monitoring and biosecurity measures are essential to mitigate potential outbreaks and safeguard wild and cultured fish populations.
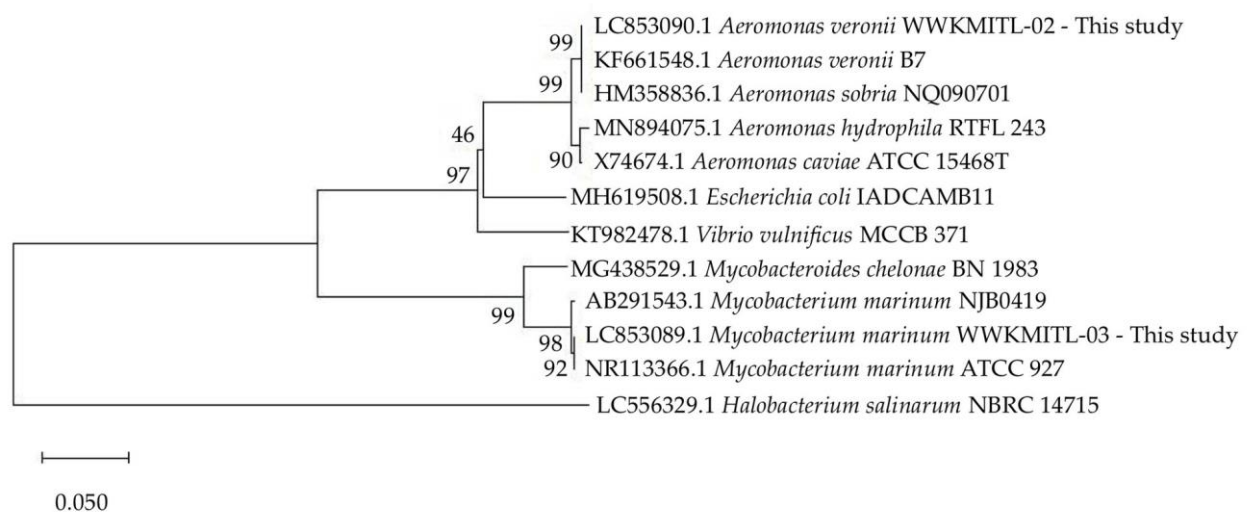
Figure 5. The phylogenetic relationship between two bacterial isolates, WWKMITL-02 (LC853090.1) and WWKMITL-03 (LC853089.1), was assessed using a tree generated via the neighbor-joining method based on 16s rRNA gene sequences. The Maximum Composite Likelihood method was applied to calculate nucleotide substitution distances. The tree was rooted with *Halobacterium salinarum* NBRC14715 (LC556329.1) as the outgroup. A scale bar indicating an evolutionary distance of 0.050 is provided to represent sequence divergence.

4. Conclusions

This study constitutes the inaugural investigation into the seasonal variations of parasitic infections among wild Siamese fighting fish within their natural water habitats, marking the first report of such observations. A distinctive facet of this research is the meticulous examination of *Henneguya* infection lesions on wild Siamese fighting fish fins, offering unprecedented insights into this hitherto unexplored dimension. The results illuminate a heightened prevalence and diversity of parasitic detection in wild Siamese fighting fish, eclipsing their ornamental counterparts. Significantly, the study discerns seasonal fluctuations in parasitic infection occurrences among wild Siamese fighting fish, underscoring the influence of water quality on both wild and aquaculture populations of Siamese fighting fish. After the rainy season, wild fish exhibit a zenith in parasitic prevalence and diversity, indicative of the conducive conditions for parasite growth during elevated temperatures.

In contrast, Siamese fighting fish from aquaculture systems and adhering to monthly or seasonal schedules exhibit negligible effects on parasite dynamics. The bacterial analysis further unravels a more excellent array of species isolated in ornamental Siamese fighting fish than in their wild counterparts, with notable identification of *M. marinum*, a genus linked to causing *Mycobacteriosis* infection. A comprehensive understanding of the complex interactions among seasonal variation, parasitic infections, and bacterial

communities is crucial for elucidating the observed associations in wild fish populations. This pursuit aims to leverage such insights for preventing infections across diverse environments, agricultural landscapes, and potential human ramifications.

5. Acknowledgements

Conflicts of Interest: We declare that we have no conflict of interest.

References

[1]   Lichak, M.R.; Barber, J.R.; Kwon, Y.M.; Francis, K.X.; Bendesky, A. Care and use of Siamese fighting fish (*Betta splendens*) for research. *Comparative Medicine.* **2022**, *72*(3), 169-180. https://doi.org/10.30802/AALAS-CM-22-000051

[2]   Poulin, R. Meta-analysis of seasonal dynamics of parasite infections in aquatic ecosystems. *International Journal for Parasitology*. **2020**, *50*, 501-510. https://doi.org/10.1016/j.ijpara.2020.03.006

[3]   Puttinaowarat, S.; Thompson, K.D.; Kolk, A.; Adams, A. Identification of *Mycobacterium* spp. isolated from snakehead, *Channa striata* (Fowler), and Siamese fighting fish, *Betta splendens* (Regan), using polymerase chain reaction-reverse cross blot hybridization (PCR-RCBH). *Journal of Fish Diseases*. **2002**, *25*, 235-243. https://doi.org/10.1046/j.1365-2761.2002.00363.x

[4]   Senapin, S.; Phiasaiya, P.; Laosinchai, P.; Kowasupat, C.; Ruenwongsa, P.; Panijpan, B. Phylogenetic analysis of parasitic trematodes of the genus *Euclinostomum* found in *Trichopsis* and *Betta* fish. *Journal of Parasitology*. **2014,** *100*(3), 368-371. https://doi.org/10.1645/13-285.1

[5]   Dong, H.T.; Senapin, S; Phiwsaiya, K.; Techatanakitarnan, C.; Dokladda, K. Histopathology and culturable bacteria associated with "big belly" and "skin nodule" syndromes in ornamental Siamese fighting fish, *Betta splendens*. *Microbial Pathogenesis*. **2018**, *122*, 46-52. https://doi.org/10.1016/j.micpath.2018.06.005

[6]   Panijpan, B.; Sriwatthanarothai, N.; Laosinchai, P. Wild betta fighting fish species in Thailand and other Southeast Asian countries. *Science Asia*. **2020**, *46*, 382-391. https://doi.org/10.2306/scienceasia 1513-1874.2020.064

[7]   Kanchan, C.; Imjai, P.; Kanchai, N.; Chaiyara, A.; Panchai, K. Occurrence of parasitic and bacterial diseases in Thai freshwater fish. *Journal of Agriculture and Crop Research*, **2020**, *8*(10), 210-214. https://doi.org/10.33495/jacr_v8i10.20.168

[8]   Mohamed, M.H.; Khalifa, E.; Sherry, Y.M.E. Detection of bacterial infections in some Red Sea fish in Hurghada. *Journal of Marine Biology and Oceanography*. **2016**, *5*, 4. https://doi.org/10.4172/2324-8661.1000164

[9]   Weerakhun, S.; Sukon, P.; Hatai, K. *Mycobacterium marinum* and *Mycobacterium fortuitum* infections in Siamese fighting fish, *Betta splendens* (Regan), in Thailand. *Thai Journal Veterinary Medicine*. **2019**, *42*(2), 137-145.

[10]   Buchmann, K.; Bresciani, J. Monogenea (Phylum Platyhelminthes) In: Fish diseases and disorders: protozoan and metazoan infections, 2nd ed.; P.T.K., Woo, CAB international, Wallingford. **2006**, *1*, 297–344. https://doi.org/10.1079/9780851990156.0297

[11]   Bhattacharya, S.B. Hanbook on Indian Acanthocephala**.** Zoological survey of India in english. **2007**. pp. 225.

[12]   Wagner, E.J. A guide to the identification of tailed Myxobolidae of the world: Dicauda, Hennegoides, Henneguya, Laterocaudata, Neohenneguya, Phlogospora, Tetrauromena, Trigonosporus and Unicauda. **2016**. Textbooks.

[13]   Khalil, L.F.; Jones, A.; Bray, R.A. Keys to the cestode parasite of vertebrates. CPI Antony Rowe, Printed. London, UK. **2006**, pp. 768.

[14]   Gibson, D.I.; Jones, A.; Bray, R.A. Keys to the Trematoda. Biddles Ltd, Printed. London, UK. **2001**, pp. 544. https://doi.org/10.1079/9780851995472.0000

[15]   Anderson, R.C.; Chabaud, A.G.; Willmott, A. Keys to the nematode parasites of vertebrates. MTC, Printed. Manila, Philippines. **2009**, pp. 462. https://doi.org/10.1079/9781845935726.0000

[16]   Hall, T.A. BioEdit: A user-friendly biological sequence alignment editor and analysis program for Windows 95/98/NT. *Nucleic Acids Symposium Series*. **1999**, *41*, 95-98

[17]   Saitou, N.; Nei, M. The neighbor-joining method: A new method for reconstructing phylogenetic trees. *Molecular Biology and Evolution*. **1987**, *4*, 406-425.

[18]   Kumar, S.; Stecher, G.; Suleski, M.; Sanderford, M.; Sharma, S.; Tamura, K. Molecular evolutionary genetics analysis version 12 for adaptive and green computing. *Molecular Biology and Evolution*. **2024**, *41*, 1-9. https://doi.org/10.1093/molbev/msae263

[19]   Thilakaratne, I.D.S.I.P.; Rajapaksha, G.; Hewakopara, A.; Rajapakse, R.P.V.J; Faizal, A.C.M. Parasitic infections in freshwater ornamental fish in Sri Lanka. *Diseases of Aquatic Organisms*. **2003**, *54*, 157-162. https://doi.org/10.3354/dao054157

[20]   Katharios, P.; Varvarigos, P.; Keklikoglou, K.; Ruetten, M.; Sojan, J.; Aktes, M.; Cascarano, M.C.; Tsertou, M.I.; Kokkari, C. Native parasite affecting an introduced host in aquaculture: cardiac henneguyosis in the Red seabream *Pagrus major* Temminck & Schlegel (Perciformes: Sparidae) caused by *Henneguya aegea* n. sp. (Myxosporea: Myxobolidae). *Parasites Vectors***. 2020**, *13*, 27. https://doi.org/ 10.1186/s13071-020-3888-7

[21]   Margarido, Y.M.M.; Adriano, E.A.; Valladão, G.M.R.; Naldoni, J.; Pilarski, F. Morphological, molecular, and histopathological characterization of a new species of *Henneguya* infecting farmed Astyanax lacustris in Brazil. *Microbial Pathogenesis*. **2021**, *158*, 104991. https://doi.org/10.1016/ j.micpath.2021.104991

[22]   Saha, M.; Bandyopadhyay, P.K. Studies on histopathological alteration of three major organs of the Goldfish, *Carassius auratus* L., of India due to myxozoan infection with special reference to scanning electron microscopic observation. *Parasitology Research*. **2017**, *116*, 511-520. https://doi.org/10.1007 /s00436-016-5314-9

[23]   Neves, L.R.; Pereira, F.B.; Tavares-Dias, M.; Luque, J.L. Seasonal influence on the parasite fauna of a wild population of *Astronotus ocellatus* (Perciformes: Cichlidae) from the Brazilian Amazon. *The Journal of Parasitology*. **2013**, *99*(4), 718-721. https://doi.org/10.1645/12-84.1

[24]   Sepúlveda, F.; Marín, S.L.; Carvajal, J. Metazoan parasites in wild fish and armed salmon from aquaculture sites in Southern Chile. *Aquaculture*. **2004**, *235*, 89-100. https://doi.org/10.1016/j.aquaculture.2003.09.015

[25]   Adugna, M. The prevalence of fish parasites of Nile tilapia (*Oreochromis niloticus*) in selected fish farms, Amhara Regional State. *Ethiopian Journal of Agricultural Sciences*. **2020**, *30*(3), 119-128.

ASEAN J. Sci. Tech. Report. **2025**, *28*(3), e257870.

13 of 13

[26] Öztürk, T.; Özer, A. Monogenean fish parasites, their host preferences and seasonal distributions in the Lower Kızılırmak Delta (Turkey). *Turkish Journal of Fisheries and Aquatic Sciences*. **2014**, *14*, 367-378.

[27] Fartade, A.; Chati, R.; Salunkhe, S.; Gavhane, U. Seasonal study of parasitic in fresh water fishes from Solapur and Osmanabad Distroct (M.S.), India. *International Journal of Fisheries and Aquatic Studies.* **2017**, *5*(5), 198-201.

[28] Cardoso, P.H.M.; Moreno, A.M.; Moreno, L.Z.; Oliveira, C.H.; Baroni, F.A.; Maganha, S.R.L.; Sousa, R.L.M.; Balian, S.C. Infectious diseases in aquarium ornamental pet fish: prevention and control measures. *Brazilian Journal of Veterinary Research and Animal Science.* **2019**, *56*(2), 16. https://doi.org/10.11606/issn.1678-4456.bjvras.2019.151697

[29] Zhu, K.; Zhang, S.; Xu, K.; Wang, H. Structural analysis and functional prediction of gut microbiota in wild and cultured Striped knifejaw (*Oplegnathus fasciatus*). *Journal of Marine Science and Engineering.* **2024,** 12, 2275. https://doi.org/10.3390/jmse12122275

[30] Ruzauskas, M.; Armalyte, J.; Lastauskienė, E.; Šiugždinienė, R.; Klimienė, I.; Mockeliūnas, R.; Bartkiene, E. Microbial and antimicrobial resistance profiles of microbiota in Common carps (*Cyprinus carpio*) from aquacultured and wild fish populations. *Animals*. **2021**, *10*, 929. https://doi.org/10.3390/ani11040929

[31] Mandrioli, L.; Codotto, V.; Annunzio, G.D.; Volpe, E.; Errani, F.; Eishi, Y.; Uchida, K.; Morini, M.; Sarli, G.; Ciulli, S. Pathological and tissue-based molecular investigation of granulomas in Cichlids reared as ornamental fish. *Animals.* **2022**, *12*, 1366. https://doi.org/10.3390/ani12111366

[32] Pleeging, C.C.F.; Moons, C.P.H. Potential walfare issues of the Siamese fighting fish (*Betta splendens*) at the retailer and the hobbyist aquarium. *Vlaams Diergeneeskundig Tijdschrift.* **2017**, *86*, 213-223. https://doi.org/10.21825/vdt.v86i4.16182

[33] Kanchan, C.; Imjai, P.; Kanchan, N.; Panchai, K.; Hatai., K. Virulence of *Aeromonas hydrophila* in Siamese fighting fish (*Betta splendens*) and the bacterium susceptibility to some herbal plants. *Iranian Journal of Fisheries Sciences.* **2019**, *18*(2), 349-354.

[34] Walczak, N.; Puk, K.; Guz, L. Bacterial flora associated with diseased freshwater ornamental fish. *Journal of Veterinary Research.* **2017**, *61*, 445-449. https://doi.org/10.1515/jvetres-2017-0070

[35] Peeler, E.; Murry, A. Disease interaction between farmed and wild fish populations. *Journal of Fish Biology.* **2004**, *65*(1). https://doi.org/10.1111/j.0022-1112.2004.0559s.x

Analysis of Profit in Organic and Conventional Paddy Farming in Two Adjoining Villages

Robert Wiliater Sibarani[1], and Buncha Somboonsuke[2*]

[1] Faculty of Natural Resources, Prince of Songkla University, Songkhla, 90110, Thailand

[2] Faculty of Natural Resources, Prince of Songkla University, Songkhla, 90110, Thailand

[*] Correspondence: buncha.s@psu.ac.id

Abstract: In Java Island, where half of Indonesia's population resides, increasing rice farming efficiency to increase rice production becomes the alternative approach. Despite some regions being vulnerable to flooding, East Java Province is one of Indonesia's top paddy producers. Compared to non-organic paddy, organic paddy produces less and is less productive. The time it takes to switch from conventional to organic farming and the significant impact of input use are the barriers to organic paddy production and productivity. This study analyzes the farmers profit from conventional and organic paddy farmers in East Java Province. The research was conducted in Mulyo 2 group with 34 conventional farmers; meanwhile, the Sumber Makmur 1 group with 32 organic farmers was used as samples. The data used in this research was data from farming during the rainy season of 2023-2024. The data was analyzed by using SPSS statistics version 26.0. The results showed that the profit farmers in Sumber Makmur 1 group made from selling their organic paddy was more than the profit farmers in Mulyo 2 group made from selling their conventional paddy. The lower variable and fixed costs incurred in the Sumber Makmur 1 farmer group support the higher profit. Compared to conventional paddy, organic paddy produces more and sells for a higher price, spending less on variable, fixed, and total costs.

Keywords: Conventional farming; Organic farming; Production paddy; Welfare

1. Introduction

Global market changes and other trends and events, like climate change, have recently put agricultural resilience to the test and raised societal concerns about environmental issues and climate change. Many people in Indonesia, an agricultural nation, live as farmers [1]. One of the industries with a significant impact on the Indonesian economy is agriculture. As a source of income, creating jobs, reducing poverty, and ensuring food security, the agricultural sector is crucial to economic growth [2]. In Indonesia, rice plants are grown in every province, and the production quantity varies. For the 2019-2022 period, ten of Indonesia largest rice-producing provinces, i.e., Aceh, North Sumatra, West Sumatra, South Sumatra, Lampung, West Java, Central Java, East Java, Banten, and South Sulawesi [3].

Both conventional and organic farming methods are being employed to maintain the resilience of Indonesia's agricultural sector, particularly in rice

ASEAN J. Sci. Tech. Report. **2025**, 28(3), e256576.

2 of 11

production. Conventional farming systems employ more chemical pesticides and fertilizers, which raises input costs and promotes production over environmental sustainability. In organic system farming, natural ingredients are used instead of chemicals, fertilizers, and pesticides, and environmental sustainability is considered while maximizing quality and productivity [4]. Input costs are typically lower than those of conventional systems because the fertilizers and pesticides used are non-chemical and are made from plant and animal waste and nitrogen-fixing cover crops. Variations in how production inputs are used will affect both the environment and output [5]. Compared to traditional farming, organic farming will produce more rice, improve product quality, and boost farmers income [6],[7]. On the other hand, the other research claims that rice production is lower in organic systems than in conventional ones [8],[9].

In 2022, total land in Indonesia was only 0.1 percent (87.195 hectares) of organic farming. Therefore, it is evident from the statistics that the majority of farmers in Indonesia continue to employ conventional farming as their primary strategy [10]. In 2023, the largest producer of paddy in Indonesia is East Java, with a total production of 9,591,422 tons [11]. In this province, there are two villages designated for paddy planting: Sumber Ngepoh village and Mulyoarjo village. Paddy is planted conventionally by every farmer in Mulyoarjo village. In the meantime, farmers in the village of Sumber Ngepoh plant rice organically. Conventional farming can have an adverse long-term effect on the environment by using chemical fertilizers, which can lower soil productivity, and pesticides, which can upset the ecosystems delicate balance. Moreover, increased chemical pesticides and fertilizers can affect crop productivity and worsen natural resource quality [12]. This claim makes it evident that conventional and organic farming profits differ. Conventional farmers prioritize their bottom line over organic farming. Consequently, every conventional farmer should thoroughly and carefully compare the profits earned switching from organic to conventional agriculture in light of the shift in profits [13].

According to the analysis of income disparities, all of these studies conclude that farmers using organic systems earn more than those using conventional systems. Regarding the various tests for income and production, they both demonstrated notable distinctions between the income and output of rice farmers using organic and conventional systems [14,15]. The findings of these investigations demonstrate that rice production in conventional and organic systems results in varying conditions in various regions and eras. This suggests a production irregularity. Farmers should practice organic farming since farming aims to make a lot of money, and organic rice farming yields higher profits than conventional rice farming. In the context of achieving sustainable livelihoods in organic and conventional farming, little is known about the difference in profits between conventional and organic paddy farming. Additionally, limited studies have analyzed the income of conventional and organic rice farming. This study compares farmers' profit margins in Sumber Ngepoh village organic paddy farming with conventional paddy farming in Mulyoarjo village. The entire cost of production serves as the foundation for the analysis (variable, fixed, and total cost) and the revenue from selling the paddy.

2. Materials and Methods

This study employs a quantitative descriptive approach, which analyzes organic and conventional paddy farming data to provide a comprehensive overview of the profits gained by farmers from their paddy farming. The research was conducted in Malang district, a rice production center in East Java province. Respondents were selected from two farmer groups: Mulyo 2 in Mulyoarjo village, consisting of 38 conventional paddy farmers, and Sumber Makmur 1 in Sumber Ngepoh village, which comprises 35 organic paddy farmers. Since this study is quantitative, the sample size from the total of farmers in each farmers group is determined using the formula developed by Krejcie and Morgan [16]. The formula is written as follows:

$$s = \frac{X^2 NP(1-P)}{d^2(N-1) + X^2 P(1-P)} \tag{2.1}$$

Where:

s   =   Required sample size

X^2 =   The table value of chi-square for 1 degree of freedom at the desired confidence level (1.960 x 1.960 = 3.841)

N   =   The population size

P   =   The population proportion (assumed to be 0.50 since this would provide the maximum sample size)

d   =   The degree of accuracy expressed as a proportion (0.05)

According to the formula, thirty-four conventional paddy farmers from farmer group Mulyo 1 and thirty-two organic paddy farmers from Sumber Makmur 2 are the respondents in this study. According to Cohen et al. [17], a minimum sample size of 30 is required for quantitative research that uses statistical analysis of the data gathered. These sample sizes meet their requirements. Furthermore, it was confirmed by Hogg et al. [18] that a sample size larger than 25 or 30 would typically yield a good approximation. Data from farming during the 2023–2024 rainy season served as the basis for this study.

Data from respondents was gathered through in-depth interviews with farmers using a structured questionnaire. The questions posed to farmers were regarding their demographic characteristics (specifically gender, age, education, marital status, and number of family members) and their paddy farming practices (specifically land area, paddy seed usage, fertilizer and pesticide application, labor usage, paddy yield, and paddy selling price). The validation process for the questionnaire was conducted by asking an expert with expertise in organic and conventional paddy farming to review and provide input on the questionnaire. A pilot testing was also conducted by piloting the questionnaire to 7 respondents to ensure that the questions can be understood and answered well.

The data was analyzed by using SPSS statistics version 26.0. The following procedures were carried out in processing data using SPSS: (a) determining the null and alternative hypothesis to test data normality and to test two farmer group means for production costs, production, revenue, and profit, (b) entering data from farmer's interview into SPSS, and (d) processing data, specifically testing data normality and also conducting the t-test.

According to Debertin [19], the costs of production that change depending on the amount of output the farmer produces are referred to as variable costs in this study, while fixed costs are those that the farmer must pay whether or not production occurs. The fixed costs in organic paddy farming are the tax of the paddy field and organic certificate issued by the Organic Certification Body (LeSOS (LSO-005-IDN)), and in conventional paddy farming is only tax on paddy fields. Meanwhile, the costs involved variable costs in organic paddy farming are the cost to rent tractors for land preparation, pay workers that plant paddy seedlings, replace dead-paddy plants, weeding, and chasing birds away as well as harvesting paddy. Meanwhile, the costs that are involved into the variable costs in conventional paddy farming are the cost of purchasing farming input (paddy seeds, fertilizers, pesticides, and bird nets) and labor payments (land preparation, planting paddy seedlings, replacing dead-paddy plants, and weeding, as well as harvesting). Since farmers in both groups only use hoes and sickles for farming activities and rent tractors for plowing, equipment depreciation was not calculated because it is not applicable in this context. Total costs are the result of adding fixed costs to variable costs. Debertin (2012) also explained that total revenue was the sale of all the output farmers produce at the going market price. Hence, the farmer's profit equals total revenue minus total cost.

Since each respondent in the two villages has a different amount of land for farming, the information about farming inputs, production costs, yields, selling prices, and profit was standardized on a per-hectare basis. The following conversion factors were used to facilitate comparison: 1 hectare is equivalent to 10,000 square meters (m²), 1 ton is equivalent to 1,000 kilograms (kg), and 1 quintal is equivalent to 100 kg.

Given that this research employs parametric statistical analysis, the data are assumed to be normally distributed. Therefore, the Kolmogorov-Smirnov test was used in this study. This is because the Kolmogorov-Smirnov test, with a significant value of more than 0.05 ($p \geq 0.05$), was employed to test whether or not a sample representing a population is normally distributed [20]. This study employs t-tests, which assume that the samples are normally distributed. The t-tests were used to compare two farmers' group means for variable

ASEAN J. Sci. Tech. Report. **2025**, *28*(3), e256576.

4 of 11

costs, fixed costs, total costs, production, revenue, and profit. The acceptance and rejection of the null hypothesis (H₀) in this test is based on a significance level (α) of 5% (0.05). If the value of t calculated is greater than that of the t table, the null hypothesis (H₀) will be rejected. The t-test's outcome will be utilized to identify the more lucrative farming.

3. Results and Discussion

3.1 Demographic characteristics of respondents

The demographic characteristics of organic farmers in the Mulyo 1 farmer group and Sumber Makmur 2 farmer group, including age, education, marital status, and household size, are essential for understanding their background characteristics. Table 1. summarizes the demographic characteristics of organic farmers in the Mulyo 1 farmer group and conventional farmers in the Sumber Makmur 2 farmer group.

Table 1. The Demographic Characteristics of Farmers

Characteristics	Organic		Conventional	
	Frequency	**%**	**Frequency**	**%**
1. Gender				
a. Male	100	100.00	100	100.00
b. Female	0	0.00	0	0.00
2. Age class				
a. 40-44 years old	0	0.00	2	5.88
b. 45-49 years old	5	15.63	2	5.88
c. 50-54 years old	7	21.88	4	11.76
d. 55-59 years old	8	25.00	7	20.59
e. 60-64 years old	4	12.50	6	17.65
f. 65-69 years old	6	18.75	8	23.53
g. 70-74 years old	2	6.25	4	11.76
h. 75-79 years old	0	0.00	1	2.94
3. Level of formal education				
a. Elementary school	27	84.38	20	58.82
b. Junior high school	5	15.63	10	29.41
c. Senior high school	0	0.00	2	5.88
d. Diploma in 3 years	0	0.00	1	2.94
e. Bachelor	0	0.00	1	2.94
4. Marital status				
a. Single	0	0.00	1	2.94
b. Married	31	96.88	31	91.18
c. Widower	1	3.13	2	5.88
5. Household size				
a. 1 person	0	0.00	1	2.94
b. 2 people	9	28.13	7	20.59
c. 3 people	13	40.63	11	32.35
d. 4 people	8	25.00	9	26.47
e. 5 people	2	6.25	4	11.76
f. 6 people	0	0.00	2	5.88

According to Table 1., it can be seen that all of the respondents are male. This indicates that as heads of households, they have a responsibility to manage their paddy fields as a source of income to meet the living needs of their household members. Furthermore, most respondents in both farmers groups fall within the age range of 50 to 69. This shows that respondents are approaching an unproductive age period. This finding is consistent with Utari et al. [21], who stated that humans are considered productive between the ages of 15 and 64.

Referring to Table 1, most respondents in both farmers groups have completed elementary or junior high school education. In terms of marital status, the majority of respondents in both farmers groups are married. Additionally, most farmers' households comprise 2-4 family members. All respondents in both farmers groups own only paddy field land. They do not have any side area farms. Additionally, respondents in the Sumber Makmur 1 farmer group rear livestock, such as cows, goats, and chickens, in their yards, where the livestock waste is a source of organic fertilizer for their paddy plants.

3.2 Kolmogorov-Smirnov test

The Kolmogorov-Smirnov test results show that all of the data collected from respondents are typically distributed. Significant (Sig.) values demonstrate that all data have values greater than 0.05. Table 2. displays the Kolmogorov-Smirnov test results.

Table 2. Tests of Normality: Kolmogorov-Smirnov test

A. Organic paddy farmer group

The data of	Statistic	df	Sig.	Std. Deviation	Mean	
					Statistic	Std. Error
Variable Cost	0.138	32	0.125	1079031.579	7099299.50	190747.637
Fixed Cost	0.139	32	0.118	68186.034	244868.06	12053.702
Total Cost	0.130	32	0.186	1100309.600	7344167.53	194509.095
Production	0.124	32	0.200	915.478	7121.81	161.835
Revenue	0.124	32	0.200	4577358.001	35609270.84	809170.221
Profit	0.114	32	0.200	4287642.882	28265103.25	757955.339

B. Conventional paddy farmer group

The data of	Statistic	df	Sig.	Std. Deviation	Mean	
					Statistic	Std. Error
Variable Cost	0.103	34	0.200	8670702.828	17122722.74	1487013.267
Fixed Cost	0.080	34	0.200	177933.109	430034.74	30515.276
Total Cost	0.101	34	0.200	8758935.743	17552757.38	1502145.087
Production	0.142	34	0.080	2390.048	6015.26	409.890
Revenue	0.144	34	0.072	10971596.461	27738962.21	1881613.270
Profit	0.139	34	0.095	7202387.264	10186204.79	1235199.225

3.3 T-test

The T-test result demonstrates differences in the means for variable costs, fixed costs, total costs, production, revenue, and profit between the two farmer groups. The findings based on Table 3. indicate that the Significant (Sig.) values are less than 0.05 in the Sumber Makmur 1 and Mulyo 2 farmers' groups. It suggests that a notable distinction exists in the economic performance components between the organic paddy farming practiced in Sumber Makmur 1 and the conventional paddy farming practiced in the farmer group of Mulyo 2.

Table 4. presents a comparison of the mean values for variable costs, fixed costs, total costs, production, revenue, and profit between the two farmer groups. The mean difference is caused by the different ways of planting paddy that respondents applied: planting paddy organically and planting paddy conventionally. The different ways lead in agricultural inputs, namely organic fertilizers and pesticides used in planting paddy organically, and chemical fertilizers and pesticides used in planting paddy conventionally. This causes differences in production expenses that need to be paid by among the respondents and the total paddy that they harvest. The sale of conventional and organic paddy in different quantities and prices causes the difference in revenue and profit earned by organic and conventional farmers.

Table 3. T-tests Results

A. Organic paddy farmer group

Mean of	Unit	N	Mean	Std. Deviation	Std. Error	t	df	Sig. (2-tailed)
Variable cost	IDR	32	7099299.50	1079031.579	190747.637	-6.686	34.085	0.000
Fixed cost	IDR	32	244868.06	68186.034	12053.702	-5.644	42.987	0.000
Total cost	IDR	32	7344167.53	1100309.600	194509.095	-6.740	34.106	0.000
Production	KG	32	7121.81	915.478	161.835	2.511	42.979	0.016
Revenue	IDR	32	35609270.84	4577358.001	809170.221	3.843	44.707	0.000
Profit	IDR	32	28265103.25	4287642.882	757955.339	12.475	54.330	0.000

B. Conventional paddy farmer group

Mean of	Unit	N	Mean	Std. Deviation	Std. Error	t	df	Sig. (2-tailed)
Variable cost	IDR	34	17122722.74	8670702.828	1487013.267	-6.686	34.085	0.000
Fixed cost	IDR	34	430034.74	177933.109	30515.276	-5.644	42.987	0.000
Total cost	IDR	34	17552757.38	8758935.743	1502145.087	-6.740	34.106	0.000
Production	KG	34	6015.26	2390.048	409.890	2.511	42.979	0.016
Revenue	IDR	34	27738962.21	10971596.461	1881613.270	3.843	44.707	0.000
Profit	IDR	34	10186204.79	7202387.264	1235199.225	12.475	54.330	0.000

Table 4. The mean of Cost, Production, Revenue, and Profit

Mean of	Unit	Organic	Conventional	Percentage Organic to Conventional
Variable cost	IDR	7,099,299	17,122,723	-141
Fixed cost	IDR	244,868	430,035	-76
Total cost	IDR	7,344,168	17,552,757	-139
Production	KG	7,122	6,015	16
Revenue	IDR	35,609,271	27,738,962	22
Profit	IDR	28,265,103	10,186,205	64

3.4 Economics Analysis of Paddy Production

The analysis of farmers' variable costs, fixed costs, total costs, production, price, revenue, and profit is shown in Table 4. In the Sumber Makmur 1 farmers group, the total cost to operate organic rice farms is 139 percent less than the total cost required in the Mulyo 2 farmers group. This indicates that the low total cost of organic paddy farming was caused by the low variable and fixed costs experienced in the Sumber Makmur 1 farmers group. This aligns with the study by [18], which states that inputs can be obtained on the farm, but input costs are frequently lower than conventional farming in organic farming.

The lower cost components of organic paddy farming than conventional paddy farming result in organic paddy farming being a more profitable option for farmers, particularly in production costs. This finding has encouraged Sumber Makmur 1 farmer group respondents to switch to planting organic paddy.

Using natural farming inputs, namely animal manure (cow, goat, and buffalo) for organic fertilizers, is why responders in the Sumber Makmur 1 farmers group reported lower variable costs than those in the Mulyo 2 farmer group to operate conventional paddy farming. Throughout the paddy planting season, a group of Mulyo 2 farmers feeds organic paddy seedlings using animal dung. Using animal manure as an organic fertilizer can reduce the expense of purchasing fertilizers, such as chemical fertilizers. Production costs can be decreased by using organic fertilizer [19]. This follows a study by [20] stating that livestock is a kind of savings. In Mulyo 2 farmers group, variable costs must incur purchasing chemical fertilizers, such as urea (N) fertilizer, za (nitrogen (N) with sulfur (S) fertilizer), NPK Phonska (compound (nitrogen (N), phosphorus (P), and potassium (K) fertilizer), and also TSP (triple super phosphate fertilizer).

Besides that, respondents in the Sumber Makmur 1 farmers group also reported that the use of organic fertilizer positively impacts the soil in their paddy fields, making it more easily cultivated. Farmers asserted that the soil became easier to cultivate since the 3rd planting season at the end of 2000, a year after they started switching from planting rice conventionally to planting rice organically, namely in the first planting season at the beginning of 1999.

Sumber Makmur 1 farmer group mentions using beneficial plants as a component of organic pesticides because they are cheaper than synthetic pesticides [21]. The grading KB (*Dioscorea composita*) is used by farmers to manage the rat (*Rattus argentiventer*), and tuber is only used to manage rat reproduction. The farmers use the daun sirsak (leaf of *Annona muricata*) and dringu daun (leaf of *Acorus calamus*) to control the sundep (*Scirpophaga innotata*). The farmers have successfully lowered the cost of purchasing pesticides by using these beneficial plants, which lowers the cost of production. The purchase of chemical pesticides, such as Decis (which is utilized to eliminate wereng (*Nilaparvata lugens*), Furadan (which is used to eradicate penggerek batang (*Tryoiryza innotata*), and also Ally (a herbicide), is the variable cost in farmers group of Mulyo 2 must bear.

In the context of tax, the average cost of IDR 218.677 to be paid in the Sumber Makmur 1 farmers group is lower than the tax of farming land that is to be paid in the Mulyo 2 farmers group, i.e., IDR 430,035. This is the reason for the lower fixed costs incurred in the Sumber Makmur 1 farmer group to run organic paddy farming as compared to fixed costs to run conventional paddy farming in the Mulyo 2 farmers group. The fact that the farmers in Sumber Makmur 1 live farther away from Lawang City, the sub-district capital, is the reason for their low tax value. Naturally, farmland is worth less when compared to the high-value farmland owned in the Mulyo 2 farmer group, which is close to Lawang City. This is in line with the study by [22], which states that land prices increase closer to the city center.

Besides the tax, Sumber Makmur 1 has the payment of an organic certificate as the fixed expense required to incur, namely IDR 33 million, and the certificate has a three-year validity period. As a result, in Sumber Makmur 1, the farmer group contributes roughly IDR 26.191 per month to the cost of the organic certificate. For the farmers, the cost of the organic certificate is mitigated by paying it jointly. Additionally, the organic certification helps improve customers' perception of their organic paddy. This is following the [23] organic certificate assures consumers that the products are free from synthetic chemicals, pesticides, and genetically modified organisms (GMOs), thereby building trust and confidence in the brand.

3.5 Estimated Production, Selling Paddy, Revenue and Profit

Based on Table 3, compared to conventional paddy produced in the farmers group of Mulyo 2, the production of organic paddy from the Sumber Makmur 1 farmers groups was higher. The production of paddy disparity between the two villages reaches 16%. It is because the quantity of production of organic paddy gotten by Sumber Makmur 1 is higher than the farmer group of Mulyo 2, namely:

1. The farming land area owned by the Sumber Makmur 1 farmers group, measuring an average of 6.313 square meters, is comparatively more significant than the agricultural land area owned by the Mulyo 2 farmers group, which measures an average of 2.735 square meters. This regard follows a study by [24] stating that the wider the cultivated land area, the higher the production.

2. The wereng (*Nilaparvata lugens*) that come into farming land owned by the farmer group of Sumber Mulyo 2 and then damage paddy plants lead to a decrease in the quantity of conventional paddy production. This aligns with the study by [25], which states that pest attacks on plants can disrupt production, reduce paddy abundance production, and lead to economic losses.

The selling price of the conventional paddy grain harvested in the farmers group of Mulyo 2 was sold for 8% less than the organic paddy grain harvested in Sumber Makmur 1 farmer group. The selling price of organic paddy is higher than that of conventional paddy. This regard is in line with a study by [26], which states that organic paddy sells for a higher price than conventional paddy. All the farmers who are members of the Sumber Makmur participate in group meetings every four months, on April 15, August 15, and December 15, to decide on the selling price for organic paddy. All the Mulyo 2 farmers group members participate in group meetings every four months, on April 15, August 15, and December 15, to decide on the

selling price for organic paddy. Two to three farmer group members surveyed the prices of paddy in the central markets of the Lawang and Malang cities before the meeting. The price obtained from the survey farmers is the cost of conventional paddy. The Sumber Makmur farmers group determines the selling price of their paddy beyond the surveyed price based on the price provided by the farmers. The farmers sell the organic paddy to the head of the Sumber Makmur farmers group. The head of the group mills the paddy grain to be rice. Furthermore, the rice is sold to loyal consumers of organic rice who can purchase the rice at a purchase price above the purchase price for conventional rice. In the meantime, the Mulyo 2 farmer group farmers sell their paddy at the central market in the cities of Lawang and Malang, paying the same price as conventional paddy.

In Sumber Makmur, there is 22% more paddy grain revenue than in Mulyo 2, and the revenue generated by paddy grain is influenced by its production and selling price. Farmer earnings within each farmer group are influenced by the amount of paddy produced and the price at which it is sold. The increased output and selling price of organic paddy can be partially attributed to the higher revenue earned in Sumber Makmur. Both this higher revenue and the farmer in Sumber Makmur spending less on total production costs contribute to their increased profit. This finding follows a study by [7],[27], which shows that organic farming yields higher profit than conventional farming. The difference in profit between the two villages is 64%. Organic paddy farming is less expensive overall, and farmers receive a higher selling price for their paddy grain. To maintain the sustainability of receiving profits for all farmers, the Sumber Makmur farmer group members should comply with the group agreement that requires each of them to sell their paddy to the head of this farmer group. Paddy sold by each farmer to the head of the farmer group will be purchased above conventional paddy's selling price. Selling their paddy only to the head of the farmer group means that all farmers only face one buyer so that they can control their paddy directly.

Conversely, the farmer group of Mulyo 2 uses a different way to sell the paddy that they harvest from their paddy fields. In this regard, they sell paddy to collecting traders, who come to Mulyoarjo village to buy conventional paddy from the farmer, or they sell paddy to owners of paddy mill, who support farmers financially by giving borrow money to them during planting season and purchase farmer paddy at harvesting season with buying price for paddy determined by the mill owners. By doing this, the farmers are forced to accept the paddy's selling price, which is determined by the collecting traders or the owners of paddy mills. This follows a study by [28],[29], where smallholder farmers are generally price takers. As price takers, farmers cannot set their own selling price for paddy that accommodates the production cost. Therefore, by receiving the selling price of paddy, which is determined by the collecting traders or the owners of the paddy mill, as a basis to sell their paddy, they receive the low revenue and, in turn, the low profit. Moreover, if the price of farming inputs increases, such as the increase in the price of chemical fertilizers or pesticides caused by scarcity in the market, then the farmer can receive a decrease in revenue and profit. This is in line with a study by [23]. As a price taker, farmers are potentially affected by an increase in farming production costs.

4. Conclusions

The profit that farmers in the Sumber Makmur 1 farmer group made from selling their organic paddy was more than the profit that farmers in the Mulyo 2 farmer group made from selling their conventional paddy. The lower fixed and variable costs incurred in the Sumber Makmur 1 farmer group support the higher profit. Furthermore, compared to conventional paddy, organic paddy produces more and sells for a higher price. This study confirms previous research results that profit from organic farming is higher than conventional farming. This study is also an early investigation of farmers' profit in organic and conventional farming. Nonetheless, respondents became disinterested due to the study lengthy questionnaire. Due to the utilization of low-cost organic fertilizers and pesticides by the Sumber Makmur 1 farmer group and the high-priced chemical fertilizers and pesticides purchased by the Mulyo 2 farmer group, the overall cost of organic paddy farming is low. As a result, we suggest that future studies focus on the availability of natural farming inputs as a crucial consideration when switching from conventional to organic farming methods. Planting organic paddy instead of conventional paddy can be accomplished by the farmers group Sumber Makmur in Mulyoarjo village by using more organic fertilizers and fewer chemical fertilizers. Farmers can decrease their use of one kilogram of chemical fertilizer during each planting season and then increase their use of one kilogram of organic fertilizer. In this manner, the full potential of organic fertilizer is realized. To help the farmer group

ASEAN J. Sci. Tech. Report. **2025**, *28*(3), e256576.

9 of 11

of Mulyo 2 in Mulyoarjo village transition from planting conventional to organic paddy, the government of Malang district must provide financial support for the purchase of livestock and enable the farmers to attend organic farming exhibitions to assist the farmers in identifying potential buyers for their organic paddy.

5. Acknowledgements

References

[1]   Khumairoh, U.; Mancini, H.; Yadav, S.; Schulte, R. P. O.; Ann, M.; Harja, D.; Joy, R.; Agustina, R.; Setiawan, A.; Nurlaelih, E. E.; Purnomo, M.; Groot, J. C. J. Linking Types of East Javanese Rice Farming Systems to Farmers' Perceptions of Complex Rice Systems. *Agric. Syst.* **2024**, *218*, 1–11. https://doi.org/10.1016/j.agsy.2024.104008.

[2]   Triyono, T.; Fahmi, M.; Al, F.; Rahmawati, N.; Rozaki, Z.; Kamarudin, M. F. The Role of Organic Rice Farm Income on Farmer Household Welfare: Evidence from Yogyakarta, Indonesia. *Open Agric.* **2024**, *9*, 1–9. https://doi.org/10.1515/opag-2022-0273.

[3]   Tamburaka, I. P. Analysis of Organic Rice Farming Income in Kulisusu North Buton District , Southeast Sulawesi. In *IOP Conf. Series: Earth and Environmental Science*, **2020**, 1–5. https://doi.org/10.1088/1755-1315/782/2/022005.

[4]   Khoiriyah, N.; Isnaini, M.; Iriany, A.; Forgenie, D. Analyzing the Cost of Paddy Rice Labor in Indonesia: A Case Study in Ten Tons Syngenta Project. *J-SEP J. Sos. Ekon. Pertan.* **2023**, *16*(2), 189–204. https://doi.org/10.19184/jsep.v16i2.38160.

[5]   Saliem, H. P.; Susilowati, S. H.; Ariningsih, E.; Agustian, A.; Muksin. Supporting Organic Rice Exports: The Success Story of West Java Organic Rice Exports. In *IOP Conf. Series: Earth and Environmental Science*; 2021; pp 1–8. https://doi.org/10.1088/1755-1315/672/1/012095.

[6]   Sardiana, I. K. Strategi Transisi Dari Pertanian Konvensional Ke Sistem Organik Pada Pertanian Sayuran Di Kecamatan Baturiti, Kabupaten Tabanan, Bali. *J. Bumi Lestari* **2017**, *17*(1), 49–57. https://doi.org/10.24843/blje.2017.v17.i01.p06.

[7]   Shennan, C.; Krupnik, T. J.; Baird, G.; Cohen, H.; Forbush, K.; Lovell, R. J.; Olimpi, E. M. Organic and Conventional Agriculture : A Useful Framing ? *Annu. Rev. ofEnvironment Resour.* **2017**, *42*, 317–346. https://doi.org/10.1146/annurev-environ-110615-085750.

[8]   Anggita, A. H.; Suprehatin. Is Organic Rice Farming More Profitable? Evidence from Pringkasap Village Subang Regency. *JEPA J. Ekon. Pertan. dan Agribisnis* **2020**, *4*(3), 561–592. https://doi.org/10.21776/ub.jepa.2020.004.03.12.

[9]   Mahmood, A.; Gheewala, S. H. A Comparative Environmental Analysis of Conventional and Organic Rice Farming in Thailand in a Life Cycle Perspective Using a Stochastic Modeling Approach. *Environ. Res.* **2023**, *235*, 1–11. https://doi.org/10.1016/j.envres.2023.116670.

[10] Adil, A.; Syarif, R.; Najib, M.; Widiatmaka. Organic Farming in Bogor, West Java, Indonesia: Measuring How Far Its Sustainability. *JPSL J. Nat. Resour. Environ. Manag.* **2023**, *13*(4), 671–682. https://doi.org/10.29244/jpsl.13.4.671-682.

[11] Kadarmanto. *Paddy Harvested Area and Production in Indonesia 2023 (Preliminary Figures)*; 2023. https://www.bps.go.id/en/pressrelease/2023/10/16/2037/paddy-harvested-area-and-production-in-indonesia-2023.

[12] Tsvetkov, I.; Atanassov, A.; Vlahova, M.; Carlier, L.; Lefort, F.; Rusanov, K.; Badjakov, I.; Dincheva, I.; Tchamitchian, M.; Rakleova, G.; Georgieva, L.; Tamm, L.; Iantcheva, A.; Herforth-rahmé, J.; Paplomatas, E.; Tsvetkov, I.; Atanassov, A.; Vlahova, M.; Carlier, L.; Christov, N.; Lefort, F.; Rusanov, K.; Badjakov, I.; Dincheva, I.; Rakleova, G.; Georgieva, L.; Tamm, L.; Iantcheva, A. Plant Organic

Farming Research – Current Status and Opportunities for Future Development. *Biotechnol. Biotechnol. Equip.* **2018**, *32*(2), 241–260. https://doi.org/10.1080/13102818.2018.1427509.

[13] Wibowo, R. P.; Raihan, A.; Sumono; Gunawan, D. Comparative Analysis of Technical Efficiency between Organic and Non-Organic Rice Farming in North Sumatera Indonesia. In *IOP Conf. Series: Materials Science and Engineering*, **2019**. https://doi.org/10.1088/1757-899X/648/1/012038.

[14] Prayuginingsih, H.; Muliasari, R. M.; Aulia, A. N. Local Wisdom of Paddy Farmer at Klungkung Village, Sub Dostrict of Sukorambi, Jember Regency to Overcome Subsidy Fertilizer Decreasing Policy. *Mimb. Agribisnis J. Pemikir. Masy. Ilm. Berwawasan Agribisnis* **2024**, *10*(2), 2447–2454. https://doi.org/10.25157/ma.v10i2.14208.

[15] Irfan; Nuraeni; Salim, M. Analisis Komparasi Usahatani Padi Organik Dan Usahatani Padi Konvensional. *Wiratani J. Ilm. Agribisnis* **2019**, *2*(2), 92–105. https://doi.org/10.33096/wiratani.v2i2.38.

[16] Krejcie, R. V; Morgan, D. W. Determining Sample Size for Research Activities. *Educ. Psychol. Meas.* **1970**, *30*(3), 607–610. https://doi.org/10.1177/001316447003000308.

[17] Cohen, L.; Manion, L.; Morrinson, K. *Research Methods in Education*, 8th ed.; Routledge, **2017**. https://doi.org/10.4324/9781315456539.

[18] Hogg, R. V; Tanis, E. A.; Zimmerman, D. L. *Probability and Statistical Inference*, Ninth Edit.; Pearson Education, Inc: United State of America, **2015**.

[19] Debertin, D. L. *Agricultural Production Economics*, Second Edi.; CreateSpace Independent Publishing Platform: New York, **2012**.

[20] Field, A. *Discovering Statistics Using SPSS*, 3rd ed.; Sage Publications Ltd: London, **2009**.

[21] Utari, W.; Eliza, E.; Yulida, R. Analisis Tingkat Kepuasan Dan Tingkat Harapan Petani Padi Terhadap Atribut Tauke Dalam Pemasaran Padi Di Nagari Sungai Rimbang. *J. Ilm. Sosio Ekon. Bisnis* **2022**, *25*(1), 8–19. https://doi.org/10.22437/jiseb.v25i01.20995.

[22] Riar, A.; Goldmann, E.; Bautze, D.; Rüegg, J.; Bhullar, G. S.; Adamtey, N.; Schneider, M.; Huber, B.; Armengot, L. Farm Gate Profitability of Organic and Conventional Farming Systems in the Tropics. *Int. J. Agric. Sustain.* **2024**, *22*(1), 1–13. https://doi.org/10.1080/14735903.2024.2318933.

[23] Etik, P.; Sudarno, S. Analysis of Greenhouse Gas Reduction by Using Organic Fertilizer in Boyolali Regency. *ICENIS 3rd Int. Conf. Energy, Environ. Inf. Syst.* **2018**, *73*, 1–5. https://doi.org/10.1051/e3sconf/20187308005.

[24] Binta BA, A.; Barbier, B. Economic and Environmental Performances of Organic Farming System Compared to Conventional Farming System: A Case Farm Model to Simulate the Horticultural Sector of the Niayes Region in Senegal. *J. Hortic.* **2015**, *02*(04), 1–10. https://doi.org/10.4172/2376-0354.1000152.

[25] Bhattacharjee, T.; Kotame, A. A.; Mahajan, A.; Ghorpade, A.; Kothadia, A.; Mohammadi, A.; Bhandarkar, A. Organic Pesticide from Non-Conventional Natural Resources. *IOP Conf. Ser. Mater. Sci. Eng.* **2023**, *1291* (1), 1–9. https://doi.org/10.1088/1757-899x/1291/1/012038.

[26] Purbalangi, G. A.; Brotosunaryo. Pengaruh Harga Lahan Terhadap Intensitas Pemanfaatan Lahan Di Koridor Jalan Mgr. Sugiopranoto-Siliwangi Semarang. *Tek. PWK* **2014**, *3*(1), 134–144. https://doi.org/10.14710/tpwk.2014.4442.

[27] Dayet, A.; Diepart, J. C.; Castella, J. C.; Sieng, S.; Kong, R.; Tivet, F.; Demenois, J. Can Organic Rice Certification Curb the Pressure of the Agrarian Transition in Cambodia? A Farming System Approach. *Agric. Syst.* **2024**, *217*, 1–14. https://doi.org/10.1016/j.agsy.2024.103953.

[28] Pradnyawati, I. G. A. B.; Cipta, W. Pengaruh Luas Lahan, Modal Dan Jumlah Produksi Terhadap Pendapatan Petani Sayur Di Kecamatan Baturiti. *Ekuitas J. Pendidik. Ekon.* **2021**, *9*(1), 93–100. https://doi.org/10.23887/ekuitas.v9i1.27562.

[29] Zenita, Z.; Hawa, Z. W. M.; Dwinata, C.; Wicaksono, A.; Samiha, Y. T.; Maryamah; Oktiansyah, R.; Aini, K.; Riswanda, J.; Miftahussaadiah. Serangga Hama Pada Tanaman Padi (Oryza Sativa L.) Pada Fase Vegetatif Dan Generatif. In *Prosiding Seminar Nasional Pendidikan Biologi*, **2020**, 98–104.

[30] Permatasari, P.; Anantanyu, S.; Dewi, W. S. Pengaruh Tingkat Adopsi Budidaya Padi Organik Terhadap Keberlanjutan Budidaya Padi Organik Di Kabupaten Boyolali. *Caraka Tani J. Sustain. Agric.* **2018**, *33*(2), 153–168. https://doi.org/10.20961/carakatani.v33i2.22296.

ASEAN J. Sci. Tech. Report. **2025**, *28*(3), e256576.

11 of 11

[31] Hazmi, M.; Suparwata, D. O. Comparative Study of Productivity of Organic and Conventional Agriculture in Maize Crops in East Java. *West Sci. Agro*. **2024**, *2*(03), 123–130.

[32] Mabuza, M. L.; Ortmann, G.; Wale, E. Effects of Transaction Costs on Mushroom Producers Choice of Marketing Channels: Implications for Access to Agricultural Markets in Swaziland. *South African J. Econ. Manag. Sci.* **2014**, *17*(2), 207–219. https://doi.org/10.4102/sajems.v17i2.494.

[33] Affandi, M. I.; Handayani, S. Marketing Efficiency of Organic Rice in Lampung Province. In *3rd Forum in Research, Science, and Technology*, **2020**, 1–8. https://doi.org/10.1088/1742-6596/1500/1/012063.

Spatial Clustering of Dormitory Density in Mueang District, Buriram Province Using the DBSCAN Algorithm

Jiravadee Yoyram[1], Prem Enkvetchakul[2], Jongkol Janruang[3], and Kittikoon Boonkate[4*]

[1] Faculty of Sciences, Buriram Rajabhat University, Buriram, 31000, Thailand
[2] Faculty of Sciences, Buriram Rajabhat University, Buriram, 31000, Thailand
[3] Faculty of Science and Liberal Arts, Rajamangala University of Technology Isan, Nakhonratchasima, 30000, Thailand
[4] Faculty of Sciences, Buriram Rajabhat University Buriram, Thailand
* Correspondence: kittikoon.bk@bru.ac.th

Abstract: Spatial distribution studies the geographical arrangement of elements within a given area, crucial for urban planning, resource allocation, and spatial decision-making. This research aimed to examine the spatial distribution of dormitories in Mueang District, Buriram Province, using the DBSCAN algorithm, and to cluster dormitory neighborhoods within the area. The methodology followed a five-step data mining process: 1) data gathering from 387 points obtained via website extraction, 2) data preparation, 3) clustering using DBSCAN, 4) visualization of results through a distribution map and clustering outcomes, and 5) validation of clustering. The findings revealed that dormitory clusters in Mueang District exhibited a dense and notable pattern. Data was classified into three clusters: Cluster 1 included Nai Mueang and Isan Subdistricts, Cluster 2 covered Samed Subdistrict, and Cluster 3 encompassed Krasang and Ban Bua Subdistricts. The Silhouette Coefficient of 0.495 indicated good clustering performance, while the Davies-Bouldin Index (DBI) of 2.785 showed acceptable results, demonstrating DBSCAN's effectiveness in clustering dormitories. The algorithm's flexibility in parameter adjustment allows for results that align with the specific context of the area, making it suitable for spatial research. It also reduces time and costs in data collection and analysis. These clusters provide valuable insights for students selecting dormitories and entrepreneurs investing in private dormitories, and hold potential for future development.

Keywords: Dormitory distribution; DBSCAN algorithm, Spatial distribution

1. Introduction

Machine Learning (ML) and Artificial Intelligence (AI) are increasingly becoming central in developing web and mobile applications called digital platforms. That means the main application task is a specialized task requiring mathematically provable computations. The technologies must support engineering simulations, automated theorem proving, scientific computing, and AI-powered math solvers, ensuring accuracy and verifiability in complex calculations. Machine Learning and Artificial Intelligence are essential tools for data analysis in various fields. For example, Convolutional Neural Networks are used for image classification of the cassava leaf to develop a Line Bot that can identify and provide information about Cassava Leaf Diseases [15], and DBSCAN (density-based spatial clustering of application with noise) is applied

in spatial analysis to decide for planning and developing the main content of the city such as hotel distribution [1][5], tourism planning [11][12][16] and analyzing an urban space [6]. These tools assist in analyzing complex data and making decisions effectively.

To demonstrate the applicability of DBSCAN in urban planning, several studies have successfully employed this clustering algorithm to support spatial decision-making. For instance, Tu et al. applied DBSCAN using point-of-interest (POI) data to analyze the spatial structure of "production–living–ecological" zones in Wuhan, China, which helped inform sustainable urban development strategies [9]. Similarly, Fauzan et al. utilized DBSCAN to cluster hotel locations in Bali, enabling tourism stakeholders to better plan post-pandemic economic recovery by identifying key zones of accommodation demand [5]. Furthermore, Camilo Alberto Caudillo-Cos and Jorge Alberto Ruiz-Pérez conducted a study titled Defining Urban Boundaries through DBSCAN and Shannon's Entropy: The Case of the Mexican National Urban System, in which they proposed a novel method for delineating urban boundaries in Mexico. This approach integrates the DBSCAN algorithm with Shannon's entropy to analyze data from multiple and diverse sources. [2].

In the context of this study, the application of DBSCAN to cluster dormitories in Mueang District, Buriram Province, follows a similar rationale. The ability of DBSCAN to identify high-density residential zones based on spatial distribution provides valuable insights for students seeking accommodation and for city planners or private entrepreneurs aiming to develop or invest in dormitory infrastructure. The algorithm's robustness in handling noise and irregular densities makes it particularly effective in modeling real-world urban patterns.

1.1 Problem Statement

Buriram Rajabhat University serves as a key educational institution driving local development. It holds a prominent position within Thailand's northeastern region, contributing to local advancement and global competitiveness. The university boasts 11,514 regular students [10], and the surrounding vicinity is home to a significant population of students, faculty, and members of the general public in the academic year 2022. It causes a substantial portion of students who originate from various regions to face challenges when selecting suitable accommodation or dormitories. Consequently, dormitories play a crucial role in addressing the accommodation needs of students, with preferences typically leaning towards options offering security, proximity to the university for ease of commuting, and affordable rental rates. Private dormitories have seen a surge in demand among university students, largely due to insufficient on-campus housing provided by the university. As the student population grows, there has been a corresponding rise in entrepreneurs venturing into the private dormitory sector. The location selection process for dormitory construction is a critical decision for these entrepreneurs.

The dormitory zones are important information for students who must find a suitable dormitory. This is because a suitable dormitory can help students reduce the cost and time spent at university. Therefore, examining the spatial distribution of dormitories in Mueang District, Buriram Province, is presented as a new approach to finding and providing information about dormitory zones for students. A new approach used the DBSCAN algorithm as a main model to support scientific computing and AI-powered math solvers. Moreover, the advantages of the DBSCAN algorithm are that it can effectively solve problems from large amounts of data, its performance is based on the overlapping and covering of points of interest, and its fast clustering speed, which can effectively handle noise points and divide high-density areas into clusters to form easier-to-recognize spatial clusters, it is applying to both convex and non-convex sample sets [9]. However, implementing DBSCAN algorithms must combine with other platforms to show the algorithms' results in visualization and results analysis, such as the Shiny web application [18] and ArcGIS [9].

To substantiate the selection of DBSCAN as the primary clustering algorithm in this study, a comparative evaluation was conducted against other well-established clustering methods, namely K-Means and Hierarchical Clustering. While widely used, K-Means assumes spherical cluster shapes and requires the number of clusters to be defined in advance—limitations that make it less suitable for spatial datasets with irregular distributions and unknown group structures [3, 12]. Hierarchical clustering, though advantageous in not requiring a pre-defined number of clusters, becomes computationally intensive and less efficient when

ASEAN J. Sci. Tech. Report. **2025**, *28*(3), e258177.

3 of 14

applied to large-scale datasets [11]. In contrast, DBSCAN offers several key advantages that align well with the characteristics of the dataset used in this study. It can effectively identify clusters of arbitrary shapes and automatically detect noise or outliers without prior knowledge of the number of clusters. Given the spatial nature of dormitory data in Mueang District, Buriram Province—characterized by varying densities and noise—DBSCAN demonstrates superior flexibility and accuracy. Its robustness in handling non-linear spatial patterns makes it particularly well-suited for uncovering meaningful dormitory clusters within this urban context [9], [13].

Based on the advantages of DBSCAN algorithms, this paper presents a new approach to analyzing dormitory distribution and clustering dormitories to identify dormitory zones. In addition, the Shiny web application displays the results of DBSCAN algorithms and is active with users. The results of the proposed approach can be used as information to support students in finding and making decisions about their suitable dormitory based on spatial distribution.

2. Materials and Methods

The research framework of the proposed approach for analysis of dormitory distribution and clustering to find the dormitory zone in Mueang District, Buriram Province. The research methodology includes the following details:

2.1 Research Framework

Clustering dormitories in Mueang District, Buriram Province, based on their density using the DBSCAN algorithm, involves extracting and retrieving location data from websites through Web Scraping. This data encompasses dormitories, apartments, mansions, and housing in the Mueang District area of Buriram Province. Subsequently, the data undergoes clustering using the DBSCAN algorithm, which hinges on the distance or proximity between points (Eps) and the minimum number of points (MinPts). The R-Studio program with R language and Shiny Web Application Framework are utilized to visualize the spatial distribution on maps and present the clustering results. The efficacy of clustering is validated using the Silhouette Coefficient concept. The research framework is illustrated in the five layers, which are shown in Figure 1.
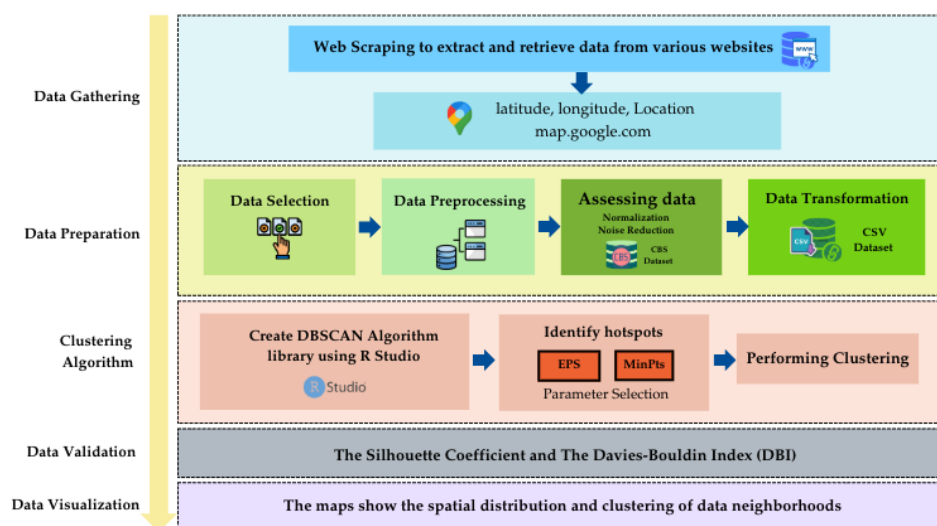
Figure 1. Research Framework

According to Figure 1, the research workflow for spatial clustering of dormitories in Mueang District, Buriram Province, using the DBSCAN algorithm, is an application of the data mining process consisting of 5 operational layers [3][4]. The main point of these steps is in a Clustering algorithm layer called the DBSCAN algorithm, which is used to identify the dormitory zones for supporting students of Buriram Rajabhat University. Finally, in the data visualization layer, the dormitory zones are displayed on the web using the

Shiny web application. Interestingly, users can set the distance (Eps) and the minimum number of points (MinPts) by themselves when the shiny web application is used as a tool to develop the user interface of the system [12], [16].

The evaluation of the proposed approach consists of two steps. First, researchers cross-check all datasets with local data sources in the areas. This cross-checking is a sub-process in data preparation and must be performed to ensure validating data accuracy. This means the dataset is corrected because it is verified before being used in the clustering model. Second, the Silhouette Coefficient and the Davies-Bouldin Index (DBI) is a statistical models used to evaluate the efficacy of clustering.

2.2 Research Methodology

Based on the Research Framework in Figure 1, this research proposes a new approach to examine dormitories' spatial distribution and cluster the dormitory zone in Mueang District, Buriram Province, using the DBSCAN algorithm. The proposed approach consists of five 5 steps, and the details of each process are shown below.

    1)   Step 1: Data Gathering

The data-gathering process entails examining the dormitory distribution in Mueang District, Buriram Province, using Web Scraping to extract and retrieve data from various websites. This process encompasses gathering the coordinates and names of each location and recording/organizing the data into an Excel spreadsheet format, delineating it into rows and columns, as illustrated in Table 1.

Table 1. Data Gathering Details

Field	Description
latitude	Latitude coordinates
longitude	Longitude coordinates
Location	Name of the place

2) Step 2: Data Preparation

Data preparation involves refining raw data to align with research objectives, comprising three key steps :

2.1) Data Selection or Acquisition: Following data extraction from websites via Web Scraping based on Google Maps, the data equals 390. The comprehensive data should encompass latitude and longitude coordinates along with location names. The dataset used in this study was selected from January 2024. The data were collected from publicly accessible sources using web scraping. No personal or sensitive information was included, and the process complied with ethical guidelines for academic use. The example of Data Selection or Data Acquisition Process is shown in Figure 2
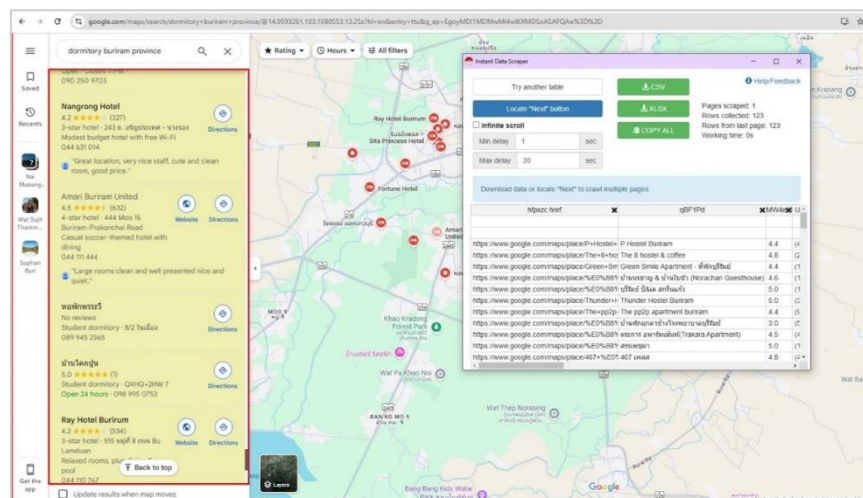
Figure 2. Example of Data Selection or Data Acquisition Process

ASEAN J. Sci. Tech. Report. **2025**, *28*(3), e258177.

5 of 14

2.2) Data Preprocessing: This step entails validating data accuracy, including latitude and longitude coordinates and location names. Researchers ensure data integrity by cross-checking all entries with local data sources in the areas. Then, data cleaning was carried out to clear the attributes with missing values, such as latitude or latitude which is loose or wrong. This is because errors from scraping via map.google.com may arise, including inaccurate latitude and longitude coordinates that deviate from the actual location. Additionally, some retrieved data may be incomplete or duplicated, such as duplicate place names or missing information, which affects data preparation, the accuracy of the clustering process, and the quality of results produced by the DBSCAN algorithm. For example, the dormitory location is incorrect when researchers cross-check all entries with local data sources in the areas. There are 3 mistakes in the locations deleted.

Based on Data Preparation, the dataset can be uploaded to the R-Studio program to analyze the distribution of dormitory locations and understand the data. For example, the distribution of dormitory is shown in Figure 3.
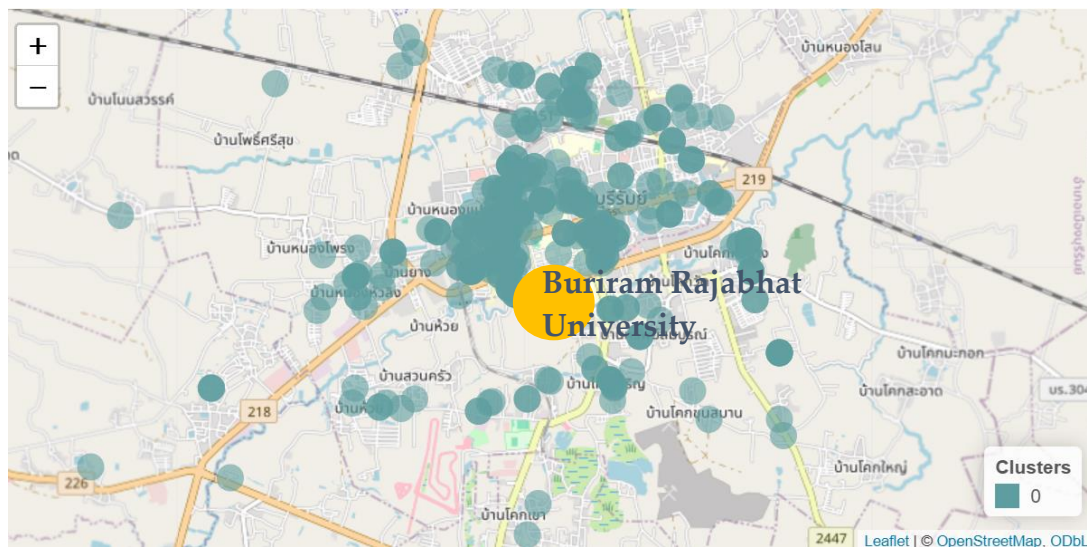
Figure 3. Example of distribution of dormitory location

According to Figure 3, dormitories are located in a high concentration in the urban area near Buriram Rajabhat University. The dataset distribution on the map shows that the dormitory location is a disordered pattern without clear planning, called unstructured distribution. Moreover, noises, outliers, or small data groups on Google Maps occur around urban areas near Buriram Rajabhat University (cycle with yellow color). This means that the dataset used as a sampling of this paper is suitable for the DBSCAN algorithm. This is because DBSCAN is an algorithm for datasets that are separated as clusters with varying shapes and sizes of cluster.

The scope of the spatial study area encompasses dormitory data within Mueang District, Buriram Province. The data scope includes dormitories, apartments, mansions, and housing. Final data was collected on January 1, 2024, referencing locations through Google Maps. The data was recorded and stored in an Excel spreadsheet comprising 387 entries. An example of data collection is illustrated in Table 2.

ASEAN J. Sci. Tech. Report. **2025**, *28*(3), e258177.

6 of 14

Table 2. Example of Dormitory Location Coordinate Data Gathering in Mueang District, Buriram Province

latitude	longitude	location
103.0942767	14.9956900	AP Apartment Buriram
103.0942767	14.9882406	Serm-Suni 4 Place Dormitory
103.0919406	15.0113636	Boonmani Dormitory
.	.	.
.	.	.
103.0818726	15.0134048	Baitong Mansion
103.0702891	14.9836372	Night for You Residence

2.3) Data Transformation: Data transformation involves converting data into a format conducive to analysis by storing files in CSV format. The CSV format consists of three fields: latitude, longitude, and the place's name (location).

3) Step 3: Clustering Algorithm

In the clustering algorithm step, the DBSCAN algorithm is chosen as the main model to find the pattern of spatial data. This is because the clustering algorithm process involves organizing spatial data using the DBSCAN algorithm, which is particularly suitable for datasets exhibiting specialized non- linear distribution patterns that cannot be effectively clustered by the K-means method [7]. The DBSCAN algorithm operates by considering the distance (Eps) and the minimum number of points (MinPts)[4][11]. Users can adjust parameter values to tailor the outcomes to the specific requirements and characteristics of the data available in the area. This customization is enabled by creating a library using clustering tools, including the RStudio program in conjunction with the R language and the Shiny Web Application Framework, an application widely utilized for spatial development tasks or spatial data analysis. Users can set the distance (Eps) and the minimum number of points (MinPts) to ensure alignment and suitability with the data in the area [13][16].

4) Step 4: Validation

Validation entails evaluating the efficacy of clustering the data by employing

4.1) The Silhouette Coefficient, introduced by Peter J. Rousseeuw in 1986 as a metric for data grouping, considering the compactness of points within clusters and the separation between clusters. The Silhouette Coefficient acts as an internal criterion for assessing the quality of cluster formation [10], utilizing the class and their interrelations. It is calculated from the inter-class cohesion and can be computed using equation (1).

$$S(i) = \frac{a(i) - b(i)}{Max\{a(i), b(i)\}} \tag{1}$$

By definition, $a(i)$ represents the number of connections between class i and any other class within the same cluster while

$b(i)$ denotes the number of connections between class i and any other class across clusters.

The range of the Silhouette coefficient is from -1 to 1, where a value close to 1 indicates that a class is highly suitable for its cluster, signifying high cohesion. Conversely, a value approaching -1 indicates low cohesion, suggesting errors in clustering. Therefore, it is highly probable that any class would need to modify its Silhouette coefficient (S(i)) calculation within each cluster to obtain the average value $\bar{s}$ for assessing intra-cluster suitability, which falls between -1 and 1. Evaluation criteria for the Silhouette coefficient are detailed in Table 3.

Table 3. Evaluation Criteria for Silhouette Coefficient

Silhouette Coefficient (S)	Interpretation
The range between 0.71 - 1	The structure of the cluster is considered excellent.
The range between 0.51 - 0.71	The structure of the cluster is acceptable.
The range between 0.26 - 0.50	The clustering should be improved.
Less than 0.25	The structure of the cluster has no relationship.

Source: Silhouettes, a graphical aid to the interpretation and validation of cluster analysis [14]

4.2) Davies-Bouldin Index

Developed to assess the quality of clustering, the Davies-Bouldin Index (DBI) utilizes Euclidean Distance as a key metric for calculation. The Davies-Bouldin Index clustering process can be computed using the following equation [17].

$$\text{Davies Bouldin} = \frac{1}{n}\sum_{i=1}^{n} \frac{max}{i \neq j}\left(\frac{\sigma_i + \sigma_j}{d(c_i, c_j)}\right) \qquad (2)$$

n: The number of clusters., c_i: The average distance within cluster i., c_j: The average distance within cluster j., σ_i: The average distance from points in cluster i to its centroid c_i. Σ_j: The average distance from points in cluster j to its centroid c_j., $d(c_i, c_j)$: The distance between the centroids c_i and c_j.

The Davies-Bouldin Index (DBI) calculation involves determining the Intra-cluster Dispersion ratio. A lower DBI value indicates better clustering quality, as the clusters exhibit less dispersion and are well-separated. Conversely, a higher DBI value suggests that the clusters overlap or cannot be effectively distinguished.

5) Step 5: Visualization

Visualization presents the results in graphical format, including maps illustrating the spatial distribution and clustering of data neighborhoods.
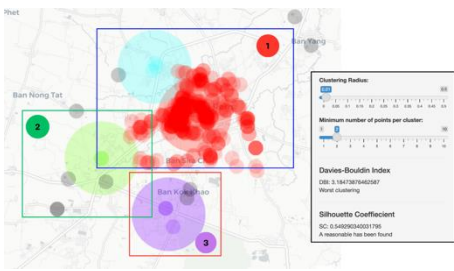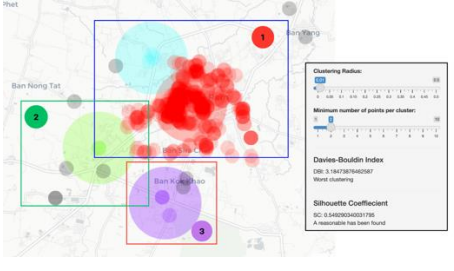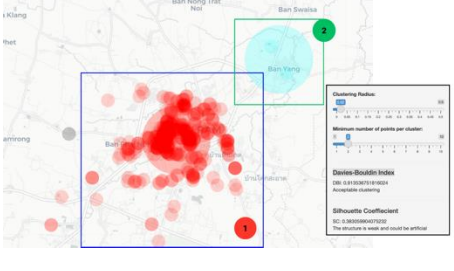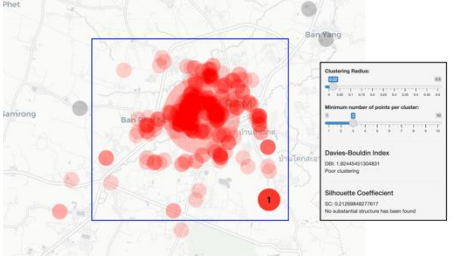
3. Results and Discussion

The spatial clustering of dormitory density using DBSCAN algorithm yielded the following outcomes**:**

3.1 Results

1) Examining the distribution of dormitories in Mueang District, Buriram Province, using the DBSCAN algorithm with the assistance of the RStudio in conjunction with the R language and the Shiny Web Application involved the visualization of maps depicting the spatial distribution of dormitories in the area. In addition, the clustering results of dormitory neighborhoods were presented. By comparing different parameter values for distance or proximity between points (Eps) and the minimum number of points (MinPts), variations in the spatial distribution and clustering of dormitory neighborhoods in Mueang District, Buriram Province, were observed, as depicted in Table 4.

ASEAN J. Sci. Tech. Report. **2025**, *28*(3), e258177.

8 of 14

Table 4. Comparison of Data Distribution across Varying Eps and MinPts Values

Eps	MinPts	Clusters	Davies-Bouldin Index/ Silhouette Coefficient/	Visualization
0.01	2	3	3.185/ 0.549	(A)
0.01	3	3	2.785/0.495	(B)
0.02	2	2	0.914/0.383	(C)
0.02	3	3	1.924/0.213	(D)

The data analysis from Table 4 reveals the spatial distribution of dormitories in Mueang District, Buriram Province, along with the clustering outcomes :

(1) Setting Eps at 0.01 and MinPts at 2 resulted in the data clustering into 3 clusters. Cluster 1 comprised areas in Nai Mueang and Isan Subdistricts containing 368 data points. Cluster 2 covered the Krasang and Ban Bua Subdistricts, containing 6 data points. Cluster 3 covered areas in the Samed Subdistrict, with 5 data points as depicted in Figure **(A).** The evaluation of the Davies-Bouldin Index (DBI) shows a value of 3.185, indicating poor clustering due to the high value. Additionally, the Silhouette Coefficient (SC) is 0.549, which suggests that the clustering structure is acceptable to some extent but can still be improved.

(2**)** With Eps set to 0**.**01 and MinPts to 3, the data formed 3 clusters**.** Cluster 1 included areas in Nai Mueang and Isan Subdistricts, containing 366 data points. Cluster 2 covered the Krasang and Ban Bua

Subdistricts, containing 5 data points. Cluster 3 covered areas in the Samed Subdistrict, with 6 data points as depicted in Figure **(B).** The clustering quality assessment using the Davies-Bouldin Index (DBI) yielded a value of 2.785, which is considered high and indicates low clustering performance. This suggests significant overlap among clusters and a lack of clear separation. Additionally, the Silhouette Coefficient (SC) was 0.495, a moderate value that implies the clustering structure is not sufficiently well-defined.

(3) When Eps was set to 0.02 and MinPts to 2, the data clustered into 2 clusters. Cluster 1 included areas in Nai Mueang and Isan Subdistricts, containing 381 data points. While Cluster 2 comprised areas in the Ban Yang Subdistrict, containing 2 data points, as illustrated in Figure **(C)**, The clustering quality assessment using the Davies-Bouldin Index (DBI) yielded a value of 0.914, which is considered acceptable. This indicates that the data points within each cluster are reasonably compact, and the clusters are fairly well-separated. However, the Silhouette Coefficient (SC) was found to be 0.383, which is considered low to moderate, suggesting that the clustering structure is not particularly strong or well-defined.

(4) When Eps was set to 0.02 and MinPts to 3, the data clustered into 1 cluster. Comprising areas in Nai Mueang and Isan Subdistricts contain 381 data points, as illustrated in Figure **(D)**. The clustering quality assessment using the Davies-Bouldin Index (DBI) yielded a value of 1.924, which is relatively high and indicates poor clustering performance. However, the Silhouette Coefficient (SC) was 0.213, indicating the lowest level with an unrelated group structure.

The findings from Table 4 illustrate how varying Eps and MinPts values influence the clustering structure and quality in the spatial distribution of dormitories. As demonstrated, the number of clusters, cluster membership, noise points, and clustering quality metrics such as DBI and Silhouette Coefficient change significantly depending on the parameter settings. Table 5 presents a consolidated overview of clustering outcomes across different Eps and MinPts combinations to highlight these variations further and enable more precise comparisons. This comparison facilitates the identification of parameter settings that yield the most reliable and interpretable clustering structure, both algorithmically and from a human-judgment perspective.

Table 5. Comparison of Data Distribution across Varying Eps and MinPts Values

Eps	MinPts	Clusters	members	noise	Silhouette Coefficient	DBI	Human (Clusters)	Clustering Quality
0.01	2	3	379	8	0.549	3.185	377	Moderate
0.01	3	3	377	10	0.495	2.785	377	Best
0.02	2	2	383	4	0.383	0.914	377	Moderate
0.02	3	1	381	6	0.213	1.924	377	Lowest

Based on the results presented in Table 5, the clustering quality varies significantly depending on the combination of Eps and MinPts values. When Eps was set to 0.01 and MinPts to 2, the clustering yielded the highest Silhouette Coefficient (0.549), indicating that the cluster structure was relatively well-defined. However, this configuration also produced the highest Davies-Bouldin Index (DBI) at 3.185, which implies poor compactness and significant overlap between clusters. Therefore, while the clusters were distinguishable, they lacked cohesion.

In contrast, Eps = 0.01 and MinPts = 3 parameter settings provided a more balanced outcome. Although the Silhouette Coefficient slightly decreased to 0.495, the DBI dropped to 2.785. This suggests that the clusters were both reasonably compact and moderately well-separated. As a result, this configuration can be considered the most appropriate overall, offering a good trade-off between intra-cluster cohesion and inter-cluster separation.

When Eps was increased to 0.02, and MinPts remained at 2, the clustering quality improved compactness, as reflected by the lowest DBI value of 0.914. However, the Silhouette Coefficient decreased to 0.383, indicating a less distinct clustering structure. This setting may be suitable when compact grouping is prioritized over structural clarity.

Finally, the configuration with Eps = 0.02 and MinPts = 3 yielded the weakest clustering performance. It produced only a single cluster with a very low Silhouette Coefficient of 0.213 and a relatively high DBI of

ASEAN J. Sci. Tech. Report. **2025**, *28*(3), e258177.

10 of 14

1.924, suggesting no meaningful or substantial cluster structure was identified. In summary, the parameter setting of Eps = 0.01 and MinPts = 3 demonstrates the best overall clustering quality, as it achieves a reasonable balance between the compactness and clarity of clusters, as shown in Figure 4.
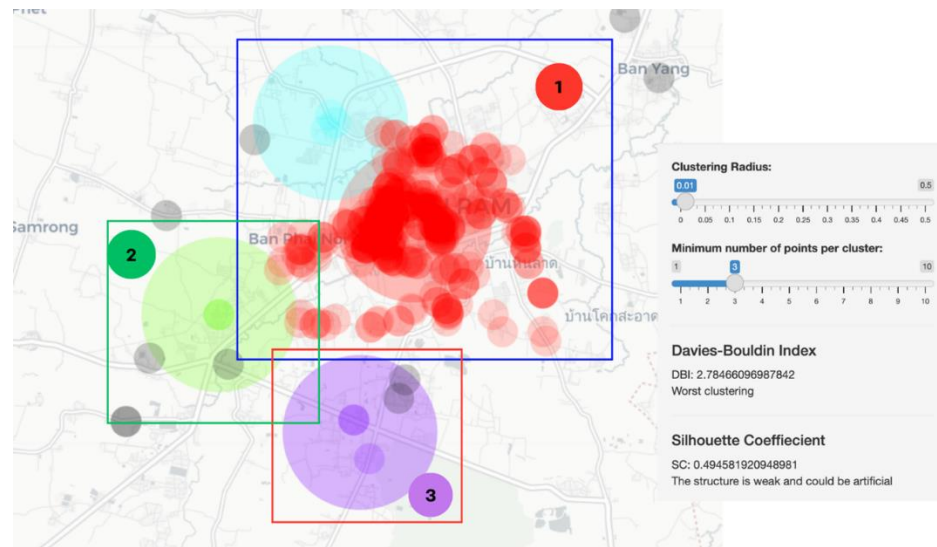
Figure 4. Clustering of Dormitory Neighborhoods in Mueang District, Buriram Province

According to Figure 4, the DBSCAN algorithm performs cluster analyses for each dataset element. The result shows that Cluster 1 (the red color) is a group of dormitories near the university (Buriram Rajabhat University). In cluster 1, the points of interest (POIs) are dormitories distributed around Nai Mueang and Isan Subdistricts. It is a bigger group than another group. This means that the suitable dormitory for students of Buriram Rajabhat University is the dormitory that occurred in cluster 1. The university can use information about dormitory groups to support students when they need to find and plan suitable dormitories. Additionally, students can utilize dormitory group information as a data source to support their decision-making when selecting a rental dormitory.

The densest cluster of dormitory neighborhoods was found in Nai Muang and Isan Subdistricts, with a total of 366 points**.** These points were primarily situated around Jira Road and near educational institutions, bus stations, restaurants, convenience stores, and shopping malls, as shown in Figure 5**.**

ASEAN J. Sci. Tech. Report. **2025**, *28*(3), e258177.

11 of 14
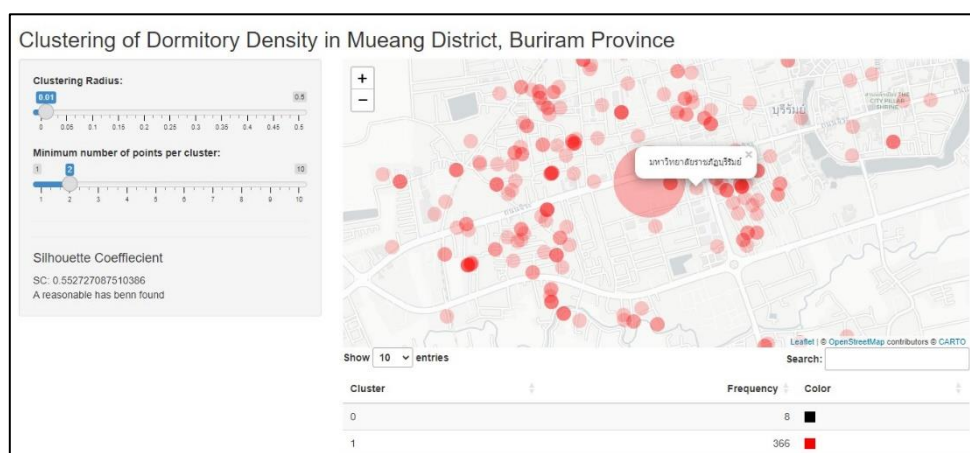
Figure 5 Clustering of High-Density Dormitory Neighborhoods in Mueang District, Buriram Province
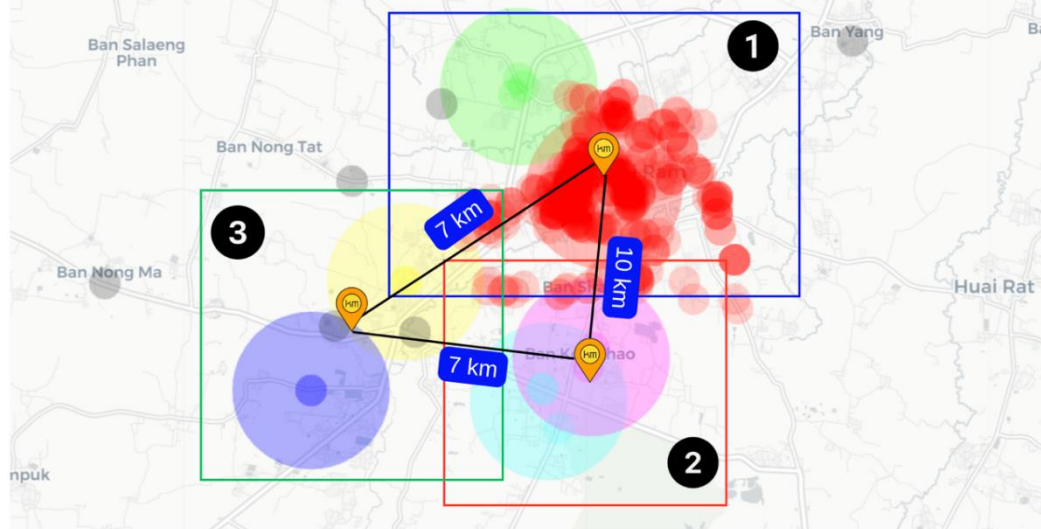
Figure 6. Example of Dormitory Neighborhood Cluster Analysis based on distance

According to Figure 6, the pattern of dormitory distribution was also found that the dormitory neighborhoods have expanded to areas outside the city, specifically in Krasang and Ban Bua Subdistricts, which are approximately 7 kilometers from the city center and 10 kilometers from Samed Subdistrict.

However, the three clusters are not significantly distant, and amenities such as convenience stores, restaurants, and public roads in Krasang, Ban Bua, and Samed Subdistricts are increasing. These clusters can potentially develop into additional dormitory neighborhoods in the future. The point where new dormitories are being constructed can lead to further analysis, providing insights into the potential development of these dormitory areas.

3.2 Discussion

Dormitory neighborhood clustering in Mueang District, Buriram Province, was analyzed using data extracted from Google Maps (https://maps.google.com/) on January 1, 2024. This data served as supplementary information for decision-making processes concerning selecting university dormitories for students at Buriram Rajabhat University and for entrepreneurs planning to invest in private dormitory businesses and selecting suitable construction locations. The clustering process identified three distinct neighborhood clusters: Cluster 1 covers areas in the Nai Muang and Isan Subdistricts, Cluster 2 encompasses areas in the Samed Subdistrict, and Cluster 3 comprises areas in the Krasang and Ban Bua Subdistricts. Additionally, it was found that the distances between the three neighborhood clusters were not significantly distant, and amenities such as convenience stores, restaurants, and public roads emerged in Krasang, Ban Bua, and Samed Subdistricts. These neighborhood clusters can potentially develop into additional dormitory neighborhoods in the future. The points where these new dormitories are being constructed can lead to further analysis, providing insights into the potential development of these dormitory areas. This concept aligns with the research of Fauzan et al. [5], who applied the DBSCAN algorithm to analyze the spatial clustering of hotels in Bali island, demonstrating that clustering hotels near tourist attractions helps managers prioritize economic recovery strategies post-COVID-19 effectively. It is also consistent with the research of Nyoman et al.[8], who conducted spatial data analysis using the DBSCAN algorithm before deciding to develop tourist destination maps based on Bali's tourism strategy, leading to equitable development and cost reduction in spatial development towards becoming tourist destinations. The clustering results offer meaningful insights for urban planning, particularly in identifying high-density dormitory zones that can guide infrastructure development and public service allocation. These insights may assist local authorities and private developers in optimizing the location and accessibility of student accommodations in the Mueang District. Furthermore, the results are consistent with previous studies that applied DBSCAN to hotel distribution in Bali [5] and urban functional

areas in Wuhan [8], affirming the algorithm's utility in spatial analysis. However, some limitations should be acknowledged. The dormitory data were collected via web scraping from Google Maps, which may result in biases such as incomplete or outdated records. Despite efforts to clean and validate the dataset, minor inaccuracies may still affect the clustering precision.

4. Conclusion

The paper presents a new approach to identifying dormitory clusters, which uses the DBSCAN clustering algorithm as a model to calculate the clustering density with the shiny web application framework. The research results conclude that the DBSCAN algorithm can serve as a tool for presenting spatial distribution data and clustering dormitory neighborhoods in Mueang District, Buriram Province. This algorithm allows parameter adjustments to align results with the context and needs of the area, facilitating data storage and analysis in spatial research, thereby efficiently reducing time and costs and examining dormitory distribution in Mueang District, Buriram Province, using the DBSCAN algorithm revealing neighborhood clusters characterized by dense and intriguing data distributions. Data clustering resulted in three neighborhoods: Cluster 1 encompassed areas in Nai Muang and Isan Subdistricts, Cluster 2 included areas in Samed Subdistrict, and Cluster 3 comprised areas in Krasang and Ban Bua Subdistricts. Validating the efficiency of clustering dormitory neighborhoods in Mueang District, Buriram Province, indicated good clustering performance, with an acceptable group structure, as reflected by a Silhouette Coefficient of 0.495 and a Davies-Bouldin Index (DBI) value of 2.785. The conclusion shows that the DBSCAN cluster analysis model is effectively characterized to identify dormitory clusters. Moreover, combining DBSCAN clustering algorithms with the shiny web application framework is a more interesting active visualization that can be applied to support information when making decisions. The proposed approach can be used as a model to develop an information system to support students who would like to find and make decisions about suitable dormitories based on spatial distribution.

5. Recommendations

The spatial clustering analysis is based on dormitory density in Mueang District, Buriram Province, utilizing the DBSCAN algorithm. Policy Recommendations: The DBSCAN algorithm is a robust tool for presenting spatial clustering data regarding dormitory density in Mueang District, Buriram Province. Tailoring parameter adjustments to suit the contextual and regional requirements facilitates its application in spatial research. This, in turn, can streamline data storage and analysis processes, thereby effectively reducing time and costs. Operational Research Recommendations: The DBSCAN algorithm facilitates the visualization and analysis of neighborhood distribution and groupings concerning dormitory data. This analytical capability can be harnessed to develop decision support systems and conduct predictive analyses using artificial intelligence methodologies, particularly for urban development and expansion initiatives.

6. Acknowledgments

References

[1]   Arifoğulları, Ö.; Orman, G. K. (2023, July 5–7). *Experimental Study of Hotel Clustering* [Conference session]. IMECS 2023: International MultiConference of Engineers and Computer Scientists, Hong Kong. https://www.iaeng.org/publication/IMECS2023/IMECS2023_pp82-87.pdf

[2]   Caudillo-Cos, C. A.; Ruiz-Pérez, J. A. Defining urban boundaries through DBSCAN and Shannon's entropy: The case of the Mexican National Urban System. *Cities*. **2024**, *149*, Article 104969. https://doi.org/10.1016/j.cities.2024.104969

[3]   Cherfi, H.; Napoli, A.; Toussaint, Y. Towards a Text Mining Methodology Using Association Rules Extraction. *Soft Computing.* **2006,** *10*(5), 431–441. https://doi.org/10.1007/s00500-005-0504-x

[4]   Ester, M.; Kriegel, H.-P.; Sander, J.; Xu, X. (1996, August 2–4). *A density-based algorithm for discovering clusters in large spatial databases with noise* [Conference session]. Proceedings of the Second International Conference on Knowledge Discovery and Data Mining (KDD-96), Portland, OR, United States. https://www.aaai.org/Papers/KDD/1996/KDD96-037.pdf.

[5]   Fauzan, A.; Novianti, A.; Ramadhani, R. M. A.; Adhiwibawa, M. A. S. Analysis of hotels spatial clustering in Bali: Density-Based Spatial Clustering of Application Noise (DBSCAN) algorithm approach. *EKSAKTA* **2022**, *3*(1), 25–38. https://doi.org/10.20885/EKSAKTA.vol3.iss1.art4

[6]   Gammanee, S.; Rattananonsathien, N.; Klaprabchone, K. Model development to increase skills in using artificial intelligence to add value to work and workability of workers in Kanchanaburi Province. *Journal of Administrative and Management Innovation.* **2023**, *11*(1), 45–53.

[7]   Janvattanavong, P.; Muenchaisri, P. (2020, November 3). Software remodularization using Tabu search [Conference session]. ICICSE 2020: International Conference on Internet Computing for Science and Engineering, Singapore. https://doi.org/10.1145/3424311.3424321

[8]   Jaya, N. M.; Wiryasa, N. M. A.; Sudarsana, D. K.; Salain, P. D. P. (2018, October 25–26). *Mapping the potential for tourism strategic areas to improve the equality of development in Bali* [Conference session]. ICAnCEE 2018: International Conference on Applied Engineering, Yogyakarta, Indonesia. https://doi.org/10.1051/matecconf/201927602008

[9]   Tu, X.; Fu, C.; Huang, A.; Chen, H.; Ding, X. DBSCAN spatial clustering analysis of urban "production–living–ecological" space based on POI data: A case study of central urban Wuhan, China. *International Journal of Environmental Research and Public Health.* **2022**, *19*(9), 5153. https://doi.org/10.3390/ijerph19095153

[10]   Office of Academic Affairs and Registration. (2023, August). Report on the number of students. Buriram Rajabhat   University.   https://oapr.bru.ac.th/wp-content/uploads/2023/08/%E0%B8%88%E0%B8%B3% E0%B8%99%E0%B8%A7%E0%B8%99-1-66.pdf

[11]   Paesrivarotai, O.; Tanaksaranond, G. (2021, June 23–25). *Study of active fire evolution in Northern Thailand using Kernel Density Estimation (KDE)* [Conference session]. The 26th National Convention on Civil Engineering (NCCE 26), Online Conference, Thailand. https://www.researchgate.net/publication/354506941.

[12]   Pensiri, F.; Visutsak, P.; Chaowalit, O. (2021, November 15–17). *Clustering tourist using DBSCAN algorithm* [Conference session]. 2021 Asia-Pacific Conference on Applied Mathematics and Statistics (AMAS 2021), Bangkok, Thailand. https://doi.org/10.1063/5.0082995

[13]   Phobphimail, S.; Janruang, J. (2021, August 19–20). *Applied DBSCAN clustering algorithm to identify tourism and hospitality zone: Case study of Sikhoraphum District at Surin Province* [Conference session]. The 10th National and the 3rd International Conference on Management Sciences: Innovation Management for Enhancing the Local Economy, Ubon Ratchathani University, Thailand.

[14]   Rousseeuw, P. J.; Silhouettes: A graphical aid to the interpretation and validation of cluster analysis. *Journal of Computational and Applied Mathematics.* **1987**, *20*, 53–65. https://doi.org/10.1016/0377-0427(87)90125-7

[15]   Yoyram, J.; Enkvetchakul, P.; Boonkate, K. Deep Learning with Convolutional Neural Networks for Cassava Leaf Diseases Via Line Bot: A Case Study of Buriram Provincial Protection Service Group, Buriram Provincial Agriculture Office. *Harbin Gongcheng Daxue Xuebao/Journal of Harbin Engineering University.* **2023**, *44*(7). https://harbinengineeringjournal.com/index.php/journal/article/view/691

ASEAN J. Sci. Tech. Report. **2025**, *28*(3), e258177.

14 of 14

[16] Yoyram, J.; Janruang, J.; Karnka, S. The study of the distribution and clustering of tourist attraction zones and facilities in Buriram Province using the DBSCAN algorithm. *Journal of Information Science Research and Practice.* **2024**, *42*(3), July–September. https://doi.org/10.14456/jiskku.2024.17

[17] Moonpen, U.; Mungsing, S.; Banditwattanawong, T. Clustering algorithm optimization model for essential attribute analysis of tour package forms inbound tourism market in Thailand. *The Journal of KMUTNB*. **2020**, *30*(4), 656–667. https://doi.org/10.14416/j.kmutnb.2020.04.006

Ecological Risk Assessment of Heavy Metal Pollution in Surface Water and Sediment of Lahug River, Cebu, Philippines

Rosalyn P. Alburo[1*], and Lora Mae G. Villegas[2]

[1] Biodiversity, Environment and Natural Resources Research Center, Cebu Technological University – Argao Campus, 6021, Cebu, Philippines

[2] Department of Chemistry, University of San Carlos, Cebu City, 6000, Philippines

* Correspondence: rosalyn.alburo@ctu.edu.ph

Abstract: The Lahug River, a significant urban waterway in Metro Cebu, was studied to assess its water quality and sediment characteristics. Physicochemical properties, such as pH and dissolved oxygen (DO), were measured in situ using a Multi-probe digital meter. At the same time, metal concentrations in both water and sediments were determined through Flame Atomic Absorption Spectroscopy (FAAS) with multiple standard addition techniques. In water, metal concentration showed a decreasing trend of Zn > Pb > Cu > Cr. Notably, copper (Cu) and chromium (Cr) exceeded the National Environmental Protection Agency (NEPA, 1989) threshold at the downstream station, while all stations exceeded the limit for zinc (Zn). In sediments, copper emerged as the most prevalent metal. Statistical analysis indicated significant correlations among Cu, Zn, Pb, and Cr, suggesting similar pollution sources or behaviors in the river environment. Ecological risk assessment revealed that the downstream area exhibited the highest risk, highlighting the urgency of rehabilitative measures to protect the river ecosystem. A comprehensive, large-scale environmental risk assessment is recommended to mitigate further degradation and ensure sustainable management of the Lahug River

Keywords: Kamputhaw river; ecological risk; water and sediment quality

1. Introduction

Metal contamination in the aquatic environment has attracted global attention due to its environmental toxicity, abundance, and persistence. Large quantities of hazardous chemicals, especially heavy metals, have been released into rivers worldwide due to rapid global population growth, intensive domestic activities, and expanding industrial and agricultural production (Srebotnjak et al. [1], Su et al. [2], Aziz et al. [3], Rizabal et al. [4]). Rivers in urban areas have also been associated with water quality problems because untreated domestic and industrial waste are discharged into the water bodies [5]. These problems of urban river pollution and ecological damage are becoming more and more critical, such that environmental monitoring and assessment are on the frontier to help environmentalists and government officials save and rehabilitate these river resources Rohde et al. [6], Richardson et al. [7]). This makes river pollution one of the most critical environmental problems of the 20th century, with agricultural, commercial, industrial, and anthropogenic activities as the main contributors Yi et al. [8], Bensig et al. [9], Maglangit et al. [10].

ASEAN J. Sci. Tech. Report. **2025**, *28*(3), e257492.

2 of 12

Barangay Lahug is in a densely populated area in Cebu City, Philippines. It has an 8.5 km long Lahug River with a basin area of 6.3 km². With the ever-increasing urbanization due to the rapid development of technology and the business process outsourcing (BPO) economy of Lahug, vast quantities of domestic and industrial wastes are disposed into its river, which leads to severe pollution and deterioration of its river ecosystem, as reported by Bensig et al. [9] and Maglangit et al. [10] that rapid oxygen depletion and high phosphorus content of the river water indicated that it is polluted. Dumping this untreated wastewater leads to an increase in pollutants present in the river. It causes dissolved oxygen (DO), biological oxygen demand (BOD), total phosphorus (TP), fecal coliform count (FC), and total coliform count (TC) in some parts of the Lahug River to exceed the Department of Environment and Natural Resources – DAO 34 (DENR-DAO 34) standards. In addition, the discharge of untreated waste into the water bodies also increases the level of metals in river water Khadse et al. [11], Venugopal et al. [12]

The introduction of metal pollutants in various forms in the environment can pose severe threats to the ecological system due to their negative impacts on most life forms (Yang et al. [13], Jaiswal et al. [14], [15]). Geolin et al. [16] reported that the univalve *Canarium labiatum* accumulated high concentrations of metals when there was a high concentration of metals in sediments. Although all life forms require some amounts of heavy metals, there is a threshold limit to this requirement (Cervantes et al. [17]). At high concentrations, heavy metal ions react to form toxic compounds in cells ([18], Choudhury et al. [19]). Another major problem with metals is their persistence, as they tend to persist indefinitely in the food chain (Gupta et al. [20], Aleem et al. [21]). Thus, assessing the concentrations and distribution of heavy metals in the Lahug riverine ecosystem is important.

2. Materials and Methods

2.1 Description of the study area

This study focused on an important urban river, the Lahug River, in the central part of Cebu City, Philippines. The river begins from the upper areas of Laguerta, passes into the midstream local communities of Kamputhaw, Capitol, and Lorega, and then courses into the downstream areas of T. Padilla, Day-as, and Tejero. This river is a natural flood drain for Cebu (Maglangit et al. [10]). The three sampling sites of Maglangit et al. [10] and Bensig et al. [9] were used as sampling sites in this study to represent the upstream, midstream, and downstream. The location of the sampling sites and their GPS coordinates are shown in Figure 1.
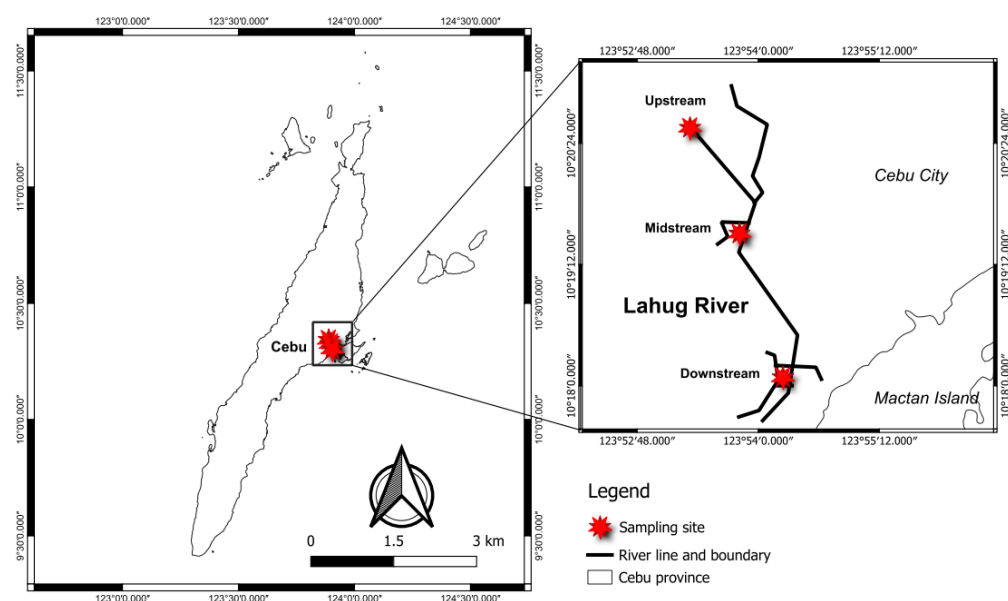
Figure 1. Location of sampling sites along Lahug River, Cebu City, Philippines.

ASEAN J. Sci. Tech. Report. **2025**, *28*(3), e257492.

3 of 12

2.2 Sampling design

As a preliminary study, the sampling for water and sediment was carried out in May, which is considered a dry season in the Philippines, with three sampling stations to represent the upstream, midstream, and downstream of the river, with a description of the stations and their coordinates tabulated in Table 1.

Table 1. Description of Sampling stations and their coordinates

Station	Coordinates	Description
Station 1 (Upstream) (5.8 km from river delta)	10° 20' 33.1" N, 123° 53' 19.4" E	Relatively clear river water. Fish and vegetation were seen; stones were covered with algae and moss; residents were seen bathing and doing laundry. A few meters up is a large construction site.
Station 2 (Midstream) (3.5 km from the river delta)	10° 19' 30.3" N, 123° 53' 48.8" E	The river water was turbid with an unpleasant smell due to the large volume of solid wastes such as feces, plastics, papers, and diapers dumped in the river. This part of the river transverses the residential and industrial areas. Concrete dikes modified the riverbanks.
Station 3 (Downstream) (900m from river delta)	10° 18' 4.90" N, 123° 54' 14.70" E	Floating solid wastes; stinky black water bubbling at the surface, plenty of households nearby; presence of fecal matter; stagnant water

2.3 Sample collection and preparation

2.3.1 Water sampling and analysis

The river water's pH and Dissolved oxygen (DO) were analyzed on-site. Approximately 30 L of river water was collected in each station and placed in a polyethylene bottle with 50% (v/v) HNO_3. The samples were then digested using the APHA method upon arrival at the laboratory. Exactly 500 mL of filtered river water was digested with 3 mL HNO_3 until the volume was about 10 mL, filtered, and diluted to the 50 mL mark of the volumetric flask. The sample was then analyzed using flame atomic absorption spectroscopy (FAAS) and the multiple standard addition technique. Five mL aliquots of the stock sample were transferred to 25-mL volumetric flasks, added with 0.00-, 0.10-, 0.20-, 0.30- and 0.40 ppm copper, chromium, lead, and zinc standards and diluted to the mark with distilled water. The samples were thoroughly mixed and analyzed in triplicates with AAS.

2.3.2 Sediment sampling and analysis

The pH of the soil was determined on-site. Composite sediment samples were collected at each sampling site using standard protocol [22]. The river bed sediment samples were taken at a 0 - 5cm depth using a core sampler. Three composite samples of mass approximately 200g were collected at each station. The samples were then chilled and contained in polyethylene bags. Upon arrival at the laboratory, the sediments were air-dried until parched, sieved at 180 μm, and homogenized using a ball mill. The homogenized samples were then oven-dried at 110°C to constant weight. The digestion method used to analyze metal concentrations in sediment was based on the USEPA Method 3050B. About 1 g of the sediment sample was placed in a 100-mL beaker and was digested with repeated additions of concentrated HNO_3 and H_2O_2 for 30 minutes to near boiling and then refluxed. The sediment digest was filtered and rinsed with hot HCl, followed by hot water. The filter paper and residue were returned to the digestion flask, refluxed with additional HCl, and then filtered again. The digest was diluted to a final volume of 100 mL and is now ready for analysis. Five mL aliquots of the sediment samples were transferred to 25-mL volumetric flasks, separately added with 0.00-, 0.10-, 0.20-, 0.30- and 0.40 ppm standards of copper, chromium, lead, and zinc and diluted to the mark with distilled water. The samples were thoroughly mixed and analyzed in triplicates with FAAS.

ASEAN J. Sci. Tech. Report. **2025**, *28*(3), e257492.

4 of 12

2.4 Instrumental analysis and quality assurance

The pH and dissolved oxygen of the river water were measured using an Orion pH meter and a Milwaukee DO meter, respectively. Metal concentrations were measured using the Shimadzu 6300 Flame Atomic Absorption Spectrophotometer (FAAS). FAAS grade MERCK Titrisol® solutions were used to prepare a calibration curve with R2 > 0.999 and were accepted for concentration calculation. All test batches were evaluated using an internal quality approach and validated if they satisfied the defined internal quality controls (IQCs). For each experiment, a run included a blank recovery test (RT), and samples were analyzed in triplicate with acceptable relative standard deviation (RSD, <5%) to eliminate any batch-specific error and provide good levels of accuracy and precision. The results were then reported in means and standard deviation of elemental values.

2.5 Statistical analysis

Means and standard deviations were calculated using Excel. A two-way Analysis of Variance (ANOVA) was performed in GraphPad Prism 6.0 to assess significant water quality differences between sampling sites. Pearson's r was used to compute the relationship between the heavy metals Cu, Pb, Cr, and Zn in the sediments.

2.6 Assessment of ecological risk

The following sediment ecological risk assessment guidelines were used to evaluate the degree to which the sediment-associated metals adversely affect aquatic organisms:

2.6.1 Pollution load index:

To assess the sediment quality, an integrated approach of the pollution load index of the four metals is calculated according to Suresh et al. [23]. The PLI is defined as the nth root of the multiplications of the contamination factor of metals (CF), as shown in the equation of

$$PLI = (CF_1 \ x \ CF_2 \ .... CF_n)^{1/n} \tag{1}$$

where the PLI value of 0 is interpreted as unpolluted, PLI of 1 means polluted, and PLI > 1 is highly polluted.

2.6.2 Contamination Factor (CF):

CF was calculated using the following equation or by dividing the content of each metal by the background values in sediment (Suresh et al. [23]):

$$CF_{metal} = C_{metal} / C_{background} \tag{2}$$

2.6.3 Geoaccumulation index (Igeo).

Geoaccumulation index values were calculated using the equation of

$$I_{geo} = log_2 (C_n / 1.5 \ B_n) \tag{3}$$

where Cn is the measured concentration of metal n in the sediment and B_n is the geochemical background value of element n in the background sample (Gao et al. [24], Islam et al. [25])

2.6.4 Potential ecological risk (PERI).

The potential ecological risk index (PERI) is also introduced to assess the degree of contamination of heavy metals in the present sediments. Equation of

$$PERI = \sum RI = \sum (T_{rf} \times CF)$$

ASEAN J. Sci. Tech. Report. **2025**, *28*(3), e257492.

5 of 12

It was used to calculate the PERI proposed by Gao et al. [24]). PERI is the comprehensive potential ecological index, the sum of RI. It represents the sensitivity of the biological community to the toxic substance and illustrates the potential ecological risk caused by overall contamination.

3. Results and Discussion

3.1 pH and dissolved oxygen

Values for river water samples ranged from 6.71 to 6.82 ppm for dissolved oxygen. The dissolved oxygen values indicate sufficient oxygen supply to support aquatic life in the river. pH values also ranged between 6.68 and 6.77 for water samples and sediments and 6.71 and 6.82 for sediments.

3.2 Metal concentration in water

The results of heavy metal concentrations in the surface waters of Lahug are shown in Table 2, revealing a significant variation ($p<0.05$) among the sites. The average concentration of the studied metals in water followed a decreasing order of Zn>Pb>Cu>Cr. The levels of all metals exceeded the threshold values of the National Environmental Protection Agency [26] at station 3, while stations (1 and 2) failed for both Cu and Zn. This means the quality of water entering the Mactan Channel failed fishery water quality standards, making all fish susceptible to metal contamination. Copper contamination downstream is attributed to domestic sewage and runoff from the widespread flower farming in the area. On the other hand, zinc contamination mostly comes from everyday human activities—industrial waste, urban runoff, and even things like the wear and tear of tires and corrosion of galvanized metal ([27], Alburo et al. [28]). Together, these pollutants can build up in aquatic life and potentially affect the ecosystem's overall health, highlighting the need for regular monitoring and better waste management practices.

Table 2. Heavy metal concentrations in surface water (ug L^{-1}).

Sampling Stations	Mean Metal Concentrations in ug/L			
	Cu	Pb	Cr	Zn
1	0.97	nd	nd	23.2
2	2.30	nd	nd	40.2
3	10.2*	15.0*	6.0*	56.4*
NEPA	0.01	0.05	0.01	0.01

* Significantly different

3.3 Metal contamination in sediments

The mean concentration of heavy metals in the sediment samples from the Lahug River is presented in Table 3. Copper was found to be the most abundant element in the river, while lead, chromium, and zinc varied in the following sequence irrespective of sampling locations: Cu>Zn>Cr/Pb. Concentrations of the metals at Station 3 were much higher than at other sites because this site is located downstream of the river, where there is extensive discharging of urban waste (Islam et al. [25], Luo et al. [29]).

To predict the heavy metal pollution in Lahug sediments, a comparative study was made with both background World Surface Rock Average (WSA) and toxicological reference values (Effect Range Low (ERL), Effect Range Medium (ERM) and Toxicity Reference Value (TRV)). Comparative results are also presented in Table 3.

ASEAN J. Sci. Tech. Report. **2025**, *28*(3), e257492.

6 of 12

Table 3. Mean ± sd metal concentrations in Lahug River and comparison with background and toxicological reference values

Metals	Sampling Stations			WSA[a]	ERL[b]	ERM[b]	TRV[c]
	1	**2**	**3**				
Copper, mg/kg	74.40 ± 1.10	94.80 ± 0.75	1152 ± 52.2	32	70	390	16
Lead, mg/kg	6.22 ± 0.26	6.733 ± 0.12	39.33 ± 0.68	20	35	110	31
Chromium, mg/kg	8.927 ± 0.48	10.15 ± 0.23	26.73 ± 0.11	97	80	145	26
Zinc, mg/kg	65.63 ± 0.55	92.13 ± 0.55	416.3 ± 0.58	129	120	270	110

[a] World Surface Rock average (Martin et al. [30]).

[b] Effect range low and effect range medium for freshwater ecosystems (Bai et al., [31]).

[c] Toxicity Reference Value (Mohiuddin et al. [32]).

Only Cu exceeded the WSA in all stations of Lahug River sediments. Lead and zinc levels exceeded WSA only at Station 3. This indicates the anthropogenic introduction of the metals in the river. Based on toxicological reference thresholds, the average concentrations of Cu at all stations exceeded the Effects Range-Low (ERL) value, while only Station 3 surpassed the Effects Range-Median (ERM). Similarly, Zn concentrations exceeded the ERM at Station 3 alone. Lead at Station 3 is also beyond its corresponding ERL value and may cause occasional biological effects on aquatic organisms in the area. In contrast, no biological effect will be observed due to Cr (Harikumar et al. [33], Marin et al. [34]). All metals at station 3 are above the TRV values. Exposures above the TRV indicate that the dose or concentration may exceed the threshold where toxic effects are likely. Depending on the organism and the substance, this can lead to adverse health effects, such as biochemical, physiological, or reproductive harm (Allard et al. [35]). Table 4 shows that all metal contaminants in the sediments are significantly correlated. According to Suresh et al. [36], a high correlation coefficient between metals signifies that the metals have common sources, mutual dependence, and identical behavior during transport.

Table 4. Pearson's correlation coefficient between the heavy metals in river sediments ($p < 0.05$).

Metals	Sampling Stations			
	Cu	**Pb**	**Cr**	**Zn**
Cu	1			
Pb	0.9993	1		
Cr	0.9975	0.9981	1	
Zn	0.9974	0.9982	0.9995	1

3.4 Ecological Risk Assessment of metal pollution in Lahug River sediments

3.4.1 Pollution Load Index

The calculated pollution load index (PLI) provides a comparative assessment of the status of sediment quality in the Lahug River, as summarized in Figure 2. Based on this information, station 3 of the river is the most polluted due mainly to the effects of urban activities.
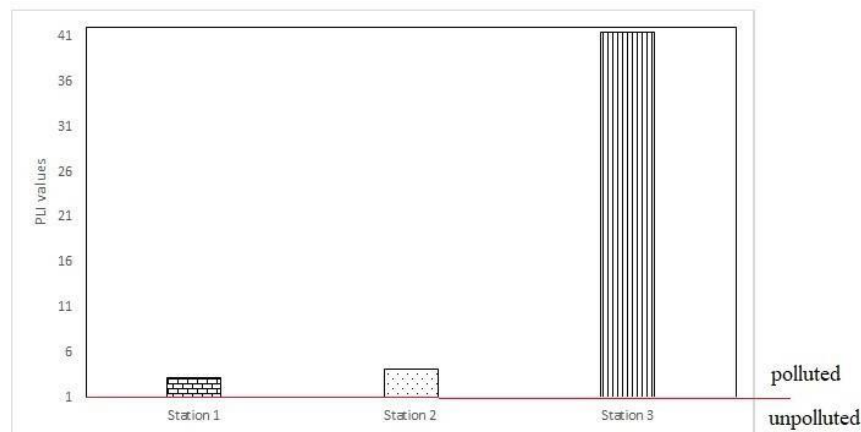
Figure 2. Pollution load index (PLI) value of heavy metals in Lahug River, Cebu, Philippines, sediment.

3.4.2 Contamination Factor

Figure 3 illustrates that the contamination factor for all metals followed a descending order of Cu > Zn > Pb > Cr. The CF values indicated a low to moderate degree of contamination (CF > 1) across all metals, except for Cu at station 3, which exhibited a considerably higher contamination level. This elevated CF for Cu suggests a significant localized source, likely linked to anthropogenic inputs such as domestic sewage, urban runoff, or corrosion of copper-containing materials. Considerable contamination of Zn levels, particularly at station 3, may be attributed to the widespread use of zinc-containing fertilizers or galvanization processes in nearby areas. The relatively lower CF values for Pb and Cr, with detections only at station 3, further support the presence of point-source pollution in the downstream portion of the Lahug River. The contamination factor (CF) of 36.01 for Cu at station 3 indicates a very high level of contamination, far exceeding the threshold for significant ecological concern. Such an elevated value suggests the presence of a major localized source, potentially stemming from continuous inputs of untreated domestic wastewater, improper disposal of copper-containing industrial effluents, or runoff from urban infrastructure and agricultural areas using copper-based agrochemicals (Oquiñena-Paler et al. [37], Cañete et al. [38]).
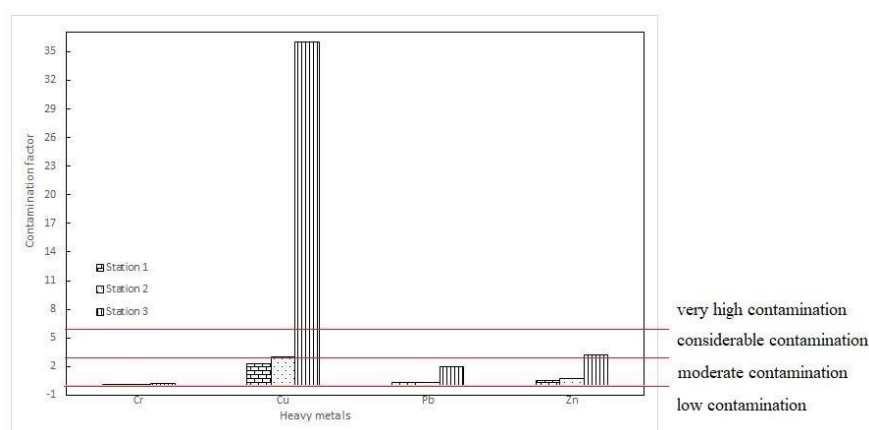
Figure 3. Contamination factor (CF) values of heavy metals in river sediments.

ASEAN *J. Sci. Tech. Report.* **2025**, *28*(3), e257492.

8 of 12

3.4.3 Geo-accumulation Index, I_{geo}

According to the Muller scale, the calculated results of Igeo values shown in Figure 4 for Cu sediment quality are considered as heavily to significantly contaminated ($4 \leq Igeo \leq 5$) for station 3, moderately contaminated at station 2, and uncontaminated to moderately contaminated at station 1. Zinc is also uncontaminated to moderately contaminated at station 2, with no contamination for Cr and Zn in all stations.
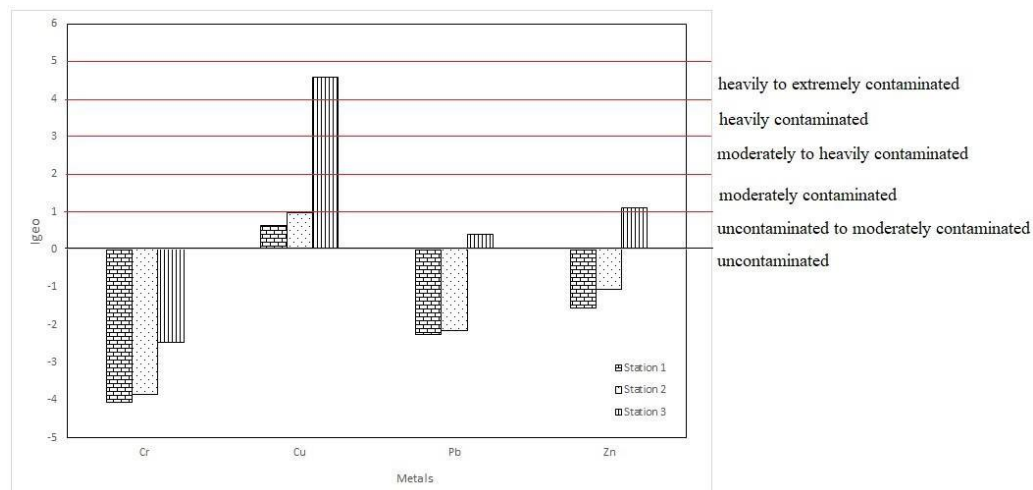
Figure 4. Geo-accumulation index (Igeo) values of heavy metals in river sediments.

3.4.4 Potential ecological risk index

The potential ecological risk index (RI) of surface sediments from the Lahug River was further calculated to confirm the other evaluations, with the results summarized in Table 6. In this study, the metals tested were copper (Cu), lead (Pb), zinc (Zn), and chromium (Cr), with the calculated Ei_r values indicating varying levels of ecological risk. Copper exhibited the highest risk, with the ecological risk coefficients following the order Cu > Pb > Zn > Cr, suggesting that copper posed the most significant potential threat to the aquatic ecosystem in the Lahug River, consistent with its elevated toxicity factor compared to the other metals. The mean Ei_r values for Pb, Cr, and Zn were all below 40, categorizing these metals under the low ecological risk classification, indicating that their concentrations in the sediments were not high enough to impact the ecosystem significantly. However, copper showed a notably higher Ei_r value, particularly at station 3, where the risk index (RI) exceeded 150, indicating a high ecological risk due to the significantly elevated copper concentrations at this site. This pronounced ecological threat highlights the need for further investigation and targeted mitigation strategies. In comparison, Villacarlos et al. [39] reported a low ecological risk classification in the sediments of the Balamban coastline, an area exposed to a diffused source of metal input from a nearby shipyard facility, suggesting that the localized and possibly point-source contamination in the Lahug River may pose a more acute environmental concern.

Table 5. Evaluation of the potential ecological risk of heavy metals pollution in sediments from Lahug River.

| Sampling Stations | Risk Index (E^i_r) | | | | Potential Ecological Risk Index (Peri) | Risk Grade [40[|
	Cu $C^i_f \times T^i_f$	Pb $C^i_f \times T^i_f$	Cr $C^i_f \times T^i_f$	Zn $C^i_f \times T^i_f$		
1	11.6	1.94	0.251	0.517	14.3	Low ecological risk
2	14.8	2.10	0.286	3.63	20.9	Low ecological risk
3	180.1	12.3	0.753	16.3	209	High ecological risk

ASEAN J. Sci. Tech. Report. **2025**, *28*(3), e257492.

9 of 12

3.4.5 Sediment Quality Guideline (SWQ) by USEPA

The chemical contaminations in the sediments were evaluated by comparison with the sediment quality guideline proposed by USEPA. These criteria are shown in Table 5. The present study indicates that all sites are heavily polluted with Cu, while Pb, Cr, and Zn exhibit varying contamination levels depending on the location. Specifically, station 2 is moderately polluted with Pb, Cr, and Zn, whereas station 1 shows no significant contamination concerning these metals. The Sediment Quality Guidelines (SQGs) established by the United States Environmental Protection Agency (USEPA) further assessed the chemical contamination levels in sediments. These guidelines benchmark for interpreting sediment contamination and potential ecological risks by providing specific contaminant concentration thresholds based on dry sediment weight. This approach directly categorizes pollution levels into not polluted, moderately polluted, or heavily polluted. In contrast, other commonly used indices such as the Contamination Factor, Geoaccumulation Index, Pollution Load Index, and Potential Ecological Risk Index rely on comparisons to background or reference values to assess anthropogenic input, making them more indicative of pollution sources rather than ecotoxicological effects.

In the present study, Cu concentrations across all three sampling stations exceeded 60 mg/kg, with values ranging from 74.40 ± 1.10 mg/kg at station 1 to 1152 ± 52.2 mg/kg at station 3, classifying all sites as heavily polluted and indicating significant anthropogenic input, particularly at station 3. Pb levels surpassed the 6 mg/kg mark in all stations, suggesting ecological risk despite the absence of a defined pollution category in the USEPA guidelines. Cr levels at station 1 (8.927 ± 0.48 mg/kg) were within the not polluted range, whereas station 3 (26.73 ± 0.11 mg/kg) slightly exceeded the 25 mg/kg threshold, indicating moderate contamination. Zn concentrations showed a gradient from not polluted at station 1 (65.63 ± 0.55 mg/kg) to heavily polluted at station 3 (416.3 ± 0.58 mg/kg), further supporting the presence of localized contamination sources.

Table 6. Environmental Protection Agency (EPA) guidelines for sediments, mg/kg dry weight

Metal	Not Polluted	Moderately Polluted	Heavily Polluted	Present Study		
				Station 1	Station 2	Station 3
Cu	<40	40-60	>60	74.40 ± 1.10	94.80 ± 0.75	1152 ± 52.2
Pb	-	-	>6	6.22 ± 0.26	6.733 ± 0.12	39.33 ± 0.68
Cr	<25	25-75	>75	8.927 ± 0.48	10.15 ± 0.23	26.73 ± 0.11
Zn	<90	90-200	>200	65.63 ± 0.55	92.13 ± 0.55	416.3 ± 0.58

4. Conclusion

The study assessed heavy metal contamination in the surface sediments of the Lahug River using multiple indices-CF, PLI, Igeo, and RI/PERI. Results showed that copper posed the highest contamination and ecological risk, particularly at station 3, where the RI exceeded 150, indicating a high ecological threat. CF and Igeo values indicated moderate to considerable Cu enrichment, while Pb, Zn, and Cr generally fell within low to moderate contamination and low-risk classifications. PLI values suggested cumulative pollution, emphasizing the impact of anthropogenic activities. When compared against the Sediment Quality Guidelines established by the U.S. Environmental Protection Agency (USEPA), Cu concentrations at all stations and Zn in station 3 exceeded the guidelines, indicating possible adverse biological effects. In contrast, Pb, Zn, and Cr were mostly below these thresholds. These results confirm that the Lahug River is experiencing localized but significant heavy metal pollution, predominantly from copper, likely due to point-source discharges. The study highlights the need for targeted pollution source identification, strengthened monitoring, and the implementation of appropriate remediation strategies to protect the river's ecological integrity.

5. Acknowledgments

Author Contributions: The following are the contributions of each author in this research: Conceptualization: Alburo, RP and Villegas, LMG; Methodology: Alburo, RP and Villegas, LMG; Software Villegas, LMG;

ASEAN J. Sci. Tech. Report. **2025**, *28*(3), e257492.

10 of 12

Validation: Alburo, RP; Formal analysis: Alburo, RP and Villegas, LMG; Investigation: Alburo, RP and Villegas, LMG; Resources: Alburo, RP; Data curation: Alburo, RP and Villegas, LMG; Writing—original draft preparation: Alburo, RP and Villegas, LMG; Writing—review and editing: Alburo, RP and Villegas, LMG; Visualization: Villegas, LMG; Supervision: Alburo, RP; Project administration: Alburo, RP; and Funding acquisition: Alburo, RP. Additionally, all authors have read and agreed to the published version of the manuscript.

Conflicts of Interest: The authors declare no conflict of interest.

The funders had no role in the study's design; in the collection, analyses, or interpretation of data; in the writing of the manuscript, or in the decision to publish the results".

References

[1] Srebotnjak, T.; Carr, G.; de Sherbinin, A.; Rickwood C. A global Water Quality Index and hot-deck imputation of missing data. *Ecol. Indic.* **2012**, *17*, 108-119. https://doi.org/10.1016/j.ecolind.2011.04.023

[2] Su, S.; Xiao, R.; Mi, X.; Xu, X.; Zhang, Z; Wu, J. Spatial determinants of hazardous chemicals in surface water of Qiantang River, China. *Ecol. Indic.* **2013**, *24*, 375-381. https://doi.org/10.1016/j.ecolind.2 012.07.01510.2965/jwet.2014.109

[3] Aziz, K. H. H.; Mustafaa, F. S.; Omer, K. M.; Hamaa, S.; Hamarawfa, R. F.; Rahman, K. O. Heavy metal pollution in the aquatic environment: Efficient and low-cost removal approaches to eliminate their toxicity: A review. *RSC Adv.* **2023**, *13*(33), 17595-17610. https://doi.org/10.1039/D3RA01317A

[4] Rizabal, T.A.C.; Villegas, L.M.G.; Alburo, H.M.A.; Velasco, L.M.; Alburo, R.P. Lead content in *Moringa oleifera* Linn. leaves and rootzone soil in the nine cities of Cebu province, Philippines. *Philipp J Sci*. **2023**, *153*(1), 133-145. https://doi.org/10.56899/153.01.14

[5] Rohde, S.; Hostmann, M.; Peter, A.; Ewald, K.C. Room for rivers: An integrative search strategy for floodplain restoration.*Landsc. Urban Plan*. **2006**. *78*, 50-70. https://doi.org/10.1016/j.landurbplan.2005.05.006

[6] Richardson, M.; Soloviev, M. The urban river syndrome: achieving sustainability against a backdrop of accelerating change. *Int. J Environ. Res. Public Health*. **2021**, *18*(12), 6406. https://doi.org/10.3390/ ijerph18126406

[7] Yi, Y.; Yang, Z.; Zhang, S. Ecological risk assessment of heavy metals in sediment and human health risk assessment of heavy metals in fishes in the middle and lower reaches of the Yangtze river basin. *Environ. Pollut*. **2011**, *159*, 2575-2585. https://doi.org/10.1016/j.envpol.2011.06.011

[8] Bensig E.; Flores M. J.; Maglangit F. Assessment of the water quality in Buhisan, Bulacao and Lahug rivers, Cebu, Philippines using fecal and total coliform as indicators. *Curr. World Environ*. **2014**, *9*(3), https://doi.org /10.12944/CWE.9.3.03

[9] Maglangit, F.; Galapate, R.; Bensig, E. Physico-chemical assessment of the water quality of Buhisan river, Cebu, Philippines. *Int. J. Res. Environ. Sci. Technol*. **2014**, *4*, 83-87.

[10] Khadse, G.K.; Patni, P.; Kelkar, P.S.; Devotta, S. Qualitative evaluation of Kanhan river and its tributaries flowing over central Indian plateau. *Environ. Monit. Assess*. **2008**, *147*, 83-92. https://doi.org /10.1007/s10661-007-0100-x

[11] Venugopal, T.; Giridharan, L.; Jayaprakash, M.; Velmurugan, P.M. A comprehensive geochemical evaluation of the water quality of River Adyar India. *Bull. Environ. Contam. Toxicol*. **2009**. *82*, 211-217. https://doi.org/10.1007/s00128-008-9533-3

[12] Yang, H.J.; Jeong, H.J.; Bong, K.M.; Jin, D.R.; Kang, T.W.; Ryu, H.S.; Han, J.H.; Yang, W.J.; Jung, J.; Hwang, S.H.; Na, E.H. Organic matter and heavy metal in river sediments of southwestern coastal Korea: spatial distributions, pollution, and ecological risk assessment. *Mar. Pollut. Bull*. **2020**, *59*, https://doi.org/ 10.1016/j.marpolbul.2020.111466

ASEAN J. Sci. Tech. Report. **2025**, *28*(3), e257492.

11 of 12

[13] Jaiswal, R.; Malik, A. Metal resistance in Pseudomonas strain isolated from soil treatment with industrial wastewater. *World J. Microbiol. Biotechnol*. **2000**, *16*, 177-182. https://doi.org/10.1023/A:1008905902282

[14] Gavrilescu, M. Removal of heavy metal from the environment by biosorption. *Eng. Life Sci*. **2004**, *4*(3), 219-232. https://doi.org /10.1002/elsc.200420026

[15] Geolin, K.R.C.; Villegas, L.M.G.; Alburo, R.P. Metallothionein response of aninikad, *Canarium labiatum* (Roding, 1798) to heavy metal concentrations in Balamban coastline, Cebu. *J. Agri. Technol. Manag*. **2021**, *24*(1), 1-12.

[16] Cervantes, C.; Corona, F.G. Copper resistance mechanisms in bacteria and fungi. *FEMS Microbiol. Rev.* **1994**, *14*, 121-138. https://doi.org/10.1111/j.1574-6976.1994.tb00083.x

[17] Nies, D.H. Microbial heavy-metal resistance. *Appl. Microbiol. Biotechnol*. **1999**, *51*, 730-750. https://doi.org /10.1007/s002530051457

[18] Choudhury, R.; Srivastava, S. Mechanism of zinc resistance in *Pseudomonas putida* strain S4. *World J. Microbiol. Biotechnol*. **2001**. *17*, 149-153. https://doi.org/10.1023/A:1016666000384

[19] Gupta, R.; Ahuja, P.; Khan, S.; Saxena, R.K.; Mohapatra, H. Microbial biosorbents: meeting challenges of heavy metal pollution in aqueous solutions. *Curr. Sci*. **2000**, *78*(8), 967–973.

[20] Aleem, A.; Isar, J.; Malik, A. Impact of long-term application of industrial waste water on the emergence of resistance traits in *Azotobacter chroococcum* isolated from rhizospheric soil. Bioresour. Technol. **2003**, *86*(1), 7-13. https://doi.org/10.1016/S0960-8524(02)00134-7

[21] U.S. EPA. Methods for Collection, Storage and Manipulation of Sediments for Chemical and Toxicological Analyses: Technical Manual. Office of Water, U.S. Environmental Protection Agency, Washington, DC. **2001**, 208pp.

[22] Suresh, G.; Sutharsan, P.; Ramasamy, V.; Venkatachalapathy, R. Assessment of spatial distribution and potential ecological risk of the heavy metals in relation to granulometric contents of Veeranam lake sediments, India. *Ecotoxicol. Environ. Saf*. **2012**, *84*, 117-124. https://doi.org/10.1016/j.ecoenv.2012.06.027

[23] Gao X.; Zhuang W.; Chem C.A.; Zhang Y. Sediment quality of the SW Coastal Laizhou Bay, Bohai Sea, China: A comprehensive assessment based on the analysis of heavy metals. *PLoS One*. **2015**, *10*, 3. https://doi.org/10.1371/journal.pone.0122190

[24] Islam, M.S.; Ahmed, M.K.; Raknuzzaman, M.; Habibullah-Al-Mamun, M.; Islam, M.K. Heavy metal pollution in surface water and sediment: a preliminary assessment of an urban river in a developing country. *Ecol. Indic*. **2015**, *48*, 282-291. https://doi.org/10.1016/j.ecolind.2014.08.016

[25] National Environmental Protection Agency. Water quality standard for metal. Beijing: GB. **1989**, 11607-89.

[26] Haque, S. E. Urban water pollution by heavy metals, microplastics, and organic contaminants. Current directions in water scarcity research. **2022**, *6*, 21-43. https://doi.org/10.1016/B978-0-323-91838-1.00001-4

[27] Alburo, R. P.; Gabrillo, S. L.; Villegas, L. M. G. Characteristic Metal Marker of Non-exhaust PM 10 Vehicular Emissions in Cebu City, Philippines. *Philipp. J. Sci.* **2023**, *152*(4), https://doi.org/10.56899/152.04.06

[28] Luo, Z.; Shao, Q.; Liu, H. Comparative evaluation of river water quality and ecological changes at upstream and downstream sites of dams/sluices in different regulation scenarios. *J. Hydrol.* **2021**, *597*, https://doi.org/10.1016/j.jhydrol.2021.126290

[29] Martin, J.M.; Meybeck, M. Elemental mass balance of materials carried by major world rivers. *Mar. Chem.* **1979**, *7*, 173-206. https://doi.org/10.1016/0304-4203(79)90039-2

[30] Bai, J.; Cui, B.; Chen, B.; Zhang, K.; Deng, W.; Gao, H.; Xiao, R. Spatial distribution and ecological risk assessment of heavy metals in surface sediments from typical plateau lake wetland. *China Ecol. Modell.* **2011**, *222*, 301-306. https://doi.org/10.1016/j.ecolmodel.2009.12.002

[31] Mohiuddin, K. M.; Zakir, H. M.; Otomo, K.; Sharmin, S.; Shikazono, N. Geochemical distribution of trace metal pollutants in water and sediments of downstream of an urban river. *Int. J. Environ. Sci. Tech.* **2010**, *7*(1), 17-28. https://doi.org/10.1007/BF03326113

[32] Harikumar, P.S.; Nasir, U.P. Ecotoxicological impact assessment of heavy metals in core sediments of a tropical estuary. *Ecotoxicol. Environ. Saf.* **2010**, *73*, 1742-1747. https://doi.org/10.1016/j.ecoenv.2010.08.022

[33] Marín, J.; Colina, M.; Ledo, H.; Gardiner, P.H.E. Ecological risk by potentially toxic elements in surface sediments of the Lake Maracaibo (Venezuela). *Environ. Eng. Res.* **2022**, *27*(4), https://doi.org/10.4491

ASEAN J. Sci. Tech. Report. **2025**, *28*(3), e257492.

12 of 12

/eer.2021.232

[34] Allard, P.; Fairbrother, A.; Hope, B.K.; Hull, R.N.; Johnson, M.S.; Kapustka, L.; Mann, G.; McDonald, B.; Sample, B.E. Recommendations for the development and application of wildlife toxicity reference values. *Integr. Environ. Assess. Manag*. **2010**, *6*, 28-37. https://doi.org/10.1897/IEAM_2009-010.1

[35] Suresh, G.; Ramasamy, V.; Meenakshisundaram, V.; Venkatachalapathy, R.; Ponnu- samy, V. Influence of mineralogical and heavy metal composition on natural radionuclide contents in the river sediments. *Appl. Radiat. Isot*. **2011**, *69*, 1466-1474. https://doi.org/10.1016/j.apradiso.2011.05.020

[36] Oquiñena-Paler, M.K.M., Ancog, R. Copper, lead and zinc concentration in water, sediments and catfish (*Clarias macrocephalus gunther*) from Butuanon River, Metro Cebu, Philippines. *IOSR J Environ Sci Toxicol Food Tech*. **2014**, *8*, 49-56. https://doi.org/10.9790/2402-081124956

[37] Cañete, R.C.; Villegas, L.M.G.; Castañares, J.M. Seasonal bioaccumulation of copper in guppy, *Poecilia reticulata* (Peters) with characterization of the hydrophobic fraction of its octanol-water emulsion. *KIMIKA*. **2014**, *25*(1), 27-37. https://doi.org/10.26534/kimika.v25i1.27-37

[38] Villacarlos, C. J. A.; Villegas, L. M. G.; Alburo, R. P. Metallothionein induction in bivalves exposed to heavy metals in sediment of the Balamban Coast, Cebu, Philippines. *Int. J. Aquat. Biol*. **2025,** *14*(2), https://doi.org/10.22034/ijab.v13i2.2425

[39] Hakanson, L. An Ecological Risk Index for Aquatic Pollution Control: A Sedimentological Approach, *Water Res*. **1980**, *14*, 975-1001. https://doi.org/10.1016/0043-1354(80)90143-8

Research article

Flooring Material from Thermoplastic Elastomer Based on Natural Rubber and Recycled Plastic Waste

Ekkawit Pianhanuruk[1], Pongpun Ratchapakdee[2], Chatree Homkhiew[3], and Uraiwan Sookyung[4*]

[1] Faculty of Science and Technology, Rajamangala University of Technology Srivijaya, Nakhon Si Thammarat, 80110, Thailand

[2] Faculty of Science and Technology, Rajamangala University of Technology Srivijaya, Nakhon Si Thammarat 80110, Thailand

[3] Faculty of Engineering, Rajamangala University of Technology Srivijaya, Songkhla 90000, Thailand

[4] Faculty of Engineering, Rajamangala University of Technology Srivijaya, Songkhla 90000, Thailand

* Correspondence: uraiwan.so@rmutsv.ac.th

Abstract: This study investigates the preparation of thermoplastic elastomer flooring materials using a blend of recycled polyethylene (Re-PE) and natural rubber (NR) through simple blending and dynamic vulcanization techniques. This study aims to provide a sustainable alternative to conventional flooring by converting plastic waste into thermoplastic elastomers (TPEs) with tailored properties suited for elderly safety. This research addresses the gap in designing flooring materials with high flexibility, shock absorption, and slip resistance, essential for fall prevention among the aging population. It was observed that the flowability of TPEs decreases as NR content increases. Thermal stability of TPEs exhibits two degradation stages: NR phase degrades at 380-400°C, and the plastic phase at 490-500°C. The degradation temperature increases with increasing plastic content. Mechanical properties of TPEs show that 100% modulus, tensile strength, impact strength, and hardness decrease as the proportion of NR increases. However, the elongation at break increases with increased NR content. Comparing the simple blending technique to dynamic vulcanization, the former yields higher impact strength while the latter results in higher values for the 100% modulus and tensile strength. The preparation of TPEs with a textured surface is obtained through the simple blending technique with a Re-PE/NR ratio of 25/75 due to its superior flowability, which allows for easier texturing. The material exhibits lower hardness and higher friction than other surfaces, reducing accident risk and injury severity. These findings highlight its potential as a practical alternative to conventional flooring, especially in elderly care where slip resistance and cushioning are critical.

Keywords: Flooring material; thermoplastic natural rubber; simple blending; dynamic vulcanization

1. Introduction

According to the United Nations (UN) report World Population Ageing 2020, Thailand faces a rapid demographic shift, with a significant increase in the elderly population. In 2020, older people accounted for 13% of Thailand's total population, which is predicted to rise to 20% by 2030 and 30% by 2050. Thailand is aging fast and has become the 2nd most aged society in ASEAN after Singapore. Currently, 20 percent of Thais are older than 60 years old. About one-third of the Thai population will be over 60 by 2030, a level not far behind what Japan is facing today [1]. As the aging population increases, so does the predominance of age-related challenges, one of the most critical of which is the risk of falling

ASEAN J. Sci. Tech. Report. **2025**, *28*(3), e257537.

2 of 12

injuries. Falls among the elderly are a leading cause of severe injuries, including fractures and internal trauma, often resulting in reduced mobility, loss of independence, and significant healthcare costs. In this context, developing safer flooring materials tailored for older people becomes a critical area of focus. TPEs derived from plastic waste offer beneficial properties such as softness, elasticity, and slip resistance, which are directly linked to minimizing fall severity and enhancing safety in elderly environments. The severity of fall-related injuries is closely linked to the type of surface on which the falls occur. Hard surfaces can exacerbate the impact of a fall, leading to more severe injuries. In contrast, surfaces with a high coefficient of friction can help reduce the risk of slipping and falling altogether. Therefore, developing flooring materials from thermoplastic elastomers (TPEs) derived from recycled waste is a promising approach to address environmental concerns and improve surface safety simultaneously.

Plastic waste has become a significant and pressing environmental issue due to the convenience and fast-paced lifestyles that generate this waste. Plastic waste is causing major environmental impacts, especially when it ends up in oceans and water sources. Technologies and materials that can replace plastic, particularly thermoplastic elastomers, are very interesting. Thermoplastic elastomers are modern materials with favorable properties, and they have garnered significant attention in current research. The advantage of thermoplastic elastomers is their combination of strength and flexibility, like rubber, but they can be reshaped like plastics [2]. These materials can be recycled and reused, making them a potential solution to the plastic waste problem. Currently, a popular research focus is thermoplastic elastomers derived from blending rubber and plastic materials. This blending can be achieved using two main techniques: simple blending and dynamic vulcanization [3, 4]. The study explores blending various rubber materials, including natural rubber [5, 6], EPDM rubber [7-9], and nitrile rubber [10-12], with different plastic materials such as polyethylene [13-15] and polypropylene [16, 17]. These thermoplastic elastomers have gained popularity for their favorable properties, and their applications extend to various fields. One notable application is the production of flooring materials, particularly in environments where safety is paramount, such as facilities for the elderly or young children. For elderly flooring, properties such as moderate softness to absorb shock and a high coefficient of friction to reduce slips are especially critical. Thermoplastic elastomers offer several advantages over traditional materials like concrete or ceramic tiles. They are less susceptible to breaking, provide flexibility, and reduce the risk of injury in case of falls. Furthermore, these materials are environmentally friendly because they can be recycled and reused. This contributes to addressing the growing environmental issues associated with plastic waste. In summary, the research aims to recycle plastic waste into thermoplastic elastomers, offering a versatile and eco-friendly solution to the plastic waste problem, particularly in applications where safety and durability are essential.

2. Materials and Methods

2.1 Materials

Natural rubber (block rubbers STR 20) was used as a blend component, produced by the Rubber Authority of Thailand (RAOT) in Nakhon Si Thammarat province, Thailand. Two cure activators for sulfur vulcanization were used, including zinc oxide (ZnO) from Lanxess, Leverkusen, Germany, and stearic acid, manufactured by Unichema International B.V., Gouda, the Netherlands. Trimethylhydroquinoline (TMQ) was used as an antioxidant obtained from Shenyang Sunnyjoint Chemicals, China. N-Cyclohexyl-2-benzothiazole sulfenamide (CBS) was obtained from Lanxess, Leverkusen, Germany. Dibenzothiazyl disulfide (MBTS) was used as an accelerator obtained from Asia Pacific Specialty Chemicals Limited, Australia. Pergan GmbH, Bocholt, Germany, manufactures sulfur curing agents.

2.2 Preparation of thermoplastic elastomer

Various blending ratios are explored to examine the effects of different compositions, including 0/100, 25/75, 50/50, 75/25, and 100/0. These proportions were chosen to represent a full spectrum of rubber-to-plastic content, enabling mechanical and thermal behavior analysis at extreme and intermediate blend ratios. This allows the identification of an optimal formulation for flooring applications. Two blending methods are compared: simple blending and dynamic vulcanization. A schematic flowchart summarizing the two preparation processes is provided in Figure 1 to illustrate the key steps involved in each method. The study

ASEAN J. Sci. Tech. Report. **2025**, *28*(3), e257537.

3 of 12

begins by preparing thermoplastic elastomers by blending natural rubber with plastic bottle waste (Re-PE). The first step for the dynamic vulcanization process involved preparing the rubber compound based on the formulation shown in Table 1. The compounding was done using a melt-mixing method in an internal mixer at a rotor speed of 60 rpm and a temperature of 60°C. The rubber was masticated for 3 minutes, followed by the sequential addition of compounding ingredients (ZnO, stearic acid, TMQ, CBS, MBTS, and sulfur), each mixed for 1 minute. The mixing process continued for an additional 2 minutes to ensure homogeneity. The resulting rubber compounds were then sheeted out using a two-roll mill and left at room temperature for at least 12 hours before further processing. Thermoplastic elastomers with various blend ratios were prepared. Before compounding, recycled polyethylene (PE) obtained from disposable plastic bottles was shredded into small pieces using a shredding machine. Thermoplastic elastomers were prepared in an internal mixer at 160°C with a rotor speed of 60 rpm. Initially, the PE was preheated in the mixing chamber without rotation for 5 minutes. It was then melted by mixing at 60 rpm for 2 minutes. Subsequently, either rubber compounds (for dynamic vulcanization) or natural rubber (for simple blending) were added to the molten PE, and the mixing was continued until the mixing torque reached a plateau, indicating the completion of blending. Finally, the blended materials were cut into small pieces. The test specimens were prepared using a compression molding machine.
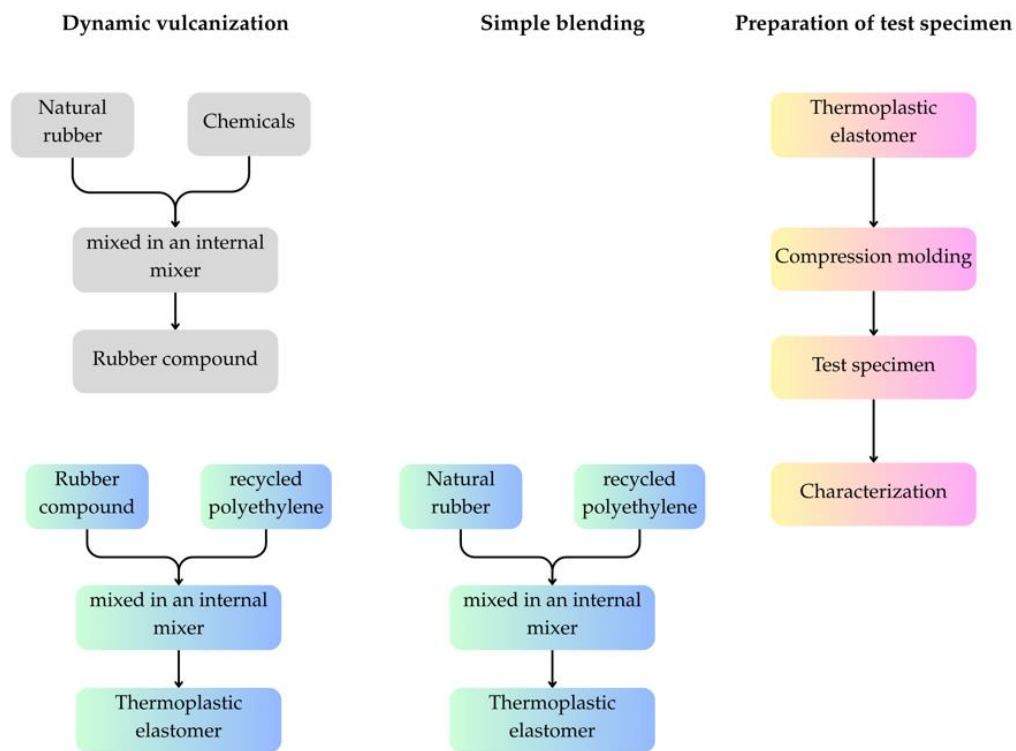

Figure 1. A schematic flowchart summarizing the two preparation processes and preparation of test specimens.

Table 1. Formulation of rubber compound.

Ingredients	Amount (phr)
Natural rubber	100
ZnO	5
Stearic acid	1
TMQ	1
CBS	1
MBTS	0.5
Sulfur	2.5

2.3 Characterization

The physical properties of thermoplastic natural rubber are studied to understand its behavior. This includes measuring hardness, tensile strength, elongation at break, 100% modulus, flow properties, and thermal decomposition using Thermogravimetric Analysis (TGA). All experimental results were analyzed using standard deviation and one-way ANOVA to determine statistical significance among formulations, with a confidence level of 95%. The tensile properties were characterized with a universal tensile testing machine (Testometric Co., Ltd.). All samples were conditioned at 25°C and 50% relative humidity for 48 hours before testing to minimize environmental variability. The samples of rubber vulcanizates were tested at room temperature according to ASTM D412 with an extension speed of 500 mm/min. The hardness of rubber vulcanizates was tested using a durometer Shore A (Rex Gauge Co., Ltd.) according to ASTM D2240, the impact resistance as per ISO180 standard by using a Zwick Roell impact tester, Germany, and the melt flow index as per ASTM D1238 standard by using a Zwick Roell Mflow, Germany. The TGA was performed using Perkin Elmer STA600 (New Shelton, USA). The samples were first placed in the platinum pan under a nitrogen atmosphere. The test was then performed with a heating rate of 10°C/min in the 30-600(C temperature range. The static friction coefficient was evaluated using the sliding angle friction method, following the ASTM D202. For elderly care flooring suitability, performance benchmarks were referenced against slip resistance values (>0.6) and Shore A hardness (<70 for comfort) as desirable for impact absorption, based on criteria outlined by Petdee et al. (2023) [18]. This method measures static friction, the force required to keep an object stationary. The specimens were mounted in this test with a sliding block featuring 3 mm of additional padding. The specimens were lifted at the incline angle of 1.5° ± 0.5° per second and held for 10 seconds. The inclination was stopped when the specimens began to move, and the angle was recorded to the nearest 0.5°. The static friction coefficient was calculated using the equation [18]: $\mu_s = \tan \theta$ where μ_s was the coefficient of static friction, and θ was the angle of testing (degree).

3. Results and Discussion

3.1 Flow Properties

Figure 2 shows the flow properties of thermoplastic natural rubber material derived from blending NR with Re-PE at various proportions (Re-PE/NR: 100/0, 75/25, 50/50, and 25/75). The flow rate of thermoplastic natural rubber is compared between simple blending and dynamic vulcanization. It was observed that the flowability of thermoplastic natural rubber decreased as the proportion of natural rubber increased. This decline in flowability is attributed to the lower plastic phase content in natural rubber, which results from the decrease in the proportion of polyethylene (PE). Polyethylene exhibits better flow properties than natural rubber, which reduces the overall flowability of thermoplastic natural rubber as the proportion of polyethylene decreases. Quantitatively, for the simple blending method, the melt flow rate (MFR) decreased from approximately 1.8 g/10 min at a 100/0 Re-PE/NR ratio to 0.9 g/10 min at 25/75, indicating a substantial reduction in flowability as the natural rubber content increased. For the dynamic blends, MFR values were consistently lower across all compositions, which can be attributed to the formation of crosslinked rubber networks that restrict polymer melt flow. Thermoplastic natural rubber obtained through simple blending exhibited better flow properties than those derived from dynamic vulcanization. This is because the natural rubber remains in its raw rubber state in simple blending, while in dynamic vulcanization, the natural rubber phase becomes vulcanized. Therefore, thermoplastic natural rubber obtained through dynamic vulcanization exhibits lower flowability. Specifically, Sobrinho et al. (2024) [19] reported that SBR/PP blends typically exhibit MFI values around 4.2 g/10 min due to the non-melting behavior of SBR, which restricts the flowability of the PP matrix. Similarly, Tasdemir et al. (2010) [20] demonstrated that dynamically vulcanized EPDM/PP blends have MFI values ranging from 1.5 to 2.2 g/10 min depending on EPDM content and vulcanization level. In contrast, our Re-PE/NR blends showed MFI values between 1.80 and 0.90 g/10 min as NR content increased, indicating reduced flowability similar to traditional TPEs. Despite this limitation, the Re-PE/NR system provides notable environmental benefits by incorporating recycled polyethylene and bio-based natural rubber. These advantages offer a sustainable alternative to petrochemical-based TPEs while still delivering essential mechanical and functional properties for applications such as slip-resistant flooring. Notably, when the proportion of natural rubber exceeds 50%, those derived from dynamic vulcanization cannot be tested for

ASEAN J. Sci. Tech. Report. **2025**, *28*(3), e257537.

5 of 12

flow properties. This is because the dispersed rubber phase, which increases with a higher proportion of natural rubber, obstructs the polymer flow [21]. Even at elevated temperatures, rubber, a thermoset, cannot flow.

Figure 2. The flow rate of thermoplastic natural rubber at various Re-PE/NR ratios was prepared using simple blending and dynamic vulcanization methods.

3.2 Thermogravimetric Analysis

As shown in Figure 3, the thermal gravimetric analysis (TGA) results reveal that thermoplastic natural rubber undergoes a two-stage decomposition process at different temperature ranges. The first stage occurs at 380-400°C), representing the natural rubber phase decomposition. The second stage takes place around 490-500°C and corresponds to the decomposition of the plastic phase. Re-PE contributes to improved thermal stability due to its higher decomposition temperature and semi-crystalline structure, which resists breakdown at elevated temperatures. The increased presence of Re-PE in the blend delays the onset of mass loss, indicating that the plastic phase plays a crucial role in sustaining the structural integrity of the composite under thermal conditions. Notably, thermoplastic natural rubber elastomers obtained through dynamic vulcanization demonstrate higher thermal stability than those derived from simple blending. The remaining portion of thermoplastic natural rubber obtained from the dynamic vulcanization process exhibits higher residual mass than the simple blending technique. This residual mass primarily consists of inorganic compounds such as sulfur and zinc oxide, in addition to chemical components used in the vulcanization recipe specific to the rubber phase of the dynamic vulcanization system. Thermoplastic elastomer prepared via dynamic vulcanization exhibited higher residual mass, suggesting improved thermal stability due to the vulcanized rubber phase and crosslinking agents. This is because vulcanized rubber forms a stable crosslinked network that resists thermal decomposition better than unvulcanized rubber. This enhanced thermal stability makes dynamically vulcanized composites suitable for applications exposed to high temperatures.

Figure 3. TGA curve of thermoplastic natural rubber at various Re-PE/NR ratios prepared using simple blending and dynamic vulcanization methods.

3.3 Mechanical Properties

The mechanical properties, including 100% modulus, tensile strength, elongation at break, and hardness, are presented in Figures 4–7, respectively. In Figure 4, it was found that the 100% modulus decreases when the proportion of natural rubber increases. It should be noted that for the 100/0 composition, the modulus was not measurable due to the extremely low flexibility and early break of specimens. This happens because the 100% modulus is influenced by the plastic continuous phase, which is stiffer than the rubber phase. At Re-PE/NR ratios of 100/0 and 75/25, the 100% modulus could not be measured due to the high plastic content, which leads to low elongation. The high hardness of Re-PE reduces flexibility, causing the test specimens to break before achieving the specified stretch, as shown in Figure 6. The elongation at break increases sharply as the proportion of natural rubber increases from 75/25 to 50/50. It increases from approximately 10% to 450%, indicating a significant increase in material elasticity. However, at 25/75, the elongation decreases slightly compared to 50/50 due to poor rubber-plastic interaction and insufficient plastic matrix for deformation. The tensile strength of thermoplastic natural rubber material is shown in Figure 5. The dynamic vulcanization process enhances the tensile strength due to the formation of crosslinked structures, whereas simple blending results in lower strength but better elongation. The plastic phase exhibits higher strength compared to the rubber phase. Several studies have indicated that higher plastic phase content improves tensile strength [22]. Then, thermoplastic natural rubber materials with a higher plastic content demonstrate increased tensile strength as the proportion of plastic increases. The mechanical properties observed in this study are consistent with previous research on PP/rubber blends. For instance, Bendjaouhdou and Bensaad (2013) [23] reported that adding 10 wt% NR to PP decreased tensile strength from 29.5 MPa to 22.1 MPa, while elongation at break increased from 6% to 20%, indicating enhanced ductility. Similarly, Kakroodi et al. (2012) [24] found that incorporating SBR into recycled PP reduced tensile strength due to interfacial incompatibility, although compatibilizer use improved it by 30%. Furthermore, Scagliusi et al. (2021) [25] noted that increasing EPDM content in PP/EPDM blends led to lower tensile strength but higher elongation. These trends align with our findings, validating the mechanical behavior of Re-PE/NR blends.

Figure 4. 100% modulus of thermoplastic natural rubber at various Re-PE/NR ratios prepared using simple blending and dynamic vulcanization methods.
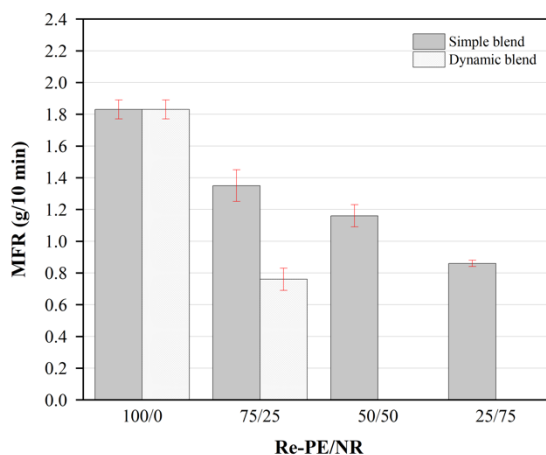

Figure 5. Tensile strength of thermoplastic natural rubber at various Re-PE/NR ratios prepared using simple blending and dynamic vulcanization methods.

ASEAN J. Sci. Tech. Report. **2025**, *28*(3), e257537.

8 of 12
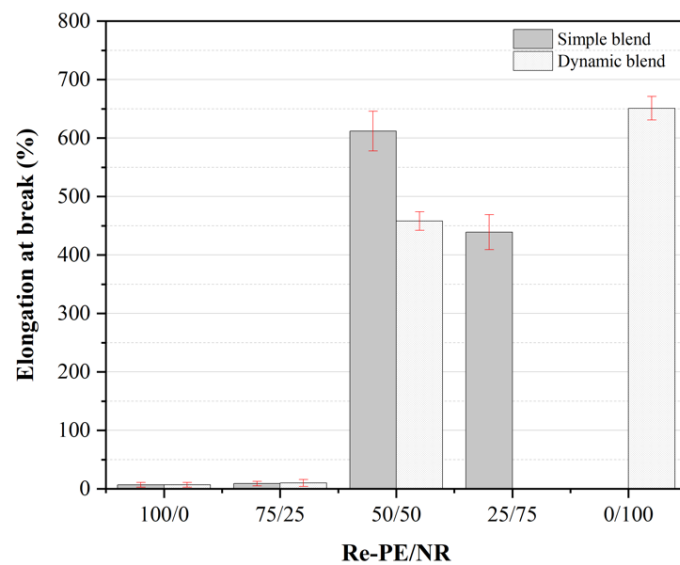
Figure 6. Elongation at break of thermoplastic natural rubber at various Re-PE/NR ratios prepared using simple blending and dynamic vulcanization methods.

Figure 7 shows that at Re-PE/NR ratios of 100/0,75/25, and 50/50, the hardness values are relatively similar, measuring around 99 Shore A. This similarity is attributed to the influence of the plastic phase on the material's properties. Figure 8 shows the impact strength properties of thermoplastic natural rubber, comparing the simple blending and dynamic vulcanization methods. It is found that the impact strength decreases with an increase in the proportion of natural rubber. It is worth noting that polyethylene is known for its excellent impact resistance properties [26]. Therefore, the impact strength depends on the material's hardness, and the values obtained correlate with the hardness values, as seen in Figure 7. In the tested samples, no signs of sample breakage occurred after testing. Thus, the test results are influenced by the decrease in hardness when the proportion of natural rubber increases.
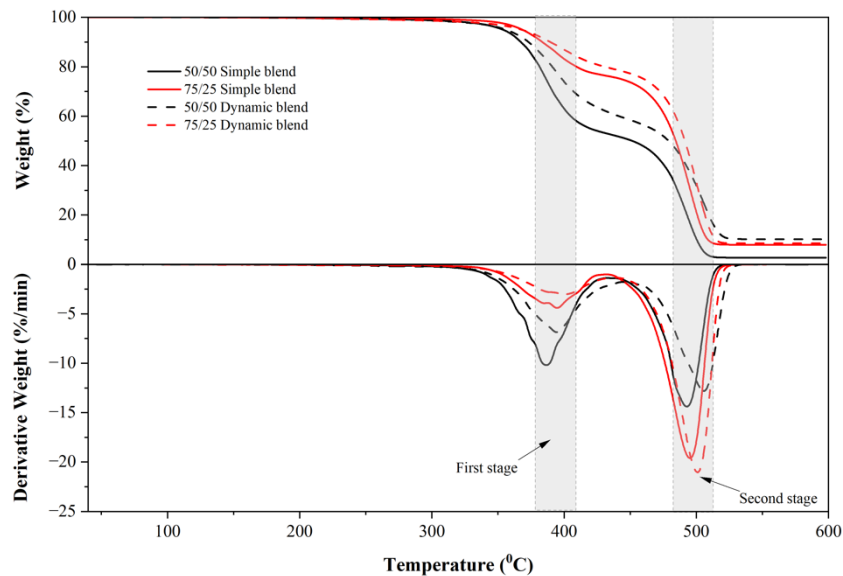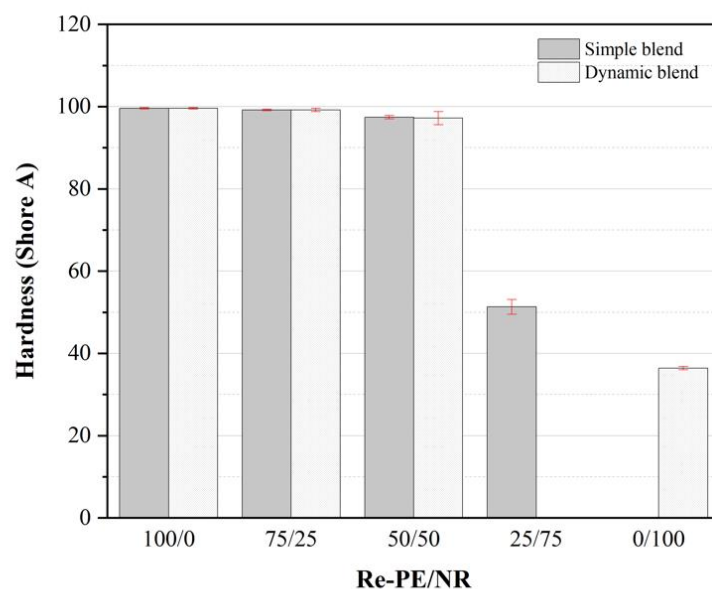

Figure 7. The hardness of thermoplastic natural rubber at various Re-PE/NR ratios prepared using simple blending and dynamic vulcanization methods.

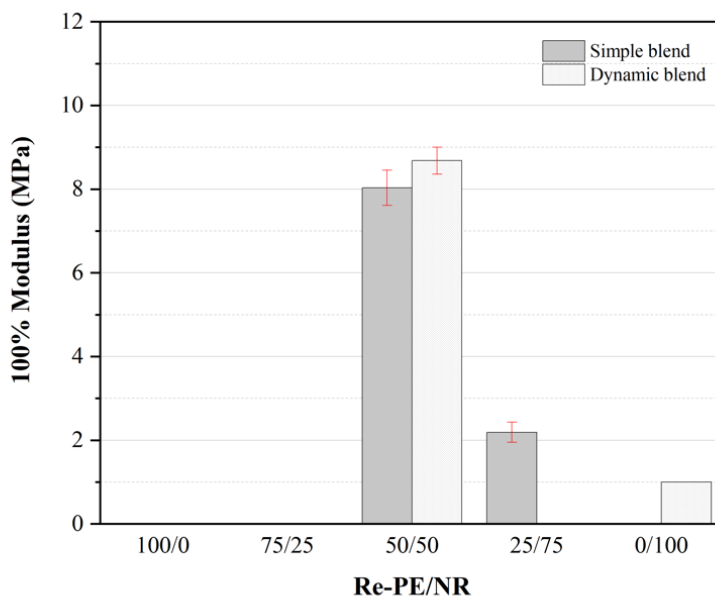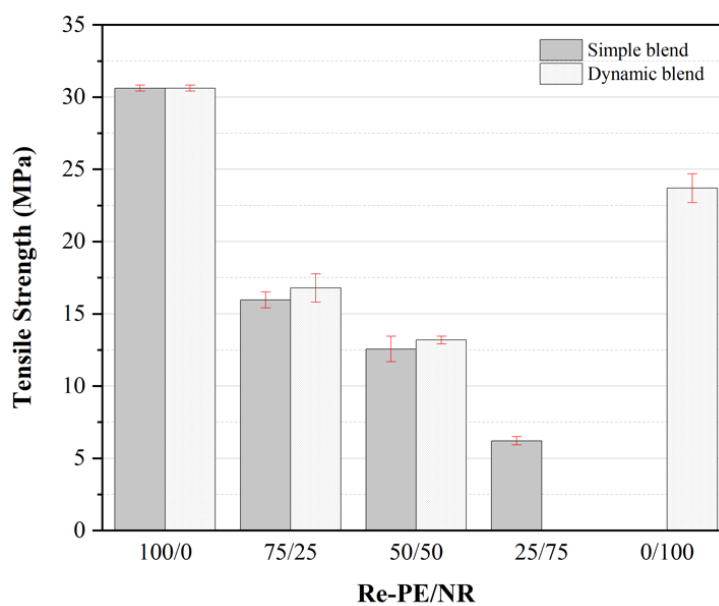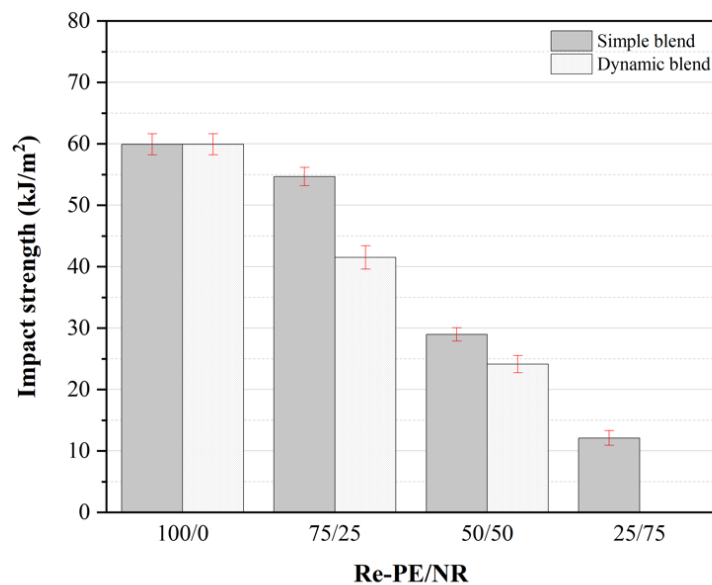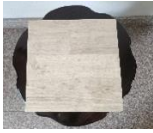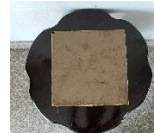**Figure 8.** Impact strength of thermoplastic natural rubber at various Re-PE/NR ratios prepared using simple blending and dynamic vulcanization methods.

3.4 Floor Molding

The experimental results indicated that thermoplastic natural rubber, in its simple blending form, is easier to mold into floor tiles than the dynamic vulcanization method. Simple blending can be molded easily in all proportions, although molding becomes more challenging as the proportion of natural rubber increases. In contrast, thermoplastic natural rubber produced through dynamic vulcanization can only be successfully molded at a 50/50 Re-PE/NR ratio, which aligns with its flowability properties shown in Figure 2. Consequently, for molding floor tiles, a decision was made to use the 50/50 and 25/75 blends from simple blending and the 50/50 blend from dynamic blending, as they were easier to mold. Table 2 shows the potential of Re-PE/NR thermoplastic elastomer as flooring materials compared to commercial flooring options (i.e., para-wood, ceramic, and granite). The hardness of Re-PE/NR dynamic blending at a 50/50 ratio is 97.2 ± 1.6 shore A, close to the hardness of ceramic and granite flooring materials, measuring 100 Shore A. In contrast, the simple blending at a 25/75 Re-PE/NR ratio displayed a significantly lower hardness of 51.3 ± 1.8. This reduced hardness enhances flexibility, making the material suitable for applications that require softer surfaces, such as flooring for elderly care facilities, where minimizing fall impact is critical. These findings are consistent with previous work by Petdee et al. (2023) [18], who optimized stair tread covers from natural rubber and wood sawdust composites and reported high slip resistance (friction coefficient ~0.63). These characteristics were validated against safety expectations for stair surfaces in elderly care environments. Therefore, this study's Re-PE/NR composites meet the safety-related material performance benchmarks for elderly flooring systems. These findings align with previous research that indicates increasing the proportion of rubber enhances flexibility while reducing hardness due to the inherent elasticity of NR [27]. As a result, the material exhibited higher flowability and softness, which facilitated molding into flooring tiles. However, the lack of vulcanization also reduced mechanical strength and hardness. This characteristic makes the unvulcanized NR blend suitable for applications that require flexibility and shock absorption, such as flooring in elderly care facilities.

The static friction coefficient indicates the slip resistance, which is important for determining surface safety. The simple blend with a 25/75 ratio exhibited the highest static friction coefficient (0.68) when compared to conventional materials such as para-wood (0.51) and ceramic (0.52). In contrast, the dynamic blend with a 50/50 ratio showed a lower slip resistance of 0.25, comparable to granite (0.33). Therefore, slip resistance is limited. The thermoplastic elastomer has a lower friction coefficient, which may result from smoother surface finishes and reduced elasticity in composites with higher plastic content.

ASEAN J. Sci. Tech. Report. **2025**, *28*(3), e257537.

10 of 12

Table 2. Comparison of the developed floor tiles with commercial materials.

Properties	Para-wood	ceramic	granite	Simple blend Re-PE/NR:25/75	Simple blend Re-PE/NR:50/50	Dynamic blend Re-PE/NR:50/50
Hardness (shore A)	100	100	100	51.3 ± 1.8	97.4 ± 0.4	97.2 ± 1.6
θ(degree)	27.17 ± 0.79	27.25 ± 0.54	18.42 ± 0.63	34.38 ± 1.10	18.10 ± 0.33	14.24 ± 0.48
Static Friction Coefficient (μ_s)	0.51	0.52	0.33	0.68	0.33	0.25
Physical appearance						

4. Conclusions

The flowability properties of thermoplastic natural rubber show that the flowability of the material decreases as the natural rubber increases. When comparing simple blending with dynamic vulcanization, dynamic vulcanization blending results in lower flowability properties than materials obtained from simple blending. Flowability properties are indicated by the material's ability to undergo deformation. Therefore, thermoplastic elastomers of natural rubber prepared from simple blending exhibit easier deformability than those prepared from dynamic vulcanization. The decomposition temperature, 100% modulus, tensile strength, hardness, and impact strength of thermoplastic natural rubber decrease as the content of natural rubber increases. While the elongation at break increases with the increasing content of natural rubber. Dynamic vulcanization blending provides materials with a higher 100% modulus and tensile strength than simple blending, indicating superior mechanical properties. However, the ability to stretch, which reflects material flexibility, is higher in simple blending. In this study, the thermoplastic elastomer was prepared by simple blending, and a Re-PE/NR ratio of 25/75 was found to be the most suitable flooring material. It has excellent processability and a high coefficient of friction. Additionally, its significantly lower hardness helps minimize the severity of injuries in the event of an accident. The results of this study are supported by previous research, including Petdee et al. (2023) [18], who reported that natural rubber-based stair tread composites exhibited impact force resistance and slip resistance, consistent with our Re-PE/NR materials. Quantitatively, the Re-PE/NR blends showed MFI between 0.90–1.8 g/10 min, elongation at break reaching 450%, and coefficient of friction up to 0.63, indicating good processability, mechanical flexibility, and slip prevention. These properties align with standards for elderly flooring, where high friction and soft underfoot cushioning are essential for preventing slips and absorbing impact. The improved tensile strength and modulus in dynamically vulcanized blends are attributed to the crosslinked network formed during vulcanization, which enhances the load-bearing capacity. In contrast, lower hardness values in simple blends offer better shock absorption, which can help mitigate fall-related injuries. This is particularly beneficial in elderly care facilities, where material compliance reduces the impact force transferred to the body upon accidental falls. These insights support the application of Re-PE/NR composites as sustainable and safe flooring materials.

5. Acknowledgements

Conflicts of Interest: The authors declare no conflict of interest.

ASEAN J. Sci. Tech. Report. **2025**, *28*(3), e257537.

11 of 12

References

[1] Anantanasuwong, D. Population Ageing in Thailand: Critical Issues in the Twenty-First Century. In *Education for the Elderly in the Asia Pacific*; Editors Narot, P., Kiettikunwong, N., Eds.; Springer Nature Singapore, Singapore. **2021**, pp. 31-56. https://doi.org/10.1007/978-981-16-3326-3_3

[2] Khatami, M.; Bairwan, R. D.; Khalil, H. A.; Surya, I.; Mawardi, I.; Ahmad, A.; Yahya, E. B. The role of natural fiber reinforcement in thermoplastic elastomers biocomposites. *Fibers and Polymers* **2024**, *25*(8), 3061-3077. https://doi.org/10.1007/s12221-024-00621-5

[3] Shahroodi, Z.; Katbab, A. A. Preparation and characterization of peroxide-based dynamically vulcanized thermoplastic elastomer of poly (lactic acid)/chloroprene rubber. *Polymer Engineering & Science* 2022, *62*(5), 1485-1495. https://doi.org/10.1002/pen.25937

[4] Urtekin, G.; Ullah, M. S.; Yildirim, R.; Ozkoc, G.; Kodal, M. A comprehensive review of the recent developments in thermoplastics and rubber blends-based composites and nanocomposites. *Polymer Composites* **2023**, *44*(12), 8303-8329. https://doi.org/10.1002/pc.27712

[5] Belhaoues, A.; Benmesli, S.; Riahi, F. Compatibilization of natural rubber–polypropylene thermoplastic elastomer blend. *Journal of Elastomers & Plastics* **2020**, *52*(8), 728-746. https://doi.org/10.1177/0095244319891231

[6] Nair, S. T.; George, S. C.; Kalarikkal, N.; Thomas, S. Enhanced mechanical and thermal performance of multiwalled carbon nanotubes-filled polypropylene/natural rubber thermoplastic elastomers. *New Journal of Chemistry* **2021**, *45*(11), 4963-4976. https://doi.org/10.1039/D0NJ05437B

[7] Lima, P.; Oliveira, J.; Costa, V. Partial replacement of EPDM by GTR in thermoplastic elastomers based on PP/EPDM: effects on morphology and mechanical properties. *Journal of Applied Polymer Science* **2014**, *131*(8), 40160. https://doi.org/10.1002/app.40160

[8] Shi, M.; Zhang, D.; Zhu, J.; Shi, Y.; Sun, J.; Ji, Y. Morphology, crystallization, and thermal and mechanical properties of dynamic vulcanization EPDM/PP thermoplastic elastomer. *Journal of Thermoplastic Composite Materials* **2019**, *32*(7), 922-935. https://doi.org/10.1177/0892705718762615

[9] Skyronka, V.; Majesté, J. C.; Carrot, C.; Chalamet, Y.; Janin, C.; Cantaloube, B.; Heuillet, P. Rheology as a powerful help for the characterization of the morphology of thermoplastic elastomers (TPE) based on PP and reclaimed EPDM rubber. *Polymer* **2024**, *313*, 127682. https://doi.org/10.1016/j.polymer.2024.127682

[10] Saha, S.; Bhowmick, A. K. Smart thermoplastic elastomers with high extensibility from poly (vinylidene fluoride) and hydrogenated nitrile rubber: processing–structure–property relationship. *Rubber Chemistry and Technology* **2018**, *91*(1), 268-295. https://doi.org/10.5254/rct-18-82676

[11] Kakhramanov, N. T.; Guliev, A. D.; Abdullin, M. I.; Allahverdieva, K. V. Thermal deformation properties of dynamically vulcanized thermoplastic elastomers based on random polypropylene and nitrile butadiene rubber. *Inorganic Materials: Applied Research* **2022**, *13*(2), 442-446. https://doi.org/10.1134/S2075113322020174

[12] Bova, T.; Tran, C. D.; Balakshin, M. Y.; Chen, J.; Capanema, E. A.; Naskar, A. K. An approach towards tailoring interfacial structures and properties of multiphase renewable thermoplastics from lignin–nitrile rubber. *Green Chemistry* **2016**, *18*(20), 5423-5437. https://doi.org/10.1039/C6GC01067A

[13] Dai, S.; Li, S.; Xu, G.; Chen, C. Direct synthesis of polar functionalized polyethylene thermoplastic elastomer. *Macromolecules* **2020**, *53*(7), 2539-2546. https://doi.org/10.1021/acs.macromol.0c00083

[14] Shaker, R.; Rodrigue, D. Rotomolding of thermoplastic elastomers based on low-density polyethylene and recycled natural rubber. *Applied Sciences* **2019**, *9*(24), 5430. https://doi.org/10.3390/app9245430

[15] Helal, E.; Pottier, C.; David, E.; Fréchette, M.; Demarquette, N. R. Polyethylene/thermoplastic elastomer/Zinc Oxide nanocomposites for high voltage insulation applications: Dielectric, mechanical and rheological behavior. *European Polymer Journal* 2018, *100*, 258-269. https://doi.org/10.1016/j.eurpolymj.2018.02.004

[16] Panigrahi, H.; Sreenath, P. R.; Bhowmick, A. K.; Kumar, K. D. Unique compatibilized thermoplastic elastomer from polypropylene and epichlorohydrin rubber. *Polymer* **2019**, *183*, 121866. https://doi.org/10.1016/j.polymer.2019.121866

[17] Benmesli, S.; Riahi, F. Dynamic mechanical and thermal properties of a chemically modified polypropylene/natural rubber thermoplastic elastomer blend. *Polymer Testing* **2014**, *36*, 54-61. https://doi.org/10.1016/j.polymertesting.2014.03.016

[18] Petdee, T.; Naemsai, T.; Homkhiew, C.; Pianhanuruk, E. Multiple response optimization of wood sawdust/natural rubber foam composites for stair tread covers. *Industrial Crops and Products* **2023**, *204*, 117312. https://doi.org/10.1016/j.indcrop.2023.117312

[19] de Melo Sobrinho, E.D.; Ferreira, E.D.S.B.; da Silva, F.U.; Bezerra, E.B.; Wellen, R.M.R.; Araújo, E.M.; Luna, C.B.B. From waste to Styrene–Butadiene (SBR) reuse: Developing PP/SBR/SEP mixtures with carbon nanotubes for antistatic application. *Polymers* **2024**, *16*(17), 2542. https://doi.org/10.3390/polym16172542

[20] Tasdemir, M.; Topsakaloglu, M.; Caneba, G.T. Dynamically vulcanized EPDM (Ethylene-Propylene-Diene Polymer)/PP (Polypropylene) polymer blend: Performance index (PI). *Journal of Polymer Materials* **2010**, *27*(4), 337.

[21] Owen, E.; Kooi, O.; Ebhodaghe, O.; Hilary, I. Enhancing the dynamic mechanical properties of thermoplastic elastomers: A study on polypropylene/natural rubber blends. *Current Chemistry Letters* **2024**, *13*(3), 633-640. https://doi.org/10.5267/j.ccl.2023.11.002

[22] Nakason, C.; Saiwari, S.; Kaesaman, A. Thermoplastic vulcanizates based on maleated natural rubber/polypropylene blends: effect of blend ratios on rheological, mechanical, and morphological properties. *Polymer Engineering & Science* **2006**, *46*(5), 594-600. https://doi.org/10.1002/pen.20498

[23] Bendjaouhdou, C.; Bensaad, S. The effects of organoclay on the morphology and balance properties of an immiscible polypropylene/natural rubber blend. *Journal of Thermoplastic Composite Materials* **2013**, *26*, 1365-1378.

[24] Kakroodi, A.R.; Rodrigue, D.; Utracki, L.A. Mechanical properties of recycled polypropylene/SBR rubber crumbs blends reinforced by birch wood flour. *Polymers and Polymer Composites* **2012**, *20*, 441-450. https://doi.org/10.1177/096739111202000503

[25] Scagliusi, S.R.; Carvalho, E.C.L.; Lugão, A.B. Introduction to the study of mechanical properties of terpolymer PP/EPDM mixtures. *Journal of Research Updates in Polymer Science* **2021**, *10*, 1-9. https://doi.org/10.6000/1929-5995.2021.10.1

[26] Khanam, P. N.; AlMaadeed, M. A. A. Processing and characterization of polyethylene-based composites. *Advanced Manufacturing: Polymer & Composites Science* **2015**, *1*(2), 63-79. https://doi.org/10.1179/2055035915Y.0000000002

[27] Tanrattanakul, V.; Bunkaew, P. Effect of different plasticizers on the properties of bio-based thermoplastic elastomer containing poly (lactic acid) and natural rubber. *Express Polymer Letters* **2014**, *8*(6), 387-396. https://doi.org/10.3144/expresspolymlett.2014.43

Archaeoastronomical Analysis of Sri Suphan Temple

Korkwan Tiansawang[1], Ponlaphat Monvucharin[2], Techin Kongjarern[3], Prissana Thamboon[4], Cherdsak Saelee[5*], and Orapin Riyaprao[6*]

[1] Science Classroom Affiliated School Project, Chiang Mai University Demonstration School, Chiang Mai, 50200, Thailand
[2] Science Classroom Affiliated School Project, Chiang Mai University Demonstration School, Chiang Mai, 50200, Thailand
[3] Science Classroom Affiliated School Project, Chiang Mai University Demonstration School, Chiang Mai, 50200, Thailand
[4] Office of research administration and Faculty of Science, Chiang Mai University, Chiang Mai, 50200, Thailand
[5] Faculty of Science, Chiang Mai University, Chiang Mai, 50200, Thailand
[6] National Astronomical Research Institute of Thailand (Public Organization), Chiang Mai, 50180, Thailand
* Correspondence: cherdsak.s@cmu.ac.th, orapin@narit.or.th

Abstract: Archaeoastronomical studies in the ancient Lanna Kingdom, centered in Chiang Mai Province in northern Thailand, have revealed the influence of *Vastu Shastra* principles, an ancient Indian treatise of architecture, on the alignments of cities and temples with auspicious stars. This paper investigates the orientation of Sri Suphan Temple, a royal Buddhist temple built in King Mueng Kaew's reign in 1503 during the Vaisakha lunar month, that has a similar orientation to the renowned Phra That Doi Suthep Temple, which was previously studied to be aligned with a star marking *Vaisakha* Nakshatra around 1537. We surveyed the site using a theodolite, a GPS device, and Stellarium astronomy software to yield the orientation of the temple with an azimuth angle of 58.94 ± 0.08°. Using precession-corrected Stellarium computation to trace stars' azimuths back in time and reveal their annual path behavior, we find Alphecca, with an azimuth of 59.45 degrees, rising on the eastern horizon during Vaisakha month as indicated in the inscription, to be the most probable star of alignment. Alphecca is a bright star in the Corona Borealis Constellation reported to be the same star used in the Doi Suthep Temple, which suggests that the Sri Suphan Temple may have been a prototype for aligning later Buddhist temples.

Keywords: Temple alignment; Stellar orientation; Sri Suphan Temple; Corona Borealis; *Vaisakha* Nakshatra

1. Introduction

Many archaeological sites around the world, including those in Italy [1], China [2], and Japan [3], have been discovered to align with astronomical phenomena connected to the Sun, Moon, classical planets, and stars, which can reflect the beliefs and culture of past civilizations. As a result, in archaeoastronomical investigation, the site's astronomical orientation should be concordant with historical data from written or unwritten sources, such as inscriptions, calendar systems, customs, and traditions [4–5]. For archaeoastronomical study in the ancient Lanna Kingdom, centered in Chiang Mai Province in northern Thailand, the founding of cities and temples may have been influenced by ancient Indian treatise of architecture known as *Vastu Shastra* principles, which was transmitted from India to Suvarnabhumi land through trade, migration, and religious dissemination since the Dvaravati and Khmer

ASEAN J. Sci. Tech. Report. **2025**, *28*(3), e257483.

2 of 10

eras [6–7]. With its tenet of promoting auspiciousness connecting dwellings on earth with the universe, *Vastu Shastra* outlines the process and rituals from site selection to top structure completion [8]. According to *Vastu* principles, the orientation of the planned structure must be decided prior to construction. The primary consideration is the cosmic orientation with reference to the Sun, for example, an alignment that coincides with the rising or setting of an auspicious star during dawn or dusk, which is believed to be the time joining the earth and cosmos. The structure aligned with a star or stellar-oriented structure usually deviates noticeably from the cardinal directions, and the chosen star is often tied to indigenous identity. Dating of the stellar-orientated structure is also possible because the wobbling of the earth's axis causes precession of the equinoxes and thus stars to shift their positions from the past (roughly 1° in a century); if the star of alignment is known, its position can be traced back in time to estimate the founding year, and *vice versa*. Previous studies include the Chiang Mai city plan, which was aligned with Plough asterism (or Orion constellation), symbolizing fertility, and was dated to between 1292 and 1296 [9], whereas Phra That Doi Suthep Temple was orientated to Corona Borealis constellation, marking *Vaisakha* Nakshatra, and was dated to around 1537 [10]. It is possible that *Vastu* principles may have been used to build other Lanna sites.

Sri Suphan Temple, located in the silversmith neighborhood of modern-day Chiang Mai and well-known for its silvery-adorned exterior, was once a royal temple in the reign of King Mueng Kaew (*r.* 1495–1524), the 11th King of the Lanna founding dynasty, Mangrai [11]. According to the temple's inscription [12], the King authorized the construction of a Buddhist temple and named it Sri Suphan on 30 January 1501 Gregorian date, which is converted from Lanna calendar date [13, p.60]. The inscription also indicates that on an auspicious New Year's Day in Vaisakha or the 6th Thai lunar month, which is equivalent to 9 April 1503 Gregorian date (or 30 March in Julian date) [13, p.62], the Grand Vihara was founded. In the 1545 Chiang Mai earthquake, the Grand Vihara remained largely unaffected, indicating its orientation has been the same since its inception. The comparable orientation of the Grand Vihara to the renowned Doi Suthep Temple, as well as the inscribed remark of Vaisakha period on the founding day, imply that the Sri Suphan Temple may have also followed *Vastu Shastra* principles, using the same star for alignment as the Doi Suthep Temple. Therefore, in this work, we aim to analyze the stellar orientation of the Grand Vihara at the Sri Suphan Temple. We conducted an archaeoastronomical survey of Sri Suphan's Grand Vihara and utilized Stellarium simulated sky software to search possible stars of alignment during the period documented in the inscription. The results from this investigation help us better understand *Vastu Shastra*'s implementation in Lanna historical sites.

2. Materials and Methods

A conclusive archaeoastronomical analysis of the site's astronomical orientations requires consistency with traces of evidence, whether recorded or not, such as inscriptions, calendars, and traditions. The astronomical orientation of Sri Suphan Temple can be determined in two steps. The first step is to conduct a site survey using the archaeoastronomical approach described in Section 2.1 to estimate the azimuth angle of the temple. The azimuth is an angle measured clockwise from the North on the horizontal plane of the observer. The second step (Section 2.2) is to use Stellarium to calculate various stars' azimuth angles changing from the past and their annual rise or set behavior to identify possible stars of alignment that corroborate with the azimuth of the temple and the period mentioned in the inscription. Stellarium is the positional astronomy software package that calculates astronomical coordinates of celestial objects in the sky [5]. For this work, we use Stellarium version 24.2.0, a free GPL software that renders realistic skies in real time with OpenGL, and with ΔT correction using the default "Espenak and Meeus (2006)" model, accounting for atmospheric refraction and extinction, and a proper motion.

2.1 Archaeoastronomical Survey of Sri Suphan Temple

We employed the archaeoastronomical site survey technique, as detailed in Riyaprao et al (2023) [10], to determine the azimuth of the site by calibrating it against the known azimuths of Polaris and other bright stars, if feasible. While using multiple stars enhances the accuracy of the azimuth calibration, Polaris is particularly favorable because it remains nearly fixed in position, providing a reliable north direction. The selection of bright stars is practical, as they must be easily visible to a survey camera or theodolite within a

ASEAN J. Sci. Tech. Report. **2025**, *28*(3), e257483.

3 of 10

vertical limit of 30 degrees. A yellow line in Figure 1 represents the orientation axis used to determine its azimuth angle of Sri Suphan Temple. A theodolite (Topcon, GTS-102N) was positioned at point A, facing towards point B along the yellow line, with horizontal angle reading was set to zero, establishing the line AB as the baseline equivalent to the temple's axis. A portable GPS device (Gamin, eTrex 32x) documented the theodolite's position as the observed location. Then, using the theodolite, we measured horizontal and vertical angles at different times of three bright stars: Polaris, Procyon, and Pollux. Readings for Polaris were taken every 5 minutes from 4:27 to 4:47 a.m., Procyon every minute from 4:51 to 4:57 a.m., and Pollux every minute between 5:00 and 5:08 a.m. We applied the least-squares method to calibrate the stars' measured angles with their respective azimuths and altitudes calculated by Stellarium, based on the observed location, date, and time. The offset value retrieved from the least-squares method is therefore the azimuth of the Sri Suphan Temple.

Figure 1. A satellite image of Sri Suphan Temple's Grand Vihara, with a yellow line indicating its axis. Points A and B are designated for a theodolite setup along the temple's axis. Map data: © OpenSteetMap contributors.

2.2 Stellarium computations of stars

The precession of the equinoxes, resulting from the wobbling of Earth's rotational axis, leads to a gradual shift in the ecliptic longitude of stars, thereby altering their azimuth angles over time. Stellarium simulates realistic skies, therefore their calculated positions are automatically precession corrected. Stellarium offers two types of calculated values: 'true' and 'apparent' values. For 'true' values, Stellarium requires only observed location, date, and time for input. For 'apparent' values, in addition to the required input, users can either use the default sky conditions or specify the observed sky conditions: Pressure, Temperature, and Extinction coefficient. The 'true' positions, as opposed to the 'apparent' ones, may not be directly observable due to the atmospheric conditions or the presence of the bright Sun, which can overwhelm the observation.

By employing precession-corrected Stellarium, we traced back in time the 'true' azimuth angle of various stars at the horizon, or zero altitude, to match with the azimuth of the temple. Stars falling within the temple's azimuthal range then underwent further analysis for their rising or setting patterns at the horizon in relation to the Sun to identify the star of orientation.

3. Results and Discussion

The parallelism of the baseline AB to the temple axis must be meticulously executed, as a misalignment of 1 cm can contribute to an angular error ($\Delta\theta$) equal to $tan^{-1}(1\ cm/|\overline{AB}|)$. The longer baseline is preferable to minimize the angular error, but it is contingent on the accessibility of the site. For the Sri Suphan Temple, the $\overline{AB}$ length measures approximately 35 m, which could lead to an angular error of approximately 0.016 degrees for 1 cm deviation. The azimuth of the baseline, hence the temple's axis, is to be determined.

3.1 Sri Suphan Temple' s azimuth

Any bright stars visible at the Sri Suphan Temple on the survey day, in addition to Polaris, the North star, can be used to determine the azimuth angle of the temple's Grand Vihara. After setting the horizontal and vertical positions of a theodolite camera on the baseline to zero, the horizontal positions (Hr) and vertical positions (or altitude) of Polaris, Procyon, and Pollux were measured in succession. The altitude of Polaris changes very little over time, with only a 0.02° variation in 5 minutes. In contrast, the altitudes of Procyon and Pollux change by approximately 0.1° and 0.5° in 1 minute, respectively. The date (21st January 2024), the location (18.778500° N, 98.983336° E, Elevation 314 m), and the time of the theodolite measurement serve as inputs for Stellarium's calculation of the azimuths and altitudes of Polaris, Procyon, and Pollux, illustrated as lines in Figure 2. The green lines are 'true' values without atmospheric effect, whereas the redlines are 'apparent' values impacted by atmospheric conditions. The parameters entered for the atmospheric conditions are pressure of 977.32 mbar, temperature of 25°C, and extinction coefficient of 1. The extinction coefficient of 1 corresponds to an increase in a star's apparent magnitude (the star appears dimmer) by one order, which provides the best fit for our data as we observed during the winter dawn with fog affecting visibility. The Stellarium values accounted for atmospheric refraction, as seen by the red lines, resulting in a higher altitude than the green lines without atmospheric effect. The blue circle markers depict the calibration of the measured Hr data to the Stellarium (with atmosphere) line, which is achieved by adjusting Hr values with the 'offset' value derived from minimizing the squared residuals, also known as the least-squares method. The 'offset' value is therefore the azimuth of the baseline, which is equivalent to the temple's azimuth.
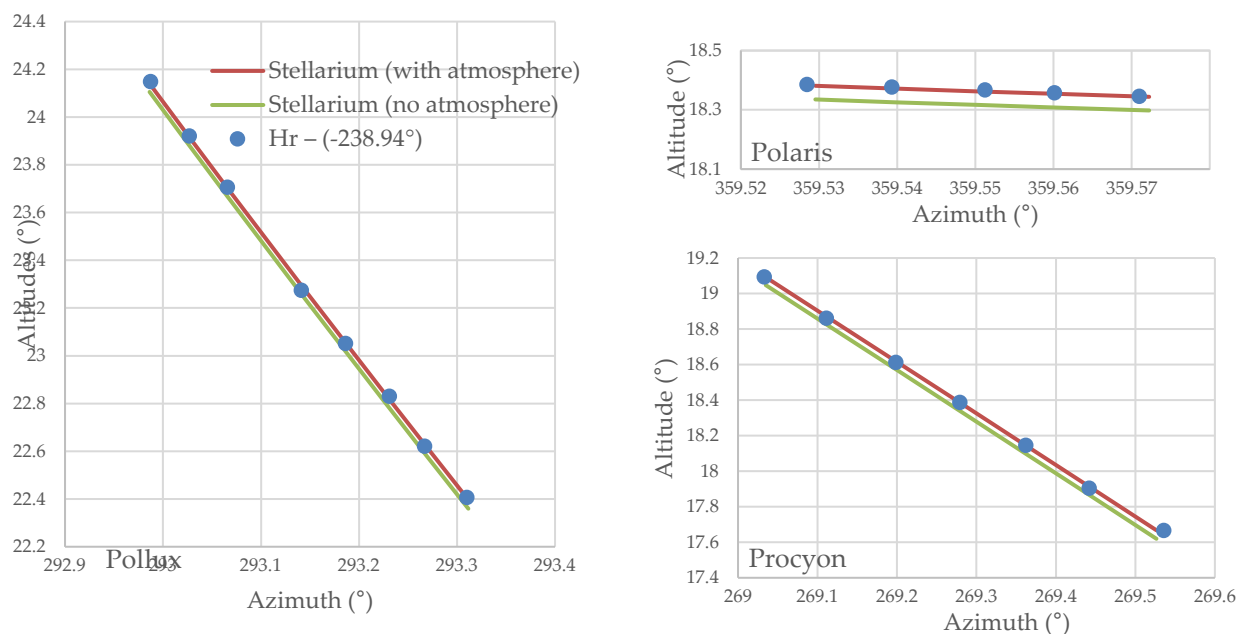
Figure 2. The altitudes and azimuths of Pollux, Polaris, and Procyon at the Sri Suphan Temple. In each graph, the red line is the computed Stellarium values with atmospheric conditions, whereas the green line is without. The blue circular markers represent the calibration of the measured Hr data to the Stellarium values of the stars.

The 'offset' values for Polaris, Procyon, and Pollux are 238.945°, 238.945°, and 238.939°, respectively, yielding an average of 238.943 ± 0.002° as the baseline's azimuth. Since the baseline points towards the back or westerly of the Vihara, the easterly azimuth of the Vihara is calculated as 238.943 – 180 = 58.943°. If we restrict the misalignment in setting up the baseline to within 5 cm, the angular error would be 0.08° (5 cm × 0.016°/1cm), resulting in the final easterly azimuth of the Sri Suphan Temple being 58.94 ± 0.08°.

3.2 Identification of the star historically used for orienting the Sri Suphan Temple

According to the *Vastu Shastra* principles, the stellar orientation of a temple should be established during sunrise or sunset, as these moments are believed to connect the earth and the cosmos. We used precession-corrected Stellarium to trace back in time and calculate the 'true' azimuth at the horizon or at zero altitude for various well-known stars. Like the Doi Suthep Temple, the Sri Suphan Temple also lacks a star aligned with its westerly azimuth. The rising azimuth of a star on 1 January every 500 years is chosen to represent the azimuth trend plotted in Figure 3, serving as an initial screening for possible stars of alignment. The Sri Suphan Temple's easterly azimuth and founding year of 1503 are overlaid in the graph, closely overlapping with azimuthal lines of Alphecca and Pollux. These two stars therefore could be utilized to set the temple's orientation in the planning process prior to construction. Alphecca is a bright star in the constellation Corona Borealis, one of three asterisms representing *Vaisakha* Nakshatra, and known in Lanna as a winnowing basket's rim star (Thai: ดาวขอบด้ง). Pollux is a bright star in the constellation Gemini, representing *Punavarsu* Nakshatra, and recognized in Lanna as the Golden Chinese Junk Boat.
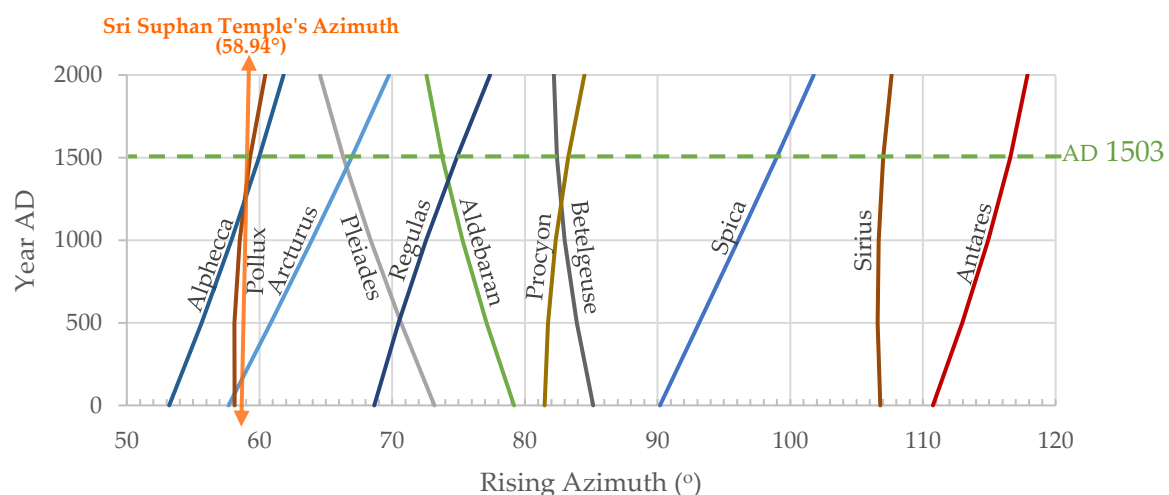
Figure 3. Rising azimuth trends tracing back in time for various well-known stars. The orange arrow locates the Sri Suphan Temple's azimuth. The dashed line indicates the founding year of the Grand Vihara.

To further identify which one is the lone star of orientation, we examine the rising behaviors of both Pollux and Alphecca during the temple's founding year, as indicated in the inscription. A star rises and sets four minutes earlier on subsequent nights, leading to four rising and setting behaviors in relation to the Sun each year, as defined in Table 1. The cosmical phenomena occur at dawn with respect to sunrise, whereas the achronycal phenomena in relation to sunset take place at dusk. In other words, these four astronomical events signify four types of stellar orientation based on the cosmic orientation rules of *Vastu Shastra* principles.

Table 1. Rising and setting behaviors of a star with respect to the Sun.

	With the star	**Opposite the star**
Sunrise at dawn	Cosmical rising (observable heliacal rising)	Cosmical setting
Sunset at dusk	Achronycal setting (observable heliacal setting)	Achronycal rising

Since we focus on the stars aligned to the east side of the temple, we plot the rising times of both Alphecca and Pollux, using the 'true' rising azimuths from Stellarium, along with sunrise and sunset times during 1503 AD in Figure 4. As indicated in the graph, the achronycal rising (AR) event refers to a star crossing the eastern horizon as the Sun sets; it is the last day a star seen rising after sunset. The cosmical rising (CS) event, on the other hand, refers to a star crossing the eastern horizon as the Sun rises; the observable one is called the heliacal rising when a star appears briefly just before the overwhelming light of sunrise. The AR and CS events of Pollux and Alphecca, as indicated in the graph, were the possible alignment times. However, only the AR of Alphecca coincided with the founding period of the Grand Vihara during the Vaisakha lunar month as noted in the inscription, which was around April to May. Hence, the star that may have been used to align the Sri Suphan Temple (azimuth ≅ 58.94°) in 1503 AD is Alphecca (azimuth ≅ 59.5°), a bright star in the constellation Corona Borealis. In Lanna, the presence of Corona Borealis with the full moon marks the Vaisakha lunar month. The full moon in Vaisakha month is known in Southeast Asia as Vaisakha Puja Day or Vesak, the Buddhist holy day commemorating the birth, enlightenment, and death of the Buddha.
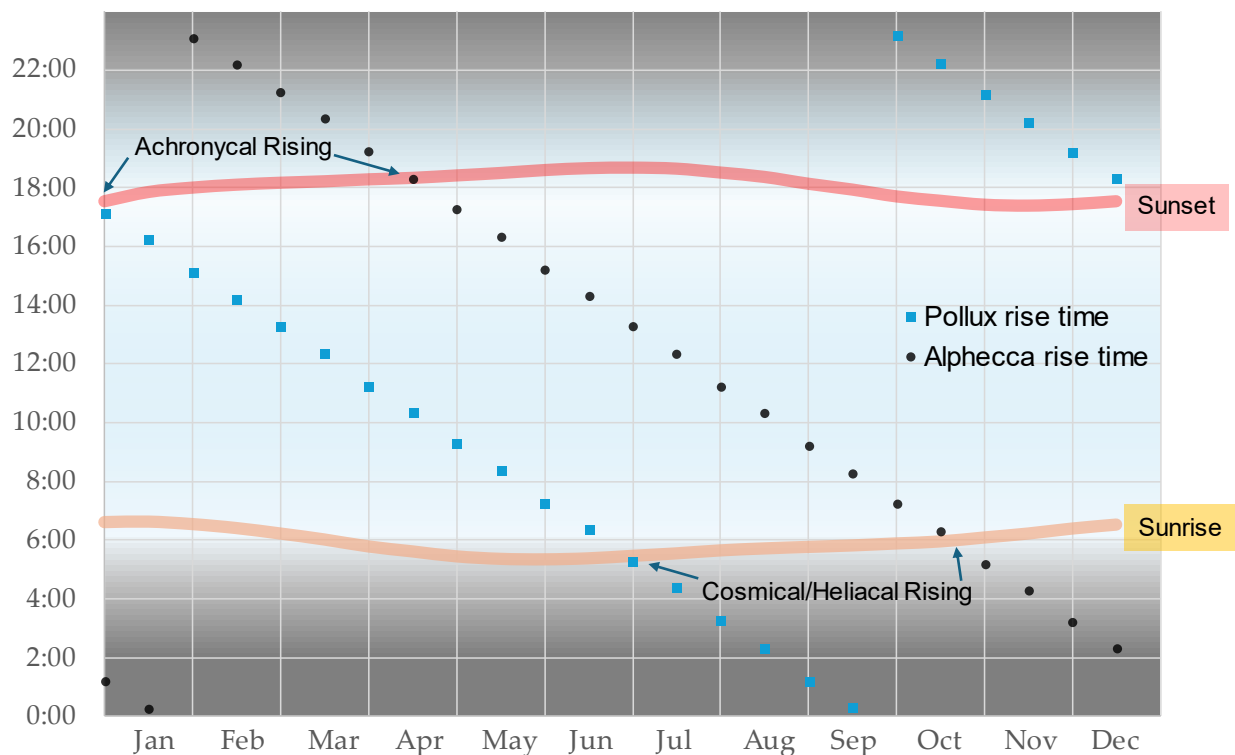
Figure 4. Rising times of Pollux (the blue squares) and Alphecca (the black dots), including sunrise and sunset times, as calculated by Stellarium for the year 1503.

3.3 Astronomical events documented on the inscription

One advantage of archaeoastronomical analysis is its ability to date an ancient site that was stellar oriented. However, it should be noted that the estimated date conveys when the stellar alignment was executed to establish the site plan, the ritual diagram *Vastu-Purusha-Mandala*, on leveled, purified ground. The germination rite, symbolized the inception of the site, was then performed, constituting a 'forecast' at the birth of the site [8]. The extent to which this process was strictly followed and how reliably it translated into the founding date noted in the inscription remains unknown. By comparing astronomical events recorded in the inscription with Stellarium simulated sky, we can gain a better understanding of how the Vastu Shastra principles were implemented in the Lanna tradition. Since Stellarium uses Julian dates to simulate the ancient

ASEAN J. Sci. Tech. Report. **2025**, *28*(3), e257483.

7 of 10

sky prior to 15 October 1582, the date that signifies the transition from the Julian to the Gregorian calendar, the dates in the Sri Suphan Inscription must first be converted to Julian dates before being checked with Stellarium.

We focused on the Vihara's founding date, which corresponds to 9 April 1503 in the Gregorian calendar and converts to 30 March 1503 in the Julian calendar [12]. This date is specified in three calendar systems: *Culasakaraj, Buddhist Nirvana Era*, and *Hontai*, as adopted in the Lanna Kingdom. In Figure 5, we present a timeline of the astronomical events recorded in and inferred from the Sri Suphan Inscription on the left side, comparing it with Stellarium simulated sky on the right side. According to the inscription, the founding date was the auspicious New Year's Day in the *Culasakaraj* lunisolar calendar, marking the moment when Sun crosses into *Mesha Rasi* (Aries). This date was determined through calculations based on the Suriyayatra treatise. Although the event itself is unobservable, the ancient practice involved marking this day with Spica, the star opposite Aries along the ecliptic, which sets at sunrise. In Thailand, the temple that may align with the New Year's Day in the *Culasakaraj* calendar using Spica is Prasat Hin Phanom Rung, which has an azimuth close to 90 degrees [14]. In the case of Sri Suphan Temple, this date appears to have been chosen only for founding the temple, and it is consistent with the Stellarium simulated sky, which reveals Spica setting around 6 a.m. The founding day was also the 4th waxing moon day in the *Buddhist Nirvana Era* lunar calendar; however, it differed slightly in the Stellarium, which indicated a moon age of 3.2 days (waxing moon). As a result, we can infer from the inscription that the full moon (15th waxing moon day) occurred on 10 April 1503, while it was 11 April 1503 for the Stellarium simulation. The full moon near Vaisakha star, Corona Borealis, also known as Vaisakha Puja Day (Vesak), is regarded as New Year's Day in the *Buddhist Nirvana Era*. Many ancient temples were aligned with stars marking calendrical New Year's Day. Sri Suphan Temple is a Buddhist temple that was aligned with the Vaisakha star, Corona Borealis; yet it was founded on the New Year's Day in the *Culasakaraj* calendar instead, which came before the Vesak. This implies that the alignment star must comply with Vastu principles, but the alignment date may be flexible. Figure 4 shows Alphecca rising in the evening until mid-April, and as the alignment procedure should be completed before the founding date of 30 March 1503, preceding evenings are possible temple alignment dates. An example of alignment event is shown in Figure 6 on the evening of 29 March 1503, with Alphecca rising on the eastern horizon at 19:32 hours, when the Sun had already fallen 18° below the horizon in the astronomical twilight. This scenario is more feasible for star observation than the ideal alignment time around 15-17 April 1503, which indicated the achronycal rising of Alphecca.

ASEAN J. Sci. Tech. Report. **2025**, *28*(3), e257483.

8 of 10

Timeline in Julian date

Possible temple alignment

*

Sri Suphan Inscription record	30 March 1503	**Stellarium simulated sky**

864 CS Thursday, New Year's Day,
Time: 6–7:30 a.m. [*Culasakaraj calendar*]

4th waxing moon day,
Vaisakha month [*Buddhist Nirvana Era*]

Kod Sa-nga day, *Ka Kai* year
[*Hontai system* (*Thai*: ระบบหนไท)]

Spica can be seen set at sunrise

Moon age 3.2 days old,
Iluminated:11.0%
Elongation: 38°42'59.8" (at midnight)

Related to Jupiter and Saturn,
need further study

| Expected Vaisakha Puja Day (full moon)
(15th waxing moon day)	10 April 1503

11 April 1503 — Moon age 14.7 days old,
Iluminated:100.0%
Elongation: 178°33'10.5" (at 17:43, full moon)

15–17 April 1503 — Ideal temple alignment via
the achronycal rising of Alphecca

Figure 5. Timeline in Julian dates of the astronomical events excerpts from the Sri Suphan Inscription (on the left) and the Stellarium simulated sky (on the right).
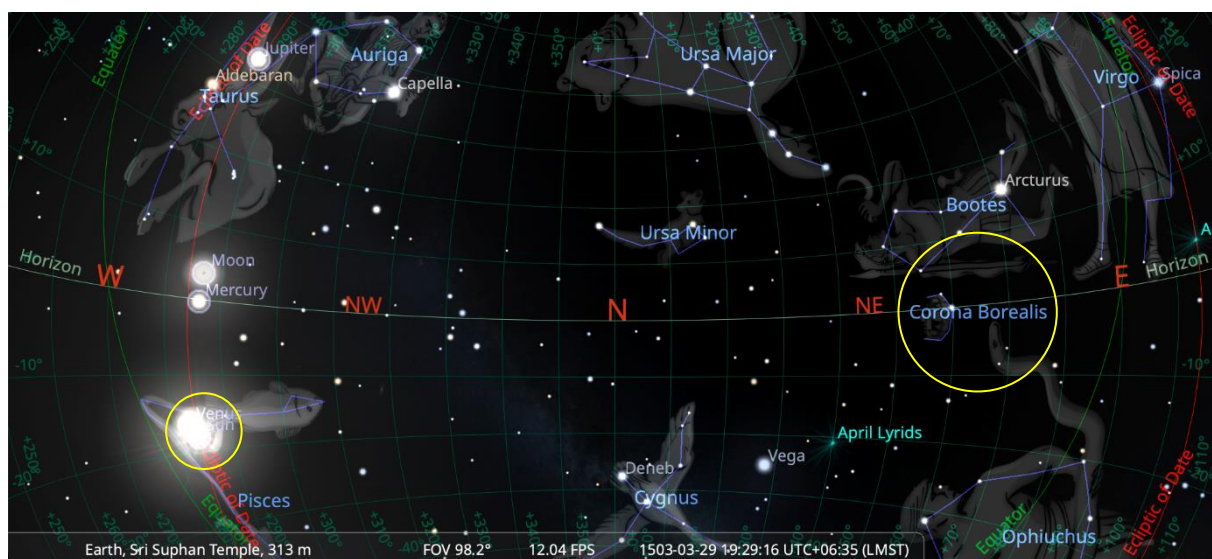
Figure 6. Stellarium simulated sky showing relative positions of Alphecca and the Sun (circled in yellow; Alphecca on the horizon, but the Sun was about 18° below the horizon at 19:32 on 29 March 1503) that could be used for the Sri Suphan Temple's alignment.

The Sri Suphan Temple and the renowned Phra That Doi Suthep Temple, two Buddhist temples built in succession in the same era, both employed the same alignment method using Alphecca in the constellation Corona Borealis, which may suggest that *Vastu Shastra* principles were widely implemented in the Lanna Kingdom, and the Sri Suphan Temple may have served as a prototype for orienting later Buddhist temples to be associated with the Vaisakha lunar month. The tradition of modern-day Buddhist temples in Chiang Mai erecting a vihara or Buddha image during Vaisakha Puja Day indicates that the preference for Vaisakha month remains, but the orientation rule has faded away with time.

Archaeoastronomical analysis possess a multi-disciplinary nature. Modern astronomy software, such as Stellarium, can be used to examine the ancient sky, but it requires traces of historical evidence to solidify its findings. Ethnoastronomy, which includes knowledge of the stars and the calendar systems of different ethnic groups, is also essential. Furthermore, even non-written traditions might contribute to the analysis. Some archeological sites might have all evidence we need, but some others might lack one or more. It is important that we continue to explore more sites to allow us to detect patterns and be able to elucidate one to another, hence filling in the missing puzzles of the ancient world.

4. Conclusions

The archaeoastronomical analysis of the Sri Suphan Temple with a measured azimuth of $58.94 \pm 0.08°$ reveals that it is closely aligned with Alphecca, a bright star in constellation Corona Borealis. The finding agrees with the inscription record that the temple was founded during the Vaisakha lunar month, which is marked by Corona Borealis and the full moon. However, the founding date, which is converted to 30 March 1503 Julian date, was New Year's Day in the *Culasakaraj* lunisolar calendar, which was before Vaisakha Puja Day, New Year's Day in the Buddhist Nirvana Era lunar calendar, and the achronycal rising of Alphecca. According to *Vastu Shastra* principles, the stellar alignment must be accomplished prior to the founding date, which leads to a possible alignment date of the preceding evening of 29 March 1503 Julian date, when Corona Borealis was still visible on the horizon. The orientation resembles the Phra That Doi Suthep Temple of a later Buddhist temple, implying that alignment knowledge was passed down from the Sri Suphan Temple.

5. Acknowledgements

Conflicts of Interest: The authors declare no conflict of interest.

References

[1]   Magli, G. Archaeoastronomy and the chronology of the Temple of Jupiter at Baalbek. *Archaeoastronomy Introduction to the Science of Stars and Stones* **2016**. https://doi.org/10.10007/978-3-319-22882-2.

[2]   Baratta, N.C.; Magli, G. The Role of Astronomy and Feng Shui in the Planning of Ming Beijing. *Nexus Network Journal* **2021**, *23*, 767-787. https://doi.org/10.1007/978-981-19-6274-5_10.

[3]   Goto, A. Archaeoastronomy and ethnoastronomy in the Ryukyu Islands: a preliminary report. *Proceedings of the International Astronomical Union*, **2011**, *7*(S278), 315-324.

[4]   Ruggles, C.L.N, ed. *Handbook of archaeoastronomy and ethnoastronomy*. Springer New York: NY; 2015. https://doi.org/10.1007/978-1-4614-6141-8.

[5]   Zotti, G.; Hoffmann, S.M.; Wolf, A.; Chéreau, F.; Chéreau, G. The Simulated Sky: Stellarium for Cultural Astronomy Research. *Journal of Skyscape Archaeology* **2021**, *6*(2), 221-258. https://doi.org/10.1558/jsa.17822.

[6]   Riyaprao, O., *et al*. *Bhumpanya Darasastr Lanna (Lanna astronomical wisdom)*, Chiang Mai: Publishing Unit, Faculty of Science, Chiang Mai University; **2021**.

[7]   Saelee, C.; Riyaprao, O.; Komonjinda, S.; Sriboonrueang, K. An archaeoastronomical investigation of Vaastu Shastra Principles (Vedic Architecture) implemented in the city planning of ancient Chiang Mai. In: Orchiston, W.; Vahia, M.N., editors. *Exploring the History of Southeast Asian Astronomy. Historical & Cultural Astronomy*. Cham: Springer **2021**, 461-485. https://doi.org/10.1007/978-3-030-62777-5_13

[8]   Kramrisch, S. The hindu temple: volume one. Delhi: Motilal Banarsidass Publ. **1976**.

[9]   Lemsonth, C.; Lorwilai, S.; Sankaokam, P.; Riyaprao, O.; Saelee, C. The off-cardinal alignment of Chiang Mai's City Plan in Relation to the Orion's Belt. *ASEAN Journal of Scientific and Technological Reports* **2023**, *26*(4), 29-37. https://doi.org/10.55164/ajstr.v26i4.249720

[10]   Riyaprao, O.; Sriboonrueang, K.; Komonjinda, S; Saelee, C. Astronomical Orientation of Phra That Doi Suthep Temple in Relation to Acronychal Rising of Corona Borealis and Visakha Bucha Day. *Journal of Astronomical History and Heritage*, **2023**, *26*(3), 701-721. https://doi.org/10.3724/SP.J.1440-2807.2023.09.68

[11]   Lertpipatworakul, T.; Chaeyklin, N. *Wat Sri Suphan Rong Roy Jaruek (Sri Suphan Temple's historical traces)*. https://www.sac.or.th/portal/th/article/detail/379 (Accessed 10 May 2024)

[12]   Princess Maha Chakri Sirindhorn Anthropology Centre. *Wat Sri Suphan Inscription* https://db.sac.or.th /inscriptions/inscribe/detail/16441 (Accessed: 16 February 2024).

[13]   Saelee, C.; Riyaprao, O. *Sobtieb Wan Duen Pee Nai Jaruk Lanna (Date Calibration of Lanna inscriptions)*. Chiang Mai: Publishing Unit, Faculty of Science, Chiang Mai University, **2023**.

[14]   Komonjinda, S.; Riyaprao, O.; Sriboonrueang, K.; Saelee, C. Relative orientation of Prasat Hin Phanom Rung Temple to Spica on New Year's Day: the chief indicator for the intercalary year of the luni-solar calendar. *Proceedings of the International Astronomical Union*, **2019**, *15*(S367), 260-264. https://doi.org/ 10.1017/S1743921321001034

The Design and Development of a Prototype Stretcher Cum Wheelchair for Radiographic Purposes

Boriphat Kadman[1], Danu Prommin[2], Parinya Junhunee[3], and Supawitoo Sookpeng[4*]

[1] Faculty of Allied Health Sciences, Naresuan University, Phitsanulok, 65000, Thailand

[2] National Metal and Materials Technology Center, National Science and Technology Agency, Pathum Thani, 12120, Thailand

[3] National Metal and Materials Technology Center, National Science and Technology Agency, Pathum Thani, 12120, Thailand

[4] Faculty of Allied Health Sciences, Naresuan University, Phitsanulok, 65000, Thailand

[*] Correspondence: supawitoos@nu.ac.th

Abstract: Background: In the hospital emergency department, X-ray imaging was crucial for ensuring the precise and prompt diagnosis of patient accidents. Recognizing the potential discomfort and risk of injury associated with transferring patients from transport beds to X-ray tables, the RT (Radiological Technology) Wheelchair was conceived and implemented as a solution to address this concern. Methods: The features and design of the RT Wheelchair were aligned with the guidelines outlined in the International Electrotechnical Commission (IEC) 60601-1 standard. The quality assessment of the carbon fiber material used in the backrest and seat cushion was conducted by evaluating X-ray transmission ratio, exposure index (EI), and image quality. Results: The reduction in radiation attenuation of the carbon fiber sheets did not exceed eight percent. The EI and image quality remained within acceptable thresholds. Consequently, the resultant images were deemed adequate for the radiologist's diagnostic purposes. Conclusions: A Stretcher Cum Wheelchair for Radiographic Purposes enhances the convenience of staff and ensures the safety of patients by minimizing the need for movement during X-ray exposure.

Keywords: Stretcher cum wheelchair; emergency department; radiography; X-ray imaging; RT wheelchair

1. Introduction

Accidents and injuries often necessitate immediate medical attention, with X-ray imaging being a fundamental diagnostic tool upon patients' arrival at hospitals [1]. Achieving proper positioning for radiographic imaging in patients with mobility limitations, such as those confined to wheelchairs or bedridden, including individuals with disabilities, accident victims, and the elderly, profoundly influences diagnostic accuracy and subsequent clinical treatment [2]. However, the process of obtaining X-ray images typically entails transferring the patient to a radiographic table, followed by repositioning the patient back onto a wheelchair or, in cases of immobility, lifting the patient's body to place the imaging receptor [3-4]. This procedure often necessitates the assistance of at least two personnel. It may lead to repeated patient injuries and distortions in X-ray images due to misalignment between the X-ray beam and the image receptor, particularly challenging for capturing images in certain positions [5]. Presently, general hospitals utilize three primary types of equipment for patient transfer: wheelchairs, wheelchair cum stretchers, and patient stretchers [6]. However,

these methods may induce further pain in patients [7], with individuals with recent falls and impaired mobility facing a heightened risk of further accidents, including falls from stretchers and examination tables [8]. Moreover, Inaccurate patient positioning can significantly degrade radiographic image quality, leading to misdiagnoses, increased repeat imaging, and unnecessary radiation exposure. Studies have identified positioning errors as a major cause of image rejection and diagnostic inaccuracies across various fields [9].

In response to the government's call for driving economic growth through innovation and Thailand's impending transition into an aging society, preparing for medical innovation becomes imperative to support the aging population's impact on the healthcare system. Recognizing the pivotal role of radiography in diagnostics, our research team has developed a specialized wheelchair, the RT (Radiological Technology) Wheelchair, tailored for radiographic imaging of elderly patients. The project aims to develop a wheelchair cum stretcher for radiographic imaging of elderly patients and analyze its operational outcomes in the field. The anticipated benefits of the RT Wheelchair for the elderly include reducing movement and time, minimizing injuries associated with patient transfers, enabling radiographic imaging directly on the wheelchair, and facilitating imaging in various positions from seated to fully reclined.

2. Materials and Methods

2.1 Feature and Safety System design

The institution granted ethical approval for this research study involving human subjects under the Certificate of Approval (COA) No. 390/2020. The study focused on selecting primary materials used in developing the structural and supportive components for X-ray imaging. Carbon fibers (CFs), known for their high strength-to-weight ratio, excellent corrosion resistance, and radiolucency, were selected as the primary material for the backrest and seat cushion of the Stretcher Cum Wheelchair for Radiographic Purposes [10,11]. These properties ensured patient safety, device durability, and optimal image quality, with minimal interference during radiographic imaging. Following material selection, the design and development of the RT Wheelchair were systematically carried out. The three seating components—the backrest, seat cushion, and support for the lower extremities—were structured considering anatomical support and compatibility with imaging requirements. Each carbon fiber panel was designed with an integrated slot to place the image receptor, thereby minimizing the risk of introducing additional artifacts. Moreover, the RT Wheelchair was modularly organized into principal structures: the mobile base frame, which houses the motor and battery system; the adjustable seating system, facilitating transition between lying and sitting positions; and the integrated support system for the image receptor, ensuring alignment with the path of the X-ray beam. Each component's function and material selection aligned with the safety requirements outlined in IEC 60601-1 for medical electrical equipment.

Ensuring electrical safety was a paramount concern during development. Therefore, the research protocol was designed to comply with IEC 60601-1 standards, delineating the minimum safety and performance requirements for medical devices before marketing and sale [12]. The RT Wheelchair incorporates folding armrests designed following clause 5.9 of IEC 60601-1, addressing patient-contacting parts [13]. The overall mechanical system includes the design of a lifting system for adjustable lying-sitting positions, an energy supply system, and a motion control system to enhance ease of operation during clinical use. Furthermore, the wheelchair was engineered to integrate a radiation-receiving panel and an adjustable support mechanism to maintain precise positioning during imaging. After design completion, comprehensive laboratory testing was conducted to validate the safety and functional performance of the RT Wheelchair. Testing included evaluations of weight-bearing capacity, radiation attenuation of materials, comparative image quality between conventional X-ray imaging and imaging performed using the RT Wheelchair, and electrical safety verification. The RT Wheelchair's ability to support a maximum patient weight of 150 kilograms was tested with a safety factor 1.5, simulating a load of 225 kilograms. Body weight distribution was based on standards from JIS T 9201:2016 and ISO 7176-11:2012, partitioned into 60% for the upper body (approximately 135 kilograms) and 40% for the lower body (approximately 90 kilograms) using a dummy model. Further testing involved positioning a simulated human body (Randy from SIMULAIDS, INC.), weighing 75 kilograms, with the same distribution assumptions and an additional load applied to the support

ASEAN J. Sci. Tech. Report. **2025**, *28*(3), e255648.

3 of 11

structure to achieve 135 kilograms. The wheelchair was evaluated over 24 hours, with adjustments to the tilt-in-space angle at 0 and 30 degrees and the sitting position at 85 degrees. A measuring device calibrated the support system to the required angles.

2.2 The effects of material on X-ray transmission

2.2.1 X-ray transmission of carbon fiber sheets

The quality of carbon fiber sheets in terms of X-ray transmission was evaluated by comparing the amount of radiation obtained from the radiation image detector when it did not pass through the material and when it passed through the material, as shown in Figure 1. This was done using voltage differences of 70, 80, and 90 kVp, tube current and exposure time values ranging from 2 to 10 mAs. The quality of the material was assessed based on the image quality using the Exposure Index (EI) value in radiographic imaging of simulated body parts, including hands, hips, and chests. A comparison was made between images obtained without passing through the carbon fiber sheets and images obtained after passing through the carbon fiber sheets.
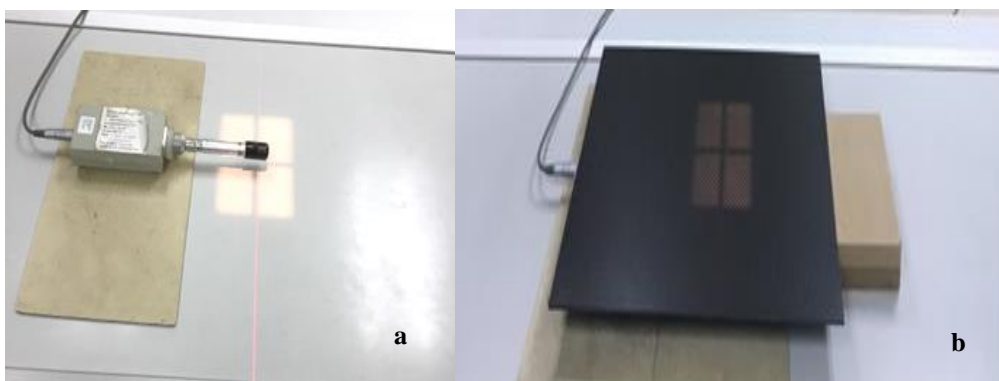
Figure 1. The radiation quantity is measured without passing through the carbon fiber sheet (a), while in the image on the right, it is measured after passing through the carbon fiber sheet (b).

The X-ray transmission rate was investigated for performance produced using carbon material [14]. Each measurement was conducted three times following established radiation measurement standards to enhance reproducibility and minimize random errors. The X-ray transmission rate is calculated using the following equation 1.

$$\text{Ratio of X-ray transmission} = (I_1/I_0) \times 100 \tag{1}$$

I_1 is the transmission value measured after passing through the carbon fiber sheet and I_0 is the initial value without passing through the carbon fiber sheet.

2.2.2 X-ray transmission of carbon fiber with human body phantom

The human body phantom was close to human attenuation. Radiographic imaging of simulated body parts, including the skull, chest, hips, and knees, was performed using conventional imaging and imaging with the RT Wheelchair at Thammasat University Hospital, employing identical exposure parameters (kVp, mAs). Although identical exposure parameters (kVp, mAs) were applied for both imaging methods, the initial radiation outputs (I_0) of the two X-ray systems were not independently measured before imaging. This may introduce variability due to inherent differences in machine output. Nevertheless, efforts were made to standardize imaging conditions, and the comparison was interpreted considering this potential limitation. Regarding patient positioning, the simulated body parts for conventional radiographic imaging were done using a radiographic table. In contrast, the positioning for radiographic imaging on the RT Wheelchair was done on the wheelchair itself, as shown in Figure 2.
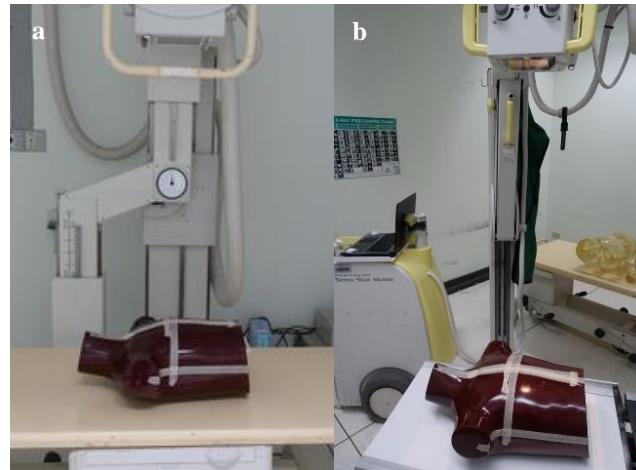
Figure 2. Evaluation of image quality of characteristic of x-ray transmission of carbon fiber with human body phantom. Comparison between exposure on the radiographic table (a) and passing through the carbon fiber sheet of the RT Wheelchair (b).

2.3 Device Satisfaction Assessment

The study incorporates user acceptance testing through interviews and satisfaction questionnaires. Participants in the research comprised three radiologists, porter staff members, and seven radiological technologists. Training and demonstration sessions for utilizing the RT Wheelchair were provided to radiological technologists and porter staff members. Satisfaction assessment encompasses various aspects, including the design, size, and appearance of the structure, the functionality of the positioning system, the usability of X-ray imaging, and overall benefits. Radiologists were interviewed regarding their satisfaction with image quality. The Likert scale was employed for scoring each item, with ratings ranging from 5-point scales with the given question, where 1-5 denotes very dissatisfied, dissatisfied, neutral, satisfied, and very satisfied, respectively [15]. Volunteer patients undergoing X-ray imaging at Phitsanuvej Hospital, Phitsanulok province, Thailand, were included in the study. X-ray imaging procedures encompassed examinations of the upper limb (hand, arm, or elbow), lower limb (foot, knee, leg, or ankle), supine chest X-ray, supine abdominal X-ray, and lateral decubitus X-ray. Volunteers capable of assisting themselves or performing activities such as sitting up, standing, and walking easily were selected to ensure safety during the preliminary testing phase.

3. Results and Discussion

3.1 Feature and Safety System design

The researcher considered the materials and properties used in developing the RT Wheelchair, as shown in Figure 3. The main structural components that can adjust between lying and sitting positions are made of aluminum and stainless steel, which provide strength, corrosion resistance, and durability. The body support areas that come into contact with X-rays are made of carbon fiber panels with low radiation attenuation properties, allowing X-rays to pass through without increasing the radiation dose compared to normal X-ray imaging. The wheelchair has a transparent slot for the X-ray imaging panel, which can be adjusted for lying positions, and it utilizes a guided navigation system with the X-ray panel and a mechanism to adjust the height of the body support. In this study, the X-ray transmission measurement described in Section 2.2 focused specifically on the carbon fiber components because these areas directly interact with the X-ray beam during imaging. Although aluminum and stainless steel were used in the frame structure, their placement was designed to avoid the primary X-ray exposure field. It did not block or overlap with the radiation pathway during clinical use. Therefore, their contribution to overall X-ray attenuation was considered negligible when evaluating transmission through the patient-contact regions directly exposed to the X-ray beam.

ASEAN J. Sci. Tech. Report. **2025**, *28*(3), e255648.

5 of 11

Figure 3. Positions of stretcher cum wheelchair for radiographic purposes driven by electronic motor. The base is made from stainless steel, the body made from 3 carbon fiber plates: the low extremity, the body, and the head part. The lower part of all fiber carbon plates has a slot for the image receptor. The motor driver can adjust the position of the image receptor.

3.2 The effects of material on X-ray transmission

3.2.1 X-ray transmission of carbon fiber sheets

The radiation reduction testing found that the difference in radiation quantities in microgray (μGy) did not exceed 8 percent. An analysis of X-ray transmission through carbon fiber sheets is detailed in Table 1.

Table 1. Exposure technique and dose between without passing and passing through the carbon fiber sheet.

Exposure Technique		Dose		Dose differences (%)	X-ray transmission
kVp	mAs	Without passing through the carbon fiber sheet (μGy)	Passing through the carbon fiber sheet (μGy)		
70	2	78.7	72.5	-7.8	92.1
	4	158.1	146.3	-7.5	92.5
	5	196.1	182.3	-7.0	93.0
	10	392.7	365.2	-7.0	93.0
80	5	267.1	249.8	-6.5	93.5
	10	536.1	500.0	-6.7	93.3
90	5	329.2	309.4	-6.0	94.0
	10	659.9	614.9	-6.8	93.2

3.2.2 X-ray transmission of carbon fiber with human body phantom

The Exposure Index and image quality evaluation results showed that the EI values obtained from photography were still within acceptable standards (Table 2), and the images' quality still showed complete anatomy, which passed the acceptance criteria. Therefore, carbon fiber sheets can be used as the main material for fabricating RT Wheelchairs and the backrest and seat cushion, which are the parts used to support organs that take X-ray images. There is no need to increase the radiation dose.

ASEAN J. Sci. Tech. Report. **2025**, *28*(3), e255648.

6 of 11

Table 2. Exposure Index (EI) values of radiographs of models of various organs when not passing through the carbon fiber sheet.

Part of the phantom	Exposure Technique	Exposure index (EI)		Criteria (EI=1800-2200)
		Without passing through the carbon fiber sheet	Passing through the carbon fiber sheet	
Hand	70 kVp, 1.4 mAs	2195	2158	Pass
Hips	85 kVp , 22 mAs	1967	1919	Pass
Thorax	66 kVp , 6.3 mAs	2198	2182	Pass

The results of the image quality assessment revealed that the anatomical features could still be observed, meeting the acceptance criteria. Therefore, carbon fiber can be used as the primary material in constructing the wheelchair frame, support parts, and seating. These components support organs during X-ray imaging without increasing radiation exposure compared to normal imaging and imaging with an RT Wheelchair, as shown in Figure 4.
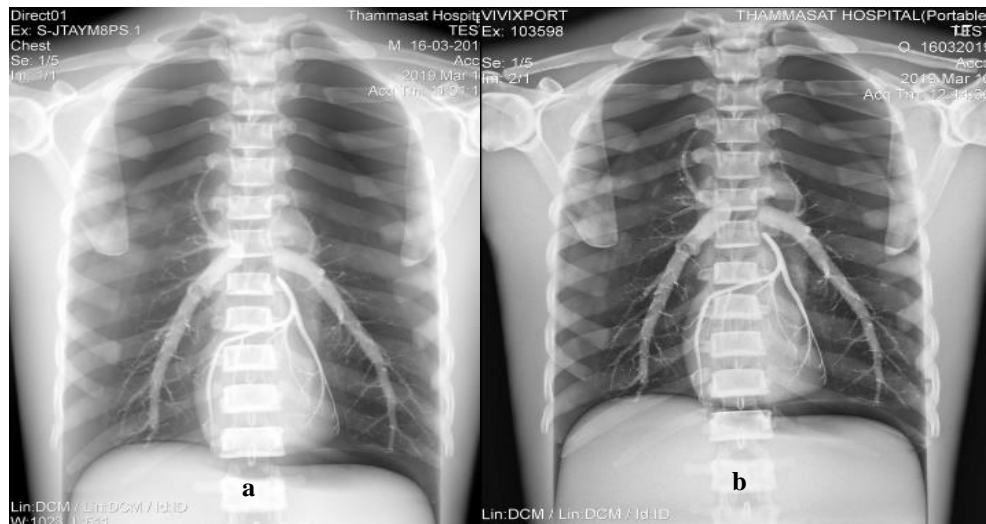
Figure 4. Chest AP 85 kV, 2.69 mAs by (a) normal imaging by exposure on the radiographic table and (b) imaging with RT wheelchair. The results of the image quality assessment revealed that the anatomical features could still be observed, meeting the acceptance criteria.

The wheelchair base is enclosed in a housing designed to prevent the spread of fire, complying with electrical safety standards for medical devices (IEC 60601-1). It is made of polycarbonate and has a lockable plastic cover. The interlock system separates the functions between usage and battery charging. The wheelchair also has a remote-control system to control the operation of the body support and the transmission of the X-ray imaging panel, as well as an electric motor system for propulsion. Electrical components and other electronic devices that control the machine are tested for electrical safety according to medical device electrical safety standards (IEC 60601-1), including protection against electromagnetic interference, as shown in Table 3.

ASEAN J. Sci. Tech. Report. **2025**, *28*(3), e255648.

7 of 11

Table 3. Specification of RT wheelchair.

Features	Details
Wheelchair weight	70 kilograms
Height in the lying position and the sitting position	80 centimeters in height (lying position) and 125 centimeters in height (sitting position)
Width	Width of 60 centimetres
Length in the lying position and the sitting position	Length of 175 centimetres (lying position) and 115 centimetres (sitting position)
Maximum patient weight capacity	Maximum weight capacity of 150 kilograms (multiplied by the Safety Factor)
Battery	24-volt dry acid battery; 21 Ampere-hours (Ah)
Degree of tilt-in-space	Tilt-in-space range of 0 to 90 degrees
Degree of leg rest adjustment	Leg rest adjustment range of 0 to 90 degrees
Maximum motor speed	Maximum speed of 12 kilometres per hour
Drive system	Electric motorized wheels without carbon brushes on both sides 24 volts and 250 watts per side
	Option to operate with electricity or manually, according to user preferences

In addition to the mechanical specifications, preliminary results from observations and inquiries regarding using the RT Wheelchair over two months (November to December 2020) were obtained. The sample group consisted of 89 volunteer participants. Among them, there were 24 elderly volunteers. The image quality of the X-ray images met the quality standards at a 100% rate. These results further underscore the effectiveness of carbon fiber materials in preserving diagnostic image quality while ensuring structural safety. Previous studies have also extensively investigated carbon fibers' mechanical and radiological properties. Unterweger et al. [16] conducted a comprehensive study employing techniques such as X-ray photoelectron spectroscopy (XPS) and scanning electron microscopy (SEM) to characterize surface properties of different types of carbon fibers. Similarly, Ho et al. [17] demonstrated that carbon fiber/polyetheretherketone (CF/PEEK) constructs enhanced biomechanical performance and minimized imaging artifacts. The widespread adoption of carbon fiber in radiotherapy couches is attributed to its superior physical resilience, reduced weight, and low beam attenuation [16,18]. However, attention must be given to dose variations introduced by carbon fiber structures, particularly at joint interfaces, necessitating accurate manufacturer data on absorption rates to ensure clinical safety [19-21].

3.2.3 Device Satisfaction Assessment

The satisfaction levels of various stakeholders concerning the RT Wheelchair were assessed, as shown in Table 4. Volunteer patients expressed that the structure's design, size, and appearance were satisfactory (4.29 ± 0.10 and 4.37 ± 0.33, respectively). Porter staff reported that the structure's design, size, and appearance were neutral level (3.45 ± 0.15) and satisfied level (3.70 ± 0.10). Radiological technologists indicated that satisfaction levels regarding the design, size, and appearance of the structure, as well as the usability of X-ray imaging and benefits, were neutral level (3.25 ± 0.34, 3.32 ± 0.40, 3.13 ± 0.18, and 3.07 ± 0.38, respectively). There were additional feedback from such as 1) The sharp edges of carbon fiber sheets cause skin abrasions during RT wheelchair use 2) The exposure factors for radiographic imaging need to be increased in certain cases 3) X-ray imaging in large-bodied patients is not feasible due to the structure of the wheelchair and the limited space for the image receptor 4) Cross-table lateral X-ray imaging is not feasible 5) Skull X-ray imaging in tall patients is not feasible 6) When adjusted to a reclined position, there is a gap between the backrest and the seat, leading to artifacts in Pelvis imaging 7) The positioning of the image receptor along the horizontal axis of the RT wheelchair is not precise during operation.

ASEAN J. Sci. Tech. Report. **2025**, *28*(3), e255648.

8 of 11

These user comments highlight several practical challenges that were not fully captured under controlled experimental conditions. In particular, the need to increase exposure factors reported by radiologic technologists can be attributed to limitations encountered during simulated use, such as phantom or volunteer body size variations, positioning difficulties, and structural interferences associated with the RT Wheelchair design. Although Exposure Index (EI) measurements under standard phantom conditions suggested that a dose increase was unnecessary, simulated practice with phantoms and volunteers revealed that certain imaging scenarios required dose adjustments to achieve acceptable image quality. This discrepancy underscores the importance of considering operational variability and user feedback before translating prototype performance into future clinical applications. The evaluation results of X-ray images conducted by radiologists underscored the high level of maneuverability and ease of use attributed to the RT Wheelchair. Despite potential concerns regarding its aesthetic appeal, the wheelchair was perceived as robust and sturdy. Crucially, the X-rays' image quality was clear and consistent, falling within the standard range and closely resembling that of conventional X-ray images. These findings affirm the practicality and efficacy of the RT Wheelchair in facilitating diagnostic imaging procedures, thereby contributing to its viability as a valuable tool in clinical settings.

In addition to the independent evaluation of images obtained using the RT Wheelchair, a comparative analysis was conducted against conventional radiographic techniques without the device. Radiologists scored the images based on positioning accuracy, anatomical visibility, and overall diagnostic acceptability. The results demonstrated no significant difference in image clarity between the two methods; however, the RT Wheelchair group exhibited improved consistency in positioning accuracy, particularly in challenging imaging views such as lateral hip and cross-table projections. This direct comparison further substantiates the RT Wheelchair's contribution to enhancing the reproducibility and reliability of radiographic positioning, supporting its potential utility in clinical practice.

Table 4. The results of satisfaction levels of various stakeholders concerning the RT Wheelchair

Stakeholders	Design and size	Appearance of the structure	X-ray imaging	Benefits
Volunteer patients	4.29 ± 0.10	4.37 ± 0.33	n/a	n/a
Porter staffs	3.45 ± 0.15	3.70 ± 0.10	n/a	n/a
Radiological Technologists	3.25 ± 0.34	3.32 ± 0.40	3.13 ± 0.18	3.07 ± 0.38

X-ray images are regarded as integral components of routine patient care. They play a pivotal role in diagnosing broken bones due to their decreased discomfort, enhanced precision, and superior lesion detection capabilities [22]. The acquisition of X-ray images facilitates prompt diagnosis by healthcare professionals, thereby expediting the commencement of treatment for patients. The RT Wheelchair, which focuses on a Stretcher Cum Wheelchair designed for Radiographic Purposes, serves as a preventive measure against patient falls within healthcare facilities. Hence, radiology departments must prioritize fall prevention and deploy interventions to mitigate harm. The initiation of preventive measures commences within emergency settings, where risk factors can be identified through appropriate tools and patient engagement [8].

Moreover, the RT Wheelchair offers versatility by seamlessly transitioning from sitting to reclining. Its carbon fiber support structure beneath the backrest facilitates precise positioning for X-ray examinations. Minimizing patient movement during diagnostic imaging procedures can significantly aid physicians in rendering timely diagnoses, potentially preserving patients' lives. The RT wheelchair has successfully undergone testing following IEC 60601 standards, which delineate safety and performance criteria for medical electrical equipment. Nevertheless, adherence to the guidance provided by regulatory bodies such as the Food and Drug Administration (FDA) is imperative for ensuring that RT Wheelchairs marketed to the intended demographic comply with safety and efficacy requisites [23]. When considering the benefits of utilizing the RT Wheelchair compared to conventional X-ray procedures, it is observed that there is no need to relocate patients to the X-ray bed. This reduces the personnel required for the procedure from 2 individuals to just 1. Additionally, the imaging time for X-ray procedures is decreased from 10 minutes to only 2 minutes.

ASEAN J. Sci. Tech. Report. **2025**, *28*(3), e255648.

9 of 11

Stakeholder satisfaction evaluations confirmed the RT Wheelchair's practical utility in hospital settings, with volunteer patients, porter staff, radiological technologists, and radiologists providing positive scores as documented in Table 3. Their valuable feedback identified several necessary improvements, including reducing carbon fiber edge sharpness, modifying the structure to accommodate horizontal 14×17-inch image receptors with grid capability, developing equipment for lateral cross-table imaging positioning, creating accessories for skull imaging in tall patients, extending the seamless seating area over the pelvis region, minimizing the gap between seat and backrest, and redesigning for more precise image receptor positioning during use. Incorporating these improvements is expected to enhance user satisfaction, optimize imaging workflows, and broaden the clinical applicability of the RT Wheelchair across a broader range of patient groups and radiographic techniques. Nevertheless, a limitation of this study is the absence of direct measurement of the initial radiation output (I_0) for the two X-ray machines. Although identical exposure settings were employed, variations in intrinsic output between systems may have influenced dose measurements. Future studies should include I_0 verification to strengthen the validity of cross-system comparisons.

4. Conclusions

Implementing the RT Wheelchair within the emergency X-ray department has effectively mitigated risks associated with patient transfers for radiographic procedures. The wheelchair's design facilitates direct radiographic imaging, enhancing workflow efficiency and reducing potential patient discomfort. Furthermore, the RT Wheelchair has successfully met the safety and performance standards mandated for medical electrical equipment. Evaluation of EI and image quality has demonstrated adherence to acceptable standards, affirming its suitability for clinical use. Significantly, the satisfaction and feedback received from volunteer patients, radiologists, radiological technologists, and porter staff members have played a pivotal role in informing and refining subsequent stages of development. Their insights have been instrumental in identifying areas for improvement and enhancing overall efficiency in the device's functionality and usability. Continuing collaboration with stakeholders and incorporating their feedback will be essential for further optimizing the RT Wheelchair's performance and ensuring its continued effectiveness in clinical settings.

5. Acknowledgements

References

[1] Warren, R.A.; Ferguson, D.G. Why do accident and emergency doctors request X-rays? *Emerg Med.* **1984**, *1*(3), 143-150. https://doi.org/10.1136/emj.1.3.143.

[2] Story, M.F.; Luce, A.C.; Leung, A.; Omiatek, E.M.; Lemke, M.R.; Rempel, D.M. Accessibility of radiology equipment for patients with mobility disabilities. *Hum Factors.* **2008**, *50*(5), 801-810. https://doi.org/10.1518/001872008X354174.

[3]   Conrad, B.P.; Rechtine, G.; Weight, M.; Clarke, J.; Horodyski, M. Motion in the unstable cervical spine during hospital bed transfers. *J Trauma Acute Care Surg.* **2010**, *69*(2), 432-436. https://doi.org/10.1097/TA.0b013e3181e89f58.

[4]   Story, M.F.; Schwier, E.; Kailes, J.I. Perspectives of patients with disabilities on the accessibility of medical equipment: Examination tables, imaging equipment, medical chairs, and weight scales. *Disabil Health J.* **2009**, *2*(4), 169-179.e1. https://doi.org/10.1016/j.dhjo.2009.05.003.

[5]   Dean, E.R.; Scoggins, M.L. Essential elements of patient positioning: A review for the radiology nurse. *J Radiol Nurs.* **2012**, *31*(2), 42-52. https://doi.org/10.1016/j.jradnu.2011.08.002.

[6]   Wallin, A.; Gustafsson, M.; Anderzen, Carlsson, A.; Lundén, M. Radiographers' experience of risks for patient safety incidents in the radiology department. *J Clin Nurs.* **2019**, *28*(7-8), 1125-1134. https://doi.org/10.1111/jocn.14681.

[7]   European Society of Radiology, European Federation of Radiographer Societies. Patient safety in medical imaging: A joint paper of the ESR and the EFRS. *Radiography.* **2019**, *25*(2), e26-e38. https://doi.org/10.1016/j.radi.2019.01.009.

[8]   Grossman, VA. Hot topics: Promoting patient safety in the radiology setting. *Insights Imaging.* **2019**, *10*(1), 1-2. https://doi.org/10.1186/s13244-019-0721-y.

[9]   European Federation of Radiographer Societies. The assessment of image quality and diagnostic value in X-ray images. *Insights Imaging.* **2022**, *13*(1), 1-10. https://doi.org/10.1186/s13244-022-01199-5.

[10]   Diaz, A.; Guizar-Sicairos, M.; Poeppel, A.; Menzel, A.; Bunk, O. Characterization of carbon fibers using X-ray phase nanotomography. *Carbon.* **2014**, *67*, 98-103. https://doi.org/10.1016/j.carbon.2013.09.066.

[11]   Wang, Y.; Yang, Y.; Zong, Z. Carbon fiber-reinforced polymer composites for X-ray transparent medical devices. *J Compos Mater.* **2019**, *54*(1), 39-50. https://doi.org/10.1177/0021998319862295.

[12]   Grob A, Biersach B, Peck J. Risk management and IEC 60601-1: Assessing compliance. *Biomed Sci Instrum.* **2013**, *49*, 55-59. https://doi.org/10.2345/0899-8205-49.s1.55

[13]   Eubanks F, Masters M. Assurance cases: A new form of requirements traceability matrix for medical devices. *INCOSE Int Symp.* **2011**, *21*(1), 1134-1144. https://doi.org/10.1002/j.2334-5837.2011.tb01271.x.

[14]   Lee, S.J.; Chung, I.S. Optimal design of sandwich composite cradle for computed tomography instrument by analyzing the structural performance and X-ray transmission rate. *Materials (Basel).* **2019**, *12*(2), 286. https://doi.org/10.3390/ma12020286.

[15]   Taherdoost, H. What is the best response scale for survey and questionnaire design: Review of different lengths of rating scale/attitude scale/Likert scale. *Int J Acad Res Manag.* **2019**, *1*(2), 1-10.

[16]   Unterweger, C.; Duchoslav, J.; Stifter, D.; Fürst, C. Characterization of carbon fiber surfaces and their impact on the mechanical properties of short carbon fiber reinforced polypropylene composites. *Compos Sci Technol.* **2015**, *108*, 41-47. https://doi.org/10.1016/j.compscitech.2015.01.004.

[17]   Ho, D.; Phan, T.H.T.; Mobbs, R.J.; Reddy, R. The use of radiolucent (carbon fibre-reinforced polymer) pedicle screw fixation for serial monitoring of clear cell meningioma: A case report. *J Surg Case Rep.* **2020**, *2020*(12), rjaa510. https://doi.org/10.1093/jscr/rjaa510.

[18]   Sedaghatian, T.; Momennezhad M, Rasta S, Makhdoomi Y, Abdollahian S. An update of couch effect on the attenuation of megavoltage radiotherapy beam and the variation of absorbed dose in the build-up region. *J Biomed Phys Eng.* **2017**, *7*(3), 279-286.

[19]   Munjal, R.; Negi, P.; Babu, A.; Sinha, S.; Anand, A.; Kataria, T. Impact of 6MV photon beam attenuation by carbon fiber couch and immobilization devices in IMRT planning and dose delivery. *J Med Phys.* **2006**, *31*(2), 67-71. https://doi.org/10.4103/0971-6203.26690.

[20]   Kong, F.; Lu, M.; Dong, J.; Wang, D.; Shi, J.; Li, Z. Effect of linear accelerator carbon fiber couch on radiotherapy dose. *PLoS One.* **2022**, *17*(11), e0277332. https://doi.org/10.1371/journal.pone.0277332.

[21]   Hufton, A.P.; Russell, J. The use of carbon fibre material in table tops, cassette fronts, and grid covers: Magnitude of possible dose reduction. *Br J Radiol.* **1986**, *59*(698), 157-163. https://doi.org/10.1259/0007-1285-59-698-157.

[22]   Howell, J.D. Early clinical use of the X-ray. *Trans Am Clin Climatol Assoc.* **2016**, *127*, 341.

ASEAN J. Sci. Tech. Report. **2025**, *28*(3), e255648.

11 of 11

[23] Miller, D.L.; Kakar, S., Jiang, L., Spelic, D.C.; Burk, L. The US Food and Drug Administration's role in improving radiation dose management for medical X-ray imaging devices. *Br J Radiol.* **2021**, *94*(1126), 20210373. https://doi.org/10.1259/bjr.20210373.

Biodiesel Production from *Chlorella sp.*

Danang Jaya[1*], Heni Anggorowati[2], Putri Restu Dewati[3], Rifka Azzahra Artha Kinara[4], and Niken Widiawati[5]

[1] Faculty of Industrial Technology, Universitas Pembangunan Nasional "Veteran" Yogyakarta, 5598, Indonesia
[2] Faculty of Industrial Technology, Universitas Pembangunan Nasional "Veteran" Yogyakarta, 5598, Indonesia
[3] Faculty of Industrial Technology, Universitas Pembangunan Nasional "Veteran" Yogyakarta, 5598, Indonesia
[4] Faculty of Industrial Technology, Universitas Pembangunan Nasional "Veteran" Yogyakarta, 5598, Indonesia
[5] Faculty of Industrial Technology, Universitas Pembangunan Nasional "Veteran" Yogyakarta, 5598, Indonesia
* Correspondence: danangjay@upnyk.ac.id

Abstract: This research utilizes the microalgae *Chlorella sp.* as a raw material for biodiesel production through the in-situ microwave-assisted transesterification method with the addition of a co-solvent. This study examines the effects of microwave power, reaction time, H_2SO_4 catalyst concentration on biodiesel yield. The study results show that using the in-situ microwave-assisted transesterification method with hexane as a co-solvent can increase the efficiency of biodiesel production from the microalgae *Chlorella sp.* The optimal conditions were a transesterification time of 7 minutes and a catalyst concentration of 0.3 M, which produced the highest biodiesel yield of 77.32%.

Keywords: Renewable energy; microalgae; biofuel; microwave; in situ transesterification

1. Introduction

Indonesia has several alternative energy potentials, including biogas, bioethanol, and biodiesel. Biodiesel has characteristics similar to those of fossil-based diesel engine fuels. It is environmentally friendly because it produces lower combustion emissions compared to petroleum-based diesel fuels and can decompose naturally. It is a renewable energy source [1, 2]. Biodiesel can be produced from various sources, such as vegetable oil, animal fat, and algae [3]. Microalgae, in particular, present a promising raw material for biodiesel production [4-5]. Among these, *Chlorella sp.* is known for its high lipid content, making it an ideal candidate for biodiesel feedstock. The oil content in *Chlorella sp.* is about 21.3%, with the major fatty acids being palmitic acid and oleic acid [6]. A practical method is needed to break down the rigid cell walls of the microalgae, allowing for more efficient oil extraction.

In situ transesterification is a cost-effective and straightforward method for biodiesel production [7-9]. This process, also known as direct transesterification [10], allows extraction and transesterification to coincide, with alcohol serving as both the solvent and the reactant [11]. Combining these steps, in situ transesterification eliminates the need for separate oil extraction and purification processes, making it highly efficient [7]. Further research is needed to explore the potential of *Chlorella sp.* microalgae for biodiesel production using in situ transesterification with an H_2SO_4 catalyst.

ASEAN J. Sci. Tech. Report. **2025**, *28*(3), e256650.

2 of 7

2. Materials and Methods

2.1 Materials

The microalgae (*Chlorella sp.*) used in this study were commercially sourced from PT. Spiralife Biotechnology Indonesia in dried powder form with a moisture content of approximately 5%. No further drying or particle size modification was conducted, and the biomass was used as received. Methanol (CH_3OH), n-hexane, ethanol, KOH, and a H_2SO_4 catalyst were obtained from Merck.

2.2 Methods

Ten grams of microalgae were placed in a 250 mL three-neck round-bottom flask, adding 150 ml of a hexane and methanol solvent mixture in a 3:2 (v/v) ratio. A catalyst was added according to the predetermined concentrations (0.1, 0.2, 0.3, 0.4, and 0.5 N). The three-neck flask was then placed in the microwave. The flask was positioned in the center of the microwave cavity and stirred with a magnetic stirrer. Microwave-assisted in-situ transesterification was conducted at five power settings: 136 W, 264 W, 440 W, 616 W, and 800 W. Each run was performed for 3, 5, 7, 9, 11, or 13 minutes in continuous mode. No intervals or cooling periods were applied during the operation. After each run, the flask was cooled at room temperature (±27 °C), and the temperature was measured using an infrared thermometer. The final mixture was then separated and analyzed.

3. Results and Discussion

3.1 Effect of Extraction Power Variation on Microalgae Oil Yield

The yield of microalgal oil influences the biodiesel yield produced. In the in situ process, the extraction and transesterification processes are carried out directly, meaning that it is not possible to analyze the yield of extracted microalgal oil using the in situ method. However, this study conducted a separate process to analyze the amount of oil that can be extracted from microalgae by varying the microwave power. This separate process was used to determine how much oil can be extracted and react to form biodiesel.
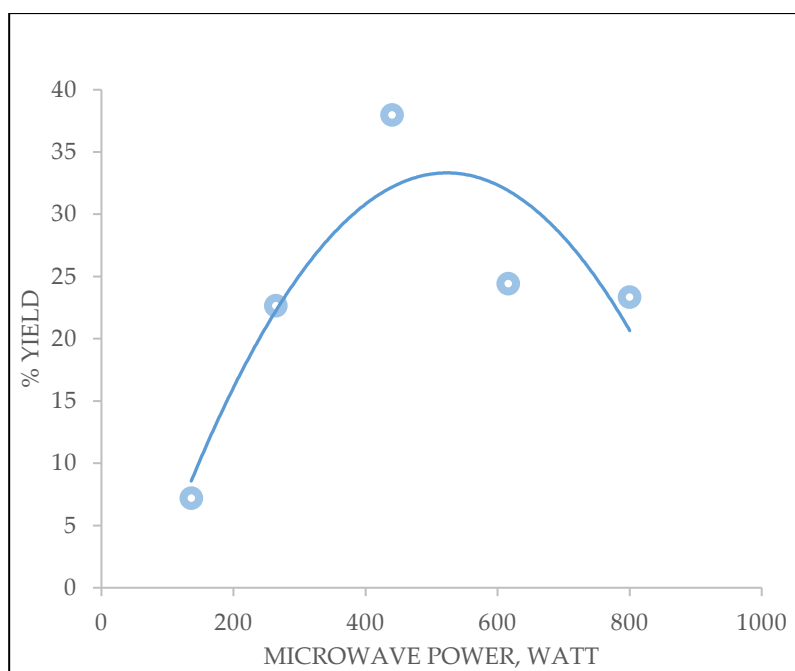
Figure 1. Relationship Between Microwave Power (136 watts, 264 watts, 440 watts, 616 watts, and 800 watts) and Microalgal Oil Yield Percentage.

Figure 1 illustrates the results of the extraction process at different microwave power levels: 136 watts, 264 watts, 440 watts, 616 watts, and 800 watts. Identifying the optimal microwave power for oil extraction from

ASEAN J. Sci. Tech. Report. **2025**, *28*(3), e256650.

3 of 7

Chlorella sp. maximizes oil yield. The findings indicate that the optimal power level, which produces the highest oil yield, is 440 watts. The data shows that 800-watt power provides a higher temperature than other powers.

Power is related to temperature [12], according to the formula:

$$P \cdot t = m \cdot c \cdot \Delta T \tag{1}$$

with: P = Microwave Power (Watt)
t   = Time (s)
m = Mass of microalgae (kg)
c   = specific heat (J kg^{-1} ^{o}C^{-1})
ΔT = temperature difference (^{o}C)

As shown in Equation 1, the relationship between power and temperature is directly proportional. This indicates that an increase in power leads to a more substantial change in temperature. High temperatures can help break down cell walls, facilitating contact between methanol and oil and producing higher yields. However, as indicated in Equation 1, a continuous increase in power will lead to even higher temperatures. Excessive heat at elevated temperatures may damage the biomass [13-15], causing it to dry out and potentially burn [16].

3.2 The Effect of Reaction Time on Biodiesel Yield

Figure 2 presents the results of a study examining the effect of transesterification time on biodiesel yield at a microwave power setting of 440 watts.
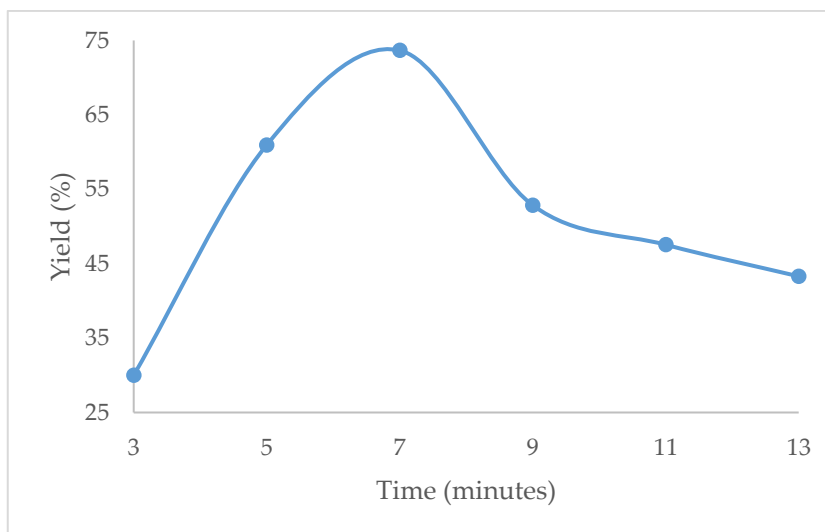
Figure 2. Effect of Extraction Time Variation (3, 5, and 7 minutes) on Biodiesel Yield

Figure 2 illustrates the results of the transesterification process conducted at a power setting of 440 watts. Biodiesel yield increased at 3, 5, and 7 minutes, with yields of 30%, 60.94%, and 73.66%, respectively. By the 7th minute, the biodiesel yield reached its optimum or equilibrium point, indicating that further reaction time would not enhance the yield. However, at the 9th minute, the yield decreased to 52.85%. Prolonged extraction times can result in excessive heating, significant solvent loss, the formation of by-products, and energy loss in the process. Compared to previous reports, the biodiesel yield of 73.66% obtained in this study after 7 minutes at 440 W is notably high. For instance, [17] reported a biodiesel yield of 68% from microalgae using microwave-assisted transesterification under similar conditions. Meanwhile, [18] achieved only 60% yield when using hexane as a co-solvent with waste cooking oil as feedstock. These differences may be attributed to the optimized microwave power applied in our study, the relatively short reaction time, and the synergistic effect of hexane as a co-solvent, which enhances methanol–lipid interaction. Furthermore, the direct use of *Chlorella sp.* with high lipid content and the simultaneous extraction–reaction strategy significantly

improve over conventional multistep methods. Integrating co-solvent and controlled microwave power likely contributed to better mass transfer and thermal efficiency, resulting in higher biodiesel yield within a shorter time frame.

The observed decline in yield at 9 minutes may be attributed to thermal degradation of fatty acid methyl esters (FAME) due to prolonged exposure to high temperatures. The excessive duration may also lead to methanol evaporation, decreasing reactant availability, or promoting side reactions such as soap formation and reverse esterification. These thermal and chemical instabilities likely reduced conversion efficiency beyond the optimal reaction time. Specifically, the decline in yield at the 9th minute may be attributed to thermal degradation of fatty acid methyl esters (FAME) due to prolonged exposure to microwave energy. Elevated temperatures can lead to ester breakdown, methanol evaporation, and reduced reactant availability. In addition, the extended heating period in the presence of an acid catalyst (H_2SO_4) may promote reverse reactions or unwanted side reactions such as saponification. These phenomena collectively reduce the efficiency of the transesterification process and result in a sharp decline in biodiesel yield after the optimal reaction time.

3.3 The Effect of H_2SO_4 Catalyst Concentration on Biodiesel Yield

This in situ transesterification process utilized microalgae powder, with methanol as solvent, hexane as co-solvent, and employed an acidic homogeneous catalyst, specifically H_2SO_4. Methanol is the reactant due to its polar nature and short carbon chain. The homogeneous acid catalyst H_2SO_4 is more effective than base catalysts because it can produce a higher yield by converting free fatty acids (FFA) into fatty acid methyl esters (FAME). During the in situ transesterification process, the addition of a co-solvent, such as hexane, results in the formation of a single-phase solution. Although hexane and methanol do not typically mix, a sufficient volume of methanol creates a homogenous solution. As a co-solvent, hexane enhances the solubility of oil in methanol [17][18]. The addition of hexane reduces the interfacial surface tension between oil and methanol, forming a single-phase liquid. This improved mixing facilitates better contact between the reactants, thereby increasing the reaction rate. A single-phase solution is a key factor in the in situ transesterification process, as it significantly enhances the yield of crude biodiesel. Initial extraction was conducted by varying the extraction time to determine the optimum duration. The extraction process involved 10 grams of powdered microalgae and time variations of 3, 5, 7, 9, 11, and 13 minutes, carried out at a microwave power setting of 440 watts, resulting in the highest yield at 7 minutes. Following extraction, transesterification was performed using a fixed biomass-to-methanol ratio of 1:15 (wt/vol) while varying the catalyst concentration. The study commenced by weighing 10 grams of microalgae powder and mixing it with methanol and hexane as co-solvents, followed by the addition of H_2SO_4 catalyst in varying concentrations of 0.1, 0.2, 0.3, 0.4, and 0.5 M.
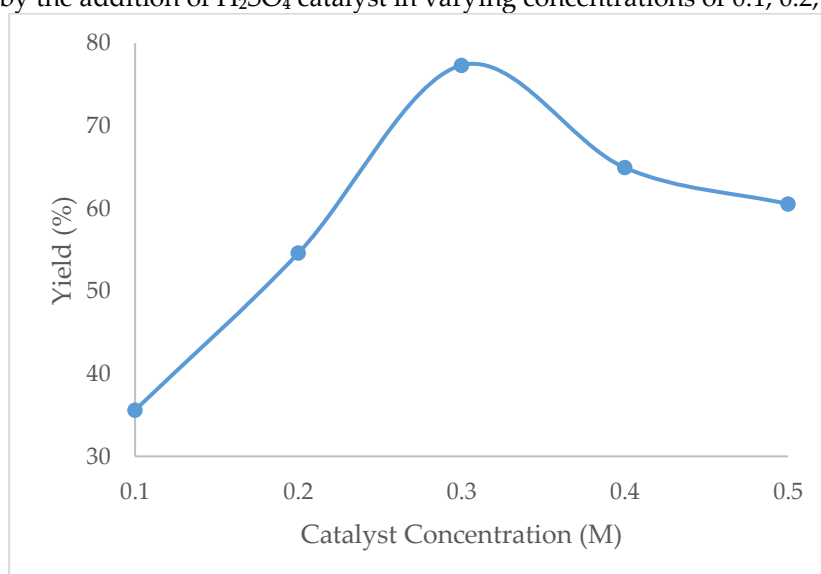
Figure 3. The Effect of H_2SO_4 Catalyst Concentration (0.1, 0.2, 0.3, 0.4, and 0.5 M) on Biodiesel Yield

Figure 3 illustrates the effect of varying H_2SO_4 catalyst concentrations on biodiesel yield. The respective yields at catalyst concentrations of 0.1, 0.2, 0.3, 0.4, and 0.5 M were 35.6%, 54.59%, 77.32%, 64.93%, and 60.53%. The results indicate that increasing the concentration of the H_2SO_4 catalyst from 0.1 M to 0.3 M leads to a substantial increase in biodiesel yield, peaking at 77.32%. This trend aligns with findings from [19], who reported that higher concentrations of H_2SO_4 catalyst reduce the percentage of free fatty acids (%FFA), thereby enhancing biodiesel production. However, as the catalyst concentration is increased beyond 0.3 M, a decline in yield is observed. This reduction may be attributed to the adverse effects of high acid catalyst concentrations, which can lead to alcohol dehydration. Such dehydration can inhibit the transesterification process, reducing overall biodiesel yield.

3.4 GC-MS Analysis Results

From the analysis, the following data was obtained:

Table 1. Results of GC-MS Analysis of Biodiesel

Compounds Analyzed	Amount (%)
9-Octadecanoic acid	19.24
Benzene, 1-ethyl-2-methyl	3.83
Decane	1.67
Hexadecanoic acid, methyl ester	10.06
Hexadecanoic acid	1.47
13-Hexyloxacyclotridec-10-en-2-one	5.65
9-Octadecenoic acid, methyl ester	46.34
Octadecenoic acid, methyl ester	11.73

Table 1 shows that the biodiesel content in the reaction product is 68.14%, with a remaining free fatty acid content of 20.72%. The remainder consists of other compounds, such as 13-Hexyloxacyclotridec-10-en-2-one, an antioxidant compound at 5.65%. The GC-MS analysis revealed that the biodiesel obtained contains 68.14% FAMEs, which does not meet the minimum standard of 96.5% set by SNI 7182:2015. This indicates that additional purification steps are necessary to enhance fuel quality before it can be applied in diesel engines. Future studies should focus on improving the transesterification efficiency and integrating purification techniques to meet the standard biodiesel quality.

4. Conclusions

The study results showed that using the in-situ microwave-assisted transesterification method with hexane co-solvent can increase the efficiency of biodiesel production from the microalgae *Chlorella sp*. The optimal conditions were found at a transesterification time of 7 minutes and a catalyst concentration of 0.3 M, which produced the highest biodiesel yield of 77.32%. Future research should explore the other variables of optimization of process parameters and evaluate the physicochemical properties of the biodiesel, including cetane number, viscosity, density, thermal, and oxidative stability. Additionally, studies focusing on the scale-up potential of this method, as well as a thorough techno-economic analysis, are essential for evaluating its feasibility in industrial applications. These aspects, which were beyond the scope of the present work, are recommended for future investigation.

5. Acknowledgements

ASEAN J. Sci. Tech. Report. **2025**, *28*(3), e256650.

6 of 7

References

[1] Edeh, I. Biodiesel Production as a Renewable Resource for the Potential Displacement of the Petroleum Diesel. In Biorefinery Concepts, Energy and Products; Beschkov, V., Ed.; IntechOpen: London, **2020**. https://doi.org/10.5772/intechopen.93013

[2] Rezania, S.; Taib, S. M.; Din, M. F. M.; Dahalan, F. A.; Kamyab, H.; Ariffin, H.; Montoya, L. H.; Mohammadi, A. A. Review on Transesterification of Non-Edible Sources for Biodiesel Production with a Focus on Economic Aspects, Fuel Properties and By-Product Applications. *Energy Convers. Manag.* **2019**, *201*, 112155. https://doi.org/10.1016/j.enconman.2019.112155.

[3] Hassan, M. H.; Kalam, M. A. An Overview of Biofuel as a Renewable Energy Source: Development and Challenges. *Procedia Eng.* **2013**, *56*, 39-53. https://doi.org/10.1016/j.proeng.2013.03.087.

[4] Zhang, S.; Zhang, L.; Xu, G.; Li, F.; Li, X. A Review on Biodiesel Production from Microalgae: Influencing Parameters and Recent Advanced Technologies. *Front. Microbiol.* **2022**, *13*, 970028. https://doi.org/10.3389/fmicb.2022.970028.

[5] Pandey, S.; Narayanan, I.; Selvaraj, R.; Varadavenkatesan, T.; Vinayagam, R. Biodiesel Production from Microalgae: A Comprehensive Review on Influential Factors, Transesterification Processes, and Challenges. *Fuel* **2024**, *367*, 131547. https://doi.org/10.1016/j.fuel.2024.131547.

[6] Mathimani, T.; Sekar, M.; Shanmugam, S.; Sabir, J. S. M.; Chi, N. T. L.; Pugazhendhi, A. Relative Abundance of Lipid Types among Chlorella sp. and Scenedesmus sp. and Ameliorating Homogeneous Acid Catalytic Conditions Using Central Composite Design (CCD) for Maximizing Fatty Acid Methyl Ester Yield. *Sci. Total Environ.* **2021**, *771*, 144700. https://doi.org/10.1016/j.scitotenv.2020.144700.

[7] Go, A. W.; Sutanto, S.; Ong, L. K.; Tran-Nguyen, P. L.; Ismadji, S.; Ju, Y. H. Developments in In-Situ (Trans) Esterification for Biodiesel Production: A Critical Review. *Renew. Sustain. Energy Rev.* **2016**, *60*, 284-305. https://doi.org/10.1016/j.rser.2016.01.070.

[8] Kasim, F. H.; Harvey, A. P.; Zakaria, R. Biodiesel Production by In Situ Transesterification. *Biofuels* **2010**, *1*(2), 355-365. https://doi.org/10.4155/bfs.10.6.

[9] Rodrigues, M. C.; Cunha, S.; Teixeira, L. S. G. In Situ Transesterification from Soybean Seed Using Mechanochemical Methods Toward Producing Biodiesel. *ACS Omega* **2023**, *8*(50), 47791-47797. https://doi.org/10.1021/acsomega.3c06269.

[10] Makareviciene, V.; Sendzikiene, E.; Gumbyte, M. Application of Simultaneous Oil Extraction and Transesterification in Biodiesel Fuel Synthesis: A Review. *Energies* **2020**, *13*(9), 2204. https://doi.org/10.3390/en13092204.

[11] Tuntiwiwattanapun, N.; Monono, E.; Wiesenborn, D.; Tongcumpou, C. In-Situ Transesterification Process for Biodiesel Production Using Spent Coffee Grounds from the Instant Coffee Industry. *Ind. Crops Prod.* **2017**, *102*, 23–31. https://doi.org/10.1016/j.indcrop.2017.03.019.

[12] Amarulloh, A.; Haikal, H.; Atmoko, N. T.; Utomo, B. R.; Setiadhi, D.; Marchant, D.; Zhu, X.; Riyadi, T. W. B. Effect of Power and Diameter on Temperature and Frequency in Induction Heating Process of AISI 4140 Steel. *Mech. Eng. Soc. Ind.* **2022**, *2*(1), 26-34. https://doi.org/10.31603/mesi.6782.

[13] Ali, M.; Watson, I. A. Microwave Thermolysis and Lipid Recovery from Dried Microalgae Powder for Biodiesel Production. *Energy Technol.* **2016**, *4*(2), 319-330. https://doi.org/10.1002/ente.201500242.

ASEAN J. Sci. Tech. Report. **2025**, *28*(3), e256650.

7 of 7

[14] Gil-Martín, E.; Forbes-Hernández, T.; Romero, A.; Cianciosi, D.; Giampieri, F.; Battino, M. Influence of the Extraction Method on the Recovery of Bioactive Phenolic Compounds from Food Industry By-Products. *Food Chem*. **2022**, *378*, 131918. https://doi.org/10.1016/j.foodchem.2021.131918.

[15] Chaves, J. O.; de Souza, M. C.; da Silva, L. C.; Lachos-Perez, D.; Torres-Mayanga, P. C.; da Fonseca Machado, A. P.; Forster-Carneiro, T.; Vázquez-Espinosa, M.; González-de-Peredo, A. V.; Barbero, G. F.; Rostagno, M. A. Extraction of Flavonoids from Natural Sources Using Modern Techniques. *Front. Chem*. **2020**, *8*, 507887. https://doi.org/10.3389/fchem.2020.507887.

[16] Bintari, Y. R.; Haryadi, W.; Rahardjo, T. J. Ekstraksi Lipida dengan Metode Microwave Assisted Extraction dari Mikroalga yang Potensial sebagai Biodiesel. JU-ke **2018**, *2*(2), 180-189.

[17] Qadariyah, L.; Mujaddid, F.; Bhuana, D. S.; Mahfud, M. Biodiesel Production from Microalgae with Trans-Esterification Method Using Microwave. *IOP Conf. Ser. Mater. Sci. Eng*. **2019**, *543*(1), 012073. https://doi.org/10.1088/1757-899X/543/1/012073.

[18] Mohadesi, M.; Moradi, G.; Ghanbari, M.; Moradi, M. J. Investigating the Effect of n-Hexane as Solvent on Waste Cooking Oil Conversion to Biodiesel Using CaO on a New Support as Catalyst. *Meas. J. Int. Meas. Confed*. **2019**, *135*, 606-612. https://doi.org/10.1016/j.measurement.2018.12.022.

[19] Ramadhas, A. S.; Jayaraj, S.; Muraleedharan, C. Biodiesel Production from High FFA Rubber Seed Oil. *Fuel* **2005**, *84*(4), 335-340. https://doi.org/10.1016/j.fuel.2004.09.016.

Reduction of Sound Pressure Levels with Noise Barriers Containing Agricultural Residues: Case Study

Pasit Tinnam[1, 2], Nantakrit Yodpijit[2*], Suparoek Junsupasen[3], Manote Sappakittipakorn[4], and Manutchanok Jongprasithporn[5]

[1] Faculty of Engineering and Industrial Technology, Bansomdejchaopraya Rajabhat University, Bangkok, 10600, Thailand
[2] Center for Innovation in Human Factors Engineering and Ergonomics (CIHFE^2), Department of Industrial Engineering, Faculty of Engineering, King Mongkut's University of Technology North Bangkok, Bangkok, 10800, Thailand
[3] Faculty of Engineering, King Mongkut's University of Technology North Bangkok, Bangkok, 10800, Thailand
[4] Faculty of Engineering, King Mongkut's University of Technology North Bangkok, Bangkok, 10800, Thailand
[5] School of Engineering, King Mongkut's Institute of Technology Ladkrabang, Bangkok, 10520, Thailand
* Correspondence: nantakrit.y@eng.kmutnb.ac.th

Abstract: Over the past decade, PM 2.5 pollution has become an increasingly serious environmental concern in Thailand, with one of its primary sources being the open burning of agricultural residues, particularly sugarcane residues. To mitigate this issue, it is essential to develop alternative applications for sugarcane leaves that eliminate the need for burning. This study investigates a sustainable approach by incorporating sugarcane leaves into producing noise insulation mortar boards. The research aims to assess these boards' acoustic performance through a combination of laboratory experiments and field testing. Employing the Design of Experiments (DOE) methodology, mortar samples were prepared with sugarcane leaf content at 2%, 4%, 6%, 8%, and 10% by cement weight to identify the optimal mixture. Analysis of variance (ANOVA) indicated that the sugarcane leaf content had a statistically significant effect on sound pressure level reduction at a 95% confidence level. Both laboratory and field results demonstrated that the 4% sugarcane leaf mixture yielded the highest performance, achieving noise reductions of 20.6 dBA and 23 dBA, respectively. These findings confirm that mortar boards reinforced with sugarcane leaves effectively reduce noise and offer a viable solution for repurposing agricultural residues. This approach contributes to noise pollution mitigation and addresses environmental concerns related to the open burning of biomass.

Keywords: Agricultural residues; noise insulation; sugarcane leaves; ANOVA

1. Introduction

PM 2.5 is a pollution problem that has affected the environment in Thailand for the past ten years. Burning waste material after sugarcane harvest is a long-standing practice of Thailand's farmers as it can be disposed of quickly and cheaply. Burning sugarcane generates high heat, causing rapid combustion and higher dust vaporization in the air at 2,250 meters and drifting up to 16 kilometers [1]. Sugarcane is one of Thailand's most important cash crops, growing mainly in northeastern and central areas. Each year, a large amount of produce is released to the market. In 2019, Thailand's sugarcane plantations exceeded 78,600 square kilometers, yielding more than 130 million tons [2]. As a

ASEAN J. Sci. Tech. Report. **2025**, 28(3), e257762.

2 of 12

result of this output, more than 22 million tons of harvest waste were generated [3]. Currently, there is an inclination to use agricultural residues materials in various production industries due to their main strengths: being cheap and environmentally friendly. Studies have shown that many types of agricultural residue materials are used in the production of sheets to study their properties in various applications, such as thermal protection properties of various fiber crops [4-6], sound control properties from hemp fibers, kenaf fibers, coconut fiber, reed grating, cork, reeds, straw bale [5-7]. Many researchers have studied the physical and structural characteristics of concrete mixed with various natural fibers, including coconut fiber [8-11], corn fiber [12], and bamboo fiber [13]. Regarding noise insulation, sound control properties from concrete mixed with date palm were studied [14]. Concrete with straw fibers has a better sound absorption ability than unmixed materials [15]. Corncob concrete has good sound absorption capabilities in the low-frequency range [16]. From comparing the sound-absorbing properties of concrete with a mixture of 5 substitute materials, it was found that corn cob slit perches with a thickness of 40 mm have the best sound absorption capacity [17]. The review results show the research on developing soundproofing materials using agricultural residues as an ingredient. Most studies focus on sound absorption properties, unlike this research, which focuses on sound transmission protection properties. The literature review [5-7,14,16-17] revealed that most research on the development of soundproofing materials using agricultural residues as a component has focused on sound absorption properties. In contrast, this study emphasizes the characteristics of sound transmission loss. Burning agricultural residues, particularly sugarcane leaves, significantly contributes to PM2.5 pollution in Thailand. This study addresses the urgent need to reduce such practices by developing sound insulation boards incorporating sugarcane leaves, thus providing a practical and environmentally beneficial alternative to waste disposal.

The major goal of this study is to develop and evaluate sound insulation boards made from agricultural residues, specifically sugarcane leaves, as a practical and sustainable solution for industrial noise mitigation. This approach also reduces air pollution, improves waste management, and promotes environmentally friendly building materials. The environmental implications of inappropriate waste disposal methodologies necessitate innovative solutions. Consequently, this research proposes the development of sound insulation panels fabricated from mortar composite incorporating sugarcane leaf waste. This approach serves the dual purpose of waste valorization and potentially mitigating the prevalent practice of agricultural residue incineration, thereby reducing particulate matter emissions and atmospheric pollution. Our methodology employed laboratory-scale prototype development utilizing design of experiments (DOE) principles and Analysis of Variance (ANOVA) for statistical validation. Subsequently, the fabricated panels were implemented in a field environment to evaluate their acoustic attenuation performance through insertion loss measurements, comparing empirical results with theoretical predictions from the laboratory phase.

2. Materials and Methods

2.1 Design of experiments to produce prototype sound insulation boards for laboratory testing

The design of experiments methodology was employed to fabricate sound insulation panels from mortar-sugarcane leaf composite materials. The independent variable in this study was the proportion of sugarcane leaf content, while the dependent variable was the sound transmission loss, measured as reduced sound pressure level. Before the primary investigation, preliminary trials were conducted to determine the maximum proportion of sugarcane leaf material to maintain structural integrity in the composite panels. Results from these preliminary experiments, testing 16%, 13%, and 10% sugarcane leaf content relative to cement weight, demonstrated that specimens with 16% and 13% leaf content failed to achieve adequate structural stability. Consequently, the maximum sugarcane leaf dosage was established at 10%, with subsequent experimental formulations decremented at 2% intervals. The mortar composition ratios utilized in this study are presented in Table 1.

ASEAN J. Sci. Tech. Report. **2025**, *28*(3), e257762.

3 of 12

Table 1. Proportion of mortar mixing

Proportion of sugarcane leaves by cement weight (%)	Item weight (kg)			
	Cement	Sand	Water	Sugarcane leave
0	2.880	6.480	1.728	0
2	2.880	6.480	1.728	0.058
4	2.880	6.480	1.728	0.115
6	2.880	6.480	1.728	0.173
8	2.880	6.480	1.728	0.230
10	2.880	6.480	1.728	0.288

The sugarcane leaves used in this research are post-harvest sugarcane leaves from Suphan Buri province, located in central Thailand. The sugarcane leaves are collected, cleaned, dried, and cut into 10-20 mm lengths before being mixed with mortar. This study employed a Portland cement-based mortar mixed by weight at a cement-to-sand ratio of 1:2.25 and a water-to-cement ratio of 0.6. This mix proportion was selected because it falls within the standard range for general-purpose mortar and was verified through preliminary trials to ensure sufficient strength and workability. All samples were subjected to 28 days of air-dried curing before testing to allow for proper hydration and material stabilization. Samples of prepared sugarcane leaves and an insulation plate sample are shown in Figure 1 (a) and (b), respectively.

The acoustic performance evaluation was conducted utilizing a custom-designed sound pressure testing chamber with a dual-compartment configuration, as illustrated in Figure 2. The apparatus consists of a source chamber and a receiving chamber separated by a test aperture where specimens are mounted. Figure 2(a) depicts the interior of the testing cabinet with the positioning of the sound source (on the left) and microphones (on the right) for precise sound pressure level measurements. In contrast, Figure 2(b) demonstrates the installation methodology of the sugarcane-cement composite insulation panel. The specimen was securely affixed between the chambers using hinged mounting brackets to ensure proper sealing and eliminate acoustic leakage. During the experimental procedure, broadband noise was generated in the source chamber, and the sound transmission loss through the test specimen was measured via calibrated microphones in both chambers. This experimental setup complies with standard measurement protocols for determining building materials' sound transmission class (STC), allowing for systematic quantification of the acoustic insulation properties of the fabricated bio-composite panels.

Figure 1. Samples of prepared sugarcane leaves(a) and insulation plate(b)

ASEAN J. Sci. Tech. Report. **2025**, *28*(3), e257762.

4 of 12
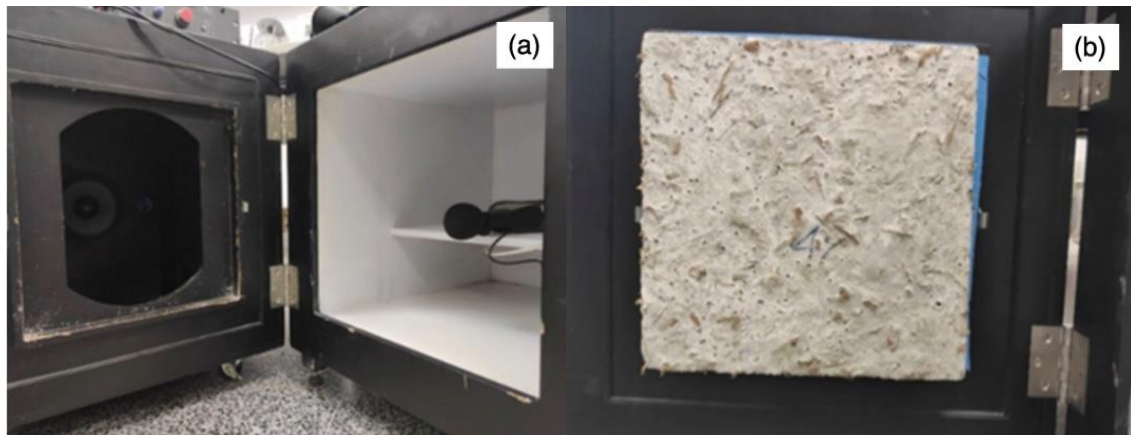
Figure 2. Sound pressure testing cabinet(a) and sample insulation plate during installation(b)

Figure 3. Sound Pressure Meter (Brüel & Kjær model 2270)

Brüel & Kjær model 2270, a noise measurement instrument shown in Figure 3, was used to measure sound pressure levels in the 200-20,000 Hz frequency range in both laboratory and field testing. This measuring device is calibrated in compliance with the IEC 61672-1 standard [18].

2.2 Design of experiments for field testing

2.2.1 Noise survey

The initial field testing phase was conducted at a block brick manufacturing facility, as illustrated in Figure 4, in Suphan Buri province, Thailand. Following site selection, researchers surveyed sound pressure levels, specifically along three sides of the factory perimeter, that generated significant noise pollution affecting the surrounding community. These critical areas were designated as Position A, B, and C, as shown in Figure 5, each representing different boundary interfaces between the industrial operation and neighboring residential zones. Subsequently, after comprehensive acoustic analysis, only the side exhibiting the highest sound pressure levels was selected for intervention. This identified location became the installation site for noise barriers constructed using the developed sugarcane leaf-incorporating mortar plates. This strategic implementation allowed researchers to evaluate the bio-composite barriers' maximum potential noise reduction capability under the most challenging real-world conditions.

Figure 4. Example of a machine used in the production of brick blocks
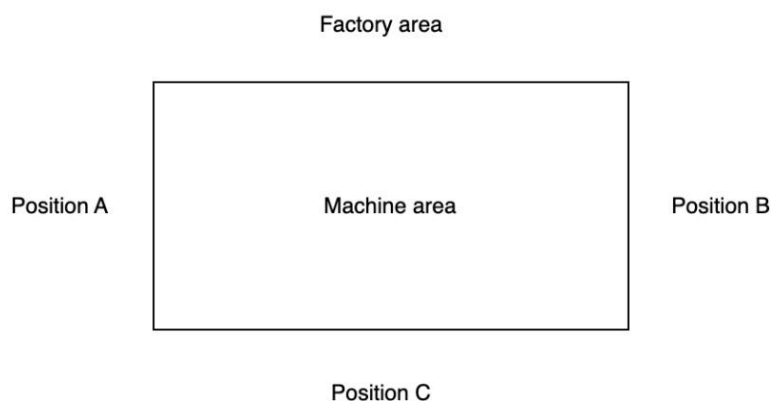
Figure 5. Position A, B, and C

2.2.2 Design and installation of noise barrier

The sample soundproof wall, a size 15 meters wide and 3 meters high, was designed and constructed from mortar mixed with sugarcane leaves and was installed in position C, as shown in Figure 6, where the sound pressure level was initially measured and found to have the highest sound pressure level to test for insertion loss. The barrier was located 3 meters from the noise source (block brick machine), as shown in Figure 7. The method for measuring in this work is a direct insertion loss measurement based on ISO 10847:1997 [19], which involves measuring the sound pressure in the same area before and after the sound barrier's installation. The sound pressure meter was positioned 5 meters away from the barrier and 1.5 meters above the ground, and the fabrication and installation of the noise barrier were illustrated in Figure 8 [20-22]. The production and installation of the noise barrier are shown in Figure 8. The findings on the mortar plate tests in the laboratory revealed that incorporating sugarcane leaves, at 2-10% by weight, resulted in a greater reduction in sound pressure levels compared to plates without sugarcane leaves. Among the tested variations, the 4% sugarcane leaf addition achieved the most significant reduction of 20.6 dBA. Based on these preliminary results, the researcher selected the 4% sugarcane leaf mixture for further testing in this field testing. Previous studies indicated that sound reflections from building ceilings and diffraction over the upper edge of partition walls are recognized transmission paths that can markedly degrade barrier performance. Ceiling reflections have been shown to lower indoor barrier insertion loss [23]. A 3-meter-high wall constructed from sugarcane leaves was strategically positioned to minimize diffraction by increasing the vertical obstruction to sound waves. In addition, an absorptive ceiling treatment using mineral wool was specified to reduce sound reflections from the ceiling surface, which is known to lower indoor barrier insertion loss. Together, these measures were intended to enhance the acoustic performance of the barrier by mitigating both ceiling reflections and diffraction-induced sound transmission, thereby improving the overall noise reduction within the enclosed space.

Figure 6. Production soundproof plate(a) and installation soundproof wall(b)
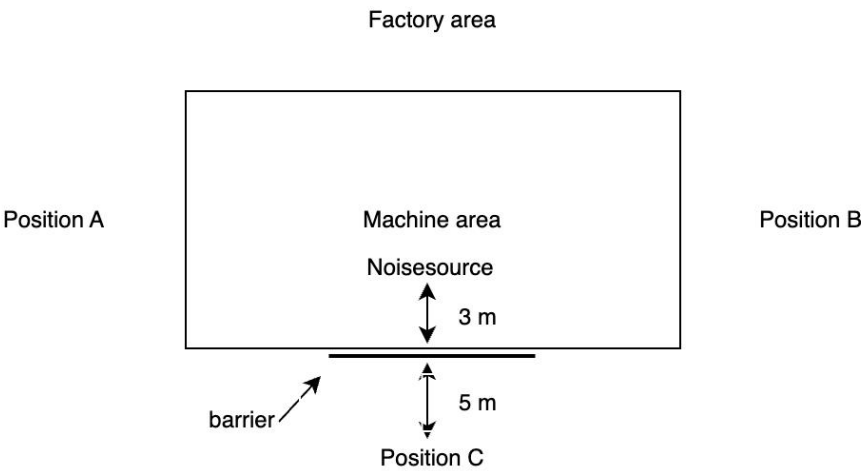
Figure 7. Position and distance for sound measurement (top view)
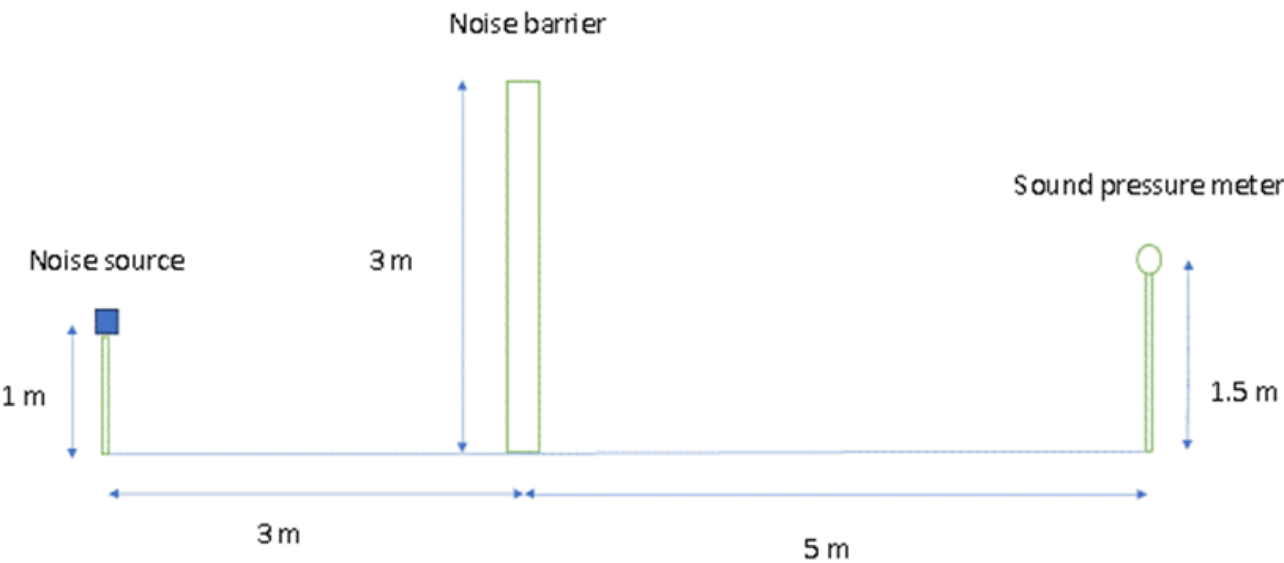
Figure 8. Position and distance for sound measurement (side view)

ASEAN J. Sci. Tech. Report. **2025**, *28*(3), e257762.

7 of 12

3. Results and Discussion

3.1 Sound pressure reduction test results and statistical analysis

The results of the laboratory sound reduction ability test are shown in Table 2.

Table 2. Test results of sound pressure reduction of sample insulation plates

Sample	Reduction of sound pressure levels at various sugarcane leaf proportions (dBA)					
	0%	2%	4%	6%	8%	10%
Sample 1	10.22	19.95	20.40	15.50	17.53	17.03
Sample 2	10.03	19.59	20.76	15.89	17.36	16.51
Sample 3	10.35	17.91	20.64	16.01	16.98	16.26
Average	10.20 ± 0.16	19.15 ± 1.09	20.60 ± 0.18	15.80 ± 0.27	17.29 ± 0.28	16.60 ± 0.39

The table shows that adding sugarcane leaves to insulation plates generally improves sound pressure reduction, with the best performance observed at a 4% proportion (average of 20.6 dBA reduction). Increasing the sugarcane leaf proportion beyond 4% decreases sound insulation effectiveness, although it remains better than the baseline (0% sugarcane leaves). There is some variation in performance between the three samples tested, but the overall trend holds. Data analysis was carried out using the Minitab program version 19. The data were analyzed for variance by determining a significance level of 0.05. The results are summarized as shown in Table 3.

Table 3. Statistics analysis results

Source	DF	Adj SS	Adj MS	F-Value	P-Value
% Sugarcane leaves	5	193.735	38.7470	150.01	0.000
Error	12	3.100	0.2583		
Total	17	196.835			

From the ANOVA, a P-value of 0.000 less than the 0.05 significant level indicates that the main hypothesis is rejected, so it can be concluded that the proportion of sugarcane leaves affects the ability to reduce the sound pressure level at a significant level of 0.05.
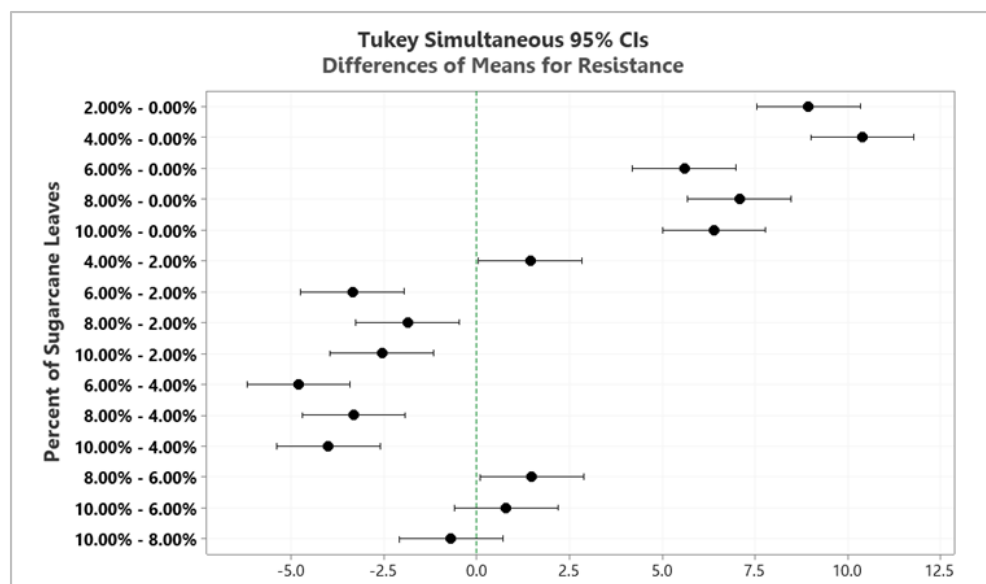
Figure 9. Comparison of Tukey Simultaneous 95%

The results of Tukey Simultaneous 95% CIs showed that the ability to decrease sound pressure level of the proportion of sugarcane leaves between (6%,10%) and (8%, 10%) are not significantly different, and all of the other pairs are significantly different as shown in Figure 9.

According to the test results, there is a difference in soundproofing properties between mortar without sugarcane leaves and sugarcane leaf blend, likely because sugarcane leaves increase pores in the mortar, which is similar to the other studies [14, 24], which concluded from the study of the sound-regulating properties of corn- crop mixing in concrete.

3.2 Preliminary sound pressure measurement results

The results of measuring sound pressure levels in the factory area at frequencies between 12.5-16000 Hz and A-Weighting at 3 positions (A, B, and C) are illustrated in Figure 10.
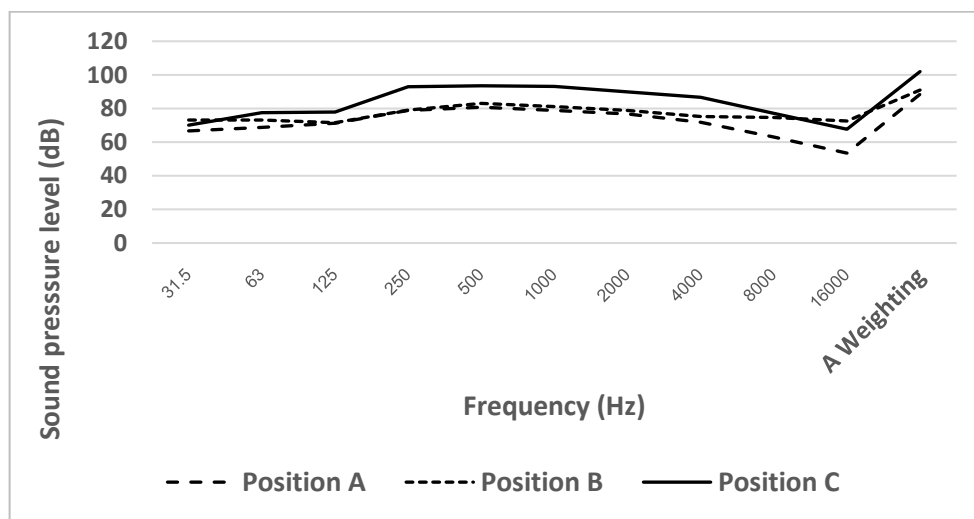
Figure 10. Sound pressure measurement results at positions A, B, and C

Sound pressure measurements in all three predetermined areas showed that the maximum sound pressure levels were measured within the frequency range of approximately 500 Hz. Sound pressure levels tend to decrease as frequency increases. A-Weighting showed that the position C region had the highest level, approximately 102 dBA, which the researcher selected to install a noise barrier.

3.3 Sound pressure measurement results after installing noise barrier

The results of the sound pressure measurement at 1/3 octave in the frequency range of 31.5-16000 Hz at position C before and after the installation of the noise barrier are shown in Figure 11. In addition, insertion loss (IL) represents the reduction in sound pressure achieved by the barrier, calculated by subtracting the sound pressure level measured after installation from the level measured before.
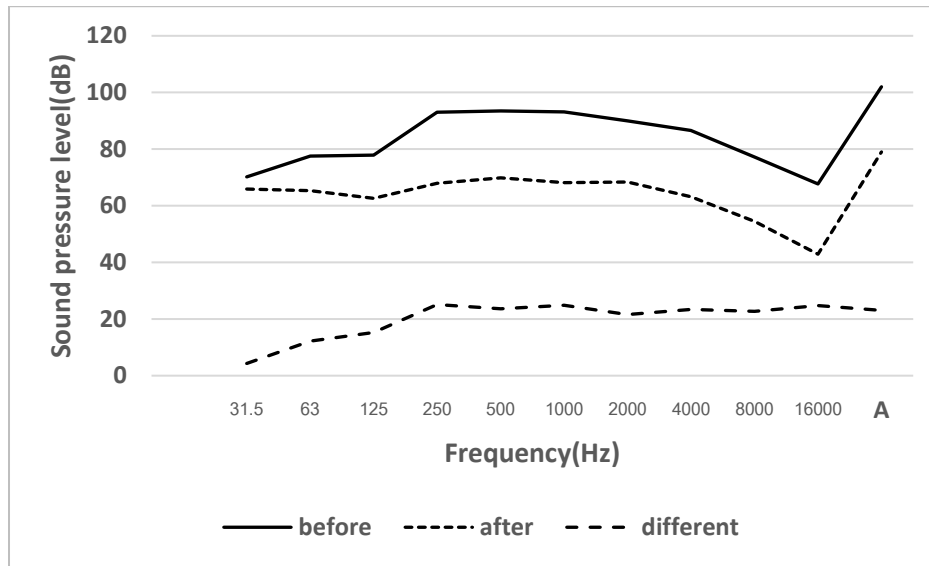
Figure 11. Sound pressure level measurement results before and after the installation of the barrier

Figure 11 shows that in the low-frequency range, the insertion loss (IL) value is small and tends to increase to the frequency level of 250 Hz. When the frequency level is greater, the IL value is relatively stable or slightly reduced, similar to the other studies [20-21], which found that IL values are high in the range of 250-8000 Hz. Similar to corn cob and sunflower stalk [25], sugarcane leaves, when incorporated, improve the sound-absorbing properties of cement-based composites. The developed sound insulation boards offer a practical and sustainable solution for industrial noise mitigation by effectively utilizing agricultural residues, such as sugarcane leaves. This approach contributes to improved waste management and reduced reliance on conventional building materials and has the potential to lower air pollution associated with open burning or improper disposal of agricultural residues. Although the experimental formulation incorporated only 4% sugarcane leaves by weight, scaling up production for industrial applications could significantly enhance the cumulative environmental benefits by promoting large-scale waste valorization and minimizing the negative impacts of traditional disposal practices. As shown in Table 4, the developed sugarcane leaf insulation panels achieved a sound pressure reduction of 20.6 dBA, outperforming lightweight concrete panels, which recorded 11.9 dBA, and demonstrating comparable performance to commercially available acrylic panels (17.35–18.26 dBA). These results highlight the potential of sugarcane leaf panels as a cost-effective and environmentally friendly alternative for industrial noise reduction applications. From an economic perspective, utilizing agricultural residues in the production of insulation boards significantly reduces raw material costs, making the product a financially viable option for manufacturers. Additionally, this approach creates value for agricultural by-products, offering potential income streams for farmers and thereby supporting economic sustainability in parallel with environmental benefits.

Table 4. Test results of the ability to reduce the sound pressure level of other types of insulation boards

Type of insulation board/thickness (mm)	Reduction of sound pressure level(dBA)
Mortar /50 mm	10.20
Mortar mixed with 4% Sugarcane leaves /50 mm	20.60
Acrylic sheet/5 mm	17.35
Acrylic sheet/10 mm	17.95
Acrylic sheet/20 mm	18.26
Lightweight Concrete/50 mm	11.90

ASEAN J. Sci. Tech. Report. **2025**, *28*(3), e257762.

10 of 12

4. Conclusions

The burning and destruction of agricultural residues is a major environmental problem in Thailand. A significant contributor to this issue is waste disposal from sugarcane harvesting, an important cash crop in the country. Addressing this problem, the researcher conceived the idea of managing such waste materials by incorporating them into mortar mixtures to enhance the noise-blocking potential of sound insulation sheets. The principles of experimental design were applied to the development and production of sample sound insulation panels to test their sound pressure reduction properties. The test results indicated that the sound insulation board with a 4% sugarcane mortar mixture achieved the highest sound pressure level reduction, equal to 20.6 dBA. This optimal proportion was then used in designing, constructing, and installing sound insulation walls for a case study in a real-world factory setting. The study's evaluation of the soundproof wall's effectiveness, determined by measuring the insertion loss, showed a reduction of 23 dBA in sound pressure level after installation. Based on these findings, it can be concluded that soundproofing walls made from mortar mixed with sugarcane leaves have significant potential for development into effective sound insulation sheets. Furthermore, developing such insulation sheets adds value to post-harvest sugarcane leaves, potentially incentivizing farmers to adopt alternative waste disposal methods and contributing to mitigating environmental problems like PM 2.5 dust in a sustainable future. Future research should focus on a comprehensive evaluation of the long-term durability and mechanical stability of the developed sugarcane leaf insulation panels under various environmental and operational conditions. In addition, further studies are required to develop and refine fabrication techniques that allow for the incorporation of higher proportions of sugarcane leaves without compromising structural integrity or acoustic performance. Investigating the scalability of the production process is also essential to determine its feasibility for widespread industrial application. Moreover, expanding the scope of research to include other types of agricultural residues, such as rice husks, coconut fibers, or corn stalks, may contribute to developing a broader range of sustainable and cost-effective insulation materials. This would further enhance the environmental and economic impact of agricultural residues in building applications.

5. Acknowledgements

Conflicts of Interest: The authors declare no conflict of interest.

References

[1] Office of The Cane and Sugar Board of Thailand. Ministry of Industry. Sugarcane Production Annaual Report **2018**. https://www.ocsb.go.th/reports-articles/ (accessed Dec 5, 2020)

[2] Office of Agricultural Economics of Thailand. Agricultural Product Production Informatio **2018**. http://www.nabc-catalog.oae.go.th/dataset/oae2025 (accessed Aug 12, 2021)

[3] Department of Alternative Energy Development and Efficiency. Electricity production from bagasse: Main contributors to the AEDP 2015 Renewable and Alternative Energy Development Plan. https://webkc.dede.go.th/testmax/node/2331 (accessed Aug 28, 2021)

[4] Faustino, J.; Pereira, L.; Soares, S.; Cruz, D.; Paiva, A.; Varum, H.; Ferreira, J.; Pinto, J. Impact sound insulation technique using corn cob particleboard. *Construction and Building Materials*, **2012**, *37*, 153-159. https://doi.org/10.1016/j.conbuildmat.2012.07.064

[5]   Asdrubali, F.; D'Alessandro, F.; Schiavoni, S. A review of unconventional sustainable building insulation materials. *Sustainable Materials and Technologies,* **2015**, *4*, 1-17. https://doi.org/10.1016/j.susmat.2015.05.002

[6]   Berardi, U.; Iannace, G. Acoustic characterization of natural fibers for sound absorption applications. *Building and Environment,* **2015**, *94*, 840-852. https://doi.org/10.1016/j.buildenv.2015.05.029

[7]   Asdrubali, F. Green and sustainable materials for noise control in buildings. 19th International Congress on Acoustics, Madrid, Spain (Sep 1, 2006).

[8]   Sivakumaresa, Chockalingam, L. N.; Rymond, N. M. Strength and Durability Characteristics of Coir, Kenaf and Polypropylene Fibers Reinforced High Performance Concrete. *Journal of Natural Fibers* **2022**, *19*(13), 6692-6700. https://doi.org/10.1080/15440478.2021.1929656

[9]   Jamshaid, H.; Mishra, R. K.; Raza, A.; Hussain, U.; Rahman, M. L.; Nazari, S.; Chandan, V.; Muller, M.; Choteborsky, R. Natural Cellulosic Fiber Reinforced Concrete: Influence of Fiber Type and Loading Percentage on Mechanical and Water Absorption Performance. *Materials,* **2022**, *15*(3), 874. https://doi.org/10.3390/ma15030874

[10]   Rumbayan, R.; Sudarno, Ticoalu, A.J.M.W.C. A study into flexural, compressive and tensile strength of coir-concrete as sustainable building material. *MATEC Web of Conferences.* **2019**, *258*, 01011. https://doi.org/10.1051/matecconf/201925801011

[11]   More, F. M. D. S.; Subramanian, S. S. Impact of Fibres on the Mechanical and Durable Behavior of Fibre-Reinforced Concrete. *Buildings,* **2022**, *2*(9), 1436. https://doi.org/10.3390/buildings12091436

[12]   Duong, N. T.; Satomi, T.; Takahashi, H. Potential of corn husk fiber for reinforcing cemented soil with high water content. *Construction and Building Materias,* **2021,** *271*, 121848. https://doi.org/10.1016/j.conbuildmat.2020.121848

[13]   Yusra, A.; Triwulan, T.; Safriani, M.; Ikhsan, M. Use of bamboo fiber on the relationship between compressive strength and split tensile strength of high strength concrete. *IOP Conference Series: Materials Science and Engineerin,* **2020**, *933*(1), 012010. https://doi.org/10.1088/1757-899X/933/1/012010

[14]   Lahouioui, M.; Ben, A. R.; Fois, M.; Ibos, L.; Ghorbal, A. Investigation of Fiber Surface Treatment Effect on Thermal, Mechanical and Acoustical Properties of Date Palm Fiber-Reinforced Cementitious Composites. *Waste and Biomass Valorization,* **2020,** *11*(8), 4441-4455. https://doi.org/10.1007/s12649-019-00745-3

[15]   Pachla, E. C.; Silva, D. B.; Stein, K. J.; Marangon, E.; Chong, W. Sustainable application of rice husk and rice straw in cellular concrete composites. *Construction and Building Materials ,* **2021**, *283*, 122770. https://doi.org/10.1016/j.conbuildmat.2021.122770

[16]   Yang, T.; Hu, L.; Xiong, X.; Petrů, M.; Noman, M. T.; Mishra, R.; Militký, J. Sound Absorption Properties of Natural Fibers: A Review. *Sustainability,* **2020,** *12*(20), 8477.   https://doi.org/10.3390/su12208477

[17]   Oancea, I.; Bujoreanu, C.; Budescu, M.; Benchea, M.; Grădinaru, C. M. Considerations on sound absorption coefficient of sustainable concrete with different waste replacements. *Journal of Cleaner Production,* **2018**, *203*, 301–312. https://doi.org/10.1016/j.jclepro.2018.08.273

[18]   International Electro Technical Commission. IEC 61672-1:2013 Electroacoustic - Sound level meters - Part 1: Specifications **2013** . https://webstore.iec.ch/publication/5708 (accessed Oct 13, 2022).

[19]   International Organization for Standardization. ISO 10847:1997 - Acoustics - In-situ determination of insertion loss of outdoor noise barriers of all types **1997**. https://www.iso.org/standard/1314.html (accessed Oct 13, 2022)

[20]   Martinez-Orozco, J. M.; Barba, A. Determination of Insertion Loss of noise barriers in Spanish roads. *Applied Acoustics,* **2022**, *186*, 108435. https://doi.org/10.1016/j.apacoust.2021.108435

[21]   Vasile, O. Insertion Loss Analysis of the Acoustic Panels with Composite Construction. *ANNALS OF EFTIMIE MURGU UNIVERSITY,* **2013**, *20*(2), 85-91.

[22]   Wayson, R.; MacDonald, J.; El-Assar, A.; Lindeman, W.; Berrios, M. Florida Noise Barrier Evaluation and Computer Model Validation. *Sage Journal,* **2003,** *1859*(1), 72-78. https://doi.org/10.3141/1859-09

[23]   Lau, S.K.; Tang, S.K. Performance of a noise barrier within an enclosed space. Applied Acoustics, 2009, *70*(1), 50–57. https://doi.org/10.1016/j.apacoust.2008.01.006

ASEAN J. Sci. Tech. Report. **2025**, *28*(3), e257762.

12 of 12

[24] Ibitoye, S.E.; Ajimotokan, H.A.; Adeleke, A.A.; Loha, C. Effect of densification process parameters on the physico-mechanical properties of composite briquettes of corncob and rice husk. *Materials todays: Proceedings,* **2023**. https://doi.org/10.1016/j.matpr.2023.08.253

[25] Chen, L.; Chen, Z.; Xie, Z.; Wei, L.; Hua, J.; Huang, L.; Yap, P.S. Recent developments on natural fiber concrete: A review of properties, sustainability, applications, barriers, and opportunities. *Developments in the Built Environment,* **2023,** *16*, 100255. https://doi.org/10.1016/j.dibe.2023.100255.

Research article

Consumer Preferences on Key Kombucha Attributes among Thais and Indonesians: A Conjoint Analysis Study for Advanced Food Product Development

Qurrata A'yuni[1], Aussama Soontrunnarudrungsri[2], and Tantawan Pirak[3*]

[1] Faculty of Agro-Industry, Kasetsart University, Bangkok, 10900, Thailand
[2] Faculty of Agro-Industry, Kasetsart University, Bangkok, 10900, Thailand
[3] Faculty of Agro-Industry, Kasetsart University, Bangkok, 10900, Thailand
* Correspondence: tantawan.k@ku.th

Abstract: Consumer preferences for healthier options have risen since post-pandemic COVID-19, thus consumers have increasingly consumed functional beverages, particularly "kombucha" due to its perceived health benefits. However, the key quality attributes that drive consumer choice when purchasing kombucha have not been well established. Hence, this study investigated the most preferred attribute of kombucha and its segmentation on consumer choices using conjoint-based rating analysis. A total of 241 participants from Thailand and Indonesia were involved in evaluating 27 concepts obtained from different combinations of each attribute level (e.g., sugar options, flavors, price, and health benefits). The results showed that consumers in both countries identified "reduced sugar content" as the most important kombucha attribute, although significant differences were found in other attribute preferences. Indonesians preferred the "original flavors" of kombucha and were willing to purchase at the "regular price" to gain the "antioxidant" benefits. Meanwhile, Thai consumers preferred kombucha with "natural fruity flavors" and sought more "affordable prices", as it was driven by the "gut health" benefits. Consumer segmentation from both countries was identified using hierarchical cluster analysis: reduced sugar-driven, healthier options, antioxidants seekers, price-driven, and sweet-tooth cravers. These insights facilitate food developers and manufacturers create kombucha that follows the most preferred attributes to meet specific market and consumer demands.

Keywords: Consumer preferences; conjoint analysis; kombucha; quality attributes.

1. Introduction

The global outbreak of COVID-19 has shifted consumer preferences toward healthy and fermented drinks due to their perceived health benefits. Among these beverages, kombucha is a famous fermented tea that offers gut health benefits and improves the immune system owing to its symbiotic microbiota [1]. The popularity of kombucha is reinforced by market growth, reaching USD 5.9 billion and growing at a CAGR of 19.4% by 2029, particularly in Western countries. However, in Southeast Asia, kombucha remains sold in niche markets, and its functionality is still relatively unfamiliar to many consumers. Furthermore, habitual kombucha consumption is primarily observed among health-conscious individuals [2]. Hence, understanding the key attribute drivers of consumer preferences for kombucha is crucial for developing new products that meet the specific needs of target market segments.

ASEAN J. Sci. Tech. Report. **2025**, *28*(3), e255936

2 of 15

Previous studies have highlighted the multi-attributes of kombucha, which are revealed across various consumer profiles with diverse market segments. Among these, sensory qualities, particularly flavor characteristics, are the essential attributes influencing the purchase decisions and intentions of the product. The flavor profile of kombucha is often described as mildly sweet, well-balanced sweetness-sourness, strong acetic, natural tea-fermented, fruity-floral, and authentic flavors [3]. In addition to flavor, the sugar option is considered critical for functional beverages, specifically in kombucha, to fit health-conscious consumers. Several products now feature sugar claims, such as reduced sugar and non-caloric sweeteners, to support body weight management and control blood glucose levels during daily consumption [4]. Another important attribute associated with kombucha is its health benefit claims, including digestive health improvement, antioxidant effects, and detoxification properties. Health benefit attributes strongly drive purchasing decisions for fermented beverages [3, 4]. According to market mapping, kombucha is currently most accessible to middle- and upper-class consumers, particularly within the premium market segment focused on healthier lifestyle choices. To expand its market reach, kombucha should become more accessible to consumers with a broader range of sociodemographic backgrounds, especially by offering affordability for lower-income consumers. In this context, price is a critical factor in affecting the purchasing decisions of functional beverages while gaining perceived product value and benefits without compromising quality and functionality [5]. No studies have identified the key kombucha attributes that drive consumer choice and purchase intentions to date.

Conjoint analysis has been widely used for various foods and beverages to identify consumer preferences for food product development, determine consumer segmentation, and conduct market simulations. The insights gained from conjoint studies are critical for food manufacturers to ensure that their products meet consumer needs and remain competitive in crowded markets [4, 6]. Ong et al. suggested that identifying the most critical product attributes enables product developers to design products that fulfill the consumer needs in specific segmented markets [6]. Lee et al. further demonstrated that consumers can be segmented based on the value benefits of product attributes [5]. Moreover, conjoint analysis aids in formulating marketing strategies to determine the most preferred product attributes and provides socio-demographic insights among consumers, which are crucial for long-term market success. Conjoint analysis has revealed that consumer preferences for product attributes vary between countries owing to differences in market segmentation and levels of understanding of product familiarity [4-6]. Cultural behaviors and consumption habits significantly influence the selection of specific product attributes, suggesting authentic preferences are shaped by cultural and socio-demographic factors [7]. Thus, conjoint analysis is valuable for identifying unique selling propositions and enhancing market opportunities.

Recent research has shown scarce information on consumer preferences for kombucha and its simulated market segmentation. Hence, this study aimed to investigate kombucha's key attributes using conjoint analysis, which consumers between Indonesians and Thais most preferred. The conjoint data was also used to determine consumer segmentation and specific kombucha attributes that fit consumer needs within specific target markets.

2. Materials and Methods

2.1 Design of conjoint analysis on the most valued key kombucha attributes

The selection of kombucha attributes and their levels for the conjoint study was determined through a focus group discussion (FGD) following a previous method [8]. The FGD involved twenty-six participants (n=26), aged between 18 and 37 years, among Thais and Indonesians, who had experienced drinking kombucha routinely. The FGD session included general and probing questions. Initially, the participants were asked about their knowledge of kombucha and their perceptions of its attributes. During the probing phase, participants identified the most preferred intrinsic and extrinsic kombucha attributes that drive consumer choice. The most frequently mentioned attributes during the FGD were selected for the conjoint study. The attributes and their levels for conjoint studies are revealed in Table 1.

ASEAN J. Sci. Tech. Report. **2025**, *28*(3), e255936.

3 of 15

Table 1. The attributes and levels of kombucha used for conjoint analysis

Parameters	Attributes	Levels
Intrinsic attributes	Flavors	Original
		Natural Fruity Flavors
		Fruity Flavor Added
	Sugar Options	Normal Sugar
		Reduced Sugar
		Sweeteners
Extrinsic attributes	Health Benefits	Antioxidant
		Good for Gut Health
		Without Health Benefits
	Price	Affordable
		Regular
		Premium

The experimental design for the conjoint analysis was determined based on a fractional factorial design, a statistical technique commonly used to reduce the number of experimental runs while maintaining statistical efficiency. The conjoint profiles were generated using the XLSTAT version 19.6 software (Addinsoft, New York, NY, USA), resulting in a total of 27 unique combinations of attributes (e.g., sugar options, flavors, health benefits, and price), and each corresponding level as shown in Table 2. The participants then evaluated each concept using a 9-point rating scale [8, 9].

Table 2. The product concepts used in the conjoint analysis to identify the most preferred attributes

No	Sugar Light	Health Benefits	Flavors	Price
1	Normal Sugar	Without Health Benefits	Natural Fruity Flavors	Premium
2	Less Sugar	Good for Gut Health	Natural Fruity Flavors	Premium
3	Normal Sugar	Good for Gut Health	Fruity Flavor Added	Premium
4	Less Sugar	Antioxidant	Natural Fruity Flavors	Premium
5	Sweeteners	Antioxidant	Natural Fruity Flavors	Affordable
6	Normal Sugar	Without Health Benefits	Fruity Flavor Added	Premium
7	Normal Sugar	Antioxidant	Fruity Flavor Added	Affordable
8	Normal Sugar	Good for Gut Health	Natural Fruity Flavors	Affordable
9	Sweeteners	Good for Gut Health	Original	Premium
10	Sweeteners	Good for Gut Health	Natural Fruity Flavors	Regular
11	Sweeteners	Without Health Benefits	Natural Fruity Flavors	Affordable
12	Sweeteners	Without Health Benefits	Original	Affordable
13	Normal Sugar	Antioxidant	Natural Fruity Flavors	Regular
14	Less Sugar	Without Health Benefits	Natural Fruity Flavors	Regular
15	Sweeteners	Without Health Benefits	Original	Premium
16	Less Sugar	Antioxidant	Original	Premium
17	Sweeteners	Antioxidant	Fruity Flavor Added	Premium
18	Less Sugar	Antioxidant	Original	Regular
19	Less Sugar	Without Health Benefits	Fruity Flavor Added	Regular
20	Sweeteners	Antioxidant	Fruity Flavor Added	Regular
21	Less Sugar	Without Health Benefits	Fruity Flavor Added	Affordable
22	Normal Sugar	Antioxidant	Original	Affordable
23	Less Sugar	Good for Gut Health	Fruity Flavor Added	Affordable
24	Less Sugar	Good for Gut Health	Original	Affordable
25	Normal Sugar	Good for Gut Health	Original	Regular
26	Normal Sugar	Without Health Benefits	Original	Regular
27	Sweeteners	Good for Gut Health	Fruity Flavor Added	Regular

ASEAN J. Sci. Tech. Report. **2025**, *28*(3), e255936

4 of 15

The levels of kombucha attributes were determined based on several considerations revealed by the FGD results and literature review. The conjoint design included four product attributes, each with three levels. The kombucha attributes were as follows: (i) Flavors were identified as a critical attribute because of their significant impact on customer satisfaction and purchasing intentions [5, 7]. The preferences for flavor quality included original fermented tea and natural or artificial fruity flavors obtained from the FGD sessions; (ii) Sugar options were selected due to rising awareness of non-communicable diseases (NCDs), particularly diabetic diseases. Participants preferred sugar content claims when purchasing functional drinks to seek healthier options without sacrificing sweetness [4]. This preference indicates a desire for consumers to control body weight and manage blood glucose levels; (iii) Health benefits were suggested as an important attribute due to consumer demand to purchase products that offer functional advantages for preventive function and well-being [5]. Kombucha is recognized as a functional drink because it can enhance gut health benefits and provide antioxidants that support healthy lifestyles. Price was identified as a crucial factor influencing consumers' buying decisions and intentions. Price levels were determined based on the product's value proposition and categorized into affordable, regular, and premium options. Pricing levels suggest consumers' willingness to spend on kombucha in alignment with their perceived value benefits [5], [6]. A conjoint study questionnaire was created using Google Forms. The questionnaire was initially drafted in English and translated into Thai and Indonesian. To ensure linguistic accuracy and cultural appropriateness, the translations were reviewed by native speakers of each language. A back-translation procedure was subsequently performed, and any discrepancies were discussed and resolved collaboratively by the Thai and Indonesian native speakers. The questionnaire included sociodemographic information, consumption habits, and conjoint stimuli profiles, which consumers from Indonesia and Thailand then assessed.

2.2 Data collection of conjoint studies on the key kombucha attributes

A total of 241 respondents participated in the survey, comprising 138 Indonesians and 103 Thais. A consumer survey was conducted between August and November 2023. The target consumers were familiar with kombucha and had previously consumed it. Data was collected using non-systematic sampling at universities and densely populated public areas. In addition, the online survey was collected using various social media platforms (e.g., WhatsApp, LINE, Facebook, and Instagram), and social media influencers assisted in the survey. Screening questions were included at the beginning of the questionnaire to ensure that all participants had prior knowledge of kombucha. Only respondents who confirmed prior experience with kombucha were allowed to proceed with the survey. Participants completed the questionnaire in approximately 10-15 minutes. The data from conjoint studies included average relative importance, overall utilities, and individual part-worth utilities. The conjoint results were used to gain deeper insights into the most preferred attributes for developing kombucha products that align with the consumer segmentation in the specific market.

2.3 Determination of consumer segmentation and its simulated market models among Thais and Indonesians

The individual part-worth utility value from the conjoint study was used to segment consumers to gain in-depth insights into their socio-demographic characteristics and the most preferred kombucha attributes, following a previous method [5]. Consumer segmentation was conducted using Ward's hierarchical cluster analysis with Euclidean distance. Each segment was classified as a consumer according to its preference for specific kombucha attributes within the target market. Individual part-worth utilities were used to simulate market conditions based on product concepts obtained from conjoint analysis to assess the acceptability of a product concept in a specific market. Market simulations were performed using the market generator tools in the XLSTAT software [9]. Different kombucha attributes and their levels defined various product concepts, which were then analysed to create simulated market models and estimate potential market shares. The product concept with the highest market share value was identified as acceptable in the target market.

2.4 Statistical analysis

The data obtained from the conjoint analysis were analyzed using XLSTAT version 19.6 software (Addinsoft, New York, NY, USA). The average relative importance of each attribute and the individual part-worth utilities were analyzed based on the rating scores evaluated by consumers. The results were further analysed

ASEAN J. Sci. Tech. Report. **2025**, *28*(3), e255936.

5 of 15

using an Independent Samples T-test with SPSS statistics software version 22.0 (Thaisoftup Co., Ltd., Bangkok, Thailand) to assess the significance of mean differences between Indonesian and Thai respondents.

3. Results and Discussion

3.1 Consumer profiles and their sociodemographic characteristics between Thais and Indonesians

It was found that the sociodemographic profiles among all Indonesians and Thais revealed distinct consumer backgrounds. Indonesians were dominated by males (49.8%), while Thais were primarily females (72.4%). Thais were predominantly aged 15-24 (51.4%), whereas Indonesians were mainly aged 24-34 (52.7%). This age difference suggested that Thais, mostly university students, had lower incomes, while Indonesians generally had professional occupations with stable incomes. Both groups were well-educated, with 95.2% of Thais and 85.1% of Indonesians holding undergraduate or postgraduate degrees. Indonesians also consumed kombucha more frequently, with 22.9% consuming it several times a week, compared to 49.5% of Thais who consumed it less than once a month. This difference in consumption habits may correlate with product familiarity, with more frequent consumption linked to a better understanding of kombucha attributes. These findings align with Sulistyawati et al. [7], who highlighted the importance of sociodemographic characteristics in understanding consumer preferences.

Table 3. Sociodemographic profiles among respondents within each identified cluster for both nationalities

Sociodemographic Profiles	Thais			Indonesians		
	Price driven	Sweet-tooth cravers	Reduced sugar driven	Antioxidant Seekers	Healthier Options	Reduced sugar driven
Gender						
Male	27%	14%	27%	65%	52%	32%
Female	73%	86%	73%	35%	48%	68%
Age (years old)						
15-24	55%	71%	44%	32%	36%	32%
25-34	25%	29%	49%	42%	56%	62%
35-44	4%	-	5%	12%	4%	3%
45-54	12%	-	2%	12%	2%	3%
>54	4%	-	-	2%	2%	-
Income (THB)						
<15.000	49%	72%	38%	32%	43%	46%
15.000-24.000	25%	14%	31%	38%	37%	41%
25.000-34.000	12%	14%	20%	20%	18%	13%
35.000-44.000	4%	-	11%	4%	2%	-
>44.000	10%	-	-	6%	-	-
Education Levels						
Primary School	2%	-	-	-	-	-
Secondary School	6%	-	2%	14%	12%	11%
Bachelor's Degree	69%	71%	69%	54%	33%	59%
Bachelor's Degree	23%	29%	29%	32%	55%	30%

The sociodemographic backgrounds of each consumer segment between Thais and Indonesians were studied as shown in Table 3. The obtained individual part-worth utility values from the conjoint analysis provided detailed insights into the sociodemographic profiles of Thais and Indonesians within each consumer segment. Specifically, the three groups among Thais and Indonesians revealed different sociodemographic characteristics regarding gender, age, income, and education levels. This analysis evaluated the influence of consumer characteristics on the selection of kombucha attributes within each segment, which will be further discussed in the following study. This result suggested that understanding consumers' sociodemographic characteristics is crucial for identifying the key factors influencing their preferences, enabling entrepreneurs

ASEAN J. Sci. Tech. Report. **2025**, *28*(3), e255936

6 of 15

to develop more effective market strategies. These findings agreed with previous studies that highlight the impact of sociodemographic factors on consumer preference and purchasing decisions among respondents in different countries [5, 6].

3.2 The consumer preferences on the most valued kombucha attributes for Thais and Indonesians

The cross-cultural study identified differences in preferred kombucha attributes between Thai and Indonesian consumers based on relative importance and utility values. The most preferred attributes were first determined at the general level for each country to evaluate the influence of nationality on kombucha preferences. A comprehensive analysis of these findings is presented in the following section.

3.2.1 The relative importance of kombucha attributes

This study revealed that the kombucha attributes' most relevant importance values differed for the two countries, as shown in Figure 1. The highest relative importance values indicate the significance of each attribute in affecting consumers' product choices [7]. Sugar options and price were the most important attributes influencing kombucha purchase decisions for Indonesian and Thai consumers. This aligns with previous research by Li et al. [4] and Ong et al. [10] highlighting the importance of sugar content and affordability in beverage choices. However, flavor and health benefits were less prioritized, consistent with the findings of Sulistyawati et al. [7] and Annunziata and Vecchio [11].
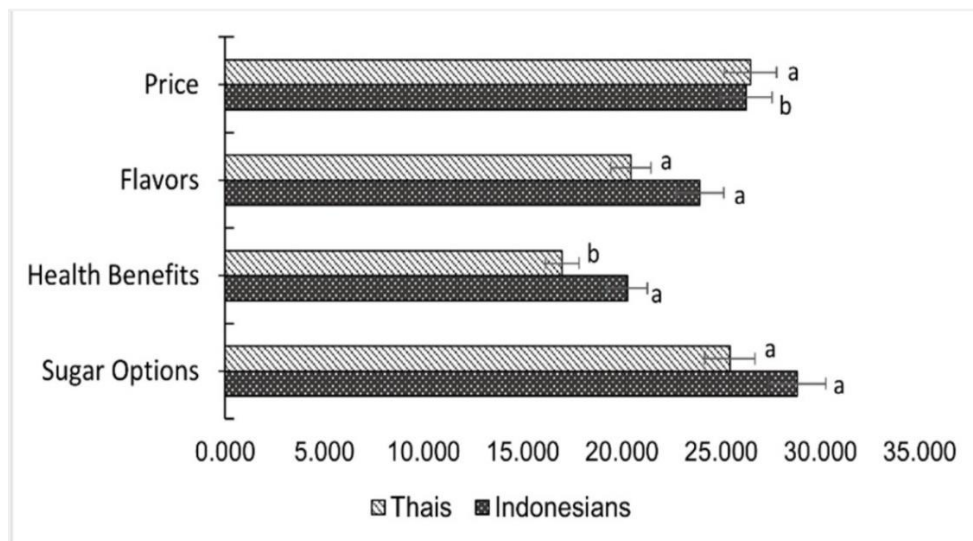
Figure 1. The average relative importance of kombucha attributes between Thais and Indonesians. Different letters exhibited significant differences in kombucha attributes between respondent groups (P < 0.05).

These findings suggested that when developing kombucha, it should be tailored to the most preferred product attributes across consumers in different countries related to sociodemographic and cultural background. Li et al. [4] reported that consumer background in specific market segments exhibited the preferences of sugar types as the key attribute in beverage choice, driven by the consumer demand for healthier options. The selection of sugar options in this study could be due to increasing consumer awareness of rising diabetes prevalence, as reported by the WHO [12]. Additionally, the prevalence of low to middle-income consumer profiles in both countries likely influenced the price preference as the most important attribute, as shown in Table 3. While flavors and health benefits were the least important attributes, they can be influenced by the perception of kombucha characteristics. This includes vinegary notes and harsh acidic taste, and its health claims have yet to affect their health or physiological functions significantly. Healthy products are often perceived as less acceptable to wider consumers, particularly due to the premium price with less appealing flavors [11]. These results suggested that kombucha products should balance sugar levels while offering competitive pricing to appeal to a broader consumer base. Moreover, reformulating flavors to address potential taste preferences and avoiding excessive health claims could enhance consumer acceptance [7, 11].

3.2.2 The overall utility values of kombucha attributes

The utility values for each kombucha attribute between Thais and Indonesians are shown in Table 4. Consumers in both countries strongly preferred reduced sugar content in kombucha, as indicated by the high positive utility values (Table 4), highlighting reduced sugar as a key attribute influencing consumer choice among health-conscious market segments. This result aligns with research by Li et al. [4] highlighting the importance of sugar reduction in beverages for seeking healthier options. A higher preference for "reduced sugar" claims may be influenced by the increasing prevalence of diabetes cases [12]. Although formulating low-sugar kombucha presents challenges, such as increased acidity and vinegary off-flavors, it remains a promising strategy to offer healthier options [3, 13]. Many commercial kombucha brands now feature "low sugar" claims to meet consumer demand [14], demonstrating that reduced-sugar formulations are feasible when using calorie-free natural ingredients, provided that sensory quality and consumer acceptance are carefully monitored [15-16]. Additionally, both groups disliked sweeteners, perceiving them as bitter and potentially harmful [15]. Despite that, Thais were more tolerant of sweeteners than Indonesians, suggesting a focus on calorie intake control [17]. The "normal sugar" attribute showed negative utility values among consumers in both countries. However, the negative value was lower for Indonesians. This could be due to Indonesians' preference for sweeter flavors, even while managing their sugar intake, and was consistent with previous studies [7, 10]. Hence, the sugar options in kombucha formulation should align with consumer preferences and target market segments to meet their needs effectively.

Table 4. The overall utility values on attributes and levels of kombucha between Indonesians and Thais.

Attributes of Kombucha	Levels of attributes	Indonesians		Thais	
		Mean	Std. deviation	Mean	Std. deviation
Sugar Options	Reduced Sugars	**0.317**[*]	0.503	**0.164**	0.424
	Normal Sugar	-0.013	0.393	-0.101	0.644
	Sweeteners	-0.304	0.495	-0.063	0.628
Health Benefits	Antioxidant	**0.045**	0.316	-0.054	0.355
	Good for Gut Health	0.030	0.324	**0.124**	0.316
	Without Health Benefits	-0.075	0.318	-0.069	0.358
Flavors	Fruity Flavor Added	-0.206	0.508	-0.104	0.438
	Natural Fruity Flavors	0.033	0.404	**0.073**	0.391
	Original	**0.174**	0.373	0.031	0.371
Price Levels	Affordable Price	0.040	0.463	**0.215**	0.507
	Premium Price	-0.122	0.635	-0.336	0.663
	Regular Price	**0.082**	0.419	0.120	0.418

[*] The bold style indicated the highest utility values as the most preferred attributes.

A significant difference in price level preference was found between consumers in both countries (Table 4). Thais, often university students with lower incomes, preferred affordable prices. This preference choice may be attributed to consumer profiles characterized by unstable incomes and product affordability benchmarks in the Thai market [10, 14]. This result was consistent with those in previous studies [10]. Meanwhile, Indonesians, with higher incomes, were more willing to pay regular prices for premium kombucha. This aligns with previous research showing income influences price level preferences [11]. Additionally, consumers in both countries exhibited less interest in "premium prices," as indicated by negative utility values (Table 4). Their unfamiliarity with kombucha's properties may have contributed to those attribute choices, as they perceived it as not worth the expense due to its less favorable taste and health benefits [5, 11]. Previous studies highlighted that consumer price preferences are affected by a product's value proposition and socio-demographic factors, particularly income [7, 11]. These findings indicated that price was the most important attribute to consumers in both countries, driving product choices and purchase decisions.

ASEAN J. Sci. Tech. Report. **2025**, 28(3), e255936

8 of 15

Flavor preferences also differed between Thais and Indonesians (Table 4). Indonesians favored traditional "original" flavors, while Thais preferred "natural fruity flavors". Cultural habits may influence these preferences, the intensity of consumption habits, and product availability benchmarks in the market [7, 11, 14]. In Indonesia, consumers prefer original traditional foods made through homemade processing, which may correlate with their preference for original flavors. This preference extends to kombucha, where traditional fermentation processes impart authentic fermented tea flavors [13, 18]. In contrast, Thais are drawn to 'natural fruity flavors' due to their familiarity with fruit characteristics and the availability of commercial kombucha products featuring fruity flavors in the Thai market [19]. Both groups showed less interest in "fruity flavors added," as indicated by negative utility values, reflecting a general aversion to artificial additives due to perceived health risks [17]. These findings suggested a consumer shift toward natural beverage ingredients, perceived as healthier options. However, it is crucial to acknowledge that incorporating natural ingredients may pose stability challenges, despite ongoing research efforts [13, 15]. Consumers in both countries valued health benefits (Table 4). Thais prioritized gut health benefits, likely due to the prevalence of fermented drinks and probiotic claims in their market [20-21]. Indonesians sought antioxidant benefits, reflecting their cultural familiarity with traditional antioxidant-rich drinks [22]. Both groups considered 'health benefits' a significant factor in their kombucha purchasing decisions. It was consistent with previous findings that the product was more acceptable when accompanied by preventive health-promoting effects [11]. Preferences for products with health benefits have influenced consumer choices over flavors, driven by awareness of the preventive effects of functional foods [22]. Annunziata and Vecchio [11] emphasized that respondents preferred food products with preventive health claims over those with generic or psychological claims in attaining consumer acceptance. While kombucha with specified health benefits attracted interest from Thais and Indonesians, health claims must adhere to local food regulations [11].

3.3 Consumer segmentation between Thais and Indonesians on valued kombucha attributes

Consumers in Indonesia and Thailand were clustered using hierarchical cluster analysis. It was revealed that the segmented consumer was divided into three clusters for each country. Although Indonesian and Thai consumers were grouped into "reduced sugar-driven" clusters, different clusters were found between Indonesian and Thai consumers to better understand market segmentation. The results were as follows:

3.3.1 Reduced sugar driven by segmented consumers

This cluster valued reduced sugar as the most crucial attribute in kombucha, showing the highest positive utility score for Indonesians and Thais as presented in Figure 2a and Figure 2b, respectively. Indonesians in this cluster preferred original flavors and were willing to pay a premium to gain gut health benefits. In contrast, while Thais assigned a lower utility score to reduced sugar, they still valued it alongside natural fruity flavors and prioritized affordable prices for similar health benefits. The preferences for kombucha attributes correlated with the sociodemographic profiles among Thais (n=45) and Indonesians (n=37), as indicated in Table 2. This cluster was dominated by well-educated females aged 25-34 across both countries. The high preference for reduced sugar in fermented kombucha is likely due to their awareness of the need to control sugar and calorie intake for weight management. This finding is consistent with previous studies [4], which indicate that reduced sugar is a highly valued attribute in functional products due to a health-conscious mindset. Consumers prioritize reduced sugar claims because of their significant association with dental health, obesity, diabetes, and weight management [23]. Higher education levels in this cluster may contribute to greater health awareness [11]. This cluster highlighted the importance of the reduced sugar claim in fermented kombucha, as consumers are aware of sugar intake limits and prioritize healthier lifestyle choices over flavor. Therefore, this group appealed to the health-conscious consumer segments in the Indonesia and Thailand markets.

(a)
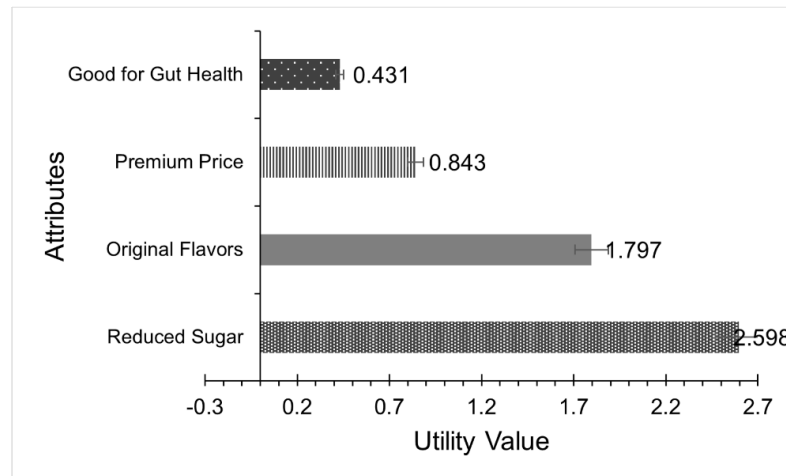
(b)
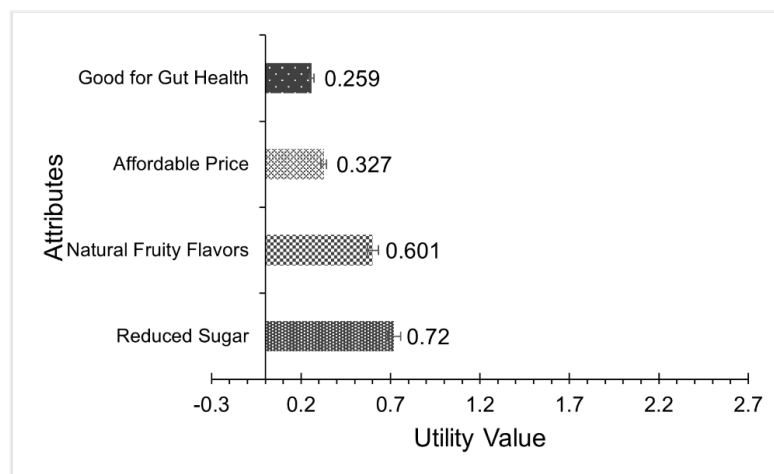
Figure 2. The preferences of "reduced sugar driven cluster" on kombucha attributes among both nationalities (a) Indonesians and (b) Thais.

3.3.2 Healthier options for segmented consumers

The healthier options segment was specific to Indonesian consumers (n=51) who prioritized reduced sugar and gut health benefits over affordable price and original flavor, as shown in Figure 3. These findings agreed with previous studies indicating that consumers favor attributes related to health benefits [5, 11]. This cluster was characterized by males as the dominant gender, with a productive age (25-34), and graduated with a bachelor's degree. Based on socio-demographic profiles, they preferred healthier option attributes when purchasing the product because of their awareness of the high prevalence of NCD cases associated with busy lifestyles and poor dietary habits [11-12]. In addition, consumers in this cluster highly preferred the original flavor of the fermented kombucha. This finding is consistent with the observations of Lee et al. [5], who reported that health-conscious consumers prefer the flavors obtained from natural ingredients over food additives. Despite this cluster being recognized as low-income consumers, they prioritized healthier option attributes over affordability due to the perceived health benefits of the kombucha.
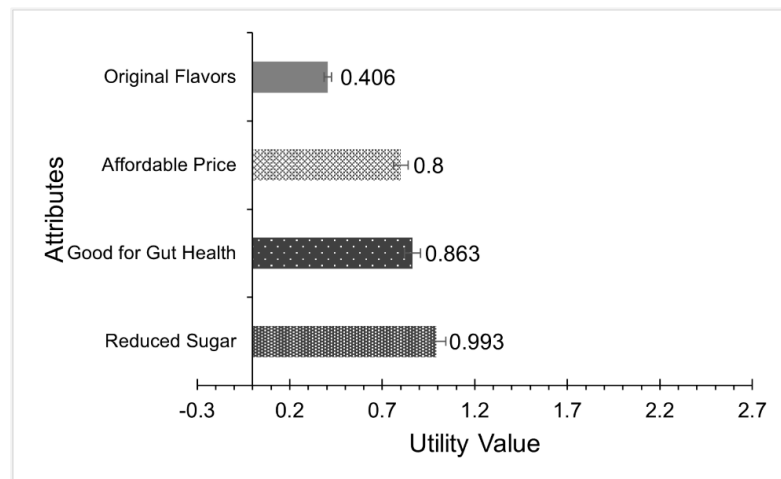
Figure 3. The preferences of the "healthier options cluster" on kombucha attributes among Indonesians.

3.3.3 Antioxidant seekers of segmented consumers

This cluster was also specific to Indonesian consumers (n=50), who prioritized antioxidant effects over affordable price, reduced sugar, and original flavors presented in kombucha, as shown in Figure 4.
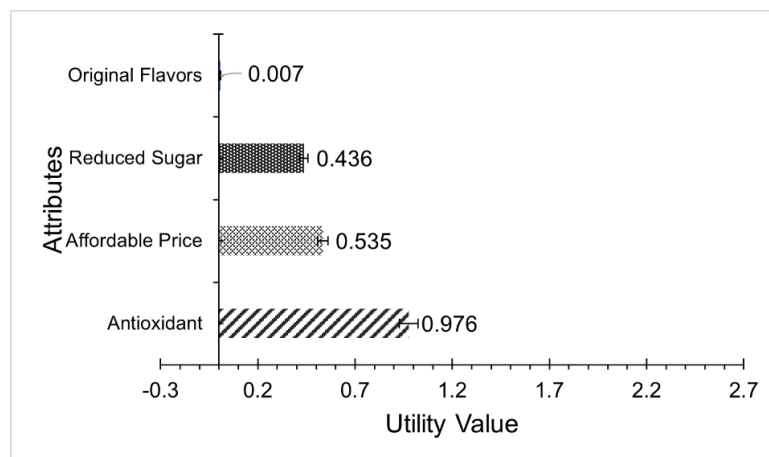
Figure 4. The preferences of the "antioxidant seekers cluster" on kombucha attributes among Indonesians.

The high preference for antioxidants could be due to the consumer perception that kombucha is made from tea substrates, which provide antioxidant benefits from polyphenols. This preference might also be influenced by Indonesian cultural habits of routinely drinking tea and other traditional drinks, "Jamu", to maintain body endurance [22]. The socio-demographic background is associated with consumer profiles in this cluster. It was dominated by males, who were in their productive age, and might seek healthiness from an antioxidant-based fermented drink, otherwise known as kombucha. Despite having stable incomes, these consumers prioritized affordability while seeking health benefits. This is consistent with Silva et al. [24], who found that consumers favor functional drinks with antioxidant claims but still consider cost-effectiveness. These insights are valuable for product developers aiming to meet consumer preferences in segmented markets focused on antioxidant benefits.

3.3.4 Price-driven by consumers

The price-driven cluster was specific to Thais (n=51), who preferred to buy kombucha for affordability, as shown in Figure 5. This cluster was characterized by the kombucha attributes, with the addition of sweeteners with original flavors and without health benefits. The most preferred kombucha attributes represented their inclination towards lower-priced options.
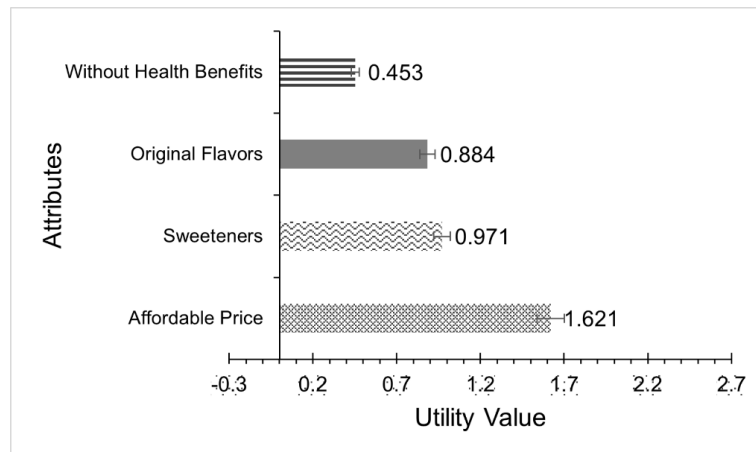
Figure 5. The preferences of "price-driven clusters" on kombucha attributes among Thais.

According to sociodemographic profiles, this cluster was recognized by females aged between 15 to 24 years and have low incomes without professional occupations. Indeed, the youngest women in this cluster preferred the kombucha attributes that indicate a preference for sweeter tastes and more robust flavors, managing their body weight, and choosing sweeteners with zero or low sugar content. However, there was also apprehension about sweeteners owing to the perceived health risks that can be obtained from the food additives [17]. Nevertheless, Fransisca et al. [25] suggested that consumers often view sweetener products as viable replacements for sucrose to reduce their sugar intake. These perceptions align with the study's findings, highlighting the importance of sweeteners in kombucha for controlling blood glucose spikes. Although this group preferred kombucha with sweeteners over health benefits, there is potential in this market segment, as affordability often precedes other attributes influencing consumer choice and purchase decisions.

3.3.5 Sweet-tooth cravers of segmented consumers

The sweet-tooth cravers cluster, specific to Thai consumers (n=7), showed a strong preference for craving sugary beverages, particularly favoring normal sugar present in kombucha. It was also found that they valued health benefits, choosing attributes suitable for gut health and original flavors, and they tended to buy at an affordable price, as shown in Figure 6. The high preference for normal sugar could be due to the dominance of females, with young generations (15-24) looking for sweet products to satisfy their desire to drink to enjoy appealing sweetness and tasty flavors [10, 26]. The preferences for normal sugar levels agreed with the findings revealed by recent studies [10, 23]. It was indicated that consumers prioritize sugar content as the most important attribute because they become habitual consumers of sweet-tooth products [10]. Although consumers opt to consume beverages with normal sugar levels, it is important to pay attention to the maximum limit of sugar in daily consumption [25]. This cluster also looked for gut health benefits, as indicated by the positive utility values in this study, and was consistent with the findings by Annunziata and Vecchio [11]. Consequently, it was suggested that a new product design should pay attention to the most preferred attribute in line with the sociodemographic characteristics of the segmented consumer in the intended market.

ASEAN J. Sci. Tech. Report. **2025**, *28*(3), e255936

12 of 15
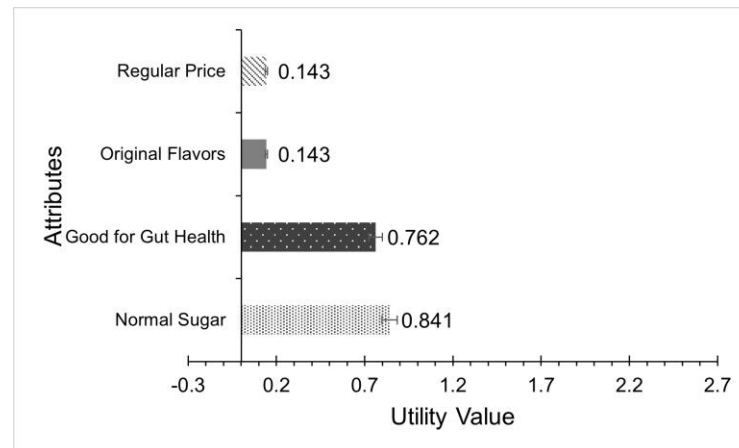
Figure 6. The preferences of "sweet-tooth cravers clusters" on kombucha attributes among Thais.

As a result, the segmented consumers in both countries have different preferences for kombucha attributes. Indonesian consumers opted for kombucha, which has health benefits, notably reduced sugar, consistent with overall utility values (Table 2). Thai consumers consistently prioritized affordable prices across all clusters, and their preference was aligned with the overall utility values among Thais. Thus, understanding these consumer segments is crucial for product developers to create functional beverages that align with the specific segmented consumers and market.

3.4 Simulated market models for product concepts that are acceptable for Thais and Indonesians

The obtained product concepts from the overall utility values and individual part-worth utility values between Indonesian and Thai consumers were analyzed. The selected product concepts for the Indonesian market are shown in Table 5, whereas those for the Thai market are presented in Table 6. Consumers in both countries showed different preferences owing to their diverse cultural backgrounds and behaviors [27].

Table 5. Market simulation for product concepts of kombucha attributes among Indonesian consumers.

Indonesian Consumer Cluster	Light	Health Benefits	Flavors	Price	Total Market Share
General Indonesian	Reduced Sugar	Antioxidant	Original	Regular Price (IDR 20.000-40.000)	23.207
Antioxidant Seekers	Reduced Sugar	Antioxidant	Original	Affordable Price (IDR <20.000)	25.464
Healthier Options	Reduced Sugar	Good for Gut Health	Original	Affordable Price (IDR <20.000)	25.422
Reduced Sugar Driven	Reduced Sugar	Good for Gut Health	Original	Premium Price (> IDR 40.000)	**25.908** [*]

[*] The bold style indicated the highest total market share value as the most acceptable product concept for kombucha development.

It was found that the product concepts for Indonesians from each segmented consumer were well-received in the simulated market (Table 5). Specifically, the "reduced sugar driven" consumer segment demonstrated the highest total market share, indicating strong consumer willingness to purchase and in alignment with the sociodemographic background in those clusters [28]. This strong value proposition also explains the acceptance of premium pricing among these consumers, particularly for the health-consciousness market segment. Moreover, an affordable price with a preference for kombucha attributes that prioritize reduced sugar, original taste, and health benefits is also in high demand, representing the second-largest market share. The market share value is differentiated based on consumer interest in the levels of antioxidant attributes and gut health benefits. Above all, Indonesians were looking for kombucha attributes to gain health

ASEAN J. Sci. Tech. Report. **2025**, *28*(3), e255936.

13 of 15

benefits with "original flavors", and they were willing to spend money based on the value of the key attributes. This implies that a product concept with a larger total market share can fulfill consumer needs and fit a specific target market. Ong et al. [6] emphasized these findings; it was revealed that the data of the conjoint studies can further determine the market segmentation while providing insights for novel products and catering to customer satisfaction [29].

Table 6. Market simulation for product concepts of kombucha attributes among Thai consumers.

Thai Consumer Cluster	Sugar Options	Health Benefits	Flavors	Price	Total Market Share
Price Driven	Sweeteners	Without Health Benefits	Original	Affordable Price (THB 15-24)	35.142
Sweet-Tooth Cravers	Normal Sugar	Good for Gut Health	Original	Regular Price (THB 25-50)	28.670
Thai General consumers or Reduced Sugar Driven	Reduced Sugar	Good for Gut Health	Natural Fruity Flavors	Affordable Price (THB 15-24)	**36.188** [*]

[*] The bold style indicated the highest total market share value as the most acceptable product concept for kombucha development.

In the Thai market, the most acceptable product concept was obtained from the overall utility values of Thai general consumers and the segmented consumers for "reduced sugar driven". The "reduced sugar" and "natural fruity flavors" attributes were identified as key factors driving Thai consumers to purchase kombucha intensely (Table 6). Interestingly, the product concept from the "price-driven" consumer segment was more interesting to consumers and suggested market opportunities for the Thai market, even if it contained "sweeteners" and "without health benefits". These findings emphasized the importance of understanding consumer profiles in specific market segments. Some consumers are motivated to buy kombucha not for its health benefits but for its affordability [30]. Lower-income consumers influenced the consumer preference to buy products for affordability due to financial constraints [6, 31]. As a result, the simulated market model and its consumer behavior guide product developers when launching new food products to ensure competitiveness and feasibility in crowded markets [32].

4. Conclusions

Consumers from Thailand and Indonesia preferred a reduced sugar kombucha. Indonesian consumers were willing to pay a regular price for kombucha, which is characterized by original flavors and provides antioxidant benefits. Meanwhile, Thai consumers sought more affordable price options and preferred kombucha with natural fruity flavors that could improve gut health. Consumer preferences on kombucha attributes were influenced by sociodemographic profile, cultural background, healthier choice lifestyle, and familiarity with kombucha attributes. When targeting the consumers, the "reduced sugar-driven segment" was indicated to have more market opportunities because it showed the highest total market share values in simulated market models across Thailand and Indonesian markets. Furthermore, the consumer segment indicated that Thais were driven by "affordability", while Indonesians were willing to purchase kombucha because they sought the health benefits and authentic fermented flavors. These findings revealed the consumer needs in the specific targeted market, which will help develop a "new functional kombucha" and other beverages.

5. Acknowledgements

ASEAN J. Sci. Tech. Report. **2025**, *28*(3), e255936

14 of 15

References

[1]   Clifford E. (2024, July 5). COVID-19 and food and drink: A year on in the UK market report 2021. *Mintel*. https://store.mintel.com/report/uk-covid-19-and-food-drink-a-year-on-market-report.

[2]   Markets and Markets. (2024, July 6). Kombucha market outlook 2024-2029. *Markets and Markets*. https://www.marketsandmarkets.com/Market-Reports/kombucha-market-211406364.html.

[3]   Kim, J; Adhikari K. Current trends in kombucha: Marketing perspectives and the need for improved sensory research. *Beverages*. **2020**, *6*(1), 2-19. doi:10.3390/beverages6010015.

[4]   Li, X. E.; Lopetcharat, K.; Drake, M. Extrinsic attributes that influence parents' purchase of chocolate milk for their children. *Journal of Food Science*. **2014**, *79*(7), S1407-S1415. https://doi.org/10.1111/1750-3841.12515.

[5]   Lee, P. Y.; Lusk, K. Mirosa, M. Oey, I. An attribute prioritization-based segmentation of the Chinese consumer market for fruit juice. *Food Quality and Preference*. **2015**, *46*, 1–8. https://doi.org/10.1016/j.foodqual.2015.06.016.

[6]   Ong, A.K.S.; Prasetyo, Y.T.; Esteller, A.J.D.; Bruno, J.E.; Lagorza, K.C.O.; Oli, L.E.T.; et al. Consumer preference analysis on the attributes of samgyeopsal Korean cuisine and its market segmentation: Integrating conjoint analysis and K-means clustering. *PLoS One*. **2023**, *18*(2), e0281948. https://doi.org/ 10.1371/journal.pone.0281948.

[7]   Sulistyawati, I.; Dekker, M.; Verkerk, R.; Steenbekkers B. Consumer preference for dried mango attributes: A conjoint study among Dutch, Chinese, and Indonesian consumers. *Journal of Food Science*. **2020**, *85*(10), 3527-3535. https://doi.org/10.1111/1750-3841.15439.

[8]   Gosine, L.; McSweeney, M.B. Consumers' attitudes towards alternative grains: a conjoint analysis study. *International Journal of Food Science and Technology*. **2019**, *54*(5), 1588-1596. https://doi.org/10.1111/ijfs.14126.

[9]   XLSTAT. (2024, May 11). Simulation for conjoint analysis and market tools. *XLSTAT Software*. https://www.xlstat.com/en/solutions/features/simulation-for-conjoint-analysis.

[10] Ong, A.K.S.; Prasetyo, Y.T.; Libiran, M.; Lontoc, Y.M.A.; Lunaria, J.A.V.; Manalo, A.M.; et al. Consumer preference analysis on attributes of milk tea: A conjoint analysis approach. *Foods*. **2021**, *10*, 1382. https://doi.org/10.3390/ foods10061382.

[11] Annunziata, A.; Vecchio, R. Consumer perception of functional foods: A conjoint analysis with probiotics. *Food Quality and Preference*. **2013**, *28*(1), 348-355. doi.org/10.1016/j.foodqual.2012.10.009.

[12] WHO. (2024, June 29). Diabetes in South-East Asia. World Health Organization. https://www.who.int /southeastasia/health-topics/diabetes.

[13] Zhang, J.; Van, J.M.; Dias, D.R.; Schwan, R.F. The chemistry and sensory characteristics of new herbal tea-based kombucha. *Journal of Food Science*. **2021**, *86*(3), 740-748. https://doi.org/10.1111/1750-3841.15613.

[14] Mintel. (2024, June 30). Global new products database for kombucha market 2019-2024. *Mintel*. https://www.mintel.com/.

[15] Medeiros, A.; Tavares, E.; Bolini, H.M.A. Descriptive sensory profile and consumer study impact of different nutritive and non-nutritive sweeteners on the descriptive, temporal profile, and consumer acceptance in a peach juice matrix. *Foods*. **2022**, *11*(2), 1-15. https://doi.org/10.3390/foods11020244.

[16] Mahato, D. K.; Keast, R.; Liem, D. G.; Russell, C. G.; Cicerale, S.; Gamlath, S. Optimisation of natural sweeteners for sugar reduction in chocolate flavoured milk and their impact on sensory attributes. *International Dairy Journal*. **2021**, *115*, 1-11. https://doi.org/10.1016/j.idairyj.2020.104922.

[17] Pang, M.D.; Goossens, G.H.; Blaak, E.E. The Impact of artificial sweeteners on body weight control and glucose homeostasis. *Front Nutr*. **2020**, *7*, 1-19. https://doi.org/10.3389/fnut.2020.598340.

[18] Fibri, D. L. N.; Frøst, M. B. Consumer perception of original and modernised traditional foods of Indonesia. *Appetite*. **2019,** *133*, 61-69. https://doi.org/10.1016/j.appet.2018.10.026.

[19] Aguilar, P. (2024, July 31). Over half of Thais want to eat healthily but budgets create barriers. *Mintel Reports Thailand*. https://www.mintel.com/press-centre/mintel-over-half-of-thai-consumers-are-committed-to-taking-healthy-eating-into-their-own-hands-but-budgets-create-barriers/.

[20] Mintel. (2024, August 1). Thai consumers seek value-added drinks amidst soaring temperatures. *Mintel Foods and Drinks*. https://www.mintel.com/press-centre/thai-consumers-seek-value-added-drinks-amidst-soaring-temperatures/.

[21] Thai FDA. (2024, August 5). Notification of the Ministry of Public Health Re: Use of probiotic microorganisms in foods. Thai Food and Drug Administration. https://food.fda.moph.go.th/.

[22] Wijaya, C. H.; Carolina, C. Consumer preference for java tea (*Orthosiphon aristatus*) extract-based functional drink as jamu. *Indonesian Journal of Food Quality*. **2022**, *9*(1), 1-9. https://doi.org/10.29244/jmpi.2022.9.1.1.

[23] Miklavec, K.; Pravst, I.; Grunert, K. G.; Klopčič, M.; Pohar, J. The influence of health claims and nutritional composition on consumers' yoghurt preferences. *Food Quality and Preference*. **2015**, *43*, 26-33. https://doi.org/10.1016/j.foodqual.2015.02.006.

[24] Silva, A. P.; Franco, M. I.; Mady, C.; Pallet, D.; Tomlins, K.; Bennett, B.; et al. Drivers of acceptance of a new beverage in Europe. *Beverages*. **2016**, *2*(2), 1-12. https://doi.org/10.3390/beverages2020012.

[25] Fransisca, F.; Palupi, N. S.; Faridah, D. N. Consumer perception in determining the purchasing decision of beverage product with less sugar claim. *Indonesian Journal of Food Quality*. **2016**, *3*(1), 50-57. http://journal.ipb.ac.id/index.php/jmp.

[26] Jensen, J. D.; Mielby, L. A.; Kidmose, U. Consumer preferences for attributes in sweet beverages and market impacts of beverage innovation. *Appetite*. **2024**, 197, 1-12. doi.org/10.1016/j.appet.2024.107329.

[27] Jeong, S.; Lee, J. Effects of cultural background on consumer perception and acceptability of foods and drinks: A review of latest cross-cultural studies. *Current Opinion in Food Science*. **2021**, *42*, 248-256. https://doi.org/10.1016/j.cofs.2021.07.004.

[28] De Pelsmaeker, S.; Schouteten, J. J.; Lagast, S.; Dewettinck, K.; Gellynck, X. Is taste the key driver for consumer preference? A conjoint analysis study. *Food Quality and Preference*. **2017**, *62*, 323-664. https://doi.org/10.1016/j.foodqual.2017.02.018.

[29] Vad Andersen, B.; Hyldig, G. Food satisfaction: Integrating feelings before, during and after food intake. *Food Quality and Preference*. **2015**, *43*, 126-134. https://doi.org/10.1016/j.foodqual.2015.03.004.

[30] A. Pimwadee. (2024, August 7). Functional food and drink of Thai consumers. *Mintel Reports Thailand*. https://www.mintel.com/.

[31] Adams, C.; Alldredge, C, K.; W. Teichner. (2024, August 7). Consumers: Spending more to buy less. McKinsey Reports. https://www.mckinsey.com/industries/consumer-packaged-goods/our-insights/consumers-spending-more-to-buy-less.

[32] Krestyanpol, L. Simulation modeling of consumer behavior within the concept of smart consumption. *Procedia Computer Science*. **2023**, *217*, 774-783. https://doi.org/10.1016/j.procs.2022.1.

Research article

Approach for Boosting the Drying Chamber's Temperature by Pulse Copper Pipes to Conduct Heat

Kitti Korbuakaew[1], and Prasit Phoosomma[2*]

[1] Faculty of Science and Technology, Dhonburi Rajabhat University, Thonburi, Bangkok, 10600, Thailand
[2] Faculty of Science and Technology, Dhonburi Rajabhat University, Thonburi, Bangkok, 10600, Thailand
* Correspondence: prasit.p@dru.ac.th

Publisher's Note:

Abstract: This research addresses a critical challenge in solar food drying: maintaining effective drying performance during low solar radiation intensity periods. We present an innovative hybrid drying system that combines thermal energy from direct solar radiation with supplementary heat provided by hot water circulating through strategically positioned copper pipes. The pulse copper pipe configuration conducts additional heat within the drying chamber, significantly enhancing thermal performance when outdoor temperatures drop or sunlight is limited. Experimental results demonstrate that this hybrid approach increases the temperature inside the drying chamber and extends drying periods by at least 10 minutes under low heat radiation conditions. Most notably, the combination of air drying with infrared radiation and hot water circulation yielded a 4.25% improvement in thermal efficiency compared to conventional methods. This approach represents a promising advancement in sustainable food preservation technology, particularly for regions with variable weather conditions.

Keywords: Conduct heat; drying chamber; pulse copper pipes; solar drying technology; hybrid thermal systems

1. Introduction

Solar radiation energy has emerged as a critical resource in contemporary sustainable technologies. While the sun has served as humanity's natural method for food drying throughout history, technological advancement has led to the development of sophisticated solar dryers that enhance this process [1,2]. Recent experimental validation has confirmed the heat efficiency of parabolic trough solar air heaters (PTSAH) utilizing U-shaped copper and aluminum heat exchangers, both with and without fins [3-4]. These systems have demonstrated considerable success in directly drying various agricultural products, including plantains, bananas, mangoes, and cassava through natural heat convection mechanisms [5-6].Innovation in this field continues with hybrid solar systems that harness the Joule effect generated by parallel-connected photovoltaic modules to efficiently dry sliced potatoes and similar food products [7-9]. Despite the availability of diverse drying technologies, comparing their effectiveness remains challenging due to variations in protective mechanisms and product-specific drying requirements. The implementation of standardized performance metrics could significantly streamline evaluation procedures.

The concept of necessary drying capability has driven improvements in solar dryers, substantially enhancing air drying capacity. Research has explored

using duck pods to increase moisture content in experimental settings, with integrated solar dryers proving particularly accessible and efficient [11-13]. These systems offer simple, expedient equipment for processing duck pods, allowing for complete same-day processing even without predetermined drying rates [12].Significant advancements in installation systems have increased annual solar energy utilization from 28.9% to 50.5%. Premium installation configurations employ adaptation tanks for solar hot water storage, connecting them in series with compact heating tanks to achieve annual performance ratings up to 50.5% [13-14]. This configuration allows larger tanks to operate at lower average temperatures while smaller, well-insulated tanks maintain higher temperatures, effectively reducing heat loss and enhancing solar engagement. Independent conventional heating systems can account for 52% of total energy needs in comparable storage conditions, with storage and reference conditions being primary factors. These parallel systems offer potentially lower investment costs while maintaining comparable performance metrics.

Heat pump-equipped solar collectors have gained widespread adoption for capturing solar energy in unfavorable sunlight conditions [15-17]. Solar water heating systems (SWHS) efficiency depends significantly on refrigerant selection, suggesting the need for developing superior refrigerants to enhance future performance [18-19]. Economic feasibility assessment requires consideration of multiple factors, while achieving consumer preference necessitates a comprehensive analysis of flow dynamics and heat transfer behaviors in solar collectors [24-26].The development of solar-powered food processing drying cabinets [10] utilizing solar-heated pipes has advanced the field further. These systems account for energy efficiency during the drying process and final product quality. Research confirms that moisture reduction correlates with increased drying time and temperature, with optimal results above 50°C. A significant advantage of these systems is their independence from electrical inputs, offering substantial energy conservation benefits.

Pulsating heat pipes have garnered significant research attention for their thermal performance and efficiency [19-23]. These innovative heat transfer devices provide enhanced thermal conductivity and have been applied across applications ranging from solar to cryogenic temperatures [21, 29]. Their integration into solar drying systems represents a promising frontier in thermal efficiency improvement.This research provides practical guidelines for food drying under suboptimal light conditions, including rainy periods, darkness, or limited sunlight exposure, expanding solar drying technologies' versatility and application scope in diverse environmental contexts. By incorporating pulse copper pipes to conduct heat within the drying chamber, we address a critical challenge in maintaining drying efficiency during periods of low solar radiation, contributing to more reliable and energy-efficient food preservation methods [27-28].

2. Materials and Methods

2.1 General (original model drying cabinet)

Farmers have traditionally relied on traditional sun-drying techniques for food preservation, as illustrated in Figure 1. This approach gained widespread adoption primarily due to economic considerations, as it significantly reduced household expenditures by eliminating the need for technological investments. The conventional methodology typically involved direct exposure of agricultural products to solar radiation in open environments. However, this traditional approach presents several substantial challenges, including contamination from environmental particulates (dust and PM 2.5) and vulnerability to insect vectors that potentially transmit pathogenic microorganisms. Researchers have developed enclosed solar drying systems to address these limitations while maintaining the benefits of solar energy utilization. These improved systems, exemplified by the solar oven configuration depicted in Figure 2, provide a protected environment that maintains drying efficiency while substantially reducing contamination risks.

Figure 1. Historically, through sun-drying

Figure 2. Original model drying cabinet

2.2 Synthesis (add to pulsed copper heating pipes)

Despite the improvements over traditional sun-drying methods, conventional solar dryers still exhibit significant operational limitations. A primary constraint is their thermal inefficiency during periods of reduced solar radiation, such as cloudy days or evening hours, when the temperature within the drying chamber decreases substantially below optimal levels. This temperature reduction compromises the drying process and extends processing time, reducing productivity and potentially affecting product quality. To address these limitations, we have developed an enhanced hybrid drying system integrating infrared radiation with controlled hot water circulation through pulsed copper heating pipes. This innovative design enables rapid thermal response, achieving significant temperature elevation within the drying chamber in approximately one minute. The system operates through convective heat transfer, storing hot water in a dedicated reservoir. Thermal energy is efficiently conducted and radiated throughout the drying chamber via strategically positioned pulsed copper heating pipes, as illustrated in Figure 3. The complete assembly of the new solar drying cabinet with the integrated pulsing heat pipe configuration is presented in Figure 4. This hybrid approach ensures consistent drying conditions even during unfavorable ambient conditions, extending operational hours and enhancing overall system reliability and efficiency.
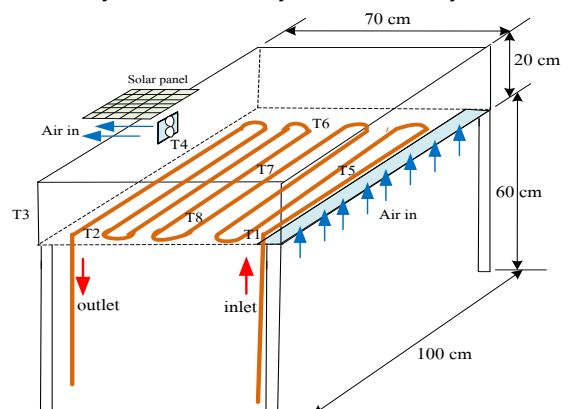
Figure 3. The pulse copper heat pipe is positioned within the drying chamber, and the temperature measurement site is displayed.

Figure 4. New solar drying cabinet and pulsing heat pipes' placement
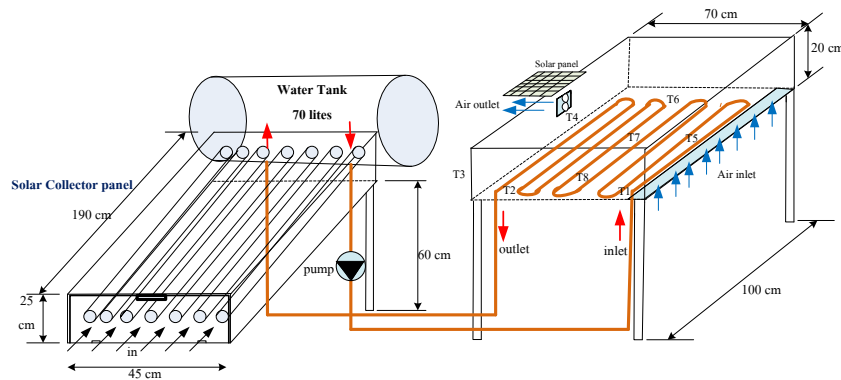
Figure 5. Infrared thermal energy drying system design

2.3 Experimental Setup and System Specifications

The experimental apparatus consists of three primary components: a solar collector, a water storage tank, and the drying chamber equipped with pulsed copper heating pipes. The solar collector (dimensions: 45 cm × 190 cm) employs a flat-plate design with a selective absorber coating to maximize thermal energy capture. The collector was oriented facing south at an inclination angle of 15° to optimize solar radiation collection at the experimental location (latitude 7.6°N, longitude 100.1°E). The water storage tank has a capacity of 70 liters and is constructed from stainless steel with 25 mm polyurethane foam insulation (thermal conductivity: 0.023 W/m·K) to minimize heat losses. A 45W solar-powered circulation pump (flow rate: 2.5 L/min) transfers heated water from the collector to the storage tank and subsequently to the pulsed copper pipe network within the drying chamber. The drying chamber measures 100 cm × 70 cm × 60 cm and is fabricated from an aluminum frame with 4 mm tempered glass on the top surface. The chamber is insulated with 20 mm polyurethane foam on all non-transparent surfaces. The pulsed copper pipe network consists of 12 mm diameter copper pipes (thermal conductivity: 401 W/m·K) arranged in a serpentine configuration with a total pipe length of 7.2 meters. The pipes are spaced 10 cm apart to ensure uniform heat distribution throughout the drying chamber. The system incorporates eight temperature measurement points (T_1-T_8) strategically positioned as shown in Figure 3 to monitor temperature distribution and gradients within the drying chamber.

2.4 Instrumentation and Data Acquisition

Temperature measurements were conducted using calibrated T-type thermocouples (measurement range: -50°C to 150°C, accuracy: ±0.5°C) connected to a data acquisition system (Agilent 34972A) with a scanning rate of 30 seconds. Solar radiation intensity was measured using a calibrated pyranometer (Kipp & Zonen CMP6, sensitivity: 5-20 μV/W/m², spectral range: 285-2800 nm) mounted on a horizontal surface adjacent to the solar collector. Ambient conditions, including temperature, relative humidity, and wind speed, were monitored using an automated weather station (Davis Vantage Pro2) with recording intervals of 5

minutes. The moisture content of food samples was determined using oven drying according to AOAC standards (Method 934.01). Samples were weighed using an analytical balance with 0.001 g precision at predetermined time intervals throughout the drying process to establish moisture reduction curves.

2.5 Experimental Procedure

The experimental trials were conducted over three months (February-April 2024) to evaluate system performance under varying weather conditions. Each experimental run was initiated at 08:00 and continued until 16:00 to capture the full diurnal cycle of solar radiation. Before each experiment, the water tank was filled with fresh water and allowed to preheat for 60 minutes. Three operational modes were evaluated to compare performance for direct sun drying (DR) - traditional open-air drying, solar drying cabinet without supplementary heating (SR), and solar drying cabinet with pulsed copper pipe heating at three temperature setpoints: 50°C, 60°C, and 70°C (SR+W50, SR+W60, SR+W70). For each operational mode, identical food samples (100 g, initial moisture content 80-85% w.b.) were prepared and distributed evenly on drying trays. Temperature readings and sample weights were recorded at 30-minute intervals throughout the drying process.

2.6 Performance Evaluation Metrics

The thermal efficiency of the solar collector and overall system was evaluated using established heat transfer equations described in Section 3. Specifically, the collector efficiency was calculated using Equation (3), while dryer efficiency was determined using Equation (4). Different operational modes were compared based on drying rate, specific energy consumption, and final product quality.Statistical analysis was performed using SPSS software (version 26.0) with a significance level of $p < 0.05$. All experiments were conducted in triplicate, and results are presented as mean values with standard deviations to ensure reproducibility and statistical validity.

3. Results and Discussion

The performance assessment of solar water heating systems requires consideration of three fundamental thermal load components. The primary component involves heating water to the desired temperature, necessitating a specific rate of sensible heat addition. This rate depends on several factors, including the mass flow rate of water, initial supply temperature, and target delivery temperature. The subsequent sections analyze the thermal efficiency parameters and solar radiation characteristics influencing the system's performance.

3.1 Thermal efficiency analysis

The useful thermal energy (Q_u) obtained from air flowing through the solar collector can be calculated using the energy balance equation [6,15]:

$$Q_u = mC_p (T_d - T_s) \qquad (1)$$

Where Q_u represents the useful thermal energy gained (W), $\dot{m}$ denotes the mass flow rate of the working fluid (kg/s), C_p is the specific heat capacity of the fluid (J/kg·K), T_d indicates the delivery temperature (°C), and T_s corresponds to the supply temperature (°C). This fundamental equation enables quantitative assessment of the thermal energy transfer within the system and provides a basis for determining operational efficiency under varying conditions.

3.2 Solar radiationcharacteristics

Solar radiation intensity at the outer boundary of Earth's atmosphere averages approximately 1361 W/m², known as the solar constant. This value represents the solar irradiance per unit area on a spherical surface surrounding the Sun at a radius equal to Earth's orbital distance (1 Astronomical Unit). From the Sun's perspective, Earth is a circular disc that consistently receives this radiation flux. The intercepting disc has an

ASEAN J. Sci. Tech. Report. **2025**, *28*(3), e254983.

6 of 14

area of πr², where r denotes Earth's radius, while the planet's total surface area (4πr²) results from its spherical geometry [7]. The daily solar energy received at a specific terrestrial location can be calculated using integration.

$$Q^{day} = -\frac{1}{2} \int_{-\pi}^{\pi} Q \, dh \tag{2}$$

Where Q^{day} represents the daily solar energy received (J/m²), Q denotes the instantaneous solar radiation intensity (W/m²), and h corresponds to the hour angle (radians). The value of Q becomes positive at sunrise, when the hour angle reaches a specific threshold dependent on the location's latitude and the solar declination angle.

3.3 The thermal efficiency of a solar collector

A solar collector's thermal efficiency (η) represents the ratio between the useful energy extracted from the system and the total solar energy input. Specifically, it quantifies the relationship between the thermal energy utilized to increase the working fluid's temperature and the incident solar radiation energy received by the collector surface. According to established thermal performance principles [4,5,6], this efficiency can be expressed mathematically as:

$$\eta = \frac{\dot{m} \times C_p \times (T_{out} - T_{in})}{A_p \times I_o} \tag{3}$$

Where $\dot{m}$ represents the fluid mass flow rate (kg/s), Cp denotes the specific heat capacity of the fluid (J/kg·K), Tout indicates the fluid temperature at the outlet (°C), Tin corresponds to the fluid temperature at the inlet (°C), Ap refers to the effective aperture area of the collector (m²), and Io designates the incident solar radiation intensity (W/m²). This efficiency parameter provides a critical performance metric for evaluating and comparing various solar collector designs and operational conditions.

3.4 Determination of dryer efficiency

Dryer efficiency quantifies the system's effectiveness in utilizing solar energy for moisture removal. It is the ratio of thermal energy employed in the evaporation process to the total solar energy incident on the dryer surface area. Following established methodologies [21,27,28], the dryer efficiency (η) can be calculated using:

$$\eta = \frac{\dot{m} \times h_{fg}}{A_p \times I_o} \tag{4}$$

Where $\dot{m}$ represents the mass flow rate of moisture removal (kg/s), hfg denotes the latent heat of vaporization for water (kJ/kg), Ap corresponds to the effective collector aperture area (m²), and Io indicates the incident solar radiation intensity (W/m²). This efficiency metric enables a comprehensive assessment of the drying system's performance under various operational conditions and design configurations.

3.5 Infrared combined heat and hot water dryer

The developed hybrid drying system integrates infrared radiation with hot water circulation, offering precise temperature control capabilities. The system permits adjusting the drying chamber temperature to three setpoints: 50 °C, 60 °C, and 70 °C, thereby accommodating various product-specific drying requirements. Supplementary thermal energy can be introduced to the drying chamber by transferring accumulated heat from the water storage reservoir. The innovative copper pipe network design facilitates efficient convective heat transfer throughout the drying chamber, ensuring uniform temperature distribution and optimized drying conditions even during periods of limited solar radiation.

3.6 Experimental results and summary

ASEAN J. Sci. Tech. Report. **2025**, *28*(3), e254983.

7 of 14

Comprehensive thermal performance data were collected from the experimental setup to evaluate the system's efficiency and temperature distribution characteristics. Temperature measurements within the drying chamber and solar radiation intensity monitoring provided insights into the system's operational dynamics under real-world conditions. Figure 6 illustrates the integrated dryer system with combined heat sources, demonstrating the physical configuration of the experimental apparatus. When operating with the thermostat set at 60 °C, the system demonstrated significant temperature elevation within the drying chamber. The ambient temperature surrounding the drying oven, recorded by sensor T_3, was 35.14 °C, while the drying chamber maintained an average temperature of 52.16 °C, indicating an effective temperature differential of approximately 17 °C. Detailed temperature measurements revealed spatial variations within the chamber, with readings from individual sensors as follows: T_1 (50.33 °C), T_2 (48.67 °C), T_4 (50.22 °C), T_5 (47.27 °C), T_6 (54.31 °C), T_7 (57.43 °C), and T_8 (57.15 °C). Throughout the experimental period, the system operated under variable weather conditions with an average solar radiation intensity of 538.92 W/m². The comprehensive temperature data collected from the chamber sensors are summarized in Table 1. The temporal evolution of temperature within the drying cabinet is graphically represented in Figure 7, while Figure 9 illustrates the solar radiation intensity fluctuations over the experimental duration. Notably, the test day featured alternating periods of clear and cloudy sky conditions, providing valuable data on system performance under variable solar input scenarios.

Figure 6. Dryer with combined heat and energy

With the thermostat configured at 60 °C, comprehensive thermal measurements were obtained throughout the experimental apparatus. The ambient temperature surrounding the drying system, recorded by sensor T_3, registered at 35.14 °C, establishing the baseline environmental condition. Concurrently, the drying chamber maintained a mean temperature of 52.16 °C, demonstrating a significant thermal enhancement of 17.02 °C above ambient conditions. Spatial temperature distribution analysis revealed notable thermal gradients within the chamber, with temperature values varying across measurement locations: T_1 (50.33 °C), T_2 (48.67 °C), T_4 (50.22 °C), T_5 (47.27 °C), T_6 (54.31 °C), T_7 (57.43 °C), and T_8 (57.15 °C). The highest temperatures were consistently recorded at positions T_7 and T_8, situated in the central region of the drying chamber. At the same time, the lowest values were observed at position T_5, located near the peripheral zones.Throughout the experimental period, the system operated under variable meteorological conditions with a mean solar radiation intensity of 538.92 W/m². The complete thermal profile data, including minimum, maximum, and average temperature values for all monitoring points, are systematically presented in Table 1. The temporal evolution of temperature within the drying cabinet is illustrated in Figure 7, exhibiting characteristic response patterns that correspond to variations in solar input. Figure 9 provides a detailed representation of solar radiation fluctuations throughout the testing period, capturing the intermittent transitions between clear sky conditions (peak intensity: 875.00 W/m²) and cloud cover events (minimum intensity: 67.50 W/m²). This variability in solar radiation presented an opportune scenario for evaluating system resilience and performance stability under realistic operational conditions.

Table 1. Compare the temperature with the intensity of solar radiation.

ASEAN J. Sci. Tech. Report. **2025**, *28*(3), e254983.

8 of 14

Temp(°C)	min	max	av
T_1	36.88	64.92	50.33
T_2	39.10	63.05	48.67
T_3	31.18	39.92	34.92
T_4	36.83	60.63	50.22
T_5	37.25	58.34	47.27
T_6	42.43	68.29	54.31
T_7	43.57	71.58	57.43
T_8	39.80	70.47	57.15
I_o(W/m^2)	67.50	875.00	538.92

Temperature measurement sensors were strategically distributed throughout the drying chamber to characterize the three-dimensional thermal profile, resulting in observable temperature gradients across the monitored volume (Figure 3). Spatial thermal analysis revealed a systematic temperature distribution pattern, with the highest temperature (57.43 °C) consistently recorded at sensor position T_7, located in the central region of the drying chamber. This central thermal maximum can be attributed to the convergence of convective currents and the cumulative radiative heat transfer from the surrounding copper pipe network. Conversely, the lowest operational temperature was documented at position T_1 (50.33 °C), situated at the inlet junction of the heat exchanger, where the introduction of the working fluid creates a localized cooling effect. This temperature differential of approximately 7.1 °C between the chamber's central and peripheral regions demonstrates the importance of thermal stratification considerations in drying system design and the need for optimized flow distribution to ensure uniform product drying conditions.
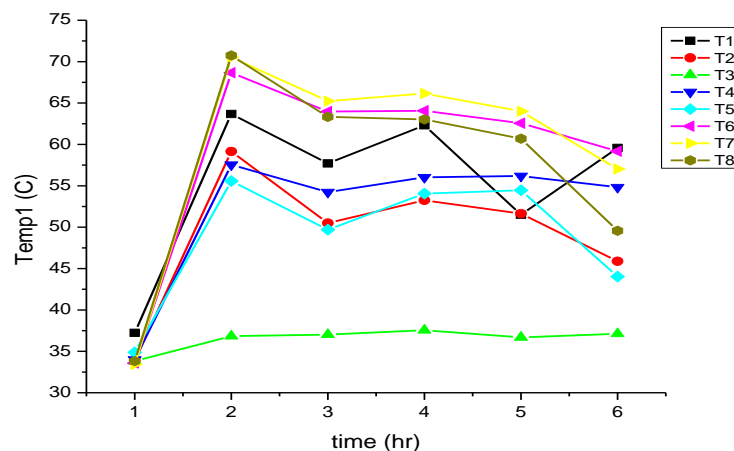
Figure7. The drying chamber's temperature

Comprehensive thermal performance data collected from the drying chamber are systematically compiled in Table 1, presenting minimum, maximum, and average temperature values for each measurement point over the experimental duration. The temporal evolution of these temperature profiles throughout the operational period (09:00-14:00) is graphically represented in Figure 7, illustrating the dynamic thermal response of the system under variable solar insolation conditions. This time interval was specifically selected to capture the maximum solar radiation availability period while documenting the system's thermal behavior during the transition from morning warming to midday peak conditions. The temperature curves demonstrate a characteristic rapid rise during the initial heating phase (09:00-10:00), followed by relative stabilization with fluctuations corresponding to ambient conditions and solar radiation intensity changes.
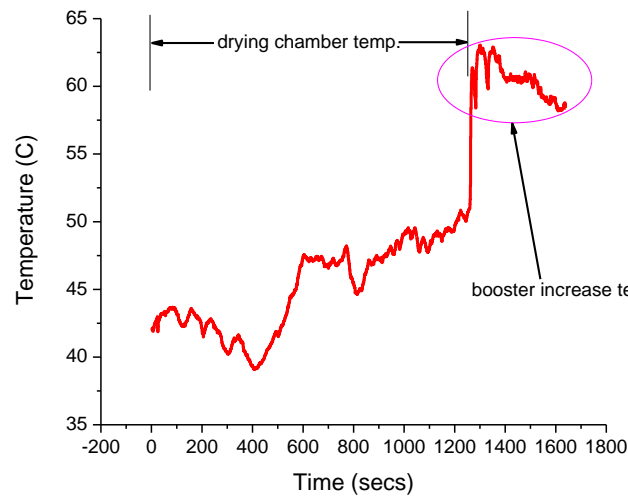
Figure8. The drying chamber's temperature, as well as the booster's increased temperature

The hybrid system demonstrated superior thermal response characteristics to conventional solar dryers, achieving rapid temperature elevation within the drying chamber in under five minutes. This accelerated heating rate can be attributed to the enhanced heat transfer mechanism facilitated by the pulsed copper pipe network, which efficiently conducts thermal energy from the hot water reservoir to the drying environment. Quantitative analysis of the temperature-time profile, as illustrated in Figure 8, revealed an initial heating rate of approximately 3°C per minute, enabling the system to reach operational temperature thresholds significantly faster than traditional passive solar dryers, which typically require 20-30 minutes to achieve comparable thermal conditions. This rapid thermal response represents a critical advancement for applications requiring prompt initiation of the drying process. It protects against transient solar radiation fluctuations by maintaining stable internal temperatures despite external environmental variations.

3.7. Environmental Conditions and Solar Resource Assessment

The experimental trials were conducted under variable meteorological conditions characterized by alternating clear sky and cloud cover periods. This weather pattern provided an opportune scenario for evaluating system performance across a spectrum of solar radiation intensities. Continuous monitoring via calibrated pyranometer recorded solar radiation fluctuations throughout the testing period, with values ranging from 67.50 W/m² during heavily clouded intervals to 875.00 W/m² during optimal clear sky conditions, yielding a mean radiation intensity of 538.92 W/m². These representative mixed-sky conditions are typical of the tropical climate at the experimental location and provide realistic operational parameters for assessing the system's resilience to radiation variability—a critical consideration for practical solar drying applications.

3.8. Dryer Efficiency Analysis

The thermal performance of the drying system was quantitatively evaluated using efficiency metrics that relate moisture removal capacity to solar energy input, as Equation (4) defines dryer efficiency as the ratio of heat energy effectively utilized for moisture evaporation to the total incident solar radiation on the collector surface. All efficiency calculations were performed using a constant aperture area (A_p) of 0.70 m² (0.7 m × 1.0 m) for analytical consistency.This efficiency parameter was calculated as:

$$\eta = \frac{\dot{m} \times h_{fg}}{A_p \times I_o} = \frac{26.53 \times 444.11}{07 \times 523.22} = 32.17\ \%$$

ASEAN J. Sci. Tech. Report. **2025**, 28(3), e254983.

10 of 14

Where the mass flow rate of moisture removal (ṁ) was 26.53 kg/hr, the latent heat of vaporization (h_{fg}) was 444.11 kJ/kg, and the average solar radiation intensity (I_o) was measured at 523.22 W/m². The resulting efficiency value of 32.17% represents a significant improvement over conventional direct sun drying methods, which typically achieve 8-10% efficiencies under similar conditions.
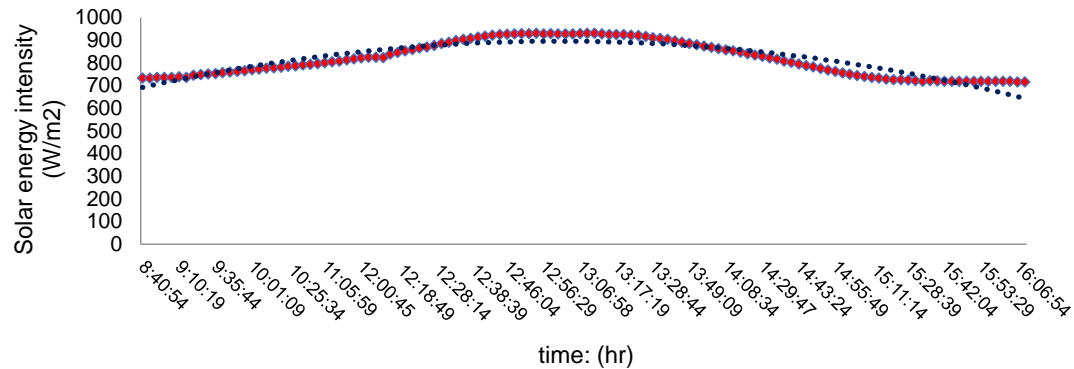
Figure 9. Solar radiation intensity

Table 2. The efficiency of the heat energy dryer, combined with hot water

Dryertype	T_{av}(°C)	ṁ (kg/hr)	I_o (W/m²)	h_{fg} (kJ/kg)	η (%)
DR	35.1	6.87	514.49	434..35	8.28
SR	46.20	8.45	523.22	435.46	10.05
SR+W50	45.10	26.53	523.22	444.11	32.17
SR+W50	47.08	26.55	531.58	446.18	31.83
SR+W50	49.43	19.61	348.73	449.21	36.08
SR+W60	51.30	15.47	552.64	450.67	18.02
SR+W60	52.16	25.94	538.92	451.53	31.12
SR+W60	54.53	22.55	496.35	453.92	29.46
SR+W70	63.67	16.51	841.29	463.13	12.98

Comparative analysis of the thermal performance data presented in Table 2 reveals significant efficiency variations among different operational configurations of the infrared combined heat and hot water dryer. The system demonstrated optimal performance at the intermediate temperature regime across the three controlled temperature setpoints (50 °C, 60 °C, and 70 °C). Specifically, the highest thermal efficiency of 36.08% was achieved when operating at an average chamber temperature of 49.43 °C, with corresponding process parameters including a moisture removal rate of 19.61 kg/s, average solar radiation intensity of 348.73 W/m², and latent heat of vaporization of 449.21 kJ/kg during the water phase transition. This peak efficiency point represents the optimal balance between thermal energy input and effective moisture removal capacity, as graphically illustrated in Figure 10. Notably, the efficiency-temperature relationship exhibits a non-linear response curve, with performance first increasing from 32.17% at 45.10 °C to the peak value of 36.08% at 49.43 °C, followed by a substantial decline to 12.98% at the highest temperature setpoint of 63.67 °C. This performance degradation at elevated temperatures can be attributed to increased thermal losses through the chamber walls and accelerated air circulation that reduces effective moisture extraction despite higher energy consumption. Identifying this optimal operational temperature range (approximately 48-52 °C) provides crucial guidance for maximizing energy utilization efficiency while maintaining effective drying capacity.

ASEAN J. Sci. Tech. Report. **2025**, *28*(3), e254983.

11 of 14
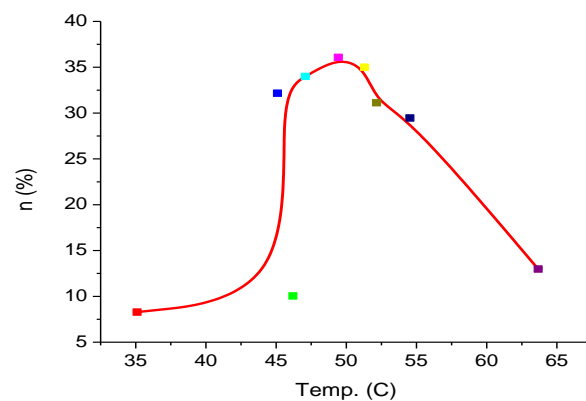
Figure 10. Efficiency of a dryer using infrared heat and hot water at a controlled temperature of 50, 60, and 70 °C

3.9 Comparative Performance of Drying Technologies

The combined infrared radiation and hot water heat dryer demonstrated exceptional thermal efficiency when operating within its optimal temperature range. At the ideal operating point, with an average chamber temperature of 49.43 °C, the system achieved a peak efficiency of 36.08%. This performance optimization occurred at the middle temperature setpoint within the experimental range (50 °C, 60 °C, and 70 °C), indicating that moderate temperature regimes provide the most favorable balance between energy input and moisture removal capacity.Comprehensive comparative analysis of the three distinct drying methodologies investigated in this study revealed substantial performance differentials:This traditional approach yielded the lowest thermal efficiency at 8.28%, reflecting substantial energy losses through uncontrolled radiation, convection, and lack of energy recovery mechanisms.The enclosed solar drying chamber showed modest improvement with an efficiency of 10.05%, representing a 21.4% increase over the direct drying method. This enhancement can be attributed to the contained environment that reduces convective losses and better directs solar radiation toward the product.The hybrid system incorporating pulsed copper pipes achieved a remarkable efficiency of 36.08%, representing a 335.7% improvement over traditional direct drying and a 259.0% enhancement compared to the conventional solar cabinet. This substantial performance gain derives from the system's ability to maintain optimal drying conditions through supplementary heating during periods of reduced solar radiation.

The superior performance of the integrated hybrid system extends beyond mere efficiency metrics. The advanced dryer design enables precise temperature control, improving product quality and consistency. Additionally, the system sustains the drying process for extended periods compared to conventional methods, allowing continuous operation even during unfavorable weather conditions or low solar insolation. This extended processing capability significantly enhances production capacity and reliability, as well as critical commercial or community-scale implementation factors.

Figure 11. Compare the DR, SR, and SR+W dryers' performances.

4. Conclusions

This research demonstrates the successful development and validation of an innovative hybrid drying system that integrates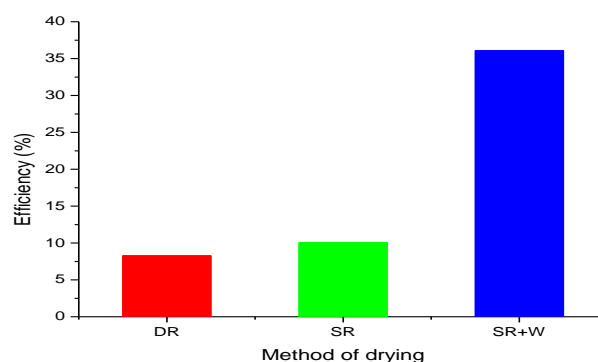 infrared radiation with hot water circulation through pulsed copper pipes. The system employs a dual thermal energy approach: primary solar energy capture via flat-plate collectors for water heating, and subsidiary thermal energy transfer to the drying chamber through an engineered copper pipe network. This configuration creates a controlled thermal environment that effectively addresses the limitations of conventional solar drying methods. Experimental performance evaluation revealed exceptional thermal efficiency of 36.08% under optimized operating conditions, specifically at an average chamber temperature of 49.43 °C, with corresponding process parameters including a moisture removal rate of 19.61 kg/s, solar radiation intensity of 348.73 W/m², and latent heat of vaporization of 449.21 kJ/kg during the phase transition of water from liquid to vapor. This efficiency represents a substantial improvement over traditional drying approaches, with performance gains of 335.7% compared to direct sun drying and 259.0% relative to conventional solar cabinet drying. The hybrid system demonstrated remarkable thermal response characteristics, achieving operational temperature within two minutes of activation and sustaining stable thermal conditions for periods exceeding one hour. This rapid heating capability, combined with extended thermal persistence, addresses a critical challenge in solar drying applications: maintaining effective drying conditions during periods of reduced solar radiation, such as cloudy weather, evening hours, or monsoon seasons. Beyond efficiency metrics, the system offers significant practical advantages, including precise temperature control for optimized product quality, extended operational hours independent of immediate solar availability, and enhanced commercial or community-scale implementation reliability. The integration of pulsed copper pipes for heat conduction represents a cost-effective technological advancement that substantially improves the versatility and applicability of solar drying systems across diverse geographical and climatic conditions. Future research directions should explore optimization of pipe configuration for further efficiency improvements, investigation of thermal storage enhancements to extend operational duration, and comprehensive product quality assessment across various agricultural commodities to establish optimal drying parameters for specific applications.

5. Acknowledgements

References

[1] Phoosomma, P. Construction and Efficiency Test of Solar Drying Cabinet for Nipa Palm Drying for Community Enterprise. In *Proceedings of the 18th International Conference on Control, Automation and Systems (ICCAS)*, PyeongChang, South Korea, 17-20 October 2018; pp. 1414-1417.

[2] Korbuakaew, K.; Phoosomma, P. Prototype a Food Processing Combination Heated Drying Cabinet. In *Proceedings of the 37th International Technical Conference on Circuits/Systems, Computers and Communications (ITC-CSCC)*, Phuket, Thailand, 4-7 July 2022; pp. 1-4. https://doi.org/10.1109/ITC-CSCC55581.2022.9894865

[3] Vengsungnle, P.; Jongpluempiti, J.; Srichat, A.; Wiriyasart, S.; Naphon, P. Thermal performance of the photovoltaic–ventilated mixed mode greenhouse solar dryer with automatic closed loop control for Ganoderma drying. *Case Stud. Therm. Eng.* **2020**, *21*, 100659. https://doi.org/10.1016/j.csite.2020.100659

[4]   Nain, S.; Ahlawat, V.; Kajal, S.; Anuradha, P.; Sharma, A.; Singh, T. Performance analysis of different U-shaped heat exchangers in parabolic trough solar collector for air heating applications. *Case Stud. Therm. Eng.* **2021**, *25*, 100949. https://doi.org/10.1016/j.csite.2021.100949

[5]   Amiri, S.; Gorji, B.; Bandpy, M.; Jahanshahi, M. Drying behaviour of lemon balm leaves in an indirect double-pass packed bed forced convection solar dryer system. *Case Stud. Therm. Eng.* **2018**, *12*, 677-686. https://doi.org/10.1016/j.csite.2018.08.007

[6]   Fadhil, A.; Jalil, J.; Bilal, G. Experimental and numerical investigation of solar air collector with phase change material in column obstruction. *J. Energy Storage* **2024**, *79*, 110066. https://doi.org/10.1016/j.est.2023.110066

[7]   Sharma, M.; Atheaya, D.; Kumar, A. Performance evaluation of indirect type domestic hybrid solar dryer for tomato drying: Thermal, embodied, economical and quality analysis. *Therm. Sci. Eng. Prog.* **2023**, *42*, 101882. https://doi.org/10.1016/j.tsep.2023.101882

[8]   Chouicha, S.; Boubekri, A.; Mennouche, D.; Berrbeuh, M.H. Solar Drying of Sliced Potatoes an Experimental Investigation. *Energy Procedia* **2013**, *36*, 1276-1285. https://doi.org/10.1016/j.egypro.2013.07.144

[9]   GaneshKumar, P.; Sundaram, P.; Sathishkumar, A.; Vigneswaran, V.S.; Chopra, T.; Thakur, U.; Kim, S.; Ramkumar, V. Exploring the performance of an indirect solar dryer by combining three augmentation approaches (trapezoidal absorber, shot blasting, and pebble stone). *J. Energy Storage* **2024**, *78*, 110109. https://doi.org/10.1016/j.est.2023.110109

[10]   Murthy, M.V.R. A review of new technologies, models and experimental investigations of solar driers. *Renew. Sustain. Energy Rev.* **2009**, *13*, 835-844. https://doi.org/10.1016/j.rser.2008.02.010

[11]   Gautam, A.; Chamoli, S.; Kumar, A.; Singh, S. A review on technical improvements, economic feasibility and world scenario of solar water heating system. *Renew. Sustain. Energy Rev.* **2017**, *68*, 541-562. https://doi.org/10.1016/j.rser.2016.09.104

[12]   Bernardo, L.; Davidsson, H.; Karlsson, B. Retrofitting Domestic Hot Water Heaters for Solar Water Heating Systems in Single-Family Houses in a Cold Climate: A Theoretical Analysis. *Energies* **2012**, *5*, 4110-4131. https://doi.org/10.3390/en5104110

[13]   Koua, K.; Fassinou, W.; Prosper Gbaha, P.; Siaka Toure, S. Mathematical modelling of the thin layer solar drying of banana, mango and cassava. *Energy* **2009**, *34*, 1594-1602. https://doi.org/10.1016/j.energy.2009.07.005

[14]   Ismail, M.A.; Idriss, E.M.I. Mathematical modelling of thin layer solar drying of whole okra (Abelmoschus esculentus (L.) Moench) pods. *Int. Food Res. J.* **2013**, *20*, 1983-1989.

[15]   Heydari, A. Experimental analysis of hybrid dryer combined with spiral solar air heater and auxiliary heating system: Energy, exergy and economic analysis. *Renew. Energy* **2022**, *198*, 1162-1175. https://doi.org/10.1016/j.renene.2022.08.110

[16]   Yang, H.; Wang, J.; Wang, N.; Yang, F. Experimental study on a pulsating heat pipe heat exchanger for energy saving in air-conditioning system in summer. *Energy Build.* **2019**, *197*, 1-6. https://doi.org/10.1016/j.enbuild.2019.05.032

[17]   Bastakoti, D.; Zhang, H.; Li, D.; Cai, W.; Li, F. An overview on the developing trend of pulsating heat pipe and its performance. *Appl. Therm. Eng.* **2018**, *141*, 305-332. https://doi.org/10.1016/j.applthermaleng.2018.05.121

[18]   Barba, M.; Bruce, R.; Bouchet, F.; Bonelli, A.; Baudouy, B. Effects of filling ratio of a long cryogenic Pulsating Heat Pipe. *Appl. Therm. Eng.* **2023**, *194*, 117072. https://doi.org/10.1016/j.applthermaleng.2021.117072

[19]   Nikolayev, V. Physical principles and state-of-the-art of modeling of the pulsating heat pipe: A review. *Appl. Therm. Eng.* **2021**, *195*, 117111. https://doi.org/10.1016/j.applthermaleng.2021.117111

[20]   Li, Z.; Sarafraz, M.M.; Mazinani, A.; Moria, H.; Iskander Tlili, I.; Tawfeeq Alkanhal, T.; Goodarzi, M.; Safaei, M. Operation analysis, response and performance evaluation of a pulsating heat pipe for low temperature heat recovery. *Energy Convers. Manag.* **2020**, *222*, 113230. https://doi.org/10.1016/j.enconman.2020.113230

[21]   Nazari, M.A.; Ahmadi, M.H.; Ghasempour, R.; Shafii, M.B.; Mahian, O.; Kalogirou, S.; Wongwises, S. A review on pulsating heat pipes: From solar to cryogenic applications. *Appl. Energy* **2018**, *222*, 475-484. https://doi.org/10.1016/j.apenergy.2018.04.020

[22]   Nikolayev, V. Effect of tube heat conduction on the single branch pulsating heat pipe start-up. *Int. J. Heat Mass Transf.* **2016**, *95*, 477-487. https://doi.org/10.1016/j.ijheatmasstransfer.2015.12.016

[23]   Jo, J.; Kim, J.; Kim, S. Experimental investigations of heat transfer mechanisms of a pulsating heat pipe. *Energy Convers. Manag.* **2019**, *181*, 331-341. https://doi.org/10.1016/j.enconman.2018.12.027

[24]   Kumar, N.; Tripathi, M.M. Design of a Novel Solar Energy Market Model for Indian Scenario. *J. Electr. Eng. Technol.* **2021**, *16*, 2783–2792. https://doi.org/10.1007/s42835-021-00802-9

[25]   Alsharif, M.; Yahya, K.; Geem, Z. Strategic Market Growth and Policy Recommendations for Sustainable Solar Energy Deployment in South Korea. *J. Electr. Eng. Technol.* **2020**, *15*, 803-815. https://doi.org/10.1007/s42835-019-00331-6

[26]   Davidsson, H.; Bernardo, R.; Hellström, B. Hybrid Ventilation with Innovative Heat Recovery-A System Analysis. *Buildings* **2013**, *3*, 245-257. https://doi.org/10.3390/buildings3010245

[27]   Mohamed, I.; Idriss, E.M. Mathematical modelling of thin layer solar drying of whole okra (Abelmoschus esculentus (L.) Moench) pods. *Int. Food Res. J.* **2013**, *20*, 1983-1989.

[28]   Chouicha, S.; Boubekri, A.; Mennouche, D.; Berrbeuh, M. Solar Drying of Sliced Potatoes. An Experimental Investigation. *Energy Procedia* **2013**, *36*, 1276-1285. https://doi.org/10.1016/j.egypro.2013.07.144

[29]   Nazari, M.; Ahmadi, M.; Ghasempour, R.; Shafii, M.; Mahian, O.; Kalogirou, S.; Wongwises, S. A review on pulsating heat pipes: From solar to cryogenic applications. *Appl. Energy* **2018**, *222*, 475-484. https://doi.org/10.1016/j.apenergy.2018.04.020

Yield and Fruit Quality of Four Melon Varieties Cultivated Using the Deep Flow Technique Hydroponic System

Poonnanan Phankaen[1*], and Warawut Kumpanuch[2]

1 Valaya Alongkorn Rajabhat University under the Royal Patronage Sa kaeo, Valaya Alongkorn Rajabhat University under the Royal Patronage, Pathum Thani, 13180

2 Public Administration Program, Faculty of Humanities and Social Science, Valaya Alongkorn Rajabhat University under the Royal Patronage, Pathum Thani, 13180, Thaland

* Correspondence: poonnanan@vru.ac.th

Abstract: This study compares the yield, fruit quality, and economic return of four melon varieties: Galia, Asahi, Khaitongkham, and Baramee. The experiment was conducted in a closed greenhouse using the Deep Flow Technique (DFT) hydroponic system in Sa Kaeo Province, Thailand. The experiment used a Completely Randomized Design (CRD) with four treatments, each replicated five times with 10 plants per replication. Data were collected from five plants per replication for analysis. The results showed that Baramee produced the highest average fruit weight (1.9875 ± 0.1021 kg), which was statistically significant ($p < 0.05$) compared to the other three varieties: Galia (1.6975 ± 0.0386 kg), Asahi (1.6225 ± 0.0866 kg), and Khaitongkham (1.5400 ± 0.1414 kg). However, the Galia exhibited the highest total soluble solids content, measuring 15.5500 ± 0.0577 °Brix, which was significantly higher ($p < 0.05$) than Baramee (14.9500 ± 0.5562 °Brix), Asahi (14.8000 ± 0.0817 °Brix), and Khaitongkham (14.1500 ± 0.0577 °Brix). Cultivating melons in a closed greenhouse system with a DFT hydroponic system effectively reduced pest and disease infestations. This resulted in high-quality fruit flesh and rind with no spoilage or cracking observed. The survival rate of all four melon varieties exceeded 97%, with no statistically significant differences. Furthermore, the Baramee variety provided the highest economic return, generating a profit of 28,750.63 THB per production cycle. These findings can be applied to improve the cultivation of melons or other crops, enhancing production efficiency and ensuring sustainable income for farmers.

Keywords: Melon; DFT hydroponic; yield; fruit quality

1. Introduction

One of the major challenges in crop cultivation is the improper use of chemicals, which leads to pesticide residues exceeding safety standards. This poses health risks to farmers and consumers and is a common issue in soil-based crop cultivation. These problems stem from soil degradation, water scarcity, climate variability, and the prevalence of plant diseases and pests often associated with traditional soil-based agricultural systems. Consequently, chemical dependency has become a common solution to address these issues [1].

Hydroponic cultivation presents an excellent alternative as it enables better control over growing conditions and reduces the risks of plant diseases and pests commonly found in soil-based cultivation systems.

Hydroponic cultivation, which involves growing plants without soil and using nutrient solutions, has gained popularity in many countries. This method allows precise control over the growing environment, enabling plants to achieve optimal growth while reducing the use of harmful chemicals and pesticides that pose risks to consumers. One popular technique for hydroponic melon cultivation in Thailand is the Deep Flow Technique (DFT). This method involves submerging plant roots in a continuously circulating nutrient solution with a depth of more than 15-20 centimeters using non-sloped planting troughs. A key advantage of this technique is the continuous supply of oxygen and nutrients to the plant roots, which promotes rapid growth and high-quality yields. The DFT method effectively addresses this issue in Thailand's hot climate, where plants often suffer from water scarcity during certain periods [2]. Additionally, hydroponic cultivation enables year-round planting. However, Thailand's hot and humid climate can lead to inconsistent yields, and off-season production remains challenging, particularly during the dry season. To overcome these obstacles, closed or controlled environment greenhouse systems are employed. These systems regulate temperature, light, and humidity, providing optimal growing conditions. The modern societal shift towards health and food safety further highlights the benefits of hydroponic cultivation. Closed greenhouse systems significantly reduce the need for chemical pesticides, enabling farmers to produce melons in greater quantities and with higher quality [3-4]. However, hydroponic cultivation requires careful monitoring and adjustment of nutrient solutions to match the specific needs of each plant species. This is crucial because different plants have varying nutrient requirements. Nutrient solution levels must be controlled by measuring the electrical conductivity (EC) to ensure appropriate nutrient concentration and monitoring pH levels to maintain proper acidity or alkalinity. These parameters must be checked daily until the harvest to ensure high-quality yields [5].

Melon (*Cucumis melo* L.), a member of the Cucurbitaceae family, is often referred to as the "queen of cucurbits" and is a commercially significant fruit in many countries. Its popularity stems from its sweet flavor, fragrant aroma, and high beta-carotene content, which varies depending on the variety. However, issues such as inconsistent sweetness, fruit weight, and susceptibility to soil-borne pests and diseases remain challenges in melon production [6]. Melons thrive in both temperate and tropical climates and are believed to have originated in India. In Thailand, two main groups of melons are commonly cultivated. The first group, *C. melo* var. *reticulatus*, includes netted melons, also known as muskmelons, characterized by their netted rinds and flesh that can be green, greenish-yellow, or orange. Popular varieties of this group include Galia and hybrids such as Asahi and Baramee. The second group, *C. melo* var. *inodorus*, consists of smooth-skinned melons like Honeydew and hybrids like Khaitongkham. These varietal differences influence the specific environmental conditions required for optimal growth [7-8].

This study focuses on four commonly grown melon varieties in Thailand, Galia, Asahi, Khaitongkham, and Baramee, each with distinct characteristics. Galia 1346/2559 produces round melon with very thin skin, initially green but turning light orange (golden-yellow) when ripe. The rind features a fine, white netted pattern, and the inner flesh is light green. The average fruit weight ranges from 1.3 - 2.5 kg, with a high total soluble solids (TSS) content ranging from 14 - 17 °Brix [9]. Asahi is characterized by its green netted rind and crisp orange flesh, with a high total soluble solids (TSS) content ranging from 1.5 to 2.4 kg and a high total soluble solids (TSS) content ranging from 14 - 16 °Brix [10]. Khaitongkham 1328/2558: Characterized by its smooth golden skin and firm orange flesh resembling apples, this variety has an average weight ranging from 1.5 to 2.3 kg and a high total soluble solids (TSS) content ranging from 12 -15 °Brix [11]. Baramee 1344/2559 has a round shape with a netted rind. Its orange flesh is crisp, fragrant, and sweet, with a high total soluble solids (TSS) content ranging from 14 - 15 °Brix. The fruits are larger, weighing between 1.8 -2.0 kg [12]. Therefore, to address the abovementioned issues, the researcher developed the concept of comparing four melon varieties suitable for cultivation in closed greenhouse systems using the DFT hydroponic system. This

ASEAN J. Sci. Tech. Report. **2025**, *28*(3), e256961.

3 of 12

study has been conducted under uniform environmental conditions and cultivation practices to develop a model that can be applied to melon farming to maximize benefits for growers.

2. Materials and Methods

2.1 Experimental Design

The study on the yield and fruit quality of four melon varieties was conducted at the Agricultural Learning Center of General Prem Tinsulanonda Statesman Foundation, Non-Mak Khaeng Subdistrict, Watthana Nakhon District, Sa Kaeo Province, Thailand. The study was carried out from May to August 2024. The experiment was designed using a Completely Randomized Design (CRD), with melon varieties as the experimental treatments. The experiment consisted of five replications, each with 10 plants. Five plants were randomly selected from each replication for data analysis.

2.2 Preparation of the Greenhouse for Melon Cultivation Using the Deep Flow Technique (DFT) Hydroponic System

This experiment was conducted in a greenhouse measuring 6 m wide, 12 m long, and 3 m high, with a total usable area of 72 m². The roof was covered with 150-micron plastic to shield the plants from sunlight and regulate the greenhouse's temperature. Additionally, insect-proof nets with 40 threads per inch mesh were installed along the sides to prevent pests from entering (Figure 1a). The cultivation system employed in the greenhouse was the Deep Flow Technique (DFT) hydroponic system, where plant roots are submerged in a nutrient solution at a depth of approximately 0.15 – 0.20 m. four planting rows made of aluminum were set up to accommodate the melon plants. Each planting row measured 0.45 m wide, 11 m long, and 0.25 m deep, with 50 planting holes per row. The planting holes were arranged in a staggered layout with a spacing of 0.30 m between them. The greenhouse could cultivate up to 200 melon plants (Figure 1b). Tap water was used as the primary water source for the hydroponic system in this experiment. Before use, the water was allowed to stand for 24 hours to allow for chlorine dissipation and ensure its suitability for plant growth. The water system utilized in the greenhouse was a recirculating system, where the nutrient solution from all planting rows flowed into a 500 L mixing tank. A float valve controlled the water level in the tank, and a water pump was used to circulate the solution back into the planting rows (Figure 1c). The pump also ensured uniform distribution of nutrients and enhanced oxygen levels in the solution to promote healthy root growth. This greenhouse setup was designed to optimize melon cultivation using the DFT hydroponic system, ensuring high-quality yields and providing knowledge that can be applied to improve production efficiency in future agricultural practices.
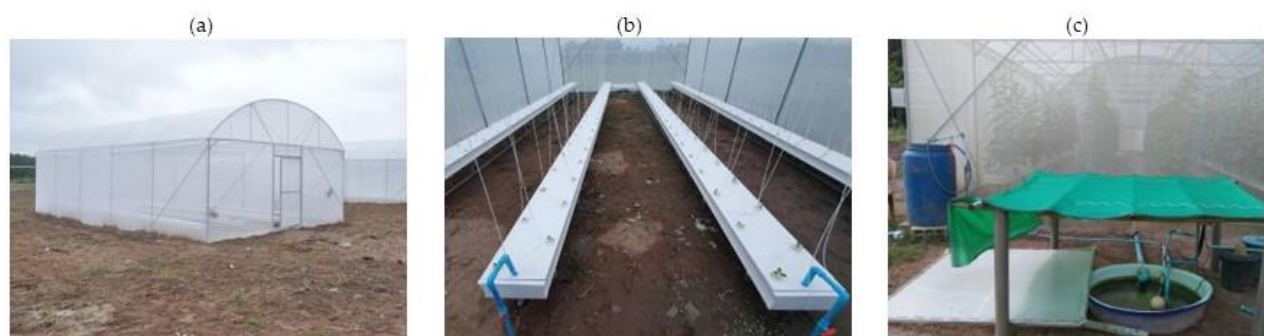

Figure 1. Characteristics of a melon growing greenhouse: (a) greenhouse, (b) growing trough, and (c) tank for mixing fertilizers A and B.

2.3 Nutrient Management and Application

The plant nutrient solution consists of two separately prepared stock solutions: Stock A and Stock B. Stock A contains Nitrogen (N), Phosphorus (P), Potassium (K), Magnesium (Mg), Sulfur (S), Molybdenum

ASEAN J. Sci. Tech. Report. **2025**, *28*(3), e256961.

4 of 12

(Mo), Boron (B), Zinc (Zn), Copper (Cu), and Manganese (Mn), while Stock B contains Calcium (Ca) and Iron (Fe). To prepare this solution, 1 kg of the stock is dissolved in 10 L of clean water, resulting in a solution concentration of 100 grams per liter. The mixture is stirred thoroughly until fully dissolved, then sealed and stored in a shaded area. When the solutions are ready, equal amounts of Stock A and B are measured and added to the mixing tank. Stock A is added first and stirred thoroughly to ensure even blending. Stock B is added and mixed into the solution until a uniform mixture is achieved. Adjusting the concentrations of Stock A and Stock B is crucial in managing the nutrient balance for melons in the hydroponic system. This study uses a 500 L mixing tank to prepare the nutrient solution. An Electrical Conductivity (EC) meter measures the total nutrient concentration in the solution. Once the nutrient solution reaches the appropriate EC level, the pH is adjusted by adding nitric acid. This process ensures that both EC and pH levels are maintained within the optimal range, as indicated in Table 1. The adjustments are carried out daily at 2 specific times: 6:00 AM and 6:00 PM, ensuring consistent nutrient availability for the plants. In addition to nutrient absorption through the roots, three types of nutrients are applied via foliar spraying according to a specific schedule to enhance plant growth and fruit quality. Calcium Boron (Ca-B) is sprayed first on days 23, 30, and 35. Following this, 2 nutrients, including Calcium Boron (Ca-B) and Potassium Sulfate (K_2SO_4), are applied together on days 38, 45, 52, 59, 66, and 73. Afterward, only Potassium Nitrate (KNO_3) is sprayed on days 42, 49, and 56. In the final stages, Potassium Sulfate (K_2SO_4) is applied on days 69, 71, 74, 76, 80, 82, and 84. From day 86 onward, all nutrient applications are discontinued to prepare the plants for the harvest phase, ensuring optimal fruit quality and readiness for collection.

Table 1. Control EC and pH levels in each stage of melon cultivation using the deep flow technique (DFT) hydroponic system.

Day	Planting Stages	EC (mS/cm)	pH
1 -13	Seedling Cultivation	0.5 – 0.8	5.6 – 6.5
14 - 35	Plant Development	1.0 – 1.3	5.6 – 6.5
36 - 42	Pollination	1.5 – 2.0	5.6 – 6.5
43 – 84	Fruit Development	2.0 – 2.3	5.6 – 6.5
85- 90	Harvest Preparation	Refrain from AB fertilizer	
91	Harvesting		

2.4 Methods of Melon Cultivation in a Hydroponic System

In melon cultivation in Figure 2**,** the seed germination process begins by soaking the melon seeds in warm water at 40– 45°C for at least 45 minutes. This step helps to activate the seeds and initiate the germination process. After soaking, the seeds are placed on a clean, damp cloth, such as muslin, and sprinkled with water to keep them moist. The cloth is then covered to maintain humidity, and the seeds are incubated at room temperature for one night (24 hours). The seeds begin to sprout during this incubation period, and small roots emerge. Once the seeds have sprouted, they are carefully transferred to a germination sponge, a hydroponic growing medium. The root tip of each seed is gently inserted into the germination sponge at a depth of approximately one-third of the cube's thickness. This ensures proper positioning and allows the roots to absorb nutrients and water effectively. The germination sponge cubes containing the seeds are then placed in seedling trays. These trays are kept moist by immersing them in water or a nutrient solution prepared using Fertilizer A and B, following the recommended EC (Electrical Conductivity) and pH levels specified in Table 1. After 14 days, the seedlings will have developed 2 - 3 cotyledon leaves. The seedlings are ready to be transplanted into the planting troughs at this stage. Carefully remove the seedlings from the trays, not damaging the roots. Place each seedling into the hydroponic planting pot in the prepared planting troughs. The nutrient levels for this stage should follow the specifications outlined in Table 1.

ASEAN J. Sci. Tech. Report. **2025**, *28*(3), e256961.

5 of 12

During the growth phase, it is essential to prune the lateral shoots (branches) emerging at nodes 1–8 to encourage optimal growth of the main stem. The nodes 9-12 are ideal for pollination and fruit setting, as they provide the most suitable conditions for fruit development. Throughout the growth period, regular care must be taken to train the plant to climb along support strings. This ensures the plants grow upright, remain stable, and develop strong stems, facilitating efficient nutrient uptake and maximizing yield potential. After transplanting, during days 36-42, the melons enter the pollination stage. Pollination should be conducted between 6:00 AM and 10:00 AM, the optimal time for adequate pollination. Following pollination, the plants are monitored for fruit set. Once the fruits reach the size of a fist, selection begins to retain only one fruit per plant. This ensures that the plant's resources are concentrated on producing a single high-quality fruit. To maintain the fruit's shape and support its growth, a string is tied around the fruit's peduncle to keep the branch parallel to the ground. At this stage, pruning is carried out by removing the apical bud at the 26th leaf. This halts further vegetative growth and redirects the plant's nutrients toward fruit development. As the melons approach the harvest stage, the plants are watered with plain water for at least 5 days before harvest. This practice reduces nutrient solution residues in the fruits, ensuring safety and quality. Harvesting typically begins around day 91, though it may occur earlier based on observations of fruit characteristics such as color, netting, fruit shape, internal appearance, and fruit skin. This careful and structured process ensures that the melons are of high quality, both in terms of appearance and flavor, meeting the desired standards for market or consumption.

Figure 2. Melon cultivation: (a) seed germination, (b) seedling nursery, (c) transferring seedlings to planting channels, (d) wrapping twine around the plant for support, (e) caring for plants and pruning side branches, (f) pollination, (g) fruit selection and (h) harvesting the produce

2.5 Analysis of Total Soluble Solids, Fruit Weight, and External and Internal Characteristics

The quality of the melons is analyzed through measurements of fresh fruit weight, total soluble solids (TSS), and observations of external and internal characteristics. The external characteristics included fruit shape, skin color, and fruit skin netting, while the internal characteristics included internal appearance. The weight of the fresh fruit is measured individually using a digital scale. Each fruit is weighed, and the weight is recorded in kilograms (kg) to determine the average weight for the sample. Next, the fruit's external and internal characteristics are observed, recorded, and evaluated using the RHS color chart, ensuring consistent and accurate grading. This process allows for a thorough assessment of the melons' physical properties. Finally, the total soluble solids (TSS) content is measured to assess the sweetness of the fruit. The process

ASEAN J. Sci. Tech. Report. **2025**, *28*(3), e256961.

6 of 12

begins by cutting the fruit and extracting the juice using a clean muslin cloth. A small amount of the extracted juice is then dropped onto the prism of a Hand Refractometer. The prism is covered with a light-shielding plate to distribute the juice evenly. The TSS value is read through the refractometer's eyepiece in a well-lit area and is expressed in degrees Brix (°Brix).

2.6 Analysis of Survival Percentage for Four Melon Varieties

The survival percentage for melon cultivation was analyzed to evaluate the resilience and adaptability of the four varieties. The experiment involved five replications, each with 10 plants, for 50 plants per variety. Data on the survival of the melon plants from each variety were collected and used to calculate the survival percentage. The survival percentage was determined using the formula by Peeracha et al. [13].

$$\text{Survival Rate (\%)} = \frac{\text{Number of surviving x 100}}{\text{Total number of plants}}$$

This calculation provides the percentage of plants that survived the experimental conditions. The results allow for a comparative analysis of the varietys' performance and suitability for cultivation in the specified hydroponic system. The survival is expressed as a percentage, offering insights into the success rate of the cultivation process.

2.7 Return on Investment for Cultivating Four Melon Varieties

The returns from cultivating 4 melon varieties per production cycle were calculated under the same environmental conditions. Each production cycle accommodates 200 plants, with an average production cost of 6,130 THB per cycle. This cost includes seeds, A and B fertilizer, germination sponge, potassium sulfate, calcium boron, trichoderma, wood vinegar, and Ridomil. However, it does not include the costs of constructing the greenhouse, hydroponic system setup, water, electricity, or labor. The analysis involves calculating the survival rate, average fruit weight, and market price. The selling price for melons is set at 90 THB per kg, which is used to compute the total revenue and profit per production cycle.

2.7.1 Survival Rate per Production Cycle

The survival rate for each variety is calculated to determine the number of surviving plants per production cycle using the formula:

$$\text{Number of surviving plants per cycle (\%)} = \frac{\text{Survival rate percentage x 200}}{100}$$

2.7.2 Revenue Calculation

The total revenue for each variety is determined by multiplying the number of surviving plants, the average fruit weight, and the selling price:

Revenue per greenhouse = Number of surviving plants per cycle × Average fruit weight (kg) × 90 THB

2.7.3 Profit Calculation

The profit for each production cycle is calculated by subtracting the production cost from the total revenue:

Profit per production cycle = Revenue per greenhouse − Production cost (6,130 THB)

2.8 Data Analysis

The analysis of recorded data included growth performance, survival rates, fruit weight (kg per fruit), and total soluble solids (TSS) to evaluate differences among the four melon varieties. The process began with an Analysis of Variance (ANOVA) to assess the variability within and between groups. This step determined

ASEAN J. Sci. Tech. Report. **2025**, *28*(3), e256961.

7 of 12

whether statistically significant differences existed among the variety for each measured parameter. If significant differences were found, Duncan's New Multiple Range Test (DMRT) was used to compare the means and identify which varieties differed significantly. This test was performed with 95% confidence to ensure reliable results. The entire analysis was carried out using statistical software to enhance the accuracy and efficiency of the calculations. This approach provided comprehensive insights into the performance and quality of the melon varieties under the given experimental conditions.

3. Results and Discussion

3.1 Analysis of Fruit Weight

The analysis of fruit weight showed that the Baramee produced the heaviest fruits, averaging 1.9875 ± 0.1021 kg, significantly different from the other varieties ($p < 0.05$). When comparing the 3 varieties, Galia, Asahi, and Khaitongkham, Their average fruit weights were 1.6975 ± 0.0386, 1.6225 ± 0.0866, and 1.5400 ± 0.1414 kg, respectively. These findings highlight that the melons' growth and fruit weight varied based on each variety's unique genetic traits. This finding aligns with Atikah and Alvianah [14], who stated that genetic factors determine each melon variety's unique characteristics and growth potential. In general, the fruit size of all melon varieties typically has a diameter of approximately 11–17 cm and a weight ranging between 1.2–2.7 kg [9][15]. Moreover, the growing environment also impacts the fruit weight of each melon variety, even when cultivated under the same conditions. Therefore, adjusting the nutrient levels and environmental factors to suit the specific requirements of the melon variety being grown is essential. This research found that the Baramee was the most suitable for achieving the highest fruit weight under the conditions and methods employed. In addition to standard nutrient applications (A and B), foliar fertilization significantly enhanced fruit yield and quality. Three key nutrients were applied as foliar sprays. The first nutrient is Calcium Boron (Ca-B). Calcium strengthens cell walls, resulting in firmer and crisper fruit texture. Meanwhile, Boron facilitates calcium absorption by the roots, enhances photosynthesis, and promotes pollen tube elongation. A boron deficiency can lead to abnormal pollen tube development, significantly reducing the success rate of pollination [16]. The second nutrient is Potassium Nitrate (13-0-46), which enhances fruit size and weight by stimulating the activity of enzymes in protein synthesis and carbohydrate metabolism [17]. The third nutrient is Potassium Sulfate (0-0-50), which enhances plant growth, yield, and fruit quality. This improvement is attributed to the sulfur content in the fertilizer. Sulfur is a critical component of coenzymes such as thiamine pyrophosphate, which metabolize plant carbohydrates and proteins. Additionally, sulfur plays a vital role in cell division, promoting the growth of plant shoots and aiding in chlorophyll synthesis [18]. Therefore, to achieve high-quality yields, paying close attention to and carefully managing every stage of the melon cultivation process is essential. Each step, from nutrient management to environmental control and foliar fertilization, plays a critical role in ensuring the production of melons that meet desired standards in both quality and yield.

3.2 Total Soluble Solid Content

The analysis of the total soluble solid (TSS) content revealed that the Galia had the highest TSS value, significantly different from the other three varieties ($p < 0.05$). The average TSS values were as follows: Galia (15.5500 ± 0.0577 °Brix), Baramee (14.9500 ± 0.5562 °Brix), Asahi (14.8000 ± 0.0817 °Brix), and Khaitongkham (14.1500 ± 0.0577 °Brix) (Table 2). However, the TSS content of all melon varieties grown using the Deep Flow Technique (DFT) hydroponic system was found to exceed the agricultural product standards set by the National Bureau of Agricultural Commodity and Food Standards (ACFS), Ministry of Agriculture and Cooperatives, which specifies a minimum of 12 °Brix [19]. For all melon varieties, the TSS standard ranges between 12 and 14 °Brix [20]. Also, soilless cultivation enables precise control of the root zone environment,

ASEAN J. Sci. Tech. Report. **2025**, *28*(3), e256961.

8 of 12

allowing plants to absorb nutrients efficiently. This contributes to improved yield and quality of melons, resulting in thicker flesh and higher total soluble solids that meet the quality standards for melon production [6].

Table 2. Weight and total soluble solids (TSS) of four cultivated varieties, including Galia, Asahi, Khaitongkham, and Baramee, cultivated using the deep flow technique (DFT) hydroponic system

Varieties	Weight (kg)	TSS (°Brix)
Galia 1346/2559	1.6975 ± 0.0386[bc]	15.5500 ± 0.0577[a]
Asahi	1.6225 ± 0.0866[bcd]	14.8000 ± 0.0817[b]
Khaitongkham 1328/2558	1.5400 ± 0.1414[cd]	14.1500 ± 0.0577[c]
Baramee 1344/2559	1.9875 ± 0.1021[a]	14.9500 ± 0.5562[b]
F-test	**	**
% CV	10.81	3.72

** Significant difference at $P < 0.05$,

[a,b,c,d] Statistically significant differences at 95% ($p < 0.05$) were determined using Duncan's new multiple range test (DMRT)

3.3 Fruit Shape, Rind Color, and Flesh Color of Four Melon varieties

The research revealed that the fruits of the Galia, Asahi, Khaitongkham, and Baramee shared a circular shape but differed significantly in their rind and flesh characteristics. Galia had a golden yellow rind, clear white netting, and light green-white flesh. Asahi featured a green rind with distinct white netting and orange flesh, while Khaitongkham had a golden smooth rind without netting and golden yellow flesh. The Baramee displayed a green rind with clear white netting and orange flesh (Table 3 and Figure 3). Research showed no evidence of pest or disease infestation during harvest, as growing melons in closed greenhouses effectively minimize the risk of pest damage. Moreover, advancements in modern genetic technology have led to the development of melon varieties with diverse characteristics, such as fruit type, peel and flesh color, flavor, and disease resistance [21]. Additionally, the differences and quality of each melon variety play a crucial role in consumer preferences and market demands. Notably, a well-formed netted rind is a key indicator of ripeness and quality, significantly influencing consumers' purchasing decisions [22].

Table 3. Fruit shape, internal appearance, fruit skin color (by RHS color chart), and fruit skin net of four cultivated, including Galia, Asahi, Khaitongkham, and Baramee.

Varieties	Fruit shape	Internal Appearance	Fruit skin color	Fruit skin net
Galia 1346/2559	Circular	Green to white	Light orange	White net
Asahi	Circular	Orange	Green	White net
Khaitongkham 1328/2558	Circular	Gold	Gold	Non-net
Baramee 1344/2559	Circular	Orange	Orange	White net

3.4 Survival of Melons

The survival of melon plants within the greenhouse from planting to harvest was assessed across five replications, with each replication consisting of 10 plants. The results showed that the Asahi had the highest survival rate at 97.75%, followed by the Galia and Baramee, which both had a survival rate of 97.50%. The variety with the lowest survival rate was Khaitongkham, at 97.25%. However, statistical analysis indicated no significant differences in survival among the four varieties ($p > 0.05$) (Table 4). The primary causes of plant loss were powdery mildew (*Oidium* sp.) and downy mildew (*Pseudoperonospora cubensis*), which affected plants during growth. Powdery mildew, commonly spread by wind, is often caused by overcrowded planting, poor air circulation, and insufficient light exposure. Early symptoms appear as light yellow spots on various parts of the plant. These spots grow larger and are covered with white, powder-like fungal spores, eventually

ASEAN J. Sci. Tech. Report. **2025**, *28*(3), e256961.

9 of 12

turning the leaves yellow-brown, brittle, and dry. Downy mildew primarily affects leaves, beginning as light yellow spots that gradually enlarge into brown lesions with angular shapes bordered by veins. The underside of the leaf corresponding to these lesions often exhibits fungal growth. Severe infections cause leaves to dry, with edges curling and eventually falling off, leading to vine death. To mitigate these issues, infected plants were promptly removed to prevent fungal spread, and weekly treatments with Trichoderma, wood vinegar, and ridomil were applied to control pests and diseases. This study underscores the importance of selecting melon varieties that are suited to local environmental conditions and resistant to diseases. These factors ensure high-quality yields and optimal production [23] [15]. Effective cultivation practices, including disease management and appropriate environmental adjustments, are necessary to achieve consistent survival rates and maintain the quality of melon production.
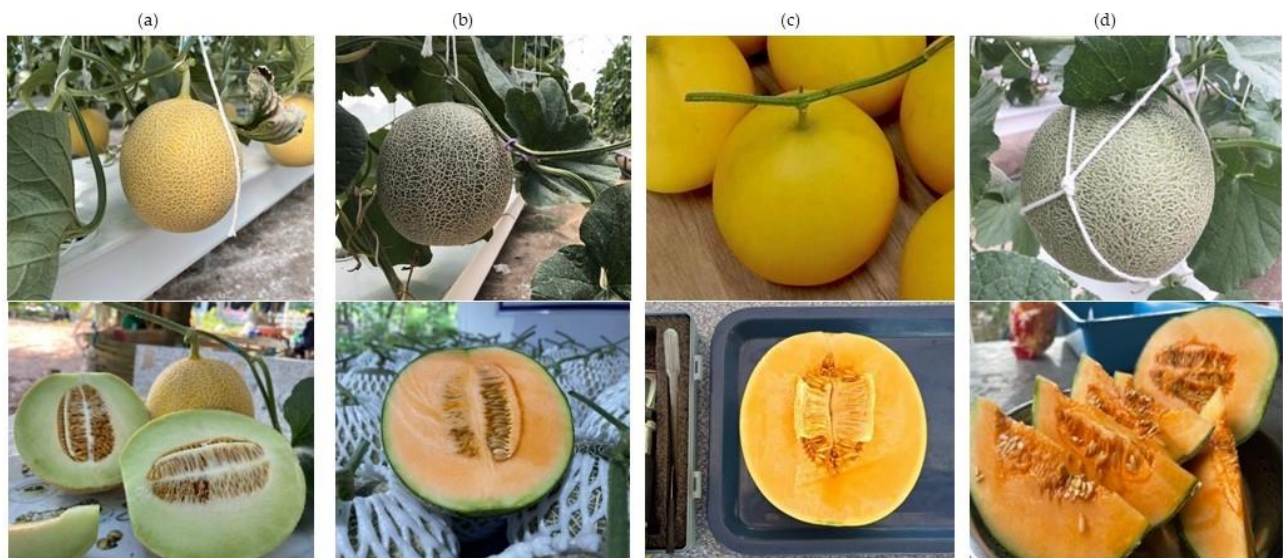
Figure 3. External and internal characteristics of four cultivated varieties: (a) Galia 1346/2559, (b) Asahi, (c) Khaitongkham1328/2558, and (d) Baramee 1344/2559

3.5 Comparison of Profits from Cultivating Four Melon Varieties

The comparison of profits generated from cultivating four melon varieties, including Baramee, Galia, Asahi, and Khaitongkham, under identical environmental conditions, reveals significant differences in economic returns. Each production cycle in a single greenhouse accommodates 200 plants, with an average production cost of 6,130 THB per cycle. Melons were sold at a fixed price of 90 THB per kg. The experiment results revealed that the Baramee achieved the highest profit due to its superior fruit weight and yield. The profits for the other varieties, in descending order, were Galia, Asahi, and Khaitongkham, with respective profits of 28,750.63, 23,661.13, 22,417.89, and 20,827.70 THB per production cycle (Table 4). These results suggest that, among the four varieties, Baramee is the most economically viable option under the specified conditions. However, the choice of variety for commercial production should also consider local environmental factors, disease resistance, and market preferences to ensure maximum profitability and sustainable melon farming.

ASEAN J. Sci. Tech. Report. **2025**, *28*(3), e256961.

10 of 12

Table 4. Return on investment for cultivating four melon varieties per production cycle per greenhouse

Varieties	% Survival	Survival/ Greenhouse (plant)	Weight (kg)	Selling price (THB)	Profit (THB)
Galia 1346/2559	97.50 ± 5.0000	195.00	1.6975	29,791.13	23,661.13
Asahi	97.75 ± 2.6300	195.50	1.6225	28,547.89	22,417.89
Khaitongkham 1328/2558	97.25 ± 3.2016	194.50	1.5400	26,957.70	20,827.70
Baramee 1344/2559	97.50 ± 5.0000	195.00	1.9875	34880.63	28,750.63
F-test	ns				
% CV	3.76				

ns = not Significant difference, Statistically significant differences at the 95% ($p < 0.05$) were determined using Duncan's new multiple range test (DMRT)

4. Conclusions

This study focused on four melon varieties' growth performance and quality, including Galia, Asahi, Khaitongkham, and Baramee. They were grown in a closed greenhouse using the Deep Flow Technique (DFT) hydroponic system. The results demonstrated that all four varieties thrived and produced high-quality yields. The Baramee had the highest average fruit weight, measuring 1.9875 ± 0.1021 kg, with statistically significant differences from other varieties ($p < 0.05$). Meanwhile, the Galia exhibited the highest total soluble solids (TSS) at 15.5500 ± 0.0577 °Brix, also with statistically significant differences ($p < 0.05$). All four varieties displayed excellent rind and flesh characteristics, with no spoilage, pest damage, or fruit cracking, resulting in a high survival percentage. However, minor losses during the growth phase were attributed to powdery mildew (*Oidium* sp.) and downy mildew (*Pseudoperonospora cubensis*). The findings indicate that cultivating the Baramee provides the highest economic return, generating 28,750.63 THB per production cycle. This research offers practical guidance for farmers to adapt or apply hydroponic melon cultivation techniques to other crops. Farmers can select varieties based on production goals, prioritizing higher yields or superior taste quality. Additionally, greenhouse management techniques, including environmental control and disease prevention, can be implemented to improve plant survival percentage. The findings can also support strategic market planning to maximize revenue from product sales. Furthermore, farmers may diversify their production by cultivating other crops using the hydroponic system, increasing income streams and reducing risks associated with market fluctuations or environmental challenges. This aligns with modern agricultural practices that emphasize value addition and sustainable development.

5. Acknowledgements

References

[1]   Pawinee Ch. The effects of bio-extract and chemical fertilizer on growth and yield of spinach (*Spinacia oleracea* L.) under a hydroponic growing system. Naresuan Phayao Journal. **2017**, *12*(3), 51-54.

[2]   Suwan, P.; Tanachod, T.; Kittipong, M.; Duannraem, P. Control hydroponics cabinets with artificial light and nanobubble technology. Journal of Innovative Technology Research. **2018**, *3*(2), 1-10.

[3]   Thanakorn, N.; Nuttapong, M. Energy conservation in the closed-system greenhouse. EAU Heritage Journal Science and Technology. **2020**, *14*(1), 1-13.

[4]   Bongkoj, S.; Mongkol, P.; Tithima, C.; Natacha, P.; Aphisit, C. Development of greenhouse and monitoring system using IoT. UBU Engineering Journal. **2012**, *14*(3), 132-143.

[5]   Pornkid, U. Automatic nutrient solution control system for planting hydroponics vegetables with internet of things (IoT). Rajamangala University of Technology Srivijaya Research Journal. **2018**, *11*(2), 146-157.

[6]   Napaporn, J.; Watcharawit, R. Effect of substrates on growth and yield of Muskmelon (*Cucumis melo* L.). Rajabhat Rambhai Barni Resaerch Journal. **2018**, *13*(2), 17-24.

[7]   Iss, S.; Sumidtra S. The study on the suitable growing medium for 'Orange Pearl' melon (*Cucumis melo* L.). Khon Kaen Agriculture Journal. **2023**, *51*(1), 547-553.

[8]   Kancharoen, S. Melon cultivation in growing media. Kasetapirom. **2021**, *7*(32), 46-49.

[9]   Supakracha, A.; Karistsapol, N.; Sujirat, S. Growth and yield of 4 muskmelon varieties cultivated under greenhouse conditions in Songkhla province. Thai Science and Technology Journal. **2019**, *28*(8), 1452-1461.

[10]   Nakonseed. **2020**. ASAHI. [Online], from: www.nakhonseeds.com/product-page/asahi. (November 25, 2024).

[11]   Kasetsart University Research and Development Institute**. 2023**. Khithongkham. [Online], from: www3.rdi.ku.ac.th/?p=82046. (November 25, 2024).

[12]   Technology Chaoban. **2018**. Mopiyanay Melon Farm. [Online], from: https://www.technologychaoban.com /agricultural-technology/article_89618. (November 25, 2024).

[13]   Peeracha, M.; San, K.; Nathawat, K.; Chongrak, W. Species trials of native fast growing tree species at Trat agroforestry research and training dtation, Mueang district, Trat province. Thai Journal of Forestry. **2015**, *34*(1), 48-56.

[14]   Atikah, T.A.; Alvianah, A. Growth of melon **(*Cucumis melo* L.)** varieties on different plant media composition in conditions of hydropanic drip irrigation. Russian Journal of Agricultural and Socio-Economic Sciences. **2023**, *5*(137), 98-108. https://doi.org/10.18551/rjoas.2023-05.10

[15]   Chiti, S; parinyawadee, S.; Pimrum, S. Greenhouse melon production technology. (1st ed.). Chiang Mai: Technology Transfer Institute to Community, Rajamangala University of Technology Lanna. **2023**, 40 p.

[16]   Teerayut, K.; Niyom, B.; Pantipa, L.; Chanpen, C. Effect of calcium-boron fertilizer application on quality of melon fruit. Journal of Agricultural. **2021**, *37*(3), 349-358.

[17]   Thimaporn, L. Effect of potassium nitrate and aeration on rubber (*Hevea brasiliensis* Muell. Arg.) seed germination and seedling growth. A Thesis Submitted in Partial Fulfillment of the Requirements for the Degree of Master of Science in Plant Science Prince of Songkla University, **2018**, *62*.

[18]   Jutathip, N.; Pornpairin, R.; Suphachai, A. Ratio of potassium chloride and potassium sulphate fertilizer on growth, yield and yield quality of cherry tomato cv. CH154. Khon Kaen Agriculture Journal SUPPL. **2020**, *1*, 202-207.

[19]   Tansinee, S.; Pariyanuj, C.; Pichittra, K. Effects of irrigation management on growth and quality of greenhouse melon (*Cucumis melo* L.). Thai Science and Technology Journal. **2021**, *29*(5), 838-849.

[20]   Phaitoon, S.; Sumit, K.; Thararat, P. Remote autonomous control system for melon planting in the greenhouse. Research funded by the income budget and the Research and Development Fund Burapha University, **2020**, *56*.

[21] Longlan, X.; Yuhua, H.; Lingli, T.; Yongyang, X.; Guangwei, Z. Genetics, Genomics, and breeding in melon. *Agronomy.* **2022**, *12*(11), 2891. https://doi.org/10.3390/agronomy12112891.

[22] Javier, O.; Juan P. F.T. Identification of melon fruit quality quantitative trait loci using near-isogenic lines. Journal of the American Society for Horticultural Science. **2018**, *133*(1), 139-151. https://doi.org /10.21273/JASHS.133.1.139

[23] Nawarat, D. Effect of Fermented Bio-extracts on Growth, Yield and quality of melon (*Cucumis melo* L.). A Thesis Submitted in Partial Fulfillment of the Requirements for the Degree of Master of Agriculture in Agricultural Resources Management School of Agriculture and Cooperatives Sukhothai Thammathirat Open University, **2018**, *53*.

Academic article

Prediction of Electricity Consumption Using Interpretable Machine Learning Approach

Theera Thongsanitkarn[1*], Prompong Sugunnasil[2], Waranya Mahanan[3], and Sumalee Sangamuang[4]

[1] Faculty of Engineering, Chiang Mai University, Chiang Mai, 50200, Thailand

[2] College of Arts, Media, and Technology, Chiang Mai University, Chiang Mai, 50200, Thailand

[*] Correspondence: theera_th@cmu.ac.th

Abstract: The continuously increasing demand for electricity presents significant issues for policymakers and utility companies. An accurate forecast of electricity usage is critical for effective energy management. This thesis provides an interpretable machine-learning approach for forecasting energy demand that incorporates macroeconomic variables such as GDP, inflation, and industrial growth. The study uses data from the World Development Indicators from 1973 to 2021 and employs the multi-model. Our findings emphasize the importance of economic considerations on electricity demand, resulting in a reliable method for forecasting energy consumption. This study adds to the body of knowledge by providing a clear model to aid in decision-making processes connected to energy management and policy creation.

Keywords: Electricity consumption; machine learning; macroeconomic; interpretable models

1. Introduction

Accurately predicting electricity consumption is critical for economic stability, policymaking, environmental sustainability, social development, and technological innovation, as it influences resource allocation, energy security, carbon reduction strategies, infrastructure planning, and the integration of smart grids. From an economic perspective, it ensures efficient resource allocation and stabilizes energy markets [1, 2]. In the political domain, reliable forecasts guide energy policy and enhance energy security by reducing dependency on foreign sources and promoting renewables [3]. Environmentally, it is crucial for carbon reduction and balancing the energy mix [4]. From a social perspective, forecasts drive urban planning and equitable energy access, ensuring reliable infrastructure in growing urban centers [5-6].

Numerous techniques have been employed in electricity consumption forecasting, including Artificial Neural Networks (ANNs) [7-8], Support Vector Machines (SVMs) [9], Autoregressive Integrated Moving Average (ARIMA) [10-11], Gradient Boosting Machines (GBMs) [12], and Long Short-Term Memory Networks (LSTMs) [13-14]. ANNs and LSTMs are highly valued for their ability to capture nonlinear relationships and long-term dependencies in consumption patterns. At the same time, SVMs and ARIMA are often used for their capability to model linear trends. Hybrid approaches combine these models and have also gained popularity for improving forecast accuracy [15]. For instance, combining ARIMA with ANNs [11] can leverage the strengths of both linear and nonlinear methods. Despite the success of these techniques,

many rely on black-box models such as ANNs and LSTMs, which provide limited interpretability and transparency. This poses a significant drawback, especially in policymaking and critical infrastructure planning, where understanding the factors influencing forecasts is crucial. As a result, there is a methodological gap in the literature, as most work emphasizes model performance without addressing the need for interpretability and explainability in electricity consumption forecasting models.

Electricity consumption is influenced by several factors, ranging from external environmental conditions to internal economic dynamics. Weather conditions are a key driver, as temperature variations directly impact heating and cooling demands [16]. Similarly, population growth is critical, as urbanization increases the demand for residential and industrial energy consumption [17-18]. Among these, macroeconomic variables such as Gross Domestic Product (GDP), inflation rates, and industrial output are particularly influential, reflecting broader economic activities that drive overall energy consumption [19-21]. However, as mentioned earlier, most forecasting techniques rely on black-box methods such as ANNs or LSTMs, making it difficult to determine how much each factor contributes to electricity consumption, leaving policymakers and planners without actionable insights into the drivers of demand.

This research addresses this issue by employing explainable/interpretable machine-learning techniques to identify and understand the factors influencing electricity consumption. Explainable machine learning models are designed to provide transparency by revealing how inputs impact predictions. These methods enhance interpretability by predicting outcomes and explaining the decision-making process behind the predictions. One significant advantage of explainable models is that they provide more precise insights into feature importance, allowing stakeholders to understand which factors drive consumption trends [22-23]. Furthermore, improved accountability is achieved through these methods, allowing model users to validate predictions and ensure that forecasts align with domain knowledge or regulatory standards [24-25]. Feature attribution and model transparency are two research domains within explainable machine learning that extract more profound insights. Feature attribution techniques, such as SHAP and LIME, help determine which variables are most influential in predicting outcomes [26-27]. On the other hand, model transparency methods, such as decision trees and generalized additive models (GAMs), provide an intuitive understanding of how input variables relate to electricity demand, offering a clear view of the decision process [28]. These techniques provide actionable insights for decision-makers, bridging the gap left by traditional black-box models.

Accurate forecasting of electricity consumption plays a crucial role in planning infrastructure, optimizing generation capacity, and ensuring the reliability of power grids. By predicting future electricity demand, policymakers can make informed decisions on infrastructure investments, such as upgrading grids and expanding generation facilities, ensuring they meet future demand without over-investment or capacity shortages [29, 30]. Demand forecasting optimizes generation capacity by allowing energy providers to adjust production based on predicted demand, reducing operational costs and minimizing waste, especially in markets with renewable energy sources that fluctuate with weather conditions [31-32]. This also enhances the integration of renewable energy into the grid by balancing demand with the intermittent supply of solar and wind power, promoting sustainability while reducing reliance on fossil fuels [33-34]. Moreover, accurate forecasts are vital for maintaining the reliability of power grids, enabling utilities to anticipate risks such as supply shortages or unexpected surges, thereby preventing blackouts and ensuring consistent service delivery [35, 36]. Through better planning and optimization, consumption forecasting strengthens infrastructure and operational efficiency and supports environmental sustainability and energy market stability.

Electricity consumption is influenced by several key factors, which include: (1) weather and climate cmiconditions, where temperature, humidity, and seasonal variations affect heating and cooling demands [37-38]; (2) economic growth and industrial activity, as higher industrial production and gross domestic product (GDP) growth drive increased electricity demand [39]; (3) population growth and urbanization, where expanding urban areas and increased population density lead to higher residential and commercial consumption [40-41]; (4) technological advancements, both increasing demand through energy-intensive technologies and decreasing it through energy-efficient solutions [42-43]; (5) energy prices and policy, where fluctuations in electricity prices and government regulations can either encourage or limit consumption [44-45]; (6) household income and consumption behavior, with wealthier households generally consuming

ASEAN J. Sci. Tech. Report. **2025**, 28(3), 257539.

3 of 27

more electricity due to higher appliance ownership, though energy-saving behavior can mitigate this effect [46-47]; and (7) technological disruptions, such as the rise of electric vehicles (EVs) increasing demand and smart grids promoting efficient consumption [48-49]. Despite identifying these factors, no comprehensive study isolates and quantifies the individual influence of each factor on electricity consumption.

The autoregressive integrated moving average (ARIMA) model is effective for short-term electricity demand forecasting, especially in cases where data exhibits linearity and stationarity, making it particularly useful for stable, predictable energy systems. However, when seasonality is a significant factor, the Seasonal autoregressive integrated moving average (SARIMA) model improves performance by accounting for seasonal variations, resulting in better forecast accuracy and reduced prediction errors [10]. While ARIMA performs well with simpler, linear datasets, it struggles with nonlinear data, as seen in the Irish study, where the artificial neural network (ANN) model outperformed ARIMA for highly variable loads [11]. Applying neural networks, particularly ANN and long short-term memory (LSTM), has significantly improved energy demand forecasting by effectively handling complex, nonlinear, and time-dependent data. ANN models have demonstrated enhanced accuracy in short-term load forecasting by closely following actual load patterns, making them beneficial for operational engineers and policymakers in optimizing energy distribution and infrastructure investment [8]. Moreover, models like LSTM, which capture periodic energy consumption patterns, have superior performance in long-term forecasts, outperforming traditional statistical methods [50]. These methods consistently demonstrate improved forecasting accuracy across multiple customer datasets, as seen in the neural basis expansion analysis for time series forecasting (N-BEATS) and bidirectional recurrent neural network (RNN) models, making them crucial for both short-term and long-term energy planning [7, 50-51]. The support vector machine (SVM) is highly effective for electricity demand forecasting, particularly in handling nonlinear, time-variant, and seasonal data. External environmental factors significantly influence electricity load by incorporating weather parameters (temperature, wind speed, and solar radiation) [52]. This approach enhances forecasting accuracy by filtering trends and seasonal fluctuations [53], and is further strengthened by integrating data preprocessing techniques such as Fourier transforms and noise reduction [9]. The combination of these strategies improves prediction accuracy and provides robust insights into demand patterns, making SVM a versatile tool for mid- and long-term electricity demand forecasting [9, 52, 53]. Ensemble learning models have consistently demonstrated superior performance in electricity demand forecasting across different contexts. A common finding among all studies is the significant improvement in forecasting accuracy when employing ensemble methods compared to single models. For instance, the gradient boosting regression tree (GBRT) and hybrid models showed lower error rates in predicting residential energy consumption [12, 54-56]. Moreover, innovative combinations like the improved coupled generative adversarial stacked auto-encoder (ICoGASA) and the novel time series ensemble approach further enhance the accuracy by addressing nonlinear patterns and stochastic fluctuations in energy demand [54-55]. This makes ensemble techniques highly valuable for policymakers and operation engineers, contributing to better grid stability and energy management [12, 54-56].

While these models demonstrate improved predictive performance, they often lack interpretability, which limits their applicability in critical decision-making. This presents a methodological gap, as current research largely focuses on accuracy and ignores the models' explainability. Addressing this gap requires integrating explainable or interpretable machine learning techniques, such as Shapley additive explanations (SHAP) or local interpretable model-agnostic explanations (LIME), into the forecasting models. The impact of filling this gap would be substantial, as it would enable more informed decisions in electricity grid management, policymaking, and sustainable planning, improving both the trust in and the utility of predictive models.

Interpretable machine learning (IML) refers to a subset of machine learning techniques designed to make the decision-making process of models transparent and understandable to humans. Unlike traditional "black box" models [19, 23], which provide little to no insight into how they arrive at their predictions, IML aims to explain each decision, making it easier to understand, trust, and manage these models. This is especially important in high-stakes fields such as healthcare, finance, and energy management, where understanding the rationale behind predictions is crucial for regulatory compliance, ethical considerations, and strategic decision-making [22, 25].

Several types of interpretable machine learning methods are categorized into intrinsic and post hoc interpretability. Intrinsic interpretability refers to inherently understandable models due to their simple structure, such as decision trees, linear regression, and rule-based models. These models are built in a way that makes their internal workings easily interpretable by humans [32]. On the other hand, post hoc interpretability applies to complex models like neural networks and ensemble methods, where interpretability is added after the model is built. Techniques such as LIME, SHAP [31], and feature importance measures help understand the model's predictions after training.

Interpretable machine learning has been effectively applied in various domains. For instance, in healthcare, IML models are used to predict patient outcomes while providing explanations that help medical professionals understand the factors contributing to these predictions. This can improve diagnosis, treatment planning, and patient management [27]. In the finance sector, IML aids in credit scoring [30], where the model's transparency helps justify credit decisions to regulators and customers. Similarly, in the energy sector, IML models can forecast electricity consumption by explaining how macroeconomic variables such as GDP growth, industrial activity, and population trends influence energy usage. This transparency is critical for policymakers and utility companies to make informed decisions.

In predicting electricity consumption, using interpretable machine learning approaches can significantly enhance the understanding of how various factors contribute to energy usage patterns. For example, using decision trees (DT) as an IML method involves employing the DT model to create an explainable reasoning structure. Using DTs to construct reasoning patterns that are easy to interpret enhances the model's accuracy. This approach is particularly effective in industrial analysis, helping to improve and optimize processes for greater efficiency in future industries. This level of detail improves the accuracy of predictions and provides actionable insights for energy management and policy formulation [29]. By leveraging IML, researchers can develop models that predict consumption accurately and explain the underlying drivers of these predictions, making the models more useful for stakeholders.

2. Materials and Methods

2.1 Overall Concept

Forecasting electricity consumption is a complex task due to factors such as seasonal variability, population growth, and technological changes [35, 57]. Traditional statistical models often struggle with this challenge because the relationship between electricity demand and its predictors tends to be nonlinear and dynamic [58–59]. In response, machine learning (ML) models have gained popularity for their ability to capture complex patterns and process large datasets [7–8]. However, their "black-box" nature raises concerns about transparency and interpretability, particularly for stakeholders like policymakers [51, 60]. As a result, integrating explainable AI techniques is essential to enhance trust and facilitate actionable insights. Macroeconomic variables—such as GDP, inflation, and interest rates—are increasingly used as predictors due to their strong links with energy demand. Economic growth typically drives up industrial and commercial electricity use [61], while downturns or inflation may suppress demand as production slows and consumers reduce usage [62]. GDP reflects overall economic activity, inflation influences household and industrial purchasing power, and interest rates affect investment decisions in energy-related technologies. Therefore, incorporating these variables is crucial for improving the accuracy and relevance of electricity consumption forecasts.

The use of machine learning models in electricity consumption forecasting has introduced a significant challenge: the issue of explainability. Traditional models, such as linear regression, offer transparency regarding how inputs relate to outputs. However, complex machine learning models often lack this transparency, especially deep learning and ensemble methods like random forests and gradient boosting. These models, though powerful, are frequently criticized as "black boxes" because they do not provide insights into the underlying relationships between input variables and the predicted outcomes [63-65]. Explainability is particularly important in electricity forecasting because energy policymakers and grid operators must understand the reasons behind the model's predictions to make informed decisions. This is where explainable artificial intelligence (XAI) comes into play, offering tools and techniques that help interpret the predictions of complex models. Methods such as SHAP and LIME provide insights into how each feature

ASEAN J. Sci. Tech. Report. **2025**, *28*(3), 257539.

5 of 27

contributes to the prediction, enabling a deeper understanding of the model's behavior. Incorporating explainability into machine learning models fosters transparency and trust, which is critical in sectors like energy, where the stakes are high, and decisions must be evidence-based. By ensuring that the models are interpretable, energy policymakers can better align forecasts with their strategic objectives, enhancing decision-making processes and improving the overall reliability of electricity consumption forecasts.

3. Results and Discussion

3.1 Data Exploration and Preprocessing

The first step in the proposed method involves collecting data from reliable, publicly available sources, such as the World Development Indicators (WDI) database, which provides macroeconomic variables (e.g., GDP, inflation rates, industrial growth) and electricity consumption data for Thailand from 1973 to 2021. These datasets offer varying levels of granularity—monthly, quarterly, and annually—and are supplemented by national economic reports and other macroeconomic resources. Once collected, the data undergoes preprocessing to resolve missing or inconsistent entries. Table 1 summarizes the variables used, offering a comprehensive view of Thailand's economic environment and its relationship to electricity consumption.

Table 1. Sources of data.

Variable	Source
Electric power consumption (kWh per capita)	WDI
Domestic credit to private sector (% of GDP)	WDI
Deposit interest rate (%)	WDI
Inflation, GDP deflator (annual %)	WDI
Industry (including construction), value added (% of GDP)	WDI
Imports of goods and services (% of GDP)	WDI
International tourism, number of arrivals	WDI
Manufacturing, value added (% of GDP)	WDI
Exports of goods and services (% of GDP)	WDI
GDP growth (annual %)	WDI
Foreign direct investment, net outflows (% of GDP)	WDI
Foreign direct investment, net inflows (% of GDP)	WDI
Trade (% of GDP)	WDI
Current account balance (% of GDP)	WDI
Interest payments (% of expense)	WDI
Interest payments (% of revenue)	WDI
Population growth (annual %)	WDI
Urban population growth (annual %)	WDI
Households and NPISHs Final consumption expenditure (annual % growth)	WDI
Official exchange rate (LCU per US$, period average)	WDI
Unemployment, total (% of total labor force) (national estimate)	WDI
Domestic credit to private sector by banks (% of GDP)	WDI

ASEAN J. Sci. Tech. Report. **2025**, *28*(3), e257539.

6 of 27

Table 1. Sources of data (continue).

Variable	Source
Gross fixed capital formation, private sector (% of GDP)	WDI
Expense (% of GDP)	WDI
Final consumption expenditure (% of GDP)	WDI
Gross domestic savings (% of GDP)	WDI

   The first data exploration phase involved a detailed analysis of the dataset's completeness and structure. It was discovered that the dataset contained no missing values, confirming the credibility of the following study. Descriptive statistics were performed to comprehend the variables' properties further, providing essential metrics such as mean, median, standard deviation, and range. Table 2 displays these descriptive statistics, which assist in illustrating the diversity and distribution of the data, providing insights into potential skewness or outliers present in specific variables.

Table 2. Statistical description of the data.

	count	mean	std	min	25%	50%	75%	max
Electric power consumption (kWh per capita)	49	1.36E+03	9.24E+02	1.67E+02	4.17E+02	1.36E+03	2.08E+03	2.90E+03
Domestic credit to private sector (% of GDP)	49	9.65E+01	4.34E+01	2.25E+01	5.69E+01	9.69E+01	1.39E+02	1.67E+02
Deposit interest rate (%)	49	5.70E+00	4.76E+00	0.00E+00	1.30E+00	3.29E+00	9.75E+00	1.37E+01
Inflation, GDP deflator (annual %)	49	4.48E+00	4.19E+00	-2.58E+00	1.78E+00	4.08E+00	5.75E+00	2.03E+01
Industry (including construction), value added (% of GDP)	49	3.47E+01	3.84E+00	2.58E+01	3.20E+01	3.63E+01	3.73E+01	3.99E+01
Imports of goods and services (% of GDP)	49	4.49E+01	1.54E+01	2.01E+01	2.93E+01	4.53E+01	5.70E+01	6.95E+01
International tourism, number of arrivals	49	1.05E+07	1.06E+07	4.28E+05	2.35E+06	6.95E+06	1.42E+07	3.99E+07
Manufacturing, value added (% of GDP)	49	2.58E+01	3.45E+00	1.87E+01	2.29E+01	2.68E+01	2.82E+01	3.09E+01
Exports of goods and services (% of GDP)	49	4.61E+01	1.96E+01	1.84E+01	2.41E+01	4.82E+01	6.60E+01	7.14E+01
GDP growth (annual %)	49	5.19E+00	4.09E+00	-7.63E+00	3.44E+00	5.37E+00	8.00E+00	1.33E+01
Foreign direct investment, net outflows (% of GDP)	49	8.38E-01	1.21E+00	-1.82E-02	9.37E-03	2.73E-01	1.24E+00	3.79E+00
Foreign direct investment, net inflows (% of GDP)	49	1.96E+00	1.50E+00	-9.89E-01	7.18E-01	1.79E+00	2.90E+00	6.44E+00
Trade (% of GDP)	49	9.10E+01	3.46E+01	3.87E+01	5.40E+01	9.51E+01	1.21E+02	1.40E+02

Table 2. Statistical description of the data.

	count	mean	std	min	25%	50%	75%	max
Electric power consumption (kWh per capita)	49	1.36E+03	9.24E+02	1.67E+02	4.17E+02	1.36E+03	2.08E+03	2.90E+03
Domestic credit to private sector (% of GDP)	49	9.65E+01	4.34E+01	2.25E+01	5.69E+01	9.69E+01	1.39E+02	1.67E+02
Deposit interest rate (%)	49	5.70E+00	4.76E+00	0.00E+00	1.30E+00	3.29E+00	9.75E+00	1.37E+01
Inflation, GDP deflator (annual %)	49	4.48E+00	4.19E+00	-2.58E+00	1.78E+00	4.08E+00	5.75E+00	2.03E+01
Industry (including construction), value added (% of GDP)	49	3.47E+01	3.84E+00	2.58E+01	3.20E+01	3.63E+01	3.73E+01	3.99E+01
Imports of goods and services (% of GDP)	49	4.49E+01	1.54E+01	2.01E+01	2.93E+01	4.53E+01	5.70E+01	6.95E+01
International tourism, number of arrivals	49	1.05E+07	1.06E+07	4.28E+05	2.35E+06	6.95E+06	1.42E+07	3.99E+07
Manufacturing, value added (% of GDP)	49	2.58E+01	3.45E+00	1.87E+01	2.29E+01	2.68E+01	2.82E+01	3.09E+01
Exports of goods and services (% of GDP)	49	4.61E+01	1.96E+01	1.84E+01	2.41E+01	4.82E+01	6.60E+01	7.14E+01
GDP growth (annual %)	49	5.19E+00	4.09E+00	-7.63E+00	3.44E+00	5.37E+00	8.00E+00	1.33E+01
Foreign direct investment, net outflows (% of GDP)	49	8.38E-01	1.21E+00	-1.82E-02	9.37E-03	2.73E-01	1.24E+00	3.79E+00
Foreign direct investment, net inflows (% of GDP)	49	1.96E+00	1.50E+00	-9.89E-01	7.18E-01	1.79E+00	2.90E+00	6.44E+00
Trade (% of GDP)	49	9.10E+01	3.46E+01	3.87E+01	5.40E+01	9.51E+01	1.21E+02	1.40E+02
Manufacturing, value added (% of GDP)	49	2.58E+01	3.45E+00	1.87E+01	2.29E+01	2.68E+01	2.82E+01	3.09E+01
Exports of goods and services (% of GDP)	49	4.61E+01	1.96E+01	1.84E+01	2.41E+01	4.82E+01	6.60E+01	7.14E+01
GDP growth (annual %)	49	5.19E+00	4.09E+00	-7.63E+00	3.44E+00	5.37E+00	8.00E+00	1.33E+01
Foreign direct investment, net outflows (% of GDP)	49	8.38E-01	1.21E+00	-1.82E-02	9.37E-03	2.73E-01	1.24E+00	3.79E+00
Foreign direct investment, net inflows (% of GDP)	49	1.96E+00	1.50E+00	-9.89E-01	7.18E-01	1.79E+00	2.90E+00	6.44E+00
Trade (% of GDP)	49	9.10E+01	3.46E+01	3.87E+01	5.40E+01	9.51E+01	1.21E+02	1.40E+02
Current account balance (% of GDP)	49	-2.76E-01	5.68E+00	-8.53E+00	-4.93E+00	-1.23E+00	3.47E+00	1.25E+01

Table 2. Statistical description of the data. (continue).

	count	mean	std	min	25%	50%	75%	max
Population growth (annual %)	49	1.30E+00	7.16E-01	1.75E-01	7.18E-01	1.28E+00	1.91E+00	2.71E+00
Urban population growth (annual %)	49	3.06E+00	1.16E+00	1.59E+00	2.03E+00	2.74E+00	4.15E+00	5.28E+00
Households and NPISHs Final consumption expenditure (annual % growth)	49	4.69E+00	3.85E+00	-1.02E+01	2.60E+00	5.03E+00	7.43E+00	1.29E+01
Official exchange rate (LCU per US$, period average)	49	2.96E+01	7.03E+00	2.03E+01	2.49E+01	3.05E+01	3.43E+01	4.44E+01
Unemployment, total (% of total labor force) (national estimate)	49	1.57E+00	1.17E+00	2.50E-01	7.50E-01	1.21E+00	2.21E+00	5.77E+00
Domestic credit to private sector by banks (% of GDP)	49	8.75E+01	3.59E+01	2.25E+01	5.68E+01	9.31E+01	1.12E+02	1.67E+02
Gross fixed capital formation, private sector (% of GDP)	49	2.05E+01	5.69E+00	1.13E+01	1.71E+01	1.86E+01	2.07E+01	3.44E+01
Expense (% of GDP)	49	1.56E+01	3.22E+00	1.03E+01	1.30E+01	1.55E+01	1.83E+01	2.44E+01
Final consumption expenditure (% of GDP)	49	7.00E+01	5.12E+00	6.26E+01	6.60E+01	6.89E+01	7.57E+01	8.00E+01
Gross domestic savings (% of GDP)	49	3.00E+01	5.12E+00	2.00E+01	2.43E+01	3.11E+01	3.40E+01	3.75E+01

ASEAN J. Sci. Tech. Report. **2025**, *28*(3), 257539.

9 of 27

This statistical variability is further explored in Figure 1, which depicts the distribution of each variable. The alignment of the data in Table 2 and the graphical representations in Figure 1 highlights the intrinsic disparities between the variables.
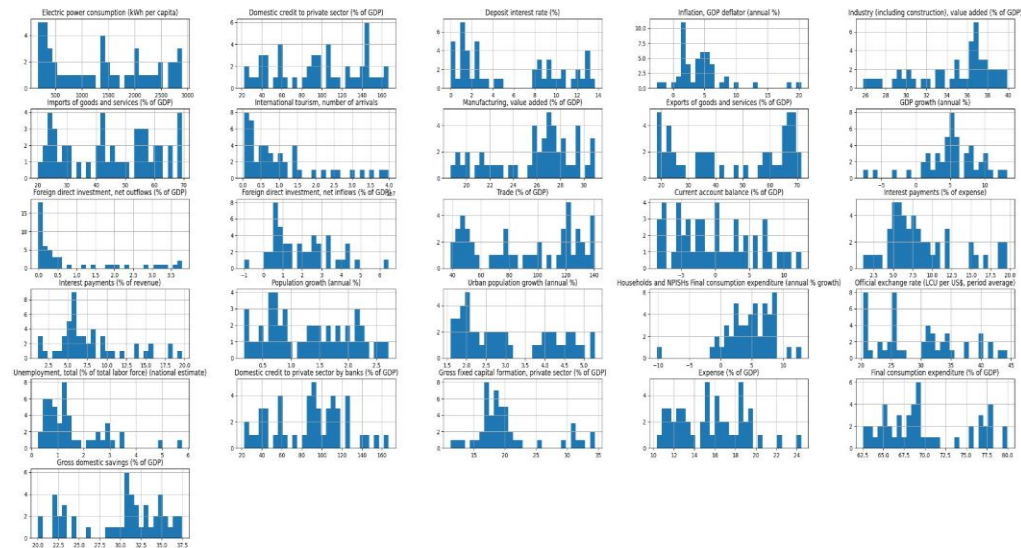

Figure 1. Frequency distribution chart of the data.

Given the diversity of the data, standardization processes were applied to ensure its accuracy. Two scaling algorithms, StandardScaler and RobustScaler, were compared to see how they handled data variability. This comparison tried to determine which technique better suited the dataset's specific characteristics. In the general structure, an economic macro variable acts as a control variable before scaling modifications are made using Normalization to reduce bias. The model is presented in equation (1) below.

$$Y = f(X1, X2, ..., X25) \tag{1}$$

Where
X1 = Domestic credit to private sector (% of GDP)
X2 = Deposit interest rate (%)
X3 = Inflation, GDP deflator (annual %)
X4 = Industry (including construction), value added (% of GDP)
X5 = Imports of goods and services (% of GDP)
X6 = International tourism, number of arrivals
X7 = Manufacturing, value added (% of GDP)
X8 = Exports of goods and services (% of GDP)
X9 = GDP growth (annual %)
X10 = Foreign direct investment, net outflows (% of GDP)
X11 = Foreign direct investment, net inflows (% of GDP)
X12 = Trade (% of GDP)
X13 = Current account balance (% of GDP)
X14 = Interest payments (% of expense)
X15 = Interest payments (% of revenue)
X16 = Population growth (annual %)

X17 = Urban population growth (annual %)

X18 = Households and NPISHs Final consumption expenditure (annual % growth)

X19 = Official exchange rate (LCU per US$, period average)

X20 = Unemployment, total (% of total labor force) (national estimate)

X21 = Domestic credit to private sector by banks (% of GDP)

X22 = Gross fixed capital formation, private sector (% of GDP)

X23 = Expense (% of GDP)

X24 = Final consumption expenditure (% of GDP)

X25 = Gross domestic savings (% of GDP)

The StandardScaler technique scales data by removing the mean and converting it to unit variance. While this strategy works well for normally distributed data, it is sensitive to outliers, as extreme values can greatly impact the mean and standard deviation. In contrast, the RobustScaler approach scales the data using the median and interquartile range (IQR), making it more resistant to outliers. Figure 2 depicts the data distribution following the use of both scaling approaches. The comparison shows that RobustScaler provides more consistent and reliable scaling, especially with outliers, which is common in macroeconomic data. Given the dataset's potential outliers from economic disruptions or rare events, RobustScaler helps prevent these from skewing the model's performance. Reducing outlier influence allows the model to focus on underlying patterns, improving prediction accuracy and generalizability. Therefore, RobustScaler was chosen for this study to ensure proper standardization and enhance analysis reliability.
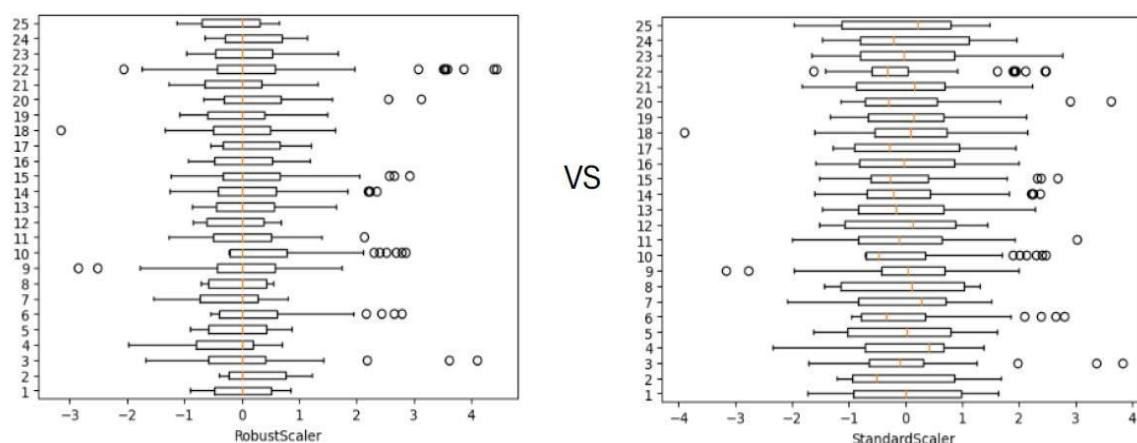

Figure 2. Comparison standardization.

A correlation analysis was conducted post-normalization to establish an understanding of how macroeconomic variables interact with electricity consumption. The correlation coefficients are summarized in Table 3, highlighting both positive and negative relationships between the variables and electricity consumption. For instance, variables like Export of Goods and industrial output showed strong positive correlations with electricity use, suggesting that economic expansion is typically accompanied by higher electricity demand. On the other hand, variables such as Deposit interest rate and inflation exhibited more complex and sometimes inverse relationships, indicating that economic instability could have varying effects on electricity usage depending on the specific context.

ASEAN J. Sci. Tech. Report. **2025**, *28*(3), 257539.

11 of 27

Table 3. Correlation between electric power consumption and macroeconomic variables.

	Electric power consumption (kWh per capita)
Exports of goods and services (% of GDP)	0.912497
Trade (% of GDP)	0.901606
Imports of goods and services (% of GDP)	0.868078
Domestic credit to private sector (% of GDP)	0.856935
International tourism, number of arrivals	0.827387
Foreign direct investment, net outflows (% of GDP)	0.812032
Manufacturing, value added (% of GDP)	0.725869
Domestic credit to private sector by banks (% of GDP)	0.708366
Expense (% of GDP)	0.680909
Official exchange rate (LCU per US$, period average)	0.678705
Industry (including construction), value added (% of GDP)	0.635421
Current account balance (% of GDP)	0.629633
Gross domestic savings (% of GDP)	0.568912
Foreign direct investment, net inflows (% of GDP)	0.380941
Gross fixed capital formation, private sector (% of GDP)	-0.227445
Unemployment, total (% of total labor force) (national estimate)	-0.364430
Households and NPISHs Final consumption expenditure (annual % growth)	-0.407281
Urban population growth (annual %)	-0.442354
GDP growth (annual %)	-0.518601
Inflation, GDP deflator (annual %)	-0.565526
Final consumption expenditure (% of GDP)	-0.568912
Deposit interest rate (%)	-0.606695
Interest payments (% of revenue)	-0.608866
Interest payments (% of expense)	-0.630804
Population growth (annual %)	-0.973860

The intensive data exploration and preprocessing methods provided a solid foundation for later model development. This study provides a credible and transparent framework for studying the determinants of power consumption in Thailand by verifying data quality, employing appropriate scaling approaches, and conducting a detailed correlation analysis. This method increases model accuracy and helps better comprehend the dynamic links between macroeconomic factors and electricity demand.

4.2 Model Performance Experiments

Before implementing and comparing the performance of different models for forecasting electricity consumption, all data underwent a standardized preprocessing procedure as described in Section 4.1. This ensured consistency and fairness across all models, allowing for reliable comparisons. Following this preprocessing stage, various models were applied, including the Multilayer Perceptron Regressor (MLP), Long Short-Term Memory Networks (LSTM), 1D Convolutional Neural Network combined with LSTM (1D CNN + LSTM), Autoregressive Integrated Moving Average (ARIMA), Decision Trees, Random Forests, and Generalized Additive Models (GAMs), to determine the most efficient approach for predicting electricity consumption.

ASEAN J. Sci. Tech. Report. **2025**, *28*(3), e257539.

12 of 27

The Grid Search technique was used to tune hyperparameters and improve model performance. This strategy searched methodically throughout a preset set of hyperparameters for each model, allowing for a thorough examination of all potential combinations. Hyperparameters such as the number of layers and neurons in neural network models, the maximum depth and number of estimators in tree-based models, and ARIMA parameters such as p, d, and q were fine-tuned to produce the optimum results.

The main advantage of Grid Search is that it performs an exhaustive search across all combinations, ensuring that no potential parameter configuration is overlooked. Unlike random search, which samples combinations randomly, Grid Search ensures that the entire search space is explored, making it more thorough in finding the best possible hyperparameters.

The evaluation of model performance was conducted using multiple metrics to capture various aspects of prediction accuracy and model behavior:

- Mean Absolute Error (MAE): A measure of the average magnitude of errors in the predictions, offering a straightforward interpretation of how much predictions deviate from actual values.
- Mean Squared Error (MSE): Emphasizes larger errors, making it sensitive to outliers. It evaluated the models' performance in scenarios where significant deviations from the actual values could occur.
- Root Mean Squared Error (RMSE): Serves as the square root of MSE and is particularly useful in understanding how model errors translate back to the original scale of electricity consumption.
- R^2 (Coefficient of Determination): Measures the proportion of variance in the dependent variable that is predictable from the independent variables, offering insights into how well each model explains the variation in electricity consumption.

The modeling process for all models involved splitting the data into training and testing sets with a 70/30 ratio to ensure consistent conditions across all models. The results after hyperparameter tuning using GridSearchCV for each model are summarized in Table 4. Following the model training and tuning through GridSearchCV, the performance of each model was measured using the previously mentioned metrics: MAE, MSE, RMSE, and R^2. The evaluation results for each model's performance are presented in Table 5.

Model performance is evaluated using MSE, MAE, RMSE, and R^2 measures. These measurements provide insights into the effectiveness of each paradigm, as seen below:

Mean Squared Error (MSE) measures the average squared differences between the predicted and actual values. It significantly emphasizes larger errors, making it helpful in identifying models sensitive to extreme deviations. A lower MSE indicates a model's ability to reduce substantial prediction errors in electricity consumption, which is critical when analyzing the impact of sudden economic shifts or outliers in electricity demand.

Mean Absolute Error (MAE) provides an average measure of absolute differences between predicted and actual values. Unlike MSE, it treats all errors equally, making it suitable for assessing models that need to minimize consistent errors across predictions. Concerning electricity use, a lower MAE suggests that the model can consistently track demand patterns, which is valuable in understanding regular economic activities and their energy implications.

Root Mean Squared Error (RMSE) is the square root of MSE, bringing the error measure back to the original scale of electricity consumption. It is beneficial for interpreting how large typical errors are in practical terms, allowing for a direct understanding of prediction accuracy in units of electricity demand. Lower RMSE values indicate models that provide accurate forecasts, which are crucial for planning and managing energy supply and are aligned with economic growth.

R-squared (R^2) indicates the proportion of variance in electricity consumption that the independent variables in the model can explain. A higher R^2 suggests that the model effectively captures the relationship between economic factors and electricity use, demonstrating how well macroeconomic variables like GDP growth, inflation, and industrial output contribute to changes in electricity demand.

Table 4. The result of each model using hyperparameter tuning.

	Model					
MLPRegresspr	**LSTM**	**1D CNN+LSTM**	**RANDOM_FORESTS**	**DECISION_TREES**	**ARIMA**	**GAMs**
Activation = relu	activation = tanh	hidden_units = 150	bootstrap = FALSE	depth = 5	p = 5	intercept = TRUE
Alpha = 0.01	dropout_rate = 0.3	learning_rate = 0.1	depth = 10	gestures = log2	q = 3	lam = 0.3
Hidden_layer_sizes = (100, 50)	hidden_units = 150	activation = relu	features = sqrt	samples_leaf = 2	d = 2	max_iter = 50
Learning_rate = constant	learing_rate = 0.01	filters = 32	samples_leaf = 1	samples_split = 5	trend = n	n_splines = 4
Learning_rate_init = 0.01	optmizer = adam	epochs = 150	samples_split = 2			spline_order = 3
Max_iter = 50		optimizer = SGD	extimators = 200			
Solver = adam						

ASEAN J. Sci. Tech. Report. **2025**, *28*(3), e257539.

14 of 27

By understanding these metrics, we can better interpret model performance in terms of its ability to predict electricity consumption accurately, which has direct implications for economic planning and policy development.

Table 5. Comparison of model performance metrics.

Model	MAE	MSE	RMSE	R-squared
MLPRegressor	0.09	0.01	0.12	0.95
LSTM	01.15	0.04	0.2	0.88
1D CNN+LSTM	0.14	0.03	0.17	0.91
RANDOM_FORESTS	0.25	0.09	0.3	0.7
DECISION_TREES	0.09	0.02	0.13	0.93
ARIMA	0.06	0.02	0.15	0.93
GAMs	0.13	0.03	0.18	0.89

Table 5 demonstrates that MLP and ARIMA outperformed the other models examined. MLP had the lowest errors (MSE: 0.01, RMSE: 0.12) and the best R^2 (0.95), suggesting its ability to capture complex patterns in the data. ARIMA fared well with a low MAE (0.06) and high R^2 (0.93), indicating its capacity to handle temporal patterns in electricity usage. Overall, MLP outperformed the other two models. It beat ARIMA with lower MSE and RMSE and a better R^2, indicating superior accuracy in modeling both linear and nonlinear interactions. MLP's advantage lies in its ability to handle complex, multi-dimensional patterns in the data, making it more adaptable to diverse factors affecting electricity consumption. While strong in modeling temporal trends, ARIMA is more limited in capturing nonlinear interactions, which may explain its slightly lower performance than MLP. On the other hand, Random Forests and LSTM exhibited the weakest performance. Random Forests had the highest errors (MAE: 0.25, MSE: 0.09) and the lowest R^2 (0.7), suggesting difficulty modeling the data's non-linearity. LSTM also struggled, with relatively high errors (MAE: 0.15, RMSE: 0.2) and a lower R^2 (0.88), indicating its limitations in this context. These findings highlight the benefits of utilizing MLP, especially when capturing complicated, nonlinear correlations in data, which is critical for effective forecasting. The complete comparison in Table 4 provides a clear standard for assessing the efficacy of various models in projecting power usage.

4.3 Feature Importance and Explainability

As shown in Table 5, the MLP model demonstrates strong predictive performance in forecasting electricity consumption, having been trained with the same variable set and consistent train-test split throughout the experiment. Following this evaluation, SHAP and LIME were applied to interpret the model's predictions and identify the macroeconomic variables with the most significant influence. While both SHAP and LIME offer local explanations by estimating feature contributions at the individual observation level, they rely on fundamentally different algorithms. To compare their effectiveness, an unsupervised clustering approach was employed using dissimilarity matrices derived from LIME weights and SHAP values, with standardized Euclidean distance as the metric. This method enabled the evaluation of which technique better captures local feature importance and provides clearer insights into variable contributions to electricity consumption.
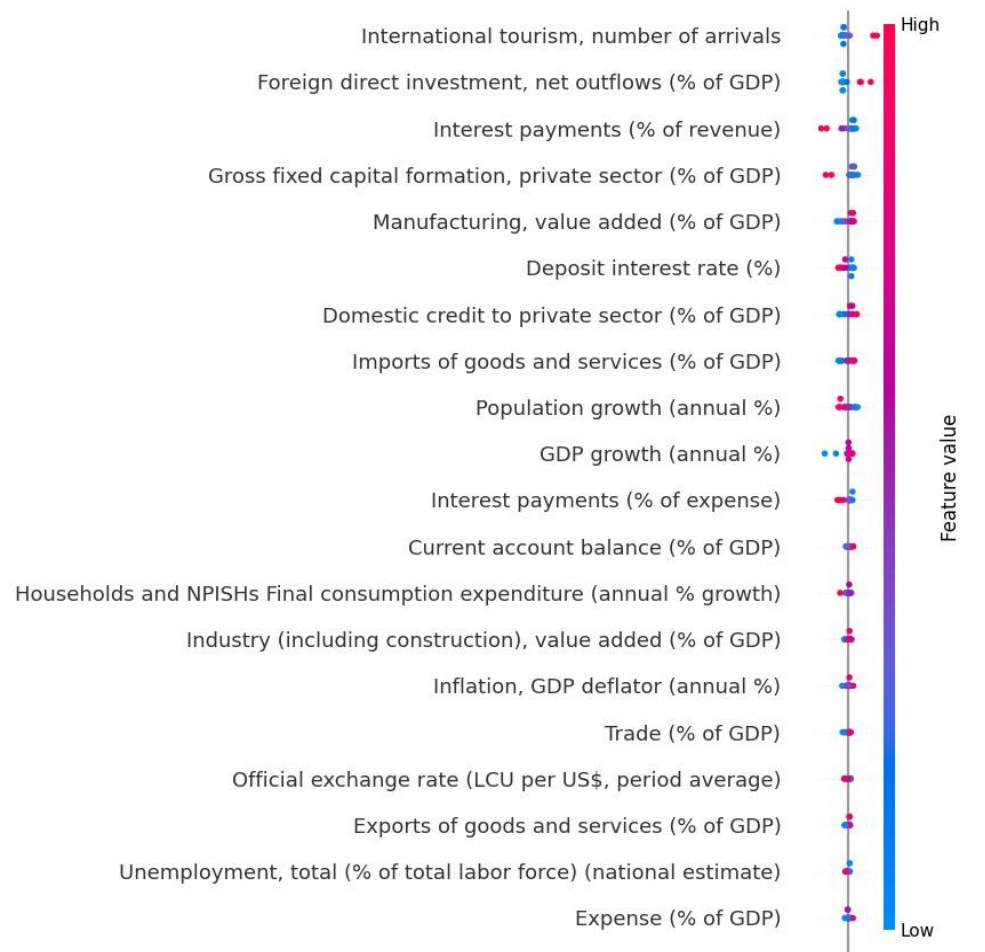
ASEAN J. Sci. Tech. Report. **2025**, 28(3), 257539.

15 of 27

Figure 3. SHAP summary plot for feature importance and impact on model predictions.

Figure 3 shows the SHAP analysis results, identifying key macroeconomic factors influencing electricity consumption. International tourism and manufacturing value-added consistently show strong positive SHAP values, indicating that growth in these sectors is linked to higher energy demand. In contrast, rising interest payments (% of revenue) are associated with negative SHAP values, suggesting that increased debt servicing may suppress electricity use due to reduced fiscal flexibility or investment capacity. As shown in Figure 4, these relationships remain consistent across individual cases, offering clearer insights into how specific variables drive or inhibit consumption. While foreign direct investment (FDI) and private sector capital formation contribute positively, their impact is generally weaker. These patterns highlight the dual role of macroeconomic variables, some acting as key drivers and others as constraints that provide helpful guidance for effective energy planning and policy design.

ASEAN J. Sci. Tech. Report. **2025**, *28*(3), e257539.

16 of 27
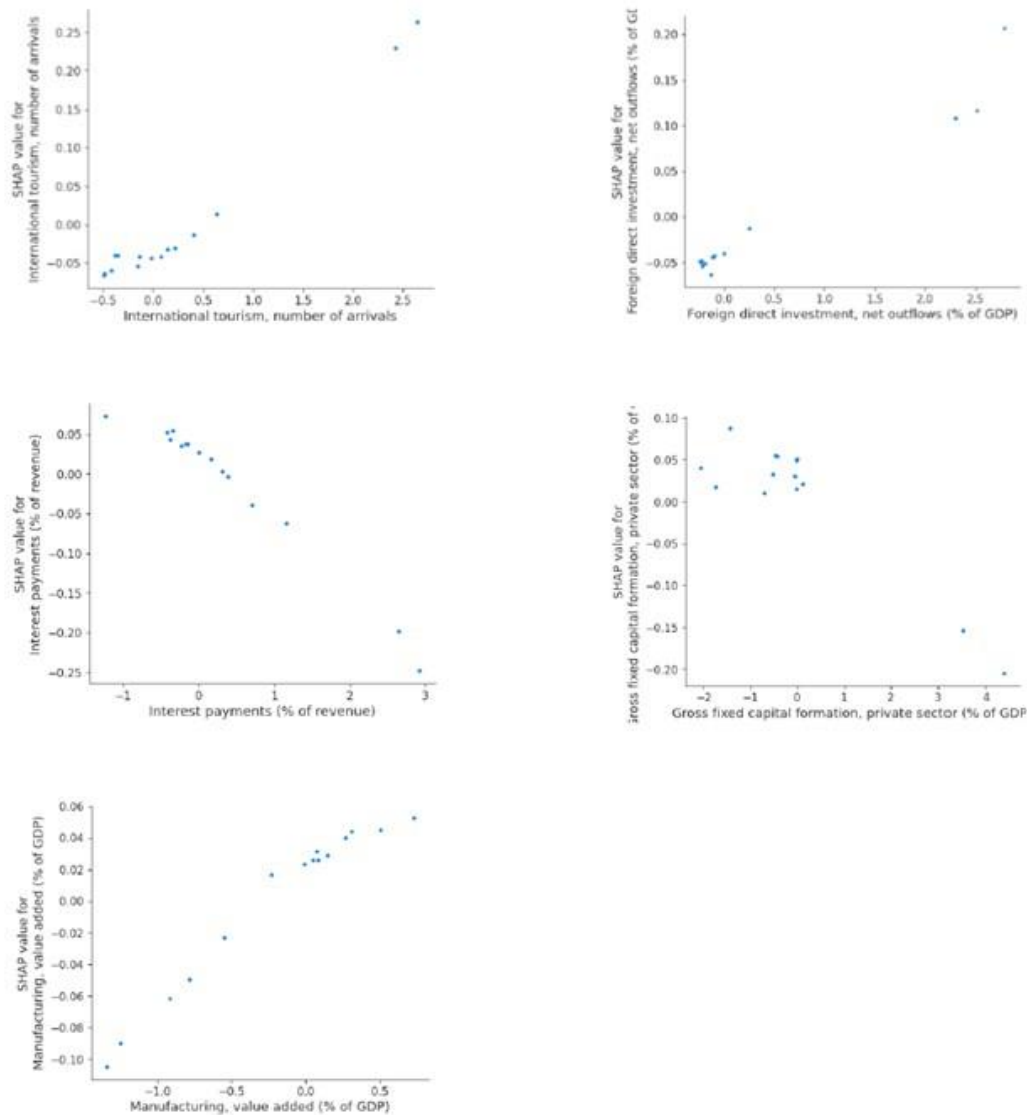
Figure 4. Top 5 SHAP for feature impact.

Locally Interpretable Model Agnostic Explanations (LIME) is a post hoc model agnostic explanation technique aiming to approximate any black box machine learning model with a local, interpretable model to explain each prediction. LIME works locally, which means it is observation-specific and provides explanations for the prediction relative to each observation, just like SHAP. It fits a local model using sample data points similar to the observation being explained, with the local model chosen from interpretable models such as linear models or decision trees. This analysis applied LIME to the MLP to understand how individual macroeconomic variables impact electricity consumption predictions at the observation level. The results of the LIME analysis are illustrated in Figure 5, which showcases the top macroeconomic factors influencing specific predictions.

ASEAN J. Sci. Tech. Report. **2025**, 28(3), 257539.

17 of 27
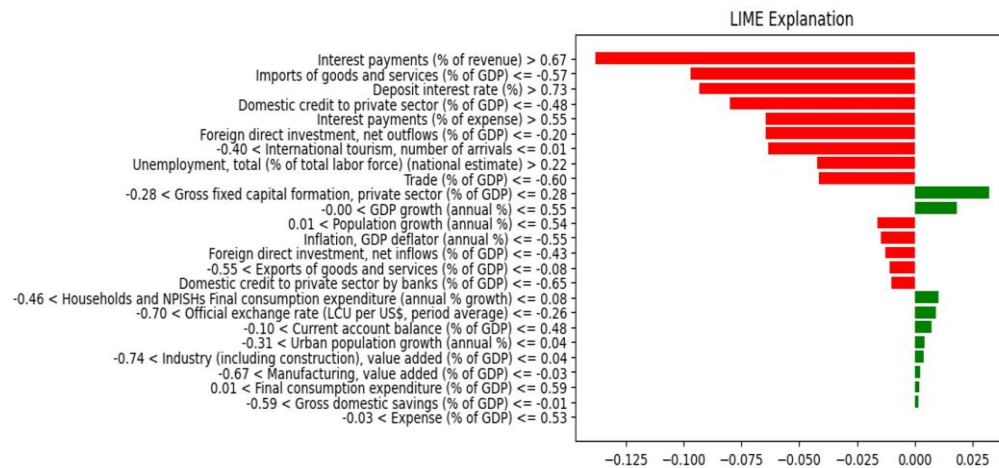
Figure 5. LIME explanation.

As shown in Figure 5, interest payments (% of revenue) have the most significant negative impact on electricity consumption, as indicated by the largest red SHAP bar, suggesting that higher financial burdens may reduce energy demand by limiting economic activity. Other variables, such as Imports of goods and services (% of GDP), Deposit interest rate (%), and Domestic credit to the private sector (% of GDP), also show negative contributions, indicating their tendency to suppress consumption in certain contexts. In contrast, Gross fixed capital formation in the private sector (% of GDP) positively influences electricity usage, reflecting increased energy needs linked to investment-driven growth. To further evaluate the interpretability of the MLP model, SHAP and LIME were compared to assess their effectiveness in explaining feature contributions. Although both methods offer local interpretability, their differing algorithms lead to unique insights. The comparison involved clustering analysis, visual inspection, and AUC-based performance evaluation. Standardized Euclidean distance was used to construct dissimilarity matrices based on SHAP values and LIME weights, followed by assessing clustering quality using Silhouette scores and the Davies-Bouldin Index (DBI) where higher Silhouette values indicate clearer cluster separation, and lower DBI suggests better internal cohesion. This analysis reveals the strengths and limitations of each method in interpreting electricity consumption forecasts under different economic scenarios.

Table 6. Clustering evaluation results.

Method	LIME	SHAP
K-means Silhouette	0.377905	0.436423
Spectral Clustering Silhouette	0.362149	0.436423
K-means DBI	1.062711	0.804729
Spectral Clustering DBI	1.008351	0.804729

Table 6 shows that SHAP outperformed LIME in terms of clustering performance. In the K-means clustering study, SHAP had a better Silhouette score (0.436423) than LIME (0.377905), indicating a clearer separation of groups. Similarly, SHAP had a lower Davies-Bouldin Index (0.804729) than LIME (1.062711), indicating that clusters were more compact. The spectral clustering analysis yielded consistent findings, with SHAP again outperforming LIME, with a higher Silhouette score (0.436423 vs. 0.362149) and a lower DBI (0.804729 vs. 1.008351). These findings indicate that SHAP is more effective at capturing the structural patterns of feature contributions, resulting in more distinct and coherent grouping.

Further, to evaluate the clustering performance of SHAP and LIME, spectral clustering was employed to visualize how each method distinguishes observations based on feature importance. This analysis aimed to assess the ability of both techniques to form distinct groups, thereby capturing different patterns of feature

contributions. The results are presented in Figure 6, with Panel A illustrating the clustering outcomes from LIME, while Panel B shows the clusters formed by SHAP.
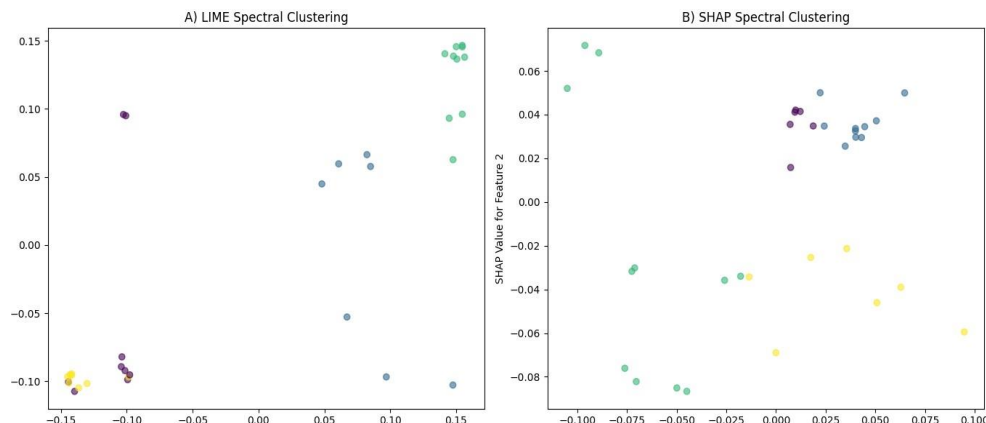

Figure 6. (A) LIME spectral clustering; (B) SHAP spectral clustering.

Figure 6 reveals key differences between the two methods. In panel A, LIME's clustering shows overlap, indicating difficulty in clearly defining boundaries based on feature importance, which may hinder local feature interpretation. In contrast, panel B shows SHAP's clusters with clearer boundaries and minimal overlap, offering a more accurate depiction of macroeconomic variable impacts on electricity consumption. SHAP better distinguishes feature influences, allowing for clearer identification of individual variable contributions to energy demand changes. Following this, ROC curves were generated to assess the predictive power of SHAP and LIME parameters.
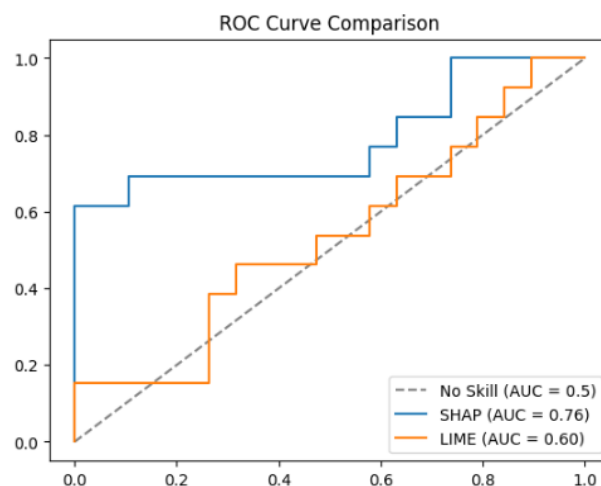
Figure 7. LIME and SHAP ROC curves.

Figure 7 shows that SHAP achieved a higher AUC (0.76) than LIME (0.60), indicating greater precision in capturing feature contributions for predicting electricity consumption. The lower AUC of LIME reflects its weaker discriminative capability. These results confirm SHAP's superiority in model interpretation.

The analysis of feature importance in predicting electricity consumption demonstrates that combining predictive accuracy with interpretability is feasible and advantageous for informed decision-making. By employing a highly accurate predictive model alongside explainability tools such as SHAP and LIME, this study reveals the value of eXplainable AI (XAI) in enhancing model performance and transparency. The results from the clustering analysis, visualization of feature importance, and overall clustering performance indicate that SHAP consistently outperforms LIME in providing clearer and more reliable feature information.

These findings affirm that SHAP is more adept at capturing the underlying structure of feature contributions, making it a more effective tool for model interpretation.

4.5 Long-term and Short-term Prediction Scenarios

Short- and long-term analyses are essential to understand the performance of the MLP in predicting electricity consumption over different time horizons. This analysis helps determine whether the model can accurately capture short-term fluctuations and predict longer-term trends. Comparing these predictions is crucial for effective energy planning and management, as economic changes have immediate and prolonged impacts. The use of interpretability tools such as SHAP and LIME in this analysis enhances our understanding of the economic factors that drive electricity consumption. SHAP provides global interpretations that cover all variables, while LIME offers localized explanations for individual predictions, making it helpful in analyzing the impact of variables over different time frames.
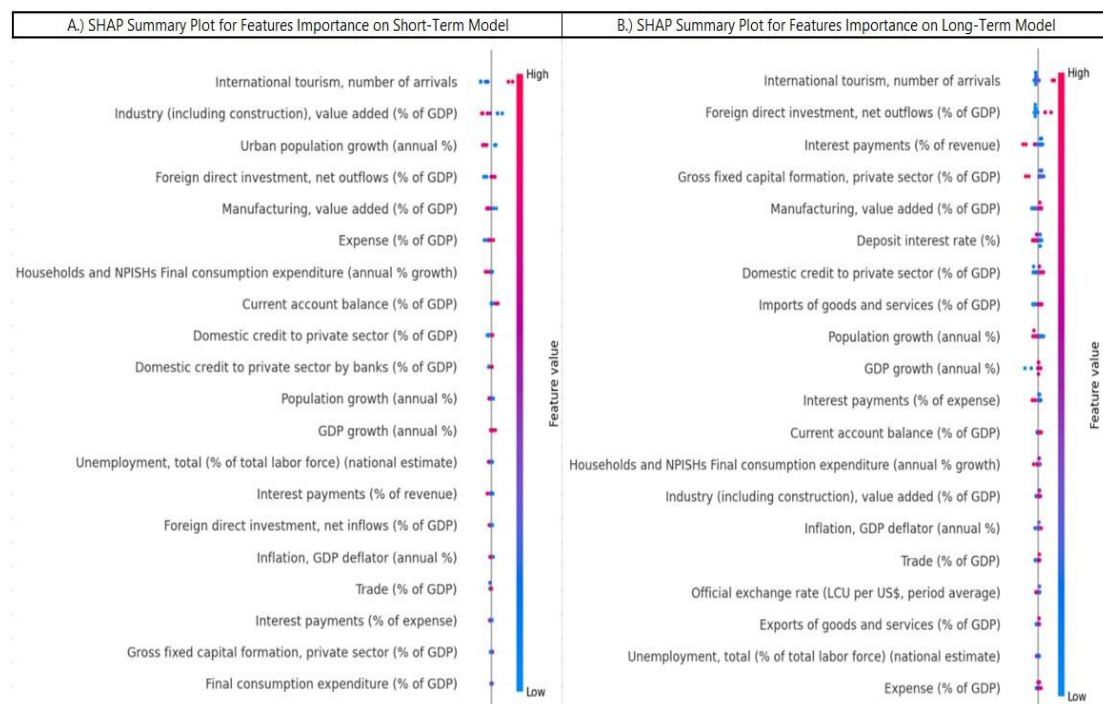
Figure 8. Comparison of the SHAP summary plot between short and long-term models.

The use of SHAP allows each model to analyze and present the influence of various variables on electricity consumption. As shown in Figure 8, the SHAP Summary Plot illustrates the importance of different features in predicting electricity consumption, separated into short-term (Panel A) and long-term (Panel B) prediction models. The results indicate that the most significant feature in both time frames is International tourism, the number of arrivals, which strongly influences electricity consumption. Additionally, in Manufacturing, value added also plays an important role, but the results differ between short-term and long-term models regarding the direction and magnitude of the influence.
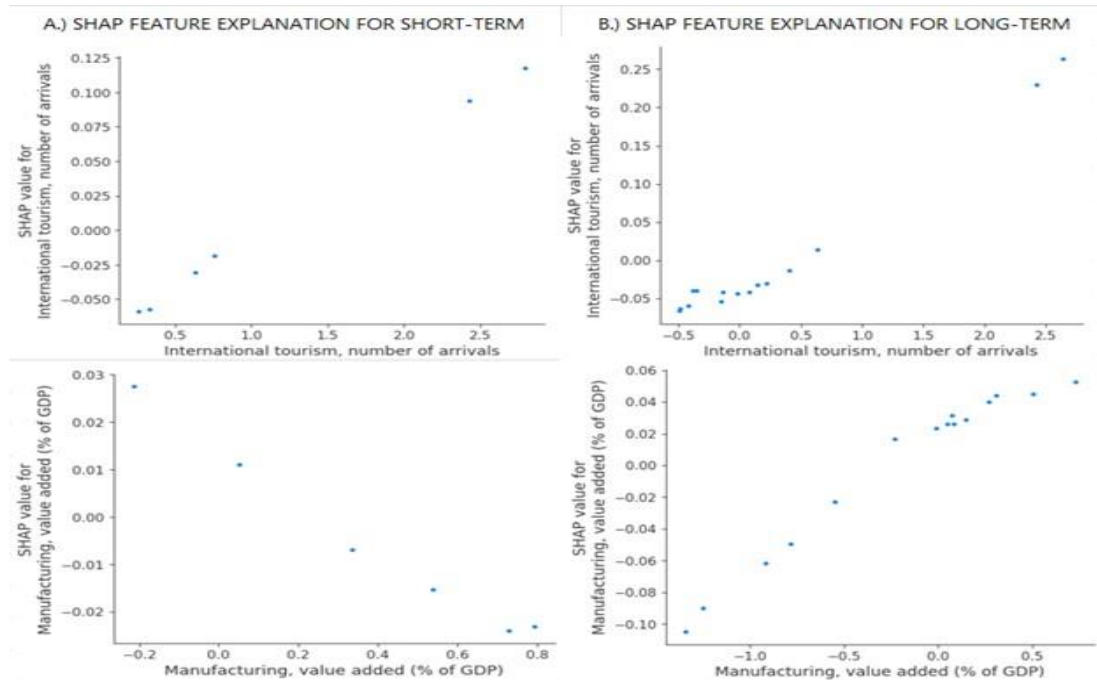
ASEAN J. Sci. Tech. Report. **2025**, *28*(3), e257539.

20 of 27

Figure 9. SHAP features explanations for short-term and long-term.

Figure 9 shows a clearer picture of how SHAP values relate to two key variables—International tourism and Manufacturing, value added—in both short-term and long-term electricity consumption predictions. For International tourism (Panels A and B), the pattern is consistent across both models: SHAP values increase as the number of tourists rises, showing a strong positive link with electricity use. However, the pattern for Manufacturing value-added changes depending on the time frame. In the short term, SHAP values decrease as manufacturing increases, suggesting that improved efficiency or temporary production adjustments might lower electricity use. In the long term, SHAP values increase with more manufacturing activity, indicating higher electricity demand as the industry grows.

SHAP helps explain which variables impact electricity consumption most, giving a broad, long-term perspective. However, a local explanation method is needed to understand how variables affect each individual prediction. That's where LIME comes in. As shown in Figure 10, LIME explains the influence of variables for each case, helping uncover how different factors affect electricity use across various periods.
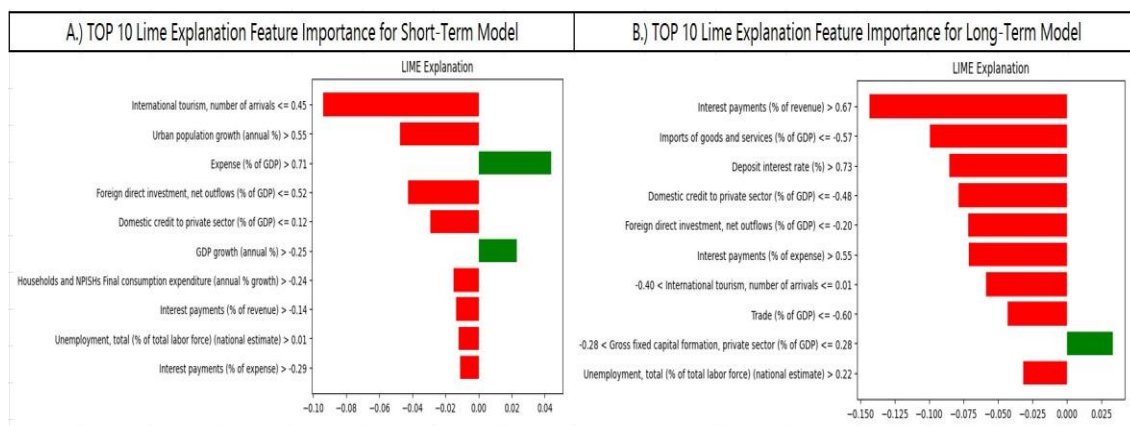
Figure 10. Top 10 LIME explanations feature importance for short-term and long-term models.

Figure 10 presents the results of the LIME analysis, comparing short-term and long-term electricity consumption predictions. This analysis highlights how the importance of variables changes over time. In the short term, international tourism has a negative impact—when tourist numbers fall below 0.5 million, electricity use drops, reflecting lower demand. Similarly, Urban population growth and Expenses (% of GDP) also have negative effects, possibly due to decreased urban energy use and short-term reductions in government spending. In contrast, the long-term analysis shows that Interest payments (% of revenue) have a strong negative influence, suggesting that rising debt payments can suppress electricity consumption over time. Other variables, like Imports of goods and services, Deposit interest rate, and Domestic credit to the private sector, also show negative effects, pointing to ongoing structural influences. Meanwhile, Trade (% of GDP) has a slight positive impact, indicating a potential rise in energy demand as trade grows. Comparing SHAP and LIME highlights their complementary roles. SHAP captures overall trends and the global influence of variables, while LIME focuses on local, case-specific explanations. LIME is beneficial for identifying short-term effects, such as the immediate impact of tourism and debt, whereas SHAP is better for understanding broader, long-term patterns. Using both methods together provides a fuller understanding of electricity consumption and supports more effective energy planning.

4.6 Comparative Study

To understand the relationship between economic determinants and electricity consumption across varying economic contexts, this study conducts a comparative analysis by grouping countries into three GDP-based categories: similar GDP (e.g., Singapore, Israel, Malaysia), higher GDP (e.g., United States, United Kingdom, Japan), and lower GDP (e.g., Iceland, Senegal, Togo). This classification enables an exploration of how economic development levels influence electricity usage and key contributing factors within each group. Using an MLP model and interpretable AI techniques—specifically SHAP and LIME—the analysis examines feature influence across different GDP levels to identify context-specific drivers of electricity consumption. All data are sourced from the World Development Indicators (WDI) to maintain consistency and comparability, following the same methodological framework used in the Thailand case study to minimize bias. The experimental process aims to determine whether GDP levels affect the significance of macroeconomic variables and how those relationships vary across countries. SHAP analysis results, illustrated in Figure 11, highlight the top five most influential economic indicators in each country, while LIME provides deeper insights into localized effects. Together, these tools offer valuable perspectives for enhancing forecasting accuracy and informing strategic energy planning tailored to diverse economic settings.
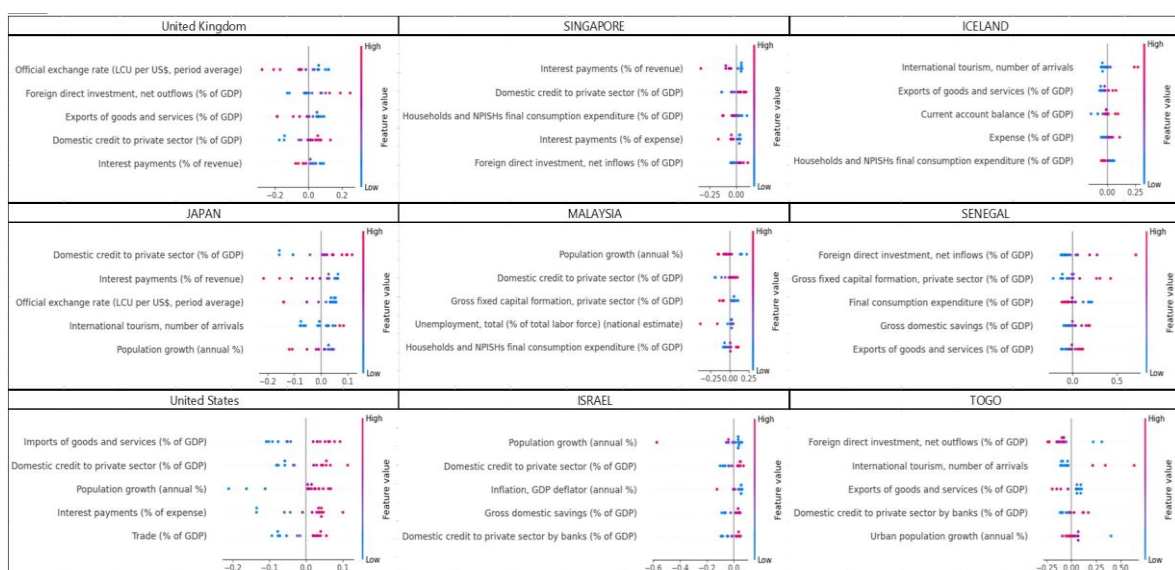

Figure 11. SHAP summary plot of feature importance for electricity consumption with different GDP levels.

ASEAN J. Sci. Tech. Report. **2025**, *28*(3), e257539.

22 of 27

The SHAP summary plot analysis comparing the influence of economic variables on electricity consumption across countries with varying GDP levels reveals distinct patterns. In high-GDP nations (e.g., the United States, United Kingdom, Japan), electricity consumption is strongly influenced by Domestic credit to the private sector and the Official exchange rate, reflecting economies driven by trade and investment. In countries with moderate GDP levels similar to Thailand (e.g., Singapore, Israel, Malaysia), Domestic credit to the private sector remains a key factor, alongside Foreign direct investment and Interest payments, which show patterns consistent with Thailand's economic context. For low-GDP countries (e.g., Iceland, Senegal, Togo), electricity usage is primarily shaped by external drivers such as Foreign direct investment and International tourism. These findings highlight how GDP level corresponds to differing economic structures and variable significance in energy demand. Building on this global SHAP analysis, we proceed to a local interpretation using LIME (see Figure 12), which offers case-specific insights into how individual variables impact electricity consumption within each country. This helps clarify which factors hold localized importance and illustrates how economic disparities influence variable behavior in electricity forecasting.
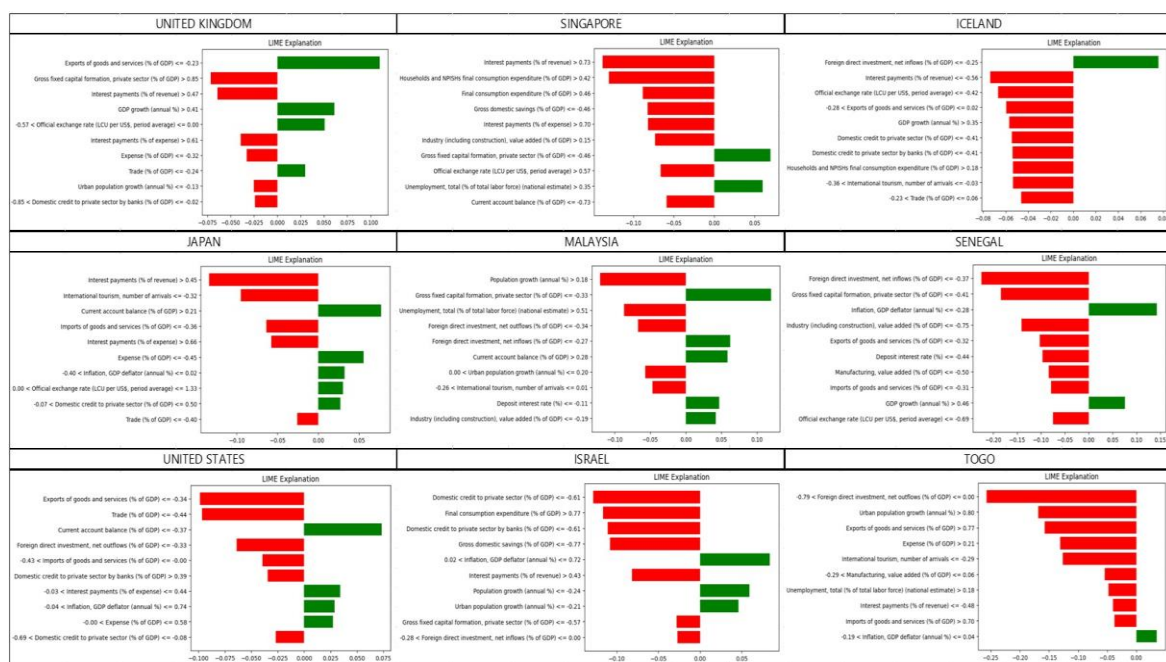

Figure 12. LIME summary plot of feature importance for electricity consumption with different GDP levels.

The LIME analysis by GDP level reveals distinct economic drivers of electricity consumption. In high-GDP countries (e.g., the UK, Japan, and the US), key factors include trade and investment, such as exports, imports, and capital formation. In mid-GDP countries (e.g., Singapore, Malaysia, Israel), population growth and domestic consumption, like household spending and FDI, are more influential. Low-GDP countries (e.g., Iceland, Senegal, Togo) rely on external factors like FDI and tourism. These findings highlight how GDP levels shape the economic variables impacting electricity consumption. SHAP and LIME analysis reveals how economic variables influence electricity consumption across GDP levels. SHAP provides a global view, showing that high-GDP countries are driven by trade and investment factors, while LIME highlights country-specific effects. Population growth and household spending are key in mid-GDP nations, whereas low-GDP countries rely on external factors like FDI and tourism. Combining SHAP and LIME offers a comprehensive understanding of economic influences on electricity consumption at both global and local scales.

ASEAN J. Sci. Tech. Report. **2025**, *28*(3), 257539.

23 of 27

4.7 Discussion

This study introduces a robust and interpretable machine learning model for forecasting electricity consumption; however, a key limitation lies in the exclusion of environmental factors such as temperature and humidity, which significantly influence energy demand—particularly in regions with extreme climates. Without these variables, the model may offer an incomplete representation of electricity usage. Future research should address this gap by incorporating environmental data and testing the model across various regions, climates, and economic contexts to enhance both accuracy and adaptability. Additionally, while the selected macroeconomic indicators and modeling techniques are appropriate, they may not fully capture the complexity of electricity consumption. Exploring alternative or ensemble methods, alongside integrating local economic factors, environmental variables, and stakeholder input, could improve predictive performance and increase the model's practical relevance in real-world energy planning.

5. Conclusion

In conclusion, this study demonstrates the effectiveness of using interpretable machine learning specifically a multilayer perceptron (MLP) integrated with SHAP and LIME to accurately forecast short- and long-term electricity consumption in Thailand while enhancing transparency into how macroeconomic variables influence energy demand. This interpretable approach offers a practical alternative to traditional black-box models, allowing stakeholders to better understand the role of economic drivers such as tourism, industrial growth, and interest rates. These insights can inform targeted policy decisions, including adjusting national energy budgets, prioritizing infrastructure in tourism-driven areas, and coordinating energy and monetary policies to manage demand more effectively. The findings show that MLP outperforms ARIMA and Random Forest models, while SHAP and LIME highlight how factors like tourism and industrial activity increase consumption, whereas interest rates and private sector investment tend to reduce it. These results support more adaptive, region-specific strategies for sustainable energy planning. However, limitations remain, such as the exclusion of geographic and environmental data—e.g., population distribution, temperature, and seasonality which future research should integrate to enhance accuracy. Incorporating regional-level data and advanced models like Transformers or other time-series techniques may also improve long-term forecasting by capturing complex, multidimensional relationships. Further, evaluating model robustness under economic uncertainty and adopting more advanced interpretability methods (e.g., integrated gradients or DeepLIFT) could deepen understanding of variable impacts and strengthen decision-making. Overall, this study advances interpretable electricity forecasting in Thailand by connecting economic indicators with energy use and lays a foundation for future improvements that support resilient, sustainable policy planning.

6. Acknowledgments

References

[1] Qureshi, M.; Arbab, M. A.; Rehman, S. ur. Deep Learning-Based Forecasting of Electricity Consumption. *Sci Rep.* **2024**, *14*(1). https://doi.org/10.1038/s41598-024-56602-4.

[2] Chung, J.; Jang, B. Accurate Prediction of Electricity Consumption Using a Hybrid CNN-LSTM Model Based on Multivariable Data. *PLoS ONE* **2022**, *17*(11), e0278071. https://doi.org/10.1371/journal.pone.0278071.

ASEAN J. Sci. Tech. Report. **2025**, *28*(3), e257539.

24 of 27

[3] Wang, T.; Zhao, Q.; Gao, W.; He, X. Research on Energy Consumption in Household Sector: A Comprehensive Review Based on Bibliometric Analysis. *Front. Energy Res*. **2024**, *11*. https://doi.org/10.3389/fenrg.2023.1209290.

[4] Altın, H. The Impact of Energy Efficiency and Renewable Energy Consumption on Carbon Emissions in G7 Countries. *International Journal of Sustainable Engineering* **2024**, *17*(1), 134-142. https://doi.org/10.1080/19397038.2024.2319648.

[5] Ferrer, A. L. C.; Thomé, A. M. T.; Scavarda, A. J. Sustainable Urban Infrastructure: A Review. Resources, Conservation and Recycling 2018, 128, 360–372. https://doi.org/10.1016/j.resconrec.2016.07.017.

[6] Angel, S. Urban Expansion: Theory, Evidence and Practice. *Buildings and Cities* **2023**, *4*(1), 124-138. https://doi.org/10.5334/bc.348.

[7] Tang, X.; Dai, Y.; Wang, T.; Chen, Y. Short-term Power Load Forecasting Based on Multi-layer Bidirectional Recurrent Neural Network. *IET Generation Trans &amp; Dist* **2019**, *13*(17), 3847-3854. https://doi.org/10.1049/iet-gtd.2018.6687.

[8] Axay J Mehta; Mehta, H. A.; T.C.Manjunath; Ardil, C. A Multi-Layer Artificial Neural Network Architecture Design For Load Forecasting In Power Systems. Zenodo **2008**. https://doi.org/10.5281/ZENODO.1059528.

[9] Jiang, P.; Li, R.; Liu, N.; Gao, Y. A Novel Composite Electricity Demand Forecasting Framework by Data Processing and Optimized Support Vector Machine. *Applied Energy* **2020**, *260*, 114243. https://doi.org/10.1016/j.apenergy.2019.114243.

[10] Goswami, K.; Kandali, A. B. Electricity Demand Prediction Using Data Driven Forecasting Scheme: Performance ARIMA and SARIMA for Real-Time Load Data of Assam. **2020** International Conference on Computational Evaluation (ComPE), **2020**, 570-574. https://doi.org/10.1109/compe49325.2020.9200031.

[11] Tarmanini, C.; Sarma, N.; Gezegin, C.; Ozgonenel, O. Short Term Load Forecasting Based on ARIMA and ANN Approaches. *Energy Reports* **2023**, *9*, 550–557. https://doi.org/10.1016/j.egyr.2023.01.060.

[12] Nie, P.; Roccotelli, M.; Fanti, M. P.; Ming, Z.; Li, Z. Prediction of Home Energy Consumption Based on Gradient Boosting Regression Tree. *Energy Reports* **2021**, 7, 1246-1255. https://doi.org/10.1016/j.egyr.2021.02.006.

[13] Abbasimehr, H.; Shabani, M.; Yousefi, M. An Optimized Model Using LSTM Network for Demand Forecasting. Computers & Industrial Engineering 2020, 143, 106435. https://doi.org/10.1016/j.cie.2020.106435.

[14] Islam, B. ul; Ahmed, S. F. Short-Term Electrical Load Demand Forecasting Based on LSTM and RNN Deep Neural Networks. *Mathematical Problems in Engineering*, **2022**, 1-10. https://doi.org/10.1155/2022/2316474.

[15] Fan, G.-F.; Wei, X.; Li, Y.-T.; Hong, W.-C. Forecasting Electricity Consumption Using a Novel Hybrid Model. *Sustainable Cities and Society* **2020**, *61*, 102320. https://doi.org/10.1016/j.scs.2020.102320.

[16] Bessec, M.; Fouquau, J. The Non-Linear Link between Electricity Consumption and Temperature in Europe: A Threshold Panel Approach. *Energy Economics* **2008**, *30*(5), 2705-2721. https://doi.org/10.1016/j.eneco.2008.02.003.

[17] Ma, S.; Li, S.; Luo, Q.; Yu, Z.; Wang, Y. Revisiting the Relationships between Energy Consumption, Economic Development and Urban Size: A Global Perspective Using Remote Sensing Data. *Heliyon* **2024**, *10*(5), e27318. https://doi.org/10.1016/j.heliyon.2024.e27318.

[18] Ahmed, M.; Huan, W.; Ali, N.; Shafi, A.; Ehsan, M.; Abdelrahman, K.; Khan, A. A.; Abbasi, S. S.; Fnais, M. S. The Effect of Energy Consumption, Income, and Population Growth on CO_2 Emissions: Evidence from NARDL and Machine Learning Models. *Sustainability* **2023**, *15*(15), 11956. https://doi.org/10.3390/su151511956.

[19] Narayan, P. K.; Smyth, R. Electricity Consumption, Employment and Real Income in Australia Evidence from Multivariate Granger Causality Tests. *Energy Policy* **2005**, *33* (9), 1109–1116. https://doi.org/10.1016/j.enpol.2003.11.010.

[20] Lu, F.; Ma, F.; Hu, S. Does Energy Consumption Play a Key Role? Re-Evaluating the Energy Consumption-Economic Growth Nexus from GDP Growth Rates Forecasting. *Energy Economics* **2024**, *129*, 107268. https://doi.org/10.1016/j.eneco.2023.107268.

[21]   Dokas, I.; Oikonomou, G.; Panagiotidis, M.; Spyromitros, E. Macroeconomic and Uncertainty Shocks' Effects on Energy Prices: A Comprehensive Literature Review. *Energies* **2023**, *16*(3), 1491. https://doi.org /10.3390/en16031491.

[22]   Gilpin, L. H.; Bau, D.; Yuan, B. Z.; Bajwa, A.; Specter, M.; Kagal, L. Explaining Explanations: An Overview of Interpretability of Machine Learning. 2018 IEEE 5th International Conference on Data Science and Advanced Analytics (DSAA), **2018**, 80-89. https://doi.org/10.1109/dsaa.2018.00018.

[23]   Brusa, E.; Cibrario, L.; Delprete, C.; Di Maggio, L. G. Explainable AI for Machine Fault Diagnosis: Understanding Features' Contribution in Machine Learning Models for Industrial Condition Monitoring. *Applied Sciences* **2023**, *13*(4), 2038. https://doi.org/10.3390/app13042038.

[24]   Bozorgpanah, A.; Torra, V. Explainable Machine Learning Models with Privacy. *Prog Artif Intell* **2024**, *13*(1), 31–50. https://doi.org/10.1007/s13748-024-00315-2.

[25]   Vishwarupe, V.; Joshi, P. M.; Mathias, N.; Maheshwari, S.; Mhaisalkar, S.; Pawar, V. Explainable AI and Interpretable Machine Learning: A Case Study in Perspective. *Procedia Computer Science* **2022**, *204*, 869-876. https://doi.org/10.1016/j.procs.2022.08.105.

[26]   Gramegna, A.; Giudici, P. SHAP and LIME: An Evaluation of Discriminative Power in Credit Risk. *Front. Artif. Intell.* **2021**, *4*. https://doi.org/10.3389/frai.2021.752558.

[27]   Ahmed, S.; Kaiser, M. S.; Shahadat Hossain, M.; Andersson, K. A Comparative Analysis of LIME and SHAP Interpreters With Explainable ML-Based Diabetes Predictions. *IEEE Access* **2025**, *13*, 37370-37388. https://doi.org/10.1109/access.2024.3422319.

[28]   Huang, A. A.; Huang, S. Y. Increasing Transparency in Machine Learning through Bootstrap Simulation and Shapely Additive Explanations. *PLoS ONE* **2023**, *18*(2), e0281922. https://doi.org/10.1371/journal.pone.0281922.

[29]   Zhang, H.; Chen, B.; Li, Y.; Geng, J.; Li, C.; Zhao, W.; Yan, H. Research on Medium- and Long-Term Electricity Demand Forecasting under Climate Change. *Energy Reports* **2022**, *8*, 1585-1600. https://doi.org/10.1016/j.egyr.2022.02.210.

[30]   Mir, A. A.; Alghassab, M.; Ullah, K.; Khan, Z. A.; Lu, Y.; Imran, M. A Review of Electricity Demand Forecasting in Low and Middle Income Countries: The Demand Determinants and Horizons. *Sustainability* **2020**, *12*(15), 5931. https://doi.org/10.3390/su12155931.

[31]   Gonçalves, A. C. R.; Costoya, X.; Nieto, R.; Liberato, M. L. R. Extreme Weather Events on Energy Systems: A Comprehensive Review on Impacts, Mitigation, and Adaptation Measures. *Sustainable Energy res.* **2024**, *11*(1). https://doi.org/10.1186/s40807-023-00097-6.

[32]   Russo, M. A.; Carvalho, D.; Martins, N.; Monteiro, A. Forecasting the Inevitable: A Review on the Impacts of Climate Change on Renewable Energy Resources. *Sustainable Energy Technologies and Assessments* **2022**, *52*, 102283. https://doi.org/10.1016/j.seta.2022.102283.

[33]   Benti, N. E.; Chaka, M. D.; Semie, A. G. Forecasting Renewable Energy Generation with Machine Learning and Deep Learning: Current Advances and Future Prospects. *Sustainability* **2023**, *15*(9), 7087. https://doi.org/10.3390/su15097087.

[34]   Ahmad, T.; Zhang, H.; Yan, B. A Review on Renewable Energy and Electricity Requirement Forecasting Models for Smart Grid and Buildings. *Sustainable Cities and Society* **2020**, *55*, 102052. https://doi.org/ 10.1016/j.scs.2020.102052.

[35]   Phuangpornpitak, N.; Prommee, W. A study of load demand forecasting models in electric power system operation and planning. *GMSARN Int. J.* **2016**, *10*, 19-24. (In Thai)

[36]   Gebre, M. T.; Hwang, J.; Biru, G. Electricity Demand Analysis and Forecasting: The Case of GADA Special Economic Zone. *Heliyon* **2024**, *10*(3), e25364. https://doi.org/10.1016/j.heliyon.2024.e25364.

[37]   Fan, J.-L.; Hu, J.-W.; Zhang, X. Impacts of Climate Change on Electricity Demand in China: An Empirical Estimation Based on Panel Data. *Energy* **2019**, *170*, 880-888. https://doi.org/10.1016/j.energy.2018.12.044.

[38]   De Felice, M.; Alessandri, A.; Ruti, P. M. Electricity Demand Forecasting over Italy: Potential Benefits Using Numerical Weather Prediction Models. *Electric Power Systems Research* **2013**, *104*, 71-79. https://doi.org/10.1016/j.epsr.2013.06.004.

[39]   Abokyi, E.; Appiah-Konadu, P.; Sikayena, I.; Oteng-Abayie, E. F. Consumption of Electricity and Industrial Growth in the Case of Ghana. *Journal of Energy* **2018**, 1-11. https://doi.org/10.1155/2018/8924835.

ASEAN J. Sci. Tech. Report. **2025**, *28*(3), e257539.

26 of 27

[40] Madlener, R.; Sunak, Y. Impacts of Urbanization on Urban Structures and Energy Demand: What Can We Learn for Urban Energy Planning and Urbanization Management?. *Sustainable Cities and Society* **2011**, *1*(1), 45-53. https://doi.org/10.1016/j.scs.2010.08.006.

[41] Salat, H.; Smoreda, Z.; Schläpfer, M. A Method to Estimate Population Densities and Electricity Consumption from Mobile Phone Data in Developing Countries. *PLoS ONE* **2020**, *15*(6), e0235224. https://doi.org/10.1371/journal.pone.0235224.

[42] Arens, M.; Worrell, E. Diffusion of Energy Efficient Technologies in the German Steel Industry and Their Impact on Energy Consumption. *Energy* **2014**, *73*, 968-977. https://doi.org/10.1016/j.energy.2014.06.112.

[43] Herring, H.; Roy, R. Technological Innovation, Energy Efficient Design and the Rebound Effect. *Technovation* **2007**, *27*(4), 194-203. https://doi.org/10.1016/j.technovation.2006.11.004.

[44] Kwon, S.; Cho, S.-H.; Roberts, R. K.; Kim, H. J.; Park, K.; Edward Yu, T. Effects of Electricity-Price Policy on Electricity Demand and Manufacturing Output. *Energy* **2016**, *102*, 324-334. https://doi.org/10.1016/j.energy.2016.02.027.

[45] Otsuka, A. Industrial Electricity Consumption Efficiency and Energy Policy in Japan. *Utilities Policy* **2023**, *81*, 101519. https://doi.org/10.1016/j.jup.2023.101519.

[46] Zhou, K.; Yang, S. Understanding Household Energy Consumption Behavior: The Contribution of Energy Big Data Analytics. *Renewable and Sustainable Energy Reviews* **2016**, *56*, 810-819. https://doi.org/10.1016/j.rser.2015.12.001.

[47] Dong, X.-Y.; Hao, Y. Would Income Inequality Affect Electricity Consumption? Evidence from China. *Energy* **2018**, *142*, 215-227. https://doi.org/10.1016/j.energy.2017.10.027.

[48] Kapustin, N. O.; Grushevenko, D. A. Long-Term Electric Vehicles Outlook and Their Potential Impact on Electric Grid. *Energy Policy* **2020**, *137*, 111103. https://doi.org/10.1016/j.enpol.2019.111103.

[49] Meliani, M.; Barkany, A. E.; Abbassi, I. E.; Darcherif, A. M.; Mahmoudi, M. Energy Management in the Smart Grid: State-of-the-Art and Future Trends. *International Journal of Engineering Business Management* **2021**, *13*. https://doi.org/10.1177/18479790211032920.

[50] Wang, J. Q.; Du, Y.; Wang, J. LSTM Based Long-Term Energy Consumption Prediction with Periodicity. *Energy* **2020**, *197*, 117197. https://doi.org/10.1016/j.energy.2020.117197.

[51] Shaikh, A. K.; Nazir, A.; Khan, I.; Shah, A. S. Short Term Energy Consumption Forecasting Using Neural Basis Expansion Analysis for Interpretable Time Series. *Sci Rep.* **2022**, *12*(1). https://doi.org/10.1038/s41598-022-26499-y.

[52] Aisyah, S.; Simaremare, A. A.; Adytia, D.; Aditya, I. A.; Alamsyah, A. Exploratory Weather Data Analysis for Electricity Load Forecasting Using SVM and GRNN, Case Study in Bali, Indonesia. *Energies* **2022**, *15*(10), 3566. https://doi.org/10.3390/en15103566.

[53] Pelka, P. Pattern-Based Forecasting of Monthly Electricity Demand Using Support Vector Machine. 2021 International Joint Conference on Neural Networks (IJCNN), **2021**, 1-8. https://doi.org/10.1109/ijcnn52387.2021.9534134.

[54] Zhang, G.; Guo, J. A Novel Ensemble Method for Residential Electricity Demand Forecasting Based on a Novel Sample Simulation Strategy. *Energy* **2020**, *207*, 118265. https://doi.org/10.1016/j.energy.2020.118265.

[55] Iftikhar, H.; Zywiołek, J.; López-Gonzales, J. L.; Albalawi, O. Electricity Consumption Forecasting Using a Novel Homogeneous and Heterogeneous Ensemble Learning. Front. *Energy Res.* **2024**, *12*. https://doi.org/10.3389/fenrg.2024.1442502.

[56] Ghareeb, A.; Al-bayaty, H.; Haseeb, Q.; Zeinalabideen, M. Ensemble Learning Models for Short-Term Electricity Demand Forecasting. 2020 International Conference on Data Analytics for Business and Industry: Way Towards a Sustainable Economy (ICDABI), **2020**, 1–5. https://doi.org/10.1109/icdabi51230.2020.9325623.

[57] Cawthorne, D.; de Queiroz, A. R.; Eshraghi, H.; Sankarasubramanian, A.; DeCarolis, J. F. The Role of Temperature Variability on Seasonal Electricity Demand in the Southern US. *Front. Sustain. Cities* **2021**, *3*. https://doi.org/10.3389/frsc.2021.644789.

ASEAN J. Sci. Tech. Report. **2025**, *28*(3), 257539.

27 of 27

[58] Ha, J.; Tan, P.-P.; Goh, K.-L. Linear and Nonlinear Causal Relationship between Energy Consumption and Economic Growth in China: New Evidence Based on Wavelet Analysis. *PLoS ONE* **2018**, *13*(5), e0197785. https://doi.org/10.1371/journal.pone.0197785.

[59] Kim, Y.-J.; Lee, S.-J.; Jin, H.-S.; Suh, I.-A.; Song, S.-Y. Comparison of Linear and Nonlinear Statistical Models for Analyzing Determinants of Residential Energy Consumption. Energy and Buildings **2020**, *223*, 110226. https://doi.org/10.1016/j.enbuild.2020.110226.

[60] Chen, G.; Hu, Q.; Wang, J.; Wang, X.; Zhu, Y. Machine-Learning-Based Electric Power Forecasting. Sustainability **2023**, *15*(14), 11299. https://doi.org/10.3390/su151411299.

[61] Surya, B.; Menne, F.; Sabhan, H.; Suriani, S.; Abubakar, H.; Idris, M. Economic Growth, Increasing Productivity of SMEs, and Open Innovation. Journal of Open Innovation: Technology, Market, and Complexity **2021**, *7*(1), 20. https://doi.org/10.3390/joitmc7010020.

[62] Bettarelli, L.; Estefania-Flores, J.; Furceri, D.; Loungani, P.; Pizzuto, P. Energy Inflation and Consumption Inequality. Energy Economics **2023**, *124*, 106823. https://doi.org/10.1016/j.eneco.2023.106823.

[63] Barbierato, E.; Gatti, A. The Challenges of Machine Learning: A Critical Review. Electronics **2024**, *13*(2), 416. https://doi.org/10.3390/electronics13020416.

[64] Freiesleben, T.; König, G.; Molnar, C.; Tejero-Cantero, A. Scientific Inference With Interpretable Machine Learning: Analyzing Models to Learn About Real-World Phenomena. arXiv **2022**. https://doi.org/10.48550/ARXIV.2206.05487.

[65] Linardatos, P.; Papastefanopoulos, V.; Kotsiantis, S. Explainable AI: A Review of Machine Learning Interpretability Methods. Entropy **2020**, *23*(1), 18. https://doi.org/10.3390/e23010018.

Article type

Type of the Paper (Article, Review, Communication, etc.) *about 8,000 words maximum*

Title (Palatino Linotype 18 pt, bold)

Firstname Lastname¹, Firstname Lastname² and Firstname Lastname²*

1   Affiliation 1; e-mail@e-mail.com
2   Affiliation 2; e-mail@e-mail.com
*   Correspondence: e-mail@e-mail.com; (one corresponding authors, add author initials)

Abstract: A single paragraph of about 400 words maximum. Self-contained and concisely describe the reason for the work, methodology, results, and conclusions. Uncommon abbreviations should be spelled out at first use. We strongly encourage authors to use the following style of structured abstracts, but without headings: (1) Background: Place the question addressed in a broad context and highlight the purpose of the study; (2) Methods: briefly describe the main methods or treatments applied; (3) Results: summarize the article's main findings; (4) Conclusions: indicate the main conclusions or interpretations.

Keywords: keyword 1; keyword 2; keyword 3 (List three to ten pertinent keywords specific to the article yet reasonably common within the subject discipline.)

1. Introduction

The introduction should briefly place the study in a broad context and highlight why it is crucial. It should define the purpose of the work and its significance. The current state of the research field should be carefully reviewed and critical publications cited. Please highlight controversial and diverging hypotheses when necessary. Finally, briefly mention the main aim of the work. References should be numbered in order of appearance and indicated by a numeral or numerals in square brackets—e.g., [1] or [2, 3], or [4-6]. See the end of the document for further details on references.

2. Materials and Methods

The materials and methods should be described with sufficient details to allow others to replicate and build on the published results. Please note that your manuscript's publication implicates that you must make all materials, data, computer code, and protocols associated with the publication available to readers. Please disclose at the submission stage any restrictions on the availability of materials or information. New methods and protocols should be described in detail, while well-established methods can be briefly described and appropriately cited.

Interventional studies involving animals or humans, and other studies that require ethical approval, must list the authority that provided approval and the corresponding ethical approval code.

3. Results and Discussion

This section may be divided by subheadings. It should provide a concise and precise description of the experimental results, their interpretation, as well as the experimental conclusions that can be drawn.Authors should discuss the results and how they can be interpreted from previous studies and the working hypotheses. The findings and their implications should be discussed in the broadest context possible. Future research directions may also be highlighted.

3.1. Subsection

3.1.1. Subsubsection

3.2. Figures, Tables, and Schemes

All figures and tables should be cited in the main text as Figure 1, Table 1, etc.

Figure 1. This is a figure. Schemes follow the same formatting.

Table 1. This is a table. Tables should be placed in the main text near the first time they are cited.

Title 1	Title 2	Title 3
entry 1	data	data
entry 2	data	data [1]

[1] Table may have a footer.

3.3. Formatting of Mathematical Components

This is example 1 of an equation:

$$a = 1,\tag{1}$$

The text following an equation need not be a new paragraph. Please punctuate equations as regular text. This is example 2 of an equation:

$$a = b + c + d + e + f + g + h + i + j + k + l + m + n + o + p + q + r + s + t + u\tag{2}$$

The text following an equation need not be a new paragraph. Please punctuate equations as regular text. The text continues here.

4. Conclusions

Concisely restate the hypothesis and most important findings. Summarize the significant findings, contributions to existing knowledge, and limitations. What are the future directions? Conclusions MUST be well stated, linked to original research question & limited to supporting results.

5. Acknowledgements

Should not be used to acknowledge funders – funding will be entered as a separate. As a matter of courtesy, we suggest you inform anyone whom you acknowledge.

References

References must be numbered in order of appearance in the text (including citations in tables and legends) and listed individually at the end of the manuscript. We recommend preparing the references with a bibliography software package, such as EndNote, ReferenceManager to avoid typing mistakes and duplicated references. Include the digital object identifier (DOI) for all references where available.

Citations and references in the Supplementary Materials are permitted provided that they also appear in the reference list here.

In the text, reference numbers should be placed in square brackets [ ] and placed before the punctuation; for example [1], [1–3] or [1, 3]. For embedded citations in the text with pagination, use both parentheses and brackets to indicate the reference number and page numbers; for example [5] (p. 100), or [6] (pp. 101–105).

Using the American Chemical Society (ACS) referencing style

[1] Author 1, A.B.; Author 2, C.D. Title of the article. *Abbreviated Journal Name* Year, *Volume*, page range.

[2] Author 1, A.; Author 2, B. Title of the chapter. In *Book Title*, 2nd ed.; Editor 1, A., Editor 2, B., Eds.; Publisher: Publisher Location, Country. **2007**, Volume *3*, pp. 154–196.

[3] Author 1, A.; Author 2, B. *Book Title*, 3rd ed.; Publisher: Publisher Location, Country, **2008**, pp. 154–196.

[4] Author 1, A.B.; Author 2, C. Title of Unpublished Work. *Abbreviated Journal Name* stage of publication (under review; accepted; in press).

[5] Author 1, A.B. (University, City, State, Country); Author 2, C. (Institute, City, State, Country). Personal communication, 2012.

[6] Author 1, A.B.; Author 2, C.D.; Author 3, E.F. Title of Presentation. In Title of the Collected Work (if available), Proceedings of the Name of the Conference, Location of Conference, Country, Date of Conference; Editor 1, Editor 2, Eds. (if available); Publisher: City, Country, Year (if available); Abstract Number (optional), Pagination (optional).

[7] Author 1, A.B. Title of Thesis. Level of Thesis, Degree-Granting University, Location of University, Date of Completion.

[8] Title of Site. Available online: URL (accessed on Day Month Year).

Reviewers sugestion

1. Name, Address, e-mail
2. Name, Address, e-mail
3. Name, Address, e-mail
4. Name, Address, e-mail

URL link:

Notes for Authors >>
https://drive.google.com/file/d/1r0zegnIVeQqe4iLQyT1xDEIinNggINPD/view?usp=sharing
https://drive.google.com/file/d/1r0zegnIVeQqe4iLQyT1xDEIinNggINPD/view?usp=sharing

Online Submissions >> https://ph02.tci-thaijo.org/index.php/tsujournal/user/register

Current Issue >> https://ph02.tci-thaijo.org/index.php/tsujournal/issue/view/16516

AJSTR Publication Ethics and Malpractice >> https://ph02.tci-thaijo.org/index.php/tsujournal/ethics

Journal Title Abbreviations >> http://library.caltech.edu/reference/abbreviations

ASEAN
Journal of Scientific and Technological Reports
Online ISSN:2773-8752